Magnetooptical Spectroscopy of Matrix-Isolated Free Radicals

A thesis

submitted in partial fulfilment

of the requirements for the Degree

of

Doctor of Philosophy in Chemistry

in the

University of Canterbury

by

Vaughan S. Langford

University of Canterbury

1997

TABLE OF CONTENTS

Continued...

Continued...

Continued...

Continued...

Continued...

Continued...

TABLE OF FIGURES

Continued...

Figure **Page**

Continued...

Figure **Page**

TABLE OF TABLES

Continued...

GLOSSARY OF ACRONYMS

A/D	analogue-to-digital
ADC	analogue-to-digital converter
CF	crystal field
CMOS	coated metal oxide semi-conductor
D/A	digital-to-analogue
DAC	digital-to-analogue converter
D/I	digital input
D/O	digital output
FWHM	full width, half maximum
$HW^{1}/_{e}M$	half width, $^{1}/_{e}$ maximum
HV	high voltage
IR	infrared
IC	integrated circuit
JT	Jahn-Teller
LIA	lock-in amplifier
LIF	laser induced fluorescence
(M)CD	(magnetic) circular dichroism
MI	matrix isolation
MOD1	simultaneous MCD/double-beam absorption spectrometer, extensively modified from a Jasco ORD/UV-5 ORD spectrometer at the University of Virginia
MOD2	high-resolution simultaneous MCD/double-beam absorption spectrometer purpose built at the University of Virginia
MOD3	simultaneous MCD/double-beam absorption spectrometer, extensively modified from a Jasco ORD/UV-5 ORD spectrometer at the University of Canterbury
MOD4	high-resolution simultaneous MCD/double-beam absorption spectrometer purpose built at the University of Canterbury as part of this research
MOD4DIAG	diagnostics software for MOD4
$Nd(ODA)_3$	$Na_3[Nd(ODA)_3].2NaClO_4.6H_2O$; a crystal with natural CD used primarily as a CD calibrant
NIR	near infrared
OD	optical density
PEM	photoelastic modulator
PMT	photomultiplier (tube)

Continued...

SATSCAN2	data-acquisition software for magnetic-field MCD saturation at a fixed wavelength
SO	spin-orbit
SOC	spin-orbit coupling
SPEC2	data-acquisition software for (M)CD and double-beam absorption, single-beam (M)CD and emission
TTL	transistor-transistor logic
UV	ultra-violet
ZFS	zero-field splitting

ACKNOWLEDGEMENTS

To my supervisor, Dr Bryce Williamson, for his tremendous advice, support, and encouragement throughout this work. The breadth and depth of his knowledge pertaining to experimental, instrumental and theoretical aspects is outstanding.

It has been a pleasure to have worked with fellow Ph.D. students Cara Dunford and Barry Prince during this research, and to have had useful discussions with them.

Helpful advice from Professor Leon Phillips, and Drs Rod Claridge and Peter Harland has been appreciated.

I am grateful to the Department's technical staff who have helped make this project a success. In particular, special mention must be made of Mr Russell Gillard and Mr Geoff Speer in the mechanical workshop, and Mr Steven Graham in the electronics workshop.

Financial support from the University of Canterbury, in the form of a Doctoral Scholarship, is gratefully acknowledged.

To Naomi Gee, and her family, whose prayers and encouragement over the past couple of months have been much appreciated!

To my family, Dad, Mum, Brent, Maree and Christie, who share very much in this project. They have helped me carry the load through the many frustrations of the first two years, particularly. Their constant love, prayers and encouragement mean a great deal much to me!

Finally, and most importantly, to my Creator, Lord and Saviour Jesus Christ. I thank Him for His all-surpassing love, and for granting me the opportunity to 'search out' this very small portion of His creation. *John 1:1-4, 14; Psalm 33:9.* He is *always* faithful.

ABSTRACT

This Ph.D. thesis presents the results of magnetooptical spectroscopic investigations of free radicals isolated in Ar matrices at cryogenic temperatures (≲20 K).

The experiments required development of a high-resolution simultaneous magnetic circular dichroism (MCD) and absorption spectrometer, MOD4. Design, construction and commission of MOD4 comprised a significant portion of this project, and its description constitutes a substantial part of the 'Experimental' chapter of the thesis.

The results of matrix-isolation experiments on the first-row radical monohydrides, CH, NH (and ND) and OH (and OD), and the theoretical analyses of the data comprise the main body of this thesis, and are presented in three chapters. Temperature and magnetic-field dependencies of the MCD and absorption over the ranges $T \approx 1.4 - 17$ K and $B = 0$ to ~4.5 T, are interpreted in terms of a spin-orbit (SO) – crystal-field (CF) model. The data are analysed by the application of quantum-mechanical and group-theoretical techniques, utilising moment analysis and (in the case of NH) spectral simulation. These allow SO and CF parameters to be extracted. Assignments of structure observed in the spectra have also been attempted.

Radical monoanions and monocations of buckminsterfullerene (C_{60}) have been investigated in Ar matrices using MCD and absorption spectroscopy, over the ranges $T \approx 1.6 - 30$ K and $B = 0 - 4$ T. Preliminary conclusions have been drawn from these data, concerning the symmetry of the molecules, but more experimental and theoretical work needs to be done.

Ferricenium, the radical cation of ferrocene, has been isolated in Ar (with a SF_6^- counter-ion) for the first time. Preliminary MCD and absorption data are presented, and show well-resolved vibronic structure; assignments to totally symmetric and Jahn-Teller-active vibrational overtones are made.

1. INTRODUCTION

Historical background

Magnetooptical spectroscopy has its origins in the pioneering work of Michael Faraday in the 1840s.[1] He observed that when polarised light passed through a borosilicate plate in a magnetic field "there was an effect produced"; specifically, he found that the plane of polarisation was rotated by the magnetic field. This phenomenon is now known as the Faraday effect.

About fifty years later a Dutch physicist, Pieter Zeeman, sought to determine whether the wavelength of light is also changed by a magnetic field.[2] To do this, he placed a sodium lamp between the poles of an electromagnet and monitored the '*D* lines' with a spectroscope. At his second attempt,[3] he observed a broadening of the lines, amounting to about one fortieth of their separation. Endeavouring to explain this phenomenon, he sought the advice of the Dutch theoretical physicist, Hendrick A. Lorentz. Lorentz (who favoured a particle model for light) supplied a theory that assumes the light is emitted from small charged particles revolving in orbits within the atom.[2] Since charged particles (electrons) travelling perpendicular to the direction of a magnetic field are deflected by the field (due to an effect that is now called the Lorentz force), a slight contraction or expansion of the orbit can be predicted depending on the direction of the orbital motion. The result is a shift in the wavelength of the radiation, which, at the limited resolution available to Zeeman, was observed as a broadening of the emission bands. (It is worthy of note that this theory of orbiting particles within the atom appeared in 1897, well before Rutherford's model of the atom, and just before J.J. Thompson had 'discovered' the electron.) From the field-induced line broadening, Zeeman and Lorentz determined the charge-to-mass ratio of these charged particles to be of the order of 1.6×10^{11} C/kg — the currently accepted value is 1.759×10^{11} C/kg for an electron. (In fact increased field strengths and spectroscopes of higher resolving power allowed some of the most accurate measurements of e/m in later years.)

Shortly thereafter, Sir Oliver Lodge and Zeeman almost simultaneously found that by using stronger magnetic fields, and spectroscopes of sufficiently high resolution, the sodium '*D* lines' actually split into a doublet and quartet. This new result could not

be explained by Lorentz's classical theory. It was not until about 30 years later, after the development of quantum mechanics and when a theory of electron spin was formulated, that an adequate explanation of this 'anomalous' Zeeman effect was furnished.

Zeeman made spectral observations both perpendicular and parallel to the magnetic field.[2] In the latter case, he found that the light was circularly polarised. As will be elaborated later in this section, this result is crucial to the work presented in this thesis since magnetic circular dichroism (MCD) relies on the fact that left and right circularly polarised light (lcp and rcp, respectively) are absorbed differently by a substance in a magnetic field.

The Zeeman effect has since found many applications in chemistry and physics, of which the spectroscopic techniques of nuclear magnetic resonance (NMR) and electron paramagnetic resonance (EPR) are perhaps the most widely employed. Analytical chemists have also used the Zeeman effect in atomic absorption spectroscopy (AAS) to reduce interference effects due to molecular absorbers. However, until the second half of this century the Zeeman effect had found only very limited application to molecular optical spectroscopy. This was primarily due to the broad absorption bands that are prevalent in molecular spectra, and to a lack of theoretical formalism to explain the phenomenon. The Faraday effect, in the form of magnetic optical rotatory dispersion (MORD), was employed by chemists to some extent, but was not well understood. (Victor Shashoua's description of the general characteristics of the spectra in 1964 provided a step forward.[4]) For example, in early 1965, Foss and McCarville[5] wrote that, "*the most useful application of MCD spectra (and MORD curves) will probably be to a classification of spectral transitions.... At present, there do not seem to be any simple relationships between the symmetry of a molecule and the presence or absence of MCD in a particular band such as exists for naturally optically active molecules.... To the best of the authors' knowledge, all known substances exhibit a Faraday effect....*" Shashoa himself wrote later that year that, "*No evidence could be obtained for relationships between the shape or the magnitude of the observed magnetic rotations and the ground-state para- or diamagnetism of the* [free-base and metallo-phthalocyanines] *molecules. Some evidence was obtained for a relation between the shape of the* [MORD] *and the polarisations of transitions in the absorption spectra.*"

It is ironic, in hindsight, that P.J. Stephens' doctoral dissertation at Oxford University, entitled "*Theoretical Studies of Magneto-Optical Phenomena*",[6] was

accepted a short time before both the Foss and McCarville[5] and Shashoua[7] articles were published. Stephens' work, which was later published in a review co-authored by A.D. Buckingham,[8] proved a turning point in the understanding of the Faraday effect, providing for the first time a sound theoretical basis for the understanding of MORD and MCD for molecular systems. (It is not the intention here to provide a review of the theory of magnetooptical phenomena; the reader is referred to a brief introduction to MCD in Section 1.3.2, and a more detailed discussion in Section 3.4.3. For full derivations, the excellent monograph by Susan Piepho and Paul Schatz[9] is recommended, which uses up-to-date conventions and powerful group-theoretical methods.) In systems with either orbital or spin degeneracy, the application of Stephens' formalism allowed the resolution of problems of band assignments for which absorption spectroscopy alone had failed. An early and classic example is the unambiguous assignment of the UV-visible $^2T_{2u} \leftarrow {}^2T_{2g}$ and $^2T_{1u} \leftarrow {}^2T_{2g}$ charge-transfer transitions of potassium ferricyanide ($K_3[Fe(CN)_6]$) by Stephens[10] and Schatz *et al.*[11]

MCD was also noted[12] to have a significant experimental advantage over MORD, because it occurs only in regions of absorption. MORD has limited usefulness as a diagnostic technique since it occurs in all regions of the spectrum — contributions from optical components, solvents and even air can be observed, posing the problem of extricating the contribution due to the species under investigation. However, at that time the benefits of MCD were not easily exploited, due to instrumental limitations.[5] MCD commonly suffered from reduced signal-to-noise (S/N) relative to MORD for the same compound.[5] The lower S/N ratio correspondingly decreased the effective sensitivity of the technique, which was otherwise theoretically determined to be comparable to MORD. Two factors were to prove crucial in facilitating measurement of MCD: development of the superconducting electromagnet and the photoelastic modulator (PEM).

Paul Schatz and coworkers at the University of Virginia (UVa) were the first to use superconducting magnets in MCD experiments,[11] finding them preferable for two main reasons. First, their high magnetic fields (relative to conventional electromagnets) increased the S/N level of the MCD. Second, their compact size allowed their incorporation into the sample compartment of commercial CD spectrometers.[12]

The PEM, which employs the photoelastic effect (Section 2.2.5.2), was invented in 1969 by Jasperson and Schnatterly,[13] primarily for their work in high-reflectivity

ellipsometry. Some time later, in 1974, the benefits of the PEM to CD and MCD were recognised by Collingwood *et al.*,[14] who employed one in their simultaneous (M)CD and double-beam absorption spectrometer. Compared to other circular-polarisation modulators (such as Pockels cells), the PEM had several advantages due to its wide spectral range, high-frequency modulation, and ease of use. Coupled with a phase-sensitive detector, such as a lock-in amplifier (Sections 1.3.3 and 2.3.8), the S/N ratio of MCD was significantly bettered, while much increasing its sensitivity. MCD became the Faraday-effect technique of choice, and today is totally dominant in the literature.

Analysis and interpretation of MCD data are facilitated when the researcher also has the corresponding absorption spectrum for the sample. However for many years these spectra had to be obtained either on independent absorption spectrometers, or on dual-purpose spectrometers with different optical paths, as noted by Collingwood *et al.*[14] In the former, problems occurred due to differing wavelength calibrations and spectral bandwidths between spectrometers. For both methods, positioning of the sample (if there are path-length or absorber-concentration differences) and its stability are very important if accurate MCD and absorption data are to be obtained. Finally, for very sharp bands, the absorption spectrum cannot be expected to remain unchanged in the presence of a magnetic field — it is best measured in the same field as the MCD.

All of these problems were eliminated when the simultaneous MCD and absorption spectrometer was developed by Collingwood *et al.* in 1974.[14] Evident, also, is the convenience of such an instrument. The evolution of simultaneous MCD and absorption spectrometers has continued from this time on, primarily through advances in electronics and by phenomenal increases in computing power. The major developments are reviewed briefly in Section 2.3, prior to description of the high-resolution instrument used in this work.

At about the same time that Collingwood *et al.*[14] built their spectrometer, Douglas, Grinter and Thomson[15] at the University of East Anglia recognised that the assignment of many electronic transitions of matrix-isolated species were made only on the basis of theoretical predictions. Matrix isolation (MI; Section 1.2) had, it seemed, yet to be coupled with the powerful spectroscopic techniques employing polarised light. However, whether strain-free (Section 1.3.4.1), optically clear matrices could be prepared, and what other requirements might be imposed through coupling of MI with MCD was unknown. Nevertheless, Douglas *et al.*[15] proceeded to develop an apparatus

whereby a matrix could be deposited on a conductively cooled sample window in the bore of a superconducting solenoid. They demonstrated that matrices of high optical quality were obtained, and that MCD spectroscopy was readily compatible with MI, providing that the deposition window was made of a suitable non-birefringent (at cryogenic temperatures) material.

There are several apparent advantages in coupling MCD and MI. First, the low temperatures used in MI are eminently suitable for temperature-dependent MCD measurements of paramagnetic systems. Second, since MCD is a polarisation technique it yields much more information about the states involved in the transitions than does absorption spectroscopy, assisting greatly in making state assignments. Further, state angular momenta can be determined. Third, other species which could not otherwise be studied using MCD (such as reactive molecular fragments and/or ions) can be probed in the solid matrix environment. That is, the scope of low-temperature MCD spectroscopy had been considerably widened: no longer were researchers limited to cubic and uniaxial crystals (Section 1.3.4.1), frozen solutions (glasses) and polymer films.

Paul Schatz and coworkers at UVa saw the potential of MI-MCD, and published their first work, on xenon halides,[16] in 1977, using the method developed by Douglas *et al.*[15] Elmars Krausz, who was a post-doctoral fellow of Paul Schatz at the time, recognised the limitations of this method,[17] such as the long sample turn-around time. He and Paul MacDonald of Oxford Instruments developed an alternative system, where matrices were made in a continuous-flow cryostat before injection into the sample chamber of the superconducting solenoid.[17] This apparatus has been employed in work done by Rose,[18] Rose *et al.*,[19] and Samet *et al.*[20] However, this early design was still limited in its usefulness.

Bryce Williamson and his group at the University of Canterbury (UoC)[21,22] have developed the matrix-injection technique first envisioned by Krausz and MacDonald[17] into the method of choice for MI-MCD. The system used by this group is without doubt the best in the world. It offers: (i) rapid sample turn-around times (2 – 3 hours); (ii) active cooling of the deposition window by liquid He; (iii) strong magnetic fields produced by a superconducting solenoid (0 – 6 Tesla); and, (iv) accurate sample temperature measurement down to ~1.4 K, because the sample is immersed in liquid He ($T \leq 4.2$ K), or in cold gas ($T > 4.2$ K). The last feature is crucial for temperature-dependent MCD studies, and is unattainable when the sample is in a vacuum.

MI-MCD employing closed-cycle He refrigerators and electromagnets, where the sample is in a vacuum and field strengths are much lower, have been used.[23,24] They are perhaps best employed for systems that lack temperature dependence, and for very economical practice depositions of matrices prior to use of a matrix injection system, as is done at UoC (Section 2.2.1).

This work

This thesis describes recent magnetooptical investigations of radical species in argon matrices at liquid He temperatures. All work was done at UoC.

The first part of this chapter (Section 1.1) provides brief and general introductions of the molecules and ions investigated in subsequent chapters. (More specific reviews of the spectroscopic literature are to be found in the introductions of those chapters.) Section 1.2 discusses the matrix-isolation (MI) method, the emphasis being on its advantages for the spectroscopic investigation of reactive molecules and ions. Finally, Section 1.3 elaborates on the preceding discussion on magnetooptical spectroscopy. It also describes in more detail the spectroscopic technique of magnetic circular dichroism (MCD) and its usefulness in probing electronic states.

1.1. The molecules and ions investigated in this work

In this thesis the radical monohydrides, CH, NH and OH, singly charged ions of buckminsterfullerene (C_{60}), and ferricenium ($Fe(cp)_2^+$) are investigated. All of these are free radicals; that is, they have at least one unpaired electron. Some are moderately to very highly reactive, but their reactivity is overcome by trapping them in a large excess of solid Ar at cryogenic temperatures (<30 K; Section 1.2), where they can be studied spectroscopically 'at leisure'. In the case of ferricenium, matrix isolation affords much sharper structure than can be observed in solution.

All of the above species are introduced below, except $Fe(cp)_2^+$ which is considered an addendum to this thesis. That work is described in its entirety in Chapter 8.

1.1.1. The radical monohydrides: CH, NH and OH

Methylidyne (methyne; CH), imidogen (imine; NH) and hydroxyl (OH) are very important radicals in a range of chemical reactions. They are generally produced in high

energy processes, such as electrical discharges, combustion or through vacuum-ultraviolet (VUV) photolysis.

It has been known for many years that all three radicals are present in organic flames.[25] In fact, the emission bands of CH ($A\,^2\Delta$, $B\,^2\Sigma^-$, $C\,^2\Sigma^+ \rightarrow X\,^2\Pi$), NH ($A\,^3\Pi \rightarrow X\,^3\Sigma^-$) and OH ($C\,^2\Sigma^+ \rightarrow X\,^2\Pi$), corresponding to the absorption bands probed in this work in Ar matrices, have all been observed. Work on combustion processes continues to the present day,[26] using sensitive techniques such as laser-induced fluorescence (LIF) to quantify radical concentrations.

Less close to home, all three monohydrides have been observed in a variety of extraterrestial environments. CH,[27] NH[28,29] and OH[30,31] have been observed in Halley's comet, and the Doppler width of OH spectral lines was used to determine the speed of the comet's outflow.[30] All three (and about 100 or so other molecules) have been identified in the interstellar medium (ISM),[32] where their lifetimes are extended because of the very low particle concentrations. They have also been detected in stars.[33-36]

In the terrestial environment, OH plays the most important role by virtue of its stability relative to CH and NH, and is the dominant oxidant in the troposphere.[37] One of the chemical routes to OH production is the destruction of ozone by hydrogen atoms (eq (1.1.1)). OH is also one of many species that catalytically destroys ozone (eq (1.1.2)), being responsible for approximately 20% of the natural ozone loss. In addition, it undergoes many other reactions, even to sea level.

$$\left.\begin{aligned} H + O_3 &\rightarrow OH + O_2 \\ OH + O &\rightarrow H + O_2 \end{aligned}\right\} \quad (1.1.1)$$

$$\left.\begin{aligned} OH + O_3 &\rightarrow HO_2 + O_2 \\ HO_2 + O &\rightarrow OH + O_2 \end{aligned}\right\} \quad (1.1.2)$$

OH is not only important in the atmosphere. Zhou and Mapper[38] found far higher concentrations of OH in seawater than models predicted, and suggested a rethink of its role in marine chemistry. It has been found to play a (generally destructive) role in many biological processes.[39,40]

The gas-phase spectra of CH, NH and OH are very well characterised,[41] but the spectra in condensed phases are less-well understood. Most of the condensed-phase work that has been conducted has involved matrix isolation (MI; Section 1.2), which allows investigation of these molecules in an inert, frozen solid at low temperature. The

first of such investigations where performed in the late 1950s (within six years of Pimentel's first publication on MI,[42]) by G. Wilse Robinson and co-workers. They prepared CH, NH and OH (and their deuterated analogues) in rare-gas lattices, and probed them using electronic absorption spectroscopy.[43-46] Attempts to assign the structure observed in the electronic absorption spectra on the basis of free rotation proved unsuccessful. During the 1960s, Marilyn Jacox and Dolphus Milligan complemented that work by looking (primarily) at the IR spectra of NH and CH in their ground electronic state.[47,48]

More recently Bondybey and co-workers have used laser-induced fluoresence (LIF) to investigate the relaxation process in OH and OD in Ne,[49] and NH and ND in Ar and Kr,[50] as well as suggesting assignment of structure for the $A\,^3\Pi \rightarrow X\,^3\Sigma^-$ transition of matrix-isolated NH and ND.[51]

The overall trend of MI studies during the late 1970s and through to the 1990s for NH and OH has been to apply sensitive techniques, such as LIF, to symmetry-forbidden transitions.[52-56] In addition, the development of theory to explain the relaxation phenomena for states of these species in matrices has been investigated.[57-60]

For the allowed transitions of CH, NH and OH isolated in Ar matrices there remains a lack of definitive assignment of the observed structure. An aim of the work reported here is to resolve this problem through use of temperature- and magnetic-field-dependent MCD and absorption spectroscopy, and the development of appropriate theoretical models (Chapters 4 – 6).

1.1.2. The singly charged anion and cation of buckminsterfullerene

A brief history of the discovery of fullerenes

The third elemental form of carbon, the cage-like fullerenes, was first recognised by Rick Smalley, Bob Curl, Harry Kroto and coworkers,[61] as products of the laser vaporisation of a graphite disk. (In 1996, Smalley, Curl and Kroto were awarded the Nobel Prize in Chemistry for their work.) The carbon clusters detected in the time-of-flight mass spectrometer showed that the 60- and 70-atom members were the most abundant. The former was deduced to have a soccer-ball structure — a truncated icosahedron — while the latter was more like a rugby ball.[62,63] Other cages were also present. By manipulation of experimental parameters, C_{60} could be formed almost

exclusively, with a small contribution from C_{70}. Their potential importance in space was discussed soon afterward, since their infrared spectrum is similar to that of the so-called diffuse interstellar bands.[64,65]

The development of a method to produce bulk amounts of C_{60} eluded these early workers. In the mean time much theoretical work was done predicting its spectroscopic and physical properties. Finally in 1989 the physicists, Huffman, Krätschmer and co-workers, showed, on the basis of theoretical work, that a 'double hump' observed (as early as 1983) in the UV spectrum of soot produced under certain conditions, could be attributed to C_{60}.[66] IR spectra of this 'camel soot' (which they had come to be able to reproduce at will) revealed four sharp absorption bands, almost coincident with energies of the four-band spectrum predicted for C_{60}. Benzene was found to extract C_{60} from the soot, giving a magenta solution. When the solvent was evaporated, tiny black crystals were left which sublimed at ~400 °C in a vacuum.

Subsequent improvement of the technique used by Huffman, Krätschmer and co-workers[66,67] saw many laboratories producing C_{60} soon afterwards (for example, Refs 68 and 69), not to mention chemical companies. Since then there has been a great rush of scientific and technological research into this new elemental form of carbon, a general review of which is beyond the purposes of this section. However, it is important to note that unlike the other known elemental forms of carbon (the 'infinite' 2- and 3-dimensional networks of graphite and diamond, respectively), the fullerenes are discrete, carbon molecules. Hence they are *pure* carbon, whereas graphite and diamond have 'dangling bonds' to which H atoms bind.

A summary of the structure, bonding and symmetry of C_{60}

Of the fullerenes, only C_{60} and its singly charged ions are investigated in this work, and in this section a brief summary is given of the geometric and electronic structure of these species.

That C_{60} has icosahedral ($\mathbf{I}_h$ or $\mathbf{K}$) symmetry is confirmed by ^{13}C-NMR measurements[68] which show that all 60 C atoms have the same environment. In many ways its bonding is like graphite — orbitals approximating graphite's sp^2 hybrids can be viewed as forming the framework, whilst orbitals approximating carbon $2p_z$ comprise the π-delocalised system. The major difference with respect to graphite is the occurrence of 5-membered rings, which enable closure. (In fact, the fullerenes are

defined as carbon cages in which exactly twelve 5-membered rings occur. The number of 6-membered rings is given by ½{n – 20}, where n is the number of carbon atoms.[62,64,65]) Although it lacks the planar structure of graphite, it is remarkably stable on account of three effects: (i) it lacks 'dangling' bonds; (ii) the strain of cage closure is distributed equally among all atoms; and (iii) there are 12500 'resonance structures'.

The $\mathbf{I}_h$ symmetry[62,63,68,70] of C_{60} gives it the highest symmetry of any molecular system, and provides a new challenge in the practical application of group-theoretical techniques to molecular systems (Chapter 3 and Appendix C). Very high symmetry introduces a high level of orbital, and hence electronic-state and vibrational-mode, degeneracy (up to 5-fold; Chapter 3). Hence, from a symmetry point of view, and on account of the large number of states, C_{60}, and particularly its ions (many of which also have non-zero total spin), are very interesting candidates for investigation using optical spectroscopy.

The singly charged ions of C_{60}

C_{60} is also remarkable in terms of its electrochemical properties. Under suitable conditions, six reversible, one-electron reductions are observed (C_{60}^{n-} / $C_{60}^{(n+1)-}$ (n = 0 – 5)).[71,72] Anions up to n = 3 are produced readily using standard methods and conditions,[71,73-75] and have been produced in thin films doped with alkali metal atoms.[76,77] Since the electrons are added sequentially to the $5t_{1u}$ orbital,[71] all of C_{60}^{-} through C_{60}^{5-} have ground states that can be probed using EPR.[73-75] Most significant, for this work, are the near-IR electronic transitions that occur for all of these anionic species in solution.[71-74]

Suggested by the electrochemical work are the low first ionisation potential[78] (7.60 eV) and relatively high electron affinity[78] (2.60 eV) of C_{60}. Consequently, simultaneous preparation of the mono-cation and anion has been achieved at low pressure in Ar in the gas phase[79] (prior to deposition on a sample window held near liquid-He temperature). (Ionising radiation ejects an electron from one C_{60} molecule, which is subsequently 'trapped' by a second molecule.) Near-infrared (NIR) spectra of the singly charged anion and cation have been obtained. The (0,0) absorption of C_{60}^{+} occurs at significantly higher energy than that of C_{60}^{-}, but there is some overlap of vibrational structure.

Despite the work described above, assignment of the NIR transitions of $C_{60}^{\pm}$

remains inconclusive. Gasyna *et al.*[79] sought to expand the amount of information available by measuring the absorption and MCD of $C_{60}^{\pm}$/Ar, but they did not measure either the temperature or magnetic-field dependencies, and were unable to provide a theoretical model to explain their results. In this thesis, the temperature and field dependencies are presented, along with a qualitative model that attempts to explain them.

1.2. Matrix isolation

The matrix-isolation (MI) technique involves trapping molecules (guests) in low concentration in a solid host at cryogenic (usually near liquid He) temperatures. An inert gas is commonly employed as the matrix, since it reduces the likelihood of reaction of unstable guests. MI is also used for investigation of stable molecules: for example, to isolate them from each other, or to limit the possibility of solvent ligation. The metalloporphyrins and metallophthalocyanines are good examples of compounds which have been probed in this way.[15,22,80-82] The insolubility of some members of these 'families' of compounds has posed difficulties in conventional solution spectral studies.[15,22] However, they are generally stable to sublimation, and are therefore eminently suitable candidates for MI.

Although the lighter rare gases can generally be regarded as chemically inert, their presence can affect the spectra of a guest through a combination of electronic, vibronic and cage effects. So MI should not be regarded as a 'quasi gas-phase' technique, and account must be taken of effects that are specific to the host medium.

1.2.1. A brief history of MI

The matrix-isolation technique was initially developed by Pimentel and co-workers in 1954.[42,83] Since that time, thousands of articles have appeared in the literature, the work being summarised in several monographs.[84-86] Among the many applications of MI are spectroscopic studies of atoms, and stable and unstable molecules using, for example, ESR, Raman, IR and UV-visible absorption methods. Species that have been studied include gas-phase reaction intermediates, and the products of *in-situ* photolysis of trapped molecules. Solid-state physicists have also been interested in MI, particularly as a means of gaining theoretical understanding of the effects of impurity defects on the properties of the host.

1.2.2. Spectroscopic advantages of MI

The cryogenic temperatures used in matrix-isolation spectroscopy are advantageous for three reasons.

First, 'hot' vibrational bands are eliminated, and generally only a few of the lowest rotational or librational (hindered-rotational) levels are populated. This tends to reduce the complexity of the low-temperature spectra relative to those obtained at higher temperatures, and hence simplifies interpretation.

Second, degenerate ground states are readily investigated at low temperatures using magnetooptical techniques, such as MCD. The lowering of ground-state degeneracy by the applied magnetic field results in a difference in Boltzmann population between the Zeeman-split states, which is reflected in the state-to-state transition intensities. The lower the temperature and/or the higher the field, the greater will be this population difference (until saturation occurs). In principle, a temperature-dependent absorption spectrum will result, but for molecules in condensed phases, the transition bandwidths are usually far too great for any change to be evident. MCD spectra, however, do show marked temperature dependence (Section 1.3.2).

Third, the bands are generally sharp relative to those obtained in other condensed phase, except single crystals.

1.2.3. Matrix effects on observed spectra

In addition to the advantages outlined in the previous section, the matrix introduces interesting perturbations into atomic and molecular spectra which are not present in the gas phase. The effects observed may include:[85]

- matrix shifts of electronic, vibrational and rotational states;
- matrix (crystal-field, CF) splitting of orbitally degenerate states because of the imposition of lower symmetry on the guest;
- librational overtones involving hindered rotations of the guest molecules;
- vibronic effects (including the Jahn-Teller effect) resulting from coupling between the electronic states of the guest and the lattice phonons (low-frequency vibrational modes) of the host;
- SOC perturbations due to, *e.g.*, the external-heavy atom effect;[20,87,88]
- orientational effects.

All of these have a potential bearing on the work reported in this thesis. However, with regard to the last point, we take the general view that the guests of interest here are most likely randomly oriented. This is despite the fact that orientation effects have been observed in the EPR spectra of larger diatomic molecules in rare-gas matrices, including VO/Ar,[89] MgF/Ne,[90] ZnF/Ne,[91] CdF/Ne[91] and BO/Ne.[92,93] (BO shows 'extreme' orientational preference in Ne matrices, but interestingly not in Ar.[92,93]) Small molecules, such as CH, NH and OH, would not be expected to remain oriented after trapping, due to their small size with respect to substitutional sites in the lattice. Theoretical treatment of preferential and random orientation in simultaneous MCD and absorption spectroscopy is discussed in Chapter 3, where moment ratios play a key role in the determination of the extent of the orientation for XH/Ar in subsequent chapters.

1.3. Magnetic circular dichroism (MCD)

A brief historical description of the Faraday and Zeeman effects was made at the beginning of this chapter. In this section, it is the intention to give: (i) a brief explanation of the similarities and differences between natural and magnetic optical activity; (ii) an overview of the bandshapes observed in MCD, and their origin; (iii) a brief look at the instrumental requirements of MCD; (iv) an account of the limitations of MCD.

Section 2.3 describes the simultaneous MCD and double-beam absorption spectrometer used in this work, while Chapter 3 develops the theory required.

1.3.1. The relationship between natural and magnetic optical activity

Although both MORD and MCD have naturally occurring analogues, the natural and magnetic phenomena have quite different origins. Natural ORD and CD are reflections of molecular (or crystal) symmetry, and are related to each other by the Kramers-Krönig transform. They arise from the interference between the electric- and magnetic-dipole transition moments, and hence can occur only in a limited number of relatively low-symmetry molecular point groups — those that contain no improper rotation axes. ORD is a consequence of a sample's different refractive indices for left and right circularly polarised light, while the CD is due to different absorption coefficients for these polarisations. On the other hand, MCD and MORD occur in all

substances independent of their symmetry, and have their explanation in the Zeeman effect, as described for MCD in the following section.

1.3.2. Faraday terms and MCD bandshapes

MCD is a longitudinal Zeeman technique; that is, it involves radiation propagating along the magnetic-field direction (Figure 1.3.1), defined as the Z axis. It is the differential absorption of left and right circularly polarised light (lcp and rcp, respectively) by a compound in the magnetic field. If the absorption of lcp and rcp at a given photon energy (E) are denoted A_L and A_R, respectively, then the MCD ΔA is defined as,

$$\Delta A' = A_L' - A_R' \qquad (1.3.1)$$

where the primes indicate field-dependent quantities. The absorption (A) is the average over the two polarisations in the absence of the field.

$$A = (A_L + A_R)/2 \qquad (1.3.2)$$

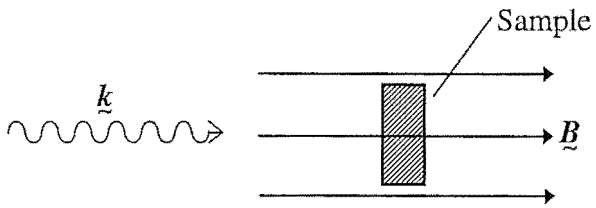

Figure 1.3.1: The longitudinal Zeeman configuration used in MCD. $\underset{\sim}{k}$ is the wave vector of the light and $\underset{\sim}{B}$ is the magnetic-field pseudovector.

The origins of MCD can be explained in terms of the Zeeman effect.[9,12] In the description due to Buckingham and Stephens,[8] the MCD comprises three types of contributions, referred to as Faraday A, B and C terms (Figure 1.3.2). A and C terms are observed as a direct consequence of first-order Zeeman splittings. B terms are the result of second-order field-induced mixing of electronic states.

Since photons have angular momenta corresponding to a quantum number $\sigma = 1$, they also have components, $m_\sigma = 0$ and ± 1. With relation to a magnetic field, Z-polarised radiation has $m_\sigma = 0$, but since the electric field must be perpendicular to the direction of propagation, Z-polarised light does not exist in the MCD experimental configuration. Lcp and rcp light have $m_\sigma = +1$ and -1, respectively. The electric vector of each follows a helical path in space, with the sense of the polarisation corresponding

to the handedness of the helix: hence, to an observer looking at a light source along the direction of propagation the electric vector of lcp light appears to rotate in an anticlockwise sense with time.

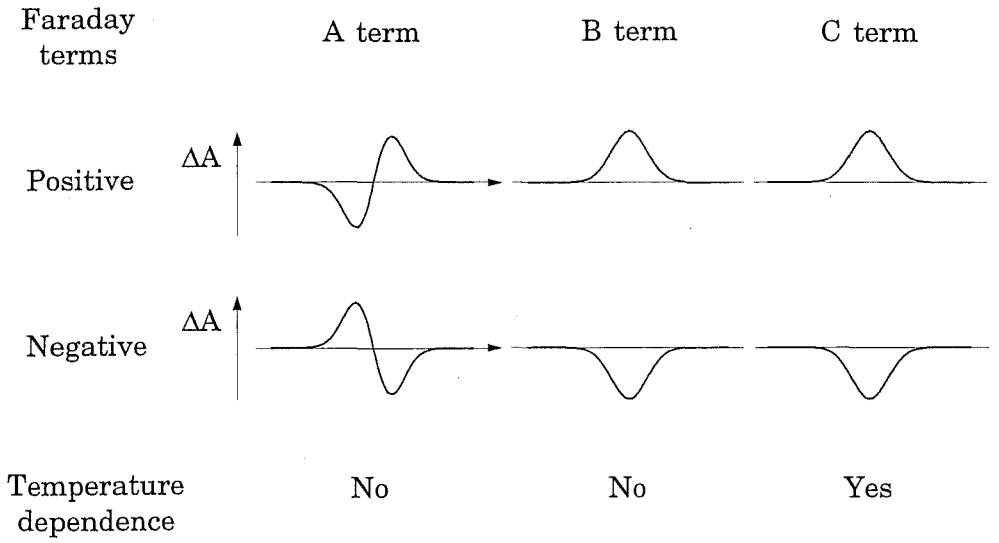

Figure 1.3.2: Dispersion forms for the Faraday *A*, *B* and *C* terms observed in MCD, and their temperature dependencies.

The circularly polarised components of the electric-field vector interact with the circularly polarised components of the electric-dipole moment of the system, given by,

$$m_{\pm 1} = \mp \tfrac{1}{\sqrt{2}}(m_x \pm i\, m_y) \qquad (1.3.3)$$

where m_i represents the relevant component of the electric-dipole moment; m_{+1} and m_{-1} are respectively lcp and rcp. The corresponding operator is proportional to the raising and lowering operators for angular momenta,

$$m_{\pm 1} = \mp \tfrac{1}{\sqrt{2}}\, m^{\pm} \qquad (1.3.4)$$

where

$$m^{\pm}\,|J\,M_J\rangle = \hbar\,(J \mp M_J)^{1/2}\,(J \pm M_J + 1)^{1/2}\,|J\,M_J \pm 1\rangle \qquad (1.3.5)$$

Hence lcp and rcp light selectively excite transitions obeying the selection rule ΔM_J = +1 and -1, respectively. Transitions between levels whose degeneracy has been lowered by the Zeeman effect will, in general, occur at different energies. However in most cases these Zeeman splittings cannot be directly resolved in molecular absorption spectra because of large bandwidths. MCD overcomes this limitation (see Section

1.3.3): it allows Zeeman splittings (among other molecular parameters) to be obtained where conventional Zeeman techniques are ineffectual.

Since MCD is a differential technique (eq (1.3.1)), spectra can have both positive and negative bands (Figure 1.3.2). Ref. 9 gives a full description of the basic dispersion forms described briefly here.

Firstly consider systems where degeneracies occur, and the magnetic field lowers those degeneracies. This is a first-order Zeeman effect, and gives rise to *C* terms if the ground state is degenerate and *A* terms if the ground and/or excited state is degenerate. *C* terms are single signed (Figure 1.3.2) and arise from the different Boltzmann populations of Zeeman-split states of the ground state. Hence they are temperature dependent, and in the so-called 'linear limit' ($\mu_B B << kT$) change intensity as $1 / T$. Their sign depends on the polarisation of the transition from the most highly populated Zeeman state according to eq (1.3.1). *A* terms have a derivative band shape and are temperature independent (Figure 1.3.2), because they are a consequence of the Zeeman splitting alone. The derivative band shape arises because of the small (relative to the bandwidth) Zeeman shifts of energies at which the lcp and rcp transitions occur. *A* terms are positive if the zero crossing has a positive slope with increasing energy (that is, if the lcp transition occurs at higher energy).

As well as the first-order Zeeman splittings, the field induces a mixing of electronic states, a second-order effect, giving rise to *B* terms. Interaction occurs only between electronic states of suitable symmetry, with the magnitude being proportional to the inverse of the energy separation. *B* terms are single-signed, and are independent of temperature (Figure 1.3.2). MCD occurs in all compounds because *B* terms, unlike *A* and *C* terms, do not depend on orbital (or spin) degeneracy.

The MCD observed for an electronic transition may be a combination of any or all of these Faraday terms. Details of the electronic structure can be determined by analysing the contributions to the total MCD from each type of term. One of the methods used to extract this information is moment analysis (the method of moments; Section 3.5.1).[9] Calculation of the first moment of the MCD by numerical integration of the spectrum yields the *A*-term magnitude. Calculation of the zeroth moment gives the sum of the *B* and *C* terms, which can be separated using the temperature dependence of the zeroth moment. (A plot of the observed intensity versus $1 / T$ yields a slope and *y*-intercept that are proportional to the *C*- and *B*-term contributions, respectively.)

Moment analysis can produce detailed information only for transitions whose band systems are well separated.[9] In some cases considered in this thesis, the individual bands due to spin-orbit and crystal-field splittings are not sufficiently well resolved to allow them to be individually characterised, and the integrations inherent in the method are carried over all the bands in the system. In that case the zeroth and first moments are invariant to crystal-field effects in excited states, and other methods are required to extricate information concerning these effects. One such method, employed in this thesis for NH/Ar, involves simulation of the absorption and MCD spectra using theoretical expressions in order to quantify the crystal-field splitting, and reproduce the fine structure.

MCD is a very useful technique for determining the angular momentum of ground and excited states in atoms and molecules, since it yields direct information on the Zeeman splitting of states. It also yields information on the field-induced mixing of states. In addition, it reveals details concerning the vibronic structure; for example, Jahn-Teller bands can be distinguished from other vibronic overtones due to alternating signs in the harmonics. And as was noted at the start of this chapter, the extra information afforded by the bisignated MCD can be used to solve difficult spectral assignments. There are limitations to the applicability of MCD which are discussed briefly in Section 1.3.4, but first the experimental aspects of MCD are considered.

1.3.3. Experimental requirements

Unlike conventional Zeeman spectroscopy, which involves direct measurement of field-induced splittings, the differential nature of MCD readily lends itself to the study of systems where resolution of splittings is not possible due to broad bands. The majority of molecules in condensed phases have bandwidths that are so large that the change in absorption of lcp and rcp light in the presence of the field is not distinguishable within the signal-to-noise (S/N) level. Nor, in general, can meaningful MCD be generated by subtracting an rcp absorption spectrum from an lcp one.

To overcome the inherent problem of low signal intensity, modern MCD spectrometers utilise phase-sensitive detection. A photoelastic modulator (PEM) produces the alternating polarisations (Section 2.3.5) giving rise to a modulated signal. A lock-in amplifier (LIA; Section 2.3.8) is then employed, enabling the very small

modulated signal due to differential absorption of (modulated) lcp and rcp light to be extracted with good S/N from the much larger dc voltage output of the detector.

1.3.4. Limitations of MCD

1.3.4.1. Physical limitations

The first problem is that in certain media, circularly polarised light cannot exist over extended ranges of space. This is generally the case in a biaxial system (for reasons discussed in Ref. 9), where there are no two equivalent crystallographic axes. (CD or MCD can still be obtained, but with significant difficulty.) Care must also be taken with uniaxial systems (which have two equivalent crystallographic axes), where CD and MCD can be obtained directly only if the circularly polarised light is propagated along the unique axis. (In cubic and isotropic systems the light can be propagated along any axis.) Generally complications only arise in solids, since gases and solutions are isotropic. Matrices are normally optically isotropic (Section 1.2), and for those investigated in this work no problems are encountered.

Secondly, the physical nature of a sample may prove unsatisfactory for CD or MCD in practice. Strain birefringence and other imperfections depolarise light. Sometimes samples that are satisfactory at room temperature are not so at low temperatures, because of a phase transition or strain development. Further, the presence of crystallites may also result in depolarisation of circularly polarised light, as, in some cases, do samples that scatter light significantly.

Depolarisation of circularly polarised light by a sample, and hence the reduction in measured MCD, can be readily quantified for molecules with no natural CD. A naturally optically active compound is placed after the sample, and the zero-field CD spectrum is collected. Subsequently the CD of the optically active compound itself is run, and the depolarisation occurring for the original sample can be determined by comparison of the two spectra. Small levels of depolarisation can be corrected. In this work the optically active crystal $Na_3[Nd(ODA)_3].2NaClO_4.6H_20$ (ODA = oxydiacetate), or aqueous solutions of *d*-10-camphorsulfonic acid (*d*-10-CSA) or *d*-$[Co(en)_3][Cl][tartrate].5H_2O$ have been used for this purpose.

1.3.4.2. Molecular symmetry

If a molecule belongs to a point group in which there are no degenerate irreducible representations (irreps), the MCD can only comprise *B* terms. Since *B* terms are the result of field-induced mixing of states, the rewards following extensive application of theory are likely to be small. Hence, the great majority of molecules studied using MCD are of 'high' symmetry; that is, they have at least two-fold degeneracy in one or more irreps. In all systems investigated in this work, the ground state is spin degenerate and, in some cases, orbitally degenerate as well; so *A* and *C* terms are observed and give rise to the dominant features of the spectrum. However, a precise quantitative analysis of the spectrum still requires consideration of *B* terms, as will be seen in later chapters.

1.4. References

1. Faraday, M. *Faraday's Diary*; G. Bell and Sons Ltd.: London, 1933; Vol. IV.
2. Zeeman, P. *Phil. Mag., 5* **1897**, *43*, 226-239.
3. Zeeman, P. *Phil. Mag., 5* **1897**, *44*, 55-60.
4. Shashoua, V. E. *J. Am. Chem. Soc.* **1963**, *84*, 2109-2115.
5. Foss, J. G.; McCarville, M. E. *J. Am. Chem. Soc.* **1965**, *87*, 228-230.
6. Stephens, P. J. Ph.D. Dissertation, Oxford University, Oxford, 1964.
7. Shashoua, V. E. *J. Am. Chem. Soc.* **1965**, *87*, 4044-4048.
8. Buckingham, A. D.; Stephens, P. J. In *Annual Review of Physical Chemistry*; Eyring, H.; Christensen, C. J.; Johnston, H. S., Eds.; Annual Reviews, Inc: Palo Alto, 1966; Vol. 17, pp. 399-432.
9. Piepho, S. B.; Schatz, P. N. *Group Theory in Spectroscopy with Applications to Magnetic Circular Dichroism*; Wiley-Interscience: New York, 1983.
10. Stephens, P. J. *Inorg. Chem.* **1965**, *4*, 1690-1692.
11. Schatz, P. N.; McCaffery, A. J.; Suetaka, W.; Henning, G. N.; Ritchie, A. B.; Stephens, P. J. *J. Chem. Phys.* **1966**, *45*, 722-734.
12. Schatz, P. N.; McCaffery, A. J. *Quart. Rev.* **1969**, *23*, 552-584.
13. Jasperson, S. N.; Schnatterly, S. E. *Rev. Sci. Instrum.* **1969**, *40*, 761-767.

14. Collingwood, J. C.; Day, P.; Denning, R. G.; Quested, P. N.; Snellgrove, T. R. *J. Phys. E: Sci. Instrum.* **1974**, *7*, 991-996.

15. Douglas, I. N.; Grinter, R.; Thomson, A. J. *Mol. Phys.* **1974**, *28*, 1377-1388.

16. Goetschalckx, M. A.; Mowery, R. L.; Krausz, E. R.; Yeakel, W. C.; Schatz, P. N.; Ault, B. S.; Andrews, L. *Chem. Phys. Lett.* **1977**, *47*, 23-27.

17. Krausz, E.; McDonald, P. *J. Phys. E: Sci. Instrum.* **1978**, *11*, 801-804.

18. Rose, J. L. Ph.D. Dissertation, University of Virginia, Charlottesville, 1987.

19. Rose, J.; Smith, D.; Williamson, B. E.; Schatz, P. N.; O'Brien, M. C. M. *J. Phys. Chem.* **1986**, *90*, 2608-2615.

20. Samet, C.; Rose, J. L.; Schatz, P. N.; O'Brien, M. C. M. *Chem. Phys. Lett.* **1989**, *159*, 567-572.

21. Dunford, C. L. Ph.D. Dissertation, University of Canterbury, Christchurch, 1997.

22. Dunford, C. L.; Williamson, B. E. *J. Phys. Chem. A* **1997**, *101*, 2050-2054.

23. Brittain, R.; Powell, D.; Voigtman, E.; Vala, M. *Rev. Sci. Instrum.* **1980**, *51*(7), 905-910.

24. Kenney, J. W., III. *Hinds Instruments PEM Applications* **1995**, *Summer*, 1-3.

25. Gaydon, A. G. *Spectroscopy and Combustion Theory*; Chapman and Hall Ltd: London, 1948.

26. Fristrom, R. M. *Flame Structure and Processes*; Oxford University Press: New York, 1995.

27. Wyckoff, S.; Telger, S.; Wehinger, P. A.; Spinrad, H.; Belton, M. J. *Astrophys. J.* **1988**, *325*, 927-938.

28. Schleicher, D. G.; Millis, R. L. *Astrophys. J.* **1989**, *339*, 1107-1114.

29. Kim, S. J.; A'Hearn, M. F.; Cochran, W. D. *Icarus* **1989**, *77*, 98-108.

30. Combi, M. R. *Icarus* **1989**, *81*, 41-50.

31. Schloerb, F. P.; Claussen, M. J.; Tacconi-Garman, L. *Astron. Astrophys.* **1987**, *187*, 469-474.

32. Smith, D. *Chemical Reviews* **1992**, *92*, 1473-1485.

33. Singh, M.; Chaturvedi, J. P. *J. P. Astrophys. Space Sci.* **1987**, *136*, 231-246.

34. Grevesse, N.; Lambert, D. L.; Sauval, A. J.; Van Dishoeck, E. F.; Farmer, C. B.; Norton, R. H. *Astron. Astrophys.* **1990**, *231*, 225-230.

35. Melen, F.; Sauval, A. J.; Grevesse, N.; Farmer, C. B.; Servais, C.; Delbouille, L.; Roland, C. *J. Mol. Spectrosc.* **1995**, *174*, 490-509.

36. Ninkov, Z.; Walker, G. A. H.; Yang, S. *Astrophys. J.* **1987**, *321*, 425-437.

37. McEwan, M. J.; Phillips, L. F. *Chemistry of the Atmosphere*; Edward Arnold Ltd: London, 1975.

38. Zhou, X.; Mapper, K. *Mar. Chem.* **1990**, *30*, 71-88.

39. Halliwell, B.; Gutteridge, J. M. C. *Free Radicals in Biology and Medicine*, 2nd ed.; Oxford University Press: Oxford, 1989.

40. Halliwell, B.; Gutteridge, J. M. C. *Methods Enzymol.* **1990**, *186*, 1-85.

41. Huber, K. P.; Herzberg, G. *Molecular Spectra and Molecular Structure, Volume 4: Constants of Diatomic Molecules*; Van Nostrand Reinhold: New York, 1979.

42. Whittle, E.; Dows, D. A.; Pimentel, G. C. *J. Chem. Phys.* **1954**, *22*, 1943.

43. McCarty, M. J.; Robinson, G. W. *J. Am. Chem. Soc.* **1959**, *81*, 4472-4476.

44. Robinson, G. W.; McCarty, M. J. *J. Am. Chem. Soc.* **1960**, *82*, 1859-1864.

45. Robinson, G. W.; McCarty, M. J. *J. Chem. Phys.* **1958**, *28*, 350.

46. Robinson, G. W.; McCarty, M. J. *Can. J. Phys.* **1958**, *36*, 1590-1591.

47. Milligan, D. E.; Jacox, M. E. *J. Chem. Phys.* **1964**, *41*, 2838-2841.

48. Milligan, D. E.; Jacox, M. E. *J. Chem. Phys.* **1967**, *47*, 5146-5156.

49. Brus, L. E.; Bondybey, V. E. *J. Chem. Phys.* **1975**, *63*, 786-793.

50. Bondybey, V. E. *J. Chem. Phys.* **1977**, *65*, 5138-5140.

51. Bondybey, V. E.; Brus, L. E. *J. Chem. Phys.* **1975**, *63*, 794-804.

52. Ramsthaler-Sommer, A.; Eberhardt, K. E.; Schurath, U. *J. Chem. Phys.* **1986**, *85*, 3760-3769.

53. Blindauer, C.; Winter, M.; Sild, O.; Jansen, G.; Hess, B. A.; Schurath, U. *J. Phys. Chem.* **1993**, *97*, 10002-10010.

54. Kaes, A.; Stuhl, F. *J. Chem. Phys.* **1992**, *97*, 4661-4668.

55. Hizhnyakov, V.; Seranski, K.; Schurath, U. *Chem. Phys.* **1992**, *162*, 249-256.

56. Blindauer, C.; van Riesenbeck, N.; Seranski, K.; Winter, M.; Becker, A. C.; Schurath, U. *Chem. Phys.* **1991**, *150*, 93-108.

57. Jansen, G.; Hess, B. A.; Marian, C. M.; Angyan, J. G. *J. Phys. Chem.* **1993**, *97*, 10011-10020.

58. Diestler, D. J.; Knapp, E. W.; Ladoucuer, H. D. *J. Chem. Phys.* **1978**, *68*, 4056-4065.

59. Fiser, J.; Vojtik, J. *Chem. Phys.* **1994**, *182*, 217-223.

60. Jansen, G.; Hess, B. A. *Chem. Phys. Lett.* **1992**, *192*, 21-28.

61. Kroto, H. W.; Heath, J. R.; O'Brien, S. C.; Curl, R. F.; Smalley, R. E. *Nature* **1985**, *318*, 162-163.

62. Curl, R. F.; Smalley, R. E. *Scientific American* **1991**, *265*, 32-41.

63. Curl, R. F. *CHEM NZ* **1992**, *47*, 3-14.

64. Kroto, H. W. *Science* **1988**, *242*, 1139-1145.

65. Kroto, H. W. *Angew. Chem. Int. Ed. Engl.* **1992**, *31*, 111-129.

66. Kratschmer, W.; Lamb, L. D.; Fostiropoulos, K.; Huffman, D. R. *Nature* **1990**, *347*, 354-358.

67. Taylor, R.; Hare, J. P.; Abdul-Sala, A. K.; Kroto, H. W. *J. Chem. Soc., Chem. Commun.* **1990**, 1423-1425.

68. Ajie, H.; Alvarez, M. M.; Anz, S. J.; Diederich, F.; Fostiropoulos, K.; Huffman, D. R.; Kratschmer, W.; Rubin, Y.; Schriver, K. E.; Sensharma, D.; Whetten, R. L. *J. Phys. Chem.* **1990**, *94*, 8630-8633.

69. Bethune, D. S.; Meijer, G.; Tang, W. C.; Rosen, H. J. *Chem. Phys. Lett.* **1990**, *174*, 219-222.

70. Chung, F.; Sternberg, S. *American Scientist* **1993**, *81*, 56-71.

71. Heath, G. A.; McGrady, J. E.; Martin, R. L. *J. Chem. Soc., Chem. Commun.* **1992**, 1272-1274.

72. Fullagar, W. K.; Gentle, I. R.; Heath, G. A.; White, J. W. *J. Chem. Soc., Chem. Commun.* **1993**, 525-527.

73. Dubois, D.; Kadish, K. M. *J. Am. Chem. Soc.* **1991**, *113*, 4364-4367.

74. Greany, M. A.; Gorun, S. M. *J. Phys. Chem.* **1991**, *95*, 7142-7144.

75. Khaled, M. M.; Carlin, R. T.; Trulove, P. C.; Eaton, G. R.; Eaton, S. S. *J. Am. Chem. Soc.* **1994**, *116*, 3465-3474.

76. Srdanov, V. I.; Saab, A. P.; Margolese, D.; Poolman, E.; Khemani, K. C.; Koch, A.; Wudl, F.; Kirtman, B.; Stucky, G. D. *Chem. Phys. Lett.* **1992**, *192*, 243-248.

77. Koh, W.; Dubois, D.; Kutner, W.; Jones, T.; Kadish, K. M. *J. Phys. Chem.* **1993**, *97*, 6871-6879.

78. Lichtenberger, D. L.; Nebesny, K. W.; Ray, C. D.; Huffman, D. R.; Lamb, L. D. *Chem. Phys. Lett.* **1991**, *176*, 203-208.

79. Gasyna, Z.; Andrews, L.; Schatz, P. N. *J. Phys. Chem.* **1992**, *96*, 1525-1527.

80. Williamson, B. E.; VanCott, T. C.; Boyle, M. E.; Misener, G. C.; Stillman, M. J.; Schatz, P. N. *J. Phys. Chem.* **1992**, *114*, 2412-2419.

81. Metcalf, D. H.; VanCott, T. C.; Snyder, S. W.; Schatz, P. N.; Williamson, B. E. *J. Phys. Chem.* **1990**, *94*, 2828-2832.

82. VanCott, T. C.; Koralewski, M.; Metcalf, D. H.; Schatz, P. N.; Williamson, B. E. *J. Phys. Chem.* **1993**, *97*, 7417-7426.

83. Pimentel, G. C. *J. Am. Chem. Soc.* **1958**, *80*, 62-64.

84. Moskovits, M.; Ozin, G. A., Eds. *Cryochemistry*; Wiley: New York, 1976.

85. Andrews, L.; Moskovits, M., Eds. *Chemistry and Physics of Matrix-Isolated Species*; Elsevier Science Publishers: Amsterdam, 1989.

86. Almond, M. J.; Downs, A. J. *Spectroscopy of Matrix-Isolated Species*; John Wiley & Sons: Chichester, 1989.

87. Pellow, R.; Vala, M. *J. Chem. Phys.* **1989**, *90*, 5612-5621.

88. Lund, P. A.; Smith, D.; Jacobs, S. M.; Schatz, P. N. *J. Phys. Chem.* **1984**, *88*, 31-42.

89. Kasai, P. H. *J. Chem. Phys.* **1968**, *49*, 4979-4984.

90. Knight, L. B. J.; Easley, W. C.; Weltner, W. J.; Wilson, M. *J. Chem. Phys.* **1971**, *54*, 322-329.

91. Knight, L. B. J.; Mouchet, A.; Beaudry, W. T.; Duncan, M. *J. Mag. Reson.* **1978**, *32*, 383-390.

92. Knight, L. B. J.; Easley, W. C.; Weltner, W. J. *J. Chem. Phys.* **1971**, *54*, 1610-1617.

93. Knight, L. B. J.; Wise, M. B.; Davidson, E. R.; McMurchie, L. E. *J. Chem. Phys.* **1982**, *76*, 126-136.

2. Experimental Apparatus and Instrumentation

There are three aspects to the acquisition of the experimental data presented in this thesis. First, the radical species are prepared in Ar at low pressures from suitable precursors using varying intensities of Ar-resonance radiation (Section 2.1). Second, the gaseous mixtures are deposited on a sapphire sample window held at ~12 K using either cold He gas or liquid He as the cryogen (Sections 2.2.1 and 2.2.2, respectively). The sample is then positioned in the bore of an electromagnet or superconducting magnet in the longitudinal Zeeman configuration, as required for MCD (Section 1.3.3). Finally, simultaneous MCD and absorption spectra are obtained using a spectrometer designed and built as part of this project (Section 2.3).

2.1. Sample preparation

In this section, the assemblies used to create the gaseous radical mixtures, prior to deposition (Section 2.2) are described. Hence, this section falls into two parts: (i) the preparation of the radical/Ar mixtures from stable first-row hydrides; and, (ii) the simultaneous production of C_{60}^{+} and C_{60}^{-} in Ar. (It is reiterated that Chapter 8 covers the work on ferricenium in its entirety.)

2.1.1. XH(D)/Ar (X = C, N, O)

Two apparatuses are described here. The first method, which employed a pulsed electrical discharge, worked only for NH/Ar. The second, using a radio-frequency (RF) discharge through quartz or glass tubing, proved successful for all monohydrides, and was used exclusively to produce the matrices investigated spectroscopically in later chapters.

2.1.1.1. Pulsed-electrical discharge method

Relatively high pressures (compared to the optimum pressure for matrix isolation) are required for an electrical discharge to be sustained through a stream of gas, placing a high load on the vacuum and producing poor-quality matrices. This can be overcome by pulsing the gas through a gap between the electrodes, where the short-duration pulses are of sufficiently high pressure for shorting, while yielding matrices of good optical quality because of a slower overall deposition rate.

The system developed in this work is based on that described by Bondybey and co-workers,[1-4] who observed NH/Ar as a discharge product from an aniline:Ar mixture using laser-induced fluorescence (LIF).[1] The discharge unit described in this thesis was designed for compatibility with existing Knudsen oven assemblies (Section 2.1.2).

The set-up used here is shown in Figure 2.1.1. A General Valve Corporation 28-V electromagnetic valve (9-442-900) is used to produce gas pulses. It is driven at a frequency of ~4 Hz by ~25-V electrical pulses of ~10 – 12-ms duration, which are generated by a home-built power supply. (The 'open time' for the pulses was not checked, because the system was not developed further. However, it is likely that it is open significantly longer than the width of the voltage pulse, since the valve is closed only by the force of gas behind it when no voltage is applied.) The backing pressure of a ~1:100 NH_3:Ar mixture (from a 1-L glass reservoir) is set using a needle valve, so that the average pressure at the pump (Section 2.2.1) is ~10^{-4} Torr. An electrical discharge occurs when the gas bridges the gap between an aluminium (high voltage) electrode and the grounded stainless-steel tube through which the gas travels. The HV electrode is held at 1000 – 1900-V potential by a Philips PW4022 HV power supply. The discharge products are deposited on a cryogenically cooled sample window (Section 2.2.1).

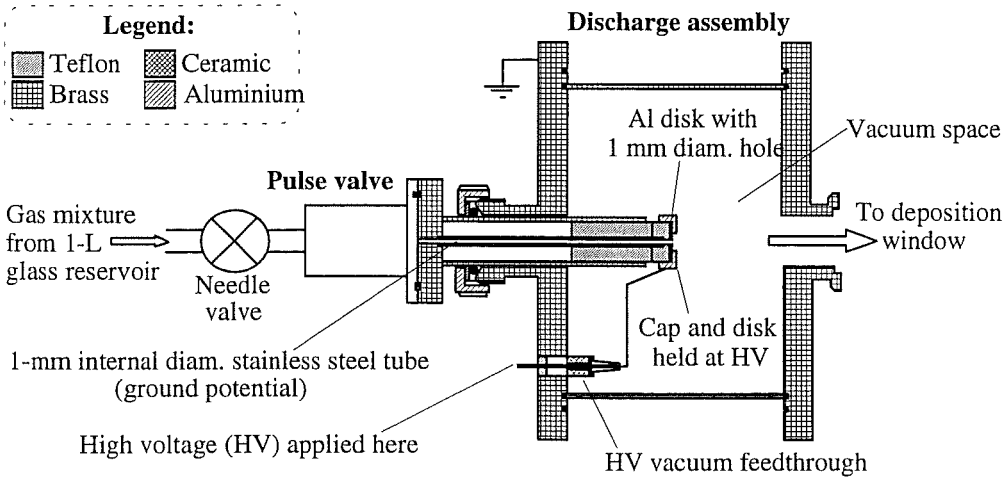

Figure 2.1.1: Schematic diagram of the pulse-discharge unit, showing the discharge assembly in cross-section.

The method was not optimised as well as it could have been, primarily because it was superseded by the technique described in the subsequent section. Several factors that could be developed include:

- construction of a dedicated discharge cavity and optimisation of discharge conditions;
- use of shorter-duration, higher-voltage pulses to open the valve, coupled with higher backing pressures, so that the valve closes rapidly after the voltage pulse decays, and lower discharge voltages are necessitated;
- placement of a suitable capacitor across the HV power supply's output that will sustain the discharge during the open period.

The low yield of NH (absorbance ~0.03) could be due to the discharge conditions being too harsh — lower discharge voltages, possible if the gas pulse is of higher pressure and shorter duration, may help in this case. (Note also that LIF is a very much more sensitive technique for detection of NH/Ar[1,2,4,5] than absorption spectroscopy, which may explain the apparent success of Bondybey's experiments in comparison with the ones conducted by this author.)

2.1.1.2. Tesla-coil method

As previously demonstrated by Rose,[6] CH, NH and OH radicals can be obtained by subjecting suitable precursors to the radio-frequency (RF) discharge produced by a Tesla coil. Rose's method[6] is briefly reiterated here. The set-up is shown schematically in Figure 2.1.2.

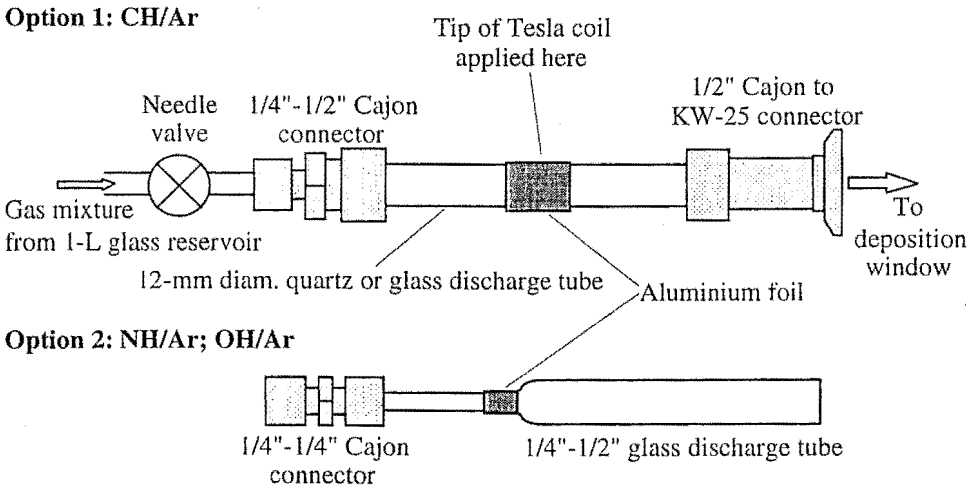

Figure 2.1.2: Schematic diagram of experimental apparatus employed to prepare XH/Ar (X = C, N, O) using the RF discharge from a Tesla coil.

A calibrated needle valve sets the flow rate of the ~1:100 precursor:Ar mixture from the 1-L glass reservoir to ~5 – 6 mmol hr^{-1}. The mixture then passes through a

quartz or glass discharge tube where it is subjected to the RF radiation produced by a Edwards High Vacuum Model TI Tesla coil. The RF discharge is sufficient to create a weak Ar-resonance radiation field inside the tube, which dissociates the precursor molecules, yielding (amongst other products) the desired radical monohydride. (The presence of other products is not a problem, because the electronic spectra are non-overlapping.)

The ~5 – 6 mmol hr^{-1} deposition rate is considerably higher than the optimum 1 – 2-mmol hr^{-1} rate for matrix preparation, but is necessary for the discharge to be sustained. Although matrices of poorer optical quality result (due to scattering of light — particularly in the UV), circularly polarised light is not depolarised (Section 1.2.4.1), so they are satisfactory for MCD studies.

Use of a microwave discharge instead of the Tesla-coil discharge was a failure, suggesting that the former is too harsh, resulting in atomisation of the precursor. Blackening in the quartz or glass discharge tubes (presumably due to deposition of elemental carbon) provided possible evidence for atomisation when CH_4:Ar and C_2H_2:Ar mixtures were used.

2.1.2. C_{60}^+ and C_{60}^-/Ar

Simultaneous production of the singly charged ions of C_{60} in an Ar atmosphere at low pressure was undertaken using the method of Gasyna, Andrews and Schatz.[7] The apparatus employed is pictured schematically in Figure 2.1.3.

C_{60} powder is sublimed at ~450 °C (under vacuum) by electrical heating in a quartz or glass Knudsen cell in the Knudsen oven. The cell is shown in cross-section in Figure 2.1.3, and is made from two pieces of tubing (one nested inside the other) sealed but for a small hole through which the sample effuses toward the deposition region (Section 2.2). The quartz Ar inlet passes through the centre of the cell (Figure 2.1.3). The cell temperature is determined approximately using the chromel-alumel thermocouple that lies inside the quartz-sheathed nichrome-wire heater coil. The current passed through the nichrome heater is controlled by a Variac.

A calibrated Whitey needle valve is employed to control the flow of Ar gas (~1 – 2 mmol hr^{-1}) from a 1-L stainless-steel reservoir. The Ar passing through the quartz discharge tube is subjected to a microwave discharge in the Evensen cavity, immediately prior to entering the Knudsen oven. Microwave radiation is produced by a 200-W

Electro-Medical Supplies Microtron 200 supply, run at full power. The discharge is tuned so that the Ar-resonance radiation is still being produced as the Ar expands out of the end of the quartz tube. Thus the VUV radiation is sufficiently intense to ionise C_{60} before deposition occurs on the cryogenically cooled sample window. C_{60} also acts as the electron trap (electron affinity[8] of 2.60 eV), forming C_{60}^-.

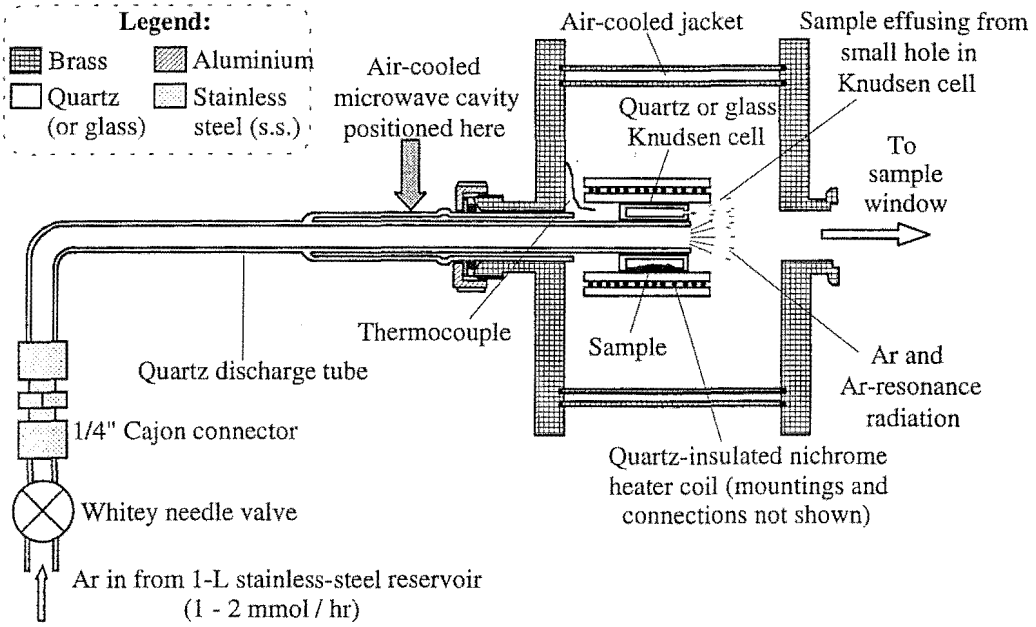

Figure 2.1.3: Simplified schematic cross-section of the Knudsen oven and discharge tube used to produce gaseous C_{60} ions.[7]

2.2. Matrix-isolation/magnet systems

The two matrix-isolation systems used in this research are described in the subsections below. Since both are bulky, heavy and need to be incorporated in the spectrometer (Section 2.3), a trolley system was developed which enables easy interchange. The two trolleys occupy the niche in the spectrometer's optical bed, shown in Figure 2.3.1 on page 42, and are positioned accurately on steel rails. The spectrometer's sample beam passes through an axial bore in each of the magnets, so that the magnetic field lies along the direction of propagation of the light, as required for MCD (Section 1.3.2).

2.2.1. He-refrigerator/electromagnet system

In this laboratory, a closed-cycle He refrigerator and electromagnet have been combined, primarily to provide an economical matrix-isolation/MCD apparatus that can

be used routinely to optimise matrix-deposition conditions.

An APD Cryogenics Inc. closed-cycle He refrigerator (comprising a HC-2D compressor and a Displex DE-202 expander) is employed, which is capable of cooling to ~12 K. The expander is shown in Figure 2.2.1, along with the modified DMX-IE shroud used for matrix-isolation spectroscopy. The vacuum is provided by a Pfeiffer Balzers TSH172 170-L s^{-1} turbo-molecular pump.

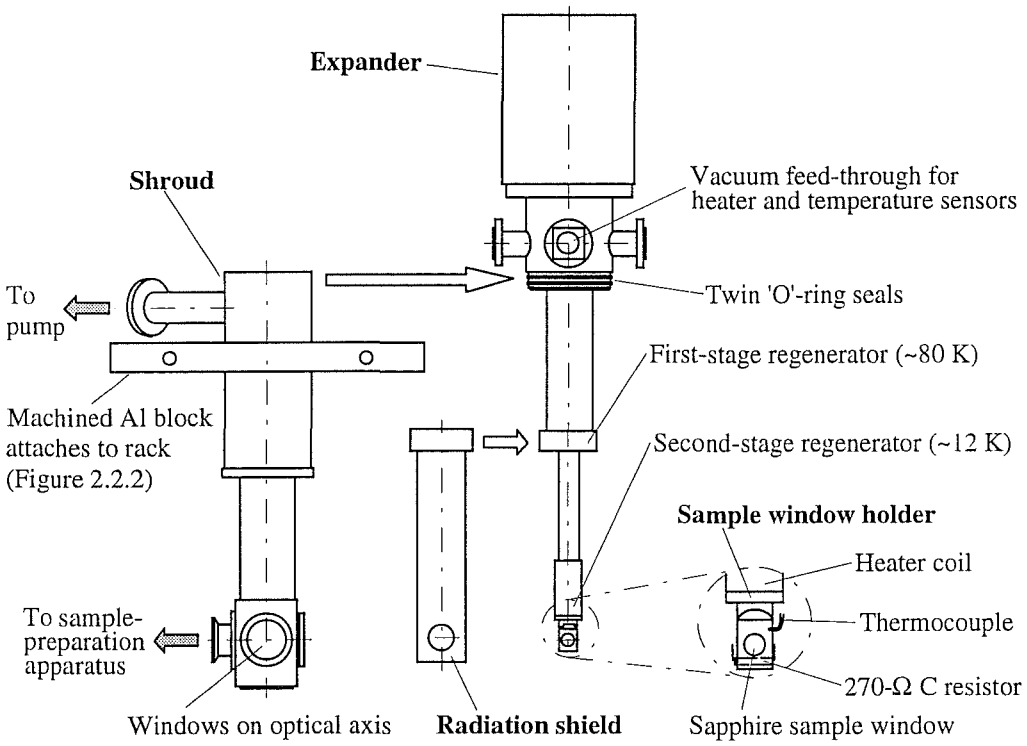

Figure 2.2.1: Simplified diagram of Displex DE-202 expander and modified DMX-IE shroud, showing detail of the sample window.

A *c*-cut sapphire sample window (~9-mm diameter) is mounted in a copper holder (Figure 2.2.1) attached to the second-stage regenerator of the expander unit, where the temperature reaches ~12 K. Thermal contact between the window and the holder, and between the holder and the regenerator, is facilitated through use of indium metal gaskets.

Two temperature sensors are used. An Au/.07%-Fe versus chromel thermocouple is pressed into a hole in the Cu block with some crycon grease for good thermal contact. It is connected to the 'Sensor 1' input of an Oxford Instruments ITC4 intelligent temperature controller (see below), which displays the temperature in Kelvin according to the programmed calibration. The thermocouple is useful over the whole temperature range (*i.e.* from room temperature to cryogenic temperatures), but is not

referenced, so drifts slightly (~2 K) with ambient temperature variations.

A carbon resistor (nominally 270 Ω) is fitted snugly into the copper block. Its temperature is determined from its resistance (measured with a digital multimeter) using a calibration curve. Carbon resistors are generally only useful below ~100 K because R changes very little with T at higher temperatures.

A nichrome-wire heater coil (resistance ~37 Ω) is used to obtain temperatures above ~12 K, and replaces the original printed-circuit heater that was burnt out (see below). Layers of teflon tape electrically insulate the heater coil from the copper body of the regenerator, and from other wiring.

Temperature control using the ITC4 is straightforward. In automatic mode, after setting the desired value on the instrument's front panel, it supplies current to the heater, while monitoring the temperature *via* the thermocouple (Sensor 1 input). Hence the ITC4 maintains the temperature through a feedback path. Similarly, if a lower temperature is set (limited by the refrigerator's cooling ability), the ITC4 reduces the current to the heater appropriately. If it is required that the temperature be accurately known, the resistance of the carbon sensor is measured. Note that large increases in temperature (>10 K) should be avoided, because the ITC4 will put a high current through the heater, which may burn it out (as occurred with the original heater). Changes should be made in small increments, so that the rate of increase of current output by the ITC4 is slow. This is also preferable to sudden temperature increases if sample integrity is to be maintained.

The chrome-plated Cu radiation shield shown in Figure 2.2.1 is held at ~80 K by the first-stage regenerator. In addition to shielding the colder second-stage regenerator from ambient IR radiation, it also protects the sample window from unwanted depositions while the Knudsen cell is being brought up to temperature.

The refrigerator's shroud is also shown in Figure 2.2.1, facing in the direction of the incident light. A vacuum port was added to the shroud, which enables the expander to be rotated once the shroud is fixed in position. Twin 'O'-rings on the expander's skirt prevent air leaks when the system is evacuated. Matrices are prepared at right angles to the optical path, as indicated by the KW-25 connection to the sample-preparation assembly (Section 2.1).

Figure 2.2.2 shows the combined refrigerator-electromagnet assembly used in this work. The refrigerator's shroud (and, consequently, the expander) is held firmly in

place on the carriage by machined aluminium blocks (see also Figure 2.2.1). The carriage allows the sample window's horizontal position to be adjusted, or completely removed from the light path. (The latter is often limited, however, by the gas- and vacuum-line connections to the shroud.)

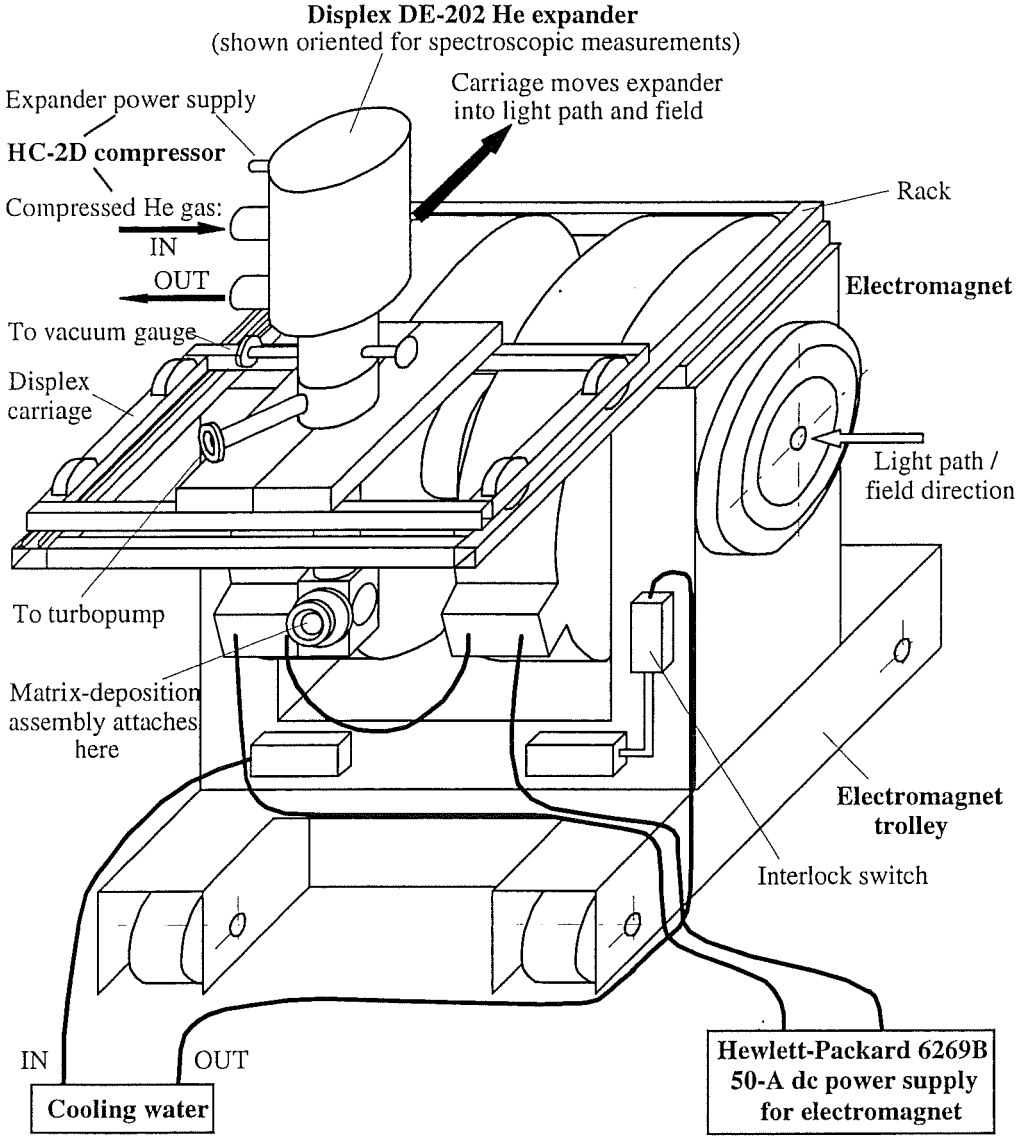

Figure 2.2.2: Simplified diagram of the APD Cryogenics Inc. Displex DE-202 He expander and Alphamagnetics 4800 electromagnet system.

The electromagnet is an Alpha Magnetics Inc. 4800 U-frame electromagnet, with pole caps removed so that MCD spectra can be obtained (Section 1.2.2). The magnet is rated for a maximum current of 50 A, which is supplied by a reconditioned Hewlett Packard 6269B 50-A, 40-V dc power supply. Since the magnet is water cooled, an interlock switch has been placed on the cooling-water return line to cut off the magnet power supply if there is no coolant flow. As mentioned in the introduction to Section

2.2, the trolley on which the electromagnet sits is designed for ease of incorporation into the spectrometer (Section 2.3).

In this work, the magnetic field has generally been determined from a calibration plot of the magnet current versus field for the pole gap used in experiments (the width of the expander shroud and windows). Calibration of the field was made over the entire current range using a Group 3 DTM-141D Digital Teslameter placed at the position of the sample window (the point of highest field). The field is reasonably homogenous in the region of the sample. (More recently, Mr. Barry Prince has calibrated a Hall probe for measurement of the field during an experiment. Nevertheless, use of the Hall probe requires that the expander/shroud carriage be shifted.)

Using the refrigerator to prepare matrices is relatively straightforward. The system is first pumped down to ~10^{-5} Torr, before the refrigerator is turned on (having ensured that the cooling water is also on). After about an hour, the temperature is <15 K, and a short while longer is required to reach ~12 K. Matrix deposition is then undertaken, after rotation of the expander through 90° to face the preparation apparatus (Section 2.1). It is important that the electromagnet has no current flowing while matrix deposition is proceeding, because the field can greatly affect the efficiency of discharges. The effect of variation of experimental conditions can be monitored easily using this system, because further depositions are easily carried out after a spectrum has been run.

The refrigerator-electromagnet system provides a very economical way to investigate the MCD of matrix-isolated species above ~12 K, with fields of up to ~0.7 T. However it suffers from two limitations relative to the matrix injection system discussed in the next section: (i) it cannot cool to the very low temperatures where MCD temperature dependence is most marked; and, (ii) it cannot provide the high fields often desirable for MCD. A significant disadvantage of the closed-cycle He refrigerator in MCD is that the sample is in a vacuum, so that it is very difficult to measure the temperature of the sample itself (as opposed to that of the refrigerator head) accurately, or to be sure that the sample is isothermal. Hence, the refrigerator cannot be used for quantitative investigation of temperature dependence. For non-temperature-dependent molecules, it may prove quite satisfactory. Nevertheless, the system's greatest utility lies in its ease of use for preliminary studies before the matrix injection system is used.

2.2.2. Matrix injection system

The matrix injection system, used to obtain the majority of the experimental data presented in this thesis, employs an Oxford Instruments CF1204 continuous-flow cryostat and SM4 superconducting cryomagnet (0 – 6 T). Although it has been described in detail previously by Dunford,[9] a brief description is made here. Figure 2.2.3 shows a schematic diagram of the apparatus, the beneficial features of which have been noted early in Chapter 1.

The matrix is first prepared in the CF1204, before being injected into the SM4 for spectroscopic investigation. The sample-preparation apparatus is attached *via* a KW-25 adaptor on the CF1204, and the cryostat pumped down to $<10^{-5}$ Torr using a Pfeiffer Balzers TSH172 170 L s^{-1} turbo-molecular pump. Active cooling of the sample window is achieved by drawing liquid He through the siphon (long sample rod) with a Compton D/189 flow pump. The flow is controlled by an Oxford Instruments VC30 flow-control console, and the temperature reaches <20 K in <30 minutes. Matrix preparation is then undertaken (Section 2.1).

Injection of the matrix into the sample chamber of the SM4 cryomagnet — which has been kept under vacuum by a Edwards High Vacuum Hg-vapour diffusion pump (Speedivac EO8, backed by a rotary pump) or a Pfeiffer Balzers TPU170 170-L s^{-1} turbo-molecular pump — occurs once the gate valve is opened. During the injection process, the first pump is used to evacuate the space between the twin 'O'-ring seals to the siphon at the top of the CFC to prevent air entering the CFC and, consequently the sample chamber. Meanwhile, the second pump maintains the vacuum in the CFC and the SM4 sample chamber. An absorption spectrum is run to assess the sample quality — if it is good the liquid He flow through the sample rod is shut off since the sample is in the cold environment of the sample chamber. Evacuation of the sample chamber is no longer necessary, and cold He gas or liquid He are siphoned into the chamber from the main reservoir of the SM4 (see below). Spectroscopic investigation begins once the current has been placed in the superconducting magnet, using the Oxford Instruments PS75 magnet power supply and SG3 sweep generator. The field is read in tesla from a digital readout constructed at the UoC. (If the matrix is poor, the siphon is carefully pulled up out of the magnet, the gate valve closed, and the rod allowed to warm up to room temperature. Using this apparatus, the matrix must be prepared in one deposition only, unlike the refrigerator.)

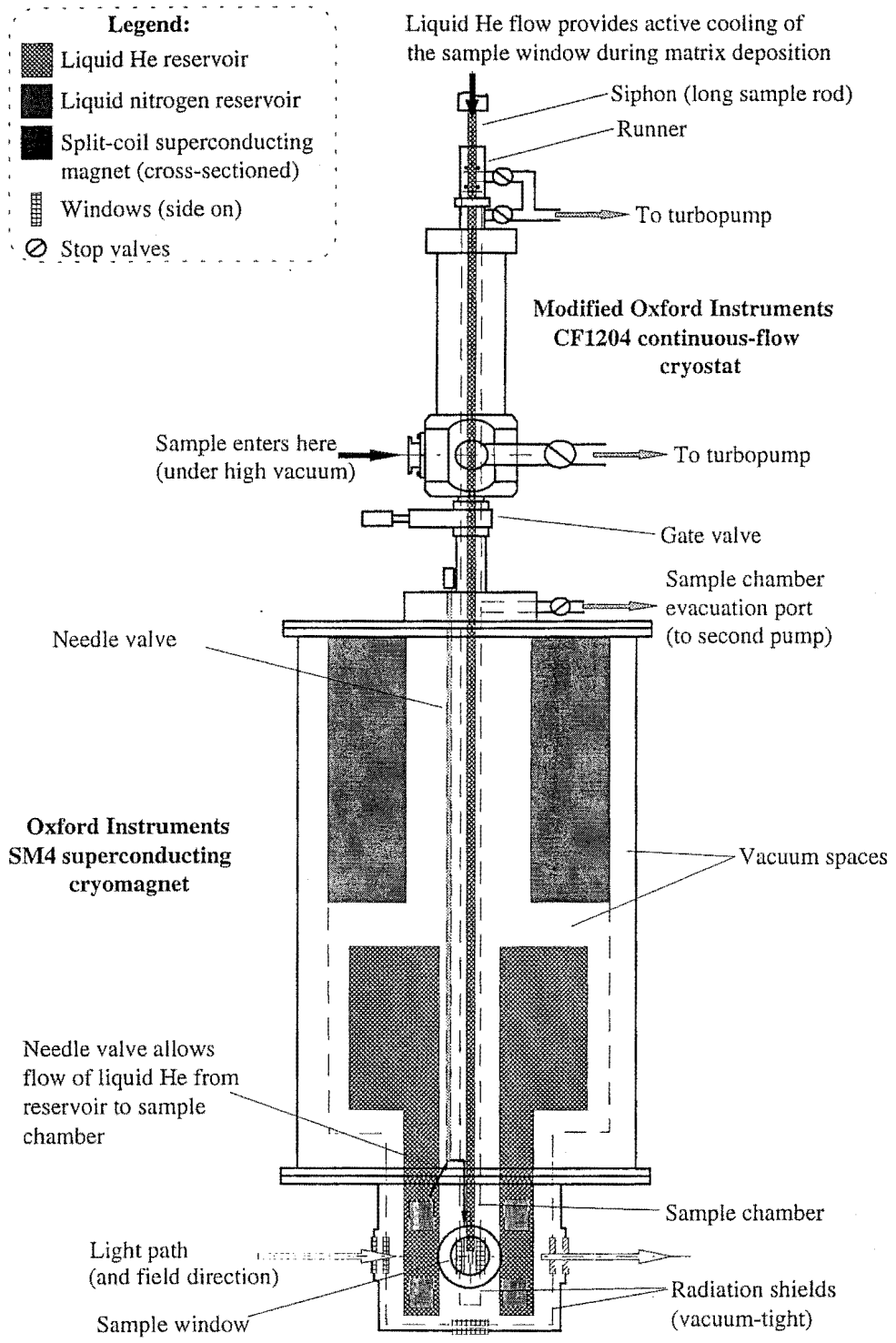

Figure 2.2.3: Schematic diagram of the matrix injection system, comprising a modified Oxford Instruments CF1204 continuous-flow cryostat and an Oxford Instruments SM4 superconducting cryomagnet.

Temperature dependence of the MCD (and absorption) is studied as follows. Firstly, spectra are obtained for temperatures above 4.216 K (b.p. of liquid He), by bleeding cold He gas from the liquid He reservoir into the sample chamber through the needle valve. The high thermal conductivity of He, and careful control of the rate at

which He comes through the needle valve (by adjusting the pressure in the sample chamber), ensures that the sample temperature is consistent for the time required to gather the spectrum. The sample temperature is determined from the resistance of a calibrated carbon resistor that lies just above the sample window on the siphon.

Temperatures at and below the boiling point of liquid He are obtained as follows. The sample chamber is flooded with liquid He from the reservoir *via* the needle valve. At 4.216 K, the vapour pressure is 1 atm. Lower temperatures, down to ~1.4 K, are achieved by pumping on the liquid with a 450-L min^{-1} Welch 1397 rotary-vane pump. An Oxford Instruments MNT manostat maintains the pressure in the chamber using mechanical feedback, while the pressure is measured using a 1000-Torr MKS Baratron capacitance manometer (type 622A13TAE). The sample temperature is easily, and precisely, calculated from the well-known relationship between the He vapour pressure and temperature.[10] In some experiments bubbling occurs between the λ-point of liquid He (2.174 K) and the boiling point. This effect ruins the absorption spectra, but fortunately, because of the way it is measured, the MCD is unaffected.

Since the completion of Dunford's work,[9] the CF1204 has been replaced by a laboratory-built matrix-isolation chamber, shown schematically in Figure 2.2.4. (The reason for making this replacement was to free the CFC for other uses to which it is more suited, such as accurate temperature-dependence runs above ~12 K.) CH/Ar and $C_{60}^{\pm}$/Ar data were obtained using the new chamber (Chapters 6 and 7, respectively).

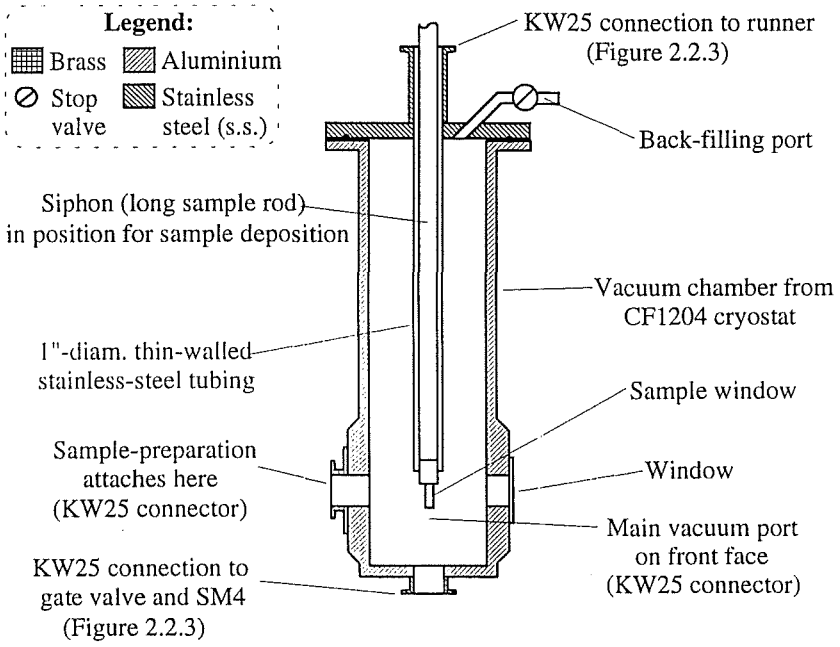

Figure 2.2.4: Schematic cross-section of the second matrix-isolation cryostat used in this work.

The matrix injection system allows very precise temperature-dependent MCD and absorption studies to be made, and also offers the high fields of a superconducting magnet. Neither of these are possible using the refrigerator/electromagnet apparatus (Section 2.2.1). Its major drawbacks relative to the refrigerator/electromagnet system are the high running cost and more difficult matrix preparation.

2.3. High-resolution simultaneous MCD/absorption spectrometer

2.3.1. Introduction

In Section 1.3.3 it was noted that the MCD (ΔA) signal is usually weak relative to the absorption. In order to obtain good S/N, it is wise to perform the experiment at a frequency (f) where background $1/f$ (or 'flicker') noise is minimised; *i.e.* at high frequency. This is accomplished by using a photoelastic modulator (PEM; Section 2.3.5.2) which modulates the light's circular polarisation at a frequency of ~50 kHz. Phase-sensitive detection, in the form of a lock-in amplifier (LIA; Section 2.3.8), is used to extract the MCD. Further signal enhancement is also obtained by increasing the magnetic-field strength, and superconducting magnets are now commonly employed. (They have the added advantage that they are more compact than conventional electromagnets.[11,12])

The mating of MCD and matrix isolation (MI-MCD; Chapter 1) was first achieved by Douglas *et al.* in the early 1970s.[11] Since the composition of matrices is liable to change with time, the development of a spectrometer capable of acquiring simultaneous absorption and MCD data was critical to the furtherance of MI-MCD. This was achieved by Collingwood *et al.*[13] at Oxford University at a similar time. Their spectrometer produced double-beam absorption spectra *via* logarithmic amplification of the reference signal, while the sample output level was kept constant through a feedback loop to the photomultiplier power supply. Circular-polarisation modulation was performed using a PEM (Section 2.3.5.2), and the MCD was extracted using a phase-sensitive detector. Spectra were recorded on chart paper.

Two simultaneous MCD/double-beam absorption spectrometers were built in the early 1980s at the University of Virginia[14] following the original design of Collingwood *et al.*[13] These instruments made use of the major advances in electronics and computer technology, with the data being accumulated on a Digital PDP 11/38 mini computer

after analogue signal processing.[14] The first, MOD1, was an extensively modified Jasco ORD/UV-5 ORD spectrometer, and of low resolution. MOD2 came later, and was a high-resolution purpose-built instrument.

More recently, Kenney and co-workers[15] at Eastern New Mexico University have developed a spectrometer that uses three LIAs. One is employed to extract the MCD in the standard manner (Sections 1.3.3 and 2.3.8), while the absorption is obtained with the other two. A two-section mechanical chopper produces the 'sample-minus-dark' and 'reference-minus-dark' signals at two different frequencies, and a LIA is devoted to accumulating each of these. A major advantage of the spectrometer is the improved absorption S/N afforded by LIA detection.

The first simultaneous MCD/spectrometer built at the University of Canterbury (MOD3) was of similar design to MOD1 and MOD2.[16] Like MOD1, it used a converted Jasco ORD/UV-5 ORD spectrometer, although its electronics were slightly more modern. Although MOD3 performs extremely well, and has been utilised in a number of studies of broad-band spectra,[9,16-19] it has a number of significant limitations which make it unsuitable for use in the work described in this thesis. The limitations include:

1. low resolution of the Jasco monochromator;
2. limited spectral range (180 to 800 nm);
3. reliance on analogue electronics to perform data acquisition and manipulation;
4. bias toward MCD in preference to absorption (short reference beam period).

Matrix-isolated species, such as NH (Chapter 5), give sharp-band spectra that require a spectrometer capable of higher resolution than that provided by MOD3. A wider spectral range is also desirable, and is a necessity for investigation of the near-IR (NIR) spectra of C_{60}^{+} and C_{60}^{-} (Chapter 7). To this end a high-resolution double-beam (M)CD/absorption spectrometer (MOD 4) was designed and constructed as part of this research project.

A wider spectral range (from the NIR to the UV) is achieved by employing a 1-m Czerny-Turner scanning monochromator with interchangeable diffraction gratings (Section 2.3.3), light sources (Section 2.3.2) and detectors (Section 2.3.7). The monochromator also gives MOD4 much greater spectral resolution than MOD3, while absorption S/N is much improved because the sample- and reference-beam sampling

periods are of the same duration. New digital techniques for data acquisition (taking advantage of the increased computing power of the mid-1990s; Section 2.3.10) obviate the necessity for much of the peripheral electronics required by the older instruments. Another significant difference is that unlike most earlier spectrometers, the sample signal is *not* maintained at a constant level by feedback circuitry. When the sample current is constant, the (M)CD is directly proportional to the ac signal level on the PMT output. Here, the sample voltage is allowed to vary, and the (M)CD is calculated digitally; the ac signal is divided by the 'sample-minus-dark' voltage for that wavelength. This method hence reduces the peripheral electronics, although Policke *et al.*[20] have shown that the sensitivity is reduced relative to the other method. (They suggest that this is because the logarithmic gain characteristic of the photomultiplier is not used.)

2.3.1.1. MOD4

Figure 2.3.1 shows a schematic diagram of MOD4. The optical table has been designed to interchangeably accommodate a superconducting magnet or an electromagnet (Section 2.2). The light from one of two sources is dispersed by the monochromator (Jarrell-Ash 78-463), then passed through a crystal polariser, to the PEM. Light is modulated between left and right circular polarisations by the PEM at a frequency of ~50 kHz. The beam is then mechanically chopped, allowing light to pass into the 'sample' and 'reference' paths during each cycle. The sample beam passes through an axial hole in a magnet, where the sample is mounted, and then to the detector. The reference beam is diverted around the magnet to the detector. Twice per cycle, a black region on the chopper prevents any light from reaching the detector, thus allowing determination of the detector 'dark' current. The output signal from the detector is then processed by electronics and accumulated by the computer.

2.3.2. Light Sources

2.3.2.1. UV/Visible: Xe-arc lamp

An ILC Technology LX300UV Xe-arc lamp (10 – 22-A power supply) is used for UV/visible studies. The user is protected from ultraviolet light and ozone (the product of oxygen photolysis at $\lambda < 190$ nm) by shielding the lamp with an aluminium hood. Air blown through the hood by a box fan acts to cool the lamp. The ozone-

contaminated air is then drawn away by a second more powerful fan and exhausted through an outside window.

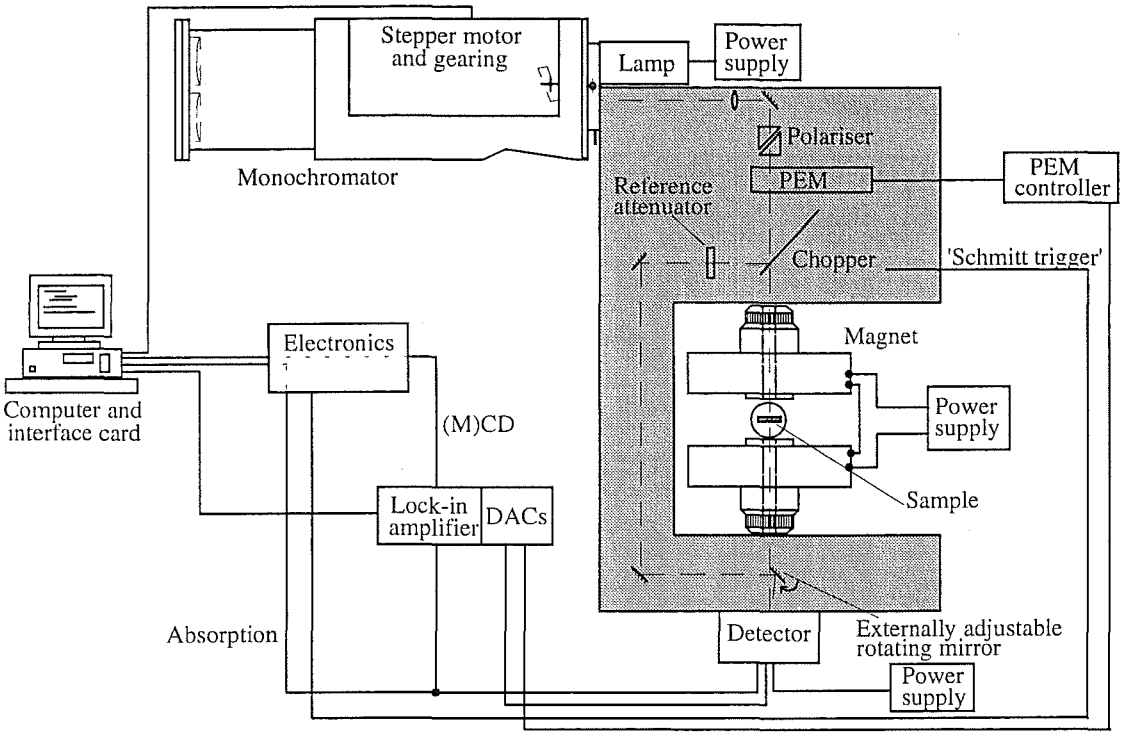

Figure 2.3.1: A schematic diagram of the MOD4 spectrometer, shown with the electromagnet in position (Section 2.2.1).

The Xe-lamp mount allows left-right and up-down adjustment relative to the monochromator entrance-slit housing. Maximum light throughput is obtained when the lamp is off centre, because one of the lamp electrodes lies in front of the discharge, causing a black spot to appear at the centre of the image when the light is collimated subsequently.

The electrical discharge through high-pressure Xe is accompanied by an inherent flicker, which adversely affects S/N. This problem is alleviated by the acquisition of multiple samples at each wavelength.

2.3.2.2. Visible/near-IR: Tungsten lamps

Two makes of tungsten-quartz-halogen lamps can be used with MOD4. The first is a 110-V, 1000-W Sylvania lamp. Unfortunately, the power supply (constructed at the University of Canterbury) could only provide ~800 W (due to a current limit of ~8 A) and was insufficiently regulated, causing small 50-Hz fluctuations in lamp intensity. Moreover, the large amount of radiant heat that was produced by the lamp led to cooling

problems.

Since, for a given colour temperature, the brightness of a tungsten lamp is independent of its total power (the filament size varies as the reciprocal of the power), it was decided to use a smaller lamp. A 24-V, 250-W tungsten-quartz-halogen lamp (Osram or Philips) was found to provide at least as much throughput as the 1000-W lamp, while reducing power consumption and heat radiation. A 24-V, 10-A line-and-load-regulated DC power supply was designed and built to run this lamp (the specifications and circuit diagram are given in Appendix A.1). The power output is regulated to within 0.25%.

Figure 2.3.2 shows the full tungsten-lamp assembly for the 250-W lamp. The lamp socket is attached to an aluminium mount, which allows lateral and height adjustment. The mount, in turn, sits on a rack that bolts directly onto the monochromator entrance-slit housing. The concave mirror behind the lamp collects and focuses light back to the filament, while the convex lens in front of the lamp focuses the light at the entrance slit. The positions of the lamp, mirror and lens can be adjusted by sliding them along two parallel slots in the rack in order to obtain optimum light throughput. A box fan blows cool air past the lamp, and the entire assembly is covered by an aluminium hood.

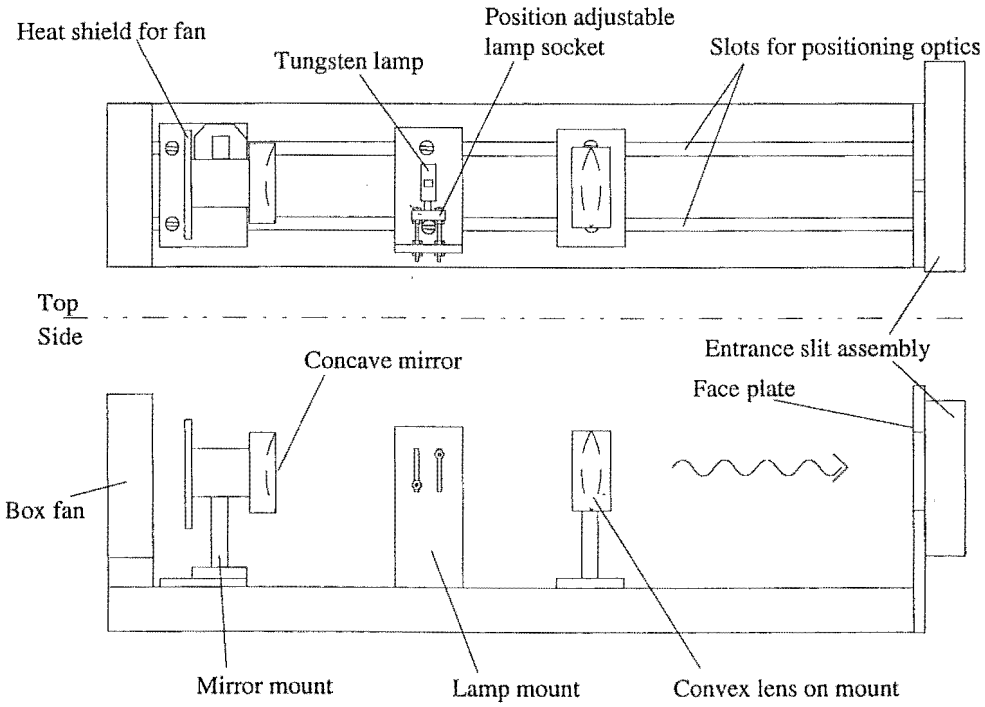

Figure 2.3.2: The rack for the W lamps (not to scale), showing in this case the mount for the 24-V, 250-W Osram or Philips lamp. The aluminium cover is not shown.

2.3.3. The monochromator

2.3.3.1. General

A Jarrell-Ash 78-463 Czerny-Turner scanning monochromator with 1-m focal length disperses the light using a diffraction grating. The Czerny-Turner optical layout is shown in many classical optics references discussing monochromators; see, for example, Ref. 21. Table 2.3.1 gives the optical specifications for this monochromator with the available diffraction gratings. The effective aperture ratio for 102 × 102 mm gratings is f / 8.7.

The diffraction gratings are relatively easily interchanged, each being mounted in its own holder. However, each time they are changed a new wavelength calibration is required. The 0.3-μm-blaze grating has higher efficiency for wavelengths less than about 800 nm, while the 1.0-μm-blaze grating is used at longer wavelengths.

A dual unilateral entrance and exit slit assembly with curved jaws (model 78-472; 63.5 mm radius of curvature) is used on the monochromator. One adjusting screw controls both slits simultaneously, within the calibrated range of 0 to 400 μm. (Detector output signal increases quadratically as a function of slit width. Within experimental error, the observed signal at slit closure (0 μm) is the dark current, while from 10 μm useable signals are obtained for absorption studies.) At 10-μm slit width, there is no loss of (first-order) resolution for slit lengths less than 20 mm. The slit length is typically set to 10 – 15 mm.

Filtering of the higher-order diffraction and stray light is described in Section 2.3.4.

Table 2.3.1: Specifications for the monochromator with diffraction gratings available for use in this work.

Grating [a]	First-order reciprocal dispersion at exit slit	Blaze wavelength	Wavelength range employed
1180 groove/mm [b]	8.2 Å/mm	0.3 μm	250 – 800 nm
590 groove/mm [c]	16.4 Å/mm	1.0 μm	800 – 1500 nm

[a] Both gratings have a ruled area of 102 × 102 mm.

[b] Counter reading at first order corresponds 1:1 with wavelength at exit slit for the 1180 g/mm grating. (The accuracy is ±5 Å over any 6000 Å range.)

[c] Reading of counter at first order corresponds 1:2 with wavelength at exit slit for the 590 g/mm grating.

2.3.3.2. Scanning mechanism

(a) Modification from synchronous-motor drive to stepper-motor control

As originally supplied, the monochromator could be scanned either by a synchronous electrical motor drive or manually. Twelve scan speeds (0.5 to 2500 Å/min) could be selected through a system of planetary gears.

To allow computer control, the scanning mechanism was converted to stepper-motor control. A Sanyo Denki Step-Syn 10823708-5 stepper motor (6 V, 1.2 A, 1.8°/step) is used to drive the original planetary gears after passing through its own gear box. The motor rotates through 1.8° per voltage pulse, producing a wavelength step of 0.05 Å at a scan rate of 2500 Å/min, which decreases linearly as lower gear settings are selected. Manual override is available *via* a front panel switch, or by having the mains switch 'off'.

(b) Stepper-motor driver and controller electronics

In this section stepper-motor driver and associated control electronics are described briefly. Their circuit diagrams are given in Appendices A.2.1 and A.2.2, respectively. Their design utilises standard components and techniques, and therefore will not be covered in detail here. Instead a general description of the scan modes and relevant (to later discussions; *e.g.* Section 10.2.1.3) signals will be given.

The stepper-motor driver provides an interface between the low-current, TTL-level controller signals and the higher-current requirements of the stepper motor, and sets the scan direction by switching in the appropriate winding of the motor.

An 'enable' line allows current from the stepper-motor drive to pass to the motor itself. Even when the monochromator is not slewing the 'hold' current locks the stepper motor in position because the enable remains active. The hold current allows the stepper motor to stop rapidly (and precisely) even from high speed. The enable passes through microswitches at either end of the monochromator worm-drive (Section 2.3.3.1), preventing the grating drive mechanism from running off the end of the drive by providing an electrical cut-out to the stepper-motor driver when they close. (This is only a safety mechanism.)

A four-way switch provides the following slew options: (i) computer-controlled scans; (ii) manual override; and, (iii) increasing, and (iv) decreasing wavelength slews independent of the computer. Each of these will be described briefly below. The switch

has multiple poles for each position, passing the clock, direction and enable signals to the stepper-motor driver (except for manual control).

In computer-controlled mode, the clock signal (CLK1) provides the pulses for driving the stepper motor (*via* the driver), and consequently the count source (Section 10.2.1.3). 'CLK1 enable' is used to check on the status of the stepper motor through a digital input (D/I) channel (Section 10.2.1.2). A TTL-high level means a slew is in progress. 'Start' is an active-high TTL pulse supplied by the computer through a digital output (D/O) channel (Section 10.2.1.2). The direction is likewise set by a D/O channel, with a stable TTL-high or TTL-low level producing a slew in the direction of increasing or decreasing wavelength, respectively. (Data collection is always undertaken with decreasing wavelength in MOD4 (see part (c)).) 'Stop' is the active-low pulse output by the counter when the terminal count is reached (Section 10.2.1.3). These connections are given in Table 2.3.2.

In this mode the slew rate is ramped from a low start speed to a higher final speed, since the stepper motor has insufficient torque to start in the latter. The initial and final speeds, and the rate of ramping between, is set by RC time constants, with the pulse train generated by the voltage-controlled oscillator of the 4046 phase-locked-loop integrated circuit (Appendix A.2.2). The maximum scan speed is about ~2400 Å/min in the 2500 Å/min gear ratio, and is reached only for longer slews.

Table 2.3.2: Connections to the stepper-motor controller.

At stepper-motor controller		At PCL-814B interface card [a]	
Signal name	Pin number(s) on D9 connector	Module	Signal name; pin number(s) on appropriate connector
Clock (CLK1)	8	Timer/counter	SRC1; 7
Direction	4	A/D	D/O 4; 5
Start	5	A/D	D/O 2; 3
Status (CLK1 enable)	2	A/D	D/I 7; 8
Stop (OUT2)	1	Timer/counter	OUT2; 13
Ground (GND)	6, 9	A/D	GND; pins of 17, 18 on D/I & D/O
		Timer/counter	GND; 17

[a] See Sections 2.3.10.2 and 2.3.11.1 for details.

The manual-slew mode does not pass the enable, clock and direction signals to the stepper-motor drive (although the oscillator continues in its present state). Since the enable is off, the stepper motor's hold current is deactivated, and manual slewing can be undertaken. On returning the switch to the computer-controlled position, the hold current is passed to the motor, and the scan mechanism is locked in position.

Computer-independent slews do not utilise the speed-ramping circuitry used in the computer-controlled mode. Instead, the low-speed pulse train that furnishes the start speed for computer control is used to scan the monochromator continuously. The scan direction is also independent of the current computer-set state, as determined by the switch position.

(c) Backlash

The grating orientation, and hence the wavelength, is determined by a worm drive (0.635-mm pitch), for which the travel over the full range of the monochromator is 100 mm. The accumulated error over this range is less than ±30 μm (0.03%). The error over smaller ranges is correspondingly less, and does not significantly affect the spectra, as long as the appropriate precautions have been taken. The most important of these is the removal of backlash. For any practical gear system there is hysteresis (backlash) when the direction of rotation is reversed. The drive mechanism of a monochromator is especially susceptible to backlash because there are frequent direction changes; after a scan the monochromator must be slewed back to the start wavelength before the next spectrum is run.

Backlash must be removed before wavelength reproducibility over the entire spectral range is obtained. Otherwise, bands near the beginning of the spectrum will appear to be anomalously shifted toward those near the end.

There are two steps that are required to eliminate the problem. First, the monochromator should always be scanned in one direction during data acquisition. For MOD4, this direction has arbitrarily been chosen to be towards increasing light energy (shorter wavelength). Second, between spectra the spectrometer must be over-slewed by a predetermined minimum amount before the direction is changed, and the starting wavelength is reset.

The required over-slew was determined by measuring the wavelength errors in the absorption spectrum (535 to 515 nm) of a $Na_3[Nd(ODA)_3].2NaClO_4.6H_2O$ crystal[22] ($Nd(ODA)_3$) at room temperature for differing backlash compensations. The results indicated that an over-slew of 20 nm is required.

2.3.4. Optical filters

Filters are used with MOD4 for two reasons. First, stray light from the monochromator (Section 2.3.2) is a problem. Second, higher orders of diffraction are

also passed to the exit slit by the grating. Optical filters are used to reduce the effect of the former, and eliminate the latter.

2.3.4.1. Stray light

A continuum source of stray light arises from light scattering within the monochromator, particularly from the gratings. Such stray light reduces the measured optical density of a sample, because the detector is not wavelength selective. Its effect is greatest in the UV, where white light can be observed at the exit slits. To reduce the level of stray light, a Corning 7-54 filter is used for spectra in the range 230-380 nm. The transmission spectrum of the filter is given in Figure 2.3.3, and shows that it cuts out light in the 400 – 700 nm range, to which the PMT is very sensitive.

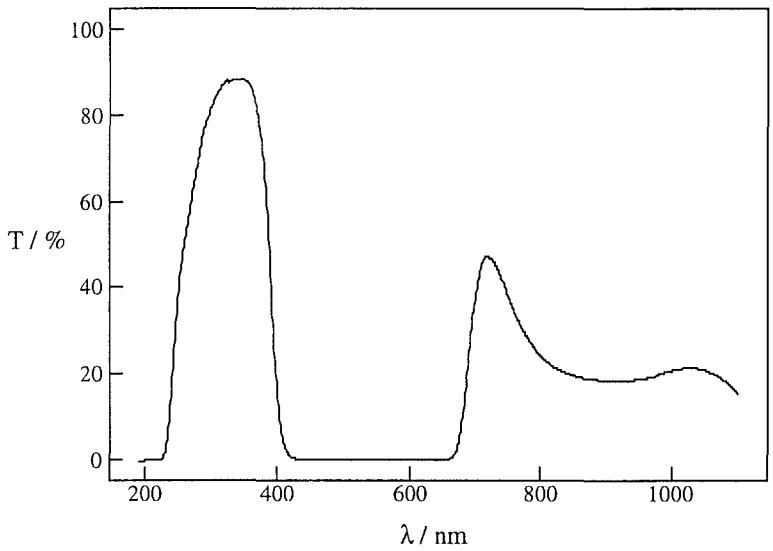

Figure 2.3.3: Transmission profile of the Corning 7-54 filter, used to reduce stray light effects in the range 250 to 380 nm.

2.3.4.2. Diffraction-order sorting

Diffraction gratings disperse radiation according to wavelength.[21] For a particular wavelength (λ), constructive interference occurs at a specific angles given by the equation $n\lambda = 2d\sin\theta$, where d is the distance between grating grooves and n = 1, 2, 3, ... is the order of diffraction. Hence for a given angle, in addition to first-order diffraction (n = 1) of wavelength λ_1, higher orders of diffraction ($n > 1$) also undergo constructive interference (with lower efficiency), having wavelengths given by $\lambda_n = \lambda_1 / n$. If the radiation leaving the monochromator is not filtered, erroneous results may result due to the response of the detector to these shorter wavelengths

In MOD4, only the first-order radiation is utilised, and the higher orders are removed by using cut-off filters, which have an effective order-sorting range of $\lambda_{cut\text{-}off}$ to $2\lambda_{cut\text{-}off}$. Since air absorbs radiation of wavelengths less than ~190 nm, it acts as an effective order-sorting filter for the range 190-380 nm (UV). For visible wavelengths, UV harmonics are filtered by an Esco Products GG-395 filter, while in the range ~660 – 1300 nm an Esco Products RG-665 filter is employed. The relevant transmission profiles are shown in Figure 2.3.4.

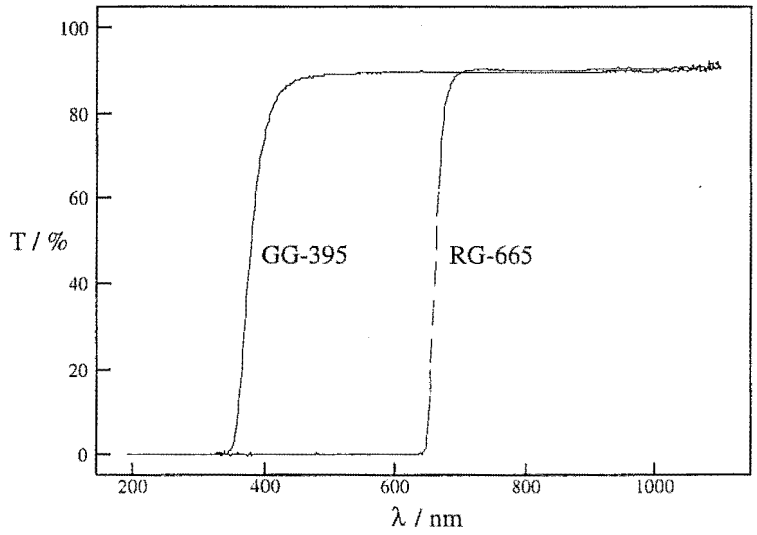

Figure 2.3.4: Transmission spectra of the Esco Products GG-395 and RG-665 cut-off filters, used to eliminate second- and higher-order diffracted light.

2.3.5. Polarisation optics

The light emerging from the monochromator is collimated by a convex lens (Figure 2.3.1), and then reflected along the main optical axis. Before circularly polarised light can be produced by the photoelastic modulator (PEM; Section 2.3.5.2), the light is plane polarised by a Glan-Taylor polariser.

2.3.5.1. Plane polarisation

A Melles-Griot 15-mm Glan-Taylor polariser is used to linearly polarise the light in the vertical plane. The Glan-Taylor method uses two calcite prisms, separated by an air gap and with internal faces at the Brewster angle. The 'ordinary' ray (O-ray) is reflected internally, and absorbed by the prism casing, while the 'extraordinary' ray (E-ray) is transmitted (Figure 2.3.5).

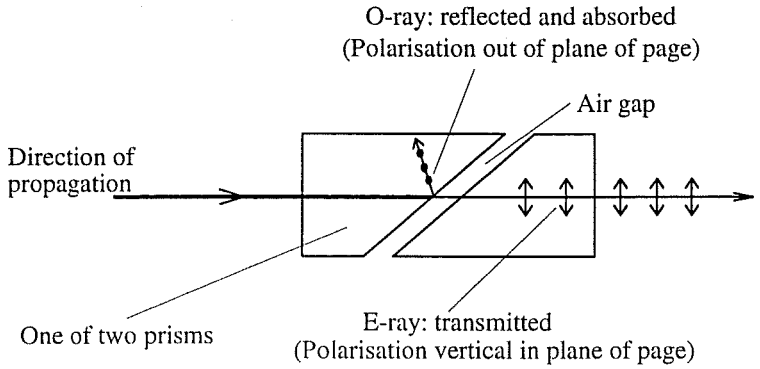

Figure 2.3.5: The principle of the Glan-Taylor polariser.

2.3.5.2. Production of circularly polarised light using the photoelastic modulator

A Hinds International PEM-80 photoelastic modulator (PEM) is used to modulate the light between left and right circular polarisations at a frequency of ~50 kHz. The basic principles of its operation are described below, followed by a discussion of its MOD4 application.

(a) PEM: Principles of operation

The PEM utilises the photoelastic effect, in which a mechanically stressed transparent medium exhibits birefringence proportional to the strain it experiences.[23] (Birefringence is the phenomenon where different polarisations of light travel at different speeds through a medium.) PEMs are resonant devices, whose birefringence oscillates at a fixed frequency (~50 kHz for the PEM-80). Advantages such as wide acceptance angle, large aperture and wide spectral range (160 to 2000 nm at quarter-wave retardation) make the PEM an attractive instrument when compared to older methods, such as Pockels cells, and quarter-wave plates. It is also readily incorporated into computer-controlled instruments[14] and is more reliable.[13]

The PEM-80 consists of a fused-silica optical element attached to a quartz-crystal piezoelectric transducer (Figure 2.3.6(a)).[23] When a voltage is applied to the piezoelectric transducer by the driver circuit (control unit) the bar vibrates along its long axis, as shown in Figure 2.3.6(b), with an amplitude determined by the voltage. The frequency of the oscillation in the fused silica (to which the quartz crystal is also matched) is determined by the length of the bar and the speed of a longitudinal sound wave propagating through fused silica.

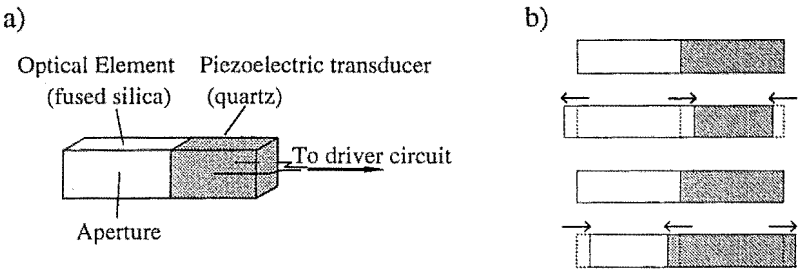

Figure 2.3.6: (a) PEM optical assembly, and (b) the PEM crystal's vibrational motion.

The control unit is matched to a particular PEM head (containing the optical element), with its electronic circuitry tuned to produce a reference frequency equal to the resonance frequency of the crystal, and the correct voltage amplitude for the required birefringence at a given wavelength. (The voltage required is linearly proportional to the wavelength.[23]) The reference signal is used for detection of the (M)CD using the lock-in amplifier (LIA; Section 2.3.8.1).

If the instantaneous length of the resonating optical element is compressed with respect to its unstressed dimension, the polarised light that lies along the 'long' axis (the horizontal component) will travel faster then the vertical component. On the other hand, if the crystal is extended, the horizontal component travels slower than the vertical one. In both cases birefringence causes a retardation of one polarisation with respect to the other.

In (M)CD, the PEM crystal is oriented at 45° to the plane polarised light (Section 2.3.5.1), so that the latter has equal projections onto the 'vertical' and 'horizontal' axes of the crystal. With the voltage across the transducer set to the quarter-wave value for the incident wavelength (half the dial reading on the control unit), the fused silica alternately causes the horizontal component to lead then lag the vertical component by a maximum of one-quarter wavelength as the light exits the crystal. At the crystal's vibrational extrema circularly polarised light is produced, because only at those points is quarter-wave retardation occurring. At one extreme the polarisation vector traces a right-hand helix about the optical axis (rcp; Figure 2.3.7(a)), while at the other the light traces a left-hand helix (lcp). In between the extrema, linear and elliptical polarisations are produced, as shown schematically in Figure 2.3.7(b). Notice that only the circular polarised light is modulated at 50 kHz, so the detection will be selective (Section 2.3.8.1).

Linear dichroism can also be studied using the PEM at 90° to the plane

polarisation (instead of 45°) and half-wave retardation. Modulated vertically and horizontally polarised light is produced in this configuration.

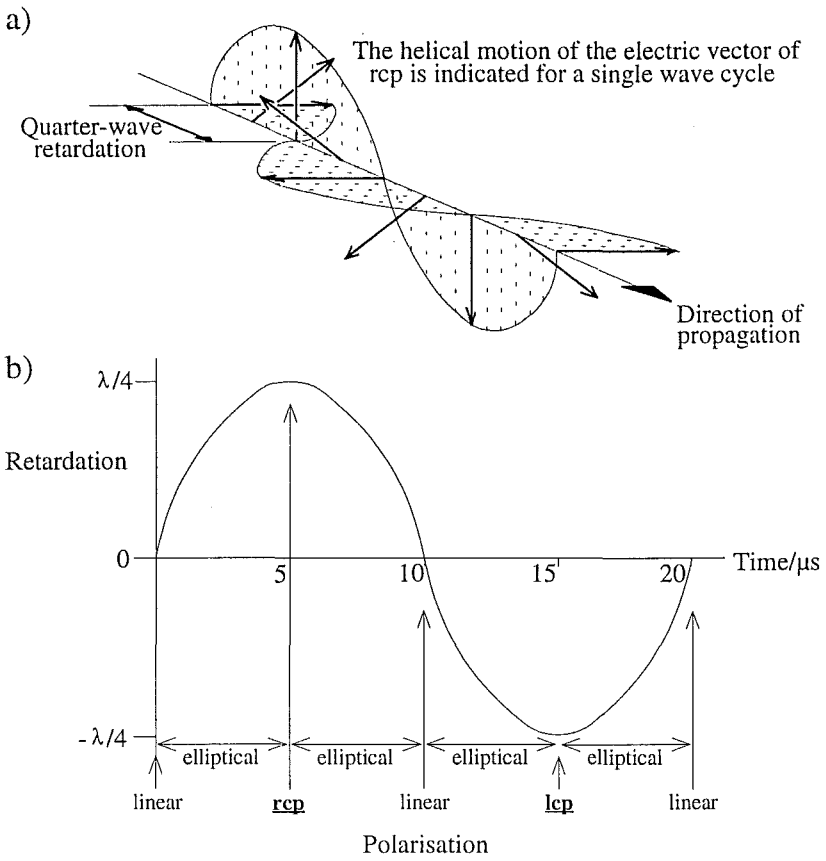

Figure 2.3.7: Production of circularly polarised light by a PEM; (a) the formation of rcp light using quarter-wave retardation, and (b) polarisation changes with time for quarter-wave retardation.

(b) Practical application in MOD4

Remote setting of quarter-wave retardation, *via* application of an analogue voltage to the PEM-80 controller (in 'remote' mode), allows the spectrometer's computer to adjust the retardation automatically as a scan proceeds. The required voltage is of such a level that standard digital-to-analogue converters (DACs) can drive it without amplification.

In MOD4, DAC channel 'X5' of the SR510 lock-in amplifier (Sections 2.3.8) is used to set the retardation at each step. The DAC full scale output is +10.24 V, and as a consequence can automatically set the quarter-wave retardation over the spectrometer's entire spectral range. The DAC is incremented bit-by-bit to the required voltage, to avoid sudden voltage changes that risk damage to the optical element.

Calibration of the remote voltage setting for quarter-wave retardation was

relatively straightforward. Measurement of the voltage output of the 'local'-mode potentiometer versus wavelength was made, and the resultant linear fit incorporated into the spectrometer software for remote programming.

2.3.6. Sample and reference beams

For measurement of absorption, it is preferable that a double-beam configuration be used.[13,14] The beam of light is split, whether by chopper or more sophisticated beam splitter, around sample and reference paths. Further, it is desirable to have a measure of the detector's dark current, which can be subtracted from the sample and reference signals. In the IR this is particularly important, due to high background-radiation levels, and detectors which generally have higher dark currents. It also eliminates effects due to a detector's preamp offset or drift. (Single-beam absorption spectrometers require multiple scans under identical conditions, followed by mathematical manipulation, to yield the absorption spectrum.)

MOD4 uses a mechanical chopper to split the beam alternately between the sample and reference paths, as well as giving a dark signal between each of these periods. The chopper is aligned so that the reference beam is deflected at 90° to the sample beam (Figure 2.3.1).

The electronics and software described in Sections 2.3.9 and 2.3.11 enable the sample's absorption to be calculated digitally.

2.3.6.1. The chopper and optical-interrupter circuitry

MOD4's chopper (Figure 2.3.8(a)) has a rotational frequency of ~11 Hz. The sample beam passes through unobstructed, the reference beam is deflected by the mirror, and the detector's dark current is obtained through absorption of light by the blackened metal strip. Available sampling times for each region are discussed in Section 2.3.9.1. Synchronisation of data collection with chopper position is achieved by using gates generated from the TTL output of an optical-interrupter circuit mounted over a slotted disk (Figure 2.3.8(b)) on the same shaft as the chopper (Figure 2.3.9). Manipulation of the signal to produce the sampling gates is described in Section 2.3.9.1.

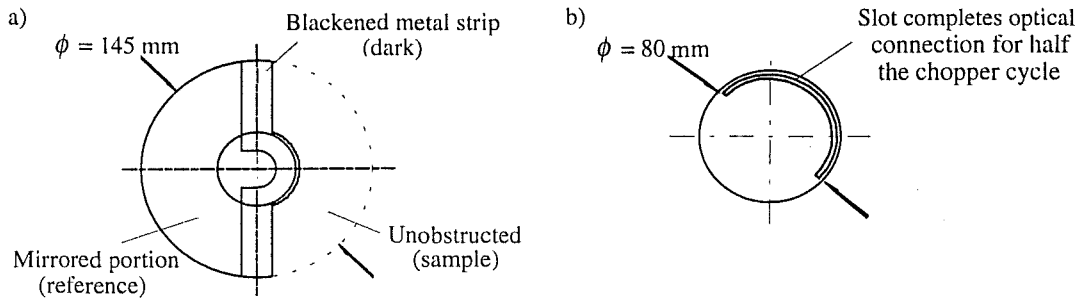

Figure 2.3.8: (a) Chopper layout for MOD4 (the rotational frequency is ~11 Hz). (b) The aluminium disk which, together with the optical interrupter (Figures 2.3.9 and 2.3.10), allows generation of sampling gates (Section 2.3.9.1).

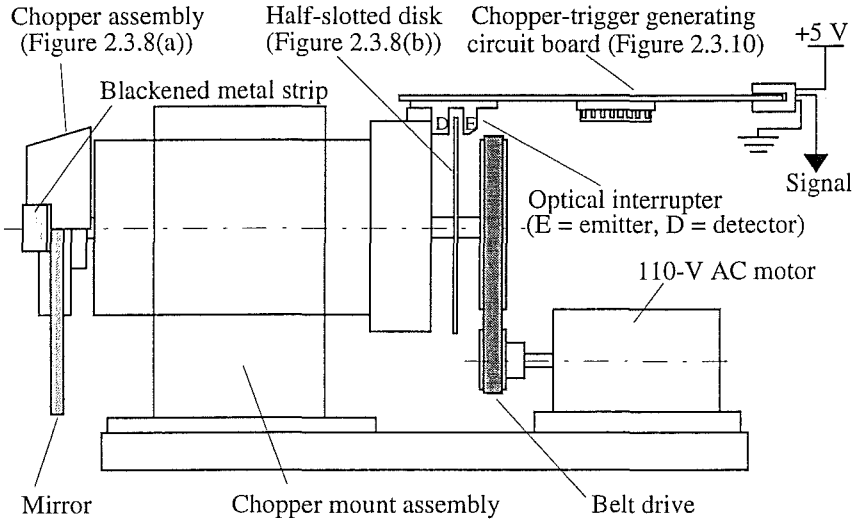

Figure 2.3.9: Schematic diagram of the chopper and optical-interrupter system.

The H21B1 optical interrupter contains an IR-emitting gallium arsenide photodiode and an IR-detecting phototransistor. A schematic diagram of the full circuit is shown in Figure 2.3.10. The slotted disk (Figure 2.3.8(a)) acts as the interrupter by sequentially transmitting and blocking light from the emitter during the chopper cycle, for which the H21B1 is configured to produce lower and higher voltages, respectively. Its output is 'sharpened' by a 4049 hex inverting buffer (*via* four inversions), yielding a TTL pulse train (Schmidt trigger) with a period of ~91 ms. The disk's orientation is chosen to give the TTL-low condition for the mirrored half-cycle (if the dark mask is ignored temporarily). (Technically, the signal is CMOS, not TTL, since the 4049 is a CMOS integrated circuit (IC). However, the 0-V and +5-V supplies used in the circuit produce TTL logic.)

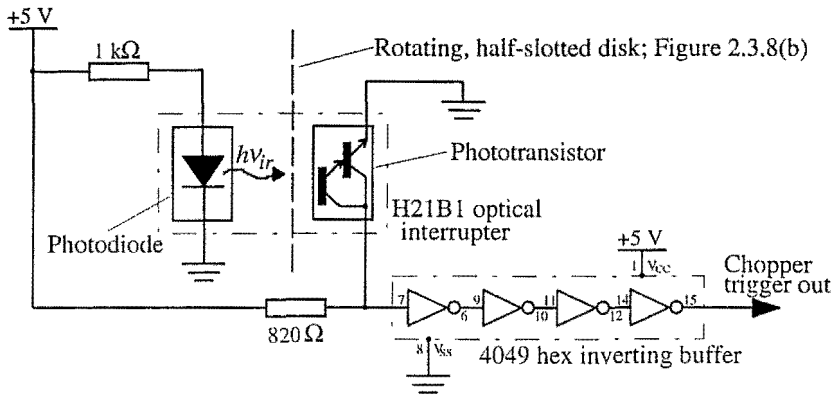

Figure 2.3.10: Optical-interrupter circuit for MOD4.

2.3.6.2. The two light paths

(a) Sample beam

The sample beam leaves the optics table and passes through an axial hole in the magnet (Section 2.2), where the sample is mounted. Following absorption, the light passes back into the spectrometer, and then to the detector.

A sample holder can be positioned on a mount prior to the detector, enabling room-temperature absorption and CD measurements. For example, calibration standards (Section 2.3.12) and samples for determination of depolarisation (Section 1.3.4.1) can be placed in it.

(b) Reference beam

Having been deflected by the mirrored portion of the chopper, the well-collimated reference beam is manually attenuated using an iris (if necessary), before being reflected by two plane mirrors around the perimeter of the optics table (Figure 2.3.1). (Attenuation of the reference beam is required when there is a high level of absorption or scattering by the sample, and for MI measurements due to the relatively small diameter of the sample window.)

The final mirror in the reference path reflects the reference-beam light to the detector. This mirror is rotatable (*via* a rod) to allow signal maximisation at the detector during operation.

2.3.7. Detection

The type of detection used depends primarily on the spectral region probed in the experiment. To a lesser extent the choice also depends on the relative sensitivity and

signal-to-noise (S/N) of the detectors if several can be employed in the same region. To cover MOD4's relatively wide spectral range, two distinct classes of detector are required: photomultiplier tubes (PMTs) in the visible and UV, and PMTs (S-1 type) or silicon photodiodes in the near infrared (NIR).

2.3.7.1. UV to NIR (190 – 1100 nm)

PMTs are efficient photon detectors in the UV and visible regions (*i.e.* for electronic transitions), although some, like the R-316, have NIR response. The essence of their operation is the photoelectric effect, and the principles of their operation have been described elsewhere.[21]

(a) PMTs used with MOD4

A number of PMTs are employed with MOD4, and comparisons of some specifications and characteristics are made in Table 2.3.3. The Hamamatsu R-376 is used most often, since it requires only moderate voltages for good signal output, has good S/N, and operates over a wide spectral range.

Table 2.3.3: Specifications and characteristics of PMTs used with MOD4.

Specification or characteristic	EMI 9514S	Hamamatsu R-292	Hamamatsu R-316	Hamamatsu R-376
Approximate spectral range / Å	3500 – 5500	1800 – 6500	4000 – 11000	1800 – 8000
Peak wavelength / Å	3800	4200	8000	4200
Window material	Borosilicate	Fused silica	Borosilicate	Fused silica
Photocathode:				
• type	Cs_3Sb	Bialkali	Ag-O-Cs	Bialkali
• diameter / mm	44	25	25	25
• Max. voltage / -V dc	2500	1500	1500	1500
Dynodes:				
• Structure	Venetian blind	Box-and-grid	Box-and-grid	Box-and-grid
• Number of stages	13	11*	11*	11*

* All have the same pin configuration, and use the same socket.

(b) Incorporation of the PMTs

Although the EMI and Hamamatsu PMTs have a different number of stages (Table 2.3.3), and use different bases, the principle of their dynode strings remains the same. Both dynode strings utilise reverse-biased 150-V Zener diodes to ensure that the voltage differential between the photocathode and first dynode is ≥150 V, which yields significantly improved efficiency in the presence of a moderate magnetic field.

Each PMT is mounted with its base in a separate housing to enable the detector

to be changed rapidly. The base incorporates a preamplifier (see (d) below), since the shorter the distance between the detector and the preamplifier the better. This introduces less noise to the small PMT current and minimises attenuation of the generally weak (M)CD signal.

Magnetic-field effects are further reduced in MOD4 by aligning the detector along the field direction, and incorporating μ-metal shields in the PMT housings.[24]

(c) HV power supply

A power supply has been built to supply the (negative) high voltage (HV) to the PMT, and ±15 V to its preamplifier ((d) below). The circuit diagram is shown in Appendix A.3. The power supply incorporates a Bertan High Voltage PMT-20C-N precision photomultiplier supply module, capable of producing 0 to -2000 V, with a maximum current rating of 2 mA. An analogue voltage (0 to 9 V) applied to pin 8 of the module yields a HV from 0 to -2000 V. This feature is used in all three of the modes of the MOD4 HV supply.

The first mode allows manual setting of the high voltage from 0 to -1000 V by a front-panel 10-turn potentiometer. (The potentiometer acts as a voltage divider, applying a fraction of the maximum 4.5 V to pin 8 of the HV module.) MOD4 calculates the absorption and (M)CD from the preamp signal produced at a fixed HV for double-beam scans, unlike earlier spectrometers which use a feedback loop to keep the 'sample' signal (Sections 2.3.9.2 and 2.3.11.2) constant.[14,16] (In addition, single-beam emission spectra obtained for wavelength calibrations use a fixed HV (Section 2.3.11.3).)

Second, and similar in principle to the manual mode, is computer control of the HV in double-beam scans. A front-panel switch on the HV power supply passes an analogue voltage to pin 8 of the HV module from digital-to-analogue channel 'X6' of the SR510 LIA (Section 2.3.8). Hence the HV can be controlled by software, a very useful feature for scans over wide wavelength ranges, where lamp, grating or PMT efficiencies can change significantly.

Finally, automatic (single-beam) mode uses a feedback loop to monitor and maintain the output current of the PMT preamp ((d) below) at a user-set level. The feedback circuitry alters the voltage applied to pin 8 of the HV module when the preamp signal changes from that level. Single-beam (M)CD spectra are obtained in this way, where the (M)CD is directly proportional to the magnitude of the ripple, *and* the current

level. (See Sections 2.3.9.2(c) and 2.3.11.4 for details.) This method's main limitation is that there is no dark-current correction, so very high voltages (*e.g.* in regions of intense absorption), and high-dark-current PMTs like the R316 can not be used in this mode without introducing significant errors. Neither are preamp offsets accounted for as they are in double-beam mode.

(d) Preamplification

Despite amplification through the dynode string of around 10^5 to 10^6 per photon, the PMT output is still only a very small current. Since small currents are susceptible to interference, they are best converted to a moderate analogue voltage by a preamplifier at the earliest opportunity. This is achieved in MOD4 by including the preamplifier circuit board in the PMT housing ((b) above).

The preamplifiers used have current-to-voltage conversions of ~5×10^5 V/A; the circuit is shown in Figure 2.3.11. The ±15-V power supplies and ground are sourced from the photomultiplier power supply ((c) above), while the input signal is the anode current of the PMT. The preamplified output goes to the MOD4 electronics in fixed-voltage (double-beam or emission) mode, or to the photomultiplier supply for automatic (single-beam (M)CD) mode.

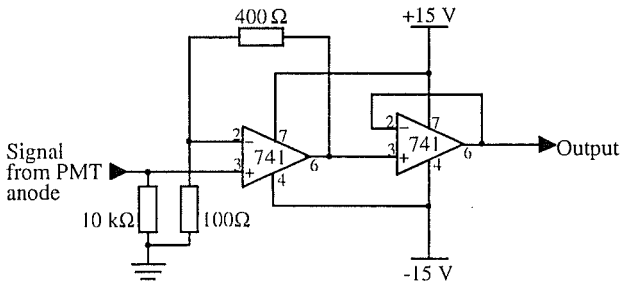

Figure 2.3.11: The photomultiplier preamplifier circuit used in MOD4. The power supplies are derived from the photomultiplier supply (see (c) above).

2.3.7.2. Photodiodes (600 – 1100 nm)

Although the PbS cell is a common, conventional NIR detector, it is unsuitable for measurement of (M)CD because of its slow response time (on the order of milliseconds) in comparison with the 50-kHz modulation frequency of the PEM.

Attempts to use Judson J16-5 and J16D Ge photodiodes as NIR detectors (wavelength range from ~800 to 1500 nm at 77 K) with MOD4 were unsuccessful due to preamp roll-off of the 50-kHz (M)CD signal. Low-light levels in MOD4, and the

consequent need for high-gain preamplification, coupled with the relatively high detector capacitance, appeared responsible for this. These detectors can be used to obtain absorption data over the wavelength range indicated above. (Note that although long-wavelength response is reduced from 1800 nm at room temperature, the S/N is much improved at 77 K.)

A Philips BPX-65 PIN silicon photodiode, with a 1-mm^2 active area, has been successfully employed in MOD4 over the wavelength range 600 to 1100 nm, and is operated at room temperature. It has a better S/N level in the 800 to 1100-nm region than the R-316 PMT operating under similar conditions, and its incorporation is described briefly in this section.

(a) Photodiode detectors

In all semiconductors there is an energy (band) gap between the occupied and conduction bands that relatively few electrons are able to cross under thermal conditions at room temperature or below. Diodes are semiconductors, of which photodiodes are a special class, undergoing electronic excitation to the conduction band and producing a small current if their *p-n* junction is exposed to photons of sufficient energy to bridge the band gap. Detector response is linear with monochromatic-photon intensity if the diode is zero- or reverse-biased (see part (c)). In MOD4 the first configuration is used, because the dark current is then reduced to near zero.

The noise level of a photodiode is reduced by decreasing the physical size of the diode, wherein the 1-mm^2 active area of the BPX-65 is advantageous. The detector's capacitance is proportional to the square of its diameter, which, as will be noted later, it is important to minimise in this application.

(b) Incorporation of the photodiodes into MOD4

The BPX-65 photodiode and its preamplifier is mounted in a small, grounded aluminium case to minimise pick-up due to radio-frequency (RF) noise. The diode protrudes from the case, and its active area is exposed to light from the spectrometer after it has been focussed by a glass convex lens ($f \sim 53$ mm) to about 1 mm^2.

The small physical size of the BPX-65 necessitates careful lateral and vertical adjustment of the diode to obtain and optimise the signal. A rack has been built for this purpose that in part utilises the monochromator's camera attachment, and replaces the PMT mount. The rack incorporates the lens described above, and is also available for

use with the Ge photodiodes in their liquid-N_2-cooled housings.

(c) Preamplification

Measurement of (M)CD requires that the photodiode-preamp combination be capable of amplifying the 50-kHz component of the signal with minimal roll-off. As noted earlier, this was not achieved for the Ge photodiodes available to the author, but it was for the Si photodiode (Philips BPX-65).

The preamp for the BPX-65 (Figure 2.3.12) incorporated an OP37 low-noise, high-speed operational amplifier. The pins of the photodiode are directly soldered to the preamp in order to minimise signal degradation and RF pick-up. The photodiode is zero-biased in this configuration, for reasons given in (a) above. The combination of a very high feedback resistance (55 MΩ) and no *added* input resistance give a large current-to-voltage amplification. No capacitor is placed across the feedback path, since this results in an RC circuit which smooths out the 50-kHz (M)CD signal. Note, however, that the preamp cannot be treated independent of the detector, since the latter has an intrinsic capacitance, C_d, which is a function of the diode type, and is proportional to the detector area. Ge photodiodes have an intrinsically higher capacitance than Si devices. This, along with the fact that the Ge photodiodes had 2 and 5-mm diameters as opposed to the 1-mm^2 area of the BPX-65, was probably responsible for the successful application of the latter in comparison with the former. The BPX-65 – preamp combination has very good 50-kHz response, and satisfactory S/N compared to the R-316 PMT.

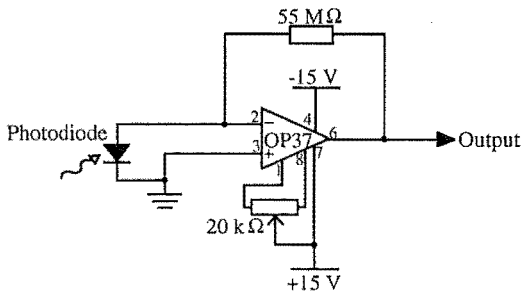

Figure 2.3.12: The photodiode preamplifier circuit. (The power supplies are derived from the photomultiplier power supply (Section 2.3.7.1(c)).)

The feedback resistance is chosen to provide suitable dc gain for measurement of absorption. Absorption S/N is reduced to a small extent because there is no feedback capacitance to filter higher frequency noise.

The preamp suffers from significant dc drift due to the very high gain. However, since the drift is very slow on the time scale of chopper rotation in double-beam mode (Section 2.3.11.2), its effect is eliminated *via* its contribution to the dark current at each wavelength step. Trimming of the 20-kΩ potentiometer allows the preamp output to be zeroed.

Note that in MOD4 there is no facility for acquisition of single-beam (M)CD data using the photodiode, since no variable-gain amplifier has been incorporated which can the sample level at a constant value *via* a feedback loop.[25]

2.3.8. Stanford Research Systems Model SR510 lock-in amplifier

The lock-in amplifier (LIA) is a phase-sensitive detector able to extract very small ac signals of a specific frequency, and amplify them, even in the presence of other much larger signals and noise components. It does this by selectively filtering and amplifying the signal component commensurate with a fixed frequency applied to the 'reference' input.

In MOD4 a Stanford Research Systems Model SR510 LIA is used to extract and amplify the small, modulated (M)CD component of the detector preamplifier output from the 'sample' signal. The (M)CD signal has a frequency of ~50 kHz corresponding to modulation frequency of the PEM (Section 2.3.5.2), and hence lies in a favourable part of the noise spectrum.[26]

In the first section, the SR510 LIA, and its application to MOD4, is described briefly. The second section covers SR510 features (including the digital-to-analogue converters) that a user needs to understand in order to run the spectrometer. The final section gives commands used to program the LIA from the spectrometer's computer (Section 2.3.10.1) *via* an industry-standard RS-232 interface.

2.3.8.1. Operation of the SR510 LIA, and its application to MOD4

The SR510 input signal is derived from the detector's pre-amplifier, after passing through the main electronics unit (Section 2.3.9; Figure 2.3.13). Line-frequency and twice-line-frequency components can be filtered from the input by selection of the notch filters.

Further filtering is provided by an auto-tracking bandpass filter with Q = 5. (The filter is set to within 1% of reference frequency.) Bandpass filtering reduces front-end

overloading of the LIA by passing only ac components very near the reference frequency. When (M)CD data are being obtained in double-beam mode, use of this filter is essential; software enforces it (Section 2.3.8.3). This filter attenuates the large, low-frequency component arising from the switching in and out of the preamplifier signal during the chopper cycle (Section 2.3.6). (The rationale behind the switching procedure is given in Section 2.3.9.2.)

Next, the signal is amplified by a high-gain ac amplifier, before passing to the phase-sensitive detector (PSD). The PSD is a linear multiplier which mixes the filtered and amplified signal with the reference sine wave (see below). The difference-frequency component of the PSD's output is a dc voltage directly proportional to the signal's amplitude. Only components of the input signal that are synchronous with the reference signal give a non-zero contribution.

Two low-pass filters smooth the dc output data by rolling off ac components that may arise from the PSD. Hence, for (M)CD data acquired in double-beam mode, the 'pre-filter' time constant is set to the minimum value, 1 ms, while the 'post-filter' time constant is switched out (0 ms). Low-pass filtering would otherwise reduce the measured signal by 'smoothing' it into the 'reference' and 'dark' regions (Sections 2.3.6 and 2.3.9.2(b)). In single-beam mode (Section 2.3.9.2(c)), it is advantageous to set the time constants to be greater than the minimum values to reduce noise, since the preamp signal is dc.

Finally, before the signal reaches the output, it is amplified by a dc amplifier. The sensitivity (10 nV to 500 mV, full scale) sets the overall gain of the LIA from the input signal for full-scale output of ±10 V. (For double-beam (M)CD measurements, the highest input sensitivity that can be utilised before overloading occurs is 5 mV when the bandpass filter is used.) The apportioning of overall gain between the ac and dc amplifiers is determined by the 'dynamic reserve'. (Dynamic reserve is the ratio of the largest noise signal to the experiment signal that the LIA can handle before the input channel overloads. The 11-Hz component of the preamp output is a large source of such noise in MOD4.) Low dynamic reserve is preferable; more of the gain is provided by the ac amplifier (before the PSD) rather than the dc amplifier, resulting in greater signal stability.

The LIA output is passed to an integrator to reduce noise in the double-beam application, or directly to the computer A/D port in single-beam mode. (Section 2.3.9.2

covers the electronics.)

The PEM reference signal provides the LIA with an exact frequency which is used to extract the ~50-kHz (M)CD signal from the detector's preamplifier output, while rejecting noise and unwanted frequency components. The PEM controller outputs a reference sine wave (peak-to-peak amplitude of 6 V) corresponding to the frequency of circular polarisation modulation (Section 2.3.5.2). This signal first passes to the input discriminator, where a sine-wave source is selected (as opposed to logic pulses). The phase-locked loop (PLL) then locks on to the reference frequency, producing a sine wave of the same frequency. The phase shifter, as its name suggests, enables the reference frequency's phase to be shifted relative to the input signal phase (allowing maximisation of the final output signal). Finally, before passing to the PSD, the phase-shifted reference signal is shaped by the precision sine-wave converter to provide a very well formed sine wave.

2.3.8.2. MOD4 settings and other SR510 features employed

Users of MOD4 should not need to set the LIA phase manually under normal circumstances. If the correct detector has been selected and the (M)CD calibration (Section 2.3.12.3) is recent (the current month, assuming no optical or electronic changes have been made), MOD4 will set the LIA phase for the type of run that is to be made (double- or single-beam, CD or MCD).

The sensitivity should be selected to satisfy two criteria in double-beam mode. First, only sensitivities of 5 mV to 500 mV can be utilised, because for higher sensitivities (2 mV or less, full scale) the LIA input is overloaded by the switching of the preamp signal due to the chopper (Section 2.3.9.2(b)). Second, the maximum sensitivity that does not cause overloading of the LIA due to the (M)CD signal should be chosen. If overloading does occur, the software reduces the LIA sensitivity; see the next section. (Note that full-scale output from the LIA will not overload the (M)CD integrator (Section 2.3.9.2(b)).)

For single-beam scans, higher sensitivities can be used, because there is no longer switching of the preamp signal due to chopper rotation.

The SR510 has four 13-bit analogue-to-digital (A/D) and two 13-bit digital-to-analogue (D/A) channels, each with a ±10.24 V range, available for user applications. In MOD4 both D/A channels are employed: one provides the voltage to remotely drive

the PEM (Sections 2.3.5.2(b) and 2.3.11.2(b)), while the other can be used to set the photomultiplier high voltage (HV) in double-beam mode (Sections 2.3.7.1(c) and 2.3.11.2). The A/D channels are unused, since this function is fulfilled by the PCL-814B interface card (Section 2.3.10.2).

2.3.8.3. Programming the SR510 via an RS-232 port

Several LIA functions are controlled by the computer *via* an RS-232 interface, using a 19200 baud rate (1 baud = 1 bit/second).

When SPEC2 (the data-acquisition program for MOD4) initialises, the auto-tracking bandpass filter is switched in automatically with the command 'B1', and the dynamic reserve is set to the low state by 'D0'.

The 'T1' and 'T2' commands set the 'pre' and 'post' time constants, respectively. In double-beam mode, the time constants are set to the minimum values (Section 2.3.8.1): '1' (1 ms) follows 'T1', and '0' (0 ms) follows 'T2'. For single-beam CD, the user must set the time constants manually using the LIA's front panel controls.

The PEM and photomultiplier HV DAC channels (Section 2.3.8.2) are programmed using the commands 'X5' and 'X6', respectively. The desired voltage is output in response to writing the voltage as a real number after the command.

A calibration file contains the current reference-phase settings for double- and single-beam (M)CD measurements. If the automatic phase-setting option is chosen by the user, these phases will be set by the computer using the command 'P', then the phase as a real number. (Note that the MCD phase differs from the CD phase by 180° on MOD4 because of the field direction, and that corrections are required for some detectors — hence the correct detector must be selected in the software.)

The LIA sensitivity (gain) is set using the command 'G', followed by an integer value corresponding to a particular sensitivity.

Before the (M)CD data are acquired at each wavelength step, the software also checks bit 4 of the SR510 status byte using the command 'Y4'. Bit 4 is then read by the software: it is zero in normal circumstances, but if the sensitivity is too high, or the dynamic reserve is too low, it registers '1' — an overload condition. (Once read, the bit returns to the zero state.) The software reduces the sensitivity in the latter case using the command 'K22', and accounts for the reduction in subsequent calculations.

2.3.9. Electronics

MOD4's electronics are conceptually quite different to those of earlier instruments in the series.[14,16] Dependence on peripheral electronics is far less than that of the previous spectrometers due to increased utilisation of computing power. The computer (Section 2.3.10) performs all mathematical manipulations, eliminating inaccuracies and noise arising from electronic components such as logarithmic amplifiers, while taking many more absorption samples.

Nevertheless, gate-generating circuitry and some electronics to manipulate the preamplifier signal (containing absorption and (M)CD data) are still required. Gating ensures that the data collection occurs at the correct time during the chopper cycle (Section 2.3.6). Maximum resolution demands that the negative voltage output of the preamplifier be inverted before passing to the Advantech PCL-814B LabCard's analogue-to-digital converter (ADC; Section 2.3.11.1(a)). The weak (M)CD signal extracted by the LIA (Section 2.3.8) during the 'sample' period is electronically integrated to reduce noise in double-beam mode.

Figure 2.3.13 shows a block diagram of MOD4's electronics. Various components have been described earlier; the monochromator stepper-motor circuitry, the PEM controller, the optical-interrupter circuit, and detector components. This section describes the remainder, except the computer hardware and software, which are covered in Sections 2.3.10 and 2.3.11, respectively.

2.3.9.1. Gating circuitry

Synchronisation of data sampling with chopper position is achieved in a straightforward manner by generating electronic gates from the Schmidt trigger produced by the optical-interrupter circuit (Section 2.3.6.1). The gates are also used for solid-state (CMOS) switching operations within the electronics.

The Schmidt trigger (Figure 2.3.14(a)) enters two parallel 74123 retriggerable monostable vibrators (Figure 2.3.15), which produce the 'sample' and 'reference' triggers, respectively. Monostables are TTL integrated circuits (ICs) with one stable state: 0 V (TTL-low). Their configuration determines whether they respond to positive or negative voltage edges. In both cases the 74123's output is a TTL-high pulse of a duration set by the time constant of either the internal RC circuit or an external one. The latter is used exclusively here; the RC circuits have front-panel-adjustable trim

potentiometers in series with fixed resistors to enable gate delays and widths to be set accurately, and easily. (The 74123 has two identical units in each package.)

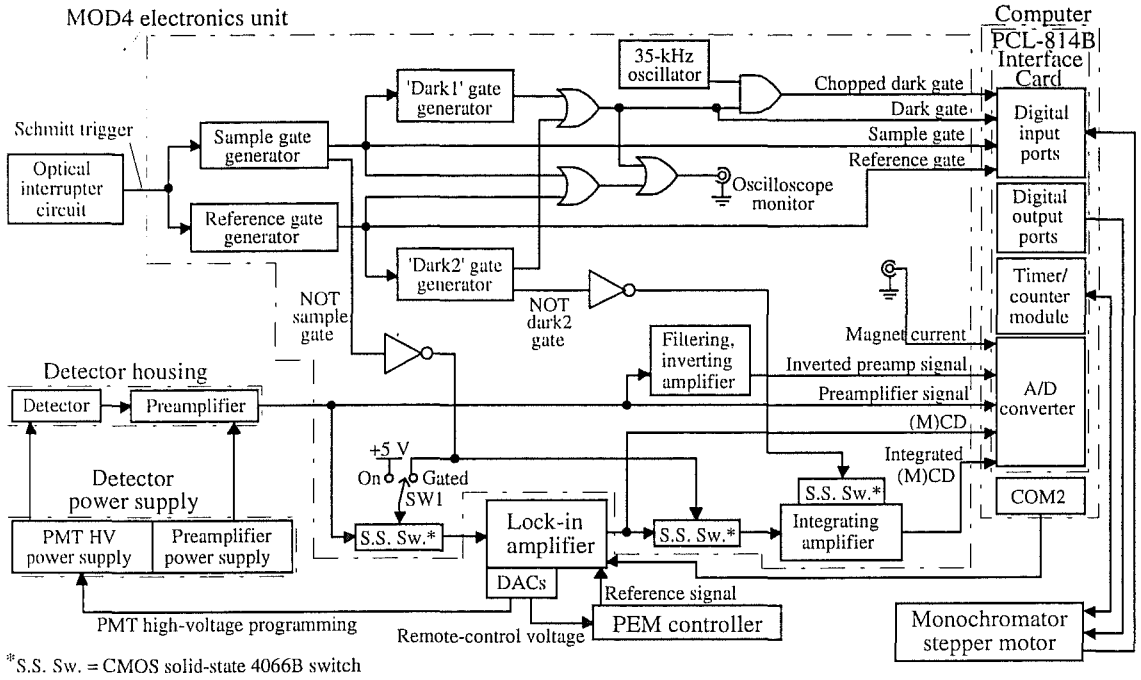

Figure 2.3.13: Block diagram of the MOD4 electronics.

All gates require a delay, because edge effects occur at the detector when the light level changes between the different sampling periods (Figure 2.3.14(e)). Here delays are generated in the first unit of the 74123 ICs (Figure 2.3.15).

The 'sample' gate is produced by the 74123 shown at top left in Figure 2.3.15. The connection to pin 'A1' for the 'sample' delay is atypical; the unit is the only one configured to trigger on a positive edge. This unit offsets the 'sample' gate from the start of the TTL-high portion of the Schmidt trigger to coincide with the start of the 'sample' period. The second unit creates the 'sample' gate's width by negatively triggering on the delay pulse. The duration of the 'sample' delay and width are shown in Figure 2.3.14(b).

The second 74123, shown at bottom left in Figure 2.3.15, generates the 'reference' gate in a similar manner to the 'sample' one, except that the delay pulse is formed by a negative trigger on the Schmidt input. Since the 'reference' and 'sample' periods are of the same duration (Figure 2.3.14(c)), the RC components have the same values.

'Dark' gates are produced by the third and fourth 74123s. The 'dark1' and 'dark2' gates follow the sample and reference gates, respectively. The gate delays are

formed by negative triggering on the 'sample' or 'reference' gate, while the gate width is generated in second unit of the 74123. For the 'dark' gates there are several additional factors that must be taken into consideration.

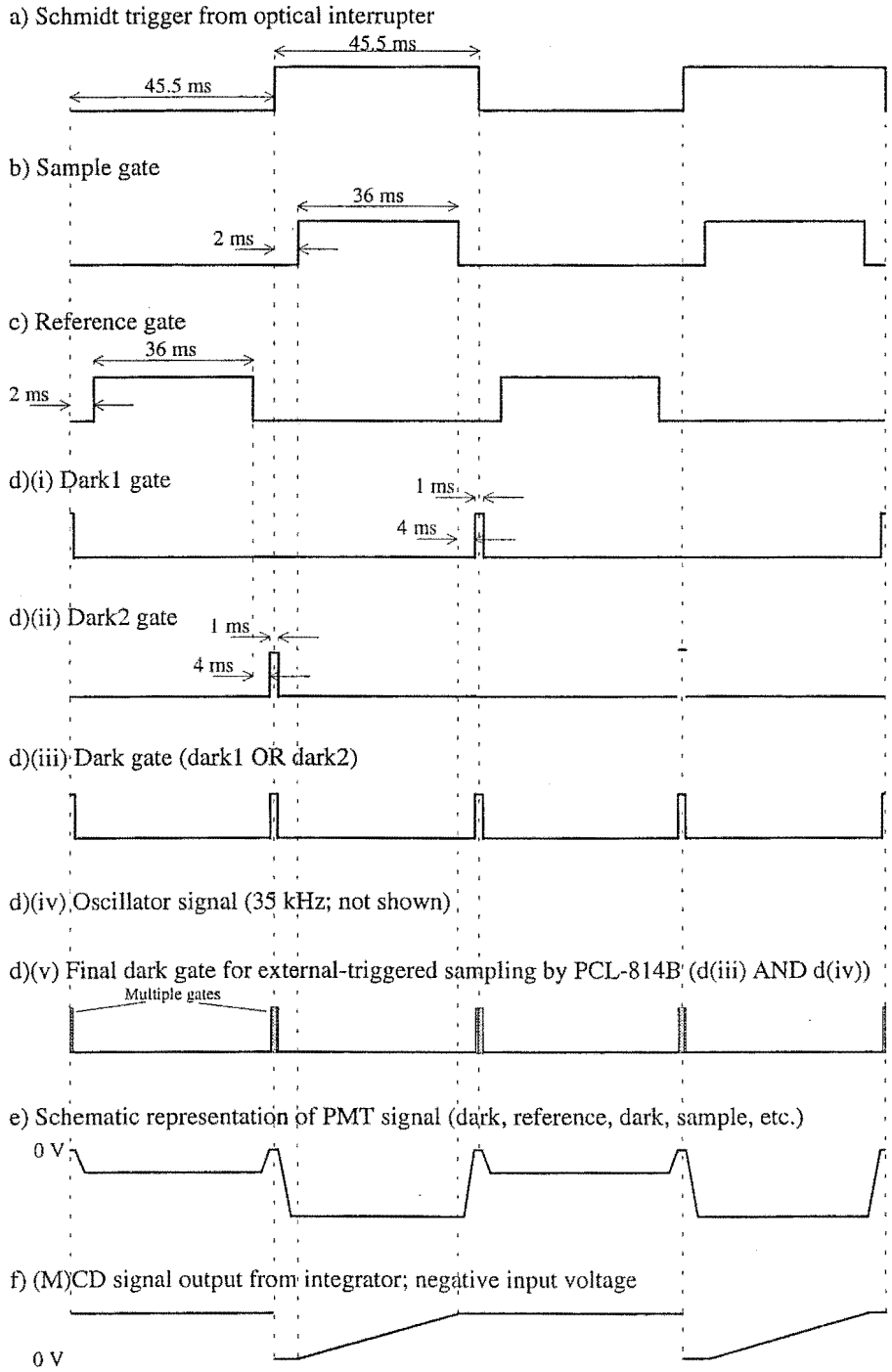

Figure 2.3.14: Timing diagram for data acquisition on the MOD4 spectrometer. (The gates are TTL low and high, while preamp and MCD signals are analogue voltages.)

First, to simplify programming it is convenient to have both of the 'dark' gates entering the digital-input port (Section 2.3.11.1(a); Table 2.3.9) of the computer on the

same channel. A 7432 quad bi-input OR gate (Figure 2.3.15) is used generate the (overall) 'dark' gate (Figure 2.3.14(d)(iii)).

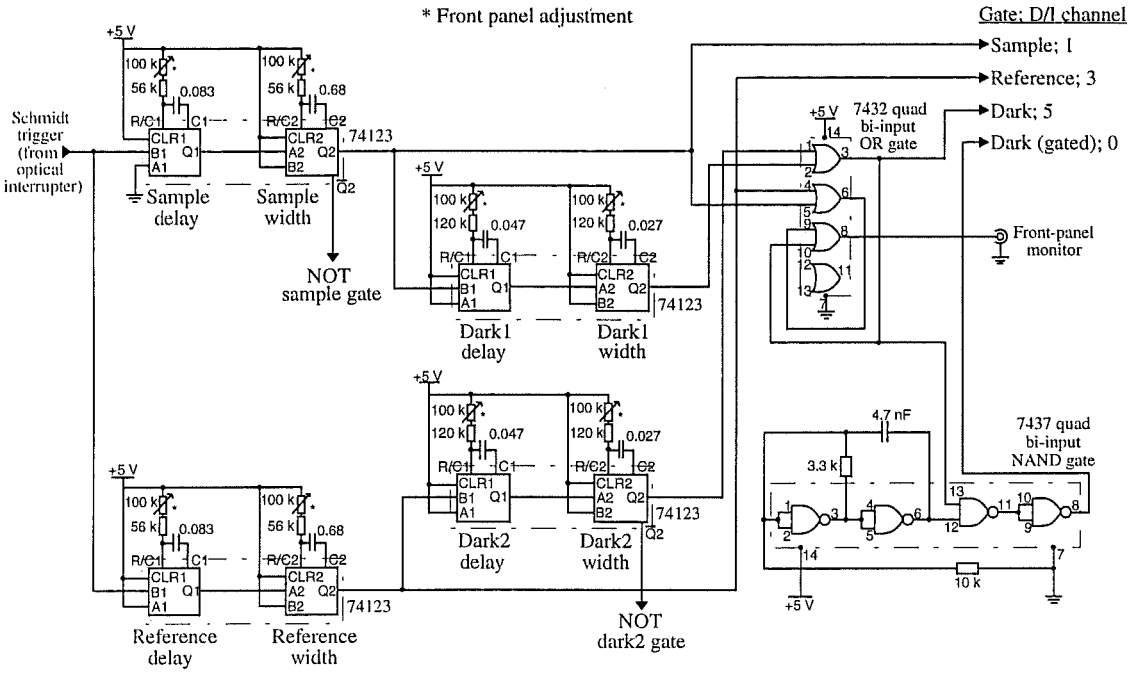

Figure 2.3.15: Schematic diagram of the MOD4 gating circuitry. NOT gates are used to operate solid-state CMOS switches (Figure 2.3.16; Section 2.3.9.2(a,b)). Section 2.3.11.1(b) describes the digital input (D/I) channels of the PCL-814B interface card. 74123 ICs are retriggerable monostable vibrators.

Second, because of the relatively short time available for acquisition of 'dark' data relative to 'sample' and 'reference' data, a different trigger mode of the PCL-814B interface card (Section 2.3.11.2) is utilised. In this mode an analogue-to-digital conversion is initiated each time digital-input channel 0 receives a positive TTL edge, up to a maximum frequency of 100 kHz (Sections 2.3.11.1(a) and 2.3.11.2). A chopped 'dark' gate is generated to provide the sampling trigger as follows. Hysteresis resulting from connection of two units of a 7437 quad bi-input NAND gate (bottom right; Figure 2.3.15) yields an TTL pulse train with a frequency of ~35 kHz when the components shown are used. A logical AND of the oscillator signal with the 'dark' gate (NAND, then NAND the result with itself), yields the chopped gate shown schematically in Figure 2.3.14(d)(v).

'Sample', 'reference' and 'dark' (unchopped) gates can be individually monitored by oscilloscope through front-panel 'tags'. An overall monitor of the gates is accessible through a front panel BNC connection. (It is produced by a logical OR of the 'sample' and 'reference' gates, and of the result with the (unchopped) 'dark' gate.)

The sampling gates are accurately positioned using the software utility MOD4DIAG, which incorporates the double-beam sampling routine of SPEC2, the spectral-data acquisition program (Section 2.3.11). In MOD4DIAG all absorption data for a chopper cycle are plotted to the computer screen, aiding setting of the gate positions, and allowing the optimal number of A/D conversions (Section 2.3.11.1) to be determined.

Gate connections to digital input channels of the PCL-814B interface card are covered in Section 2.3.11.1(b), while their use in acquisition of double-beam data is described in Section 2.3.11.2.

2.3.9.2. Analogue circuitry

Minimal electronic circuitry is used to manipulate the analogue preamplifier output. Absorbance is calculated from the filtered and amplified detector signal (part (a)). The (M)CD is electronically integrated over the entire sample period in double-beam experiments to reduce noise (part (b)). However, single-beam (M)CD requires a slightly different approach, which is outlined in part (c).

A final feature of the main electronics unit is the programmable-gain and inverting amplifiers (part (d)), available for use with weak signals or detectors whose preamp output is positive.

(a) Filtering, inverting amplifier for absorption data

Absorbance is calculated digitally in MOD4, following analogue-to-digital (A/D) conversion of the preamplifier signal by the PCL-814B interface card. The subtraction and logarithmic amplifiers (which are subject to drift and noise) used in earlier spectrometers[14,16] have been eliminated.

The 14-bit resolution of the PCL-814B A/D module is fully utilised by choosing unipolar gains (Section 2.3.11.1(a)), and inverting the negative PMT preamp signal. The inverting amplifier is shown at centre top of Figure 2.3.16 (gain = 4.11).

A third feature of the amplifier is its filtering characteristic. The reference-beam mirrors contribute a large linear dichroism component to the 'reference' signal at twice the frequency of circular polarisation modulation (~50 kHz; Section 2.3.5.2). (The frequency appears lower due to 'aliasing' with the 69-kHz sampling rate of the PCL-814B.) This contribution is removed by the RC circuit forming the feedback portion of the amplifier. As a consequence, however, some rounding of the sharp 'dark' edges

(Figure 2.3.14) occurs, reducing the accuracy of 'dark' data from this source. Therefore the preamp signal itself is sampled for the 'dark' signal (Section 2.3.11.1(a)), and multiplied by the amplifier's gain (-4.11).

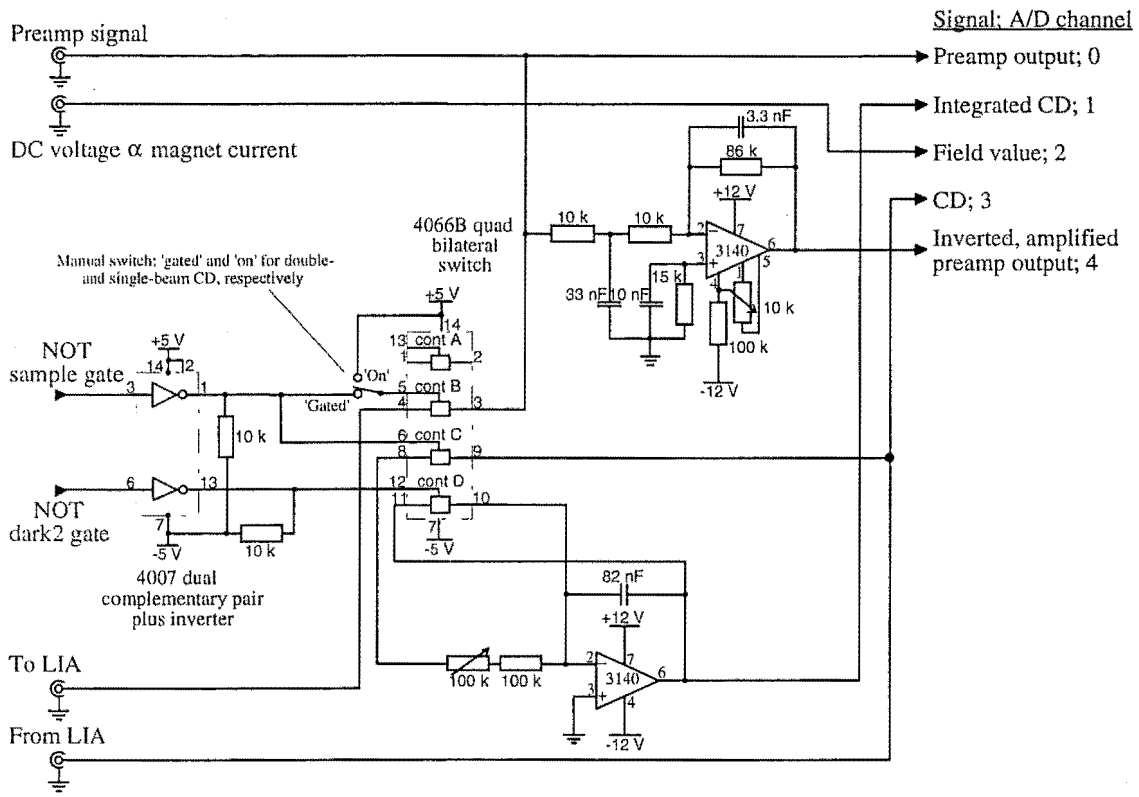

Figure 2.3.16: Data-sampling and manipulation electronics for MOD4. (Figure 2.3.15 shows the gate-generating circuitry.)

The inverted, filtered and amplified signal is passed to channel 4 of the A/D converter, while the original preamp signal goes to channel 0. The former can be observed on the oscilloscope by clipping a probe on to the tag labelled 'analogue output' on the electronics unit, and the latter by direct link to the preamp output.

(b) Integration of the (M)CD signal in double-beam experiments

During the 'sample' period a small, 50-kHz ac component of the preamplifier output carries the (M)CD signal. The LIA is used to extract and amplify the ac contribution, producing a dc output voltage of ±10 V full scale (Section 2.3.8). The (M)CD electronics do two jobs: first, they electronically gate the preamp output to the LIA (cutting out the 'reference' and 'dark' signals), and; second, they electronically integrate the LIA output.

Switching of the LIA input was alluded to in Section 2.3.8.1, and is performed by a CMOS 4066B quad bilateral switch. The 'sample' component of the preamp signal

is gated to the LIA (the input is 0 V for the remainder of the chopper cycle) by the CMOS equivalent of the TTL 'sample' gate. (The CMOS gate is generated from the NOT output of the 'sample' gate 74123 (Figure 2.3.15), by passing the TTL gate through a CMOS 4007 dual complementary pair plus inverter configured as an inverter (Figure 2.3.16).) The 'reference' beam is not passed, because the linear dichroism of the mirrors (Section 2.3.9.2(a)) creates a large 'ghost' (M)CD signal, which may cause overloading of the LIA input.

The dc output of the LIA is rather noisy; in part due to the lack of time-constant smoothing (Section 2.3.8.1), but also because the (M)CD signal is weak. An (inverting) integrating amplifier (bottom right in Figure 2.3.16) is used to sum the (M)CD over the 'sample' period, reducing noise. Like the LIA, the integrator's input is switched through another unit of the 4066B switch by the CMOS 'sample' gate, so that 0 V is summed for the remainder of the chopper cycle.

A 3140 operational amplifier is utilised in the integrator, because its large input impedance results in little integration of noise, and it has high output stability. The magnitude of the feedback capacitor and input resistor (Figure 2.3.16) are chosen to give the integrator an output of less than the ±5 V full scale (to match the PCL-814B interface card; Section 2.3.10.2), when the LIA output is full scale (±10 V) for the duration of the 'sample' period (~35 ms). Because the input is 0 V for the remainder of the cycle, the integrator output remains constant, and is ready for sampling (Section 2.3.11.2).

The integrator is reset prior to the next 'sample' period by shorting the feedback capacitor. A CMOS equivalent of the TTL 'dark2' gate is generated by the 4007 (see above), and closes a third unit ('D') of the 4066B switch when high (~5 V). The capacitor is shorted, and the energy is rapidly dissipated in the 125-Ω internal resistance of the closed switch.

Figure 2.3.14(f) gives an idealised representation of the integration procedure for a constant input voltage. Section 2.3.11.2 describes the calculation of the (M)CD from the integrator output.

(c) Single-beam (M)CD

Single-beam (M)CD scans (Section 2.3.11.4), including field-saturation scans (using SATSCAN2 software; Section 2.3.11.5), can also be run using MOD4. The

chopper is off in this mode, so (M)CD integration is not feasible, and the (M)CD is sampled directly from the LIA output *via* channel 3 of the PCL-814B A/D module (Figure 2.3.16; Section 2.3.11.4). Time-constant filtering can be utilised in single-beam mode (Section 2.3.8.1), because the signal is solely due to the sample. A restriction is that the time constant must not cause smoothing between wavelength steps.

The feedback ('automatic') mode of the photomultiplier supply is used (Section 2.3.7.1(c)), with the (M)CD directly proportional (*via* an empirical calibration constant) to the ac signal and the fixed dc voltage.[14,25] Note that for the spectrum to be consistent with the calibration, it must be run at the same feedback voltage. However, because no account is made for dark current in the single-beam experiments, low-dark-current detection (*i.e.* not the R-316 PMT) and well-trimmed preamplifiers are essential. Single-beam mode is not used often, since the data have similar S/N to (M)CD acquired in double-beam mode for a scan of the same duration.

One final setting needs to be changed in addition to the HV supply feedback mode, and having the chopper off. The front-panel 'preamp signal' switch must be set to the 'on' position (from 'gated') to ensure that the preamp signal is passed to the LIA. (This toggle switch closes unit B of the 4066B (Figure 2.3.16) continuously, passing the preamplifier signal to the LIA. In double-beam mode the signal is gated by the switch (Section 2.3.9.2(b)).)

(d) Programmable amplifier and switchable inverting amplifier

In some situations it may be desirable to amplify and/or invert the preamp signal before it reaches the main electronics board (parts (a) – (c)). This requirement is satisfied by a six-setting programmable amplifier (gains of $2^{(n-1)}$ for n = 1 to 6), and an option to switch in an inverting amplifier with unity gain. The circuit diagram is given in Appendix A.4. Use of the programmable amplifier requires that the BNC cable carrying the detector preamp signal be connected to the front panel of the electronics unit, while the board's output goes to the preamp signal input of the main board. This amplifier circuit has not been made a permanent part of the electronics, because additional switches and amplifiers that are not frequently required only serve to increase noise.

The amplifiers are switched in, and the gain selected, using channels of a 4066B quad bilateral switch controlled by TTL logic derived from digital-output (D/O) channels of the PCL-814B interface card (Section 2.3.10.2; the connections are given in

Section 2.3.11.1(b)). The table on the circuit diagram (Appendix A.4) shows the required D/O settings for a particular gain: channels 13, 14 and 15 set the gain (A, B and C, respectively). The inverter is switched in by a TTL-high signal on channel 12.

2.3.10. Computer hardware

MOD4 is a computer-based instrument. An IBM-compatible PC controls wavelength scanning and data acquisition *via* an Advantech PCL-814B interface card, and digitally computes the spectra.

The SR510 LIA is programmed *via* a RS-232 interface (Section 2.3.8.3), providing digital-to-analogue conversion (Section 2.3.8.2) for remote control of PEM retardation (Section 2.3.5.2), and (optionally) for PMT HV programming (Section 2.3.7.1). (Section 2.3.11 covers the software aspects of spectrometer control and data acquisition.)

2.3.10.1. The computer

A 486SX-based computer has been used in MOD4. Pacer- and external-triggered analogue-to-digital (A/D) conversions and direct-memory-access (DMA) data transfer are features of the PCL-814B that allow it to operate independent of the CPU. The computer is freed from involvement in acquisition, enabling it to sort and sum data collected during an earlier sampling period. There is CPU dependence in this respect, but since data is being collected concurrently it is not important.

LIA functions and digital-to-analogue (D/A) conversions are also controlled by the computer *via* an RS-232 interface to the SR510 (Section 2.3.8.3).

2.3.10.2. The Advantech PCL-814B LabCard and timer/counter module

The PCL-814B interface card provides a major technological advance over earlier simultaneous absorption/CD spectrometers, because it allows a large quantity of data to be gathered rapidly. Hence much of the peripheral electronics in previous instruments[14,16] are no longer required (Section 2.3.9). Programming of the PCL-814B is described in Section 2.3.11.1. The PCL-814B occupies 16 consecutive data-bus addresses, with a base address of 200 (Hex).

The PCL-814B incorporates a 16-channel, 14-bit analogue-to-digital converter (ADC) capable of sampling at a (programmable) rate up to 100 kHz. The software driver supplied by Advantech is used to control all ADC functions, where MOD4's

software provides the driver with a 'parameter table' of settings (Section 2.3.11.1(a)).

Three triggering options are offered by the ADC, all of which are utilised in MOD4. External triggering converts data when positive TTL edges occur on digital-input channel 0, while pacer (internal) triggering uses the output of the cascaded programmable counters 1 and 2 (of an Intel™ 8254) as the trigger source. Each of these modes can undertake multiple conversions per software initiation, with the count provided by counter 0. Software triggering instigates a single conversion, and is dependent on the CPU. Converted data can be transferred to the data buffer using either DMA or interrupt transfer for the first two trigger modes (each independent of the CPU speed), or *via* software for software triggering (CPU-dependent).

The ADC also features software-programmable unipolar and bipolar gains (from 1× to 8× in each case), with a maximum range of 0 to 10 V and -5 to +5 V, respectively. These features are discussed more fully in Section 2.3.11.1(a). In addition to the ADC, there are 16 digital-input (D/I) and 16 digital-output (D/O) channels on the PCL-814B. Their application is described in Section 2.3.11.1(b).

Unfortunately, no units of the Intel™ 8254 programmable counter on the PCL-814B's main board are available for user applications. However, this function is provided by an add-on timer/counter module (PCL-814-TC-1), utilising an Am9513A system timing controller. The programmable counter is used to control slewing of the monochromator stepper motor (Section 2.3.3.2(b)), independent of the computer CPU. The Am9513A has five 16-bit counters, independently and simultaneously operable in any of 24 modes. (Only Mode A is utilised here — 'software-triggered strobe with no hardware gating'.) The source for each counter is programmable, as is the choice of output pulse on terminal count, and many other features. The Am9513A has also enabled slews of greater than 65535 counts to be undertaken, because the counters can be internally concatenated. A brief description of the software developed for the timer/counter module is given in Section 2.3.11.1(c). Pin connections are given in the relevant places in Section 2.3.11.1.

2.3.11. Computer software

All aspects of MOD4 programming are performed in Microsoft QuickBASIC 4.5. Standard (M)CD and double-beam absorption, single-beam (M)CD and emission studies are undertaken using SPEC2 software, while single-beam field-saturation scans

employ SATSCAN2 software. SPEC2 is an extensively modified version of a simultaneous MCD/absorption spectrometer control program developed at the University of Virginia,[14] and modified for use with MOD3 at the University of Canterbury.[16]

Section 2.3.11.1 describes the software developed for use of the PCL-814B interface card with MOD4. Subsequent sections outline the application of this software to the sampling routines for (M)CD/double-beam absorption, emission, single-beam (M)CD and saturation scans. Programming of the SR510 LIA was covered in Section 2.3.8.3.

2.3.11.1. PCL-814B software, with applications to MOD4

In this section the fundamentals of the PCL-814B software in its MOD4 application are described. Part (a) covers programming of the A/D converter used to obtain the experimental data from the signals of Section 2.3.9.2. The channel and pin numbers are included, to give a clear relationship to the diagrams and discussion of Section 2.3.9.2.

Programming of D/I and D/O operations are discussed in part (b). Channel and pin numbers are included to allow correlation with the description of the electronics given in Sections 2.3.3.2(b), 2.3.9.1 and 2.3.9.2(d).

Software developed for the add-on timer-counter module (Section 2.3.10.2) is outlined in part (c). Included is the application to monochromator control in MOD4 (Section 2.3.3.2(b)).

(a) ADC programming

Basic procedures, and the ADC features employed in MOD4, are discussed in this section, which concludes with a summary of the channels utilised, and their hardware connections.

A/D conversions are performed *via* the driver program (PCL816.EXE) supplied with the PCL-814B. Use of the driver requires two steps. First, arrays for each data type are established by the software — these arrays are termed 'parameter tables'. Later, the software calls the driver with a 'function call' and the appropriate parameter table. The function call tells the driver what operation the ADC is to perform, while the parameter table contains the ADC settings.

The A/D module is selected by writing a 'zero' to the highest data-bus address

(20F, Hex) occupied by the PCL-814B.

(i) Parameter tables

The form of the parameter table is shown in Table 2.3.4, where MOD4 settings are given in the third column. A brief summary of the important parameters will be given here.

Table 2.3.4: Parameters used when programming the PCL-814B ADC

Parameter number	Name / purpose	Value
1	Board number	0 = first board
2	Base address	&H200
3	DMA channel for A/D data buffer A	3
4	Interrupt request level	2
5	Pacer rate, C1	12
6	Pacer rate, C2	12
7	A/D trigger mode	Varies*
8	A/D conversion mode	0 = non-cyclic
10	Offset of data array address to A/D data buffer A	Varies*
11	Segment of data array address to A/D data buffer A	Varies*
14	A/D conversion number	Varies*
15	A/D start channel	Varies*
16	A/D stop channel	Varies*
17	Overall gain code	Determined by signal level**
45	Error return	0 = no error; 1 = error
46	Return value	Varies†

* See Table 2.3.5 for the values used.

** Discussed in Section 2.3.11.2.

† Usage with MOD4 involves checking the status of pacer- or external- triggered A/D conversions only, although there are many other applications. In this case, '1' indicates that the conversion process is active, while '0' reveals its completion. See (b) below.

Each of the three A/D trigger modes available using parameter 7 (P7) are utilised in SPEC2. The PCL-814B has an on-board programmable timer/counter (Intel 8254; Section 2.3.10.2). Channels 1 and 2 are cascaded in a fixed-divider configuration, providing a pacer for A/D conversion ('pacer trigger') if P7 is set to zero. The sampling frequency is given by eq (2.3.1), where C_1 and C_2 are defined by parameters 5 and 6 (P5 and P6), and must have a value from 2 to 65535.

$$\text{Pacer rate (kHz)} = 10^4 \text{ kHz} / (C_1 \times C_2) \qquad (2.3.1)$$

Pacer triggering is used to rapidly (~69 kHz) gather 'sample' and 'reference' data in double-beam mode (Section 2.3.11.2), and emission and single-beam (M)CD data in their respective modes (Sections 2.3.11.3 and 2.3.11.4). (Sampling rates above ~69 kHz were found to cause random errors that 'crashed' the computer, despite a specification of 100 kHz.) Data acquisition is independent of CPU speed when using DMA data

transfer (see below).

Because software is used to initiate acquisition, pacer triggering is unsuitable for gathering 'dark' data (double-beam mode); the computer's system interrupts do not occur consistently within the short time available for sampling (Figure 2.3.14(e)). The interrupts delay software response to the 'dark' gate going TTL-high, and variations cause non-dark data to be obtained during some 'dark' sampling periods. The second A/D triggering method — external triggering (P7 = 1) — provides the solution, because the ADC is initialised well before a dark period and the ADC is not affected by system interrupts. External triggering is similar to pacer triggering, except that an A/D conversion occurs each time a positive TTL edge is detected on (only) D/I channel 0 (part (b)). In MOD4 the trigger source is provided by the chopped 'dark' gate (Section 2.3.9.1 and Figure 2.3.14(d)(v)), which during the dark period has TTL edges at a frequency of ~35 kHz.

For both pacer- and external-triggered A/D conversions, direct-memory-access (DMA) data transfer is utilised, providing rapid, CPU-independent transfer of data into the allocated data arrays. The method of data transfer is specified by the function call (see below), while parameter 3 sets the DMA channel for A/D data buffer A (buffer B is not used).

While pacer and external triggering are limited to making more than one conversion per call on the driver, the third mode — software triggering (P7 = 2) — is not. Software triggering is employed in MOD4 to obtain the single (M)CD datum per chopper cycle (double-beam mode), since integration occurs over the entire sample period (Section 2.3.9.2(b)). Data transfer is achieved by software in this case, not DMA or interrupt. Software A/D triggering with software data transfer does not return control to the calling software until the conversion and transfer process is complete, and is therefore CPU-speed dependent. More detail is given in part (ii).

Note that although the pacer is not used during external- or software-triggered A/D conversions, P5 and P6 must have values within the limits specified above (Table 2.3.5).

Data arrays are dimensioned for each data type in double-beam mode (sample, reference, dark1, dark2 and (M)CD; Table 2.3.4), enabling them to be summed at a suitable time during the chopper cycle. Consequently, parameter tables for each data type must be set up (Tables 2.3.5 and 2.3.6), and as the chopper cycle proceeds the A/D

module must be re-initialised for each table (data type). The contents of each data array are overwritten during the next cycle (parameter 8 is 'non-cyclic'). Parameter 14 specifies the number of samples that the A/D module is to make. In double-beam mode P14 is chosen with the help of the utility MOD4DIAG (Section 2.3.9.1). Consideration of the CPU-dependent summing of data (Section 2.3.11.2) must be made such that CPU time is not wasted, nor is the computer still summing old data when new data sampling should be occurring.

Table 2.3.5: PCL-814B programming parameters dependent on data type.

Parameter number*	Data types				
	Sample	Reference	Dark1	Dark2	(M)CD
7	0 = Pacer	0 = Pacer	1 = External	1 = External	2 = Software
10**	DatSample%	DatRef%	DatDark1%	DatDark2%	DatCD%
11**	DatSample%	DatRef%	DatDark1%	DatDark2%	DatCD%
14	1000	1000	30	30	1
15	4	4	0	0	1
16	4	4	0	0	1

* See Table 2.3.4 for the variable that the parameter number refers to.
** The QuickBASIC VARPTR and VARSEG memory-allocation functions operate on the relevant data array for parameters 10 and 11, respectively, to give the address of the variable for the PCL-814B driver.

For all scan modes only one data type is sampled at any time, so the start and stop channels (parameters 15 and 16) are the same — automatic scanning over multiple A/D channels is not utilised here.

Parameter 17 sets the programmable gain level for all A/D channels to the same value — individual gains can be set in a 'gain-code table', where use of parameters 18 and 19 specify the memory location. Here, an overall gain setting is used since data are sampled from only one channel at a time, and the A/D is re-initialised before the next data type is collected. The available bipolar and unipolar gains are shown in Table 2.3.6. Sections 2.3.11.2 – 2.3.11.5 include a discussion of the application of the programmable gain feature.

Table 2.3.6: Input ranges, recommended gains and gain codes for the A/D module.

Input range	Recommended gain	Gain code
-5 to +5 V	×1	0
-2.5 to +2.5 V	×2	1
-1.25 to +1.25 V	×4	2
-0.625 to +0.625 V	×8	3
0 to +10 V	×1	4
0 to +5 V	×2	5
0 to +2.5 V	×4	6
0 to +1.25 V	×8	7

(ii) Function calls

When the PCL-814B driver is called by the SPEC2 software, a function number and the appropriate 'parameter table' are passed to the program as 'parameters'. This is termed a 'function call', where the function number (an integer) tells the driver program what operation the PCL-814B is to perform, and the parameter table gives the driver the settings. Table 2.3.7 summarises the PCL-814B function calls that are used in SPEC2.

Table 2.3.7: Function calls used in SPEC2.

Function number	Function's effect
3	Driver initialisation
4	A/D module initialisation
5	Performs software-triggered A/D conversion
6	Performs pacer- or external-triggered A/D conversion with DMA transfer
7	Gets operation status of function 6*

* See Table 2.3.4; return value is obtained from the value of parameter 46.

Driver initialisation is invoked before the scan begins, ensuring that the PCL-814B is functioning correctly. Initialisation of the A/D module is required prior to sampling each data type during every chopper cycle in double-beam mode, because the parameter tables differ. The A/D module is then ready to undertake conversions.

Software-triggered A/D conversions are initiated using function 5, and only return control to SPEC2 after the data is transferred, as noted earlier. This function is only utilised for the integrated (M)CD signal (double-beam mode).

Pacer- and external-triggered A/D conversions give the option of DMA or interrupt data transfer; only the former is used here. DMA allows rapid data transfer to the data buffer specified by parameters 10 and 11, and is hence independent of CPU speed. The process is initiated using function 6, while the status of the conversion/transfer is checked using function 7. (In actual fact, in double-beam mode SPEC2 uses the CPU to sum other data while the PCL-814B is sampling independently (Section 2.3.11.2), before checking the conversion status.) Parameter 46 is unity if the conversion is still occurring, and zero when complete. (The conversion process can be halted using function 8, an option that is not employed.) The data types obtained using these A/D trigger modes were described earlier.

(iii) Connections

The external connections to the female D-37 connector of PCL-814B A/D module are given in Table 2.3.8 for all channels in use. All signals are derived from the

MOD4 electronics unit.

Table 2.3.8: Connections and signals into the A/D converter.

Channel	Pin number (high, low*)	Signal	Section
0	1, 19	Preamp signal**	2.3.9.2.(a)
1	2, 20	Integrated (M)CD	2.3.9.2(b)
2	3, 21	Voltage proportional to magnetic field	2.3.11.5
3	4, 22	Single-beam (M)CD	2.3.9.2(c)
4	5, 23	Filtered, inverted preamp signal	2.3.9.2(a)

* 'Low' is connected to the MOD4 electronics unit ground.
** Containing 'raw' double-beam absorption or emission data.

(b) Digital input/output programming

The PCL-814B A/D module also incorporates 16 D/I and 16 D/O channels. Although the PCL-814B driver program can be used to perform D/I and D/O operations, direct addressing is achieved almost as simply, while requiring less CPU time. Access to the D/I and D/O channels is through the two lowest locations occupied by the PCL-814B (200 and 201 (Hex); Section 2.3.10.2).

Reading the low and high bytes give the status of D/I channels 0 to 7, and 8 to 15, respectively. Whether a particular channel is TTL-high or TTL-low is determined by a logical AND of the byte with the appropriate binary value for the channel.

Five input channels are used by MOD4 (Table 2.3.9). Channel 7 carries the monochromator status (Sections 2.3.3.2(b) and 2.3.11.1(c)), while the remainder carry the sampling gates used in double-beam-mode (Sections 2.3.9.1 and 2.3.11.2).

Table 2.3.9: Digital-input channels used, their purpose and connection number.

Digital input channel	Signal	Pin number on D/I 20-pin connector at PCL-814B board*
0**	Dark gate AND oscillator	1
1	Sample gate	2
3	Reference gate	4
5	Dark gate	6
7	Stepper motor status	8

* Pin number is the same at the 40-pin connector on the electronics unit.
** Special input channel used for external-triggering of A/D conversions (Section 2.3.11.1(a)).

D/O operations involve writing a byte to the same locations. For each bit, a value of one yields a TTL-high output for the corresponding D/O channel, whereas a zero produces a TTL-low signal.

The D/O channels used by MOD4 are shown in Table 2.3.10. The first three are

used for stepper-motor control (Section 2.3.3.2), while the remainder control the optional programmable-gain amplifier (Section 2.3.9.2(d)).

Table 2.3.10: Digital-output channels used, their purpose and connection number

Digital output channel	Signal	Pin number on D/O 20-pin connector at PCL-814B board*
2	Trigger**	3
4	Stepper motor direction**	5
6	Gate**	7
12	Switch inverting amplifier in†	13
13	First gain-setting bit†	14
14	Second gain-setting bit†	15
15	Third gain-setting bit†	16

* For 40-pin connector on the electronics unit, add 20 to these pin numbers.
** Monochromator stepper-motor interfacing; Section 2.3.3.2(b) gives the overall connectivity, and Section 2.11.1.1(c) the use in software.
† Programmable-gain amplifier interfacing (Section 2.3.9.2(d)). TTL-high closes 4046B switch unit.

(c) Programming the timer/counter module

As noted in Sections 2.3.3.2(b) and 2.3.10.1, the MOD4 monochromator stepper-motor circuitry requires a programmable counter to undertake wavelength slewing. In this section, programming of the Am9513A-based timer/counter add-on module to the PCL-814B in the MOD4 application is described.

Of the 24 counter modes available, only mode A ('software-triggered strobe with no hardware gating') is used and hence covered here. This mode is employed with either one (part (i)) or two (part (ii)) counters.

The timer/counter module is installed in Slot 1 of the PCL-814B, and is selected by writing '1' to address 20F (Hex). It has several registers which are relevant to the current discussion. The registers are accessed by writing to the 8-bit 'Control Port' (location 201 (Hex)), and contents read or written through the 16-bit 'Data Port' (200 (Hex)). In addition to addressing registers, the 'command register' can be accessed directly by writing to the Control Port. (Register addresses all have zeroes for the three most-significant bits, while commands have non-zero values. Several of the commands are utilised; see (i) and (ii).) Reading the Control Port returns the status byte.

Overall settings for the Am9513A are written to the 'master mode register' *via* the Data Port, which is itself addressed by writing '17' (Hex) to the Control Port. The only setting worthy of note is that the bus width is set to 8 (not 16) bits; the low byte of 16-bit data is transferred first. (No delay between reading or writing the two bytes is required with the computer described in Section 2.3.10.1.) The master mode register is

one of the control group registers.

Each of the five counters has its own 'mode', 'load' and 'hold' registers. The 16-bit counter mode register contains the counter's settings, such as its operating mode (*e.g.* mode A). In both parts (i) and (ii), binary counting on rising TTL edges is used; settings that differ are mentioned in each section. The load register contains the 16-bit count. The 16-bit hold register can be written to (as an alternative load register), or used to store the counter's current count for reading from the data port (see (i)).

Note that the count source is provided by the pulse train that drives the stepper motor (Section 2.3.3.2(b)). Table 2.3.11 gives the connections to the 20-pin connector of the timer/counter module. The GATE2 connection is not used for mode A, because there is no hardware gating.

Table 2.3.11: PCL-814B timer/counter module connections.

Signal	Pin number on 20-pin connector (CN1)*	Pin number on D9 connector at monochromator
GATE2	3	[D/O channel 6; Table 2.3.10]
SRC1	7	8
OUT2	13	1
GND	17	6, 9

* See Section 2.3.3.2 for connections to stepper motor circuitry and PCL-814B D/I and D/O ports.

(i) Normal counting using a single counter

A single 16-bit counter is able to control slews of up to ~3250 Å at the highest monochromator scan speed (that is, the biggest wavelength step per count; Section 2.3.3.2). For slower scan speeds the slew range is reduced in direct proportion to the reduction in gear ratio. Concatenation of two counters to undertake longer scans is dealt with in the next section.

The counter is programmed as follows. Having selected the timer/counter module, the 16-bit mode register of counter 2 is selected by writing '2' to the Control Port. The settings are then written to the register through the Data Port. They include non-repetitive counting down to zero, using SRC1 as the count source, and having counter 2's dedicated output (OUT2) go TTL-low on terminal count (see Section 2.3.3.2(b)).

The second step is to load the count corresponding to the scan length (and scan speed — see (iii)). Counter 2's load register is selected by writing '10' to the Control Port, and the count is loaded into the register through the Data Port.

Finally, counter 2 must have its count loaded from the load register, and be

activated for counting. These two functions can be performed simultaneously using the 'load and arm' command, which for counter 2 involves writing 62 (Hex) to the Control Port.

Note also that counter 2's current count can be read by the software, although this feature is not utilised in SPEC2. First, the current count is saved to the counter's hold register by writing 'A2' (Hex) to the Control Port. Second, counter 2's hold register is addressed by writing '12' (Hex) to the Control Port. Finally the count is retrieved by reading the Data Port.

(ii) Concatenation (or linking) of counters

Slews requiring more than 2^{16} steps of the stepper motor are performed by means of internal concatenation of two adjacent counters in the Am9513A. By connecting the counters in this manner up to 2^{32} counts can be made, although it unlikely that greater than 2^{18} counts will ever be required. The programming procedure generally follows that employed for a single counter, although one counter has some quite different settings to those described in (i).

Once the timer/counter module has been selected, the counter 1 and 2 mode registers must be set. Counter 1 (the lower-order counter) is selected by writing a '1' to the Control Port, and its settings are then loaded through the Data Port. This counter is programmed to count upwards (with repetitive counting), using SRC1 as the count source, and have an inactive (external) output (on OUT1) on terminal count (each time 65535 is counted through).

The counter 2 mode register is addressed as described in (i). (It is the higher-order counter.) The settings loaded differ only for the count source, and the direction of counting (upwards here, like counter 1). The source is TCN-1, an internal connection in the Am9513A to the terminal-count output of counter 1, from which counter 2 makes its count. Like the single-counter application in (i), counter 2 has an active-low output (OUT2; see Section 2.3.3.2(b)) on terminal count.

The next step is to load the count for each of the counters. The load register is accessed through the Control Port by writing a '9' or '10' for counters 1 and 2, respectively. The method used for both counters is analogous to (i), except that the count is split, and must be manipulated for upward counting. (Counter 2 will most often have a value of ten (set arbitrarily), while counter 1 cycles continuously through one tenth of the total count. If division of the total count by ten gives a remainder greater

than unity, a short correction slew of the type described in part (i) is undertaken before the long slew. However, if the remainder is unity (the counters cannot count one), or the quotient (counter 1's count) is greater than 65 000, the divisor is incremented by one, and the above repeated before the slew is undertaken.)

The last step is to 'load and arm' the counters (see (i)). This is achieved for both counters simultaneously by writing 63 (Hex) to the Control Port.

(iii) General procedure for scanning of the monochromator wavelength

This section briefly describes the procedure used to undertake all wavelength slews in SPEC2.

First, the stepper motor's 'status' is checked by reading the most significant bit (channel 7) of the D/I low byte (Section 2.3.11.1(b)). For program execution to continue the status must be TTL-low, indicating that the monochromator is inactive (Section 2.3.3.2(b)). If it is high, a slew is in progress, and the software loops until the input line goes low.

Second, the subroutine calls the appropriate slewing routine (determined by the number of counts the stepper motor is to take, as described in parts (i) and (ii), respectively). The direction (positive or negative) and number of counts required for the slew are passed as parameters.

Both slewing routines can be generalised as follows. The timer/counter module is selected, and the counters programmed and activated, as described in (i) and (ii). Then the monochromator is set to slew by selecting the A/D module, then simultaneously writing the start pulse and slew direction to the D/O low byte (Section 2.3.11.1(b)). The rising edge produced by D/O channel 2 going TTL-high initiates the slew, the direction of which is of either increasing or decreasing wavelength, obtained by holding D/O channel 4 high or low, respectively. Immediately after triggering the scan, the same D/O byte is written again, retaining the direction, but resetting the start signal to low. Finally, a check of the monochromator status (D/I channel 7) is made to ensure that the scan has started.

Control is then returned to the calling subroutine. Note that the stepper motor is stopped when counter 2's output (OUT2) goes TTL-low (Section 2.3.3.2(b)) at terminal count. The CPU, with no further role in the slewing procedure, is left free to perform other operations.

(iv) Incorporation of wavelength scanning into SPEC2

This section very briefly introduces the general slewing procedure used in MOD4, and the inclusion of variable monochromator scan speeds and diffraction gratings into the SPEC2 software.

On entering SPEC2, the user gives the current wavelength of the monochromator. From this point the software can take care of all slewing. The effect of backlash in the monochromator's scanning mechanism (Section 2.3.3.2(c)) is eliminated by always acquiring spectral data with decreasing wavelength, after undertaking a 20-nm slew to the start wavelength. The backlash slew is performed at the start of each scan.

After data are collected at the first wavelength, and for each subsequent step through the scan (Sections 2.3.11.2 – 2.3.11.4), the monochromator is activated to move to the next wavelength, leaving the CPU free to complete other tasks. Before obtaining data at the next step, the monochromator status is checked, as described in (iii). At the completion of data collection, or if it is aborted, the monochromator will automatically slew back to the start wavelength (allowing for backlash correction), if the option is set.

SPEC2 allows either of the three fastest scan speeds, approximately 2500, 1250 and 500 Å/min., to be used, with one step of the stepper motor equal to 0.05, 0.025 and 0.01 Å, respectively. This gives a minimum wavelength slew for each scan speed. In addition, for small step sizes, some modification by the software may be necessary for the two fastest scan speeds if the stepper motor step, when divided into the wavelength step, leaves a remainder. The total number of steps to be taken by the stepper motor for a slew is calculated by dividing the scan in angstroms by the wavelength of a single stepper motor step for the scan speed.

Two diffraction gratings are available for use with MOD4 (Section 2.3.3.1). The wavelength counter reading corresponds 1:1 with the wavelength for the 1180-groove/mm grating, and because it is most commonly used, the software is based around it. For the 580-groove/mm grating, the wavelength is double the counter reading, so correction is made for slewing *via* a variable. The true wavelength must be entered, but the counter setting is half this. Backlash compensation remains 200 counter units, since it is of mechanical origin.

2.3.11.2. (M)CD and double-beam absorption

In this section the sampling procedure for simultaneous (M)CD and double-beam absorption is summarised. The relevant subroutine in SPEC2 is 'Samp'.

Before the scan begins, the monochromator is slewed to the start wavelength to eliminate backlash (Section 2.3.3.2(b)). If (M)CD data are to be acquired the PEM control voltage is incremented to the voltage corresponding to the initial wavelength (Sections 2.3.5.2(b) and 2.3.8.3). If selected, the initial PMT HV is also programmed (Section 2.3.7.1(c)).

When the monochromator backlash slew (or any wavelength step during the scan) is complete, the software first ensures that the LIA input has not overloaded (Section 2.3.8.3). If it has, the sensitivity is reduced, and this change is subsequently accounted for by the software in the calculations.

Next, the PCL-814B gain is optimised for each data type, to make best use of the ADC's 14-bit resolution (Section 2.3.11.1(a)). The gains are initially set to unity, then data are gathered during a single chopper cycle using the subroutine SamplingRoutine. Instead of generating a running sum (as it does during later data acquisition), SamplingRoutine sorts each data type in order to find the value of the largest magnitude. From the maximal values the appropriate gain is determined and inserted into the ADC parameter tables (Section 2.3.11.1(a)).

At this point, if the user has selected remote HV programming of the PMT, the software checks that the sample and reference voltages satisfy certain criteria before proceeding to gather the data. If they do not, the HV is adjusted and the gain-optimisation procedure is repeated until they do satisfy the criteria.

Now the absorption and (M)CD data are obtained for the wavelength step. On entering the subroutine SamplingRoutine, the 'dark' gate (Section 2.3.9.1) is monitored, although the 'sample' data are to be gathered first. This ensures that acquisition does not begin in the middle of the 'sample' gate which would entail a risk of overrunning the 'sample' period. After the 'dark' gate has gone TTL-high, the main sampling loop is entered. The 'sample' data are gathered after the 'sample' gate goes high. If it is the second or subsequent cycle, the previous cycle's 'reference' data will be summed as the DMA transfer occurs. 'Dark1' data are gathered when their gate goes high, and 'dark2' data are summed if it's the second or later cycle. 'Reference' data acquisition follows 'dark1', while the current cycle's 'sample' data are summed. The CD datum for the

chopper cycle (Section 2.3.9.2(b)) is then read from channel 1. Finally, 'dark2' data are obtained while 'dark1' data are summed. The process continues until the number of chopper cycles is complete, with the data summed in running totals. After the final cycle, the last 'reference' and 'dark2' data are summed, before leaving the subroutine SamplingRoutine and returning to Samp.

The slew to the next wavelength is initiated (Section 2.3.11.1(c)), freeing the computer to manipulate the data, and perform other tasks, such as plotting to the screen. Averaging of the 'sample', 'reference', 'dark' and (M)CD data are performed, including normalisation to the minimum gain value, before the true absorption and (M)CD are calculated as follows.

The absorption at a given wavelength is

$$A = -\log_{10}(I / I_0) \tag{2.3.2}$$

where I_0 is the intensity of the light incident on the sample, and I is the intensity transmitted by the sample. In double-beam absorption spectroscopy, I is measured in the sample beam, while I_0, or a fraction (k) thereof, is measured in the reference beam. MOD4 measures kI_0 in the reference beam, due to some extent of reference attenuation (Section 2.3.6.2). Because absorption is a logarithmic scale, k only causes a shift (C) of the whole spectrum, which is easily subtracted later. Mathematically,

$$\begin{aligned} A_{\text{meas}} &= -\log_{10}(I / k I_0) \\ &= -\log_{10}(I / I_0) + \log_{10}(k) \\ &= A + C \end{aligned} \tag{2.3.3}$$

The final consideration before calculating the absorption is the detector dark current (Section 2.3.6.1), and/or any non-zero offsets in subsequent amplification stages. These contributions are removed in a straightforward manner by subtracting the no-light signal of the 'dark' period from the 'sample' and 'reference' signals. Therefore the absorbance of the sample at any given wavelength is,

$$A_{\text{meas}} = -\log_{10}\left(\frac{V_{\text{sample}} - V_{\text{dark}}}{V_{\text{reference}} - V_{\text{dark}}}\right) \tag{2.3.4}$$

since the intensities are measured as voltages.

The (M)CD signal at the integrator (ΔA_{int}) is proportional to the sample-beam intensity, the LIA sensitivity (L, in mV), and an empirical calibration factor (f;

determined for a LIA sensitivity of 10 mV). ΔA_{int} is corrected using,

$$\Delta A_{meas} = \frac{\Delta A_{int}\, L\, f}{(10\text{ mV})\,(V_{sample} - V_{dark})} \qquad (2.3.5)$$

where $(V_{sample} - V_{dark})$ is the averaged 'sample-minus-dark' intensity, and ΔA_{meas} is the (M)CD in units of ellipticity (millidegrees). The absorption, 'sample-minus-dark', 'reference-minus-dark' and (M)CD data are then saved to the appropriate arrays. The new (M)CD and/or absorption points are also plotted to the screen.

If (M)CD data are being collected, output of DAC channel 'X5', which controls the PEM (Section 2.3.8.3), will be incremented to the voltage for the next wavelength (Section 2.3.5.2(b)). Various other operations are performed before the software continues the loop for each wavelength step.

When this procedure has been performed for the entire spectrum, the user is given an opportunity to save or reject the data. The spectrum is saved in binary format, with the (M)CD in millidegrees.

2.3.11.3. Emission

This option is included within SPEC2, and utilises 'Samp' for control of data collection. It is used primarily for wavelength calibrations employing the Hg lamp (Section 2.3.12.1). Neither the chopper nor the LIA are used, and manual HV control is enforced.

Emission data are acquired from ADC channel 4; that is, the inverting amplifier (Section 2.3.9.2(a)) is utilised to obtain the favourable positive signal for the PCL-814B unipolar gains (Section 2.3.11.1(a)). The subroutine 'EmissionSR' collects the data at each wavelength. Like the double-beam case (Section 2.3.11.2), the first time 'EmissionSR' is called by 'Samp' it is used to set the gain according to the average signal level obtained (in this case) over one thousand samples. Having set the gain, the user-selected number of samples is obtained using pacer-triggered A/D conversion (Section 2.3.11.1(a)). The chopper-cycle basis for data acquisition is retained, and for every 'cycle' 1000 emission samples are taken.

At the completion of the scan, the data are saved as ADC 'counts' ($0 - 2^{16}$ from the averaged and gain-normalised ADC reading) to the binary file. A flag in the saved file is set to indicated that the file contains an emission, rather than an absorption, spectrum.

2.3.11.4. Single-beam (M)CD

The accumulation of single-beam (M)CD spectra (Section 2.3.9.2(c)) differs in three ways from the case in the double-beam mode: (i) the chopper is off; (ii) the mode of detector operation is different; and, (iii) the acquisition method is different. Subroutine Samp (Section 2.3.11.2) is still used to control data collection (the required hardware settings for the scans were outlined in Section 2.3.9.2(c)), but the ADC samples the LIA output directly in this method. This results in a minor problem – whereas the maximum input range of the former is ±5-V, the maximum output range of the latter is ±10 V. Hence only half of the full-scale range of LIA can be employed if overloading of the ADC is to be avoided.

Data are gathered from ADC channel 3 using the subroutine EmissionSR (Section 2.3.11.3), which employs pacer-triggered DMA-transfer A/D conversion. As in the emission mode, EmissionSR is called twice, once to set the PCL-814B gain, and once to obtain the spectral data. The true (M)CD is obtained by multiplying the measured value by an empirical calibration constant, obtained using a LIA sensitivity of 10 mV and PMT power-supply feed-back voltage of 1 V. *It is imperative that the same feedback voltage be used, if the spectrum is to be consistent with the calibration.*

The data are saved in millidegrees (the units of ellipticity).

2.3.11.5. Magnetic-field saturation scans using SATSCAN2

Saturation scans are (in the context of this work) plots of MCD versus magnetic field at a *fixed* wavelength. The program SATSCAN2 collects single-beam MCD data at a fixed wavelength, using the settings given in Sections 2.3.9.2(c) and 2.3.11.4. At the same time, the magnetic field is monitored directly by the computer, as follows. The Oxford Instruments PS75 magnet power supply produces an analogue voltage, which is proportional to the current through the coil of the Oxford Instruments SM4 superconducting magnet (Section 2.2.2). This voltage is amplified to give 1:1 correspondence with the field (0 to 6 V corresponds to 0 to 6 T) before being read (*via* a BNC connector on the front panel of the MOD4 electronics unit) by ADC channel 2 using the 0 to 10 V range.

Because the wavelength is fixed, the PEM voltage is set at the start of the subroutine 'Samp', and henceforth is not altered. The magnetic-field scan direction (controlled by the Oxford Instruments SG3 sweep generator) can be positive or

negative, depending on the user's choice of the initial and final field settings. The scan rate is also entered by the user, but because the sweep generator is not interfaced to the computer, its values must coincide with those set physically on the sweep generator.

Before the MCD signal is gathered, the magnet field must be scanning; subroutine Samp monitors the field until the user-chosen initial value is obtained. (Subroutine 'FieldRead' performs this task, using pacer-triggered DMA-transfer A/D conversions (Section 2.3.11.1(a)).) The MCD data are then acquired *via* ADC channel 3 by the subroutine 'SamplingRoutine' after the gain has been optimised by an earlier call to the same subroutine (see, *e.g.*, Section 2.3.11.3). The field reading is measured again, and this and the initial value are averaged. For subsequent data acquisition steps there is no wait time; the measurement cycle field/MCD data/field is repeated until the final field value is reached. Data are then saved in a binary file of the standard format, except that the abscissa data are magnetic-field values, rather than wavelengths. A flag is set in the saved file to indicate to subsequent manipulation and fitting programs that it contains saturation data.

2.3.12. Calibrations

In this section the wavelength, absorption and (M)CD calibrants and calibration procedures for MOD4 are described.

2.3.12.1. Wavelength

There are two types of wavelength calibration performed on MOD4. The first involves calibration over the entire spectral range using a number of emission lines from a low-pressure mercury lamp, and is sufficient for broad-band spectra investigated over moderate to large wavelength ranges. The second, for sharp spectra, involves more precise single- or double-point calibrations using lines within, or very near to, the appropriate scan region. A low-pressure Philips 125-W Hg ballast lamp was employed for all wavelength calibrations done in this work. Suitable moderate and high-intensity lines were chosen from the listing in Ref. 27.

2.3.12.2. Absorption

MOD4 absorption data do not (in principle) require calibration (Section 2.3.11.2). Nevertheless, a periodic check of the absorption is made, to bring potential problems to light. (For example, excessive stray light will cause a decrease in measured

optical density.) Broad-band absorbers (such as $K_3[Fe(CN)_6]$ in the visible and *d*-10-camphorsulfonic acid (*d*-10 CSA) in the UV) are commonly used to compare MOD4 with commercial spectrometers, since their absorbance is essentially independent of spectrometer resolution. A crystal calibrant, $Na_3[Nd(ODA)_3].2NaClO_4.6H_2O$ ($Nd(ODA)_3$)[22] has also been utilised. This sample has advantages over solutions, because its composition (and hence optical densities) does not change with time and it has many absorption bands over a wide spectral range (with a great variety of optical densities). In addition, its natural optical activity makes it a very convenient standard for the (M)CD calibration (Section 2.3.12.3), for which purpose it is employed almost exclusively. The optical densities of a variety of absorption bands were calibrated after it was determined that MOD4 obtains true optical density values.

2.3.12.3. (M)CD

In this section the calibrants and methods used for double- and single-beam CD calibrations are described. The CD calibration applies to the MCD also, apart from a 180° phase change at the LIA to account for the magnetic-field direction.

Initial calibration of the CD for MOD4 was performed using an optically pure solution of *d*-$[Co(en)_3][Cl][tartrate].5H_2O$. Calibration factors were derived for the single- and double-beam modes by taking the ratio of the true CD to that measured using MOD4.

The advantages of the $Nd(ODA)_3$ crystal as a calibrant were outlined in Section 2.3.12.2. Its natural optical activity and abundance of transitions of varying intensities mean that it is a convenient multiple-point standard for CD calibrations. A crystal has been standardised for use in our laboratory.

Because the detectors available for use with MOD4 (Section 2.3.7) have differing responsitivity to the 50-kHz (M)CD signal, they require different calibrations. For convenience, their calibrations have all been normalised to that of the Hamamatsu R-376, which has a wide spectral range, and a good S/N ratio. Table 2.3.12 shows the multipliers that SPEC2 uses to correct (M)CD spectra if the R-376 is not used.

Seven to ten bands in the CD spectrum of $Nd(ODA)_3$ (between 545 and 495 nm) are used for the multi-point CD calibrations. (Since the $Nd(ODA)_3$ crystal is uniaxial, it is important that it is correctly oriented with its unique (*c*) axis aligned exactly along the path of light propagation. See Section 1.3.4.1.)

Table 2.3.12: Multiplier required to obtain true (M)CD when the Hamamatsu R-376 detector is not used.

Detector	Multiplier	Signal/noise*
EMI 9514S	0.90	Good
Hamamatsu R-292	0.99	Good
Hamamatsu R-316	0.94	Poor
Philips BPX-65 photodiode	1.44	Satisfactory

* The R-376 was found to have the best S/N.

The LIA phase is set by using the following procedure: the wavelength is scanned to a point at which the CD is non-zero, then the phase is adjusted to give a zero CD reading. The correct phase is then set by shifting the phase by either +90° or –90° to obtain the maximum signal of the correct sign. (The zero reading can be determined much more precisely than an extremum, because the rate of signal change with respect to phase is greatest at that point.) The 'Control Panel' option in SPEC2 greatly enhances the accuracy of this process, because it averages the integrated CD signal over 10 chopper cycles in double-beam mode, or 10000 samples in single-beam mode. It is very much more difficult to set the phase using the digital or analogue displays of the LIA (particularly so for double-beam mode, due to switching of the preamp signal; Section 2.3.9.2(b)). Note that different phase settings are required for single- and double-beam modes, since they employ different signal-processing electronics.

In double-beam mode it is essential that the 'sample' gate (Section 2.3.9.1) be set correctly before performing a calibration. The gate must not intrude into the 'dark' portions of the preamp signal, yet it should fill the 'sample' region as far as possible. (Note that it is stable, and does not normally require adjustment.) Once the CD has been calibrated the 'sample' gate cannot be changed without affecting the calibration. The other system settings were covered in Sections 2.3.8.2 and 2.3.9.2(b).

Settings for single-beam mode were given in Section 2.3.9.2(c). Since the (M)CD signal is proportional to the preamp voltage maintained by the feedback loop on the HV power supply (Section 2.3.7.1(c)), calibrations are obtained using 1 V.

2.4. References

1. Schlacta, R.; Lask, G.; Tsay, S. H.; Bondybey, V. E. *Chem. Phys.* **1991**, *155*, 267-274.

2. Thoms, A.; Wurfel, B. E.; Schlacta, R.; Lask, G.; Bondybey, V. E. *J. Phys. Chem.* **1992**, *96*, 7231-7235.

3. Stangassinger, A.; Schuenchenpflug, J.; Prinz, T.; Bondybey, V. E. *Chem. Phys.* **1993**, *178*, 533-546.

4. Wurfel, B. E.; Thoma, A.; Schallmoser, G.; Lammers, A.; Bondybey, V. E. *J. Chem. Phys.* **1994**, *100*, 8003-8009.

5. Bondybey, V. E.; Brus, L. E. *J. Chem. Phys.* **1975**, *63*, 794-804.

6. Rose, J. L. Ph.D. Dissertation, University of Virginia, Charlottesville, 1987.

7. Gasyna, Z.; Andrews, L.; Schatz, P. N. *J. Phys. Chem.* **1992**, *96*, 1525-1527.

8. Lichtenberger, D. L.; Nebesny, K. W.; Ray, C. D.; Huffman, D. R.; Lamb, L. D. *Chem. Phys. Lett.* **1991**, *176*, 203-208.

9. Dunford, C. L. Ph.D. Dissertation, University of Canterbury, Christchurch, 1997.

10. Durieux, M.; Rusby, R. L. *Metrologia* **1983**, *19*, 67-72.

11. Douglas, I. N.; Grinter, R.; Thomson, A. J. *Mol. Phys.* **1974**, *28*, 1377-1388.

12. Schatz, P. N.; McCaffery, A. J.; Suetaka, W.; Henning, G. N.; Ritchie, A. B.; Stephens, P. J. *J. Chem. Phys.* **1966**, *45*, 722-734.

13. Collingwood, J. C.; Day, P.; Denning, R. G.; Quested, P. N.; Snellgrove, T. R. *J. Phys. E: Sci. Instrum.* **1974**, *7*, 991-996.

14. Misener, G. C. Ph.D. Dissertation, University of Virginia, Charlottesville, 1987.

15. Kenney, J. W., III. *Hinds Instruments PEM Applications* **1995**, *Summer*, 1-3.

16. Upton, A. H. P. M.Sc. Thesis, University of Canterbury, Christchurch, 1991.

17. Upton, A. H. P.; Williamson, B. E. *J. Phys. Chem.* **1994**, *98*, 71-76.

18. Dunford, C. L.; Williamson, B. E. *J. Phys. Chem. A* **1997**, *101*, 2050-2054.

19. van Hale, R. J. BSc(Hons) Project Report, University of Canterbury, Christchurch, 1991.

20. Policke, T. A.; Schreiner, A. F.; Trexler, J. W.; Knopp, J. A. *Rev. Sci. Instrum.* **1990**, *61*, 2073-2079.

21. Moore, J. H.; Davis, C. C.; Coplan, M. A. *Building Scientific Apparatus. A practical guide to design and construction*; Addison-Wesley Publishing Company, Incorporated: Reading, 1983.

22. Albertsson, J. *Acta Chem. Scand.* **1968**, *22*, 1563-1578.

23. Jasperson, S. N.; Schnatterly, S. E. *Rev. Sci. Instrum.* **1969**, *40*, 761-767.

24. *Co-Netic & Netic Magnetic Shielding Alloys; Material and Fabrication Guide*; Magnetic Shield Corp., Perfection Mica Company, Bensenville, Illinois, 1988.

25. Williamson, B. E. MOD2 Laboratory Notes; University of Virginia, 1985.

26. *Model SR510 Lock-in Amplifier Manual*; Stanford Research Systems, Sunnyvale, CA, 1989.

27. Lide, D. R., Ed. *CRC Handbook of Chemistry and Physics*, 71st ed.; CRC Press, Inc: Boca Raton, 1990.

3. THEORY

In 1983 Piepho and Schatz[1] published a significant monograph on group theory and MCD. The elementary theory of MCD was presented, explaining and quantifying the MCD dispersion forms (Section 1.3.2). It also applied very powerful group-theoretical techniques to the derived equations, which eased computational effort by reducing them to the calculation of a minimal number of symmetry-unrelated matrix elements. Worked examples of the applications of these and the appropriate quantum-mechanical methods were given. The group-theoretical conventions, and extensive tabulations of high-symmetry coupling coefficients due to Butler[2] were used throughout, and the relations between various MCD conventions were concisely summarised in appendices. Aspects of that work pertaining particularly to this thesis are presented in this chapter, and developed in a logical, concise form. All of the conventions of Piepho and Schatz[1] are followed, with the exception of transition moments, where the more standard convention[3] of bras and kets is utilised. Quantum mechanical conventions employed are described in Section 3.1.

There are many fine texts on group theory and its application to chemistry and spectroscopy.[1,2,4-6] The purpose of this chapter is not to reproduce the basic principles, but to introduce their application to the theoretical analyses performed in this work. To this extent, the description of group theory in Section 3.2 is directed toward the applications of subsequent sections.

The method used to generate molecular wavefunctions, and evaluate matrix elements, is covered in Section 3.3. Following a discussion of selection rules for electronic transitions, and the evaluation of transition moments, MCD and absorption theory are introduced in Section 3.4. The equations presented are applied and developed in later chapters. Data-analysis methods are summarised in Section 3.5. First, moment analysis is used over entire band systems.[1] Second, spectral simulations are employed to elucidate contributions to fine structure.

3.1. Quantum mechanical conventions

This section describes two important quantum mechanical conventions that are used in this work.

3.1.1. Vector operators[1]

For a vector (or pseudo-vector) operator $\boldsymbol{V}$, there are real, Cartesian components V_x, V_y and V_z,

$$\boldsymbol{V} = (V_x, V_y, V_z) \tag{3.1.1}$$

which are related to complex, spherical components by,

$$V_{\pm 1} = \mp \frac{1}{\sqrt{2}} (V_x \pm iV_y)$$

$$V_0 = V_z \tag{3.1.2}$$

where $i = \sqrt{-1}$. Spherical tensors are a favourable form for use in MCD, since they are defined to have identical transformation properties to the $|jm\rangle$ of the angular momentum basis ($\mathbf{SO}_3 \supset \mathbf{SO}_2$; see Section 3.2.2), *i.e.* $V_{\pm 1} \sim |1 \pm 1\rangle$ and $V_0 \sim |1\ 0\rangle$.

3.1.2. Bra-ket notation[1,7]

Matrix elements are integrals of the form shown on the left-hand side of eq (3.1.3).

$$\int \psi_J^* \, \boldsymbol{O} \, \psi_A \, d\tau \equiv \langle \psi_J | \boldsymbol{O} | \psi_A \rangle \equiv \langle J | \boldsymbol{O} | A \rangle \tag{3.1.3}$$

$\boldsymbol{O}$ is an operator, and ψ_A and ψ_J are wavefunctions. The asterisk denotes complex conjugation, while integration is over all space ($d\tau$).

In this thesis, matrix elements are written using Dirac's bra-ket notation, which abbreviates the definite integral to the forms shown on the right-hand side of eq (3.1.3). In this notation, $|\psi_A\rangle$ is a 'ket' and $\langle \psi_J|$ is a 'bra', with

$$|\psi_J\rangle^\dagger = \langle \psi_J| \tag{3.1.4}$$

i.e. a bra is the adjoint (or tranjugate) of a ket.

In the remainder of this thesis, the notation $\langle J|\boldsymbol{O}|A\rangle$ is chosen, where A and J represent the transformation properties of ψ_A and ψ_J, respectively.[1] This choice is made because of the importance of group theory in relating various matrix elements (see next section).

Note that here *all* operators are taken to act on the ket, including transition-moment matrix elements (Section 3.4.2). This follows the convention of Herzberg,[3] but not that employed by Piepho and Schatz.[1]

3.2. Group theory

The wavefunctions of molecular states transform as the irreducible representations (irreps) of the molecular point group.[1] Hence group theory supplies a relatively straightforward method by which approximate wavefunctions (of exact symmetry) can be generated for the states (Section 3.3.1). In addition, symmetry can be used to find exact relationships between matrix elements, without the need for calculations (*i.e.* matrix elements need not be evaluated using quantum-mechanical methods for much useful information to be obtained).

This section gives a brief introduction to relevant group-theoretical notation, conventions and methods. Detailed presentations are given in Piepho and Schatz[1] and Butler.[2]

3.2.1. Notation

The group-theoretical notation used in this work is a mixture of the standard Mulliken notation[1,2] and the so-called natural (or Butler[2]) notation. The former is more familiar to chemists. However the latter readily lends itself to mathematical manipulations. Therefore, the use of Mulliken notation is limited to the labelling of terms and states. Butler's notation is utilised during the derivation of these terms and states (*i.e.* to evaluate direct products, *etc.*), and also to generate wavefunctions. It is also used to label double-group irreps, and other quantities, as will be made clear during the discussion. In terms of notational correlation, there is a simple label-for-label exchange between the two systems. For each point group used in this work, the equivalent irreps are shown in a table at the beginning of the appropriate theoretical discussion.

3.2.2. Chains of groups and branching rules[1,2]

The chain-of-groups approach used by Butler[2] provides a clear picture of the origin of the partners of degenerate irreps in the molecular point group. The chain is denoted by $\mathbf{A} \supset \mathbf{B} \ldots \supset \mathbf{F}$ (where **A**, **B**, ... are point group labels). The partners result from the reduction of symmetry to a lower point group where all irreps have a dimension of unity. The same chain of groups is also utilised to calculate the $2jm$ and $3jm$ described below. Butler shows branching diagrams for the molecular and crystallographic point groups, and gives branching-rule tables for each reduction,

showing how the irreps in the higher-symmetry point group correlate to those in the lower-symmetry group.

3.2.3. High-symmetry coupling coefficients: the 2*jm* phase and 3*jm* coefficient

In this work, the coupling coefficients of Butler are utilised, following the suggestion made by Piepho and Schatz.[1] The main reason for employing these conventions is that a nearly complete tabulation is given by Butler[2] for most molecular point groups. For those groups that are not documented (*e.g.* $\mathbf{D}_{5d}$), standard methods for deriving consistent coefficients are provided.

Butler's high symmetry coupling coefficients (HSCC) allow application of the very powerful methods of Racah algebra developed for use in the rotation groups $\mathbf{SO}_3$ and $\mathbf{O}_3$. ($\mathbf{O}_3 \equiv \mathbf{R}_3$ is the symmetry of a sphere. $\mathbf{SO}_3$ is the point group obtained by removing the centre of symmetry.) Here, only the small portion of the method required for use in this work is presented.

*3.2.3.1. 3*jm *coefficient*

The 3*jm* coefficient $\begin{pmatrix} a & b & c^* \\ \alpha & \beta & \gamma^* \end{pmatrix}^r$ is defined by Butler[2] in terms of Clebsch-Gordan (or vector) coupling coefficients, $(a\alpha, b\beta|c\gamma)$

$$(a\alpha, b\beta|rc\gamma) = |c|^{1/2} \begin{pmatrix} c \\ \gamma \end{pmatrix} \sum_r \begin{pmatrix} a & b & c^* \\ \alpha & \beta & \gamma^* \end{pmatrix}^r \qquad (3.2.1)$$

Here a, b and c are irreps with components (partners) α, β and γ, respectively. The sum is over the r repeated irreps. (Of the molecules investigated in this project, repeated irreps are only encountered in the icosahedral group; Appendix C.) $\begin{pmatrix} c \\ \gamma \end{pmatrix}$ is a 2*jm* phase (Section 3.2.3.1), and $|c|$ is the dimensionality of the irrep c. When working in $\mathbf{SO}_3$ or $\mathbf{O}_3$ an additional phase factor $H(abc)$ is generally added to make the phase conventions compatible with the historical Condon-Shortley phases in the angular momentum basis; in $\mathbf{SO}_3$ and $\mathbf{O}_3$, $H(abc) = H(j_1\, j_2\, j_3) = (-1)^{-j_1+j_2-j_3}$.[1]

Tables of 3*jm* for the point groups $\mathbf{C}_{\infty v}$ and $\mathbf{I}_h$ are given in Appendix B. The tables are not complete because the former has an infinite number of irreps, while the latter has a very large number irreps of which only those tabulated are required. Only the non-zero 3*jm* are given, although not all possible combinations are listed explicitly because they can be readily derived by permutation relations. 3*jm* are invariant under

cyclic (even) permutation of their columns. Some are also invariant under non-cyclic (odd) permutations; those that change sign under non-cyclic permutation are marked by a dagger (†) superscript.

Finally, the 3*jm* and its complex conjugate 3*jm** are related by,

$$\begin{pmatrix} a & b & c \\ \alpha & \beta & \gamma \end{pmatrix}^{*^r} = \begin{pmatrix} a \\ \alpha \end{pmatrix}\begin{pmatrix} b \\ \beta \end{pmatrix}\begin{pmatrix} c \\ \gamma \end{pmatrix}\begin{pmatrix} a^* & b^* & c^* \\ \alpha^* & \beta^* & \gamma^* \end{pmatrix}^r \qquad (3.2.2)$$

*3.2.3.2. 2*jm *phase*

Hereafter simply called a '2*jm*', the 2*jm* phase relates the transformation properties of a bra and ket. That is, using Dirac's bra-ket notation[7] (Section 3.1.2),

$$\langle a\alpha| \equiv |a\alpha\rangle^\dagger \sim \begin{pmatrix} a \\ \alpha \end{pmatrix}|a\alpha\rangle^* \equiv \begin{pmatrix} a \\ \alpha \end{pmatrix}|a^*\alpha^*\rangle \qquad (3.2.3)$$

where the bra and ket functions are represented by their transformation properties (a and α) and the symbol '~' means 'transforms as'. In the chain $\mathbf{SO}_3 \supset \mathbf{SO}_2$, $\begin{pmatrix} j \\ m \end{pmatrix} = (-1)^{j-m} = \pm 1$; in molecular point groups $\begin{pmatrix} a \\ \alpha \end{pmatrix}$ also takes a value of either +1 or −1.

2*jm* for the point groups $\mathbf{C}_{\infty v}$ and $\mathbf{I}_h$ are given in Appendix B. Only a partial list is given for the former, because it has an infinite number of irreps.

3.2.4. The Wigner-Eckart theorem

The Wigner-Eckart theorem[1] is used extensively in this work to reduce matrix elements to a partner-independent form, called a 'reduced matrix element'. The reduced matrix element is common to a (generally) larger number of matrix elements, and is dependent on the functions and their irreps, but *not* their partners. Coefficients that depend *only* on the transformation properties of the functions (that is, their irreps and partners) relate the reduced to the unreduced matrix elements. This very important theorem, and the great orthogonality theorem upon which it rests, will be presented here without proof.

The great orthogonality theorem[1] states that the irreps of a point group are all orthogonal to each other, and that a partner of an irrep is orthogonal to all other partners of the same irrep. Hence if there are two functions with irreps a and b and partners α and β, respectively, then non-zero overlap requires $a = b$ and $\alpha = \beta$. This can be expressed as,

$$\langle a\alpha|b\beta\rangle = \delta_{ba}\,\delta_{\alpha\beta}\,|a|^{1/2}\,\langle a||b\rangle \qquad (3.2.4)$$

where δ is the Kronecker delta, and $\langle a||b\rangle$ is the reduced overlap, which is independent of α and β.

The Wigner-Eckart theorem extends the concept of irrep and partner orthogonality to matrix elements. The theorem in terms of high-symmetry coupling coefficients is,

$$\langle a\alpha|\mathcal{O}^f_\phi|b\beta\rangle = \begin{pmatrix} a \\ \alpha \end{pmatrix} \sum_r \begin{pmatrix} a^* & f & b \\ \alpha^* & \phi & \beta \end{pmatrix}^r \langle a||\mathcal{O}^f||b\rangle_r \qquad (3.2.5)$$

where $\mathcal{O}^f_\phi$ is an operator that transforms as partner ϕ of irrep f, and $\langle a||\mathcal{O}^f||b\rangle$ is the reduced matrix element. The coefficients in these expressions are independent of the particular function, and are readily tabulated. Hence the coefficients and reduced matrix elements describe all matrix elements involving irreps a, b and f. Moreover the matrix element is non-zero only when the direct product $f \otimes b$ contains the irrep a.

3.3. Molecular states

The method by which molecular wavefunctions are constructed is described in this section; then the procedures used to compute a variety of matrix elements are outlined.

3.3.1. Construction of molecular wavefunctions

In this section, group theory is used to construct state wavefunctions from molecular orbitals (MOs) formed from properly symmetrised linear combinations of atomic orbitals (LCAO).[7,8]

3.3.1.1. Molecular orbitals (MO) and configurations

(a) Construction of MOs from valence atomic orbitals

Two approaches are used for obtaining MOs. Those for small molecules are readily derived by forming linear combinations of the valence atomic orbitals which can be mixed by symmetry.[7,8] This is known as the LCAO-MO method, and forms the basis for many quantum chemical calculations.[7] For larger molecules, the MOs utilised originate from such calculations. Spectroscopic data often play an important role in

checking such results.

(b) Determination of molecular configurations

In simple cases the ground-state molecular configuration can be unambiguously determined by filling MOs with valence electrons (the Aufbau principle). However in other cases, where for example several MOs lie close in energy, the exact ordering of MOs may not be clear and electron pairing energies may become important. Here the ground-state configuration is usually determined by recourse to experimental data, such as ESR or magnetic susceptibility. Such measurements also provide a good check of the results of MO calculations.

3.3.1.2. Molecular term symbols from electronic configurations

(a) Orbital irreps

The possible many-electron orbital irreps for a given electron configuration are determined by calculating the direct product of the single-electron orbital irreps ($h(1)$, $h(2)$...). Filled (or empty) subconfigurations are not considered, because they transform as the totally symmetric irrep (0 in Butler's basis[2]). For example, for a three electron problem,

$$\begin{aligned} h(1) \otimes h(2) \otimes h(3) &= (h(1) \otimes h(2)) \otimes h(3) \\ &= (h_1' \oplus h_2' \oplus h_3' \oplus \ldots) \otimes h(3) \\ &= h_1 \oplus h_2 \oplus h_3 \oplus \ldots \end{aligned} \qquad (3.3.1)$$

The direct product of the first two irreps, $h(1)$ and $h(2)$, gives the 'intermediate' irreps h_1', h_2'... For each of these irreps, the direct product is then taken with $h(3)$, resulting in the three-electron orbital irreps, h_1, h_2, h_3...

(b) Spin irreps

Many-electron spin irreps are determined in a similar manner to the orbital irreps, but with some significant differences. Firstly, all spins have the same magnitude; $s_1 = s_2 = s_3 \ldots = ½$. Secondly, since spins are unaffected (in the absence of spin-orbit coupling) by electric fields, it is convenient to treat them in the chain $\mathbf{SO}_3 \supset \mathbf{SO}_2$, irrespective of the molecular symmetry. Hence for three electrons,

$$s_1 \otimes s_2 \otimes s_3 = \tfrac{1}{2} \otimes \tfrac{1}{2} \otimes \tfrac{1}{2}$$

$$= (\tfrac{1}{2} \otimes \tfrac{1}{2}) \otimes \tfrac{1}{2} = (0 \oplus 1) \otimes \tfrac{1}{2}$$

$$= (\tfrac{1}{2}) \oplus (\tfrac{1}{2} \oplus \tfrac{3}{2}) \qquad (3.3.2)$$

The many electron spin irrep in $\mathbf{SO}_3$ is denoted $\mathcal{S}$. Hence, for example, in eq (3.3.2), $\mathcal{S}$ can take the values $\frac{1}{2}$, $\frac{1}{2}$ or $\frac{3}{2}$.

(c) Term symbols

In accordance with the convention for molecular electronic states,[3] the term symbol is written ${}^{2\mathcal{S}+1}h$, where h is the many-electron orbital irrep (in Mulliken notation) and $2\mathcal{S}+1$ is the spin multiplicity.

In deriving such terms, when two or more electrons reside in the same orbital, care must be taken to ensure that the Pauli exclusion principle is not violated (see below); in other words, that the resultant wavefunctions are antisymmetric with respect to the exchange of two electrons. For some cases, the appropriate precautions are intuitively obvious (*e.g.* in the many-electron atomic case, a ${}^3D$ state from a p^2 configuration), but others will not be so clear.

3.3.1.3. Orbital and spin wavefunctions for a sub-configuration[1]

(a) Orbital wavefunctions

The orbital functions of the electrons corresponding to the partially filled orbitals of a given single subconfiguration or shell are coupled according to,

$$|(h_1\ h_2)\ r\ h\ \theta\rangle = |h|^{1/2} \begin{pmatrix} h \\ \theta \end{pmatrix} \sum_{\theta_1\,\theta_2} \begin{pmatrix} h_1 & h_2 & h^* \\ \theta_1 & \theta_2 & \theta^* \end{pmatrix}^{*\,r} |h_1\theta_1\rangle\, |h_2\theta_2\rangle \qquad (3.3.3)$$

where h and θ are the orbital irrep and partner for the many-electron wavefunction. h_1 and h_2 are the irreps of the orbital functions to be coupled, and the summation is made over all partners θ_1 and θ_2 for which the $3jm$s are non-zero. In certain point groups the chain of groups leads to repeated representations which are indexed by $r = 0, 1\ldots$

(b) Spin wavefunctions in the group SO_3

Spin wavefunctions are generated in $\mathbf{SO}_3$ by sequentially coupling spins using

$$|(s_1\ s_2)\ \mathcal{S}\ \mathcal{M}\rangle = (-1)^{s_1-s_2+\mathcal{S}}\,|\mathcal{S}|^{1/2}\,(-1)^{\mathcal{S}-\mathcal{M}} \sum_{m_1 m_2} \begin{pmatrix} s_1 & s_2 & \mathcal{S} \\ m_1 & m_2 & -\mathcal{M} \end{pmatrix} |s_1\ m_1\rangle\ |s_2\ m_2\rangle \qquad (3.3.4)$$

$\mathcal{S}$ is the spin irrep in $\mathbf{SO}_3$ of the many-electron spin function, and $\mathcal{M}$ is its partner. The s_1 and s_2 irreps correspond to the electron spins to be coupled. Their partners are m_1 and m_2, respectively, over which the summation must occur for all non-zero $3jm$s.

3.3.1.4. Formation of SL wavefunctions[1]

SL wavefunctions (the nomenclature of Ref. 1 is followed here) are (in a simple view) obtained by directly coupling the spin and orbital wavefunctions above *without* symmetrisation to the molecular point group. (The symmetrisation is covered in Section 3.3.1.5.) However in reality, because of the requirements of the Pauli exclusion principle and the need for Slater determinants, the situation is often more complicated.

The result of these steps is to have the functions expressed as products of one-electron spin-orbitals. In the kets corresponding to the individual spin-orbitals, the shorthand generally used is as follows. The spin-orbitals are described by the orbital partner (in Butler notation) and spin partner as a superscript '+' or '–' corresponding to spin orientation, unless the orbital is full (and a superscript '2' is used). Thus, for example, an α (up) spin in a -1 partner of a Π orbital is designated $|\text{-}1^{+}\rangle$.

(a) One open shell, a^n

Here the case is considered of one open shell, designated by the irrep a and containing n electrons. The Pauli exclusion principle is only obeyed when symmetric orbital and antisymmetric spin wavefunctions, or vice versa, are coupled together. For symmetric wavefunctions, the exchange of any two particles does not result in a change of sign. In contrast, an antisymmetric function will change sign when two particles are exchanged.

Having determined the exchange symmetry of the wavefunctions, the following equation summarises the formation of the coupled orbital and spin states that are desired:

$$|\mathcal{S}\ h\ \mathcal{M}\ \theta\rangle = |(h_1\ h_2)\ r\ h\ \theta\rangle\ |(s_1\ s_2)\ \mathcal{S}\ \mathcal{M}\rangle \qquad (3.3.5)$$

Note that the SL wavefunctions ($|\mathcal{S}\ h\ \mathcal{M}\ \theta\rangle$) obtained in this manner may require antisymmetrisation in order to form Slater determinants.[7]

(b) More than one open shell, $a^n\ b^m\ c^l$...

To couple electrons from more than one open shell, $a^n\ b^m\ c^l$ ..., wavefunctions for each subconfiguration are coupled sequentially using,

$$|(a^m(\delta_1\ h_1),\ b^n(\delta_2\ h_2))\ \delta\ h\ \mathcal{M}\ \theta\rangle\ =\ (-1)^{\delta_1-\delta_2+\delta}\ |\delta|^{1/2}\ (-1)^{\delta-\mathcal{M}}\ |h|^{1/2}\begin{pmatrix} h \\ \theta \end{pmatrix}\times$$

$$\sum_{\mathcal{M}_1\mathcal{M}_2}\begin{pmatrix} \delta_1 & \delta_2 & \delta \\ \mathcal{M}_1 & \mathcal{M}_2 & -\mathcal{M} \end{pmatrix}\sum_{\theta_1\theta_2}\begin{pmatrix} h_1 & h_2 & h^* \\ \theta_1 & \theta_2 & \theta^* \end{pmatrix}^*\ |a^m\ \delta_1\ h_1\ \mathcal{M}_1\ \theta_1\rangle\ |b^n\ \delta_2\ h_2\ \mathcal{M}_2\ \theta_2\rangle \quad (3.3.6)$$

where $|a^m\ \delta_1\ h_1\ \mathcal{M}_1\ \theta_1\rangle$ is the SL wavefunction corresponding to the a^m subconfiguration. The newly coupled wavefunction requires antisymmetrisation, and this is performed using,

$$|\mathcal{A}(a^m(\delta_1\ h_1),\ b^n(\delta_2\ h_2))\ \delta\ h\ \mathcal{M}\ \theta\rangle\ =\ [m!\ n!\ (m+n)!]\ (-1)^{\delta_1-\delta_2+\delta}\ |\delta|^{1/2}\ (-1)^{\delta-\mathcal{M}}\times$$

$$|h|^{1/2}\begin{pmatrix} h \\ \theta \end{pmatrix}\sum_{\mathcal{M}_1\mathcal{M}_2}\begin{pmatrix} \delta_1 & \delta_2 & \delta \\ \mathcal{M}_1 & \mathcal{M}_2 & -\mathcal{M} \end{pmatrix}\sum_{\theta_1\theta_2}\begin{pmatrix} h_1 & h_2 & h^* \\ \theta_1 & \theta_2 & \theta^* \end{pmatrix}^*\times$$

$$\sum_{\nu=1}^{(m+n)!}(-1)^{\nu}\ \mathbf{P}_\nu\ |a^m\ \delta_1\ h_1\ \mathcal{M}_1\ \theta_1\rangle\ |b^n\ \delta_2\ h_2\ \mathcal{M}_2\ \theta_2\rangle \quad (3.3.7)$$

where $\mathcal{A}$ is the antisymmetrisation operator, and $\mathbf{P}_\nu$ permutes the electrons.[1]

The resulting SL wavefunction can now be simplified to the required Slater determinant(s), as described in texts on quantum chemistry,[7] which are written here in the form of kets.

SL wavefunctions are often written as $|^{2\delta+1}h\ \mathcal{M}\ \theta\rangle$, were the orbital irrep is given in Mulliken notation, as this notation relates the functions more directly to the molecular term symbols ($^{2\delta+1}h$) of Section 3.3.1.2 than does the $|\delta\ h\ \mathcal{M}\ \theta\rangle$ nomenclature.

(c) The hole-particle formalism

Often the effort required to generate SL wavefunctions can be reduced if the hole-particle formalism is invoked.[1] An example of hole-particle equivalent configurations is π^1 and π^3 in $\mathbf{C}_{\infty v}$. For such equivalents the same $|\delta\ h\ \mathcal{M}\ \theta\rangle$ labels apply, but the actual wavefunctions differ, as shown in Table 3.3.1. Once the relationship between the hole and particle is understood the method poses no problems, and its implementation saves a considerable amount of time.

Table 3.3.1: Hole-particle equivalent SL wavefunctions for π^1 and π^3 in $\mathbf{C}_{\infty v}$.

$\|\delta\ h\ \mu\ \theta\rangle$	π^1	π^3
$\|\frac{1}{2}\ 1\ \pm\frac{1}{2}\ \pm1\rangle$	$\|\pm1^{\pm}\rangle$	$\|-1^{+}\ \pm1^{\pm}\ 1^{-}\rangle$
$\|\frac{1}{2}\ 1\ \pm\frac{1}{2}\ \mp1\rangle$	$\|\mp1^{\pm}\rangle$	$\|-1^{\pm}\ \mp1^{\mp}\ 1^{\pm}\rangle$

The use of the standard basis relations and antisymmetrisation criteria outlined in the preceding subsections does not necessarily result in a unique phase choice within the hole-particle formalism. The convention adopted here to ensure that the phases are consistent is summarised by,[1]

$$|a^{2|a|}\ 0\ 0\ 0\ 0\rangle = \sum_{\delta_1\ h_1} |\delta_1|^{1/2}\ |h_1|^{1/2} \left[\frac{(2|a|)!}{n!\,(2|a|-n)!}\right] |(a^{n}(\delta_1\ h_1),\ a^{2|a|-n}(\delta_2\ h_2))\ 0\ 0\ 0\ 0\rangle \tag{3.3.8}$$

3.3.1.5. Spin-orbit wavefunctions[1]

The aim here is to obtain symmetry-adapted $|\delta\ S\ M\rangle$ basis functions, where S and M are respectively the spin irrep and partner in the molecular double group. Hence we must correlate the spin quantum numbers (effectively δ and μ of $\mathbf{SO}_3$) with S and M in the molecular double group.

The spin-orbit (SO) irreps for the molecule of interest are found by forming the direct product of the spin irrep in molecular double group (correlated from the spin quantum number in $\mathbf{SO}_3$) with the orbital irrep. The SO irrep is designated t;

$$t = S \otimes h \tag{3.3.9}$$

and has partners τ.

Once the SL wavefunctions have been obtained, the SO basis (that is, wavefunctions diagonal in the SO operator) can be derived using,

$$|(\delta\ S,\ h)rt\tau\rangle = |t|^{1/2} \begin{pmatrix} t \\ \tau \end{pmatrix} \sum_{M\ \theta} \begin{pmatrix} S & h & t^* \\ M & \theta & \tau^* \end{pmatrix}^{*r} |\delta\ S\ h\ M\ \theta\rangle \tag{3.3.10}$$

The summation is made over all spin (M) and orbital (θ) partners for which the $3jm$ is non-zero, and the SO wavefunctions thus obtained are normalised and mutually orthogonal.

The $|(\lambda S, h)rt\tau\rangle$ functions that form the SO basis are normally written as $|^{2\lambda+1}h_t\ \tau\rangle^r$.

3.3.2. Calculation of matrix elements in the SO basis

The matrix elements considered here are those involving inter-electron repulsion, spin-orbit coupling, crystal fields and the Zeeman effect (in Section 3.3.4). Another important set of matrix elements are the transition moments, which are dealt with in Section 3.4.2.

3.3.2.1. Electron repulsion[7]

When several terms result from a single configuration, the most important effect in determining their splitting is usually electron repulsion. The corresponding operator transforms as the totally symmetric irrep of the molecular point group, and is given by,

$$\mathcal{H}_{\text{Rep}} = \sum_{i=1} \sum_{j>i} e^2 / r_{ij} \tag{3.3.11}$$

in cgs (Gaussian) units. For two electrons i and j in orbitals a and b the matrix elements of this operator are:

$$J_{ab} = \iint a^* b^* \frac{e^2}{r_{ij}} ab\, d\tau_i\, d\tau_j = \langle a|\langle b|\frac{e^2}{r_{ij}}|a\rangle|b\rangle \equiv (ab|ab) \tag{3.3.12}$$

$$K_{ab} = \iint a^* b^* \frac{e^2}{r_{ij}} ba\, d\tau_i\, d\tau_j = \langle a|\langle b|\frac{e^2}{r_{ij}}|b\rangle|a\rangle \equiv (ab|ba) \tag{3.3.13}$$

where J_{ab} is the Coulomb integral, and K_{ab} is the exchange integral. Note that $J_{ab} = J_{ba}$ and $K_{ab} = K_{ba}$ from the Wigner-Eckart theorem, and that $J_{aa} = K_{aa}$. The Condon-Slater rules are used to evaluate these matrix elements for states with more than one electron in an open shell, or several open shells. For a Slater determinant $|\psi\rangle = |\phi_1\ \phi_2\ \phi_3\ \ldots\rangle$ (where the ϕ_i are spin orbitals), the non-zero matrix elements are given by the following:

1. Diagonal matrix elements.

$$\langle\psi|\mathcal{H}_{\text{Rep}}|\psi\rangle = \sum_{i<j} \{(\phi_i\ \phi_j|\phi_i\ \phi_j) - (\phi_i\ \phi_j|\phi_j\ \phi_i)\} \tag{3.3.14}$$

2. Off-diagonal matrix elements;

   (a) one element different.

$$\langle \psi | \mathcal{H}_{\text{Rep}} | \psi_{j \to j'} \rangle = \sum_{i \neq j} \{ (\phi_i \, \phi_j | \phi_i \, \phi_{j'}) - (\phi_i \, \phi_j | \phi_{j'} \, \phi_i) \} \tag{3.3.15}$$

(b) two elements different.

$$\langle \psi | \mathcal{H}_{\text{Rep}} | \psi_{i \to i', \, j \to j'} \rangle = (\phi_i \, \phi_j | \phi_{i'} \, \phi_{j'}) - (\phi_i \, \phi_j | \phi_{j'} \, \phi_{i'}) \tag{3.3.16}$$

The Wigner-Eckart theorem can be used to determine which of these matrix elements are zero by symmetry, without having to evaluate the matrix element itself. Since $\mathcal{H}_{\text{Rep}}$ transforms as the totally symmetric irrep in the molecular point group, there are no non-zero matrix elements between SO wavefunctions that transform as different irreps or different partners. However, there will, in general, be off-diagonal (or cross) terms between different SL wavefunctions that have the same transformation properties (Section 3.3.1.4).

3.3.2.2. Spin-orbit matrix elements[1,7]

The relativistic interaction between spin and orbital angular momenta is called spin-orbit coupling (SOC).

The SO operator $\mathcal{H}_{\text{SO}}$ is defined by:

$$\mathcal{H}_{\text{SO}} = \sum_k \xi(r_k) \, \boldsymbol{l}(k) \bullet \boldsymbol{s}(k) = \sum_k \boldsymbol{s}(k) \bullet \boldsymbol{u}(k) \tag{3.3.17}$$

The sum over k in eq (3.3.17) is made over all electrons in open shells. $\xi(r_k)$, $\boldsymbol{l}(k)$ and $\boldsymbol{s}(k)$ are respectively the spin-orbit coupling coefficient, orbital angular momentum and spin angular momentum of the kth electron. $\boldsymbol{u}(k) = \xi(r_k) \, \boldsymbol{l}(k)$.

$\boldsymbol{s} \bullet \boldsymbol{u}$ on the right-hand side of eq (3.3.17) can be expanded in terms of its components (Section 3.1.1),

$$\begin{aligned} \boldsymbol{s} \bullet \boldsymbol{u} &= s_z u_z + s_y u_y + s_x u_x \\ &= s_z u_z - \tfrac{1}{2} s_{+1} u_{-1} - \tfrac{1}{2} s_{-1} u_{+1} \end{aligned} \tag{3.3.18}$$

where $s_{\pm 1}$ and $u_{\pm 1}$ are spherical components of $\boldsymbol{u}$ and s, defined by eq (3.1.2). Generalising l and s as j, j_{+1} and j_{-1} are related to the raising and lowering operators, j^+ and j^-,

$$j_{\pm 1} = \mp \tfrac{1}{\sqrt{2}} j^{\pm} \tag{3.3.19}$$

The raising and lowering operators act on the $|j\,m\rangle$ of the $\mathbf{SO}_3 \supset \mathbf{SO}_2$ basis as shown in eq (3.3.20), while j_z operates on the $|j\,m\rangle$ according to eq (3.3.21).

$$j^{\pm}\,|j\,m\rangle = \hbar\,(j \mp m)^{1/2}\,(j \pm m + 1)^{1/2}\,|j\,m\pm1\rangle \tag{3.3.20}$$

$$j_z\,|j\,m\rangle = m\hbar\,|j\,m\rangle \tag{3.3.21}$$

For $s_z u_z$, the only non-zero matrix elements in the SL basis (Section 3.3.1.4) are those where the bra and ket are identical.

Whether or not the matrix elements of $s_{+1}u_{-1}$ and $s_{-1}u_{+1}$ need to be evaluated depends on the molecular symmetry and the degree of precision of the calculation. For example, in linear molecules, to first order, only the matrix elements of $s_z u_z$ need be considered since all irreps are doubly degenerate (with the exception of 0 and $\tilde{0}$); the (two) orbital partners of these irreps cannot be connected by step operators since $\Delta m_l > 1$. However for C_{60}, which has icosahedral symmetry (point group $\mathbf{I}_h$), the partners of degenerate irreps *can* be connected by the step operators.

Because eqs (3.3.20) and (3.3.21) apply to the $\mathbf{SO}_3 \supset \mathbf{SO}_2$ basis, evaluation of SO matrix elements necessitates correlation back to that basis. Tables exist for such correlations.[1,2] Although for many point groups there are no difficulties when a correlation is not performed, it is not advisable to ignore it. (This was found to be particularly important in the case C_{60}^{+} in $\mathbf{I}_h$ symmetry (Appendix C), where several of the phase choices turn out to be very critical to the final result.)

3.3.2.3. Crystal-field matrix elements

A crystal field (CF) perturbs a state only if it transforms as a partner of the symmetric square $[h^2]$ of the orbital part of the wavefunction. Consider, for example, the symmetric square of a Π term in $\mathbf{C}_{\infty v}$, as encountered in the $^2\Pi$ ground states of OH and CH (Chapters 4 and 6) and the $^3\Pi$ excited state of NH (Chapter 5). In Mulliken notation,

$$[\Pi^2] = \Sigma^+ \oplus \Delta \tag{3.3.22}$$

whereas in Butler notation,

$$[1^2] = 0 \oplus 2 \tag{3.3.23}$$

Σ^+ (0) is the totally symmetric irrep in $\mathbf{C}_{\infty v}$. The corresponding components of the CF shifts all states, but has no effect on orbital degeneracy. (This can be considered a contributor to the commonly observed wavelength shift from gas to condensed phases.) On the other hand, a CF of Δ symmetry (which transforms as $|2\ \pm2\rangle$ in the complex basis) will lower the orbital degeneracy of the Π term, causing a CF splitting. The differing CFs are illustrated in Figure 3.3.1.

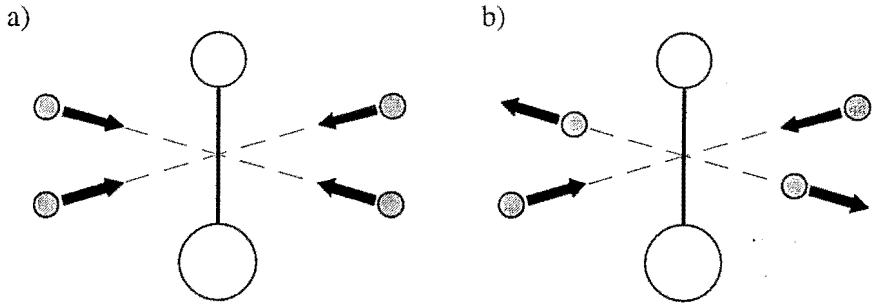

Figure 3.3.1: Crystal fields with different transformation properties derived from the symmetric square of a π orbital of a diatomic molecule. A symmetric field (Σ^+), which does not lower orbital degeneracy, but affects both orbital components equally, is shown in (a). In (b), a quadrupolar (or orthorhombic) field of Δ symmetry is illustrated, which does lower degeneracy.

The CF diagonalises the orbitals in a real basis, so the Δ-field components should be chosen to transform as xy and x^2-y^2. The choice of component is arbitrary (one is shown in Figure 3.3.1(b)), but normally x^2-y^2 is used, for which the tesseral harmonic is,

$$Z_{22}^{C} = \frac{1}{\sqrt{2}}(|2\ 2\rangle + |2\ -2\rangle) \tag{3.3.24}$$

Using this relationship, the real CF operator $\mathcal{H}_{CF}$ is defined as,

$$\mathcal{H}_{CF} = \frac{1}{\sqrt{2}}(V_2^2 + V_{-2}^2) \tag{3.3.25}$$

where $V_{\pm2}^2$ are the spherical components.

The matrix elements of $V_{\pm2}^2$ are evaluated in the SO basis using the fact that the CF (which is an electric field) does not affect spin. The only non-zero one-electron elements have the form $\langle\pi\ \pm1|V_{\pm2}^2|\pi\ \mp1\rangle$ ($\equiv \langle\pm1|V_{\pm2}^2|\mp1\rangle$). These can be related to each other using the Wigner-Eckart theorem (Section 3.2.4),

$$\langle 1\ \pm1|V_{\pm2}^2|1\ \mp1\rangle = \frac{1}{\sqrt{2}}\langle 1||V^2||1\rangle = \frac{V}{\sqrt{2}} \tag{3.3.26}$$

where V is the magnitude of the splitting of the orbital components.

3.3.3. SO-CF wavefunctions

Eigenfunctions of the simultaneous action of SO and CF operators are obtained by diagonalisation of a Hamiltonian matrix containing both SO and CF matrix elements. In the case of two-fold orbital degeneracy (as exists in $\mathbf{C}_{\infty v}$), this can be done analytically.

First, the eigenvalues of the Hamiltonian are calculated from the secular (determinantal) equation. The difference between the eigenvalues of the two orbital states is dependent on the magnitude of the SOC and CF, and the net SO-CF splitting parameter is labelled Δ in this work.

Substitution of each of the eigenvalues into the secular equation yields the eigenvectors, which are then normalised appropriately. The mixing coefficients α and β are functions of the SO and CF strengths. Since they are normalised, $|\alpha|^2 + |\beta|^2 = 1$. Other useful product relationships are given in the relevant sections. Note that the phases are to some degree arbitrary, but the final result is independent of the choice. For consistency, these phases are chosen so that the SO-CF eigenfunctions tend to the SO wavefunctions as V vanishes.

3.3.4. Zeeman matrix elements and *g* values

The interaction between two states, $|A\alpha\rangle$ and $|K\kappa\rangle$, in the presence of a magnetic field is given by,

$$H'_{A\alpha,K\kappa} = \langle K\kappa|\mathcal{H}_B|A\alpha\rangle \tag{3.3.27}$$

where $\mathcal{H}_B$ is the Zeeman operator. For the magnetic field along the laboratory Z axis,

$$\mathcal{H}_B = -\mu \bullet \boldsymbol{B} = -\mu_Z B = (L_Z + g_e S_Z)\mu_B B \tag{3.3.28}$$

Here μ is the electronic magnetic moment, and $\boldsymbol{B}$ is the magnetic field with magnitude B. μ is generated by spin and orbital angular momenta, the operators for which have components S_Z and L_Z, respectively, along Z (in units of $\hbar$). μ_B is the Bohr magneton (0.4667 cm^{-1} T^{-1}), and g_e is the electron's g value ($g_e \approx 2$).

This work involves MCD, which is a longitudinal Zeeman technique; that is, the light is propagated along the direction of $\boldsymbol{B}$. When $|A\alpha\rangle \equiv |K\kappa\rangle$, $H'_{A\alpha,A\alpha}$ represents a

first-order Zeeman energy,

$$E_B(A\alpha) \equiv H'_{A\alpha A\alpha} = \langle A\alpha|\mathcal{H}_B|A\alpha\rangle \tag{3.3.29}$$

For any two adjacent states from a degenerate (at zero magnetic field) manifold, the Zeeman splitting is,

$$\Delta E_B = |E_B(A\alpha) - E_B(A\beta)| \equiv g\mu_B B \tag{3.3.30}$$

So determination of a g value essentially involves evaluation of matrix elements $\langle A\alpha|L_Z + g_e S_Z|A\alpha\rangle$. These elements generally depend on molecular orientation.

3.3.4.1. Zeeman matrix elements when the field is parallel to the z axis

For isotropic molecules or molecules aligned with their z axis along the field,

$$\mu_Z = \mu_z = -\mu_B (L_z + g_e S_z) \tag{3.3.31}$$

Here L_z and S_z are respectively the spin and orbital angular momentum operators along the *molecular* z axis. The Zeeman matrix elements are now,

$$H'_{A\alpha K\kappa} = \langle K\kappa|L_z + g_e S_z|A\alpha\rangle \mu_B B \tag{3.3.32}$$

Generally, z is taken to represent the major symmetry axis of the molecule, so evaluation of these matrix elements is usually quite simple. This is especially so for isotropic and axial molecules. More generally, the molecules are oriented in other directions, or randomly oriented; these cases will be treated below.

The matrix elements of L_z and S_z are evaluated by expanding the many-electron operators L_z and S_z in terms of the one-electron operators $l_z(k)$ and $s_z(k)$. That is,

$$L_z + g_e S_z = \sum_k l_z(k) + g_e s_z(k) \tag{3.3.33}$$

Since only L_z and S_z are evaluated, the SL wavefunctions (Section 3.3.1.4), linear combinations of which form the SO wavefunctions (Section 3.3.1.5), must be the same for a possible non-zero contribution to the Zeeman energy (*i.e.* $\Delta M_L = 0$ and $\Delta M_S = 0$).

$$\langle \lambda\ h\ \mathcal{M}\ \theta\ |L_z + g_e S_z|\lambda'\ h'\ \mathcal{M}'\ \theta'\rangle = \langle h\theta\ |L_z|h\theta\rangle\ \delta_{h\,h'}\ \delta_{\theta\,\theta'} + g_e \mathcal{M}\ \delta_{\lambda\lambda'}\delta_{\mathcal{M}\mathcal{M}'} \tag{3.3.34}$$

This does not mean that SO wavefunctions are exactly diagonal in the Zeeman effect, since more than two states can have the same h, θ, λ, and $\mathcal{M}$. However, unless the

states are close in energy the off-diagonal elements cause little mixing, and hence the MCD *B* terms are generally very weak.

*3.3.4.2. Molecular z-axis not aligned parallel to **B***

When an axial molecule is not aligned with its z axis parallel to $\boldsymbol{B}$, matrix elements involving μ_x and μ_y (or $\mu_{\pm1}$; Section 3.1.1) can be non-zero. This section describes their evaluation, while Section 3.3.4.3 shows how they are used to compute $g_\perp$.

The complex operators $\mu_{\pm1}$ are related to raising and lowering operators, as shown in eq (3.3.19). In terms of the angular momentum operators,

$$\mu_{\pm1} = -\mu_B (L_{\pm1} + g_e S_{\pm1}) \qquad (3.3.35)$$

in analogy to μ_z. Like μ_z (eq 3.3.33), these many-electron operators are evaluated in terms of the one-electron operators, $l_{\pm1}$ and $s_{\pm1}$. Hence, for a matrix element to be non-zero, the bra and ket must differ by one unit of spin and/or orbital angular momentum (*i.e.* $\Delta M_L = \pm1$ and/or $\Delta M_S = \pm1$).

Note that for the axial molecules treated in this work, $l_{\pm1}$ cannot convert between π components ($\Lambda = 1$, $M_\Lambda \equiv M_L = \pm1$ in $\mathbf{C}_{\infty v}$ symmetry), so that only $s_{\pm1}$ needs to be considered.

3.3.4.3. g values

For isotropic molecules the g matrix (tensor) is isotropic. Axial molecules have two g values; g_z is unique while $g_x = g_y$. They are described as being parallel, and perpendicular, to the molecular z axis; $g_\parallel \equiv g_z$ and $g_\perp \equiv g_x$.

The value of $g_\parallel$ is specified by the Zeeman splitting when $\boldsymbol{B}$ is parallel to the molecular z axis, while $g_\perp$ is defined by the Zeeman splitting when $\boldsymbol{B}$ is perpendicular to the molecular z axis. Matrix elements of $\mu_{\pm1}$ are used to calculate $g_\perp$.

3.4. Spectroscopy

This section describes those aspects of the interaction of light with molecules that are important in this work. The molecules considered are either axial (CH, NH and OH) or isotropic (C_{60}^+ and C_{60}^-), so the equations presented below are relevant to those situations.

3.4.1. Selection rules for electronic transitions

3.4.1.1. Molecules with inversion symmetry

If the molecular point group has inversion symmetry, the Laporte selection rule must be applied: allowed transitions are $g \leftrightarrow u$. Parity must change during an electronic transition because the electric-dipole operator is odd (u) with respect to inversion. Note, however, that although the purely electronic excitation may be disallowed, there may be a process occurring which allows vibronic structure to be observed (for example, the Herzberg-Teller mechanism).

3.4.1.2. Spin selection rule

Electronic transitions generally only occur between terms of the same spin multiplicity ($\Delta S = \Delta M_S = 0$). Sometimes SOC may allow transitions with $\Delta S \neq 0$ and/or $\Delta M_S \neq 0$ by mixing levels with the same SO irrep and partner ($t\tau$), but different spin multiplicity.

3.4.1.3. Orbital selection rule

Orbital symmetry requirements are as follows. First, the transformation properties of the electric-dipole operator $\boldsymbol{m}$ in the molecular point group must be determined. The real vector components of $\boldsymbol{m}$ in $\mathbf{SO}_3 \supset \mathbf{SO}_2$ (m_x, m_y and m_z) transform as the functions x, y and z, which are normally given in the point-group character table, with irrep(s) M. The spherical (complex) components used in MCD are obtained using eq (3.1.2). An allowed transitions $J \leftarrow A$ fulfils the requirement,

$$M \otimes A \supset J \qquad (3.4.1)$$

Here A and J are the initial and final orbital irreps. Alternatively, $J \otimes M \otimes A$ must contain the totally symmetric irrep (0 in Butler notation[2]).

3.4.2. Transition moments[1]

The general principles of the interaction of electromagnetic radiation with matter are described in detail elsewhere.[1,7,8] Transitions of the type investigated here involve (in a simplistic view) excitations between molecular orbitals (MOs), for which the spin quantum numbers remain unchanged ($\Delta s = \Delta m_s = 0$).

The convention employed in this work is that lower energy states are given on the right and the higher energy states on the left.[3] For absorption, these are, respectively, the final and initial states, so transition-moment matrix elements in Dirac notation have the final and initial orbitals or states forming the 'bra' and 'ket', respectively.

The probability, $P_{j\leftarrow a}$, of a one-electron excitation $j \leftarrow a$ is,

$$P_{j\leftarrow a} \propto I_0 \, |\langle j|\boldsymbol{m}|a\rangle|^2 \qquad (3.4.2)$$

I_0 is the light intensity, and $\langle j|\boldsymbol{m}|a\rangle$ is the electric-dipole transition moment. The electric-dipole operator, $\boldsymbol{m}$, has spatial components (m_x, m_y, m_z). However it is often useful to take linear combinations of these real components (eq (3.1.2)) to give the complex components, which correspond to circular (m_{-1}, m_{+1}) and z ($m_0 \equiv m_z$) polarised transitions. The utility of the latter choice lies with the fact that these raise (m_{+1}), lower (m_{-1}) or leave unchanged (m_0) the orbital angular momentum. In MCD, the radiation is circularly polarised so the transition moments are most conveniently calculated in terms of m_{+1}, m_{-1} and m_0.

Real situations are complicated by SO interactions and inter-electronic repulsion, which mean that each configuration is (generally) associated with more states than there are orbital partners. Hence, each excitation will give several transitions, amongst which the total transition intensity is shared. Moreover, each transition can actually comprise an admixture of excitations (configuration interaction). Group theory, through the Wigner-Eckart theorem (Section 3.2.4), gives the relative intensity of the allowed transitions, eliminates those that are zero by symmetry, and reduces the number of transition moments requiring evaluation.

Two steps are employed in the evaluation of transition moments. The first involves the definition of one-electron reduced transition moment(s) for the excitation(s). The second involves rewriting the state-to-state transition moments as linear combinations of one-electron moments

3.4.2.1. One-electron transition moments

The one-electron transition moments for an electronic transition $|j\lambda\rangle \leftarrow |a\alpha\rangle$ (a and j are MO irreps with partners α and λ, respectively) are written down in a straightforward manner. Using the Wigner-Eckart theorem (Section 3.2.4), the lcp and

rcp transitions for an axial (or higher symmetry) molecule can be related to each other,

$$\langle j\lambda|m^1_{\pm1}|a\alpha\rangle = c^1_{\pm1}\,\langle j||m^1||a\rangle \equiv c^1_{\pm1}\,\mathcal{M} \qquad (3.4.3)$$

$\mathcal{M} = \langle j||m^1||a\rangle$ is a reduced one-electron transition moment common to transitions of both polarisations, while $c^1_{\pm1}$ is a symmetry coefficient determined from the $2jm$ and $3jm$ factors. $\mathcal{M}$ is exceedingly useful in that it allows all transitions arising from the introduction of electron-repulsion, SO coupling and CF effects to be related *via* a single parameter — *i.e.* from symmetry considerations alone we can derive *relative* transition intensities.

Reduced one-electron transition moments for z-polarised transitions (m_0) are derived in a similar manner. If the molecular symmetry is sufficiently high they will also be related to $\mathcal{M}$ (for example, in the $\mathbf{I}_h$ point group; Appendix C).

Note that the total intensity I_{Total} is given by,

$$I_{\text{Total}} \propto |\mathfrak{s}| \sum_i |\langle j\lambda|m^1_i|a\alpha\rangle|^2 \qquad (3.4.4)$$

where the sum is over all polarisations, and $|\mathfrak{s}|$ is the spin degeneracy.

3.4.2.2. Transitions between molecular states

Inclusion of electron spin, electron repulsion, SOC, and CF effects results in redistribution of total intensity of the excitation amongst its component transitions. First, the Wigner-Eckart theorem is employed to relate the intensities of individual transitions between SO or SO-CF levels to common reduced transition moments.

The full matrix elements are then evaluated using Slater's rules[7] to give a coefficient and a one-electron transition moment. (The bra and ket in a non-zero element must differ by one orbital (*not* spin), and that difference must be commensurate with the component of the electric-dipole operator.) Hence each transition moment can be written in terms of the $\mathcal{M}$ of eq (3.4.2), and the *relative* transition intensities can be determined without recourse to a quantum-mechanical calculation.

3.4.3. MCD and absorption

A brief introduction to MCD was given in Section 1.3, where the occurrence of the three dispersion forms found in MCD spectra (*A*, *B* and *C* terms) was described. This section presents the equations of MCD and absorption (as they are conventionally

expressed in the so-called 'linear limit'[1]) without derivation. References 1, 9 and 10 provide those derivations. Some of the phase choices and the appearance of some equations may differ from those earlier publications due to the conventions employed in this thesis (Section 3.1.2).

The absorbance (or optical density), A, of a homogeneous sample containing a chromophore of concentration c, is,

$$A = \log_{10}\frac{I}{I_0} = -\varepsilon c l \qquad (3.4.5)$$

I_0 is the incident light intensity, and I is the transmitted intensity. ε is the molar absorption (extinction) coefficient, in mol^{-1} L cm^{-1}, and l is the path length of the sample in cm.

Absorption of light occurs over an energy range, due to homogeneous and inhomogeneous broadening. For molecular systems the bandwidths of the transitions are generally much greater than the Zeeman shifts of the states (Section 3.1.4), so the Zeeman splittings are usually obscured in conventional absorption spectroscopy. Therefore it is convenient (and usually very accurate) to assume that the absorption is unchanged by the application of a magnetic field, and treat the zero-field case.

Because in MCD the light propagates along the direction of the field, $\boldsymbol{B}$, (the Z-axis of the laboratory frame), there can be no Z-polarised light. The absorption is then defined as an average absorbance of the two circular polarisations (eq (1.3.2)) used to measure the MCD. In eq (1.3.2), A_L and A_R are, respectively, the absorbance of left- and right-circularly polarised (lcp and rcp) light.

The absorbance shows dispersion (dependence on the energy, E, of the incident photons) which is represented by a bandshape function. This is made explicit by the equation,

$$\frac{A(E)}{E} = \gamma c l D_0 f(E) \qquad (3.4.6)$$

where γ is a collection of physical constants, and $f(E)$ is the normalised bandshape function;

$$\int f(E)\, dE = 1 \qquad (3.4.7)$$

D_0 is the dipole strength defined by eq (3.4.8). Its use (instead of ε or oscillator strengths) requires the factor $1 / E$ on the left-hand side of eq (3.4.6).

$$D_0 = \tfrac{1}{2} \sum_{\alpha\lambda} P_\alpha \left(|\langle J\lambda | M_{+1} | A\alpha \rangle|^2 + |\langle J\lambda | M_{-1} | A\alpha \rangle|^2 \right) \qquad (3.4.8)$$

Here P_α is the zero-magnetic-field fractional population of the partner α within the A manifold. The $\langle J\lambda | M_{\pm 1} | A\alpha \rangle$ are transition moments for the electronic transition $J \leftarrow A$, derived according to Section 3.4.1, and $M_{\pm 1}$ are the cp electric dipole operators in the *laboratory* reference frame.

Eq (3.4.8) is general to all cases considered in this thesis. However to be usefully employed it must be transformed into the molecular reference frame and averaged over all possible orientations.

The MCD, $\Delta A'$ (the prime indicates field dependence), is defined as the differential absorption of lcp and rcp light (eq (1.3.1)). Expansion of eq (1.3.1) gives,

$$\frac{\Delta A'(E)}{E} = \gamma c l \sum_{\alpha\lambda} P_\alpha' \left(|\langle J\lambda | M_{+1} | A\alpha \rangle'|^2 - |\langle J\lambda | M_{-1} | A\alpha \rangle'|^2 \right) f'_{\alpha\lambda}(E) \qquad (3.4.9)$$

P_α' is the fractional population of the partner state α within the A manifold,

$$P_\alpha' = \frac{\exp(-E_\alpha/kT)}{\sum_\alpha \exp(-E_\alpha/kT)} = \frac{\exp(-E_\alpha/kT)}{Q} \qquad (3.4.10)$$

where Q is the partition function, k is the Boltzmann constant (0.6954 cm^{-1} K^{-1}), T is the temperature (in K), and E_α is the Zeeman energy (Section 3.3.4) given by,

$$E_\alpha = \langle A\alpha | L_Z + g_e S_Z | A\alpha \rangle \, \mu_B B \qquad (3.4.11)$$

The transition moments, state populations and line-shape functions of eq (3.4.9) are all field dependent, which substantially complicates the theory of MCD. Conventionally, the MCD is treated in the linear limit,[1] where the field is regarded as a weak perturbation and first-order perturbation theory is applied. In essence, the criterion for the linear limit is $\mu_B B << kT$.

In conventional treatments, the Born-Oppenheimer and Franck-Condon approximations (BO-FC) are generally assumed, so the vibrations of the molecule do not need to be considered explicitly. However, there are deviations from these (such as the Jahn-Teller effect) where more complicated treatments must be undertaken. Additionally, the ground term is considered to be the only one populated, and the rigid-shift model (RS) is assumed; *i.e.*, the Zeeman shifting of bands does not affect their bandshape.

The overall MCD for a transition $J \leftarrow A$ within the 'BO-FC-RS' approximation[1] is,

$$\frac{\Delta A'(E)}{E} = \gamma c l \mu_B B \left[A_1 \left(-\partial f(E)/\partial E\right) + \left(B_0 + C_0/kT\right) f(E)\right] \qquad (3.4.12)$$

where equations for the so-called Faraday parameters, A_1, B_0 and C_0, are given below.

The following equations for A_1, B_0 and C_0 are applicable for molecules in isotropic point groups (such as $\mathbf{I}_h$) or for molecules which are preferentially oriented with their z axis (molecular reference frame) along the direction of the magnetic field and incident radiation (Z). They require that the basis states be (first-order) diagonal in the Zeeman effect. In these cases the laboratory-fixed operators $M_{\pm 1}$ coincide with the molecule-fixed operators $m_{\pm 1}$.

For A terms,

$$A_1 = \frac{1}{|A|} \sum_{\alpha\lambda} \left(\langle J\lambda|L_0 + g_e S_0|J\lambda\rangle - \langle A\alpha|L_0 + g_e S_0|A\alpha\rangle\right) \times \left(|\langle J\lambda|m_{+1}|A\alpha\rangle|^2 - |\langle J\lambda|m_{-1}|A\alpha\rangle|^2\right) \qquad (3.4.13)$$

For B terms,

$$B_0 = \frac{2}{|A|} \mathcal{R}_e \sum_{\alpha\lambda} \Bigg\{ \sum_{K\kappa(K\neq J)} \frac{\langle J\lambda|L_0 + g_e S_0|K\kappa\rangle}{W_K^0 - W_J^0} \times \left(\langle J\lambda|m_{+1}|A\alpha\rangle \langle A\alpha|m_{-1}|K\kappa\rangle - \langle J\lambda|m_{-1}|A\alpha\rangle \langle A\alpha|m_{+1}|K\kappa\rangle\right) + \sum_{K\kappa(K\neq A)} \frac{\langle K\kappa|L_0 + g_e S_0|A\alpha\rangle}{W_K^0 - W_A^0} \times \left(\langle J\lambda|m_{+1}|A\alpha\rangle \langle K\kappa|m_{-1}|J\lambda\rangle - \langle J\lambda|m_{-1}|A\alpha\rangle \langle K\kappa|m_{+1}|J\lambda\rangle\right) \Bigg\} \qquad (3.4.14)$$

where $\mathcal{R}_e$ represents the real part of all to the right, and the W_X^0 are zeroth-order level energies. And for C terms,

$$C_0 = -\frac{1}{|A|} \sum_{\alpha\lambda} \langle A\alpha|L_0 + g_e S_0|A\alpha\rangle \times \left(|\langle J\lambda|m_{+1}|A\alpha\rangle|^2 - |\langle J\lambda|m_{-1}|A\alpha\rangle|^2\right) \qquad (3.4.15)$$

3.4.3.1. Basis-invariant MCD equations

In eqs (3.4.13) – (3.4.15) the basis must be diagonal in the Zeeman operator. In some systems it is desirable to work in a non-diagonal basis. Eqs (3.4.16) and (3.4.17) give the appropriate expressions for A_1 and C_0, while B_0 is still given by eq (3.4.14).

$$A_1 = -\frac{1}{|A|}\sum_{\alpha\alpha'\lambda\lambda'}(\langle J\lambda|L_0 + g_e S_0|J\lambda'\rangle\,\delta_{\alpha\alpha'} - \langle A\alpha'|L_0 + g_e S_0|A\alpha\rangle\,\delta_{\lambda\lambda'}) \times (\langle J\lambda|m_{+1}|A\alpha\rangle\langle A\alpha'|m_{-1}|J\lambda'\rangle - \langle J\lambda|m_{-1}|A\alpha\rangle\langle A\alpha'|m_{+1}|J\lambda'\rangle) \tag{3.4.16}$$

$$C_0 = \frac{1}{|A|}\sum_{\alpha\alpha'\lambda}\langle A\alpha'|L_0 + g_e S_0|A\alpha\rangle(\langle J\lambda|m_{+1}|A\alpha\rangle\langle A\alpha'|m_{-1}|J\lambda\rangle - \langle J\lambda|m_{-1}|A\alpha\rangle\langle A\alpha'|m_{+1}|J\lambda\rangle) \tag{3.4.17}$$

If diagonal Zeeman elements are encountered for the ground and excited states, simplification of these equations may be possible using the relationship,

$$\langle J\lambda|m_{\pm 1}|A\alpha\rangle^* = -\langle A\alpha'|m_{\mp 1}|J\lambda\rangle \tag{3.4.18}$$

Note that these equations still apply only to Z-oriented molecules or those in an isotropic point group.

3.4.3.2. Orientational averaging for axial molecules

To treat randomly oriented molecules, the first step is to transform the absorption and MCD equations from space-fixed (X, Y, Z) to molecule-fixed (x, y, z) coordinates. This is performed using the conventions of Goldstein[11] and the Euler angles ϕ, θ and ψ defined in Figure 3.4.1.

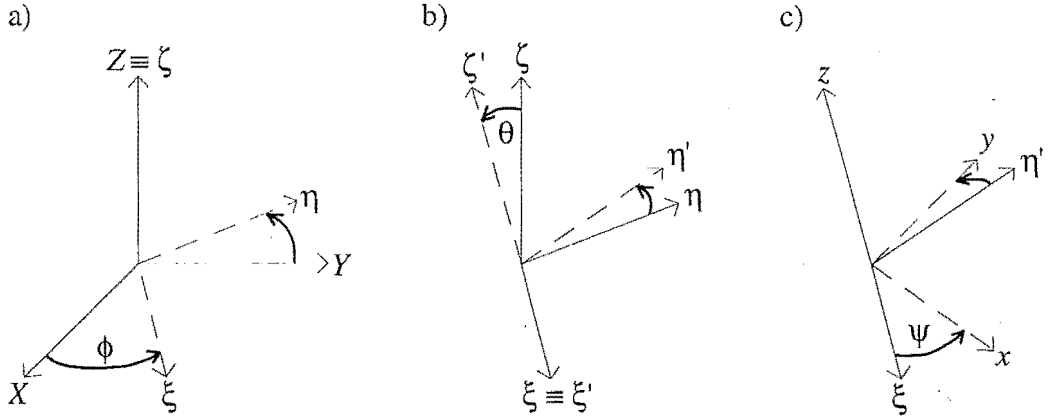

Figure 3.4.1: The Euler angle convention following Goldstein:[11] (a) rotation by ϕ about Z; (b) by θ about ξ; and, (c) by ψ about ζ'.

Then,

$$\begin{pmatrix} x \\ y \\ z \end{pmatrix} = \boldsymbol{R} \begin{pmatrix} X \\ Y \\ Z \end{pmatrix} \tag{3.4.19}$$

where

$$\boldsymbol{R} = \begin{pmatrix} \cos\psi\cos\phi - \sin\psi\cos\theta\sin\phi & \cos\psi\sin\phi + \sin\psi\cos\theta\cos\phi & \sin\psi\sin\theta \\ -\sin\psi\cos\phi - \cos\psi\cos\theta\sin\phi & -\sin\psi\sin\phi + \cos\psi\cos\theta\cos\phi & \cos\psi\sin\theta \\ \sin\theta\sin\phi & -\sin\theta\cos\phi & \cos\theta \end{pmatrix} \tag{3.4.20}$$

Since $\boldsymbol{R}$ is unitary, the inverse relationship is,

$$\begin{pmatrix} X \\ Y \\ Z \end{pmatrix} = \boldsymbol{R}^{\mathrm{T}} \begin{pmatrix} x \\ y \\ z \end{pmatrix} \tag{3.4.21}$$

Hence for a vector (or pseudo-vector) operator $\boldsymbol{O}$,

$$\begin{aligned} O_{\mathrm{X}} &= R_{11}O_{\mathrm{x}} + R_{21}O_{\mathrm{y}} + R_{31}O_{\mathrm{z}} \\ O_{\mathrm{Y}} &= R_{12}O_{\mathrm{x}} + R_{22}O_{\mathrm{y}} + R_{32}O_{\mathrm{z}} \\ O_{\mathrm{Z}} &= R_{13}O_{\mathrm{x}} + R_{23}O_{\mathrm{y}} + R_{33}O_{\mathrm{z}} \end{aligned} \tag{3.4.22}$$

These components are related to the spherical form by eq (3.1.2).

First we apply the last result to the transition moments, then average over the Euler angles ϕ and ψ using the result for an arbitrary function $F(\theta,\phi,\psi)$,

$$\bar{F}(\theta) = \frac{1}{4\pi^2} \int_{\psi=0}^{2\pi} \int_{\phi=0}^{2\pi} F(\theta,\phi,\psi)\, \mathrm{d}\phi\, \mathrm{d}\psi \tag{3.4.23}$$

Eq (3.4.21) is then used to transform from the laboratory-fixed transition moments of eq (3.4.12) to the molecular-fixed coordinates we require.

Note that the transitions of OH, NH and CH that are considered in this work are all x,y-polarised, and hence the terms involving $\langle J\lambda|m_z|A\alpha\rangle$ are zero. The absorption result is, after starting with eq (3.4.6) and (3.4.8), and averaging over ϕ and ψ,

$$\frac{\bar{A}(E,\theta)}{E} = \tfrac{1}{4}\,(1 + \cos^2\theta) \sum_{\alpha\lambda} P_\alpha \left(|\langle J\lambda|m_{+1}|A\alpha\rangle|^2 + |\langle J\lambda|m_{-1}|A\alpha\rangle|^2\right) f_{\alpha\lambda}(E) \tag{3.4.24}$$

$\bar{A}(E,\theta)/E$ gives the absorption for an axial molecule oriented with its z axis at an angle θ with respect to the laboratory Z axis. Likewise, the MCD for such molecules is obtained

beginning with eq (3.4.9), and averaging over ϕ and ψ,

$$\frac{\overline{\Delta A}'(E,\theta)}{E} = \gamma c l \cos\theta \sum_{\alpha\lambda} P_\alpha' \left(|\langle J\lambda|m_{+1}|A\alpha\rangle'|^2 - |\langle J\lambda|m_{-1}|A\alpha\rangle'|^2\right) f'_{\alpha\lambda}(E) \qquad (3.4.25)$$

Note that eqs (3.4.24) and (3.4.25) are completely general expressions for the *x,y*-polarised absorption and MCD of axial molecules oriented with their *z* axis at an angle θ to the *Z* axis. MCD field dependence is expressed in the population factor P_α' (eq (3.4.10)), the transition moments and the bandshape function (eq (3.4.9)). Eqs (3.4.24) and (3.4.25) are the starting points for the analyses of OH, NH and CH in Chapters 4 to 6.

If the molecules are randomly oriented, eqs (3.4.24) and (3.4.25) must be orientationally averaged over θ. Integration of a function $\bar{F}(\theta)$ over θ is performed using,

$$\bar{F} = \frac{1}{2}\int_{-1}^{1} \bar{F}(\theta)\, d\cos\theta \qquad (3.4.26)$$

where $\bar{F}$ is the orientationally averaged function.

The orientationally averaged absorption for axial molecules with $\langle J\lambda|m_z|A\alpha\rangle = 0$ is,

$$\frac{\bar{A}(E)}{E} = \frac{1}{3}\gamma c l \sum_{\alpha\lambda} P_\alpha \left(|\langle J\lambda|m_{+1}|A\alpha\rangle|^2 + |\langle J\lambda|m_{-1}|A\alpha\rangle|^2\right) \qquad (3.4.27)$$

Likewise, the orientationally averaged MCD is, assuming that the population factor is independent of orientation (not generally the case in this thesis),

$$\frac{\overline{\Delta A}'(E)}{E} = \frac{1}{3}\gamma c l \sum_{\alpha\lambda} P_\alpha' \left(|\langle J\lambda|m_{+1}|A\alpha\rangle'|^2 - |\langle J\lambda|m_{-1}|A\alpha\rangle'|^2\right) f'_{\alpha\lambda}(E) \qquad (3.4.28)$$

If working within the linear limit, eq (3.4.28) reduces to the form of eq (3.4.12). The orientationally averaged Faraday parameters in this case are denoted by placing a bar over them.

$$\bar{A}_1 = \frac{1}{3|A|}\sum_{\alpha\alpha'\lambda\lambda'} \left(\langle J\lambda|L_0 + g_e S_0|J\lambda'\rangle\, \delta_{\alpha\alpha'} - \langle A\alpha'|L_0 + g_e S_0|A\alpha\rangle\, \delta_{\lambda\lambda'}\right)$$
$$\times \left(\langle J\lambda|m_{+1}|A\alpha\rangle\, \langle A\alpha'|m_{-1}|J\lambda'\rangle - \langle J\lambda|m_{-1}|A\alpha\rangle\, \langle A\alpha'|m_{+1}|J\lambda'\rangle\right) \qquad (3.4.29)$$

$$\bar{B}_0 = -\frac{2}{3|A|}\,\mathcal{R}e\sum_{\alpha\lambda}\Big\{\sum_{K\kappa(K\neq J)}\frac{\langle J\lambda|L_0+g_eS_0|K\kappa\rangle}{W_K^0-W_J^0}\times(\langle J\lambda|m_{+1}|A\alpha\rangle\langle A\alpha|m_{-1}|K\kappa\rangle - \langle J\lambda|m_{-1}|A\alpha\rangle\langle A\alpha|m_{+1}|K\kappa\rangle) + \sum_{K\kappa(K\neq A)}\frac{\langle K\kappa|L_0+g_eS_0|A\alpha\rangle}{W_K^0-W_A^0}\times(\langle J\lambda|m_{+1}|A\alpha\rangle\langle K\kappa|m_{-1}|J\lambda\rangle - \langle J\lambda|m_{-1}|A\alpha\rangle\langle K\kappa|m_{+1}|J\lambda\rangle)\Big\} \tag{3.4.30}$$

$$\bar{C}_0 = -\frac{1}{3|A|}\sum_{\alpha\alpha'\lambda}\langle A\alpha'|L_0+g_eS_0|A\alpha\rangle(\langle J\lambda|m_{+1}|A\alpha\rangle\langle A\alpha'|m_{-1}|J\lambda\rangle - \langle J\lambda|m_{-1}|A\alpha\rangle\langle A\alpha'|m_{+1}|J\lambda\rangle) \tag{3.4.31}$$

Likewise for the absorption, the orientationally averaged dipole strength $\bar{D}_0$ (eq (3.4.8)) is,

$$\bar{D}_0 = \frac{1}{3|A|}\sum_{\alpha\lambda}(|\langle J\lambda|m_{+1}|A\alpha\rangle|^2 + |\langle J\lambda|m_{-1}|A\alpha\rangle|^2) \tag{3.4.32}$$

where the fact that $\sum_{\alpha} P_\alpha = |A|^{-1}$ has been used.

3.5. Data-analysis methods

Two methods employed in this work to test theoretical models on experimental data are described in this section. The first, moment analysis (Section 3.5.1), is used to extract molecular parameters from MCD and absorption data, by integrating over an *entire* band system. The second involves a spectral simulation of discrete bands (Section 3.5.2) in order to reproduce the structure observed in the band envelope.

3.5.1. Moment analysis

3.5.1.1. A brief introduction to moments

Moment analysis is essentially the statistics of continuous distributions. It was first applied to MCD by Schnatterly *et al.* in 1965,[12] and has been used extensively since that time. A summary has been given by Piepho and Schatz.[1] Only a brief overview is furnished here.

The method of moments provides a fairly rigorous method by which the suitability of a theoretical model can be tested on experimental data. Its major limitation is that strictly it should only be applied over complete and well-separated band systems — that is, the function (A or ΔA in this work) must fall to zero at the integration limits, or there must be some reasonably objective means of deconvoluting the part of the spectrum of interest.

The nth moment of a function $\phi(E)$ (dependent on variable E) is given by,

$$\langle\phi\rangle_n^{E^0} = \int \phi(E)\,(E - E^0)^n\,dE \qquad (3.5.1)$$

where E^0 is the energy about which the moment is taken. Integration is carried out between limits E_1 and E_2 at which $\phi(E) = 0$.

The zeroth moment is simply the integrated area of $\phi(E)$, given by,

$$\langle\phi\rangle_0 = \int \phi(E)\,dE \qquad (3.5.2)$$

It is independent of E^0, and is therefore designated $\langle\phi\rangle_0$. The average energy (barycentre) of the band is denoted $\bar{E}$, and is defined so that $\langle\phi\rangle_1^{\bar{E}} = 0$, which yields,

$$\bar{E} = \langle\phi\rangle_1^0 / \langle\phi\rangle_0 \qquad (3.5.3)$$

Higher moments are normally taken about the band barycentre;

$$\langle\phi\rangle_n^{\bar{E}} = \int \phi(E)\,(E - \bar{E})^n\,dE \qquad (3.5.4)$$

For absorption spectra $\phi(E) = A(E)/E$, while in MCD $\phi(E) = \Delta A'(E)/E$. $\bar{E}$ is defined according to the absorption, and is the same for both types of data. Since A and ΔA are expressed in terms of a normalised bandshape $f(E)$ (eq (3.4.7)), these moments really involve integration of functions derived from $f(E)$, as will be seen in Section 3.5.1.2.

The method of moments is applied by numerically integrating the experimental data as required for the desired moment, and comparing the result with that given by a theoretical model. This procedure is outlined in the following section for the moments computed in this work.

3.5.1.2. The moment equations in MCD and absorption spectroscopy ($\mathbf{A}_0$, $\mathbf{M}_0$ and $\mathbf{M}_1$)

Theoretical expressions for the absorption (A/E) and MCD ($\Delta A'/E$) (Section 3.4.3) are substituted into eq (3.5.1), from which the nth moment ($\mathbf{A}_n$ and $\mathbf{M}_n$, respectively) is computed. In this thesis only the zeroth moment of the absorption, and zeroth and first moments of the MCD, have been utilised.

The zeroth absorption moment is,

$$\mathbf{A}_0 \equiv \langle A/E \rangle_0^{\bar{E}} = \int (A/E)\,(E-\bar{E})^0\,\mathrm{d}E = \gamma c l\, D_0 \int f(E)\,\mathrm{d}E$$

$$= \gamma c l\, D_0 \qquad (3.5.5)$$

where eqs (3.4.6) and (3.4.7) have been used. $\mathbf{A}_1$ is zero due to the definition of the band barycentre.

The zeroth MCD moment is,

$$\mathbf{M}_0 \equiv \langle \Delta A'/E \rangle_0^{\bar{E}}$$

$$= \gamma c l \mu_B B\,(B_0 + C_0/kT) \qquad (3.5.6)$$

where the last step assumes the linear limit. Eq (3.5.6) uses eqs (3.4.7) and (3.4.12), and the fact that

$$\int (-\partial f(E)/\partial E)\,\mathrm{d}E = 0 \qquad (3.5.7)$$

since $f(E) = 0$ at the integration limits.

The first MCD moment is slightly more complicated, because of the factor $(E-\bar{E})$.

$$\mathbf{M}_1 \equiv \langle \Delta A'/E \rangle_1^{\bar{E}}$$

$$= \gamma c l \mu_B B \left[\int A_1\,(-\partial f(E)/\partial E)(E-\bar{E})\,\mathrm{d}E + \int (B_0 + C_0/kT)\, f(E)(E-\bar{E})\,\mathrm{d}E\right]$$

$$= \gamma c l \mu_B B\, A_1 \qquad (3.5.8)$$

using eqs (3.4.7), (3.4.12), (3.5.3) and (3.5.7), and the fact that,

$$\int (-\partial f(E)/\partial E)\, E\,\mathrm{d}E = 1 \qquad (3.5.9)$$

In this thesis, the band systems over which moment analysis is performed generally consist of several overlapping (i = 1, 2, ...) component bands. For each

component there is a local barycentre, $\bar{E}_i$, and moments $\mathbf{A}_0(i)$, $\mathbf{M}_0(i)$ and $\mathbf{M}_1(i)$, which, in principle, can be determined by deconvolution followed by the use of eqs (3.5.5), (3.5.6) and (3.5.8), respectively. It is usually more practical (and often more useful) to determine the overall moments for the whole band system. Overall $\mathbf{A}_0$ and $\mathbf{M}_0$ are obtained simply by summing over $\mathbf{A}_0(i)$ and $\mathbf{M}_0(i)$, respectively, weighted by population factors,

$$\mathbf{A}_0 = \sum_i P_i \, \mathbf{A}_0(i) \tag{3.5.10}$$

$$\mathbf{M}_0 = \sum_i P_i \, \mathbf{M}_0(i) \tag{3.5.11}$$

where P_i represents the population of the initial state of the transition.

The total $\mathbf{M}_1$ is found as follows. Defining the displacement of band i from the overall barycentre $\bar{E}$ as Δ_i, gives,

$$\bar{E} = \bar{E}_i - \Delta_i \tag{3.5.12}$$

Substitution of eq (3.5.12) into eq (3.5.8), followed by summing over all components of the band system, yields,

$$\mathbf{M}_1 = \sum_i P_i \, [\mathbf{M}_1(i) + \Delta_i \, \mathbf{M}_0(i)] \tag{3.5.13}$$

Hence B_0 and C_0 may contribute to $\mathbf{M}_1$ when $\bar{E}_i \neq \bar{E}$.

An important and complicating factor in the calculation of $\mathbf{M}_1$ is the potential temperature dependence of $\bar{E}$, because it is derived from the absorption *via* eqs (3.5.3) and (3.5.4), and can change with temperature and/or field if the populations P_i are affected by these parameters.

One of the potentially useful aspects of moment analysis is that the zeroth and first MCD and absorption moments are invariant to unitary transformations of the excited-state basis.[1] As a consequence, a great deal of information can be extracted concerning, for example, symmetries, angular momenta and spin-orbit coupling of excited states without concern for fine details of the spectra. On the other hand, a potentially adverse consequence is that moment analysis provides little direct information concerning first-order vibronic (*e.g.* Jahn-Teller) and crystal-field effects in the excited state. When the latter are judged to be important, other methods (such as simulation of the structure in the spectrum — see Section 3.5.2) are necessary.

3.5.1.3. MCD/absorption ratios

Since $\mathbf{A}_0$, $\mathbf{M}_0$ and $\mathbf{M}_1$ (eqs (3.5.5), (3.5.6) and (3.5.8), respectively) are all linearly proportional to γ, c and l, the ratio of MCD to absorption can be used to eliminate these dependencies. In addition, because the Faraday parameters and dipole strengths are all expressed in terms of the square of the reduced one-electron transition moment $|m|^2$ (Section 3.4.2), this factor also cancels. Fortunately, group theory, and in particular the Wigner-Eckart theorem (Section 3.2.4), allow theoretical values of such ratios to be derived in a straightforward manner. Hence many molecular parameters can be extracted from MCD and absorption data (obtained simultaneously) *via* numerical integration of the spectral data and by the taking of ratios. Most of the spectral data reported in this thesis were analysed in this way.

3.5.2. Spectral simulation

Computer generation of molecular spectra is most useful in cases where overlapping bands are present, and/or where moment analysis is insensitive to the perturbation of interest (*e.g.* crystal-field effects in the excited state). Moment analysis (Section 3.5.1) can then be applied only over the entire band system, and the number of molecular parameters obtained is sometimes significantly reduced.

In this thesis spectral simulation was employed for NH/Ar, in an attempt to quantify the CF splitting in the $A\,^3\Pi$ excited term, and reproduce the fine structure associated with it (Section 5.6.2). A computer program was written by the author to perform this task, and a brief description of the procedure employed is given here.

Fractional populations are calculated for each Zeeman level of the ground-state term for the user-chosen temperature and field, assuming random orientation of the radical. Various mixing coefficients and splitting parameters are calculated from the SOC constant ζ_π, previously determined using moment analysis (Section 3.5.1), and the chosen CF parameter, V. Theoretical expressions derived for the absorption and MCD intensity of the component transitions are then used to compute the simulated spectrum as follows. The MCD and absorption for each component transition of the band system is treated sequentially. A normalised Gaussian bandshape and its first derivative are evaluated; the former is used to generate the absorption, and B- and C-term contributions to the MCD, while the latter is used for A terms. All of the various contributions to the spectra are then summed, and the calculated spectra are plotted to

the computer screen. The final result can also be saved to a binary data file for comparison with the experimental spectrum.

3.6. References

1. Piepho, S. B.; Schatz, P. N. *Group Theory in Spectroscopy with Applications to Magnetic Circular Dichroism*; Wiley-Interscience: New York, 1983.
2. Butler, P. H. *Point Group Symmetry Applications*; Plenum Press: New York, 1981.
3. Herzberg, G. *Molecular Spectra and Molecular Structure Volume 1: Spectra of Diatomic Molecules*, 2nd ed.; Krieger: New York, 1950.
4. Davidson, G. *Group Theory for Chemists*; MacMillan Education Ltd: London, 1991.
5. Tsukerblat, B. S. *Group Theory in Chemistry and Spectroscopy*; Academic Press, Ltd: London, 1994.
6. Bishop, D. M. *Group Theory and Chemistry*; Clarendon Press: Oxford, 1973.
7. Levine, I. N. *Quantum Chemistry*, 4th ed.; Prentice-Hall, Inc: Englewood Cliffs, 1991.
8. Atkins, P. W. *Physical Chemistry*, 4th ed.; Oxford University Press: Oxford, 1990.
9. Buckingham, A. D.; Stephens, P. J. In *Annual Review of Physical Chemistry*; Eyring, H.; Christensen, C. J.; Johnston, H. S., Eds; Annual Reviews, Inc: Palo Alto, 1966; Vol. 17, pp. 399-432.
10. Schatz, P. N.; McCaffery, A. J. *Quart. Rev.* **1969**, *23*, 552-584.
11. Goldstein, H. *Classical Mechanics*; Addison-Wesley: Reading, 1950.
12. Henry, C. H.; Schnatterly, S. E.; Slichter, C. P. *Phys. Rev.* **1965**, *137*, A583-A602.

4. OH/Ar

4.1. Introduction

As noted in Section 1.1.1, the hydroxyl free radical (OH) occurs in a wide variety of terrestial and extra-terrestrial environments, and is important in a large range of chemical processes. There has been much work done on OH in the gas phase, but to a lesser extent in ice and rare-gas matrices. A brief history of these previous investigations follows as part of this introduction. The main body of the chapter covers the candidate's research on the MCD and electronic absorption of the $A\,^2\Sigma^+ \leftarrow X\,^2\Pi$ transition of OH (and OD) trapped in a solid Ar matrix. It presents temperature- and magnetic field-dependent data which are interpreted in terms of a spin-orbit (SO) – crystal-field (CF) model in which the orbital angular momentum is partially quenched by CF interactions with neighbouring species in the matrix.

4.1.1. Observation and early assignments of gas-phase OH absorption and emission

For many years the UV emission spectrum due to the $^2\Sigma^+ \rightarrow {}^2\Pi$ transition of OH was observed in sources, such as Giesler tubes, containing water vapour or moist H_2 or O_2. However, it was not until 1924 that Watson[1] correctly assigned the well-developed band systems with heads at 3064 Å (0,0) and 2811 Å (1,0) to OH.

In 1927, Mulliken[2] published a detailed work on the theoretical interpretation of electronic states and band spectra in diatomic molecules, which he applied to the then-known bands of the hydroxyl radical. Johnston and co-workers, in a later series of papers,[3-5] reported further bands, which they were able to observe due to improved experimental conditions and longer photographic-plate exposure times. Since that time there have many investigations into gas-phase OH, and, to a lesser extent, OD, which are summarised by Huber and Herzberg.[6]

4.1.2. OH in ice

In the late 1950s, Piette *et al.*[7] tentatively assigned a strong EPR resonance at $g \approx 2$ in β-irradiated ice (at 4.2 and 77 K) to OH. Assignment was based on the doublet splitting due to hyperfine coupling with the proton of OH, in spite of a g value

suggestive of almost completely quenched orbital angular momentum for $X\,^2\Pi_{3/2}$ of OH. Later work by Siegel *et al.*[8] (g = 2.008) and Brivati *et al.*[9] ($g_{\parallel}$ = 2.05, $g_{\perp}$ = 2.008) on γ-irradiated ice, and a theoretical study by Symons,[10] confirmed this assignment. The quenching of the orbital contribution to the angular momentum was suggested to be due to strong interactions of the ice lattice with the hydroxyl radical, particularly *via* hydrogen bonding. This interaction lowers the degeneracy of the π orbitals — a large CF splitting (Section 3.3.2.3).

4.1.3. Matrix-isolated OH and OD

The electronic absorption spectrum of OH/Ar was first observed by Robinson and McCarty in 1958.[11] The OH radicals were produced in an electrodeless discharge through *moist* hydrazine and Ar, and the resultant mixture was deposited on a liquid-He-cooled sample window. The (0,0) absorption band for the $A\,^2\Sigma^+ \leftarrow X\,^2\Pi$ transition of matrix-isolated OH was found to be red-shifted by about 300 cm^{-1} from the gas-phase energy. In a (slightly) more comprehensive work they later published electronic absorption spectra for both OH/Ar and OD/Ar.[12] They observed fine structure, but were unable to assign it to guest rotation. For Ar and Kr hosts the structure is very similar, and changes only slightly between OH and OD.[13] This is contrary to the gas-phase observation,[14] in which significant changes in rotational structure between isotopomers were observed.[15] Hence if rotation is responsible for the fine structure, it is strongly perturbed. Wei corroborated McCarty and Robinson's results in unpublished work,[16] while finding that OH and OD in Xe have fine structure similar to that in Ar and Kr.

Absorption and emission spectra of OH/Ne and OD/Ne at 4.2 K were reported by Tinti in 1968.[17] The structure found in Ne matrices differed from that of the other rare-gas matrices and showed isotopic variation. The spectra were partially interpreted in terms of slightly perturbed rotation of OH and OD in the solid. A larger perturbation of OH than OD in Ne suggested that translation-rotation coupling in the solid might be important. Subsequently, Brus and Bondybey[18] used time- and wavelength-resolved fluorescence spectroscopy to probe OH/Ne and OD/Ne, finding that there was "intermediate strong coupling" (or resonant mixing) occurring between rotational and lattice-phonon levels. Nevertheless, OH and OD in Ne matrices were found to rotate almost freely.

In 1986, Rose[19] reported the first MCD and absorption spectra of OH/Ar, at four temperatures from ~3 to 8.3 K. Although spectral resolution was insufficient for structure to be observed, the magnitude of the MCD was found to increase with decreasing temperature, indicating the presence of *C* terms (Section 1.3.2). This result suggests that, unlike OH in β- and γ-irradiated ice (Section 4.1.2),[7-10] the orbital angular momentum of OH/Ar is *not* totally quenched. However, Rose's study[19] failed to find a reliable measure of the orbital reduction factor because of MCD and thermometry calibration problems. In particular, the magnetic field was applied the wrong way, and temperatures were uncertain because the matrix was in a vacuum. The former is easily overcome, while the latter is dealt with by using the matrix injection system described in Section 2.2.2.

The work in this thesis reports high-resolution simultaneous MCD and absorption spectra of OH/Ar at temperatures from 1.735 to 6.9 K, and for magnetic fields up to 4 T. A quantitative measure of the ground-state orbital angular momentum, and hence orbital reduction factor, are given by means of a SO-CF model (Section 3.1.3). MCD and absorption spectra of OD/Ar are also presented for temperatures of ~12 and 17 K, and provide qualitative assistance in the assignment of structure observed here and by Robinson and McCarty.[12]

4.2. Experimental

OH/Ar and OD/Ar were prepared using the apparatus described in Section 2.1.1.2, employing the ¼" → ½" discharge tube shown at the bottom of Figure 2.1.2.

Distilled water was freeze-thaw purified several times before being mixed with Ar (1:100 mole ratio using standard gas-handling techniques) in a 1-L glass reservoir to a final pressure of about 1 atm. In like manner, D_2O was mixed with Ar in a new, *oven-dried* 1-L reservoir. OH(OD)/Ar matrix preparation times were ~15 minutes, with $H_2O(D_2O)$:Ar flow rates ~6 mmol hr^{-1}.

MOD4 (Section 2.3) was used to gather all spectral data. The Xe-arc lamp and 1180-groove/mm grating were utilised in conjunction with either the Hamamatsu R-376 or R-292 photomultiplier tubes. A Corning 7-54 filter was used to remove stray visible light exiting the monochromator.

The following subsections describe aspects of the experimental work that are specific to OH/Ar and OD/Ar.

4.2.1. OH/Ar

Preliminary matrix depositions were performed in the He refrigerator – electromagnet system described in Section 2.2.1. The deposition temperature was typically 12 to 14 K. Despite the somewhat cloudy appearance of the matrices, the depolarisation of cpl by the matrix was found to be negligible.

These experiments showed that annealing OH/Ar matrices above ~17 K resulted in only a small amount of band sharpening, but did not reveal any new structure. Overall, annealing OH/Ar matrices was detrimental: it reduced the OH concentration, and caused further clouding of the matrices. In subsequent experiments OH/Ar matrices were not annealed.

Reduction of the H_2O concentration (to 1:250 H_2O/Ar mole ratio) yielded slightly less OH/Ar than for 1:100 mixtures. The spectral appearance was unchanged, so 1:100 mole ratios were used subsequently.

The fine structure observed for OH/Ar and OD/Ar is moderately broad. Slit-width dependence of the MCD and absorption spectra revealed no increase in resolution below a setting of 150 μm. While there was some loss of resolution above 150 μm, bands were not obscured. Hence, the spectra shown in Section 4.3.1 were obtained using 200-μm slits (spectral resolution ~0.16 nm). Although resolution was compromised slightly, higher light intensity afforded better S/N.

Data for quantitative analysis were obtained using the CF1204–SM4 matrix-isolation–cryomagnet system (Section 2.2.2). During deposition of the sample, the window temperature was less stable than the He refrigerator (due to the tendency of liquid-He flow to surge) and varied within the range ~12 – 20 K.

4.2.2. OD/Ar

Since D_2O is easily contaminated with H_2O, the deposition assembly was pumped to $<10^{-5}$ Torr before OD/Ar runs were done. Spectral data (Section 4.3.2) reveal no evidence of OH contamination.

The yield of OD/Ar was reduced from OH/Ar, which made the collection of high-quality data difficult. Consequently, the OD/Ar spectra presented in Section 4.3.2 were obtained using the He refrigerator – electromagnet system (Section 2.2.1) and are intended for qualitative and semi-quantitative purposes only.

4.3. Results

4.3.1. OH/Ar

Figure 4.3.1 shows the averaged, temperature-independent absorption (16 individual spectra) and temperature-dependent MCD (from 1.735 to 6.9 K) of OH/Ar. (The OD/Ar absorption spectrum is shown for comparison; see Section 4.3.2.) Each spectrum exhibits a pair of maxima, and a number of shoulders spaced at approximately regular intervals. The barycentres for these bands (1 – 5) are given in Table 4.3.1, which also lists the wavenumbers of the three most intense absorption bands (2 – 4) observed by McCarty and Robinson,[12] and the single maximum observed by Rose.[19]

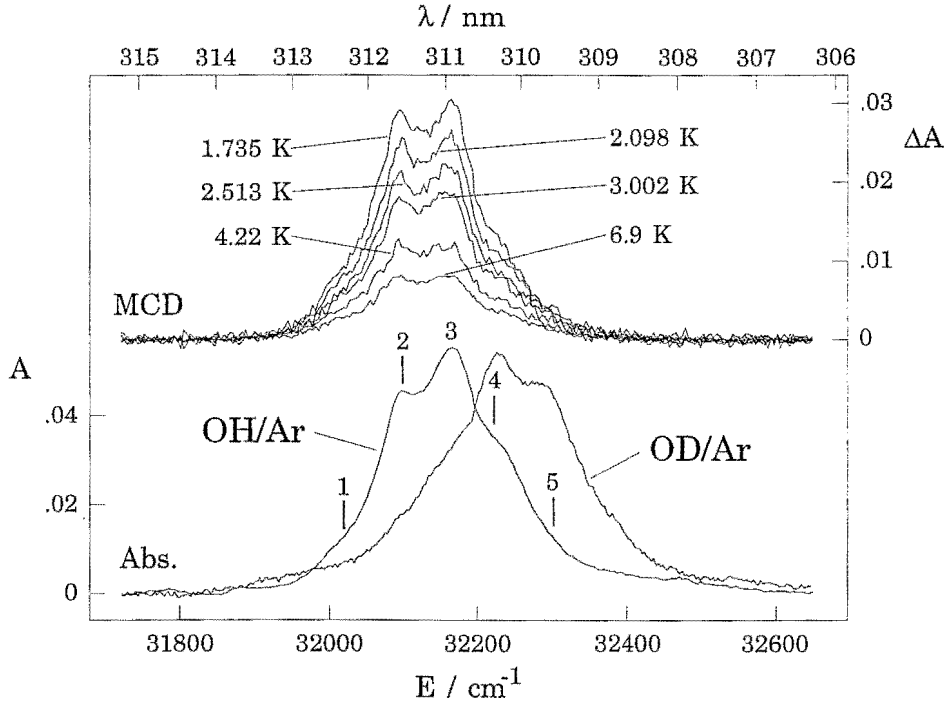

Figure 4.3.1: Top: MCD (ΔA) of OH/Ar from 1.73 to 6.9 K (B = 0.5 T or 1.0 T). Bottom: averaged (16 temperature- and field-independent spectra) absorption spectrum of OH/Ar, with OD/Ar shown for comparison. The absorption bands are labelled for cross-referencing with Tables 4.3.1 and 4.5.2, and Figure 4.5.3.

The MCD is single-signed and shows the temperature dependence indicative of *C* terms (Section 1.3.2). Further evidence for the presence of *C* terms is provided by the saturation behaviour exhibited by the field-dependence data shown in Figure 4.3.2. The significance of the changes of relative intensity between bands 2 and 3 with field variation will be discussed in Section 4.5.

Table 4.3.1: Band barycentres for fine structure in the $A\ ^2\Sigma^+ \leftarrow X\ ^2\Pi$ system of OH/Ar and OD/Ar.[a]

Band [b]	OH/Ar			OD/Ar
	McCarty and Robinson [c]	Rose [d]	This work [e]	This work [e]
1			32 025	32 145
2	32 090		32 095	32 230
3	32 155	31 980	32 165	32 295
4	32 225		32 230	32 370
5			32 285	

[a] Wavenumbers given in cm^{-1}.
[b] Numbering for cross-reference with Figures 4.3.1 and 4.5.2, and Table 4.5.1.
[c] Ref. 12.
[d] Ref.19.
[e] Band barycenters $\pm 10\ cm^{-1}$.

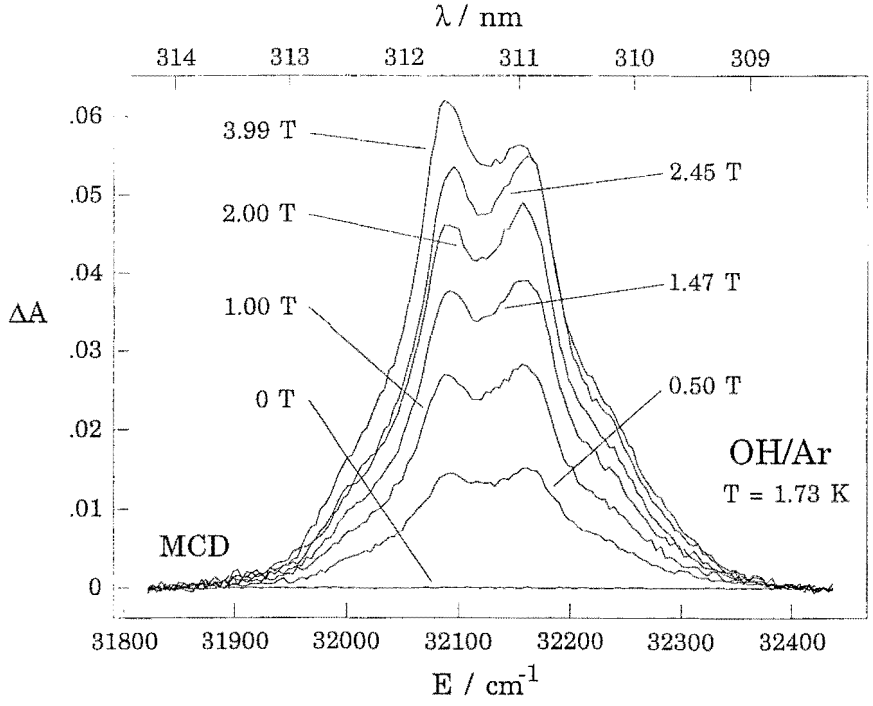

Figure 4.3.2: Magnetic-field dependence, from 0 to 4 T, of the MCD of OH/Ar at 1.73 K.

4.3.2. OD/Ar

Figure 4.3.3 shows the temperature-independent absorption and temperature-dependent MCD (~12 and 17 K) of OD/Ar. Data were acquired using the He-refrigerator – electromagnet system (Section 2.2.1), at a field of 0.6 T. The system is blue-shifted by ~1 nm relative to OH/Ar. The absorption spectrum bears a resemblance

to OH/Ar, in terms of the separation of bands (Section 4.5.2), although there are intensity variations.

MCD S/N is poor relative to OH/Ar due to a reduced yield of OD/Ar, and because only higher temperatures are available using the closed-cycle He refrigerator. Nevertheless, like OH/Ar, the MCD is single-signed and positive, showing reciprocal temperature dependence.

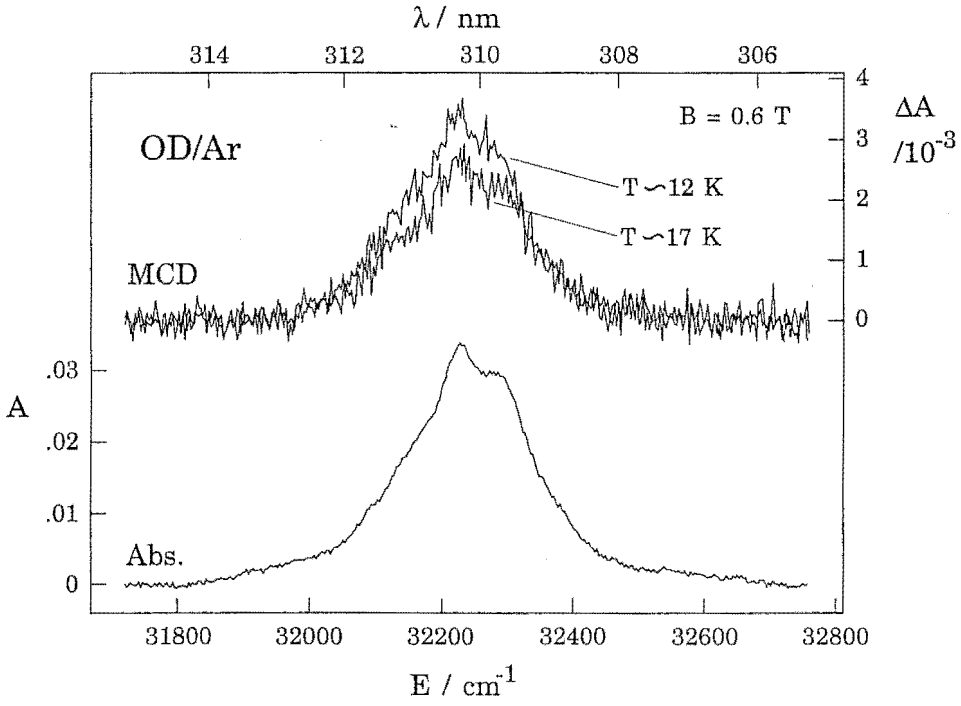

Figure 4.3.3: Absorption and temperature-dependent MCD of OD/Ar at ~12 K and 17 K, with B = 0.6 T.

4.3.3. Moment analysis

In order to quantify the temperature and field dependencies, dimensionless zeroth moment parameters (Section 3.5.1) are defined. Using eq (3.5.2), the zeroth absorption and MCD moments, $\mathbf{A}_0$ and $\mathbf{M}_0$, are,

$$\mathbf{A}_0 = \int \frac{A(E)}{E} \mathrm{d}E \qquad (4.3.1)$$

$$\mathbf{M}_0 = \int \frac{\Delta A(E)}{E} \mathrm{d}E \qquad (4.3.2)$$

where E is the energy of the incident radiation, A is the absorption, and ΔA is the MCD.

The $\mathbf{M}_0/\mathbf{A}_0$ ratios for the OH/Ar temperature- and field-dependence data are plotted against $\mu_B B/2kT$ in Figure 4.3.4. The saturation behaviour attributable to *C* terms is again clearly evident. Problems with the absorption baseline for OD/Ar preclude inclusion of $\mathbf{M}_0/\mathbf{A}_0$ for that system.

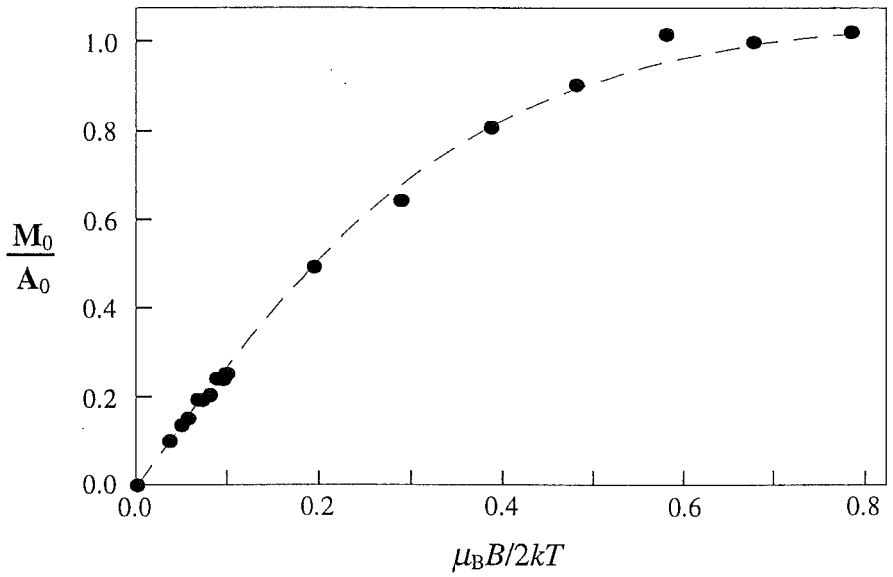

Figure 4.3.4: Magnetisation saturation for the moment ratio $\mathbf{M}_0/\mathbf{A}_0$ as a function of $\mu_B B/2kT$ for OH/Ar. The broken curve is a best fit to the data of Section 4.3.1 using eq (4.4.39) assuming random orientation of the guest radical and ζ_π = 125 ± 10 cm^{-1}, and was obtained with an orbital reduction factor of 0.79 ± 0.02.

4.4. Theory

In this section, a SO-CF model is developed that is used in the subsequent section to explain the observed data. Chapter 3 describes in detail the technique used here, although the MCD and absorption theory of Section 3.4.3 is extended considerably for use with data obtained outside the so-called 'linear limit',[20] and accounts for the effects of orientational averaging.

4.4.1. Spin-orbit wavefunctions for OH

OH belongs to the point group $\mathbf{C}_{\infty v}$, the irrep and partner labels for which are given in Table 4.4.1. (Reasons for mixing notations are given in Section 3.2.1.) In this work, term labels are given using the 'standard' notation.

Table 4.4.1: Irreps and partner label notations for the $C_{\infty v}$ point group.

Butler notation[*21]		Standard notation	Mulliken notation
Irreps	Components		
0	0	Σ^+	A_1
$\tilde{0}$	0	Σ^-	A_2
$\frac{1}{2}$	$\pm\frac{1}{2}$	$E_{1/2}$	$E_{1/2}$
1	±1	Π	E_1
$\frac{3}{2}$	$\pm\frac{3}{2}$	$E_{3/2}$	$E_{3/2}$
2	±2	Δ	E_2
$\frac{5}{2}$	$\pm\frac{5}{2}$	$E_{5/2}$	$E_{5/2}$

[*] M.F. Reid, *J. Phys. A: Math. Gen.*, **17** (1984), 1755-9.

Figure 4.4.1 shows a schematic MO diagram for OH. The lowest-energy configuration is $1\sigma^2\ 2\sigma^2\ 3\sigma^2\ 1\pi^3$, while the first-excited configuration is $1\sigma^2\ 2\sigma^2\ 3\sigma^1\ 1\pi^4$. Since both of these configurations involve only one partially occupied orbital, determination of the orbital irreps is quite simple. The $1\pi^3$ open shell is a hole equivalent of π^1 (Section 3.3.1.4), producing a $^2\Pi$ ground term. The excited term has a partially occupied σ^+ orbital, giving rise to a $^2\Sigma^+$ excited term.

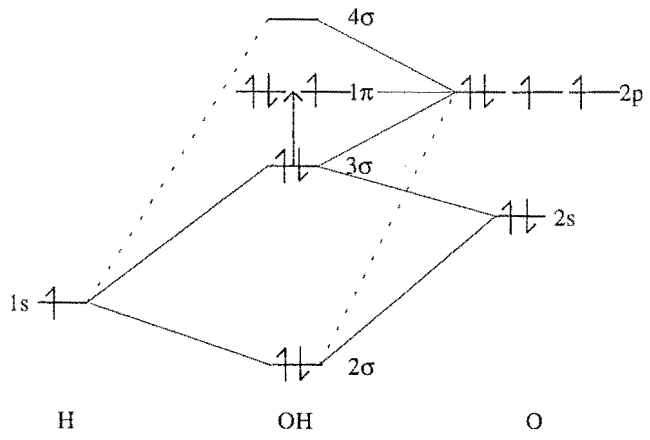

Figure 4.4.1: Schematic MO diagram for OH. (The 1σ MO is essentially pure O(1s), and is not shown.) The dashed arrow shows the lowest-energy electronic excitation investigated in this work.

4.4.1.1. SL wavefunctions

Eqs (4.4.1) and (4.4.2) give SL wavefunctions $|^{2\delta+1}h\ m\ \theta\rangle$ for the ground and first-excited configurations, respectively, obtained as described in Section 3.3.1.4.

$$|^2\Pi\ \pm\tfrac{1}{2}\ +1\rangle = |0^2\ -1^{\pm}\ 1^2\rangle \qquad (4.4.1a)$$

$$|^2\Pi\ \pm\tfrac{1}{2}\ -1\rangle = |0^2\ -1^2\ 1^{\pm}\rangle \qquad (4.4.1b)$$

$$|^2\Sigma^+\ \pm\tfrac{1}{2}\ 0\rangle = |0^{\pm}\ -1^2\ 1^2\rangle \qquad (4.4.2)$$

4.4.1.2. SO wavefunctions

SO coupling (SOC) is treated using the method of Section 3.3.1.5. Table 4.4.2 gives the spin correlations for $\delta = ½$ that are required to form the symmetry-adapted basis for $\mathbf{SO}_3$ in $\mathbf{C}_{\infty v}$, and summarises the SO irreps and partners that arise for the $X\ ^2\Pi$ and $A\ ^2\Sigma^+$ terms.

Table 4.4.2: SOC irreps and partners resulting from the $X\ ^2\Pi$ and $A\ ^2\Sigma^+$ terms of OH.

Term	Orbital irrep	Spin irrep		SOC		
	$\mathbf{C}_{\infty v}$	$\mathbf{SO}_3$	$\mathbf{C}_{\infty v}$	Irreps (t)	Partners (τ)	Level
$^2\Pi$	1	$\frac{1}{2}$	$\frac{1}{2}$	$\frac{3}{2}$	$\pm\frac{3}{2}$	$^2\Pi_{3/2}$
				$\frac{1}{2}$	$\pm\frac{1}{2}$	$^2\Pi_{1/2}$
$^2\Sigma^+$	0	$\frac{1}{2}$	$\frac{1}{2}$	$\frac{1}{2}$	$\pm\frac{1}{2}$	$^2\Sigma^+_{1/2}$

The SO wavefunctions for each level were derived using eq (3.3.10), and are shown in eqs (4.4.3) and (4.4.4) for the ground- and first-excited configurations, respectively. The $|^{2\delta+1}h_{\Omega}\ M_{\Omega}\rangle$ notation is described in Section 3.3.1.5. In $\mathbf{C}_{\infty v}$, the SO irrep and partner (t and τ, respectively) correspond to the total angular momentum quantum number, Ω, and its magnetic quantum number, M_{Ω}.

$$|^2\Pi_{3/2}\ \pm\tfrac{3}{2}\rangle = -|0^2\ -1^+\ \pm1^{\pm}\ 1^-\rangle \qquad (4.4.3a)$$

$$|^2\Pi_{1/2}\ \pm\tfrac{1}{2}\rangle = \mp|0^2\ -1^{\mp}\ \pm1^{\pm}\ 1^{\mp}\rangle \qquad (4.4.3b)$$

$$|^2\Sigma^+_{1/2}\ \pm\tfrac{1}{2}\rangle = |0^{\pm}\ -1^2\ 1^2\rangle \qquad (4.4.4)$$

4.4.2. Matrix elements

4.4.2.1. Spin-orbit matrix elements

SO matrix elements were evaluated as described in Section 3.3.2.2. The $A\,^2\Sigma^+$ term exhibits no first-order SOC, since it is orbitally non-degenerate. The ground term has both orbital and spin degeneracy, and the non-zero matrix elements are,

$$\langle {}^2\Pi_{1/2}\,\pm\tfrac{1}{2}|\mathscr{H}_{SO}|{}^2\Pi_{1/2}\,\pm\tfrac{1}{2}\rangle = \tfrac{1}{2}\zeta_\pi$$

$$\langle {}^2\Pi_{3/2}\,\pm\tfrac{3}{2}|\mathscr{H}_{SO}|{}^2\Pi_{3/2}\,\pm\tfrac{3}{2}\rangle = -\tfrac{1}{2}\zeta_\pi \qquad (4.4.5)$$

where ζ_π is an empirical SO splitting constant for a 1π electron in OH,

$$\zeta_\pi = \langle \pi\ 1|u_z|\pi\ 1\rangle = -\langle \pi\ {-1}|\,u_z\,|\pi\ {-1}\rangle \qquad (4.4.6)$$

The energies of the SO levels are therefore,

$$E({}^2\Pi_\Omega) = -\zeta_\pi\,\Lambda\,(\Omega-\Lambda) \qquad (4.4.7)$$

where Λ and Ω are, respectively, the total orbital angular momentum and SO quantum numbers. The leading negative sign on the right-hand side accounts for the $X\,^2\Pi$ term of OH being an inverted SO system, since ζ_π is positive.

The SO levels of the ground-state term are shown towards the left in Figure 4.4.2.

4.4.2.2. Crystal-field matrix elements

CF matrix elements are evaluated as described in Section 3.3.2.3. In fact, the example given there for the CF splitting of Π orbital components in $\mathbf{C}_{\infty v}$ is directly applicable to the $X\,^2\Pi$ ground term of OH. (The $^2\Sigma^+$ can have no CF-induced lowering of symmetry, since it is only spin degenerate.) The CF matrix elements are hence,

$$\langle {}^2\Pi_{1/2}\,\pm\tfrac{1}{2}|\mathscr{H}_{CF}|{}^2\Pi_{3/2}\,\mp\tfrac{3}{2}\rangle = \mp\tfrac{1}{2}V$$

$$\langle {}^2\Pi_{3/2}\,\pm\tfrac{3}{2}|\mathscr{H}_{CF}|{}^2\Pi_{1/2}\,\mp\tfrac{1}{2}\rangle = \pm\tfrac{1}{2}V \qquad (4.4.8)$$

where $V = \langle 1\pi\|V^2\|1\pi\rangle$ is a one-electron reduced CF matrix element, which represents the magnitude of the splitting of the $|\Pi\ \pm1\rangle$ orbital components in the absence of SOC. Figure 4.4.2 illustrates the effect of CF splitting on the SO levels.

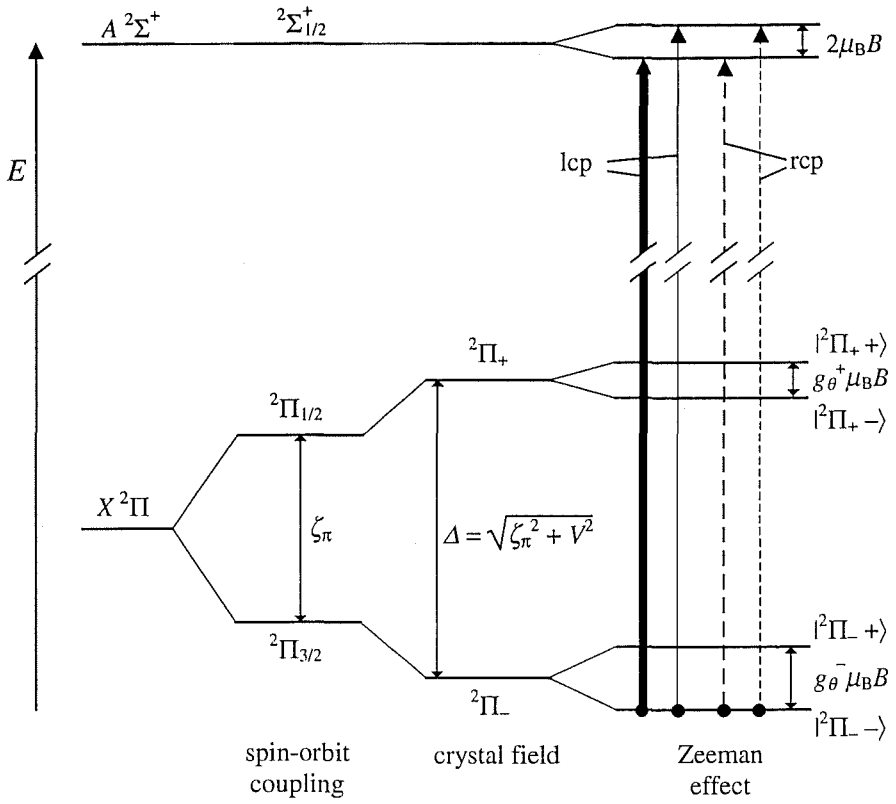

Figure 4.4.2: Energy-level diagram showing the effects of SO, CF and Zeeman interactions on the $X\,^2\Pi$ and $A\,^2\Sigma^+$ states of OH/Ar. The relative intensities of left- (lcp) and right-circularly polarised (rcp) transitions originating from the $|^2\Pi_-\rangle$ state and terminating in the $A\,^2\Sigma^+$ manifold are indicated by the thickness of the lines.

4.4.3. SO-CF wavefunctions for OH/Ar

The simultaneous presence of SO and CF effects alters the energies of the levels by mixing eigenstates of either operator. The new SO-CF eigenfunctions and the corresponding eigenvalues for the $^2\Pi$ term were obtained by diagonalising the SO-CF hamiltonian matrix (Section 3.3.3), and yield a splitting (Δ) in the $^2\Pi$ manifold of,

$$\Delta = \sqrt{\zeta_\pi^2 + V^2} \qquad (4.4.9)$$

ζ_π and V have been defined in preceding sections, and the value of ζ_π will be reduced from the gas-phase values.[22,23] The SO-CF eigenstates are then,

$$|^2\Pi_+ \pm\tfrac{1}{2}\rangle = \pm\beta\,|^2\Pi_{3/2}\,\pm\tfrac{3}{2}\rangle + \alpha\,|^2\Pi_{1/2}\,\mp\tfrac{1}{2}\rangle$$

$$|^2\Pi_- \pm\tfrac{1}{2}\rangle = \alpha\,|^2\Pi_{3/2}\,\pm\tfrac{3}{2}\rangle \mp \beta\,|^2\Pi_{1/2}\,\mp\tfrac{1}{2}\rangle \qquad (4.4.10)$$

where $^2\Pi_+$ and $^2\Pi_-$ respectively designate the upper and lower SO-CF levels, and $\pm\frac{1}{2}$ in the left-hand kets denotes the value of M_S. The mixing coefficients α and β are given by

$$\alpha = \frac{V}{\sqrt{V^2 + (\Delta - \zeta_\pi)^2}} \tag{4.4.11}$$

$$\beta = \frac{\Delta - \zeta_\pi}{\sqrt{V^2 + (\Delta - \zeta_\pi)^2}} \tag{4.4.12}$$

These coefficients obey the relations,

$$\alpha^2 + \beta^2 = 1 \tag{4.4.13}$$

$$\alpha^2 - \beta^2 = \zeta_\pi / \Delta \equiv \kappa \tag{4.4.14}$$

$$2\alpha\beta = V / \Delta \equiv \eta \tag{4.4.15}$$

Here $0 \leq \kappa \leq 1$ and $0 \leq \eta \leq 1$.

4.4.4. Zeeman matrix elements and *g* values

Section 3.3.4 covers the evaluation of Zeeman matrix elements and g values.

4.4.4.1. $X\,^2\Pi$ ground term

Angular momentum matrix elements for the SO-CF states of the $X\,^2\Pi$ term are listed in Table 4.4.3 for the z and x components (molecular reference frame) of $\boldsymbol{L}$ and $\boldsymbol{S}$ (Sections 3.3.4.1 and 3.3.4.2). The g values are given by,

$$g_\parallel^{\pm} \equiv 2\,\langle {}^2\Pi_\pm\, {+\tfrac{1}{2}} | L_z + 2S_z | {}^2\Pi_\pm\, {+\tfrac{1}{2}} \rangle = 2(1 \mp \kappa\Lambda) \tag{4.4.16}$$

$$g_\perp \equiv 2\,\langle {}^2\Pi_\pm\, {+\tfrac{1}{2}} | L_x + 2S_x | {}^2\Pi_\pm\, {-\tfrac{1}{2}} \rangle = 2\eta \tag{4.4.17}$$

$g_\parallel^+$ and $g_\parallel^-$ are the g values for the upper and lower SO-CF levels, respectively, when the molecular z axis is aligned parallel to $\boldsymbol{B}$. $g_\perp$ was computed assuming that $g_x = g_y$, although due to higher-order interactions they are not equal. Such differences cannot be resolved in this work, and are unimportant to the following analysis. Notice that the g values are not mutually independent, since $\kappa^2 + \eta^2 = 1$ (eqs (4.4.13) – (4.4.15)). Figure 4.4.3 illustrates their dependencies on κ.

From eq (4.4.16) and Figure 4.4.3, κ can be seen to act as an orbital reduction factor for the lower ($^2\Pi_-$) SO-CF level. With $\kappa = 1$ (no CF), $g_\perp = 0$, $g_\parallel^- = 4$ and the

orbital angular momentum makes its full contribution to the magnetic moment. With κ = 0, the orbital angular momentum is totally quenched, and the g values take their spin-only values.

Table 4.4.3: Angular momentum matrix elements for the $X\,^2\Pi$ SO-CF states of OH/Ar[a] and CH/Ar.[b]

$L_z + 2S_z$	$\|^2\Pi_- -\frac{1}{2}\rangle$	$\|^2\Pi_- \frac{1}{2}\rangle$	$\|^2\Pi_+ -\frac{1}{2}\rangle$	$\|^2\Pi_+ \frac{1}{2}\rangle$
$\langle^2\Pi_- -\frac{1}{2}\|$	$-\frac{1}{2}g_\parallel^-$	0	$\frac{1}{2}g_\perp$	0
$\langle^2\Pi_- \frac{1}{2}\|$	0	$\frac{1}{2}g_\parallel^-$	0	$\frac{1}{2}g_\perp$
$\langle^2\Pi_+ -\frac{1}{2}\|$	$\frac{1}{2}g_\perp$	0	$-\frac{1}{2}g_\parallel^+$	0
$\langle^2\Pi_+ \frac{1}{2}\|$	0	$\frac{1}{2}g_\perp$	0	$\frac{1}{2}g_\parallel^+$

$L_x + 2S_x$	$\|^2\Pi_- -\frac{1}{2}\rangle$	$\|^2\Pi_- \frac{1}{2}\rangle$	$\|^2\Pi_+ -\frac{1}{2}\rangle$	$\|^2\Pi_+ \frac{1}{2}\rangle$
$\langle^2\Pi_- -\frac{1}{2}\|$	0	$\frac{1}{2}g_\perp$	0	$-\kappa$
$\langle^2\Pi_- \frac{1}{2}\|$	$\frac{1}{2}g_\perp$	0	κ	0
$\langle^2\Pi_+ -\frac{1}{2}\|$	0	κ	0	$\frac{1}{2}g_\perp$
$\langle^2\Pi_+ \frac{1}{2}\|$	$-\kappa$	0	$\frac{1}{2}g_\perp$	0

[a] Parameters are defined by eqs (4.4.14), (4.4.16) and (4.4.17).
[b] See Section 6.4.4.1. Parameters are defined as for OH/Ar, except that $g_\parallel^\pm$ is given by eq (6.4.14) rather than eq (4.4.16)

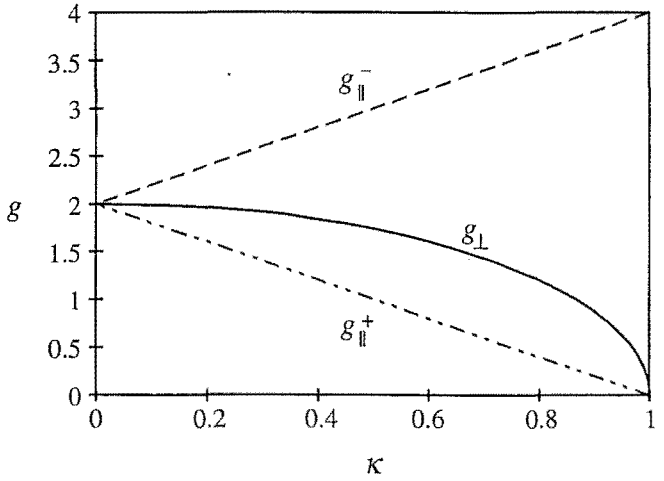

Figure 4.4.3: Dependence of g values for the $X\,^2\Pi$ term of OH/Ar on the orbital reduction factor, κ.

4.4.4.2. A $^2\Sigma^+$ excited term

In the $A\,^2\Sigma^+$ term, there is no orbital angular momentum and no CF splitting. Hence the Zeeman splitting is nearly isotropic, with $g \approx g_e \approx 2$. The relevant matrix elements (Section 3.3.4.1) are,

$$\langle {}^2\Sigma^+_{1/2} \pm\tfrac{1}{2}|L_z + 2S_z|{}^2\Sigma^+_{1/2} \pm\tfrac{1}{2}\rangle = \pm 1 \qquad (4.4.18)$$

4.4.5. Transition-moment matrix elements

Transition-moment matrix elements for $A\,{}^2\Sigma^+ \leftarrow X\,{}^2\Pi$ were evaluated as described in Section 3.4.2. The non-zero transition moments are summarised in Table 4.4.4, where the initial states are shown along the top row and the final states down the left hand column. $\mathcal{M}$ is the one-electron reduced transition moment (Section 3.4.2.1) for the orbital excitation $1\pi \leftarrow 3\sigma$,

$$\mathcal{M} = \langle 1\pi \| m^1 \| 3\sigma \rangle \qquad (4.4.19)$$

Table 4.4.4: Transition moments for the $^2\Sigma^+ \leftarrow {}^2\Pi_\pm$ SO-CF transitions of OH/Ar.[a]

m^1_{+1}	$\lvert{}^2\Pi_- -\frac{1}{2}\rangle$	$\lvert{}^2\Pi_- \frac{1}{2}\rangle$	$\lvert{}^2\Pi_+ -\frac{1}{2}\rangle$	$\lvert{}^2\Pi_+ \frac{1}{2}\rangle$
$\langle {}^2\Sigma^+_{1/2} -\frac{1}{2}\rvert$	$\frac{1}{\sqrt{2}}\alpha\mathcal{M}$	0	$-\frac{1}{\sqrt{2}}\beta\mathcal{M}$	0
$\langle {}^2\Sigma^+_{1/2} \frac{1}{2}\rvert$	0	$\frac{1}{\sqrt{2}}\beta\mathcal{M}$	0	$-\frac{1}{\sqrt{2}}\alpha\mathcal{M}$

m^1_{-1}	$\lvert{}^2\Pi_- -\frac{1}{2}\rangle$	$\lvert{}^2\Pi_- \frac{1}{2}\rangle$	$\lvert{}^2\Pi_+ -\frac{1}{2}\rangle$	$\lvert{}^2\Pi_+ \frac{1}{2}\rangle$
$\langle {}^2\Sigma^+_{1/2} -\frac{1}{2}\rvert$	$\frac{1}{\sqrt{2}}\beta\mathcal{M}$	0	$\frac{1}{\sqrt{2}}\alpha\mathcal{M}$	0
$\langle {}^2\Sigma^+_{1/2} \frac{1}{2}\rvert$	0	$\frac{1}{\sqrt{2}}\alpha\mathcal{M}$	0	$\frac{1}{\sqrt{2}}\beta\mathcal{M}$

[a] $\mathcal{M}$ is defined in eq (4.4.19).

4.4.6. MCD and absorption

In this work, OH was initially assumed to be orientationally averaged, and the averaging procedure outlined in Section 3.4.3.2 was employed. However, much of the data for OH/Ar were obtained *outside* the linear limit,[20] so the starting point for the MCD theory is eq (3.4.25), which considers the most general case in the molecular reference frame.

The gas-phase SO splitting in $X\,{}^2\Pi$ of OH is ~139 cm^{-1},[15] which will be slightly quenched in a matrix by the external heavy atom effects of the host atoms.[22,23] However, the net SO-CF splitting of OH/Ar will certainly be close to this value or greater (eq (4.4.4)). Hence at temperatures lower than 7 K, the population of the upper ($^2\Pi_+$) level will be entirely negligible; *i.e.* $P_{\pm1/2}{}'(^2\Pi_+) = 0$.

The zeroth moment of the MCD ($\mathbf{M}_0$; Section 3.5.1) comprises contributions from *B* and *C* terms, and was treated as follows. First, *C* terms were determined explicitly, by diagonalisation of the molecular Hamiltonian matrix, including Zeeman elements. Then in Section 4.4.6.2 first-order perturbation theory was used to deal with the field-induced mixing of states that gives rise to *B* terms.

4.4.6.1. Absorption and MCD C terms

At first pure *C* terms were assumed for OH/Ar, and the radicals were taken to be preferentially oriented with their *z* axis at an angle θ to the field axis *Z* (Section 3.4.3.2; Figure 3.4.1). Since only *C* terms are treated initially (Section 4.4.6.2 deals with *B* terms), the field-dependent transition moments $\langle J\lambda|m_{\pm1}|A\alpha\rangle'$ of eq (3.4.25) are approximated by field-independent $\langle J\lambda|m_{\pm1}|A\alpha\rangle$, as given in Table 4.4.4. Likewise, the bandshape function $f'_{\alpha\lambda}(E)$ is replaced by $f_{\alpha\lambda}(E)$ within the rigid-shift approximation.[20] Using eq (3.4.24), the absorption is ($P_\alpha = ½$ for $^2\Pi_-$),

$$\frac{\overline{A}(E,\theta)}{E} = \frac{1+\cos^2\theta}{8}\gamma c l \sum_{M_\Omega M_S} (|\langle {}^2\Sigma^+_{1/2}\, M_\Omega|m_{+1}|{}^2\Pi_-\, M_S\rangle|^2 + |\langle {}^2\Sigma^+_{1/2}\, M_\Omega|m_{-1}|{}^2\Pi_-\, M_S\rangle|^2) f_{M_\Omega M_S}(E) \qquad (4.4.20)$$

while applying eq (3.4.25) gives the MCD,

$$\frac{\overline{\Delta A}'(E,\theta)}{E} = \gamma c l \cos\theta \sum_{M_\Omega M_S} P_{M_S}{}' (|\langle {}^2\Sigma^+_{1/2}\, M_\Omega|m_{+1}|{}^2\Pi_-\, M_S\rangle|^2 - |\langle {}^2\Sigma^+_{1/2}\, M_\Omega|m_{-1}|{}^2\Pi_-\, M_S\rangle|^2) f_{M_\Omega M_S}(E) \qquad (4.4.21)$$

The population factors $P_{M_S}{}'$ in eq (4.4.21) are not easily dealt with, due to the dependence of the state energies on $g_\parallel$ and $g_\perp$, whose contributions change with θ (Section 3.4.3.2). That is, the anisotropy of the *g* values in the $X\ ^2\Pi$ term (due to non-zero orbital angular momentum) necessitate the following treatment.

Using the angular momentum matrix elements given in Table 4.4.3, and the following relationship derived according to Section 3.4.3.2 for transformation to the laboratory reference frame,

$$\mu_Z = \cos\theta\,\mu_0 + \frac{i}{\sqrt{2}}\sin\theta\,[\exp(-i\psi)\mu_{-1} + \exp(i\psi)\mu_{+1}] \qquad (4.4.22)$$

non-zero matrix elements of μ_Z in the $^2\Pi_-$ level are,

$$\langle {}^2\Pi_- \pm\tfrac{1}{2}|\text{-}\mu_Z B|{}^2\Pi_- \pm\tfrac{1}{2}\rangle = \pm\tfrac{1}{2}\cos\theta\, g_{\|}\mu_B B \tag{4.4.23}$$

$$\langle {}^2\Pi_- \pm\tfrac{1}{2}|\text{-}\mu_Z B|{}^2\Pi_- \mp\tfrac{1}{2}\rangle = \mp\tfrac{i}{2}\sin\theta\exp(\pm i\psi)\, g_{\perp}\mu_B B \tag{4.4.24}$$

ψ is the Euler angle defined in Figure 3.4.1. The Zeeman splitting as a function of θ is obtained by solving a secular equation for the Zeeman interaction. The energies are,

$$E_B(\pm) = \pm\tfrac{1}{2} g_\theta^- \mu_B B \tag{4.4.25}$$

Here $E_B(\pm)$ gives the energies of the raised and lowered magnetic-field-mixed SO-CF basis functions, and g_θ^- is,

$$g_\theta^- = \sqrt{(g_{\|}^- \cos\theta)^2 + (g_\perp \sin\theta)^2} \tag{4.4.26}$$

The eigenfunctions in the Zeeman effect for the $^2\Pi_-$ term are then,

$$|{}^2\Pi_- \pm\rangle = a|{}^2\Pi_- \pm\tfrac{1}{2}\rangle \pm b|{}^2\Pi_- \mp\tfrac{1}{2}\rangle \tag{4.4.27}$$

where the '+' and '–' subscripts respectively represent the raised and lowered states corresponding to eq (4.4.25). The mixing coefficients a and b satisfy,

$$|a|^2 = \frac{(g_\perp \sin\theta)^2}{2g_\theta^-(g_\theta^- - g_{\|}^- \cos\theta)} \tag{4.4.28}$$

$$|a|^2 + |b|^2 = 1 \tag{4.4.29}$$

$$|a|^2 - |b|^2 = \frac{g_{\|}^- \cos\theta}{g_\theta^-} \tag{4.4.30}$$

Using eq (4.4.25), the Boltzmann populations are given by,

$$P_\pm = \frac{1}{Q}\exp\left(\mp\frac{g_\theta^- \mu_B B}{2kT}\right) \tag{4.4.31}$$

where P_+ and P_- are the populations of the '+' and '–' levels and Q is the partition function,

$$Q = \exp\left(\frac{g_\theta^- \mu_B B}{2kT}\right) + \exp\left(-\frac{g_\theta^- \mu_B B}{2kT}\right) = 2\cosh\left(\frac{g_\theta^- \mu_B B}{2kT}\right) \tag{4.4.32}$$

so,

$$P_+ - P_- = \tanh\left(\frac{g_\theta^- \mu_B B}{2kT}\right) \tag{4.4.33}$$

Now returning to eqs (4.4.20) and (4.4.21), the absorption and MCD moments (Section 3.5.1.2) are defined as $\mathbf{A}_0^\theta$ and $\mathbf{C}_0^\theta$, respectively (where the latter accounts for only the *C*-term contribution to $\mathbf{M}_0$). For transitions originating from the Zeeman eigenstates (±) of eq (4.4.27), these moments are given by eqs (4.4.34) and (4.4.35). (The principle of spectroscopic stability[20] has been utilised in the choice of excited-state basis functions.) The superscript θ indicates that the moment is specified for a particular orientation of the molecule with respect to the field axis (*Z*).

$$\mathbf{A}_0^\theta(\pm) = \frac{1+\cos^2\theta}{8}\gamma c l \sum_{M_\Omega} \left(|\langle {}^2\Sigma^+_{1/2}\, M_\Omega | m_{+1} | {}^2\Pi_- \pm\rangle|^2 + |\langle {}^2\Sigma^+_{1/2}\, M_\Omega | m_{-1} | {}^2\Pi_- \pm\rangle|^2\right) \tag{4.4.34}$$

$$\mathbf{C}_0^\theta(\pm) = \gamma c l \cos\theta \sum_{M_\Omega} P_\pm \left(|\langle {}^2\Sigma^+_{1/2}\, M_\Omega | m_{+1} | {}^2\Pi_- \pm\rangle|^2 - |\langle {}^2\Sigma^+_{1/2}\, M_\Omega | m_{-1} | {}^2\Pi_- \pm\rangle|^2\right) \tag{4.4.35}$$

The transition moments from the Zeeman eigenstates of $^2\Pi_-$ to the $^2\Sigma^+$ manifold are readily calculated from Table 4.4.4 and eq (4.4.27). Using these transition moments with eqs (4.4.34) and (4.4.35), and eqs (4.4.14), (4.4.15) and (4.4.29) – (4.4.33), the absorption and MCD zeroth moments are,

$$\mathbf{A}_0^\theta = \frac{\gamma c l\,(1+\cos^2\theta)\,|\mathcal{M}|^2}{8} \tag{4.4.36}$$

$$\mathbf{C}_0^\theta = \frac{\gamma c l\,\kappa g_\parallel^- \cos^2\theta\,|\mathcal{M}|^2}{2g_\theta^-} \tanh\left(\frac{g_\theta^- \mu_B B}{2kT}\right) \tag{4.4.37}$$

where $\mathcal{M}$ was defined in eq (4.4.19).

Some immediate qualitative conclusions can be drawn from eq (4.4.37). Firstly, the existence of a *C*-term contribution to the MCD requires $\kappa \neq 0$; that is, the quenching of the orbital angular momentum of OH is incomplete in an Ar host. Secondly, since all of the parameters are either squared or intrinsically positive, the *C*-term component of the MCD is positive, as observed experimentally. This result is represented diagrammatically in Figure 4.4.2, where the relative intensities of the transition originating from the $|^2\Pi_- -\rangle$ state are indicated by the thickness of the lines; the total lcp

intensity is greater, so the MCD is positive at low temperatures. Thirdly, the existence of the tanh factor (essentially the population difference $P_- - P_+$) accounts for the saturation behaviour exhibited in Figures 4.3.2 and 4.3.4.

Eqs (4.4.36) and (4.4.37) allow the ratio $\mathbf{C}_0/\mathbf{A}_0$ to be determined for any angle θ. A particularly simple result is obtained for the case where $\theta = 0$, whence

$$\mathbf{C}_0^0/\mathbf{A}_0^0 = 2\kappa \tanh\left(\frac{\bar{g}_\parallel \mu_B B}{2kT}\right) \tag{4.4.38}$$

However, it is far more likely that the OH molecules are randomly oriented, in which case $\mathbf{A}_0$ and $\mathbf{C}_0$ are obtained by averaging over θ (Section 3.4.3.2), with the result,

$$\bar{\mathbf{C}}_0/\bar{\mathbf{A}}_0 = 3\kappa \int_0^1 \frac{\bar{g}_\parallel \cos^2\theta}{\bar{g}_\theta} \tanh\left(\frac{\bar{g}_\theta \mu_B B}{2kT}\right) d\cos\theta \tag{4.4.39}$$

which cannot be solved analytically. Numerical integration is used to extract various parameters including κ from the saturation curve (Figure 4.3.4), as described in Section 4.5.1.

Invoking the linear limit[20] (Section 3.4.3), where $\mu_B B << 2kT$, allows the approximation,

$$\tanh\left(\frac{\bar{g}_\theta \mu_B B}{2kT}\right) \approx \frac{\bar{g}_\theta \mu_B B}{2kT} \tag{4.4.40}$$

which gives for the *Z*-oriented case,

$$\mathbf{C}_0^0/\mathbf{A}_0^0 \approx \frac{\kappa \bar{g}_\parallel \mu_B B}{kT} = \frac{2\kappa(\kappa+1)\mu_B B}{kT} \tag{4.4.41}$$

and for the orientationally averaged case,

$$\bar{\mathbf{C}}_0/\bar{\mathbf{A}}_0 \approx \frac{\kappa \bar{g}_\parallel \mu_B B}{2kT} = \frac{\kappa(\kappa+1)\mu_B B}{kT} \tag{4.4.42}$$

Note that the $\bar{\mathbf{C}}_0/\bar{\mathbf{A}}_0$ ratio in the linear limit is half that of $\mathbf{C}_0^0/\mathbf{A}_0^0$. Also, comparing eqs (4.4.39) and (4.4.42), it is clear that $g_\perp$ (through its contribution to $\bar{g}_\theta$; eq (4.4.26)) is only important outside the linear limit.[24]

4.4.6.2. MCD B *terms*

B-term contributions to the MCD[24] are now considered by allowing field-induced mixing of $|^2\Pi_-\rangle$ and $|^2\Pi_+\rangle$. The Zeeman eigenfunctions $|^2\Pi_- \pm\rangle$ (eq (4.4.27)) become,

$$|^2\Pi_- \pm\rangle = |^2\Pi_- \pm\rangle^0 + |^2\Pi_- \pm\rangle' \tag{4.4.43}$$

where the ^{0} and $'$ respectively denote the states in the absence of the perturbation, and the correction for the perturbation. The *B* term arises from the second of these, which can be expressed as,

$$|^2\Pi_- \pm\rangle' = -\frac{\mu_B B}{\Delta} \sum_{M_S=\pm 1/2} |^2\Pi_+ M_S\rangle^0 \langle ^2\Pi_+ M_S|L_Z + 2S_Z|^2\Pi_- \pm\rangle^0 \tag{4.4.44}$$

where from here on the ^{0} superscript on the unperturbed wavefunctions is dropped, and spectroscopic stability has been invoked for the $^2\Pi_+$ states. Since the Zeeman matrix element is expressed in terms of laboratory-fixed coordinates, eq (4.4.44) must be transformed to the molecular reference frame, in terms of the operators L_z, S_z and L_x, S_x. Following the usual procedure (Section 3.4.3.2) the corrections are,

$$|^2\Pi_- \pm\rangle' = -\frac{\mu_B B}{2\Delta} \left[(\tfrac{1}{2}\cos\theta\, a g_\perp - \sin\theta\, b\kappa)|^2\Pi_+ \pm\tfrac{1}{2}\rangle \pm \right.$$

$$\left. (\tfrac{1}{2}\cos\theta\, b g_\perp + \sin\theta\, a\kappa)|^2\Pi_+ \mp\tfrac{1}{2}\rangle \right] \tag{4.4.45}$$

Transition moments from these corrected functions are computed in the usual manner (Section 3.4.2), where the principle of spectroscopic stability in the choice of the excited-state basis (Section 4.4.1.2) is utilised.[20] These corrections to the transition moments are then combined with the unperturbed ones, as follows, to give the total transition moments.

$$|\langle J|m_{\pm 1}(|A\rangle + |A\rangle')|^2 = |\langle J|m_{\pm 1}|A\rangle|^2 + (\langle J|m_{\pm 1}|A\rangle \langle J|m_{\pm 1}|A\rangle'^*) + (\langle J|m_{\pm 1}|A\rangle^* \langle J|m_{\pm 1}|A\rangle')$$

$$= |\langle J|m_{\pm 1}|A\rangle|^2 + 2\mathcal{R}_e(\langle J|m_{\pm 1}|A\rangle \langle J|m_{\pm 1}|A\rangle'^*)$$

$$\equiv |\langle J|m_{\pm 1}|A\rangle|^2 + [J|m_{\pm 1}|A]^2 \tag{4.4.46}$$

Here the terms of second-order in the perturbation have been omitted, and the fact that $X + X^* = 2\mathcal{R}_e(X)$ has been used. In this analysis, $\langle J| = \langle ^2\Sigma^+ \pm\tfrac{1}{2}|$ and $|A\rangle = |^2\Pi_- \pm\rangle$.

Evaluation of the $[J|m|A]^2$ (defined by the last two lines of eq (4.4.46)) enables

calculation of the *B*-term contribution to the MCD for an orientation θ. This involves differences such as $\cos\theta\,([J|m_{+1}|A]^2 - [J|m_{-1}|A]^2)$. The *B*-term contribution to the zeroth MCD moment, $\mathbf{B}_0^{\theta}$, is then obtained by summing over all non-zero transitions, weighted by their ground-state population factor, and multiplying by γcl. The result is,

$$\mathbf{B}_0^{\theta} = \frac{\gamma cl\,(g_{\perp}\cos\theta)^2\,\mu_B B\,|m|^2}{4\Delta} \tag{4.4.47}$$

Eq (4.4.47) shows that the *B*-term contribution to $\mathbf{M}_0$ does not saturate, but (while $\mu_B B \ll \Delta$) increases linearly with field strength. When combined with eq (4.4.36), the results for the *Z*-oriented ($\theta = 0$) and randomly oriented cases are, respectively,

$$\mathbf{B}_0^0/\mathbf{A}_0^0 = \frac{g_{\perp}^2\mu_B B}{\Delta} \tag{4.4.48}$$

$$\bar{\mathbf{B}}_0/\bar{\mathbf{A}}_0 = \frac{g_{\perp}^2\mu_B B}{2\Delta} \tag{4.4.49}$$

No other *B*-term contributions are considered, because higher excited states are too distant to allow significant mixing. (The second excited term, $B\,^2\Sigma^+$, lies at 69774 cm^{-1} in OH and 69775 cm^{-1} in OD.[6])

4.5. Data analysis and discussion

This section falls into two parts. First, the orbital reduction factor (κ) for the ground term $X\,^2\Pi$ of OH/Ar is deduced from moment analysis of the entire $A\,^2\Sigma^+ \leftarrow X\,^2\Pi$ band system. Second, possible origins of the transition's fine structure are discussed.

4.5.1. Orbital reduction in $X\,^2\Pi$

The expressions for the moment ratios given by eqs (4.4.39) and (4.4.49) are functions of only three independent parameters, one of which is the angle θ. The second is the SO coupling constant, for which the value $\zeta_{\pi} = 125 \pm 10$ cm^{-1} is chosen, slightly less than the gas-phase value.[22,23] The third is chosen to be κ, the orbital reduction factor.

Initially, random orientation is assumed, and κ is varied to obtain the best fit to

the data of Figure 4.3.4 using eqs (4.4.39) and (4.4.49), and the fact that $\mathbf{M}_0 = \mathbf{B}_0 + \mathbf{C}_0$ (Section 4.4.6). Standard steepest-descent methods are employed, evaluating the required integrals by Simpson's rule. By choosing κ as the unconstrained parameter, the effects of the uncertainty in ζ_π can be largely restricted to $\mathbf{B}_0$, which is significantly the smaller contribution to $\mathbf{M}_0$. Hence the value of κ is quite insensitive to changes of ζ_π within the estimated range of uncertainty. The best-fit value is $\kappa = 0.79 \pm 0.02$; the V and g values derived from this result are summarized at the bottom of Table 4.5.1.

Table 4.5.1: Parameters for the $A\,^2\Sigma^+ \leftarrow X\,^2\Pi$ bands of OH/Ar.

Band[a]	E / cm^{-1} [b]	$\mathbf{A}_0(i)/\mathbf{A}_0$ [c]	κ	V / cm^{-1}	$g_{\parallel}$	$g_{\perp}$
1	32 025	0.08	1.00	0	4.0	0.0
2	32 095	0.29	0.91	56	3.8	0.8
3	32 165	0.35	0.77	103	3.5	1.3
4	32 230	0.19	0.54	194	3.1	1.7
5	32 285	0.09	0.55	189	3.1	1.7
overall[d]	32 170	1.00	0.79 ± 0.02	97 ± 10	3.58 ± 0.04	1.23 ± 0.05

[a] Numbering for cross-reference with Figures 4.3.1 and 4.5.2, and Table 4.3.1.
[b] Band barycenters ± 10 cm^{-1}.
[c] Zeroth absorption moments, expressed as a fraction of the total $\mathbf{A}_0$, obtained by least-squares fitting of the OH/Ar absorption spectrum in Figure 4.3.1 using Gaussian bands (see Figure 4.5.3).
[d] Obtained from a least-squares fit to the data in Figure 4.3.4, assuming random molecular orientation and $\zeta_\pi = 125 \pm 10$ cm^{-1}.

The best fit, illustrated by the dashed curve in Figure 4.3.4, provides an accurate representation of the experimental magnetisation behaviour. However, it assumes a single effective site for the guest molecules, whereas the structure of the spectra provides evidence that the individual bands represent different sites. This is discussed in the next section.

Evidence has been produced elsewhere to show that larger diatomic molecules (*e.g.* metal oxides[25-28] and fluorides[29,30]) can assume preferential orientations in rare-gas matrices, with their internuclear axes either parallel or perpendicular to the plane of the deposition window. For OH/Ar, the former case would eliminate the possibility of observing C terms (eq (4.4.37)), and so can be rejected. For the latter, eqs (4.4.38) and (4.4.48) are applicable. Fitting the data of Figure 4.3.4 using these expressions yields a substantially smaller orbital reduction factor ($\kappa = 0.48$), but also gives a significantly

poorer fit, doubling the sum of the squared residuals. Although the possibility of preferential orientation (with $\theta = 0$) can not be definitively excluded, it is believed to be unlikely.

4.5.2. Structure

In this section possible origins of the fine structure observed in the MCD and absorption spectra of OH/Ar and OD/Ar are discussed.

4.5.2.1. Rotation and hindered rotation OH/Ar and OD/Ar?

Here an attempt to assign fine structure to free rotation is described.

The $X\,^2\Pi$ ground state of OH and OD is Hund's case (a), since the SOC in each isotopomer is moderately strong.[15] This means that there is no $J = \frac{1}{2}$ total angular momentum quantum number for the ground $\Omega = \frac{3}{2}$ level. On the other hand, $A\,^2\Sigma^+$ has no orbital angular momentum and is therefore a Hund's case (b) state. The transition is thus commonly designated $A\,^2\Sigma^+ \leftarrow X\,^2\Pi(a)$. The rotational structure of OH will be considered first, followed by OD.

The OH ground-state gas-phase rotational constant $B(v = 0) \equiv B_0$ has a value of 18.550 cm^{-1}.[31] The rotational levels in Hund's case (a) are given by eq (4.5.1), where it is noted that allowed levels have $J \geq \Omega$.[15]

$$F_0(J) = B_0 [J(J+1) - \Omega^2] \qquad (4.5.1)$$

Centrifugal distortion $D_0[J^2(J+1)^2]$ and higher-order effects are neglected in this treatment, since the small energy changes resulting from their inclusion are not resolvable in our experiments. Λ-doubling is also omitted. The left-hand side of Figure 4.5.1 shows the gas-phase rotational levels for OH.

Likewise, for the $A\,^2\Sigma^+$ excited state, the rotational levels are obtained using the following equations,[15]

$$F_1(N) = B_0 N(N+1) + \tfrac{1}{2}\gamma_0 N \qquad (4.5.2)$$

$$F_2(N) = B_0 N(N+1) - \tfrac{1}{2}\gamma_0 (N+1) \qquad (4.5.3)$$

where $F_1(N)$ and $F_2(N)$ are the energies for each N (the total angular momentum quantum number apart from spin) corresponding to $J = N + \frac{1}{2}$ and $J = N - \frac{1}{2}$, respectively. B_0 = 17.36 cm^{-1} for $A\,^2\Sigma^+$, and γ_0 is an effective spin-rotation coupling

constant, with a value of 0.201 cm^{-1}.[6] Again centrifugal distortion and higher-order terms are ignored. The rotational levels are shown in Figure 4.5.1, where the small spin splitting is neglected.

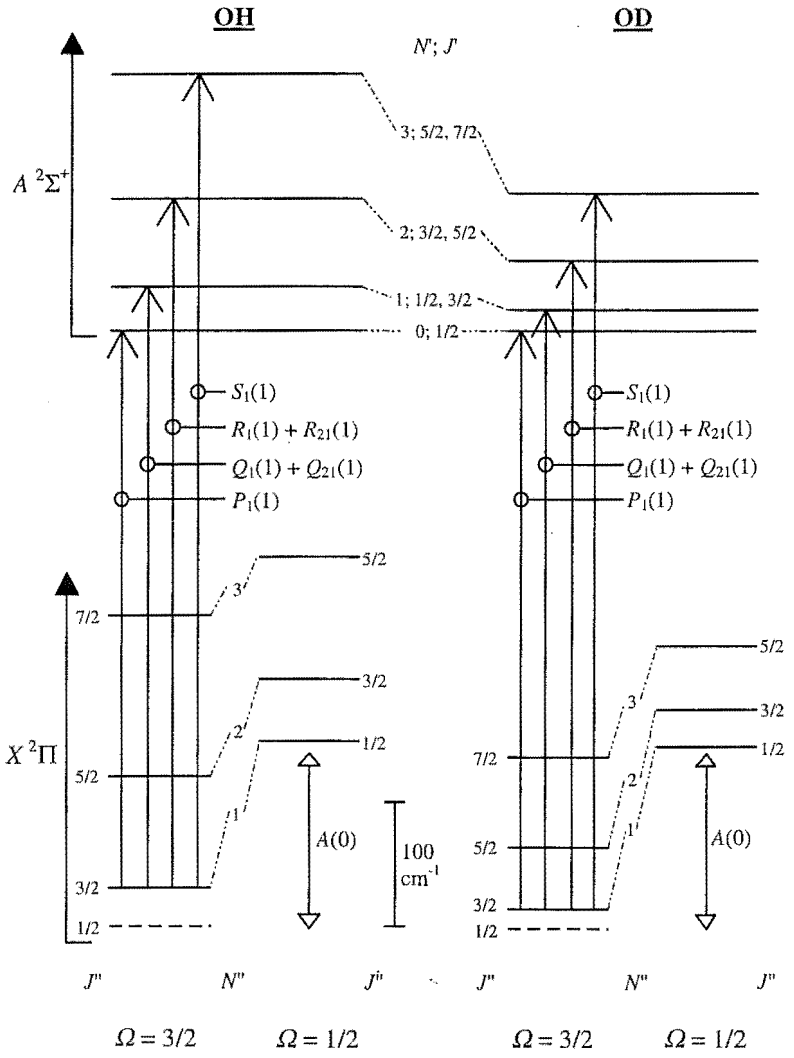

Figure 4.5.1: Rotational energy-level diagrams (approximately to scale within the $X\,^2\Pi$ and $A\,^2\Sigma^+$ terms) for the (0,0) band of gas-phase OH and OD radicals. The dashed lines representing the $J'' = 1/2$ total angular momentum level of $\Omega = 3/2$ are not allowed (see text). At liquid helium temperature, only the lowest level of $\Omega = 3/2$ will be occupied, from which the allowed transitions are indicated. The SOC parameter $A(0)$ is indicated, the magnitude of which is very similar for the two isotopomers.

At 20 K, the thermal populations of the $X\,^2\Pi$ rotational levels are such that only transitions from the lowest rotational level ($J'' = 3/2$) will be observed. Hence there are relatively few possible transitions shown in Figure 4.5.1.[15,17] (Note that the quantum number N'' shown in the $X\,^2\Pi$ term is only used for the purpose or correlation between

$X\ ^2\Pi$(a) and $A\ ^2\Sigma^+$(b), since different quantum numbers apply.[15] It enables the *P*, *Q*, *R* and *S* branches ($\Delta N = -1$, 0, +1 and +2, respectively) to be labelled appropriately.) The approximate energies of these transitions, and their separations, are given in Table 4.5.2.

Table 4.5.2: Approximate relative energies and separations for gas-phase OH and OD ($^2\Sigma^+$, $N' = 0, 1, 2, 3 \leftarrow {}^2\Pi(a)$, $N'' = 1$, $J'' = 3/2$).

Transition(s)†	N' for $A\ ^2\Sigma^+$	OH		OD	
		Energy – $P_1(1)$ (cm^{-1})	Separations (cm^{-1})	Energy – $P_1(1)$ (cm^{-1})	Separations (cm^{-1})
$P_1(1)$	0	0		0	
			35		18
$Q_1(1)$, $Q_{21}(1)$	1	35		18	
			69		36
$R_1(1)$, $R_{21}(1)$	2	104		54	
			104		54
$S_1(1)$	3	208		108	

† Spin splitting has been ignored; hence there can be two transitions to the same *N* level.

For OD the rotational constant, B_0, is reduced from OH because deuteration increases the molecule's moment of inertia. In the ground and first excited terms, B_0 = 9.8831 cm^{-1} and 9.0342 cm^{-1}, respectively.[32] Following the methodology described for OH, the rotational levels of OD can be calculated according to the same approximations (*e.g.*, for $^2\Sigma^+$, γ_0 = 0.1201 cm^{-1}). The low levels are shown on the right-hand side of Figure 4.5.1, as are the allowed transitions at cryogenic temperatures. Approximate transition energies, and splittings, are given in Table 4.5.2.

Table 4.5.2 reveals that the gas-phase rotational separations for OD are just over half those of OH. Hence OH and OD cannot be undergoing free rotation in an Ar matrix because of the similar band separations observed in the solid (Figures 4.3.1 and 4.3.3). In addition, the separations for gas-phase OH do *not* correspond to those obtained from Table 4.3.1 for OH/Ar.

4.5.2.2. Site structure

Site structure is a very probable cause of the fine structure observed for several reasons. First, such an interpretation is consistent with the relative invariance of the band spacings to isotopic substitution (Figures 4.3.1 and 4.3.3) and host lattice.[12,13,16] Second, in preliminary investigations the relative intensities of the bands showed slight variations with annealing and from one deposition to another. Third, these intensities

exhibit different magnetic-field and temperature dependencies (Figures 4.3.1 and 4.3.2), suggesting different κ values.

The last of these points is emphasised in Figure 4.5.2, the data for which were obtained by simultaneously fitting the MCD and absorption spectra of Figure 4.3.1 with five Gaussian bands, as illustrated at upper left for the MCD. (An example of such a fit is given in Figure 4.5.3 for both absorption and MCD.) The data illustrated in Figure 4.5.2 pertain to temperature dependence within the linear limit, hence eqs (4.4.42) and (4.4.49) are applicable and *rough* κ values can be estimated from the slopes. As in Section 4.5.1, random orientation is assumed, and $\zeta_\pi = 125 \pm 10$ cm^{-1}. These are summarised, along with other parameters derived from them, are given in Table 4.5.1. It is emphasised that these values must be treated with caution because of the inherent uncertainties in the fitting procedure in the case of strongly overlapping bands. However, it seems clear that κ does vary across the envelope of the transition, from higher values at the red end to lower values at the blue. In addition, the fit shown in Figure 4.3.4 can be quite closely reproduced using these parameters.

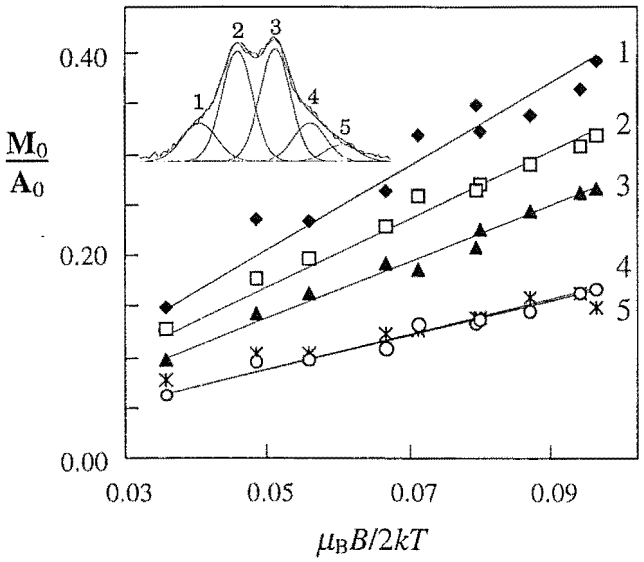

Figure 4.5.2: Temperature dependence (at B = 0.5 T or 1 T) of the ratios $\mathbf{M}_0/\mathbf{A}_0$ for the individual bands (1 to 5) of Figure 4.3.1. The inset illustrates the deconvolution of the 1.73-K MCD spectrum into five Gaussian components (see also Figure 4.5.3). The straight lines are best fits to the temperature dependence data using eqs (4.4.42) and (4.4.49). Approximate parameters derived from these fits, assuming random orientation of OH and $\zeta_\pi = 125$ cm^{-1}, are summarised in Table 4.5.1.

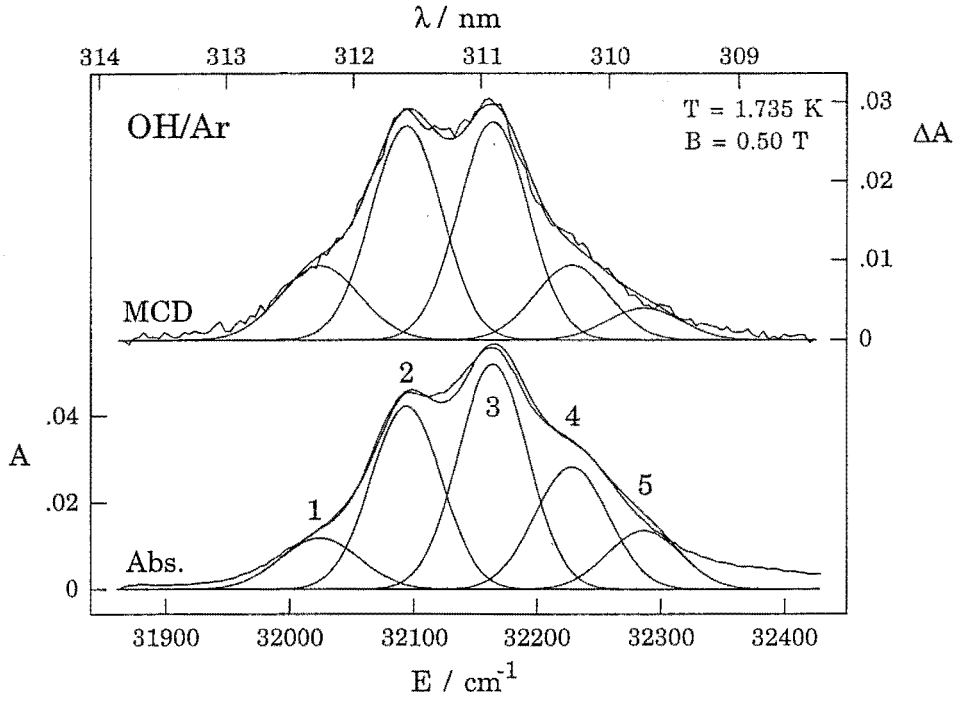

Figure 4.5.3: Experimental (dotted) and fitted (full) MCD and absorption spectra of OH/Ar at 1.735 K and B = 0.5 T.

4.6. Conclusion

The MCD and absorption spectra of OH/Ar confirm a partial quenching of the orbital angular momentum of the lowest electronic level of the guest. A model in which the reduction of angular momentum is due to a low-symmetry crystal field adequately accounts for the observed temperature and magnetic-field dependencies of the MCD. Assuming the radicals to be randomly oriented, the effective average orbital reduction factor is $\kappa = 0.79 \pm 0.02$, corresponding to a crystal field of $V = 97 \pm 10$ cm^{-1}. However, closer considerations of the structure observed in the spectra suggests that the guest radicals occupy at least five discrete sites, with orbital reduction factors varying from $\kappa \approx 1$ to 0.5 across the envelope of the transition. Site structure is also consistent with the similar structure observed for OD/Ar in this work, and by other workers for OH and OD in Kr and Xe matrices.[13,16]

Comparison of the g values for OH/Ar presented in Table 4.5.1 with those obtained by EPR for OH in ice[7-10] (Section 4.1.2) reveals significant differences between these media. Quenching of the orbital angular momentum in the $X\,^2\Pi$ term is

almost complete in ice, but only partial in Ar. The most likely explanation for this difference is that strong hydrogen bonding between OH and the host molecules of the ice lattice results in a CF splitting of the π orbitals[8-10] that is much larger than is the case in the weakly interacting Ar environment. This final point suggests a tentative explanation for the variation of CF splitting observed for OH/Ar sites (Table 4.5.1). The red-most site (site 1) corresponds to a highly symmetric Ar cage with no CF splitting. Moving to the blue, the CF splitting increases, possibly due to interactions with neighbouring undissociated H_2O precursor molecules, which inevitably must be trapped in the matrix.

4.7. References

1. Watson, W. W. *Astrophys. J.* **1924**, *60*, 145-158.
2. Mulliken, R. S. *Phys. Rev.* **1928**, *32*, 388-416.
3. Johnston, H. L.; Dawson, D. H.; Walker, M. K. *Phys. Rev.* **1933**, *43*, 473-480.
4. Johnston, H. L.; Dawson, D. H. *Phys. Rev.* **1933**, *43*, 580.
5. Dawson, D. H.; Johnston, H. L. *Phys. Rev.* **1933**, *43*, 980-991.
6. Huber, K. P.; Herzberg, G. *Molecular Spectra and Molecular Structure, Volume 4: Constants of Diatomic Molecules*; Van Nostrand Reinhold: New York, 1979.
7. Piette, L. H.; Rempel, R. C.; Weaver, H. E.; Fluornoy, J. M. *J. Chem. Phys.* **1959**, *30*, 1623-1624.
8. Siegel, S.; Baum, L.; Skolnik, S.; Fluornoy, J. M. *J. Chem. Phys.* **1960**, *32*, 1623-1624.
9. Brivati, J. A.; Symons, M. C. R.; Tinling, D. J. A.; Wardale, H. A.; Williams, D. O. *Chem. Commun.* **1965**, 402-403.
10. Symons, M. C. R. *J. Chem. Soc. London* **1963**, *32*, 570-576.
11. Robinson, G. W.; McCarty, M. J. *J. Chem. Phys.* **1958**, *28*, 350.
12. Robinson, G. W.; McCarty, M. J. *Can. J. Phys.* **1958**, *36*, 1590-1591.
13. McCarty, M. J. Ph.D. Dissertation, The John Hopkins University, Baltimore, 1960.
14. Johnston, H. L. *Phys. Rev.* **1934**, *45*, 79-81.
15. Herzberg, G. *Molecular Spectra and Molecular Structure Volume 1: Spectra of Diatomic Molecules*, 2nd ed.; Krieger: New York, 1950.

16. Wei, S. *Unpublished data* **1968.**

17. Tinti, D. S. *J. Chem. Phys.* **1968**, *48*, 1459-1464.

18. Brus, L. E.; Bondybey, V. E. *J. Chem. Phys.* **1975**, *63*, 786-793.

19. Rose, J. L. Ph.D. Dissertation, University of Virginia, Charlottesville, 1987.

20. Piepho, S. B.; Schatz, P. N. *Group Theory in Spectroscopy with Applications to Magnetic Circular Dichroism*; Wiley-Interscience: New York, 1983.

21. Butler, P. H. *Point Group Symmetry Applications*; Plenum Press: New York, 1981.

22. Samet, C.; Rose, J. L.; Schatz, P. N.; O'Brien, M. C. M. *Chem. Phys. Lett.* **1989**, *159*, 567-572.

23. Lund, P. A.; Smith, D.; Jacobs, S. M.; Schatz, P. N. *J. Phys. Chem.* **1984**, *88*, 31-42.

24. Schatz, P. N.; Mowery, R. L.; Krausz, E. R. *Mol. Phys.* **1978**, *35*, 1537-1557.

25. Kasai, P. H. *J. Chem. Phys.* **1968**, *49*, 4979-4984.

26. Knight, L. B. J.; Easley, W. C.; Weltner, W. J. *J. Chem. Phys.* **1971**, *54*, 1610-1617.

27. Knight, L. B. J.; Wise, M. B.; Davidson, E. R.; McMurchie, L. E. *J. Chem. Phys.* **1982**, *76*, 126-136.

28. Williamson, B. E.; Roser, D. C.; Vala, M. *J. Phys. Chem.* **1994**, *98*, 3624-3630.

29. Knight, L. B. J.; Easley, W. C.; Weltner, W. J.; Wilson, M. *J. Chem. Phys.* **1971**, *54*, 322-329.

30. Knight, L. B. J.; Mouchet, A.; Beaudry, W. T.; Duncan, M. *J. Mag. Reson.* **1978**, *32*, 383-390.

31. Mizushima, M. *Physical Review A* **1972**, *5*, 143-157.

32. Coxon, J. A. *J. Mol. Spectrosc.* **1975**, *58*, 1-28.

5. NH/Ar

5.1. Introduction

The imidogen free radical (NH) is an important flame species, and occurs in a variety of extra-terrestrial environments, such as comets and in the interstellar medium (Section 1.1.1). There has been much work done on NH in the gas phase, but to a lesser extent in rare-gas matrices. A brief history of these previous investigations follows as part of this introduction. The main body of the chapter presents the candidate's research on the electronic absorption and MCD of the $A\,^3\Pi \leftarrow X\,^3\Sigma^-$ transition of NH (and ND) trapped in a solid Ar matrix. It gives temperature- and magnetic-field-dependence data that are explained in terms of a spin-orbit (SO) – crystal-field (CF) model in which the orbital angular momentum of the excited state is partially quenched by CF interactions with the matrix. The analysis also enables determination of the ground-state zero-field splitting (ZFS).

5.1.1. Gas-phase investigations of NH and ND

The $A\,^3\Pi - X\,^3\Sigma^-$ transition of NH was first observed by Eder late last century.[1] In the mid 1930s, Funke observed the (0,0) and (1,1) bands in emission[2] and absorption,[3] and made rotational assignments. (The (0,0) band of $^3\Pi \leftarrow {}^3\Sigma^-$ occurs at around 29 800 cm^{-1}.)

In 1959, Dixon published the high-resolution gas-phase absorption spectrum of the (0,0) and (1,0) systems of NH ($A\,^3\Pi \leftarrow X\,^3\Sigma^-$),[4] assigning bands in the (0,0) system that Funke had not observed, and correcting some previous assignments. The ZFS (D) in the $X\,^3\Sigma^-$ term and the excited-state SO coupling constant (ζ_π) were found to be 1.856 cm^{-1} and 35.02 cm^{-1}, respectively. Bollmark *et al.* performed an analysis of the (0,0) band of ND in 1970, obtaining D = 0.91 cm^{-1}, and ζ_π = 34.56 cm^{-1}.[5] Later work by Veseth[6] gives D = 1.67 cm^{-1} and ζ_π = 34.79 cm^{-1} for NH, and D = 1.79 cm^{-1} and ζ_π = 34.58 cm^{-1} for ND.

Huber and Herzberg summarise the gas-phase results for NH and ND in their book.[7]

5.1.2. Investigations of the $^3\Pi \leftarrow {}^3\Sigma^-$ system of NH/Ar and ND/Ar

A year before Dixon published his definitive work on the gas-phase $A\,^3\Pi \leftarrow X\,^3\Sigma^-$ transition,[4] the first evidence for NH isolated in an Ar matrix (NH/Ar) was published in a letter to the *Journal of Chemical Physics* by McCarty and Robinson.[8] NH was produced when a 1:25 mixture of hydrazine and Ar was subjected to an electrodeless discharge. The following year the same workers published a comprehensive article on NH and ND isolated in rare-gas matrices (Ar, Kr and Xe).[9] From the electronic absorption spectra of these species, they concluded that NH and ND undergo nearly free rotation in rare-gas lattices. In addition, some vibrational parameters of NH and ND in rare-gas matrices were deduced.

In 1975, Bondybey and Brus[10] described time- and wavelength-resolved laser-induced fluorescence (LIF) experiments used to probe vibrational relaxation of NH and ND in Ar and Kr matrices. From the structure of the temperature-dependent local-phonon spectra they concluded that near-free rotation occurs in the $X\,^3\Sigma^-$ term, whilst in the $A\,^3\Pi$ term, the molecule undergoes libration.

There are few MCD studies of matrix-isolated NH in the literature. NH/Ar and NH/Xe have been investigated by Lund *et. al.*,[11] but poor spectrometer resolution and limited temperature control meant that few conclusions were reached. Rose[12] made a comprehensive experimental investigation of NH/Ar and NH/Xe, and made a cursory examination of NH/Kr spectra. These data have not been published because of the lack of a satisfactory theory. She found that she had to assume that the molecules were essentially oriented at the lowest temperatures (<1.5 K), and that as the temperature increased orientational disordering occurred, being complete by 15 K. This seems physically unreasonable, since it is difficult to see how the molecules will orient as the matrix is cooled after deposition at warmer temperatures.

The aim of this project is to produce a SO-CF model that satisfactorily explains the observed temperature and magnetic-field dependencies of the MCD and absorption of NH/Ar and ND/Ar $A\,^3\Pi \leftarrow X\,^3\Sigma^-$. Assignment of fine structure is also attempted. To this end, ND/Ar was investigated to allow comparison of fine structure with NH/Ar; ND and NH in the gas phase have similar ground-state ZFS and excited-state SOC (Section 5.1.1), but due to the isotope effect, rotational levels are compressed in ND with respect to NH.

5.2. Experimental

NH/Ar and ND/Ar were prepared using the apparatus described in Section 2.1.1.2, employing the ¼" → ½" discharge tube shown at the bottom of Figure 2.1.2. NH_3 (dry laboratory reagent) or ND_3 (Isotec, Inc.) were mixed with Ar (1:100 mole ratio using standard gas-handling techniques) in a 1-L glass reservoir to a final pressure of about 1 atm. NH(ND)/Ar matrix preparation times were ~15 minutes, with $NH_3(ND_3)$:Ar flow rates of ~5 mmol hr^{-1}.

MOD4 (Section 2.3) was used to gather all spectral data. The Xe-arc lamp and 1180-groove/mm grating were utilised in conjunction with either the Hamamatsu R-376 or R-292 PMTs. A Corning 7-54 filter was used to remove stray visible light exiting the monochromator (Section 2.3.4.1).

Data for quantitative analysis were obtained using the CF1204–SM4 matrix injection system (Section 2.2.2). During deposition of the sample, the window temperature was less stable than the He refrigerator (due to the tendency of liquid He to surge) and varied within the range ~12 – 20 K. The matrices were not annealed, preparation in this system seemingly having accomplished the purpose already.

The following subsections elaborate more specific aspects of the experimental aspects of the NH/Ar and ND/Ar systems.

5.2.1. NH/Ar

Preliminary matrix depositions were performed in the He-refrigerator/ electromagnet system described in Section 2.2.1. The deposition temperature was typically 12 to 14 K. Despite the somewhat cloudy appearance of the matrices, the depolarisation of circularly polarised light by the matrix was found to be negligible.

These experiments showed that annealing NH/Ar matrices above ~20 K yielded significant band sharpening, even at slit widths as wide 100 μm (Figure 5.2.1). Further, new fine structure was resolved when suitably small spectral slit widths were used (Figure 5.2.2; 30 μm corresponds to a spectral resolution of ~0.025 nm). However, the NH concentration was reduced a little, and the matrix underwent further clouding.

Reduction of the NH_3 concentration (to 1:250 and 1:500 NH_3/Ar mole ratio) yielded much less NH/Ar than for 1:100 mixtures. A major reason for this seems to be that the percentage of NH_3 adsorbed to the glass reservoir and stainless-steel deposition

line is much higher for lower NH_3/Ar mole ratios, so little NH_3 actually gets to the discharge region. The appearance of the spectra was unchanged for the less concentrated mixtures, so 1:100 mole ratios were used subsequently.

As noted above, and illustrated in Figure 5.2.2, the fine structure observed for NH/Ar is sharp, requiring a slit width of ≤30 μm. However, for satisfactory S/N to be obtained in the MCD, a great deal of data averaging has to be performed. (Note that the spectra shown in Figure 5.2.2 have data averaging in the ratio 1:2:2.5 for slit settings of 100:50:30 μm.) This was not a problem when using the He refrigerator (Section 2.2.1), but for the matrix injection system (Section 2.2.2) these long scan times are undesirable, due to the expense of liquid He, and temperature-control considerations. Hence, when the latter system was used, resolution was compromised slightly by employing 50-μm slits, affording better S/N due to increased light throughput. The spectra shown in Section 5.3.1 were obtained at this resolution.

5.2.2. ND/Ar

After problems with NH/Ar contamination in preliminary experiments (*i.e.* when using the He refrigerator; Section 2.2.1), the data presented in Section 5.3.2, were obtained with a mixture and deposition line prepared as follows. The gas-mixing apparatus was pumped overnight with a diffusion pump, before ~11 Torr of ND_3 was allowed to fill the line and passivate the surface for about 20 minutes. The pressure was then reduced to ~7.5 Torr, and the 1:100 ND_3/Ar mixture made. The deposition lines were prepared by pumping with a turbopump (with heating) until a vacuum of $<0.5 \times 10^{-5}$ Torr was obtained. The components were then assembled with minimum exposure to the atmosphere. However, the data of Section 5.3.2 show some NH/Ar contamination, which is suggested to be related to problems encountered with H_2O outgassing in the CH/Ar experiments (Section 6.2). In that case OH/Ar partially overlapped the CH/Ar $C\,^2\Sigma^+ \leftarrow X\,^2\Pi$ transition. Here, photolysis of H_2O would leave H atoms free to attach to N, yielding NH/Ar. Contamination by water in the matrix injection system appears to be a major problem.

ND/Ar spectra revealed less fine structure than NH/Ar, although some sharpening did occur after the sample was annealed. The data presented in Section 5.3.2 were obtained using 100-μm slits (spectral resolution ~0.082 nm).

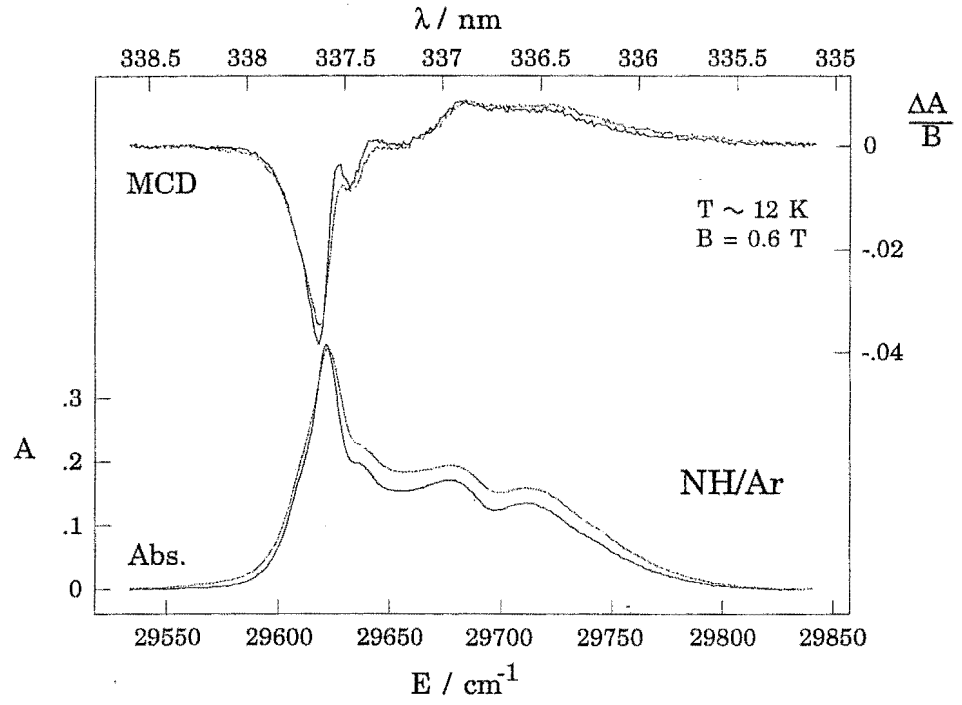

Figure 5.2.1: NH/Ar MCD and absorption spectra at ~12 K (B = 0.6 T) before and after (dotted and full curves, respectively) annealing the matrix at $T \approx 20$ K. (Slit width of 100 μm.)

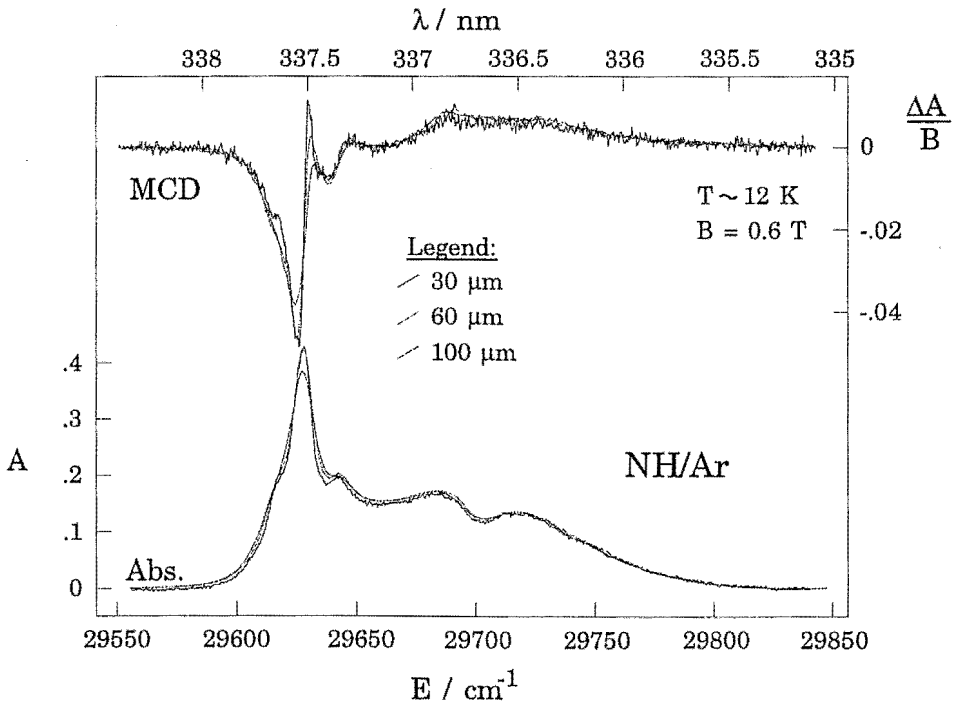

Figure 5.2.2: Slit-width dependence of NH/Ar MCD and absorption spectra at $T \approx 12$ K (B = 0.6 T) after an anneal at $T \approx 20$ K.

5.3. Results

5.3.1. NH/Ar

Temperature dependencies of the MCD and absorption of NH ($A\,^3\Pi \leftarrow X\,^3\Sigma^-$) from 1.58 to 16.2 K are shown in Figure 5.3.1. The spectra exhibit several maxima; those bands at low energy are relatively sharp (FWHM $\approx$ 8 cm^{-1}), but they become increasingly broad as energy increases. This broadening may be indicative of fast relaxation between SO and rotational levels in the excited state.[10] The positions of the bands indicated on Figure 5.3.1 (1 – 7 and 1') are given in Table 5.3.1, where the band positions observed by McCarty and Robinson,[9] and Rose,[12] are given for comparison. Although the absolute transition energies differ, the splittings observed in this work compare best with those obtained by McCarty and Robinson.[9] Also indicated are the assignments made previously;[9,12] these will be discussed in Section 5.5.2.

The MCD is bisignated, and shows the temperature dependence indicative of *C* terms (Section 1.3.2). Further evidence for the presence of *C* terms is provided by the saturation behaviour exhibited by the field-dependence data (B = 0 to 4.49 T) and shown in Figure 5.3.2. There also exists good evidence for the presence of *A* or pseudo-*A* terms, even at low temperatures, in the region between the strong negative and positive features. Assignments based on these observations will be described in Section 5.5.2.

The absorption is temperature independent within the S/N level until $T \approx 10$ K. At higher temperatures, band broadening increases and hot bands begin to grow in.

5.3.2. ND/Ar

Figure 5.3.3 shows the temperature-dependent MCD and absorption of ND/Ar ($A\,^3\Pi \leftarrow X\,^3\Sigma^-$) from 1.73 to 14.3 K. (A small amount of NH/Ar contamination is indicated by the arrow; Section 5.2.2. Note that the small (0,0) shift of ~22 cm^{-1} with respect to NH/Ar is due to the similarity of the potential surfaces of the ground and excited terms for the isotopomers.[9,13]) The spectra show a general similarity to those of NH/Ar (Figure 5.3.1), but also exhibit significant differences. Like NH/Ar, the bands broaden with increasing energy, and the entire band envelope encompasses approximately the same energy range as NH/Ar. The MCD shows the same general

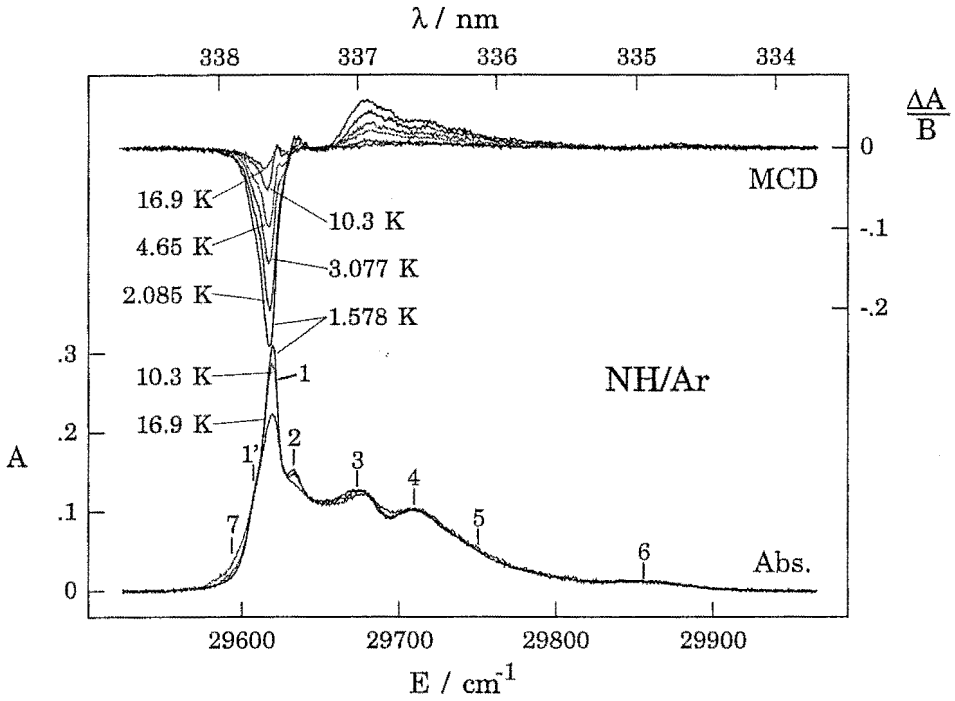

Figure 5.3.1: MCD (ΔA; top) and absorption (A; bottom) spectra of NH/Ar from 1.58 to 16.2 K (B = 0.5 or 1 T). The absorption bands are labelled for cross-referencing with Table 5.3.1 and Section 5.5.2.

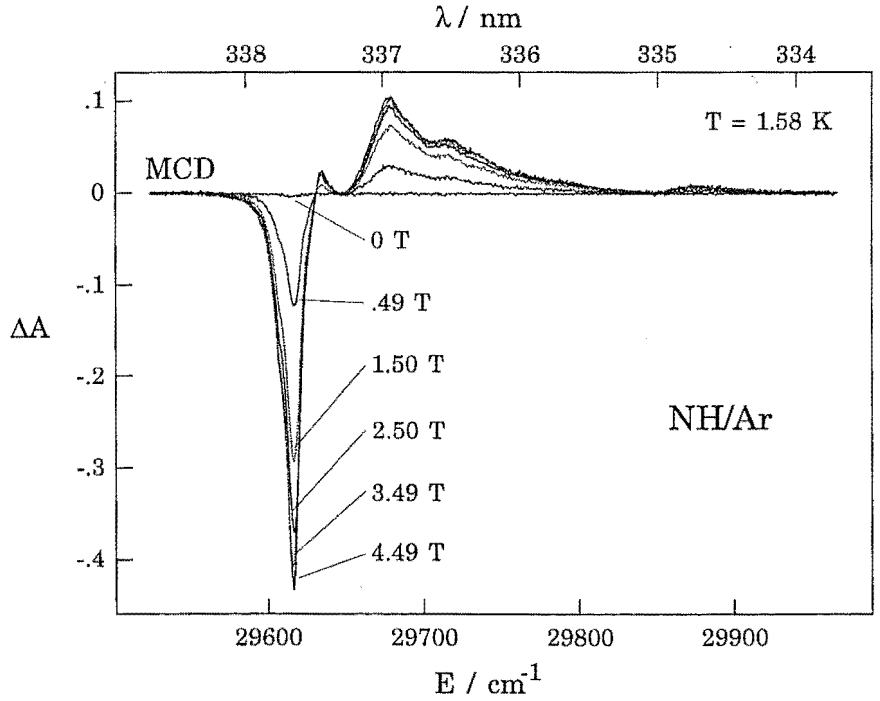

Figure 5.3.2: Magnetic-field dependence, from 0 to 4.49 T, of the MCD of NH/Ar at 1.58 K.

Table 5.3.1: Bands in the $A\,^3\Pi \leftarrow X\,^3\Sigma^-$ system of NH/Ar and ND/Ar.[a]

Band numbers; assignments [b]	Band energy / cm^{-1}				
	McCarty and Robinson [c]		Rose [d]	This work [e]	
	NH/Ar	ND/Ar	NH/Ar	NH/Ar	ND/Ar [f]
1; $R_1(1)$ [1'; $R_1(1)$]	29581	29608	29551	29620 ± 1 [29608 ± 3 sh][g]	29642 ± 2
2; $^RQ_{21}(1)$	29597		29562	29633 ± 2 (13)	29657 ± 3 (15)
3; $^RP_{31}(1)$	29642		29616	29674 ± 3 (54)	29712 ± 6 (70)
4; $^SQ_{31}(1)$	29671		29650	29708 ± 3 (88)	sh
5; $^TR_{31}(1)$			29682	sh	sh
$R_1(2)$; hb			29565		
$^RP_{31}(2)$; hb			29643		
6				29853 ± 10 (233)	sh ?
7; hb				29595 ± 5; sh	

[a] Wavenumbers are given in cm^{-1}. sh = shoulder; hb = hot band

[b] Band numbering is shown on Figures 5.3.1 and 5.3.3. Rotational assignments are those made previously by McCarty and Robinson[9] and Rose,[12] based on the gas-phase work of Dixon.[4] These assignments are discussed in Section 5.5.2.

[c] Ref. 9. [d] Ref. 12.

[e] Bracketed values give the displacement from band 1.

[f] The shoulder to the red of band 1 in Fig 5.3.3 is attributed to NH/Ar, since it lies at 29621 ± 5 cm^{-1}.

[g] The value in square brackets is attributed to a second site.

trend as NH/Ar; it is bisignated, decreases with temperature, and saturates with increasing magnetic-field strength (as shown for 0 to 4.0 T at $T \approx 1.72$ K in Figure 5.3.4). Band positions for ND/Ar are also given in Table 5.3.1. Unfortunately, although McCarty and Robinson obtained spectra of ND/Ar, they only published vibrational parameters, with no reference to any structure.[9]

ND/Ar reveals much less structure than NH/Ar, probably due to the broader bands and the compression of rotational levels as a consequence of deuteration.[7,13] In fact, the spectra are reminiscent of those obtained by Rose for NH/Kr.[12] In the MCD of ND/Ar the structure observed for NH/Ar (Figures 5.3.1 and 5.3.2) between the large positive and negative lobes is absent. However, notice that the associated absorption band (band 2 of Figure 5.3.3) is still present as a shoulder, suggesting that the MCD has been overlapped by stronger *C*-term components to lower and higher energy. The second broad band observed for NH/Ar (band 4 in Figure 5.3.1 and Table 5.3.1) is not resolved in ND/Ar. Its assignment as a transition to a (slightly hindered) rotational level seems reasonable, in that the splitting would be expected to decrease for ND/Ar relative to NH/Ar (Sections 5.1.2 and 5.5.2).

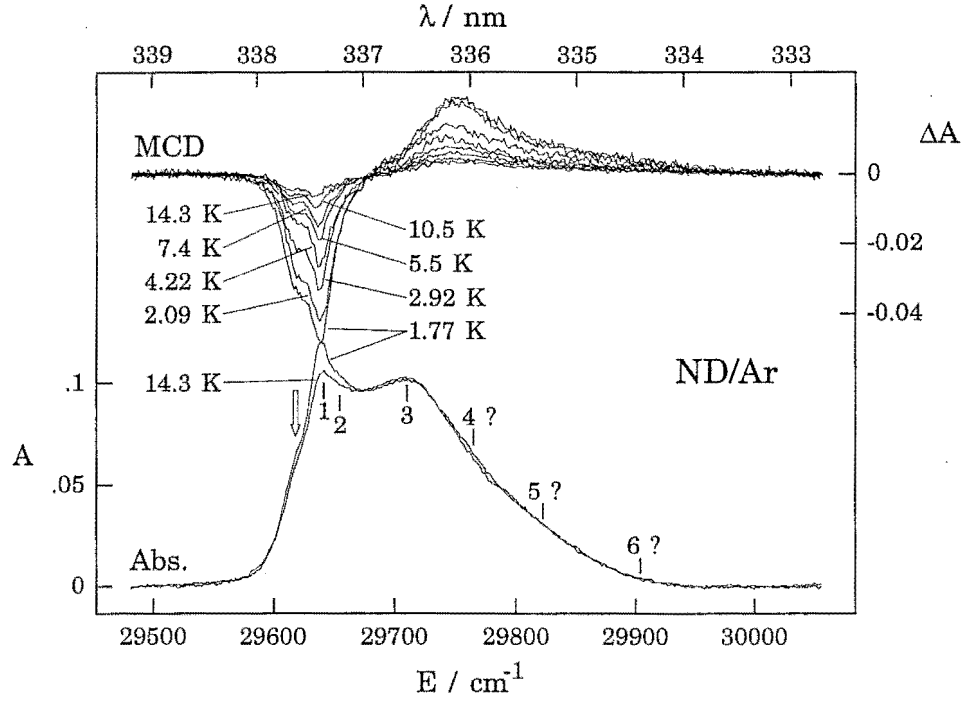

Figure 5.3.3: MCD (ΔA; top) and absorption (A; bottom) spectra of ND/Ar from 1.73 to 14.3 K ($B = 0.5$ or 1 T). The absorption bands are labelled for cross-referencing with Table 5.3.1, and Section 5.5.2.

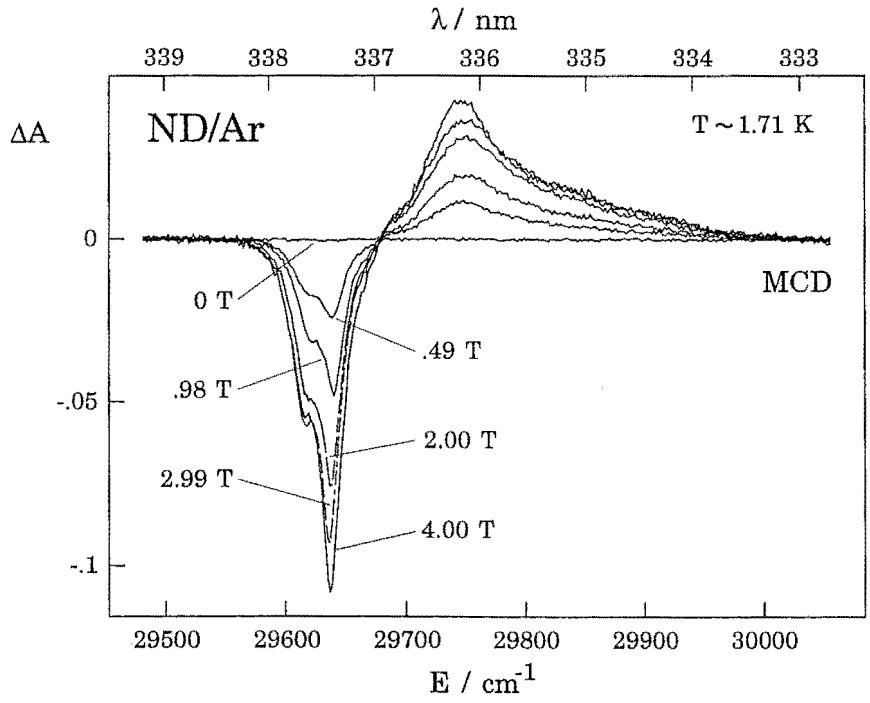

Figure 5.3.4: Magnetic-field dependence, from 0 to 4 T, of the MCD of ND/Ar at $T \approx 1.72$ K.

5.3.3. Moment analysis

In order to quantify the temperature and field dependencies, dimensionless zeroth absorption and first MCD moment parameters (Section 3.5.1) are defined. (For NH/Ar and ND/Ar the zeroth MCD moment is zero; Section 5.4.6.) The zeroth absorption moment $\mathbf{A}_0$ is given by eq (4.3.1). Using eq (3.5.4), the first MCD moment, $\mathbf{M}_1$, is,

$$\mathbf{M}_1 = \int \frac{\Delta A(E)}{E} (E - \bar{E})\, dE \qquad (5.3.1)$$

where E is the energy of the incident radiation, and ΔA is the MCD.

Figures 5.3.5 and 5.3.6 show the $\mathbf{M}_1/\mathbf{A}_0$ ratios (scaled by $\mu_B B$) plotted versus $1/kT$ for NH/Ar and ND/Ar, respectively, for fields of 0.5 T (below T = 5 K) and 1.0 T above (T = 5 K), which lie within the regime of the linear limit.[14] The experimental MCD saturation curves for NH/Ar (T = 1.58 K) and ND/Ar (T = 1.72 K) are shown in Figures 5.3.7 and 5.3.8, respectively, plotted against $\mu_B B$. The lines are best fits obtained as described in Section 5.5.1.

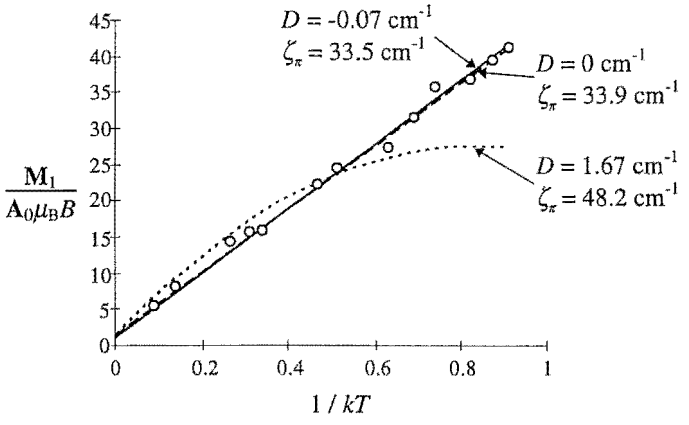

Figure 5.3.5: $\mathbf{M}_1/(\mathbf{A}_0\mu_B B)$ vs $1/kT$ for NH/Ar data obtained in the linear limit.[14] Fits were computed using eq (5.4.55) with the parameters shown (Table 5.5.1; Section 5.5.1) after simultaneous least-squares fitting of these and the saturation data (Figure 5.3.7).

5.4. Theory

In this section SO-CF theory is developed for NH/Ar (and ND/Ar), which will be applied to the experimental data of Section 5.3 in the following section. The treatment follows that of Chapter 3, although the MCD and absorption are dealt with in

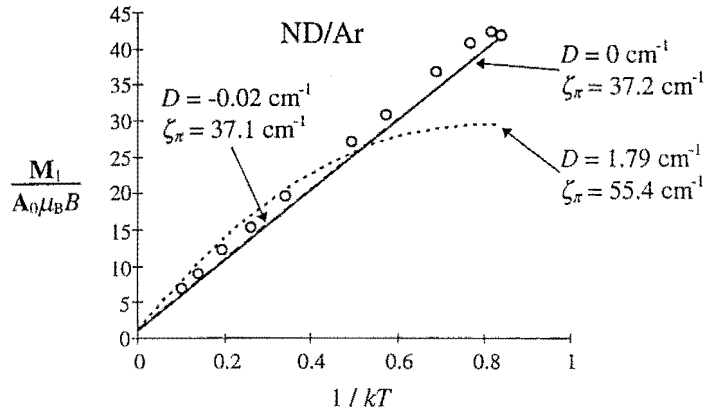

Figure 5.3.6: $M_\perp/(A_0\mu_B B)$ plotted against $1/kT$ for ND/Ar data obtained in the linear limit.[14] Fits were computed using eq (5.4.55) with the parameters shown (Table 5.5.1; Section 5.5.1) after simultaneous least-squares fitting of these and the saturation data (Figure 5.3.8).

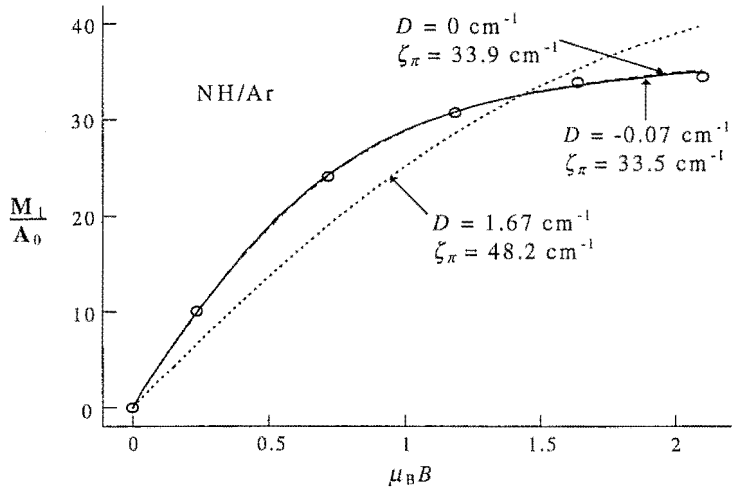

Figure 5.3.7: $M_\perp/A_0$ vs $\mu_B B$ for NH/Ar MCD saturation data obtained at 1.58 K.[14] The points are experimental data, while the curves represent the fits calculated using eq (5.4.55). The best fit (full curve) and other parameters as shown on the diagram.

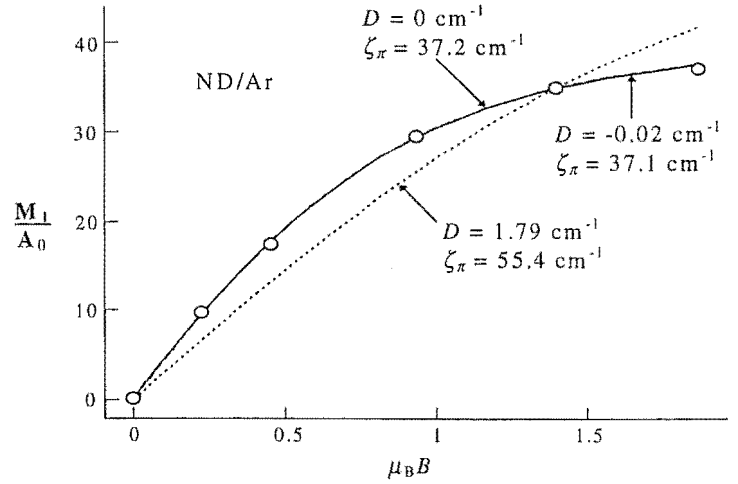

Figure 5.3.8: $M_\perp/A_0$ vs $\mu_B B$ for ND/Ar MCD saturation data obtained at ~1.72 K.[14] The points are experimental data, while the curves represent fits calculated using eq (5.4.55). The best fit (full curve) and other parameters as shown on the diagram.

a different manner. Like OH/Ar (Section 4.4.6), the theory is developed so that data obtained outside the linear limit[14] can be employed, and accounts for orientational averaging.

The $X\,^3\Sigma^-$ ground term of NH has no orbital angular momentum, and as such the g value is due only to spin ($g \approx g_e \approx 2$). The ZFS D, resulting from spin-spin and second-order SO splittings (Sections 5.4.2.3 and 5.4.2.2, respectively), is considered explicitly. For $D = 0$, many simplifications to the computation of the MCD moments are possible, and these are presented in Section 5.4.6.

The $A\,^3\Pi$ term, with non-zero orbital angular momentum, is susceptible to SO and CF effects (Section 3.3.2), and the full SO-CF treatment of Section 3.3.3 is used. It is helpful to note that the zeroth absorption and zeroth and first MCD moments are independent of CF splittings in the excited state (Sections 3.5.1.2 and 5.4.6).[14]

5.4.1. Spin-orbit wavefunctions for NH

NH has $\mathbf{C}_{\infty v}$ point-group symmetry, irrep and partner labels for which are given in Table 4.4.1. A schematic MO diagram for the radical is shown in Figure 5.4.1. The lowest-energy configuration is $3\sigma^2\ 1\pi^2$, while the first excited configuration is $3\sigma^1\ 1\pi^3$.

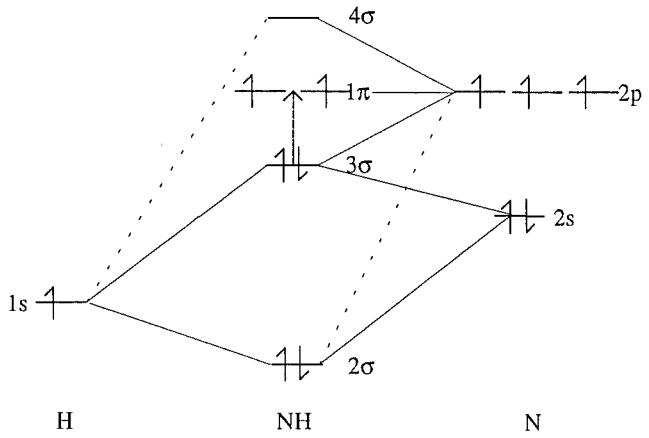

Figure 5.4.1: MO diagram for NH. (The 1σ MO is essentially pure N(1s), and is not shown.) The dashed line shows the lowest-energy electronic excitation, which is investigated in this work.

The orbital irreps of the states arising from a given configuration are found by calculating the direct product of the orbital irreps of the valence electrons (Section 3.3.1.2(b)). Using Table B.1.2 of Appendix B, these irreps are $\pi \otimes \pi = \Sigma^+ \oplus \Sigma^- \oplus \Delta$ for the ground configuration, and $\sigma^+ \otimes \pi = \Pi$ for the first excited configuration (where the

hole-particle formalism (Section 3.3.1.4(b) is employed). Spin irreps are found by coupling individual spin irreps (Section 3.3.1.2(c)). For both the ground and excited configurations $\delta = 1, 0$; and a triplet and singlet result.

The allowed terms for NH are obtained as described in Section 3.3.1.2(c). In order of increasing energy, they are $^3\Sigma^-$, $^1\Delta$ and $^1\Sigma^+$ in the ground configuration, and $^3\Pi$ and $^1\Pi$ in the first excited configuration.

Orbital and spin wavefunctions for the ground and first-excited configurations are generated following Section 3.3.1.3(a). MOs are coupled using eq (3.3.3), where the notation is also described. For the $3\sigma^2\ 1\pi^2$ ground configuration, ignoring the filled $3\sigma^2$ subconfiguration, the orbital wavefunctions are,

$$|(1\ 1)\ 2\ \pm2\rangle \equiv |\Delta\ \pm2\rangle = |1\ \pm1\rangle\,|1\ \pm1\rangle$$

$$|(1\ 1)\ \tilde{0}\ 0\rangle \equiv |\Sigma^-\ 0\rangle = \tfrac{1}{\sqrt{2}}\{|1\ -1\rangle\,|1\ 1\rangle - |1\ 1\rangle\,|1\ -1\rangle\}$$

$$|(1\ 1)\ 0\ 0\rangle \equiv |\Sigma^+\ 0\rangle = \tfrac{1}{\sqrt{2}}\{|1\ -1\rangle\,|1\ 1\rangle + |1\ 1\rangle\,|1\ -1\rangle\} \qquad (5.4.1)$$

Orbital wavefunctions for the σ^1 and π^3 subconfigurations of the first excited configuration are given in eqs (5.4.2) and (5.4.3), respectively, where the π^3 function was derived using the hole-particle equivalent, π^1 (Section 3.3.1.4(c)). They are not coupled until each has had the spin contribution included (Section 3.3.1.4(b)).

$$|\sigma^1\ 0\ 0\rangle \equiv |\Sigma^+\ 0> = |0\ 0\rangle \qquad (5.4.2)$$

$$|\,\pi^3\ 1\ \pm1\rangle \equiv |\pi^1\ 1\ \pm1\rangle \equiv |\Pi\ \pm1\rangle = |1\ -1\rangle\,|1\ \pm1\rangle\,|1\ 1\rangle \qquad (5.4.3)$$

The (general) two-electron spin wavefunctions, which apply for both configurations, were formed in the full-rotation group ($\mathbf{SO}_3$) using eq (3.3.4). Eqs (5.4.4) and (5.4.5) correspond to the triplet and singlet, respectively.

$$|(\tfrac{1}{2}\ \tfrac{1}{2})\ 1\ 1\rangle = |\tfrac{1}{2}\ \tfrac{1}{2}\rangle\,|\tfrac{1}{2}\ \tfrac{1}{2}\rangle$$

$$|(\tfrac{1}{2}\ \tfrac{1}{2})\ 1\ 0\rangle = \tfrac{1}{\sqrt{2}}\{|\tfrac{1}{2}\ \tfrac{1}{2}\rangle\,|\tfrac{1}{2}\ -\tfrac{1}{2}\rangle + |\tfrac{1}{2}\ -\tfrac{1}{2}\rangle\,|\tfrac{1}{2}\ \tfrac{1}{2}\rangle\}$$

$$|(\tfrac{1}{2}\ \tfrac{1}{2})\ 1\ -1\rangle = |\tfrac{1}{2}\ -\tfrac{1}{2}\rangle\,|\tfrac{1}{2}\ -\tfrac{1}{2}\rangle \qquad (5.4.4)$$

$$|(\tfrac{1}{2}\ \tfrac{1}{2})\ 0\ 0\rangle = \tfrac{1}{\sqrt{2}}\{|\tfrac{1}{2}\ \tfrac{1}{2}\rangle\,|\tfrac{1}{2}\ -\tfrac{1}{2}\rangle - |\tfrac{1}{2}\ -\tfrac{1}{2}\rangle\,|\tfrac{1}{2}\ \tfrac{1}{2}\rangle\} \qquad (5.4.5)$$

5.4.1.1. SL wavefunctions

The SL wavefunctions, $|^{2\delta+1}h\ \mathcal{M}\ \theta\rangle$, were formed using the method, and follow the notation, described in Section 3.3.1.4. The ground configuration of NH has a single open shell, so eq (3.3.5) of Section 3.3.1.4(a) applies, yielding,

$$|^3\Sigma^-\ \pm1\ 0\rangle = |0^2\ \text{-}1^{\pm}\ 1^{\pm}\rangle$$

$$|^3\Sigma^-\ 0\ 0\rangle = \tfrac{1}{\sqrt{2}}\{|0^2\ \text{-}1^{+}\ 1^{-}\rangle + |0^2\ \text{-}1^{-}\ 1^{+}\rangle\}$$

$$|^1\Delta\ 0\ \pm2\rangle = |0^2\ \pm1^{+}\ \pm1^{-}\rangle$$

$$|^1\Sigma^+\ 0\ 0\rangle = \tfrac{1}{\sqrt{2}}\{|0^2\ \text{-}1^{+}\ 1^{-}\rangle - |0^2\ \text{-}1^{-}\ 1^{+}\rangle\} \qquad (5.4.6)$$

where the fully occupied σ (0) orbital is included for completeness.

Since the first excited configuration has two open shells (σ^1 and π^3), coupling is performed using eq (3.3.6). $|\sigma^1\ \delta_1\ h_1\ \mathcal{M}_1\ \theta_1\rangle$ and $|\pi^3\ \delta_2\ h_2\ \mathcal{M}_2\ \theta_2\rangle$ wavefunctions are generated by inspection — the latter *via* the hole-particle formalism. The SL wavefunctions are,

$$|^3\Pi\ \pm1\ \pm1\rangle = |0^{\pm}\ \text{-}1^{+}\ \pm1^{\pm}\ 1^{-}\rangle$$

$$|^3\Pi\ 0\ \pm1\rangle = \tfrac{1}{\sqrt{2}}\{|0^{+}\ \text{-}1^{\mp}\ \pm1^{\pm}\ 1^{-}\rangle + |0^{-}\ \text{-}1^{+}\ \pm1^{\pm}\ 1^{\mp}\rangle\}$$

$$|^3\Pi\ \mp1\ \pm1\rangle = |0^{\mp}\ \text{-}1^{\mp}\ \pm1^{\pm}\ 1^{\mp}\rangle$$

$$|^1\Pi\ 0\ \pm1\rangle = \tfrac{1}{\sqrt{2}}\{|0^{+}\ \text{-}1^{\mp}\ \pm1^{\pm}\ 1^{-}\rangle - |0^{-}\ \text{-}1^{+}\ \pm1^{\pm}\ 1^{\mp}\rangle\} \qquad (5.4.7)$$

5.4.1.2. SO wavefunctions

The SO coupling (SOC) described here follows the method of Section 3.3.1.5. After spins are correlated, the SO irreps and partners are derived for terms of the ground and excited configurations using eq (3.3.7). They, and the resulting SO levels, are given in Table 5.4.1.

SO wavefunctions for each of the levels shown in Table 5.4.1 were derived using eq (3.3.10), and are given in eqs (5.4.8) and (5.4.9) for the ground and first-excited configurations, respectively. The $|^{2\delta+1}h_{\Omega}\ M_{\Omega}\rangle$ notation follows the convention described in Section 3.3.1.5, where in $C_{\infty v}$, $t \equiv \Omega$ and $\tau \equiv M_{\Omega}$.

Table 5.4.1: SO irreps and partners resulting from the ground and first-excited configurations of NH.

Term	Orbital irrep	Spin irrep		SOC		
	$C_{\infty v}$	SO_3	$C_{\infty v}$	Irreps	Partners	Level
$X\,^3\Sigma^-$	$\tilde{0}$	1	1	1	±1	$^3\Sigma_1^-$
	$\tilde{0}$	1	$\tilde{0}$	0	0	$^3\Sigma_0^-$
$a\,^1\Sigma^+$	0	0	0	0	0	$^1\Sigma_0^+$
$b\,^1\Delta$	2	0	0	2	±2	$^1\Delta_2$
$A\,^3\Pi$	1	1	1	0	0	$^3\Pi_{0+}$
				$\tilde{0}$	0	$^3\Pi_{0-}$
				2	±2	$^3\Pi_2$
	1	1	$\tilde{0}$	1	±1	$^3\Pi_1$
$c\,^1\Pi$	1	0	0	1	±1	$^1\Pi_1$

$$|^3\Sigma_0^-\,0\rangle = -\tfrac{1}{\sqrt{2}}\{|0^2\,{-1}^+\,1^-\rangle + |0^2\,{-1}^-\,1^+\rangle\}$$

$$|^3\Sigma_1^-\,\pm1\rangle = \mp|0^2\,{-1}^\pm\,1^\pm\rangle$$

$$|^1\Delta_2\,\pm2\rangle = |0^2\,\pm1^2\rangle$$

$$|^1\Sigma_0^+\,0\rangle = \tfrac{1}{\sqrt{2}}\{|0^2\,{-1}^+\,1^-\rangle - |0^2\,{-1}^-\,1^+\rangle\} \qquad (5.4.8)$$

$$|^3\Pi_2\,\pm2\rangle = |0^\pm\,{-1}^+\,\pm1^\pm\,1^-\rangle$$

$$|^3\Pi_1\,\pm1\rangle = \pm\tfrac{1}{\sqrt{2}}\{|0^\pm\,{-1}^\mp\,\pm1^\pm\,1^\mp\rangle + |0^\mp\,{-1}^+\,\pm1^\pm\,1^-\rangle\}$$

$$|^3\Pi_{0\pm}\,0\rangle = \tfrac{1}{\sqrt{2}}\{|0^+\,{-1}^2\,1^+\rangle \pm |0^-\,{-1}^-\,1^2\rangle\}$$

$$|^1\Pi_1\,\pm1\rangle = \tfrac{1}{\sqrt{2}}\{|0^+\,{-1}^\mp\,\pm1^\pm\,1^-\rangle - |0^-\,{-1}^+\,\pm1^\pm\,1^\mp\rangle\} \qquad (5.4.9)$$

Electron-repulsion, SO, spin-spin and CF matrix elements were computed using these wavefunctions.

5.4.2. Hamiltonian matrix elements

$$\mathcal{H} = \mathcal{H}_0 + \mathcal{H}_{Rep} + \mathcal{H}_{SO} + \mathcal{H}_{SS} + \mathcal{H}_{CF} \qquad (5.4.10)$$

5.4.2.1. Electron-repulsion matrix elements

Electron-repulsion matrix elements for NH were derived using the method of Section 3.3.2.1, where the notation is also described. In $C_{\infty v}$, the *a* and *b* labels, 0, 1 and

-1, are partners of the σ (0) and π (±1) orbitals. The results obtained for the terms of the ground and first-excited configurations of NH are given in eq (5.4.11).

$$\langle {}^3\Sigma^-|\mathcal{H}_{Rep}|{}^3\Sigma^-\rangle = J_{1\text{-}1} - K_{1\text{-}1}$$

$$\langle {}^1\Delta|\mathcal{H}_{Rep}|{}^1\Delta\rangle = J_{11}$$

$$\langle {}^1\Sigma^+|\mathcal{H}_{Rep}|{}^1\Sigma^+\rangle = J_{1\text{-}1} + K_{1\text{-}1}$$

$$\langle {}^3\Pi|\mathcal{H}_{Rep}|{}^3\Pi\rangle = 3J_{01} - 2K_{01} + 2J_{1\text{-}1} - K_{1\text{-}1} + J_{11}$$

$$\langle {}^1\Pi|\mathcal{H}_{Rep}|{}^1\Pi\rangle = 3J_{01} + 2J_{1\text{-}1} - K_{1\text{-}1} + J_{11} \qquad (5.4.11)$$

5.4.2.2. Spin-orbit matrix elements

SO matrix elements were evaluated as described in Section 3.3.2.2. As mentioned there, elements involving the raising and lowering operators can be ignored in $\mathbf{C}_{\infty v}$.

There are no non-zero diagonal SO matrix elements within the ground configuration of NH, because the terms are orbitally and/or spin non-degenerate. Off-diagonal matrix elements occur between the ${}^3\Sigma_0^-$ and ${}^1\Sigma_0^+$ levels, since they share the same SO irrep and partner. They are,

$$\langle {}^3\Sigma_0^- 0|\mathcal{H}_{SO}|{}^1\Sigma_0^+ 0\rangle = 2\zeta_\pi$$

$$\langle {}^1\Sigma_0^+ 0|\mathcal{H}_{SO}|{}^3\Sigma_0^- 0\rangle = 2\zeta_\pi \qquad (5.4.12)$$

where ζ_π is the SO splitting of an electron in a NH(1π) orbital, and is given by,

$$\zeta_\pi = \pm\tfrac{1}{2}\langle \pi\,\pm1|u_z|\pi\,\pm1\rangle \qquad (5.4.13)$$

Due to the large energy separation of the ${}^3\Sigma_0^-$ and ${}^1\Sigma_0^+$ levels (~21200 cm^{-1} in the gas phase[7]), the second-order SO splitting in the ${}^3\Sigma^-$ term is small (~0.2 cm^{-1}).[7,15]

In the ${}^3\Pi$ excited term, the diagonal SO matrix elements are,

$$\langle {}^3\Pi_2\,\pm2|\mathcal{H}_{SO}|{}^3\Pi_2\,\pm2\rangle = -\zeta_\pi$$

$$\langle {}^3\Pi_1\,\pm1|\mathcal{H}_{SO}|{}^3\Pi_1\,\pm1\rangle = 0$$

$$\langle {}^3\Pi_{0^\pm}\,0|\mathcal{H}_{SO}|{}^3\Pi_{0^\pm}\,0\rangle = \zeta_\pi \qquad (5.4.14)$$

giving the first-order energies,

$$E(^3\Pi_\Omega) = -\zeta_\pi \Lambda (\Omega - \Lambda) \qquad (5.4.15)$$

where Λ and Ω are, respectively, the orbital angular momentum and SO quantum numbers. The leading negative sign on the right-hand side accounts for the $A\ ^3\Pi$ term of NH being an inverted SO system, since ζ_π is positive. The SO levels of the $A\ ^3\Pi$ term are shown near the left-hand side of Figure 5.4.2.

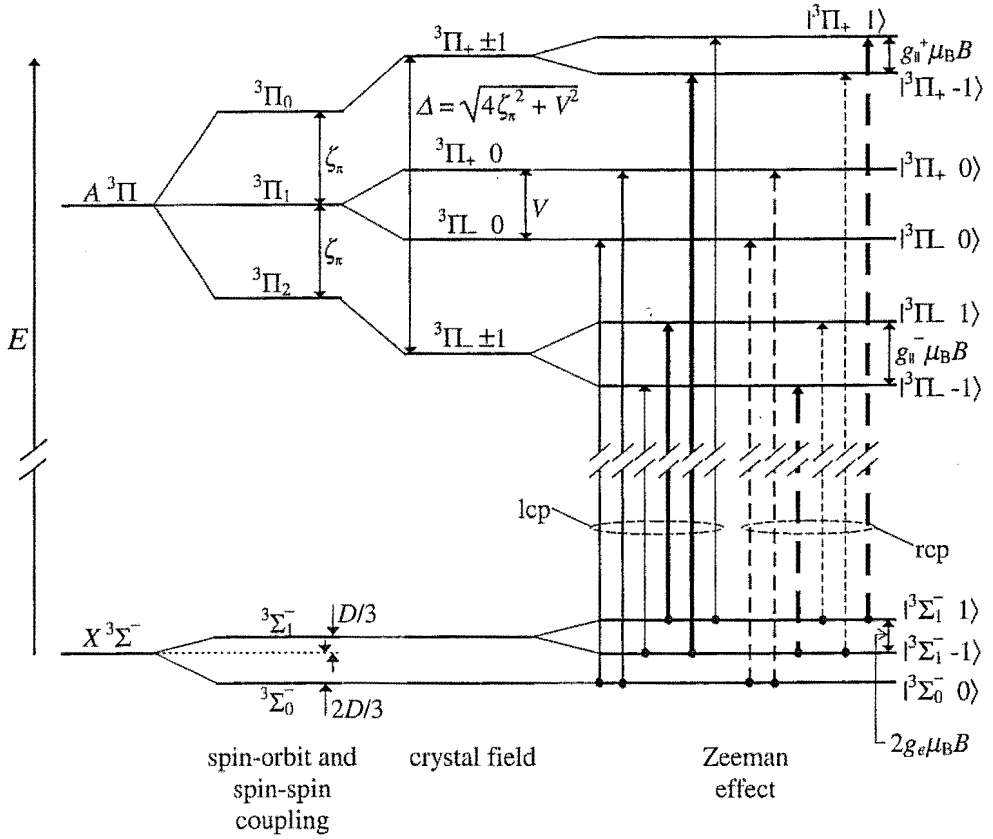

Figure 5.4.2: Energy-level diagram showing the effects of SO, spin-spin, CF and Zeeman interactions on the $X\ ^3\Sigma^-$ and $A\ ^3\Pi$ terms of NH/Ar. Approximate relative intensities of left- (lcp) and right-circularly polarised (rcp) transitions are indicated by full and dashed arrows, respectively, assuming that NH is *Z*-oriented. (Singlet terms arising from the ground and first-excited configurations (Section 5.4.1) are omitted for clarity.) All $^3\Sigma^-$ states are given in SO notation (Section 5.4.1.2), as are the $^3\Pi$ SO levels. However, introduction of the CF gives $^3\Pi_\pm$ states which are designated by their M_S value (Section 5.4.3).

The $^1\Pi$ excited term has no first-order SOC, but has the same total angular momentum as $^3\Pi_1$; there occur non-zero off-diagonal matrix elements coupling these terms,

$$\langle {}^1\Pi_1 \pm 1 | \mathcal{H}_{SO} | {}^3\Pi_1 \pm 1 \rangle = \zeta_\pi$$

$$\langle {}^3\Pi_1 \pm 1 | \mathcal{H}_{SO} | {}^1\Pi_1 \pm 1 \rangle = \zeta_\pi \qquad (5.4.16)$$

Higher-order SOC also causes ZFS of the $^3\Pi_{0+}$ and $^3\Pi_{0-}$ levels (~3 cm^{-1} in the lowest rotational level).

5.4.2.3. Spin-spin coupling[16]

Spin-spin coupling is calculated to be the major contributor to the ZFS in the $X\,^3\Sigma^-$ term.[6,7,15,17] Evaluation of the spin-spin matrix elements of the ground-state term are described here. (In the excited $A\,^3\Pi$ term the spin-spin contribution is small relative to the (first-order) SOC, and is neglected here.)

The classical Hamiltonian $\mathcal{H}_d$ describing the interaction of two magnetic dipoles is given by,

$$\mathcal{H}_d = [r_{12}^2(\mu_1 \bullet \mu_2) - 3(r_{12} \bullet \mu_1)\,(r_{12} \bullet \mu_2)]\, r_{12}^{-5} \qquad (5.4.17)$$

If the dipoles are the consequence of the spins of two electrons at positions r_1 and r_2, then $\mu_i = g_e \mu_B s_i$, $r_{12} = r_2 - r_1$ and $r_{12} = |r_{12}|$. It can be shown that the quantum-mechanical spin-spin interaction Hamiltonian $\mathcal{H}_{SS}$ is,

$$\mathcal{H}_{SS} = \sum_p \sum_q D_{pq} S_p S_q = \boldsymbol{S} \bullet \boldsymbol{D} \bullet \boldsymbol{S} \qquad (5.4.18)$$

where $p, q = x, y, z$, D_{pq} is an element of the ZFS tensor $\boldsymbol{D}$, and $\boldsymbol{S} = (S_x, S_y, S_z)$. A unitary transformation diagonalises $\boldsymbol{D}$, with the result,

$$\mathcal{H}_{SS} = D_{xx} S_x^2 + D_{yy} S_y^2 + D_{zz} S_z^2 = D(S_z^2 - \tfrac{1}{3}S^2) + E(S_x^2 - S_y^2) \qquad (5.4.19)$$

$D = \frac{3}{2}D_{zz}$, and $E = \frac{1}{2}(D_{xx} - D_{yy})$. The matrix elements of $\mathcal{H}_{SS}$ in a triplet system are found from the action of the operator on the spin wavefunctions. The spin-spin matrix elements are given in Table 5.4.2 for the spin wavefunctions $|S\ M_s\rangle$ (Section 3.3.1.3(c)).

Table 5.4.2: Spin-spin matrix elements for a triplet spin system ($S = 1$).[a]

$\mathcal{H}_{SS}$	$\|1\ 1\rangle$	$\|1\ 0\rangle$	$\|1\ -1\rangle$
$\langle 1\ 1\|$	$D/3$	0	E
$\langle 1\ 0\|$	0	$-2D/3$	0
$\langle 1\ -1\|$	E	0	$D/3$

[a] Bras and kets (Section 3.1.2) give $|S\ M_s\rangle$.

The eigenvalues of the matrix are $\lambda_\pm = D/3 \pm E$, and $\lambda_0 = -2D/3$. In $C_{\infty v}$, x and y are equivalent and E vanishes, giving eigenvalues of $-2D/3$ and $D/3$ for $^3\Sigma^-_0$ and $^3\Sigma^-_1$, respectively, and a splitting of D.

In this thesis, the second-order SO splitting (Section 5.4.2.2) is included in D; *i.e.* the ZFS is treated as an effective Hamiltonian, and the overall splitting parameter D comprises both spin-spin and SO contributions.

5.4.2.4. Crystal-field matrix elements

Section 3.3.2.3 describes the method used to evaluate the CF matrix elements of a $^3\Pi$ term. The CF matrix elements are,

$$\langle {}^3\Pi_2 \pm2|\mathcal{H}_{CF}|{}^3\Pi_{0+}\ 0\rangle = -\tfrac{1}{\sqrt{8}}V$$

$$\langle {}^3\Pi_{0+}\ 0|\mathcal{H}_{CF}|{}^3\Pi_2 \pm2\rangle = -\tfrac{1}{\sqrt{8}}V$$

$$\langle {}^3\Pi_2 \pm2|\mathcal{H}_{CF}|{}^3\Pi_{0-}\ 0\rangle = \mp\tfrac{1}{\sqrt{8}}V$$

$$\langle {}^3\Pi_{0-}\ 0|\mathcal{H}_{CF}|{}^3\Pi_2 \pm2\rangle = \mp\tfrac{1}{\sqrt{8}}V$$

$$\langle {}^3\Pi_1 \pm1|\mathcal{H}_{CF}|{}^3\Pi_1 \mp1\rangle = \tfrac{1}{2}V \qquad (5.4.20)$$

where $V = \langle 1\|V^2\|1\rangle$ is a one-electron reduced CF matrix element. V represents the magnitude of the splitting of the $|\Pi \pm1\rangle$ orbital components in the absence of SOC (or other competing effects). The effect of the CF splitting is illustrated in Figure 5.4.2.

5.4.3. SO-CF wavefunctions for NH($A\ ^3\Pi$)/Ar

The simultaneous presence of SO and CF effects alters the energies of the levels by mixing eigenstates of either operator. The 6×6 secular determinant formed from the first-order SO and CF matrix elements (Section 3.3.3) of eqs (5.4.14) and (5.4.20), respectively, can be factored into two blocks; a 2×2 matrix corresponding to $S = \tilde{0}$ ($M_S = 0$), and a 4×4 matrix for $S = 1$ ($M_S = \pm1$). (The spin quantum numbers are given in the symmetry-adapted SO basis for $\mathbf{C}_{\infty v}$ (Table 5.4.1; Section 5.4.1.2), where in this case $M_S \equiv \mathcal{M}_{\tilde{S}}$.) The former has no non-zero SO contributions, so the splitting arises from the CF only, and has a magnitude V (Section 5.4.2.4). The corresponding eigenfunctions are,

$$|{}^3\Pi_\pm\ 0\rangle = \tfrac{1}{\sqrt{2}}\{|{}^3\Pi_1\ {-1}\rangle \pm |{}^3\Pi_1\ {+1}\rangle\} \qquad (5.4.21)$$

$^3\Pi_+$ and $^3\Pi_-$ respectively designate the upper and lower SO-CF levels, and the '0' in the left-hand ket denotes the value of M_S. The kets on the RHS are the SO wavefunctions of eq (5.4.7).

Diagonalisation of the 4×4 determinant (S = 1) yields the remaining SO-CF eigenfunctions and eigenvalues for the $^3\Pi$ term. The splitting (Δ) of these components is given by,

$$\Delta = \sqrt{4\zeta_\pi^2 + V^2} \tag{5.4.22}$$

SO-CF eigenstates were obtained with a little more effort than was necessary for OH/Ar (Section 4.4.3). Mixtures of M_S values were eliminated by an appropriate choice of coefficients for the raised states, and for the lowered states by taking linear combinations. The eigenstates are,

$$|^3\Pi_- \pm 1\rangle = \beta\,|^3\Pi_2 \pm 2\rangle \mp \tfrac{1}{\sqrt{2}}\alpha\,\{|^3\Pi_{0^-}\,0\rangle \pm |^3\Pi_{0^+}\,0\rangle\} \tag{5.4.23a}$$

$$|^3\Pi_+ \pm 1\rangle = \pm\alpha\,|^3\Pi_2 \pm 2\rangle + \tfrac{1}{\sqrt{2}}\beta\,\{|^3\Pi_{0^-}\,0\rangle \pm |^3\Pi_{0^+}\,0\rangle\} \tag{5.4.23b}$$

where the notation was described subsequent to eq (5.4.21). The arbitrary choice of coefficients was shown to be satisfactory, because the wavefunctions diagonalise the Hamiltonian correctly, and reduce to the appropriate SO eigenstates (eq (5.4.7)) as $V \rightarrow 0$ ($\alpha \rightarrow 0$ and $\beta \rightarrow 1$; see eqs (5.4.28) and (5.4.29)). The mixing coefficients α and β are given by,

$$\alpha = \frac{2\zeta_\pi - \Delta}{\sqrt{V^2 + (2\zeta_\pi - \Delta)^2}} = \frac{V}{\sqrt{V^2 + (2\zeta_\pi + \Delta)^2}} \tag{5.4.24}$$

$$\beta = \frac{V}{\sqrt{V^2 + (2\zeta_\pi - \Delta)^2}} = \frac{2\zeta_\pi + \Delta}{\sqrt{V^2 + (2\zeta_\pi + \Delta)^2}} \tag{5.4.25}$$

These coefficients obey the normalisation relationship of eq (4.4.13), but eqs (4.4.14) and (4.4.15) become,

$$\alpha^2 - \beta^2 = 2\zeta_\pi / \Delta \equiv \kappa \tag{5.4.26}$$

$$2\alpha\beta = -V / \Delta \equiv -\eta \tag{5.4.27}$$

Here $0 \le \kappa \le 1$ and $0 \le \eta \le 1$. Other useful relationships are,

$$\alpha^2 = \tfrac{1}{2} - \zeta_\pi / \Delta = \tfrac{1}{2}(1 - \kappa) \tag{5.4.28}$$

$$\beta^2 = \tfrac{1}{2} + \zeta_\pi / \Delta = \tfrac{1}{2}(1 + \kappa) \qquad (5.4.29)$$

5.4.4. Zeeman matrix elements and *g* values

The angular momentum matrix elements and g values were evaluated as described in Section 3.3.4.

5.4.4.1. $X\,^3\Sigma^-$ ground term

In the $X\,^3\Sigma^-$ term, there is no orbital angular momentum and no CF splitting. Although the Zeeman splitting is nearly isotropic, with $g \approx g_e \approx 2$, because of ZFS and orientational averaging (Section 5.4.6) matrix elements for both the z and x components (molecular reference frame) of $\boldsymbol{L}$ and $\boldsymbol{S}$ (Sections 3.3.4.1 and 3.3.4.2) are presented in Table 5.4.3.

Table 5.4.3: Angular momentum matrix elements for the $X\,^3\Sigma^-$ states of NH/Ar.

$L_z + g_e S_z$	$\lvert^3\Sigma_1^-\ -1\rangle$	$\lvert^3\Sigma_0^-\ 0\rangle$	$\lvert^3\Sigma_1^-\ +1\rangle$
$\langle^3\Sigma_1^-\ -1\rvert$	$-g_e$	0	0
$\langle^3\Sigma_0^-\ 0\rvert$	0	0	0
$\langle^3\Sigma_1^-\ +1\rvert$	0	0	g_e

$L_x + g_e S_x$	$\lvert^3\Sigma_1^-\ -1\rangle$	$\lvert^3\Sigma_0^-\ 0\rangle$	$\lvert^3\Sigma_1^-\ +1\rangle$
$\langle^3\Sigma_1^-\ -1\rvert$	0	$-g_e/\sqrt{2}$	0
$\langle^3\Sigma_0^-\ 0\rvert$	$-g_e/\sqrt{2}$	0	$g_e/\sqrt{2}$
$\langle^3\Sigma_1^-\ +1\rvert$	0	$g_e/\sqrt{2}$	0

5.4.4.2. $A\,^3\Pi$ excited term

Angular momentum matrix elements for the SO-CF states of the $A\,^3\Pi$ term are listed in Table 5.4.4 for the z and x components (molecular reference frame) of $\boldsymbol{L}$ and $\boldsymbol{S}$ (Sections 3.3.4.1 and 3.3.4.2). $g_\parallel^+$ and $g_\parallel^-$ are the g values for the upper and lower $S = 1$ SO-CF levels (eq (5.4.23)), respectively, when the molecular z axis is aligned parallel to $\boldsymbol{B}$. They are given by,

$$g_\parallel^\pm \equiv 2\,\langle^3\Pi_\pm +1 | L_z + g_e S_z | ^3\Pi_\pm +1\rangle = 2(g_e \mp \kappa\Lambda) \qquad (5.4.30)$$

where Λ is the total orbital angular momentum quantum number.

Table 5.4.4: Angular momentum matrix elements for the $A\,^3\Pi$ SO-CF states of NH/Ar.[a]

$L_z + g_e S_z$	$\|^3\Pi_- -1\rangle$	$\|^3\Pi_- 1\rangle$	$\|^3\Pi_- 0\rangle$	$\|^3\Pi_+ 0\rangle$	$\|^3\Pi_+ -1\rangle$	$\|^3\Pi_+ 1\rangle$
$\langle^3\Pi_- -1\|$	$-\frac{1}{2}g_{\|\|}^-$	0	0	0	$-A\eta$	0
$\langle^3\Pi_- 1\|$	0	$\frac{1}{2}g_{\|\|}^-$	0	0	0	$-A\eta$
$\langle^3\Pi_- 0\|$	0	0	0	$-A$	0	0
$\langle^3\Pi_+ 0\|$	0	0	$-A$	0	0	0
$\langle^3\Pi_+ -1\|$	$-A\eta$	0	0	0	$-\frac{1}{2}g_{\|\|}^+$	0
$\langle^3\Pi_+ 1\|$	0	$-A\eta$	0	0	0	$\frac{1}{2}g_{\|\|}^+$

$L_x + g_e S_x$	$\|^3\Pi_- -1\rangle$	$\|^3\Pi_- 1\rangle$	$\|^3\Pi_- 0\rangle$	$\|^3\Pi_+ 0\rangle$	$\|^3\Pi_+ -1\rangle$	$\|^3\Pi_+ 1\rangle$
$\langle^3\Pi_- -1\|$	0	0	$\frac{1}{2}g_e(\alpha-\beta)$	$-\frac{1}{2}g_e(\alpha+\beta)$	0	0
$\langle^3\Pi_- 1\|$	0	0	$\frac{1}{2}g_e(\alpha-\beta)$	$\frac{1}{2}g_e(\alpha+\beta)$	0	0
$\langle^3\Pi_- 0\|$	$\frac{1}{2}g_e(\alpha-\beta)$	$\frac{1}{2}g_e(\alpha-\beta)$	0	0	$\frac{1}{2}g_e(\alpha+\beta)$	$-\frac{1}{2}g_e(\alpha+\beta)$
$\langle^3\Pi_+ 0\|$	$-\frac{1}{2}g_e(\alpha+\beta)$	$\frac{1}{2}g_e(\alpha+\beta)$	0	0	$\frac{1}{2}g_e(\alpha-\beta)$	$\frac{1}{2}g_e(\alpha-\beta)$
$\langle^3\Pi_+ -1\|$	0	0	$\frac{1}{2}g_e(\alpha+\beta)$	$\frac{1}{2}g_e(\alpha-\beta)$	0	0
$\langle^3\Pi_+ 1\|$	0	0	$-\frac{1}{2}g_e(\alpha+\beta)$	$\frac{1}{2}g_e(\alpha-\beta)$	0	0

[a] Parameters are defined by eqs (5.4.24), (5.4.25), (5.4.27) and (5.4.30).

5.4.5. Transition-moment matrix elements

Transition-moment matrix elements for $A\,^3\Pi \leftarrow X\,^3\Sigma^-$ were evaluated using the method of Section 3.4.2. The non-zero transition moments are summarised in Table 5.4.5, where initial states are shown along the top row and the final states down the left hand column. $\mathcal{M}$ is the one-electron reduced transition moment (Section 3.4.2.1) for the orbital excitation $1\pi \leftarrow 3\sigma$,

$$\mathcal{M} = \langle 1\pi \| m^1 \| 3\sigma \rangle \qquad (5.4.31)$$

5.4.6. MCD and absorption

Expressions for the zeroth absorption and zeroth and first MCD moments within the SO-CF model are derived in this section. Complete orientational disorder is assumed. Equations are first presented which apply for non-zero D, before the simpler case where $D = 0$ is considered. Note that although $\mathbf{A}_0$, $\mathbf{M}_0$ and $\mathbf{M}_1$ are independent of first-order CF effects (Section 3.5.1.2),[14] the CF is retained in the hope that individual component bands may explain some peculiarities of the fine structure. Although the invariance of the moments over the entire band system should be universally true, it was

specifically checked and confirmed for NH/Ar; analytically for $D = 0$, and numerically for $D \neq 0$.

Table 5.4.5: Transition moments for the $^3\Pi_\pm \leftarrow {}^3\Sigma^-$ SO-CF transitions of NH/Ar.[a]

m^1_{+1}	$\|^3\Sigma^-_1\ -1\rangle$	$\|^3\Sigma^-_0\ 0\rangle$	$\|^3\Sigma^-_1\ 1\rangle$
$\langle^3\Pi_-\ -1\|$	$-\frac{1}{\sqrt{2}}\alpha\mathcal{M}$	0	0
$\langle^3\Pi_-\ 1\|$	0	0	$-\frac{1}{\sqrt{2}}\beta\mathcal{M}$
$\langle^3\Pi_-\ 0\|$	0	$\frac{1}{2}\mathcal{M}$	0
$\langle^3\Pi_+\ 0\|$	0	$-\frac{1}{2}\mathcal{M}$	0
$\langle^3\Pi_+\ -1\|$	$-\frac{1}{\sqrt{2}}\beta\mathcal{M}$	0	0
$\langle^3\Pi_+\ 1\|$	0	0	$-\frac{1}{\sqrt{2}}\alpha\mathcal{M}$

m^1_{-1}	$\|^3\Sigma^-_1\ -1\rangle$	$\|^3\Sigma^-_0\ 0\rangle$	$\|^3\Sigma^-_1\ 1\rangle$
$\langle^3\Pi_-\ -1\|$	$-\frac{1}{\sqrt{2}}\beta\mathcal{M}$	0	0
$\langle^3\Pi_-\ 1\|$	0	0	$-\frac{1}{\sqrt{2}}\alpha\mathcal{M}$
$\langle^3\Pi_-\ 0\|$	0	$-\frac{1}{2}\mathcal{M}$	0
$\langle^3\Pi_+\ 0\|$	0	$-\frac{1}{2}\mathcal{M}$	0
$\langle^3\Pi_+\ -1\|$	$\frac{1}{\sqrt{2}}\alpha\mathcal{M}$	0	0
$\langle^3\Pi_+\ 1\|$	0	0	$\frac{1}{\sqrt{2}}\beta\mathcal{M}$

[a] $\mathcal{M}$ is defined in eq (5.4.31).

General case: $D \neq 0$

Expressions are first developed for radicals with their z axes at an angle θ to the magnetic-field axis Z (Section 3.4.3.2; Figure 3.4.1). Using eq (3.4.24), the absorption is,

$$\frac{A(E,\theta)}{E} = \tfrac{1}{4}(1+\cos^2\theta)\,\gamma c l \sum_{\sigma=\pm}\sum_{M_S M_\Omega} P_{M_\Omega}\left(|\langle^3\Pi_\sigma M_S|m_{+1}|^3\Sigma^- M_\Omega\rangle|^2 + |\langle^3\Pi_\sigma M_S|m_{-1}|^3\Sigma^- M_\Omega\rangle|^2\right) f_{\lambda,M_S}(E) \qquad (5.4.32)$$

where $\sigma = \pm$ is a label representing a state raised or lowered by the CF, with a spin component M_S (eqs (5.4.21) and (5.4.23)). M_Ω are the SO partner labels for the ground state (the Ω subscript has been omitted from the term symbol). Applying eq (3.4.25) gives the MCD,

$$\frac{\Delta A'(E,\theta)}{E} = \gamma c l \cos\theta \sum_{\sigma=\pm} \sum_{M_S M_\Omega} P_{M_\Omega} (|\langle {}^3\Pi_\sigma M_S|m_{+1}|{}^3\Sigma^- M_\Omega\rangle|^2 - |\langle {}^3\Pi_\sigma M_S|m_{-1}|{}^3\Sigma^- M_\Omega\rangle|^2) f_{\lambda,M_S}(E) \qquad (5.4.33)$$

The population factors P_{M_Ω} of the $^3\Sigma^-$ levels in eqs (5.4.32) and (5.4.33) are not easily dealt with analytically. The levels are separated by spin-spin (Section 5.4.2.3) and second-order SO (Section 5.4.2.2) coupling, and in the presence of a magnetic field are both split and mixed, the latter as a consequence of non-zero S_x matrix elements. The extent of mixing is angle-dependent, and necessitates the construction of angle-dependent eigenfunctions as follows.

Using the angular momentum matrix elements in Table 5.4.3, eq (4.4.22) for transformation to the laboratory reference frame, and including the ZFS (Table 5.4.2), the Hamiltonian matrix for the $X\,^3\Sigma^-$ term is given by Table 5.4.6.

Table 5.4.6: Full ZFS and Zeeman Hamiltonian matrix for NH/Ar $X\,^3\Sigma^-$.

$-\mu_Z B + \mathcal{H}_S$	$\|^3\Sigma_1^-\ -1\rangle$	$\|^3\Sigma_0^-\ 0\rangle$	$\|^3\Sigma_1^-\ +1\rangle$
$\langle^3\Sigma_1^-\ -1\|$	$-g_e\cos\theta\,\mu_B B + D/3$	$-g_e\sin\theta\,\mu_B B/\sqrt{2}$	0
$\langle^3\Sigma_0^-\ 0\|$	$-g_e\sin\theta\,\mu_B B/\sqrt{2}$	$-2D/3$	$g_e\sin\theta\,\mu_B B/\sqrt{2}$
$\langle^3\Sigma_1^-\ +1\|$	0	$g_e\sin\theta\,\mu_B B/\sqrt{2}$	$g_e\cos\theta\,\mu_B B + D/3$

Although analytical eigenfunctions can be derived when $D \neq 0$, their form is far too complicated for practical application. Instead numerical methods are employed. The general factor has the form,

$$|^3\Sigma^- M_\Omega'\rangle = \sum_{M_\Omega} C_{M_\Omega,M_\Omega'} |^3\Sigma^- M_\Omega\rangle \qquad (5.4.34)$$

where the mixing coefficients $C_{M_\Omega,M_\Omega'}$ are determined by diagonalisation of the matrix in Table 5.4.6. The primes are used to indicate new angle-dependent eigenfunctions (M_Ω') that are admixtures of the original eigenfunctions, and have eigenvalues $E_{M_\Omega'}$. Their fractional Boltzmann populations $P_{M_\Omega'}$ are given by,

$$P_{M_\Omega'} = \frac{1}{Q}\exp(-E_{M_\Omega'}/kT) \qquad (5.4.35)$$

Q is the partition function,

$$Q = \sum_{M_\Omega'} \exp(-E_{M_\Omega'}/kT) \tag{5.4.36}$$

Considerable simplifications can be made when the radicals are *Z*-oriented. $E_{M_\Omega'}$ can be replaced by E_{M_Ω}, because the wavefunctions are not mixed, so,

$$P_{M_\Omega} = \frac{1}{Q}\exp(-E_{M_\Omega}/kT) \qquad (\theta = 0) \tag{5.4.37}$$

A useful relationship for calculation of the MCD in this case is,

$$P_{-1} - P_{+1} = \frac{2\sinh\left(\dfrac{g_e\mu_B B}{kT}\right)}{\exp\left(\dfrac{D}{3kT}\right) + 2\cosh\left(\dfrac{g_e\mu_B B}{kT}\right)} \qquad (\theta = 0) \tag{5.4.38}$$

In the linear limit,[14] $\sinh(x) \rightarrow x$ and $\cosh(x) \rightarrow 1$, and eq (5.4.38) becomes,

$$P_{-1} - P_{+1} = \frac{2g_e\mu_B B}{(\exp(D/3kT) + 2)\ kT} \qquad (\theta = 0,\ \mu_B B << kT) \tag{5.4.39}$$

Returning to eqs (5.4.32) and (5.4.33), the zeroth absorption moment and *C*-term contribution to the zeroth MCD moment (Section 3.5.1.2) are defined as $\mathbf{A}_0^\theta$ and $\mathbf{C}_0^\theta$, respectively. For transitions originating from the Zeeman eigenstates M_Ω' of the $X\,^3\Sigma^-$ term, and terminating in the $|^3\Pi_\sigma M_S\rangle$ of $A\,^3\Pi$, these moments are given by eqs (5.4.40) and (5.4.41). The superscript θ indicates that the moment is specified for a particular orientation of the molecule with respect to the field axis (*Z*).

$$\mathbf{A}_0^\theta(^3\Pi_\sigma M_S \leftarrow M_\Omega') = \tfrac{1}{4}(1 + \cos^2\theta)\ \gamma c l\ P_{M_\Omega'} \sum_{M_\Omega} |C_{M_\Omega M_\Omega'}|^2 \times$$
$$(|\langle ^3\Pi_\sigma M_S|m_{+1}|M_\Omega\rangle|^2 + |\langle ^3\Pi_\sigma M_S|m_{-1}|M_\Omega\rangle|^2) \tag{5.4.40}$$

$$\mathbf{C}_0^\theta(^3\Pi_\sigma M_S \leftarrow M_\Omega') = \gamma c l \cos\theta\, P_{M_\Omega'} \sum_{M_\Omega} |C_{M_\Omega M_\Omega'}|^2 \times$$
$$(|\langle ^3\Pi_\sigma M_S|m_{+1}|M_\Omega\rangle|^2 - |\langle ^3\Pi_\sigma M_S|m_{-1}|M_\Omega\rangle|^2) \tag{5.4.41}$$

Here the angle-dependent coefficients $C_{M_\Omega M_\Omega'}$ are defined by eq (5.4.34). The populations $P_{M_\Omega'}$ are computed using eqs (5.4.35) and (5.4.36) after the $C_{M_\Omega M_\Omega'}$ have been found *via* numerical diagonalisation of the Hamiltonian matrix for the ground-state term (Table 5.4.6).

Using the transition moments of Table 5.4.5, expressions for $\mathbf{A}_0^{\theta}({}^3\Pi_\sigma\, M_S \leftarrow M_\Omega')$ and $\mathbf{C}_0^{\theta}({}^3\Pi_\sigma\, M_S \leftarrow M_\Omega')$ can be developed. These and their summations are given in Table 5.4.7. Notice that in the final row of Table 5.4.7, the total absorption moment $\mathbf{A}_0^{\theta}(A\,{}^3\Pi \leftarrow X\,{}^3\Sigma^-)$ is independent of population factors and D, and that the total $\mathbf{C}_0^{\theta}(A\,{}^3\Pi \leftarrow X\,{}^3\Sigma^-)$ is zero.

Table 5.4.7: Zeroth absorption moments ($\mathbf{A}_0^{\theta}$) and C-term contributions ($\mathbf{C}_0^{\theta}$) to the zeroth MCD moment for the $A\,{}^3\Pi \leftarrow X\,{}^3\Sigma^-$ band system of NH/Ar, when $D \neq 0$.[a]

Transition	$\mathbf{A}_0^{\theta}$ [b]	$\mathbf{C}_0^{\theta}$ [c]
${}^3\Pi_\pm\ \pm1$ [d] $\leftarrow {}^3\Sigma^-\, M_\Omega'$	$K_A\, P_{M_\Omega'}\, \lvert C_{\pm1,M_\Omega'}\rvert^2\, \mathcal{M}^2$	$-K_M\, \kappa P_{M_\Omega'}\, \lvert C_{\pm1,M_\Omega'}\rvert^2\, \mathcal{M}^2$
${}^3\Pi_\mp\ \pm1$ [d] $\leftarrow {}^3\Sigma^-\, M_\Omega'$	$K_A\, P_{M_\Omega'}\, \lvert C_{\pm1,M_\Omega'}\rvert^2\, \mathcal{M}^2$	$K_M\, \kappa P_{M_\Omega'}\, \lvert C_{\pm1,M_\Omega'}\rvert^2\, \mathcal{M}^2$
${}^3\Pi_\pm\ 1$ [e] $\leftarrow {}^3\Sigma^-$	$K_A\, \mathcal{M}^2 \sum_{M_\Omega'} P_{M_\Omega'} \times$ $(\lvert C_{-1,M_\Omega'}\rvert^2 + \lvert C_{+1,M_\Omega'}\rvert^2)$	$\pm\tfrac{1}{2}\gamma c l \cos\theta\, \kappa\, \mathcal{M}^2 \times$ $\sum_{M_\Omega'} P_{M_\Omega'}\, (\lvert C_{-1,M_\Omega'}\rvert^2 - \lvert C_{+1,M_\Omega'}\rvert^2)$
${}^3\Pi_\pm\ 0$ [d] $\leftarrow {}^3\Sigma^-\, M_\Omega'$	$K_A\, P_{M_\Omega'}\, \lvert C_{0,M_\Omega'}\rvert^2\, \mathcal{M}^2$	0
${}^3\Pi_\pm\ 0$ [e] $\leftarrow {}^3\Sigma^-$	$K_A\, \mathcal{M}^2 \sum_{M_\Omega'} P_{M_\Omega'}\, \lvert C_{0,M_\Omega'}\rvert^2$	0
$A\,{}^3\Pi \leftarrow X\,{}^3\Sigma^-$	$\tfrac{1}{4}\gamma c l\, (1 + \cos^2\theta)\, \mathcal{M}^2$	0

[a] $C_{i,j}$ coefficients and populations are computed numerically after diagonalisation of the ground-state Hamiltonian matrix shown in Table 5.4.6.

[b] $K_A = \gamma c l\, (1 + \cos^2\theta)\, /\, 8$.

[c] $K_M = \gamma c l \cos\theta\, /\, 2$.

[d] Notation is ${}^3\Pi_\sigma\, M_S$.

[e] Notation is ${}^3\Pi_\sigma\, S$.

Next, the B-term contributions ($\mathbf{B}_0^{\theta}$) to the zeroth MCD moment are evaluated. The only important interactions are taken to be those between states of the $A\,{}^3\Pi$ excited term, because both the $X\,{}^3\Sigma^-$ and $A\,{}^3\Pi$ terms are well separated from other terms.[7] From Table 5.4.4 it can be seen that $L_z + g_e S_z$ mixes states with the same M_S in the raised and lowered SO-CF levels, while $L_x + g_e S_x$ mixes states which differ by $\Delta M_S = \pm1$, both within and between the SO-CF levels. Denoting the ground-state level $|{}^3\Sigma^-\, M_\Omega'\rangle$ as $|i\rangle$, the excited-state level $|{}^3\Pi_\sigma\, M_S\rangle$ as $|j\rangle$, and the states with which mixing occurs as $|k\rangle$, the zeroth MCD moment due to B terms ($\mathbf{B}_0$) in the *laboratory* reference frame (using eqs (3.4.14), (3.4.18) and (3.5.6)) is,

$$\mathbf{B}_0(j \leftarrow i) = -2\gamma c l \mu_B B \, \mathcal{R}e \sum_{k \neq j} P_i \frac{\langle j|L_Z + g_e S_Z|k\rangle}{E_k - E_j} (\langle k|M_{+1}|i\rangle \langle j|M_{+1}|i\rangle^* - \langle k|M_{-1}|i\rangle \langle j|M_{-1}|i\rangle^*) \qquad (5.4.42)$$

Here L_Z, S_Z, M_{+1} and M_{-1} are operators in the laboratory frame that must be converted to the molecular reference frame using the method described in Section 3.4.3.2. The expressions derived are (since $m_0 = 0$ for NH/Ar),

$$L_Z + g_e S_Z = \cos\theta\,(L_z + g_e S_z) + \sin\theta\,(L_x + g_e S_x) \qquad (5.4.43)$$

$$|\langle j|M_{+1}|i\rangle|^2 - |\langle j|M_{-1}|i\rangle|^2 = \cos\theta\,(|\langle j|m_{+1}|i\rangle|^2 - |\langle j|m_{-1}|i\rangle|^2) \qquad (5.4.44)$$

where L_z, S_z, L_x, S_x, m_{+1} and m_{-1} are operators in the molecular frame.

A general analytical expression for $\mathbf{B}_0^{\theta}(j \leftarrow i)$ and various sums are given in Table 5.4.8. (Tables 5.4.4 and 5.4.5, and the fact that the transition moments are real, have been used.)

Table 5.4.8: *B*-term contributions ($\mathbf{B}_0^{\theta}$) to the zeroth MCD moment for the $A\,^3\Pi \leftarrow X\,^3\Sigma^-$ band system of NH/Ar, when $D \neq 0$.[a]

Transition	$\mathbf{B}_0^{\theta}$
$^3\Pi_-\,\pm1$ [b] $\leftarrow {}^3\Sigma^-\,M_{\Omega'}$	$2K_M \mu_B B \, \mathcal{m}^2 P_{M_{\Omega'}} [-\frac{\cos\theta\,\eta^2\Lambda}{\Delta} \lvert C_{\pm1,M_{\Omega'}}\rvert^2 + \frac{\sin\theta\, g_e}{\sqrt{2}\,\zeta_\pi} C_{\pm1,M_{\Omega'}} C_{0,M_{\Omega'}}]$
$^3\Pi_-\,1$ [c] $\leftarrow {}^3\Sigma^-\,M_{\Omega'}$	$2K_M \mu_B B \, \mathcal{m}^2 P_{M_{\Omega'}} [-\frac{\cos\theta\,\eta^2\Lambda}{\Delta} (\lvert C_{-1,M_{\Omega'}}\rvert^2 + \lvert C_{+1,M_{\Omega'}}\rvert^2) + \frac{\sin\theta\, g_e}{\sqrt{2}\,\zeta_\pi} C_{0,M_{\Omega'}} (C_{-1,M_{\Omega'}} + C_{+1,M_{\Omega'}})]$
$^3\Pi_\pm\,0$ [b] $\leftarrow {}^3\Sigma^-\,M_{\Omega'}$	$2K_M \mu_B B \, \mathcal{m}^2 P_{M_{\Omega'}} [\pm\frac{\cos\theta\,\Lambda}{V} \lvert C_{0,M_{\Omega'}}\rvert^2 - \frac{\sin\theta}{\sqrt{2}\,\zeta_\pi} C_{0,M_{\Omega'}} (C_{+1,M_{\Omega'}} + C_{-1,M_{\Omega'}})]$
$^3\Pi_\pm\,0$ [c] $\leftarrow {}^3\Sigma^-\,M_{\Omega'}$	$2K_M \mu_B B \, \mathcal{m}^2 P_{M_{\Omega'}} [\pm\frac{\cos\theta\,\Lambda}{V} \lvert C_{0,M_{\Omega'}}\rvert^2 - \frac{\sin\theta}{\sqrt{2}\,\zeta_\pi} C_{0,M_{\Omega'}} (C_{+1,M_{\Omega'}} + C_{-1,M_{\Omega'}})]$
$^3\Pi_+\,\pm1$ [b] $\leftarrow {}^3\Sigma^-\,M_{\Omega'}$	$2K_M \mu_B B \, \mathcal{m}^2 P_{M_{\Omega'}} [\frac{\cos\theta\,\eta^2\Lambda}{\Delta} \lvert C_{\pm1,M_{\Omega'}}\rvert^2 + \frac{\sin\theta\, g_e}{\sqrt{2}\,\zeta_\pi} C_{\pm1,M_{\Omega'}} C_{0,M_{\Omega'}}]$
$^3\Pi_+\,1$ [c] $\leftarrow {}^3\Sigma^-\,M_{\Omega'}$	$2K_M \mu_B B \, \mathcal{m}^2 P_{M_{\Omega'}} [\frac{\cos\theta\,\eta^2\Lambda}{\Delta} (\lvert C_{-1,M_{\Omega'}}\rvert^2 + \lvert C_{+1,M_{\Omega'}}\rvert^2) + \frac{\sin\theta\, g_e}{\sqrt{2}\,\zeta_\pi} C_{0,M_{\Omega'}} (C_{-1,M_{\Omega'}} + C_{+1,M_{\Omega'}})]$

[a] $K_M = \gamma c l \cos\theta / 2$. $C_{i,j}$ coefficients and populations are computed numerically after diagonalisation of the ground-state Hamiltonian matrix shown in Table 5.4.6.

[b] Notation is $^3\Pi_\sigma\,M_S$.

[c] Notation is $^3\Pi_\sigma\,S$.

Now the first MCD moment $\mathbf{M}_1^\theta$ is considered. Since there are multiple component transitions i, both $\mathbf{M}_0^\theta(i)$ (= $\mathbf{B}_0^\theta(i)$ + $\mathbf{C}_0^\theta(i)$; eq (3.5.6)) and $\mathbf{M}_1^\theta(i)$ must be accounted for (eq (3.5.13)). First, A terms are treated by defining the angle-dependent components $\mathbf{A}_1^\theta({}^3\Pi_\sigma S \leftarrow {}^3\Sigma^-)$, which contribute to $\mathbf{M}_1^\theta$ as shown in eq (3.5.8). $\mathbf{A}_1^\theta({}^3\Pi_\sigma S \leftarrow {}^3\Sigma^-)$ is evaluated according to eq (5.4.45), where it is noted that they are formed by summing the individual $\mathbf{C}_0^\theta({}^3\Pi_\sigma M_S \leftarrow M_\Omega')$ of Table 5.4.7.

$$\mathbf{A}_1^\theta({}^3\Pi_\sigma S \leftarrow {}^3\Sigma^-) = \sum_{M_S}\sum_{M_\Omega'} \mathbf{C}_0^\theta({}^3\Pi_\sigma M_S \leftarrow M_\Omega')(E_B({}^3\Pi_\sigma M_S) - E_B(M_\Omega')) \quad (5.4.45)$$

Here, $E_B({}^3\Pi_\sigma M_S)$ and $E_B(M_\Omega')$ are the Zeeman shifts in the excited and ground terms, respectively. The results are,

$$\mathbf{A}_1^\theta({}^3\Pi_\pm 1 \leftarrow {}^3\Sigma^-) = \pm\tfrac{1}{2}\gamma c l\, \kappa \cos^2\theta\, |\mathcal{M}|^2 \times$$
$$\left[g_\parallel^\pm \mu_B B \sum_{M_\Omega'} P_{M_\Omega'} (|C_{-1,M_\Omega'}|^2 + |C_{+1,M_\Omega'}|^2) - \right.$$
$$\left. \sum_{M_\Omega'} P_{M_\Omega'} E_B(M_\Omega') (|C_{-1,M_\Omega'}|^2 - |C_{+1,M_\Omega'}|^2)\right] \quad (5.4.46a)$$

$$\mathbf{A}_1^\theta({}^3\Pi_\pm 0 \leftarrow {}^3\Sigma^-) = 0 \quad (5.4.46b)$$

where $g_\parallel^\pm$ is given by eq (5.4.30). The total A-term contribution to $\mathbf{M}_1^\theta$ is simply the sum over the component bands (eq (3.5.13) in eq (5.4.46); *i.e.*,

$$\mathbf{A}_1^\theta(A\,{}^3\Pi \leftarrow X\,{}^3\Sigma^-) = \gamma c l \mu_B B\, \Lambda\kappa^2 \cos\theta\, |\mathcal{M}|^2 \sum_{M_\Omega'} P_{M_\Omega'} (|C_{-1,M_\Omega'}|^2 + |C_{+1,M_\Omega'}|^2) \quad (5.4.47)$$

The expression for $\mathbf{M}_1^\theta$ obtained by integration over the whole band system is (eq (3.5.13)),

$$\mathbf{M}_1^\theta(A\,{}^3\Pi \leftarrow X\,{}^3\Sigma^-) = \mathbf{A}_1^\theta(A\,{}^3\Pi \leftarrow X\,{}^3\Sigma^-) + \sum_I (\mathbf{B}_0^\theta(I) + \mathbf{C}_0^\theta(I))\,\Delta_I \quad (5.4.48)$$

where the sum is over the I individual Zeeman transition components of $\mathbf{C}_0^\theta$ and $\mathbf{B}_0^\theta$ (Tables 5.4.7 and 5.4.8, respectively) and Δ_I is the energy shift from $\bar{E}$. Hence,

$$\mathbf{M}_1^\theta(A\,{}^3\Pi \leftarrow X\,{}^3\Sigma^-) = \gamma c l \cos\theta\, |\mathcal{M}|^2 \left[\Lambda\mu_B B \cos\theta + \right.$$
$$\left. \zeta_\pi \sum_{M_\Omega'} P_{M_\Omega'} (|C_{-1,M_\Omega'}|^2 - |C_{+1,M_\Omega'}|^2)\right] \quad (5.4.49)$$

Eq (5.4.49) must be treated numerically, unless $\theta = 0$, whence,

$$\mathbf{M}_1^0(A\,^3\Pi \leftarrow X\,^3\Sigma^-) = \gamma c l\,|m|^2\,[\Lambda\mu_B B + \zeta_\pi\,(P_{-1} - P_{+1})] \qquad (5.4.50)$$

since $C_{-1,-1'} = C_{+1,+1'} = 1$ are the only non-zero coefficients in eq (5.4.34). The populations are those of the pure M_Ω states; *i.e.* they are given by the P_{M_Ω} of eq (5.4.37). The term $P_{-1} - P_{+1}$ is given by eq (5.4.38). Calculating $\mathbf{A}_0^0$ from the last line of Table 5.4.7 gives,

$$\mathbf{M}_1^0/\mathbf{A}_0^0(A\,^3\Pi \leftarrow X\,^3\Sigma^-) = 2\,[\Lambda\mu_B B + \zeta_\pi\,(P_{-1} - P_{+1})] \qquad (5.4.51)$$

It is far more likely that NH radicals are randomly oriented in Ar matrices, so $\mathbf{A}_0^\theta$ and $\mathbf{M}_1^\theta$ are averaged over θ (Section 3.4.3.2). Averaging of the individual component transitions of Tables 5.4.7 and 5.4.8 and eq (5.4.46) can only be achieved numerically.

However, it is possible to obtain analytical averages for the zeroth moments over the whole band system. The bottom line of Table 5.4.7 yields,

$$\bar{\mathbf{A}}_0(A\,^3\Pi \leftarrow X\,^3\Sigma^-) = \tfrac{1}{3}\gamma c l\,|m|^2 \qquad (5.4.52)$$

and,

$$\bar{\mathbf{M}}_0(A\,^3\Pi \leftarrow X\,^3\Sigma^-) = 0 \qquad (5.4.53)$$

$\bar{\mathbf{M}}_1$ is found by averaging eq (5.4.49), which yields,

$$\bar{\mathbf{M}}_1(A\,^3\Pi \leftarrow X\,^3\Sigma^-) = \gamma c l\,|m|^2\,[\tfrac{1}{3}\Lambda\mu_B B + \tfrac{1}{2}\zeta_\pi \int_0^1 \cos\theta \sum_{M_\Omega'} P_{M_\Omega'}\,(|C_{-1,M_\Omega}|^2 - |C_{+1,M_\Omega}|^2)\,\mathrm{d}\cos\theta\,] \qquad (5.4.54)$$

which can only be evaluated by numerical diagonalisation and integration. The ratio $\bar{\mathbf{M}}_1/\bar{\mathbf{A}}_0$ is then,

$$\bar{\mathbf{M}}_1/\bar{\mathbf{A}}_0(A\,^3\Pi \leftarrow X\,^3\Sigma^-) = \Lambda\mu_B B + \frac{3}{2}\zeta_\pi \int_0^1 \cos\theta \sum_{M_\Omega'} P_{M_\Omega'}\,(|C_{-1,M_\Omega}|^2 - |C_{+1,M_\Omega}|^2)\,\mathrm{d}\cos\theta \qquad (5.4.55)$$

It is this equation that is used to extract best-fit values for D and ζ_π (Section 5.5.1) from all the NH/Ar and ND/Ar data illustrated in Figures 5.3.5 and 5.3.7 and Figures 5.3.6 and 5.3.8, respectively.

It is interesting (though perhaps of little practical use) to note that in the linear limit, and when $\theta = 0$, eq (5.4.55) reduces to a relatively simple analytical expression,

$$\mathbf{M}_1^0/\mathbf{A}_0^0(A\,^3\Pi \leftarrow {}^3\Sigma^-)_{\text{Lin. limit}} \approx 2\mu_B B\left[\Lambda + \frac{2g_e\zeta_\pi}{(\exp(D/3kT)+2)\,kT}\right] \qquad (5.4.56)$$

Here, eq (5.4.39) has been utilised. This final equation provides a check against the standard equation, and confirms the absence of errors in the preceding algebra.

Special case: D = 0

Now the special case is considered where $D = 0$. (This section pre-empts Section 5.5.1, which shows that near-best fits are obtained using $D = 0$.) This scenario affords major simplifications to many of the general equations, as will be demonstrated below, since analytical angle-dependent wavefunctions are obtained.

The ground-state Zeeman splitting is now obtained by solving the secular equation arising from Table 5.4.6 with $D = 0$, giving (independent of θ),

$$E_B(0') = 0 \qquad (5.4.57a)$$

$$E_B(\pm 1') = \pm g_e\mu_B B \approx \pm 2\mu_B B \qquad (5.4.57b)$$

The eigenvalues show the near-isotropy of the $X\,^3\Sigma^-$ term in the Zeeman effect. The (normalised) wavefunctions are still θ dependent, but have simple forms;

$$|^3\Sigma^-\,0'\rangle = \cos\theta\,|^3\Sigma^-\,0\rangle - \tfrac{1}{\sqrt{2}}\sin\theta\,[|^3\Sigma^-\,{-1}\rangle + |^3\Sigma^-\,{+1}\rangle] \qquad (D=0) \qquad (5.4.58a)$$

$$|^3\Sigma^-\,\pm 1'\rangle = \tfrac{1}{\sqrt{2}}\sin\theta\,[|^3\Sigma^-\,0\rangle \mp \tfrac{1}{\sqrt{2}}\sin\theta\,((1\pm\cos\theta)^{-1}\,|^3\Sigma^-\,{-1}\rangle - (1\mp\cos\theta)^{-1})\,|^3\Sigma^-\,{+1}\rangle] \qquad (D=0) \qquad (5.4.58b)$$

Note that when $\theta = 0$, the $|^3\Sigma^-\,M_\Omega'\rangle$ reduce to the $|^3\Sigma^-\,M_\Omega\rangle$ of the right-hand side, as required.

Using eq (5.4.57), the fractional Boltzmann population $P_{M_\Omega'}$ of the M_Ω' state is given by eq (5.4.59).

$$P_{M_\Omega'} = \frac{1}{Q}\exp\left(\frac{M_\Omega'\,g_e\mu_B B}{kT}\right) \qquad (D=0) \qquad (5.4.59)$$

where Q, the partition function, is now,

$$Q = \sum_{M_\Omega} P_{M_\Omega'} = 1 + 2\cosh\left(\frac{g_e\mu_B B}{kT}\right) \qquad (D=0) \qquad (5.4.60)$$

A useful relationship for the MCD is,

$$P_{-1} - P_{+1} = \frac{2\sinh\left(\frac{g_e\mu_B B}{kT}\right)}{1 + 2\cosh\left(\frac{g_e\mu_B B}{kT}\right)} \qquad (D = 0) \qquad (5.4.61)$$

In the linear limit,[14] $\sinh(x) \to x$ and $\cosh(x) \to 1$, yielding,

$$P_{-1} - P_{+1} = \frac{2g_e\mu_B B}{3kT} \qquad (D = 0) \qquad (5.4.62)$$

Now the moment expressions for the case $D = 0$ are considered. The coefficients $C_{M_\Omega M_\Omega'}$ defined by eq (5.4.34) have a practically applicable analytical form, and linear combinations provide significant simplifications from the case $D \neq 0$. Using the following relations,

$$\sum_{M_\Omega'} P_{M_\Omega'} \left(|C_{-1,M_\Omega}|^2 + |C_{+1,M_\Omega}|^2\right) = \tfrac{1}{2}\left[1 + \cos^2\theta + P_0(1 - 3\cos^2\theta)\right] \qquad (5.4.63a)$$

$$\sum_{M_\Omega'} P_{M_\Omega'} |C_{0,M_\Omega}|^2 = \tfrac{1}{2}\left[\sin^2\theta + P_0(2 - 3\sin^2\theta)\right] \qquad (5.4.63b)$$

$$\sum_{M_\Omega'} P_{M_\Omega'} \left(|C_{-1,M_\Omega}|^2 - |C_{+1,M_\Omega}|^2\right) = (P_{-1} - P_{+1})\cos\theta \qquad (5.4.63c)$$

the expressions for $\mathbf{A}_0^\theta({}^3\Pi_\sigma\, M_S \leftarrow M_\Omega')$ and $\mathbf{C}_0^\theta({}^3\Pi_\sigma\, M_S \leftarrow M_\Omega')$ shown in Table 5.4.7 become those of Table 5.4.9.

Likewise, the expressions for B terms given in Table 5.4.8 can be simplified using eq (5.4.63a) and,

$$\sum_{M_\Omega'} P_{M_\Omega'} C_{0,M_\Omega'} \left(C_{-1,M_\Omega'} + C_{+1,M_\Omega'}\right) = \frac{\sin\theta\cos\theta}{\sqrt{2}}\left[3P_0 - 1\right] \qquad (5.4.64)$$

The result is, in $|{}^3\Pi_\pm\, S\rangle$ notation,

$$\mathbf{B}_0^\theta({}^3\Pi_\pm\, 1 \leftarrow {}^3\Sigma^-)^{D=0} = \tfrac{1}{2}\gamma c l\mu_B B \cos^2\theta\, |m|^2 \left[\pm\frac{\eta^2\Lambda}{\Delta}\left(1 + \cos^2\theta + P_0(1 - 3\cos^2\theta)\right)\right.$$
$$\left. - \frac{g_e}{\zeta_\pi}\sin^2\theta\,(1 - 3P_0)\right] \qquad (5.4.65a)$$

$$\mathbf{B}_0^\theta({}^3\Pi_\pm\, 0 \leftarrow {}^3\Sigma^-)^{D=0} = \tfrac{1}{2}\gamma c l\mu_B B \cos^2\theta\, |m|^2 \left[\pm\frac{\Lambda}{V}\left(\sin^2\theta + P_0(2 - 3\sin^2\theta)\right)\right.$$
$$\left. + \frac{g_e}{\zeta_\pi}\sin^2\theta\,(1 - 3P_0)\right] \qquad (5.4.65b)$$

When $D = 0$, the $\mathbf{A}_1^\theta({}^3\Pi_\pm\, 1 \leftarrow {}^3\Sigma^-)$ of eq (5.4.46) become,

Table 5.4.9: Zeroth absorption moments $\mathbf{A}_0^\theta$ and C-term contributions ($\mathbf{C}_0^\theta$) to the zeroth MCD moment for the $A\,^3\Pi \leftarrow X\,^3\Sigma^-$ band system of NH/Ar, when $D = 0$.[a]

Transition	$\mathbf{A}_0^{\theta}$ [b]	$\mathbf{C}_0^{\theta}$ [c]
$^3\Pi_\pm$ ±1 [d] $\leftarrow {}^3\Sigma^-$ M_Ω'	$K_A P_{M_\Omega} \lvert C_{\pm1,M_\Omega'}\rvert^2 \lvert m\rvert^2$	$-K_M \kappa P_{M_\Omega} \lvert C_{\pm1,M_\Omega'}\rvert^2 \lvert m\rvert^2$
$^3\Pi_\mp$ ±1 [d] $\leftarrow {}^3\Sigma^-$ M_Ω'	$K_A P_{M_\Omega} \lvert C_{\pm1,M_\Omega'}\rvert^2 \lvert m\rvert^2$	$K_M \kappa P_{M_\Omega} \lvert C_{\pm1,M_\Omega'}\rvert^2 \lvert m\rvert^2$
$^3\Pi_\pm$ 1 [e] $\leftarrow {}^3\Sigma^-$	$\frac{1}{2}K_A \lvert m\rvert^2 (1 + \cos^2\theta + P_0 (1 - 3\cos^2\theta))$	$\pm\frac{1}{2}\gamma c l \cos^2\theta \kappa \lvert m\rvert^2 (P_{-1} - P_{+1})$
$^3\Pi_\pm$ 0 [d] $\leftarrow {}^3\Sigma^-$ M_Ω'	$K_A P_{M_\Omega} \lvert C_{0,M_\Omega'}\rvert^2 \lvert m\rvert^2$	0
$^3\Pi_\pm$ 0 [e] $\leftarrow {}^3\Sigma^-$	$\frac{1}{2}K_A \lvert m\rvert^2 (\sin^2\theta + P_0 (2 - 3\sin^2\theta))$	0
$A\,^3\Pi \leftarrow X\,^3\Sigma^-$	$\frac{1}{4}\gamma c l (1 + \cos^2\theta) \lvert m\rvert^2$	0

[a] $C_{i,j}$ coefficients have the analytical form given in eq (5.4.58). Populations are obtained from eq (5.4.59).
[b] $K_A = \gamma c l (1 + \cos^2\theta) / 8$.
[c] $K_M = \gamma c l \cos\theta / 2$.
[d] Notation is $^3\Pi_\sigma M_S$.
[e] Notation is $^3\Pi_\sigma S$.

$$\mathbf{A}_1^\theta(^3\Pi_\pm\, 1 \leftarrow {}^3\Sigma^-)^{D=0} = \tfrac{1}{4}\gamma c l \mu_B B \kappa \cos^2\theta \lvert m\rvert^2 \times$$

$$[\kappa\Lambda(1 + \cos^2\theta + P_0 (1 - 3\cos^2\theta)) \pm g_e \sin^2\theta (1 - 3P_0)] \qquad (5.4.66a)$$

$$\mathbf{A}_1^\theta(^3\Pi_\pm\, 0 \leftarrow {}^3\Sigma^-)^{D=0} = 0 \qquad (5.4.66b)$$

Here eqs (5.4.63a) and (5.4.67) have been used, and the fact that $P_{M_\Omega'} = P_{M_\Omega}$.

$$P_1(\lvert C_{1,1'}\rvert^2 - \lvert C_{-1,1'}\rvert^2) - P_{-1}(\lvert C_{1,-1'}\rvert^2 - \lvert C_{-1,-1'}\rvert^2) = \cos\theta (1 - P_0) \qquad (5.4.67)$$

$\mathbf{A}_1^\theta$ for the whole band system (eq (5.4.47)) is then,

$$\mathbf{A}_1^\theta(A\,^3\Pi \leftarrow X\,^3\Sigma^-)^{D=0} = \tfrac{1}{2}\gamma c l \mu_B B \Lambda\kappa^2 \cos^2\theta \lvert m\rvert^2 \times$$

$$[1 + \cos^2\theta + P_0 (1 - 3\cos^2\theta)] \qquad (5.4.68)$$

$\mathbf{M}_1^\theta$ may be obtained from eq (5.4.49),

$$\mathbf{M}_1^\theta(A\,^3\Pi \leftarrow X\,^3\Sigma^-)^{D=0} = \gamma c l \cos^2\theta \lvert m\rvert^2 [\Lambda\mu_B B + \zeta_\pi (P_{-1} - P_{+1})] \qquad (5.4.69)$$

where eq (5.4.63c) has been used.

The moment ratio $\mathbf{M}_1/\mathbf{A}_0$ can be determined for any angle θ, by using eq (5.4.69) and the expression for $\mathbf{A}_0^{\theta}(^3\Pi \leftarrow {}^3\Sigma^-)$ in Table 5.4.7. If NH is *Z*-oriented, eq (5.4.51) gives $\mathbf{M}_1^0/\mathbf{A}_0^0$, and the $P_{-1} - P_{+1}$ term is given by eq (5.4.61).

Now orientational averaging of the NH radical is treated. The analytical form of the $C_{M_\Omega M_{\Omega'}}$ (eq (5.4.34)) in eq (5.4.58) allow orientationally averaged parameters for the component bands to be derived, and they are given in Table 5.4.10.

Table 5.4.10: Orientationally averaged parameters for component bands in the $A\ ^3\Pi \leftarrow X\ ^3\Sigma^-$ band system of NH/Ar, when $D = 0$.

Parameter	Transition	Value
$\bar{\mathbf{A}}_0$	$^3\Pi_\pm\ 1 \leftarrow {}^3\Sigma^-$	$\frac{1}{60}\gamma c l \lvert m \rvert^2 (7 - P_0)$
	$^3\Pi_\pm\ 0 \leftarrow {}^3\Sigma^-$	$\frac{1}{60}\gamma c l \lvert m \rvert^2 (3 + P_0)$
$\bar{\mathbf{C}}_0$	$^3\Pi_\pm\ 1 \leftarrow {}^3\Sigma^-$	$\pm\frac{1}{6}\gamma c l\ \kappa \lvert m \rvert^2 (P_{-1} - P_{+1})$
	$^3\Pi_\pm\ 0 \leftarrow {}^3\Sigma^-$	0
$\bar{\mathbf{B}}_0$	$^3\Pi_\pm\ 1 \leftarrow {}^3\Sigma^-$	$\pm\frac{1}{15}\gamma c l \mu_B B \lvert m \rvert^2 \left[\frac{\eta^2 \Lambda}{\Delta}(4 - 2P_0) \mp \frac{g_e}{\zeta_\pi}(1 - 3P_0)\right]$
	$^3\Pi_\pm\ 0 \leftarrow {}^3\Sigma^-$	$\pm\frac{1}{15}\gamma c l \mu_B B \lvert m \rvert^2 \left[\frac{\Lambda}{V}(1 + 2P_0) \pm \frac{g_e}{\zeta_\pi}(1 - 3P_0)\right]$
$\bar{\mathbf{A}}_1$	$^3\Pi_\pm\ 1 \leftarrow {}^3\Sigma^-$	$\frac{1}{30}\gamma c l \mu_B B\ \kappa \lvert m \rvert^2 [\kappa\Lambda(4 - P_0) \pm g_e(1 - 3P_0)]$
	$^3\Pi_\pm\ 0 \leftarrow {}^3\Sigma^-$	0

Averaging over the entire band system sees $\bar{\mathbf{M}}_1/\bar{\mathbf{A}}_0$ takes a much simpler form than that of eq (5.4.55),

$$\bar{\mathbf{M}}_1/\bar{\mathbf{A}}_0(A\ ^3\Pi \leftarrow X\ ^3\Sigma^-)^{D=0} = [\Lambda\mu_B B + \zeta_\pi (P_{-1} - P_{+1})] \qquad (5.4.70)$$

or half the value for *Z*-oriented NH given in eq (5.4.50). (The expression for $P_{-1} - P_{+1}$ is given by eq (5.4.61).)

Invoking the linear limit[14] yields eq (5.4.62) for all θ, which upon substitution into eq (5.4.50) yields,

$$\mathbf{M}_1^0/\mathbf{A}_0^0(A\ ^3\Pi \leftarrow X\ ^3\Sigma^-)^{D=0}_{\text{Lin. limit}} \approx 2\ \mu_B B\left[\Lambda + \frac{2 g_e \zeta_\pi}{3kT}\right] \qquad (5.4.71)$$

in the *Z*-oriented case, and

$$\bar{\mathbf{M}}_1/\bar{\mathbf{A}}_0(A\,^3\Pi \leftarrow X\,^3\Sigma^-)^{D=0}_{\text{Lin. limit}} \approx \mu_B B\left[\Lambda + \frac{2g_e\zeta_\pi}{3kT}\right] \qquad (5.4.72)$$

when the NH molecules are randomly oriented. Note again that $\bar{\mathbf{M}}_1/\bar{\mathbf{A}}_0$ is half that of $\mathbf{M}_1^0/\mathbf{A}_0^0$.

Finally, it is re-emphasised that the overall expressions for $\mathbf{A}_0$, $\mathbf{M}_1$ and $\mathbf{M}_1/\mathbf{A}_0$ are all independent of the choice of excited-state basis. However, although the *overall* moment is insensitive to this choice, fine-structure changes occur with inclusion of a CF (there are four $A\,^3\Pi \leftarrow X\,^3\Sigma^-$ transitions as opposed to three in the absence of a CF), and consequently the component bands have differing moments. In the absence of a CF (the SO-only case), the appropriate moments for individual bands may be derived from those presented in this section by letting $V = 0$.

5.5. Data analysis and discussion

The two parts of this section are as follows. First, the SO coupling constant ζ_π of the $A\,^3\Pi$ term, and the ZFS D of the $X\,^3\Sigma^-$ term are determined for NH/Ar and ND/Ar by performing moment analysis over the entire $A\,^3\Pi \leftarrow X\,^3\Sigma^-$ band system. Second, possible sources of structure are discussed.

5.5.1. Ground- and excited-state ZFS in NH/Ar and ND/Ar

The moment ratio given by eq (5.4.55), is a function of only three independent parameters, one of which is the angle θ. The second is the SOC constant, ζ_π, of the $A\,^3\Pi$ term, and the third is the ZFS, D, of the $X\,^3\Sigma^-$ ground term.

Complete orientational disorder was assumed (and is justified in Section 5.5.2). ζ_π and D were varied to obtain the best fit to the data of Figures 5.3.5 and 5.3.7 for NH/Ar, and Figures 5.3.6 and 5.3.8 for ND/Ar. Standard steepest-descent methods were employed. Matrix diagonalisations and integral evaluations were achieved numerically for each value of θ. The best-fit values extracted by simultaneously fitting temperature- and field-dependence data for NH/Ar and ND/Ar are summarised in Table 5.5.1, and yield the full curves shown in Figures 5.3.5 to 5.3.8.

Fits obtained by fixing D at the gas-phase value (1.67 and 1.79 cm^{-1} for NH and ND, respectively[6]), and at zero, and optimising ζ_π are also given in Table 5.5.1. These

Table 5.5.1: Parameters extracted using moment analysis over the entire $A\,^3\Pi \leftarrow X\,^3\Sigma^-$ band system of NH/Ar and ND/Ar.

Parameter	NH (gas) [a]	NH/Ar		
		Best fit	Fit with $D = 0$	Fit with gas-phase D
D / cm^{-1}	1.67	-0.08 ± 0.03	0 (fixed)	1.67 (fixed)
ζ_π / cm^{-1}	34.79	33.5 ± 0.3	33.9 ± 0.5	48.2 ± 6.4
SSR [b]	—	1.57	1.66	104

Parameter	ND (gas) [a]	ND/Ar		
		Best fit	Fit with $D = 0$	Fit with gas-phase D
D / cm^{-1}	1.79	-0.02 ± 0.06	0 (fixed)	1.79 (fixed)
ζ_π / cm^{-1}	34.58	37.1 ± 1.0	37.2 ± 1.0	55.4 ± 7.2
SSR [b]	—	3.20	3.20	90

[a] Ref. 6.

[b] Sum-of-squared residuals from non-linear least-squares fit to the data.

fits are illustrated in Figures 5.3.5 to 5.3.8 as the dotted and dashed curves, respectively. Comparison of the best-fit and $D = 0$ curves (Figures 5.3.5 to 5.3.8) reveal that they both provide an accurate representation of the experimental magnetisation behaviour *and* the temperature dependence. The fits obtained using the gas-phase D values are very poor. Hence for NH/Ar and ND/Ar it can only be concluded that the ground-term ZFS is essentially completely quenched in the matrix. The mechanism by which this should occur is not understood. However, Herzberg has commented (p 222 of Ref. 13), without extensive explanation, that "...non-rotating molecule multiplet Σ states are single ...". It therefore seems possible that the observed absence of ZFS in this work is purely a consequence of the fact that spin-spin and second-order SO interactions are not manifest in the lowest rotational level of a $^3\Sigma^-$ term; *i.e.* the rotations are not built on a ZFS splitting in the electronic term, but the ZFS is evident only in higher rotational levels. The results of fitting would then be consistent with the expectation that most of the ground-state NH radicals should be in their lowest rotational (librational) level in an Ar matrix at the temperatures used in this work.

Unlike OH/Ar (Section 4.5.1), ζ_π for NH/Ar is only slightly reduced from its gas-phase value (Table 5.5.1). The value obtained for ND/Ar (Table 5.5.1) is slightly larger than in the gas phase, probably as a consequence of uncertainties in determining the absorption baseline that were not as acute for NH/Ar, because of the sharper structure and greater optical density. It is also possible that some contamination of the ND sample by NH (Section 5.2.2) may have a bearing on this result.

5.5.2. CF splitting and spectral structure

$\mathbf{M}_l$ does not yield any information about CF effects in the $A\,^3\Pi$ term (Section 5.4.6), so the likely magnitude of V can only be determined by considering the structure observed in the spectra. That, along with attempts to assign some of the other structure, is the aim of this section.

5.5.2.1. NH/Ar

CF splitting

For OH/Ar (Chapter 4), $V = 97 \pm 15$ cm^{-1}, and it might be expected that NH/Ar experiences a CF of similar, or perhaps slightly smaller magnitude (since the dipole moment of the $A\,^3\Pi$ term of NH[7] is lower than that of OH $X\,^2\Pi$[18]).

Assuming the SO-CF model is correct, and ignoring (for the moment) vibrational and librational overtones, there will be four bands in the spectra. The two lowest-energy bands should terminate in the $|^3\Pi_-\,\pm1\rangle$ and $|^3\Pi_-\,0\rangle$ states; their separation will be $x = \frac{1}{2}(\Delta - V)$. Using eq (5.4.22), identification of these two bands and measurement of their separation will provide an estimate of V, according to,

$$V = (\zeta_\pi^2 - x^2) / x \qquad (5.5.1)$$

It is tempting to assign bands 1 and 2 (Figure 5.3.1 and Table 5.3.1) to these transitions. Their separation (~13 cm^{-1}) then gives $V \approx 75$ cm^{-1}, slightly lower than for OH/Ar, as predicted above. The reasonableness of these assignments can be tested by using spectral simulations generated from the orientationally averaged absorption and MCD parameters for the individual bands (Table 5.4.10). Computed spectra were generated using Gaussian bandshapes with *ad hoc* widths (HW^1/eM) of 5 cm^{-1} for the $^3\Pi_- \leftarrow {}^3\Sigma^-$ bands, and 30 cm^{-1} for the $^3\Pi_+ \leftarrow {}^3\Sigma^-$ bands. Figures 5.5.1 and 5.5.2 show the simulated MCD temperature dependence (B = 1 T) and magnet-field dependence obtained for NH/Ar using $\zeta_\pi = 33.5$ cm^{-1} and $D = 0$ cm^{-1}. The absorption spectrum corresponds to T = 1.6 K, and shows little temperature dependence.

The simulated spectra in Figures 5.5.1 and 5.5.2 are to be compared with the experimental data in Figures 5.3.1 and 5.3.2, respectively. This reveals a general agreement between theory and experiment. Firstly, the C-term behaviour, a negative

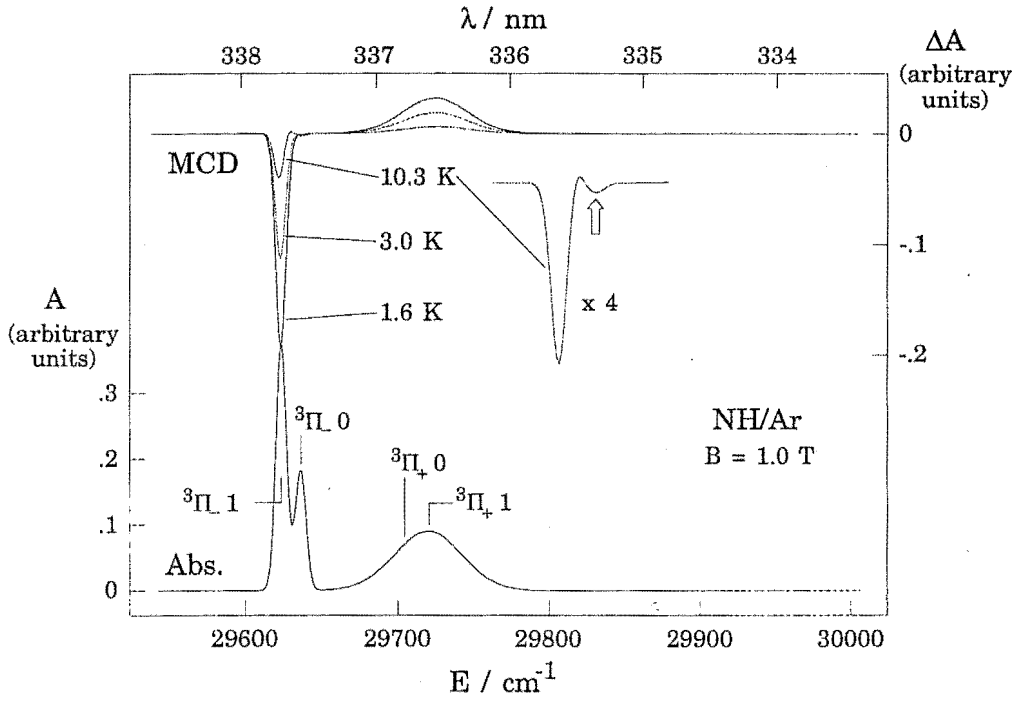

Figure 5.5.1: Simulated MCD (ΔA; top) from 1.6 to 10.3 K (B = 1 T) and absorption (A; bottom) spectrum (T = 1.6 K) of NH/Ar obtained using ζ_π = 33.5 cm^{-1} and D = 0 cm^{-1}. Gaussian bandshapes with *ad hoc* widths (HW^1/*e*M) of 5 cm^{-1} for the $|^3\Pi_- S\rangle \leftarrow |^3\Sigma^-\rangle$ bands, and 30 cm^{-1} for the $|^3\Pi_+ S\rangle \leftarrow |^3\Sigma^-\rangle$ bands have been used. The arrow in the expanded MCD spectrum at T = 10.3 K indicates a negative B term — see text.

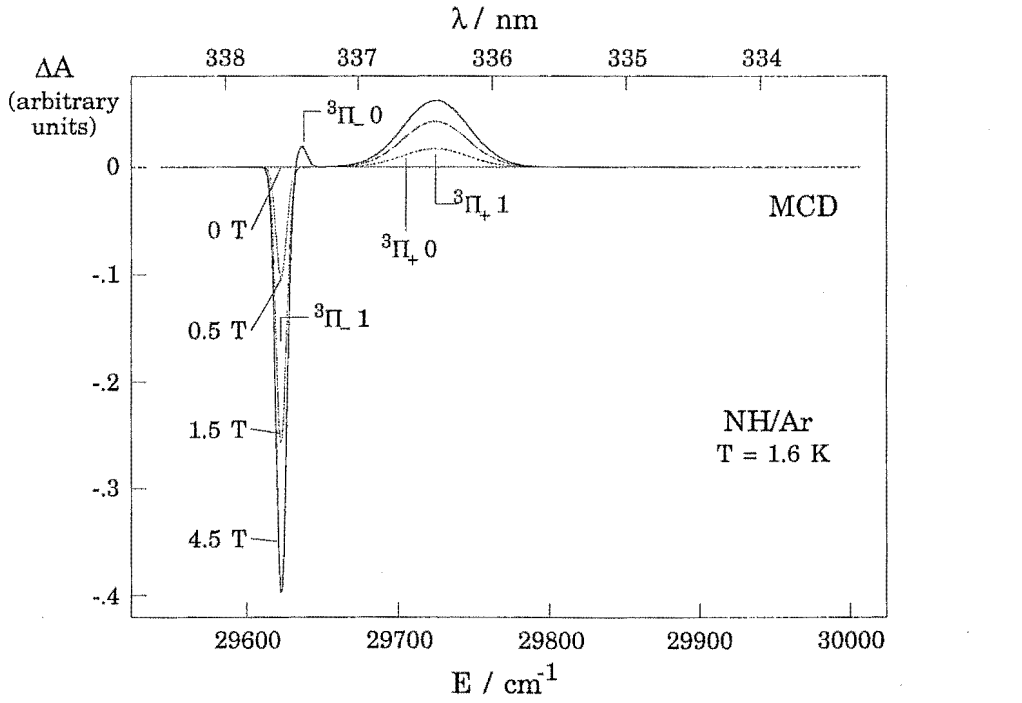

Figure 5.5.2: Simulated MCD magnetic-field dependence of NH/Ar from B = 0 to 4.5 T at T = 1.6 K. See caption for Figure 5.5.1.

band at low energy and a positive band at higher energy, is reproduced, with the correct temperature and field dependencies, as well as the right $\Delta A/A$ ratios. Secondly, the MCD dispersion of the $|^3\Pi_- 1\rangle \leftarrow |^3\Sigma^-\rangle$ band tends to that of an A term at high temperatures. Thirdly, and more subtly, the $|^3\Pi_- 0\rangle \leftarrow |^3\Sigma^-\rangle$ band exhibits a B-term, which shows qualitatively correct temperature and field dependence.

The last point is worthy of further comment, since B terms are usually regarded as being independent of temperature and linearly dependent on magnetic-field strength. In the case of the $|^3\Pi_\pm 0\rangle \leftarrow |^3\Sigma^-\rangle$ transitions of NH/Ar, this situation is changed since the magnitudes of the B terms are partly determined by the populations of the ground-state Zeeman levels (Section 5.4.6); this is made explicitly evident in Table 5.4.10 by the presence of factors that depend on P_0. Consider the transitions terminating in the $|^3\Pi_- 0\rangle$ level which are sharp enough for the (relatively weak) B terms to be resolved. The first term of the relevant expression contains the population factor $-(1 + 2P_0)$, and arises from magnetic-field-induced interaction with the $|^3\Pi_+ 0\rangle$ state *via* the operators L_z and S_z. This gives a negative B term, whose magnitude (in the temperature regime used in these experiments) increases with P_0 as the temperature is increased and/or the field is decreased. That this is the case can be seen by close inspection of the experimental spectra in Figure 5.3.1 for $T > 5$ K, and is even more evident in the higher-temperature (and lower-field) spectra of Figures 5.2.1 and 5.2.2. It is reproduced in the 10.3-K simulated spectrum of Figure 5.5.1, where it is indicated in an expansion by an arrow. The second term contains the population factor $(1 - 3P_0)$, which arises from the combined magnetic-field-induced interactions with the $|^3\Pi_+ 1\rangle$ and $|^3\Pi_- 1\rangle$ states *via* the spin operator S_x. This term produces a positive B term, which increases with decreasing temperature and/or increasing magnetic field. So one would expect the B term to change from negative to positive as temperature is decreased or field is increased, exactly as observed in Figures 5.3.1 and 5.3.2. In the simulations the B term clearly becomes more positive with decreasing temperature and increasing field. At $T = 1.6$ K and $B = 4.5$ T, it looks very much like that observed experimentally.

Despite the optimism of the preceding paragraph, there are significant problems with the details of the simulation. First, the $|^3\Pi_+ 1\rangle \leftarrow |^3\Sigma^-\rangle$ transition is calculated to be coincident with the experimental band 4, whereas the true intensity is spread (predominantly) over bands 3 and 4 (Figures 5.3.1 and 5.3.2). Second, the B-term

intensities for $|^3\Pi_- 0\rangle \leftarrow |^3\Sigma^-\rangle$ are calculated to have quantitatively different field and temperature behaviour than observed experimentally for band 2.

Now consider the possibility that preferential orientation of the NH radical could help to account for some of the discrepancies between the simulated and experimental data. First, it is noted that the molecule can not be oriented perpendicular to the magnetic field, since all *A* and *C* terms would be quenched due to their dependence on $\cos\theta$ (eq 5.4.46 and Table 5.4.7). Hence, only the possibility of *Z*-oriented NH was tested. Non-linear least-squares fitting of the data using eq (5.4.51), gave a sum-of-squared residuals comparable to the randomly oriented result (Table 5.5.1), with $\zeta_\pi \approx 16$ cm^{-1}, which might be considered more in accord with the expectation that the matrix will partially quench SOC. However there are several reasons why this model is unappealing. Firstly, the fit gives a physically unreasonable value for the ground-state ZFS, $D \approx -1$ cm^{-1} (*i.e.*, the $M_S = \pm 1$ levels lie lower than $M_S = 0$; *cf.* Section 5.4.2.3). Secondly, if the radical is *Z*-oriented, then the *B* terms that arise from coupling of the $S = 0$ and $S = 1$ SO-CF levels vanish, since they depend on $\sin\theta$ (Table 5.4.8); hence the positive *B* terms for band 2 at low temperature and high field would not be observed. And finally, a convincing physical mechanism by which preferential orientation along the *Z* axis could occur is difficult to imagine.

In previous work on NH/Ar, Rose[12] (who employed only a SOC model for the $A\ ^3\Pi$ term) suggested that the guest radicals are randomly oriented at high temperatures (>15 K) and become increasingly *Z*-oriented at low temperature (being completely oriented at <1.5 K), but she did not propose a mechanism by which this could occur. More recently Rivoal and co-workers[19] have suggested that Mn_5 clusters (which are relatively large molecules, with potentially large magnetic moments) can be oriented in inert matrices by a magnetic field, because they observed (zero-field) circular and linear dichroisms only after application of the field. Hence there seems to be some possibility that magnetic orientation occurs for NH at low temperature, which is disrupted by thermal effects at warmer temperatures. There are major obstacles for this model, however. For instance, the torque on NH due to the magnetic field should be minute in comparison with CF effects of the order of ~100 cm^{-1}. But perhaps more damaging to its credibility, it would predict that the $|^3\Pi_- 0\rangle$ *B* term would get *smaller* with decreased

temperature and/or increased magnetic-field strength, whereas exactly the opposite occurs.

This author is inclined to believe, from the results presented in this chapter, that the NH radicals remain randomly oriented under all conditions. However, on the basis of the discussion in this section, the value for the CF splitting ($V \approx 75$ cm^{-1}) must be regarded as somewhat tentative. The assumption that the splitting between bands 1 and 2 is primarily a consequence of SO-CF effects in the $A\,^3\Pi$ term seems reasonable, but it also seems very likely that other matrix-induced effects could perturb the energy levels and affect the way in which they are coupled by the magnetic field. Some speculations regarding such effects follow in the next section.

Other structure

The remainder of this section considers previous assignments of the structure observed in the spectra in light of the SO-CF model proposed above for the $A\,^3\Pi$ term, and on the basis of the data reported in this chapter.

In Section 5.5.1 it was shown that ζ_π for the $A\,^3\Pi$ term of NH/Ar is only slightly reduced from the gas-phase value.[6] Hence the orbital angular momentum of $A\,^3\Pi$ is *not* totally quenched by the matrix (*via* CF effects), and any interpretation in terms of low-lying rotational levels should still follow Hund's case (a).[4,13] The levels rapidly convert to Hund's case (b),[4] but this does not justify Bondybey and Brus' use of this case for their analysis of librational structure.[10] (With no orbital angular momentum, the $X\,^3\Sigma^-$ term of NH is Hund's case (b).[13]) However, their suggestion that the increasing breadth of the structure toward the blue is due to fast relaxation between excited-state levels may have some validity.[10]

In previous work McCarty and Robinson[9] and Rose[12] have assigned some of the NH/Ar structure to rotations in the $A\,^3\Pi$ term, slightly perturbed by the matrix environment. Their assignments are given in Table 5.3.1, and are based on the gas-phase results of Dixon.[4] (Figure 5.5.3 shows some of the allowed lines for a $^3\Pi \leftarrow {}^3\Sigma^-$ system.) Variation of splittings from the gas-phase values were explained in terms of differing matrix interactions with the $A\,^3\Pi$ SO levels and their rotations. Bands 1 – 3 were taken to correspond to transitions between the lowest rotational levels of $X\,^3\Sigma^-$ and the Ω = 2, 1 and 0 components, respectively, of $A\,^3\Pi$ (Figure 5.4.2). Band 4 was

assigned to the $^{S}R_{21}(1)$ transition (Figure 5.5.3) by McCarty and Robinson;[9] but the positive, temperature-dependent MCD clearly associates it with a transition to $^{3}\Pi_{0}$, so Rose reassigned it to a librational level derived from $^{S}Q_{31}(1)$.[12] (Note: the $^{S}R_{21}(1)$ transition may underlie the band system, but there is no direct evidence for it.) Rose assigned band 5 (which is not well resolved in the spectra shown in this thesis) to $^{T}R_{31}(1)$ (Figure 5.5.3). Although this transition was not observed by Dixon in the gas phase, matrix perturbations to the radical's rotational structure (*i.e.* librational motion[10]) could conceivably result in its appearance. She also assigns two hot bands, arising from the first librational level of $X\,^{3}\Sigma^{-}$ at ~10 cm^{-1} in Ar:[12] $R_{1}(2)$ and $^{R}P_{31}(2)$ (Table 5.3.1; Figure 5.5.3). These are feasible, although the bands themselves are not clearly evident in the spectral data (either hers or those reported here), due to the broadening of the spectra observed at higher temperatures (Figure 5.3.1). However, the $R_{1}(2)$ assignment seems unlikely because no corresponding negative MCD is observed.

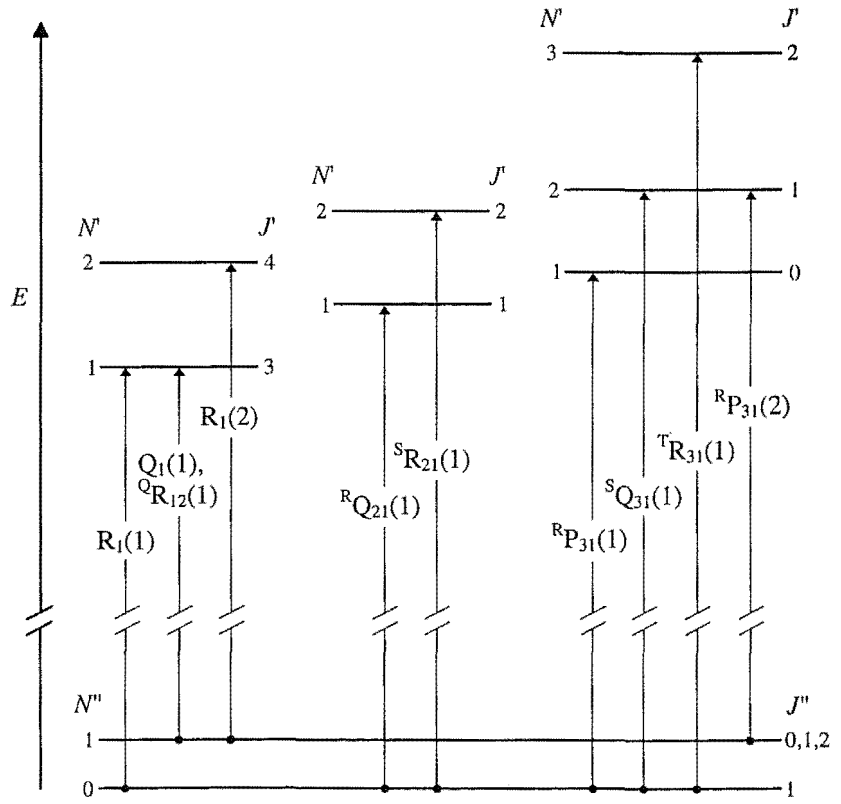

Figure 5.5.3: Energy-level diagram (approximately to scale within the terms) for the lines of a $^{3}\Pi \leftarrow {}^{3}\Sigma^{-}$ transition that are relevant to NH/Ar. *J'* and *N'* labels in the $^{3}\Pi$ term are for Hund's cases (a) and (b), respectively. (The small spin-spin and second-order SO splittings in $^{3}\Sigma^{-}$ ($N = 1$) and λ-doubling in $^{3}\Pi$ are ignored, since this work cannot resolve them.)

Now modification of these assignments in terms of the SO-CF model presented in this chapter are considered.

Clearly band 1 (Figure 5.3.1) can be attributed to transitions terminating in the lower SO-CF level $|^3\Pi_- 1\rangle$, which arises predominantly from the gas-phase $|^3\Pi_2\rangle$ level. This is essentially in agreement with the assignments made by McCarty and Robinson[9] and Rose.[12] Associated with band 1, because of its negative MCD, is a hot band (band 7; Figure 5.3.1), which is assigned to a librational component of the gas-phase $Q_1(1)$ and $^QR_{12}(1)$ transitions. ($Q_1(1)$ and $^QR_{12}(1)$ originate in different J'' levels of $X\,^3\Sigma^-$ $N'' = 1$;[13] Section 4.5.2). Band 7 lies ~25 cm^{-1} to the red of band 1 (Table 5.3.1); the gas-phase splitting is ~32.5 cm^{-1},[4] suggesting that rotation in the $X\,^3\Sigma^-$ term of NH/Ar is slightly hindered; a result in qualitative agreement with that of Bondybey and Brus who observed 'near-free rotation' in the librational levels using LIF.[10]

Band 2 is attributed to $|^3\Pi_- 0\rangle \leftarrow |^3\Sigma^-\rangle$, arising from the CF-split $|^3\Pi_1\rangle \leftarrow |^3\Sigma^-\rangle$ transition (see above). Again the similarity with earlier assignments is evident,[9,12] but whereas they could not explain the marked deviations from the SO splittings observed for the $A\,^3\Pi$ term in the gas phase, this chapter provides a rationale by invoking CF splitting in that term.

The upper CF component derived from the $|^3\Pi_1\rangle$ level, $|^3\Pi_+ 0\rangle$, should lie to the blue of $|^3\Pi_- 0\rangle$, and its MCD should comprise *B* terms, which are weak. On the basis of the simulated spectra (Figures 5.5.1 and 5.5.2), it would be tempting to assign band 3 (Figure 5.3.1) to this transition. However, band 3 is too intense in absorption, and its MCD shows definite *C*-term behaviour (~1 / *T* and field-saturation dependencies), more suited to assignment as a transition terminating in the $|^3\Pi_+ 1\rangle$ level, which arises predominantly from the gas-phase $|^3\Pi_0\rangle$ level. It is therefore concluded that in the region of band 3 there are in fact overlapping broad contributions from transitions to both $|^3\Pi_+ 0\rangle$ and $|^3\Pi_+ 1\rangle$, with the MCD dominated by latter. The MCD in Figures 5.3.1 and 5.3.2 appears slightly truncated to the red, which may be indicative of the presence of the weaker $|^3\Pi_+ 0\rangle$ transition.

The problems encountered in assigning the structure evident in the region of bands 1 – 3 warrant a short digression to comment on two possible causes of the divergence of experiment and theory. Firstly, it is possible that the upper SO-CF $|^3\Pi_+ S\rangle$ ($S = 0, 1$) levels are close in energy to librational levels built on the $|^3\Pi_- S\rangle$ components,

which could lead to perturbations that shift energies and broaden bands. Secondly, there may be some sort of matrix-mediated interactions acting to bring the $|^3\Pi_{-}\ 1\rangle$ and $|^3\Pi_{-}\ 0\rangle$ levels closer together than predicted by eq (5.4.22). In this case the true CF splitting would be *smaller* than that calculated above ($V \approx 75$ cm^{-1}) using eq (5.5.1). This would bring the spectral simulations into closer agreement in the sense that it would contract the range of the calculated spectrum.

Bands 4 and 5 could be librations built on band 3, as suggested by Rose.[12] Alternatively, they could be the result of coupling to phonon modes of the Ar lattice.[20] Band 6 is broad, weak and lies at significantly higher energy, and as such is almost certainly due to local-phonon overtones.

The shoulder at ~12 cm^{-1} to the red of band 1 (band 1'; Table 5.3.1) has constant intensity relative to band 1, independent of temperature. It is therefore not a hot band, and is interpreted to indicate the presence of a second stable (but less favoured) site for NH in an Ar matrix. Hence, the higher-energy bands will have associated site structure, which will increase the apparent broadening. It is conceivable that this site also exhibits spectra with different structure to the main site because of different site symmetry, CF effects and/or lattice interactions;[21-24] an interesting possibility that the present data are unable to resolve. Band sharpening after the matrix is annealed (Section 5.2.1) is also consistent with the presence of multiple sites, with unstable sites being annihilated at warmer temperatures (Figures 5.2.1).

5.5.2.2. ND/Ar

MCD and absorption spectra for ND/Ar (Figures 5.3.3 and 5.3.4) exhibit broader bands than NH/Ar (Figures 5.3.1 and 5.3.2), although like NH/Ar band widths increase with energy (Section 5.5.2.1). Band 2 (Table 5.3.1; Figure 5.3.3) becomes a shoulder in the absorption, while in the MCD the intriguing temperature dependencies observed in that region for NH/Ar (Figure 5.3.1 and Section 5.5.2.1) are obscured. Broad bands are probably a result of shorter lifetimes due to the compression of rotational levels relative to NH (causing greater overlap), and different interactions with phonons of the Ar lattice.

Since ζ_π is roughly the same for NH/Ar and ND/Ar, the larger splitting observed between bands 1 and 3 for ND/Ar relative to NH/Ar may be a consequence of overlap in

ND/Ar of the two bands labelled 3 and 4 for NH/Ar (Figure 5.3.1). (The average splitting from band 1 is 71 cm^{-1} for NH/Ar, compared to 70 cm^{-1} for ND/Ar.)

No other fine structure is resolved for ND/Ar, and hence the uncertainty in the position of bands 4, 5 and 6. Broad bands also preclude identification of secondary sites. Note that although the shoulder to the red of band 1 (Figure 5.3.3) is attributed to a small amount of NH/Ar because of the isotope shift (27 cm^{-1} in Ref. 9, and ~22 cm^{-1} here; see Section 5.2.2), it could conceivably be due to a second site.

Broadening of the absorption at higher temperatures occurs as for NH/Ar, and is suggestive of a low-lying hindered rotational level. However, here the broad bands do not allow its approximate energy to be determined.

5.6. Conclusion

Absorption and temperature- and field-dependent MCD data for NH/Ar and ND/Ar have been successfully interpreted in terms of a model which treats SO-CF effects in the $A\,^3\Pi$ term, and ZFS splitting in the $X\,^3\Sigma^-$ term. Simultaneously fitting all $\mathbf{M}_l/\mathbf{A}_0$ data, assuming orientational averaging, shows that the ground-state ZFS is essentially totally quenched in an Ar matrix. Further, the SOC parameters in the $A\,^3\Pi$ term are very similar to the gas-phase values, with $\zeta_\pi = 33.5 \pm 0.3$ cm^{-1} for NH/Ar, and $\zeta_\pi = 37.1 \pm 1.0$ cm^{-1} for ND/Ar.

Excited-state CF splittings cannot be determined from the first MCD moment. The NH/Ar spectra are better resolved than ND/Ar, and allow a tentative value to be proposed for the former: $V \approx 75$ cm^{-1}. Spectral simulations using $V = 75$ cm^{-1} and $\zeta_\pi =$ 33.5 cm^{-1} yield semiquantitative agreement with experiment, but other effects and perturbations clearly have to considered to obtain more exact agreement.

The sharp structure in NH/Ar reveals the presence of a second stable site at slightly lower energy than the primary site. The ND/Ar spectra are broader, and do not show any resolved site structure. Temperature dependence in the absorption spectra of both species is accounted for by thermal population of the first rotational level of the ground state, which lies ~25 cm^{-1} above the lowest rotational level for NH/Ar, and is only slightly hindered in the Ar matrix. Broad bands to the blue are attributed to hindered rotation in the $A\,^3\Pi$ term, or coupling with lattice phonons.

5.7. References

1. Eder, J. M. *Denskschr. Wien. Akad.* **1893**, *1*, 60.
2. Funke, G. *Z. Physik* **1935**, *96*, 787-798.
3. Funke, G. *Z. Physik* **1936**, *101*, 104-112.
4. Dixon, R. N. *Can. J. Phys.* **1959**, *37*, 1171-1186.
5. Bollmark, P.; Kopp, I.; Rydh, B. *J. Mol. Spectrosc.* **1970**, *34*, 487-499.
6. Veseth, L. *J. Phys. B: Atom. Molec. Phys.* **1972**, *5*, 229-241.
7. Huber, K. P.; Herzberg, G. *Molecular Spectra and Molecular Structure, Volume 4: Constants of Diatomic Molecules*; Van Nostrand Reinhold: New York, 1979.
8. Robinson, G. W.; McCarty, M. J. *J. Chem. Phys.* **1958**, *28*, 350.
9. McCarty, M. J.; Robinson, G. W. *J. Am. Chem. Soc.* **1959**, *81*, 4472-4476.
10. Bondybey, V. E.; Brus, L. E. *J. Chem. Phys.* **1975**, *63*, 794-804.
11. Lund, P. A.; Hasan, Z.; Schatz, P. N.; Miller, J. H.; Andrews, L. *Chem. Phys. Lett.* **1982**, *91*(6), 437-439.
12. Rose, J. L. Ph.D. Dissertation, University of Virginia, Charlottesville, 1987.
13. Herzberg, G. *Molecular Spectra and Molecular Structure Volume 1: Spectra of Diatomic Molecules*, 2nd ed.; Krieger: New York, 1950.
14. Piepho, S. B.; Schatz, P. N. *Group Theory in Spectroscopy with Applications to Magnetic Circular Dichroism*; Wiley-Interscience: New York, 1983.
15. Weltner, W. J. *Magnetic Atoms and Molecules*; Dover Publications: Mineola, 1989.
16. Carrington, A.; McLaclan, A. D. *Introduction to Magnetic Resonance with Applications to Chemistry and Chemical Physics*; Harper and Row: New York, 1969.
17. Wayne, F. D.; Radford, H. E. *Mol. Phys.* **1976**, *32*, 1407-1422.
18. Lide, D. R., Ed. *CRC Handbook of Chemistry and Physics*, 71st ed.; CRC Press: Boca Raton, 1990.
19. Lignieres, J.; d'Humieres, B.; Rivoal, J.-C. *Z. Phys. D - Atoms, Molecules and Clusters* **1991**, *19*, 207-209.
20. Rebane, K. K. *Impurity Spectra of Solids*; Plenum Press: New York, 1970.

21. Blindauer, C.; Winter, M.; Sild, O.; Jansen, G.; Hess, B. A.; Schurath, U. *J. Phys. Chem.* **1993**, *97*, 10002-10010.

22. Jansen, G.; Hess, B. A.; Marian, C. M.; Angyan, J. G. *J. Phys. Chem.* **1993**, *97*, 10011-10020.

23. Flygare, W. H. *J. Chem. Phys.* **1963**, *39*, 2263-2273.

24. Bowers, M. T.; Flygare, W. H. *J. Chem. Phys.* **1966**, *44*, 1389-1404.

6. CH/Ar

6.1. Introduction

The methylidyne free radical (CH) is an important flame species, and occurs in a variety of extra-terrestrial environments, such as comets and in the interstellar medium, as was noted in Section 1.1.1. Although there is a significant literature on CH in the gas phase, there is a relative dearth of investigations in rare-gas matrices. A brief history of these investigations follows as part of this introduction. The substance of this chapter describes the candidate's research on the MCD and electronic absorption spectra of the $A\,^2\Delta$, $B\,^2\Sigma^-$ and $C\,^2\Sigma^+ \leftarrow X\,^2\Pi$ transitions of CH isolated in a solid Ar matrix. Temperature- and magnetic field-dependence data are presented, and interpreted in terms of a spin-orbit (SO) – crystal-field (CF) model in which the orbital angular momentum is partially quenched by CF interactions with neighbouring species in the matrix.

6.1.1. Gas-phase studies

Spectroscopic investigations of gas-phase CH have been summarised by Herzberg,[1] and more recently Huber and Herzberg.[2] Constants for the ground, and first, second and third excited spin-doublet terms have been given in these references.

In 1973, Veseth and co-workers[3] published a comprehensive article on the doublet terms of CH that are investigated in this thesis. They recalculated molecular parameters and term values from earlier experimental data, obtaining them with greater precision than had been achieved previously. Gas-phase values quoted here reference that work exclusively.

6.1.2. Matrix-isolated CH

Matrix-isolated CH and CD radicals were first observed by Robinson and McCarty.[4] Mixtures of diazomethane (and its mono- and bi-deuterated analogues) with Kr were subjected to photolysis at different UV wavelengths. The resulting transients were trapped in a Kr matrix and probed using electronic absorption spectroscopy. When photolysis wavelengths longer than 3400 Å were used, sharp features resulted in the

vicinity of 3000 Å, which were attributed to the previously undetected CH_2, CHD and/or CD_2 radicals. Further photolysis using higher-energy radiation bleached these, yielding spectral features that corresponded to gas-phase transitions of CH and CD.[1,2] In Kr matrices, the $A\,^2\Delta$, $B\,^2\Sigma^-$ and $C\,^2\Sigma^+ \leftarrow X\,^2\Pi$ transitions were observed to occur at 23121 ± 15, 25368 ± 15 and 31497 ± 20 cm^{-1} for CH, and were not shifted measurably for CD/Kr.

Keyser,[5] a later student of Robinson's, prepared CH/Ar by X-ray irradiation of a ~5-K 1:100 CH_4/Ar matrix, achieving a yield of about 8% after eight hours. Absorption and emission spectra were obtained for all three transitions at ~12 K. The $A\,^2\Delta$, $B\,^2\Sigma^-$ and $C\,^2\Sigma^+ \leftarrow X\,^2\Pi$ transitions were observed at 23217 ± 3, 25496 ± 3 and 31670 ± 5 cm^{-1}. Some structure in the second and third of these band systems was assigned to free rotation.

IR and UV-visible spectra of CH and CD were obtained by Milligan and Jacox[6] after vacuum-UV (VUV) photolysis of methane and *d*-methane, respectively, *in situ* in Ar at 14 K. The electronic transitions assigned by Keyser[5] for CH were again observed, as were those of CD.

MCD and absorption spectra for the $A\,^2\Delta \leftarrow X\,^2\Pi$ and $B\,^2\Sigma^- \leftarrow X\,^2\Pi$ systems of CH/Ar were obtained by Rose,[7] who followed Keyser's assignments of fine structure, and added others besides. She used orbital-reduction arguments to explain the observed temperature-dependent MCD. (In the gas phase, there is no quenching of orbital angular momentum for a $^2\Pi_{1/2}$ level, and the Zeeman splitting is essentially zero, in the limit that $g_e \approx 2$, due to cancellation of the spin and orbital contributions.)

This thesis aims to explain the structure observed for all three transitions, while developing a more rigorous model to quantify the orbital angular momentum of the $X\,^2\Pi$ term.

6.2. Experimental

CH/Ar was prepared using the apparatus described in Section 2.1.1.2, employing the ½" → ½" discharge tube shown in Figure 2.1.2. (Use of the ¼" → ½" tube yielded no CH, although a black residue, indicative of carbon, was deposited on the tube during such attempts.) Ultra-high-purity (UHP) CH_4 was mixed with UHP Ar (1:100 mole ratio using standard gas-handling techniques) in a 1-L glass reservoir to a final pressure

of about 1 atm. CH/Ar matrix preparation times were ~15 minutes, with CH_4:Ar flow rates ~5 mmol hr^{-1}.

MOD4 (Section 2.3) was employed to gather all spectral data, but a modified version of the data-acquisition software SPEC2 (Section 2.3.11) was utilised, which allowed several wavelength step sizes and levels of data averaging within a single scan. (Small steps were used in regions of sharp structure, and larger steps in less structured regions.) The Xe-arc lamp and 1180-groove/mm grating were utilised in conjunction with a Hamamatsu R-376 photomultiplier tube. An Esco Products GG-395 filter was employed to eliminate second-order UV light (Section 2.3.4.2) for the $A\,^2\Pi$ and $B\,^2\Sigma^-$ $\leftarrow X\,^2\Pi$ transitions, while a Corning 7-54 filter was used to remove stray visible light (Section 2.3.4.1) for the $C\,^2\Sigma^+ \leftarrow X\,^2\Pi$ transition. The $A\,^2\Pi$ and $C\,^2\Sigma^+ \leftarrow X\,^2\Pi$ systems exhibit sharper fine structure than the $B\,^2\Sigma^- \leftarrow X\,^2\Pi$ transition; the monochromator slits were set to 100 μm (spectral resolution ~0.08 nm) and 200 μm (~0.16 nm), respectively.

Preliminary matrix depositions were undertaken in the He-refrigerator/ electromagnet system (Section 2.2.1). Deposition temperatures of 12 to 14 K were typical. These experiments showed that annealing CH/Ar matrices above ~20 K resulted in some band sharpening for the transitions to $A\,^2\Delta$ and $C\,^2\Sigma^+$, but not to the extent observed for NH/Ar (Section 5.2.1). (Fine structure in the $B\,^2\Sigma^-$ transition is less well resolved and did not show the same effect.) However, a reduction in the (already small) CH concentration also occurred (as was observed for OH/Ar and NH/Ar), as well as increased clouding of the sample.

Temperature and field dependencies of the MCD for all three transitions were measured using the matrix injection system (Section 2.2.2). The samples were deposited over the temperature range ~8-20 K, but were not annealed because of the risk of degrading the S/N for the gain of only slightly sharper spectra. The data are presented in Section 6.3. In the course of these experiments, a problem with OH/Ar contamination was encountered to an extent not observed with the He refrigerator. The $A\,^2\Sigma^+ \leftarrow X\,^2\Pi$ transition of OH/Ar partially overlaps the $C\,^2\Sigma^+ \leftarrow X\,^2\Pi$ transition of CH/Ar with the optical densities being approximately equal. Despite a great deal of care, this result was obtained in two separate experimental runs. It seems apparent that water contamination is a major problem in the matrix injection system, probably due to condensation onto cool surfaces which are not readily outgassed before the sample is

prepared. For this reason, the analysis of the data for $C\,^2\Sigma^+ \leftarrow X\,^2\Pi$ is subject to a greater level of uncertainty than for the other transitions.

6.3. Results

In this section, spectral data for the $A\,^2\Delta$, $B\,^2\Sigma^-$ and $C\,^2\Sigma^+ \leftarrow X\,^2\Pi$ transitions, and the results of moment analyses (Section 3.5.1), are presented. The absorption data are similar to those of Keyser,[5] while the MCD for the $A\,^2\Delta$ and $B\,^2\Sigma^- \leftarrow X\,^2\Pi$ systems agrees with that of Rose.[7] This work gives the first MCD spectra of the $C\,^2\Sigma^+ \leftarrow X\,^2\Pi$ transition.

Observed for all transitions was the significant broadening of spectral features with increasing energy across the band systems. The MCD associated with the broad absorption features is very much weaker than that corresponding to the sharper low-energy bands.

6.3.1. $A\,^2\Delta \leftarrow X\,^2\Pi$

Figure 6.3.1 shows the averaged absorption spectrum (seven individual spectra) and temperature-dependent MCD (from 1.41 to 15.8 K) for the $A\,^2\Delta \leftarrow X\,^2\Pi$ transition of CH/Ar. Band positions are given in Table 6.3.1, which also lists the wavenumbers of the structure observed by Keyser[5] and Rose.[7] The spectra in the region of band 1 showed some broadening with increasing temperature.

The MCD is single-signed and positive at low temperatures and low fields, and shows the temperature dependence indicative of *C* terms (Section 1.3.2). (Note that relative to OH/Ar, which also has a $^2\Pi$ ground term, the MCD of CH/Ar is quite weak.) Further evidence for the presence of *C* terms is provided by the saturation behaviour exhibited by the field-dependence data shown for four temperatures (1.41, 1.73, 2.13 and 4.65 K) in Figures 6.3.2 to 6.3.5. Negative features in the MCD as temperature and field increase are due to a strong positive *A*-term component (Sections 6.4.6.3 and 6.5.1), which is (apart from broadening) temperature independent (Section 1.3.2), and does not saturate (Section 6.4.6.3).

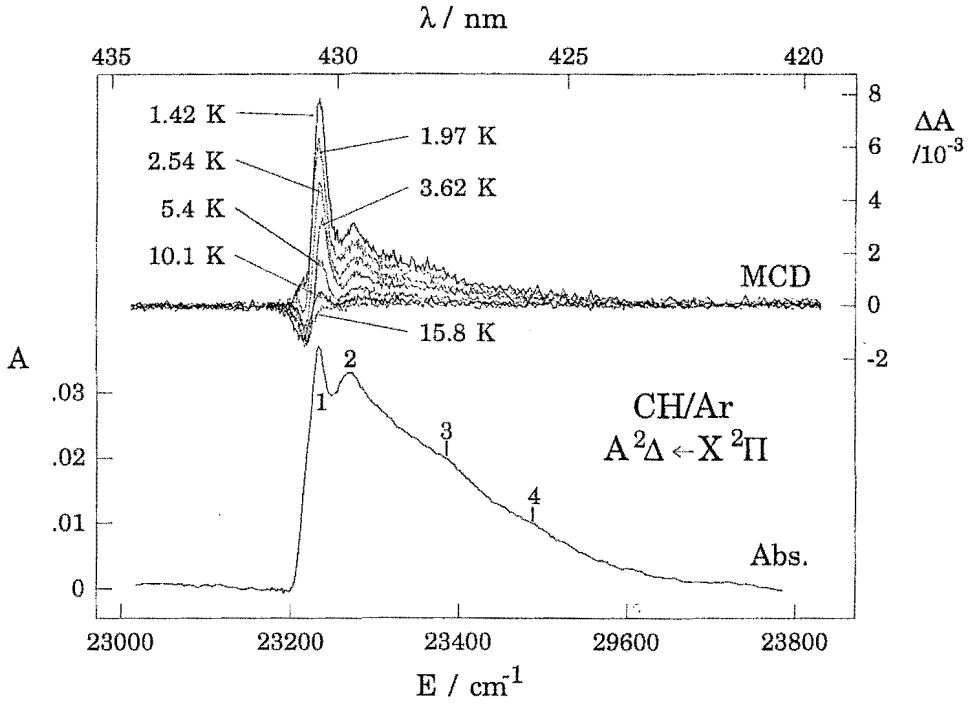

Figure 6.3.1: Top: MCD (ΔA) of the $A\,^2\Delta \leftarrow X\,^2\Pi$ transition of CH/Ar from 1.42 to 15.8 K (B = 1 T). Bottom: averaged (seven spectra) absorption spectrum for the same transition. The absorption bands are labelled for cross-referencing with Table 6.3.1.

Table 6.3.1: Bands in the $A\,^2\Delta$, $B\,^2\Sigma^-$ and $C\,^2\Sigma^+ \leftarrow X\,^2\Pi$ systems of CH/Ar.[a]

Band [b]	Band energy / cm^{-1}		
	Keyser [c]	Rose [d]	This work [e]
$A\,^2\Delta \leftarrow X\,^2\Pi$			
1	not measured	23200	23234 (0)
2	23217	23230	23271 (37)
	23271		
	23331		
3			23388 (sh; br) * (154)
4			23501 (sh; br) * (267)
$B\,^2\Sigma^- \leftarrow X\,^2\Pi$			
1	25496	25475	25507 (0)
2		25510	25544 (37)
3	25572	25547	25587 (80)
4		25581	25622 (115)
$C\,^2\Sigma^+ \leftarrow X\,^2\Pi$			
1	31670		31706 (sh) (0)
2	31710		31739 (33)
3	31738		31780 (74)

[a] Wavenumbers given in cm^{-1}. sh = shoulder; br = broad.
[b] Band numbering is shown on Figures 6.3.1, 6.3.6 and 6.3.11.
[c] Ref. 5. [d] Ref. 7.
[e] Band position ±5 cm^{-1}, except for * which are approximate only. Bracketed values give the separation from band 1.

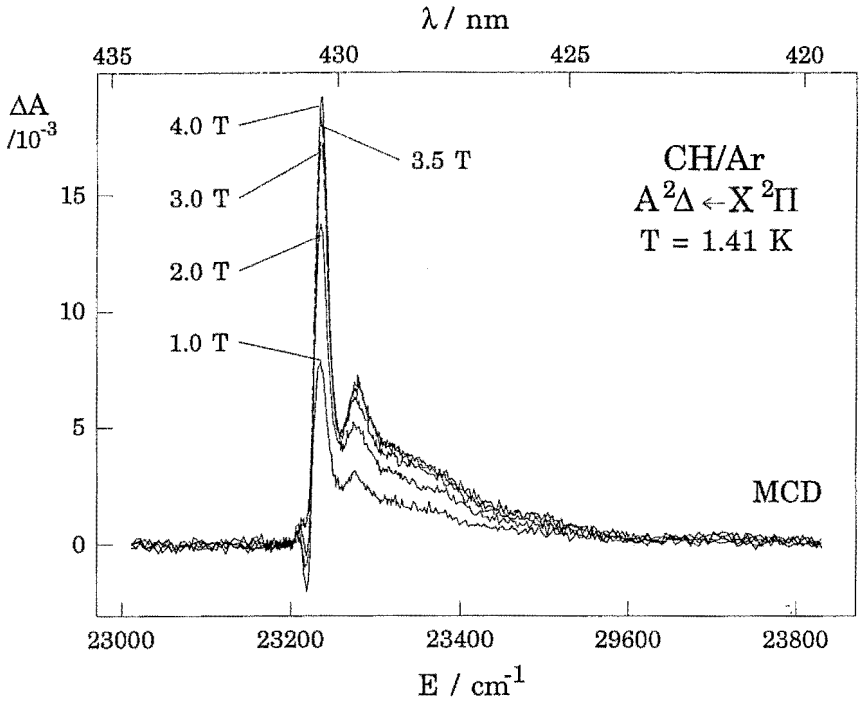

Figure 6.3.2: Magnetic-field dependence, from 1 to 4 T, of the MCD of the $A\,^2\Delta \leftarrow X\,^2\Pi$ transition of CH/Ar at 1.41 K.

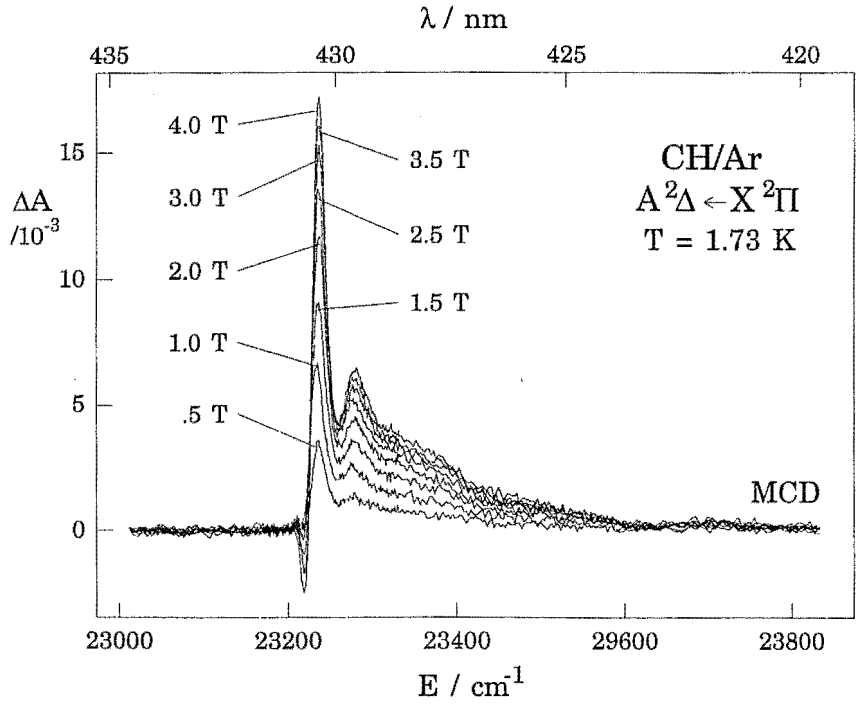

Figure 6.3.3: Magnetic-field dependence, from 0.5 to 4 T, of the MCD of the $A\,^2\Delta \leftarrow X\,^2\Pi$ transition of CH/Ar at 1.73 K.

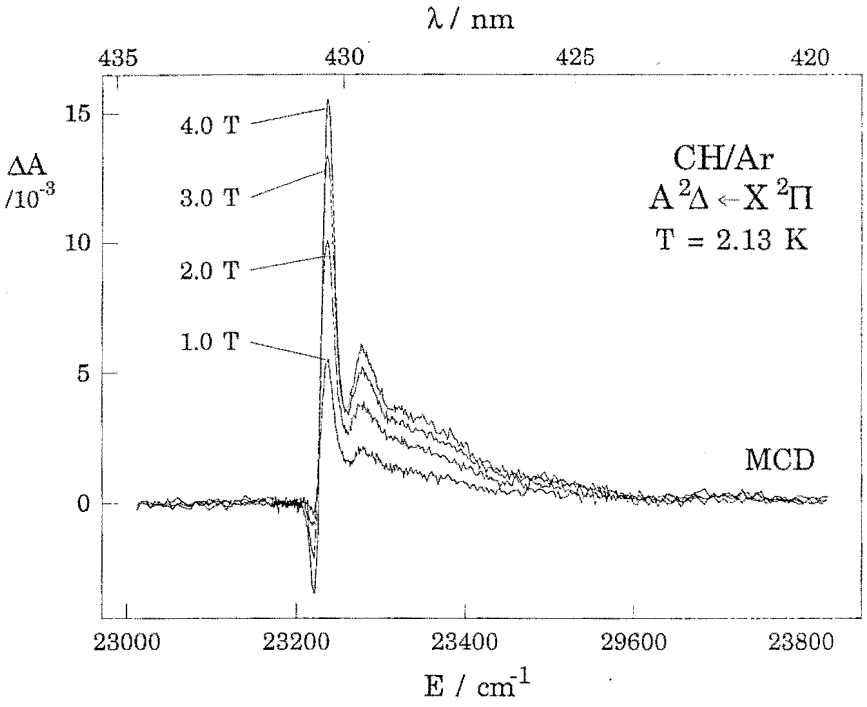

Figure 6.3.4: Magnetic-field dependence, from 1 to 4 T, of the MCD of the $A\,^2\Delta \leftarrow X\,^2\Pi$ transition of CH/Ar at 2.13 K.

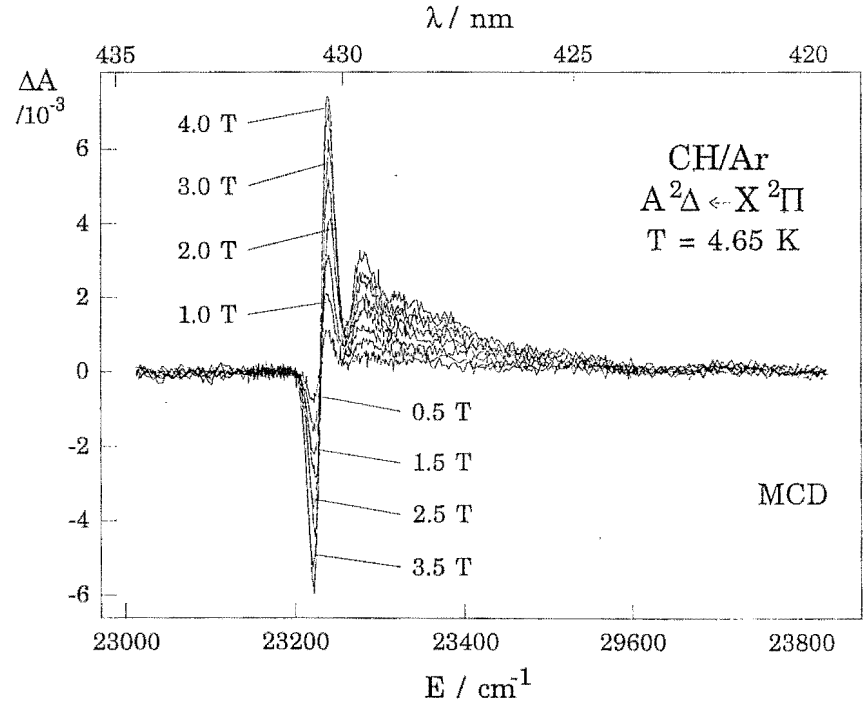

Figure 6.3.5: Magnetic-field dependence, from 0.5 to 4 T, of the MCD of the $A\,^2\Delta \leftarrow X\,^2\Pi$ transition of CH/Ar at 4.65 K.

6.3.2. $B\,^2\Sigma^- \leftarrow X\,^2\Pi$

MCD temperature dependence (1.41 to 15.9 K) and an absorption spectrum (average of five spectra at $T \approx 2$ K) for the $B\,^2\Sigma^- \leftarrow X\,^2\Pi$ system of CH/Ar are shown in Figure 6.3.6. The spectra have a similar appearance to those reported by earlier workers,[5,7] but have much better S/N. Band positions are given in Table 6.3.1, with those of Keyser[5] and Rose[7] included for comparison.

The MCD is single-signed and negative; its absolute magnitude decreases with increasing temperature, reaching zero within the S/N level at 15.9 K. Such temperature dependence is characteristic of *C* terms (Section 1.3.2). MCD saturation with increasing magnetic field is another feature of *C* terms, particularly at lower temperatures, and is shown in Figures 6.3.7 to 6.3.9 for 1.73, 2.13 and 4.68 K, respectively. MCD of the opposite phase is not observed to grow in with variation of temperature or field, unlike $A\,^2\Delta \leftarrow X\,^2\Pi$ (Figures 6.3.1 to 6.3.5). This indicates that the *A*-term component predicted by Section 6.4.6.3 is weak, which is consistent with the observation of a strong positive *A* term for $A\,^2\Delta \leftarrow X\,^2\Pi$ (Section 6.5.1).

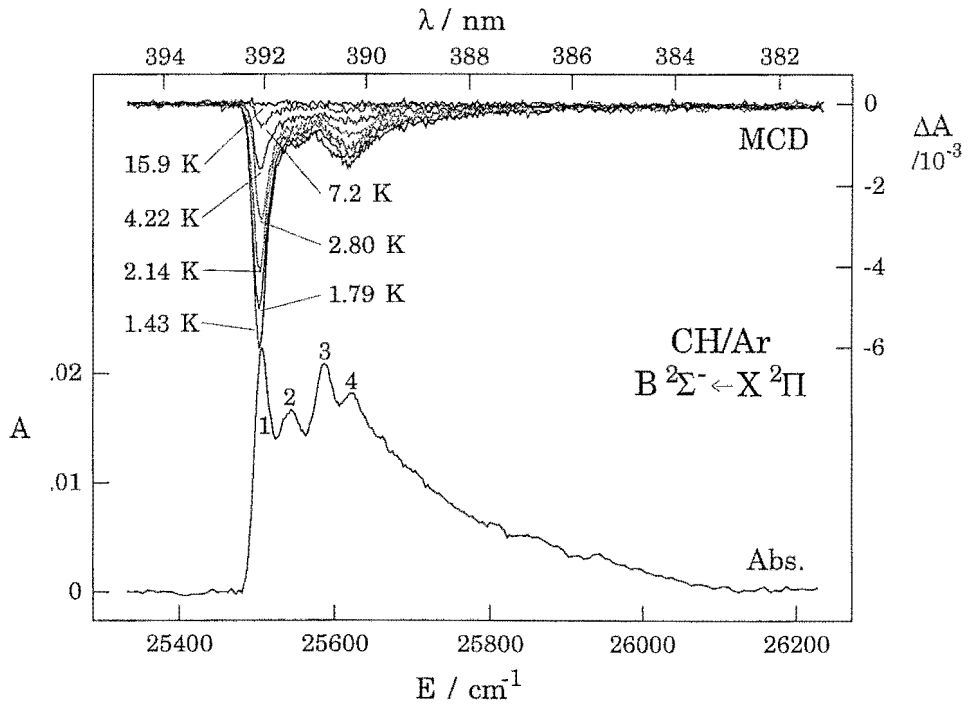

Figure 6.3.6: Top: MCD (ΔA) of the $B\,^2\Sigma^- \leftarrow X\,^2\Pi$ transition of CH/Ar from 1.43 to 15.9 K (B = 1 T). Bottom: averaged (five spectra at $T \approx 2$ K) absorption spectrum for the same transition. The absorption bands are labelled for cross-referencing with Table 6.3.1.

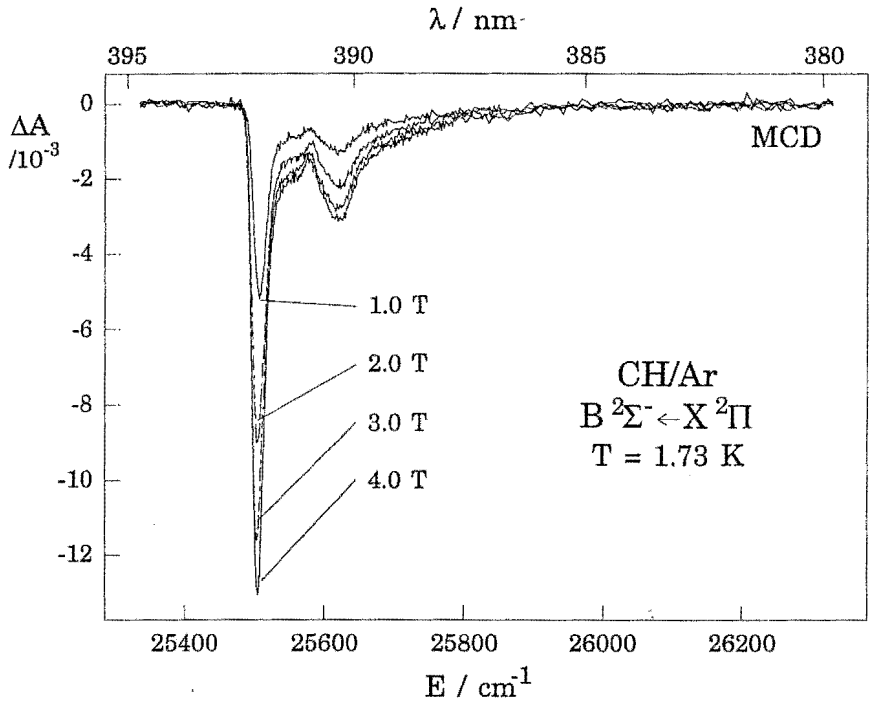

Figure 6.3.7: Magnetic-field dependence, from 1 to 4 T, of the MCD of the $B\,^2\Sigma^- \leftarrow X\,^2\Pi$ transition of CH/Ar at 1.73 K.

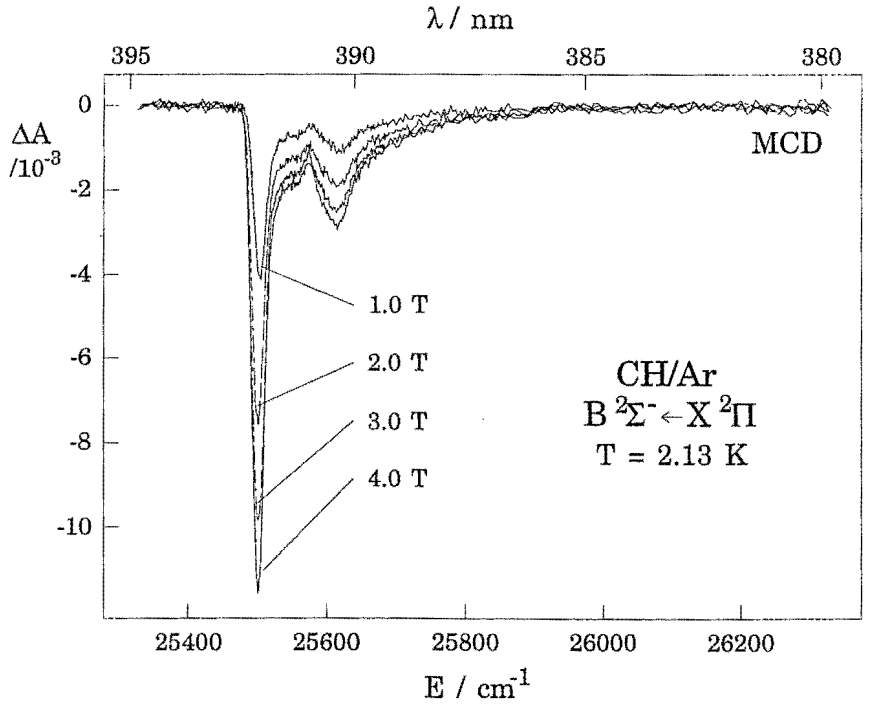

Figure 6.3.8: Magnetic-field dependence, from 1 to 4 T, of the MCD of the $B\,^2\Sigma^- \leftarrow X\,^2\Pi$ transition of CH/Ar at 2.13 K.

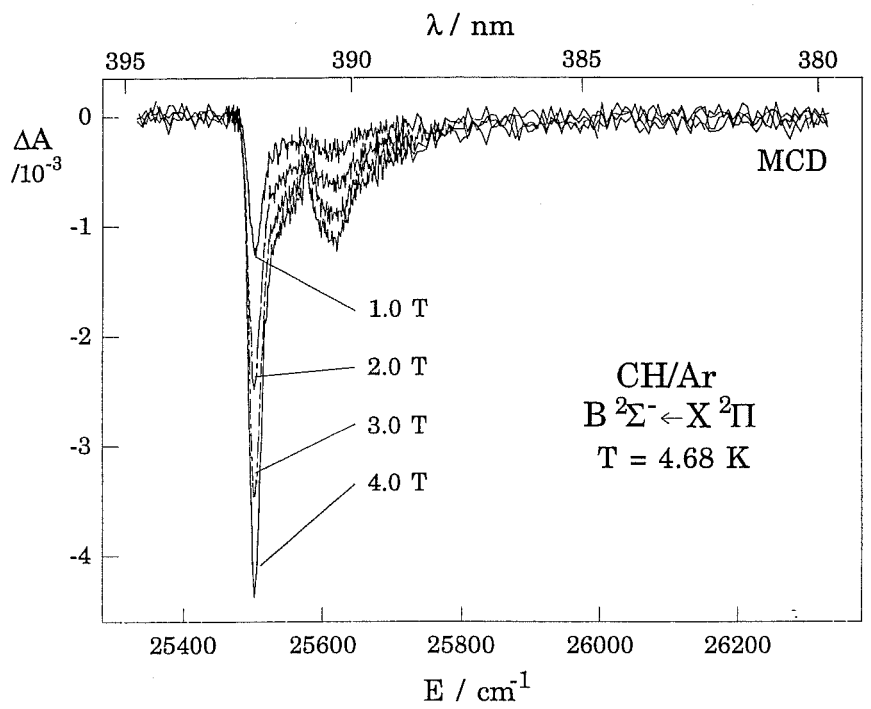

Figure 6.3.9: Magnetic-field dependence, from 1 to 4 T, of the MCD of the $B\,^2\Sigma^- \leftarrow X\,^2\Pi$ transition of CH/Ar at 4.68 K.

6.3.3. $C\,^2\Sigma^+ \leftarrow X\,^2\Pi$

Figure 6.3.10 shows the correction applied to MCD and absorption data for the $C\,^2\Sigma^+ \leftarrow X\,^2\Pi$ transition of CH/Ar because of OH/Ar contamination (Section 6.2). Absorption spectra were corrected by replacing the OH/Ar contribution with a portion of a scaled absorption spectrum (dashed in Figure 6.3.10; $T \approx 14$ K) in which there was minimal OH/Ar. The inserted portion was obtained using the He-refrigerator/ electromagnet system (Section 2.2.1). This method cannot be employed for the MCD, because at ~14 K the MCD for this transition is nearly zero within the S/N level. Instead a smooth curve (dashed in Figure 6.3.10) was generated that decays to zero in a similar manner to the MCD of $B\,^2\Sigma^- \leftarrow X\,^2\Pi$ (Figures 6.3.6 – 6.3.9). The curve was used to replace the OH/Ar-contaminated portion after appropriate scaling; temperature-dependence data at $1/T$, while for field-dependence data the factor had to be further modified to account for saturation. Hence the data for $C\,^2\Sigma^+ \leftarrow X\,^2\Pi$ are subject to a larger degree of uncertainty than the other transitions.

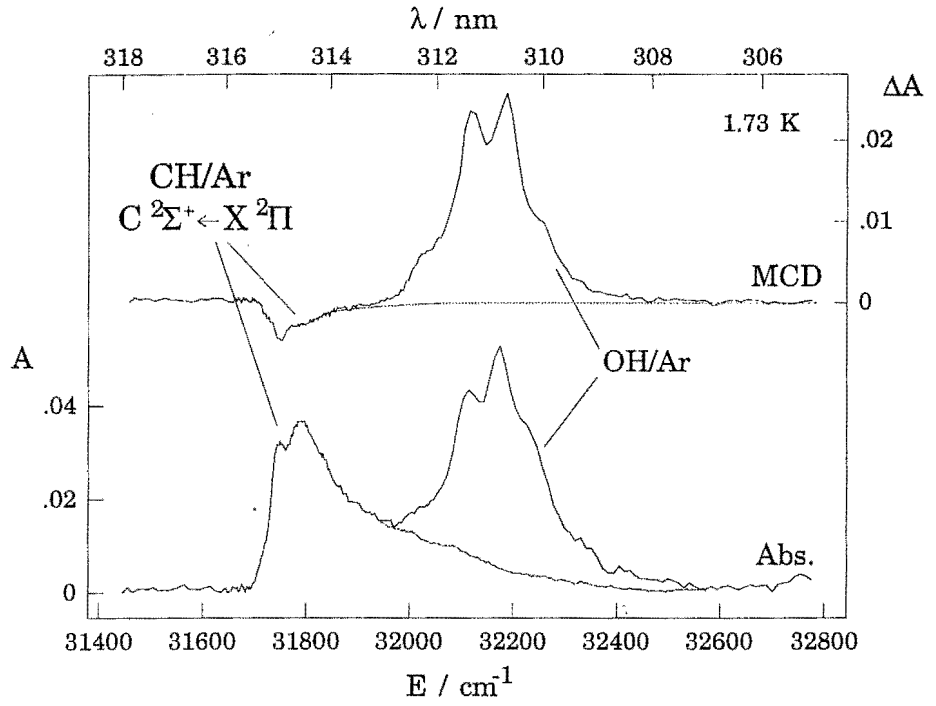

Figure 6.3.10: Demonstration of the methodology employed to overcome effects of OH/Ar contamination in the $C\,^2\Sigma^+ \leftarrow X\,^2\Pi$ transition of CH/Ar. The full curves show the extent of contamination (*cf.* Figure 4.3.1). Top: MCD at 1.73 K, with the dashed curve showing the expected behaviour of the MCD in the absence of OH/Ar (*cf.* $B\,^2\Sigma^- \leftarrow X\,^2\Pi$; Figure 6.3.6). Bottom: a representative absorption spectrum; the dashed curve was generated from a suitably scaled spectrum that was nearly free of OH/Ar, obtained using the He refrigerator.

Figure 6.3.11 shows the MCD temperature dependence (1.41 to 4.69 K) and an absorption spectrum (average of seven spectra at $T \approx 4.7$ K) for the $C\,^2\Sigma^+ \leftarrow X\,^2\Pi$ transition of CH/Ar. Absorption fine structure is quite sharp, although the data obtained using the matrix injection system are broader than those gathered using the He-refrigerator system. The inset in Figure 6.3.11 shows an expanded portion of an absorption spectrum obtained at ~14 K in the latter. Here band 1, which appears as a shoulder in the main spectrum, is more clearly resolved. These spectra are in good agreement with those obtained by Keyser,[5] but with a much improved S/N level. Within the S/N level of the individual spectra, the absorption data are temperature independent from ~1.42 to 4.7 K. Band positions for this work, and those of Keyser[5] are given in Table 6.3.1. (Rose did not report this transition.[7])

The MCD is single-signed and negative at all temperatures investigated, with temperature dependence that is typical of *C* terms (Section 1.3.2). Temperatures higher

than ~4.7 K were not used, because earlier work that employed the He refrigerator ($T_{minimum} \approx 14$ K) was unable to detect MCD within the S/N level. MCD saturation with increasing magnetic field is another feature of C terms, particularly at lower temperatures, and is shown in Figure 6.3.12 for 1.74, 2.13 and 4.68 K. (The same ordinate applies for all temperatures.) The single-signed nature of the MCD agrees with the results obtained for $B\,^2\Sigma^- \leftarrow X\,^2\Pi$ (Section 6.3.2), and is indicative of only a weak A-term contribution (Section 6.5.1).

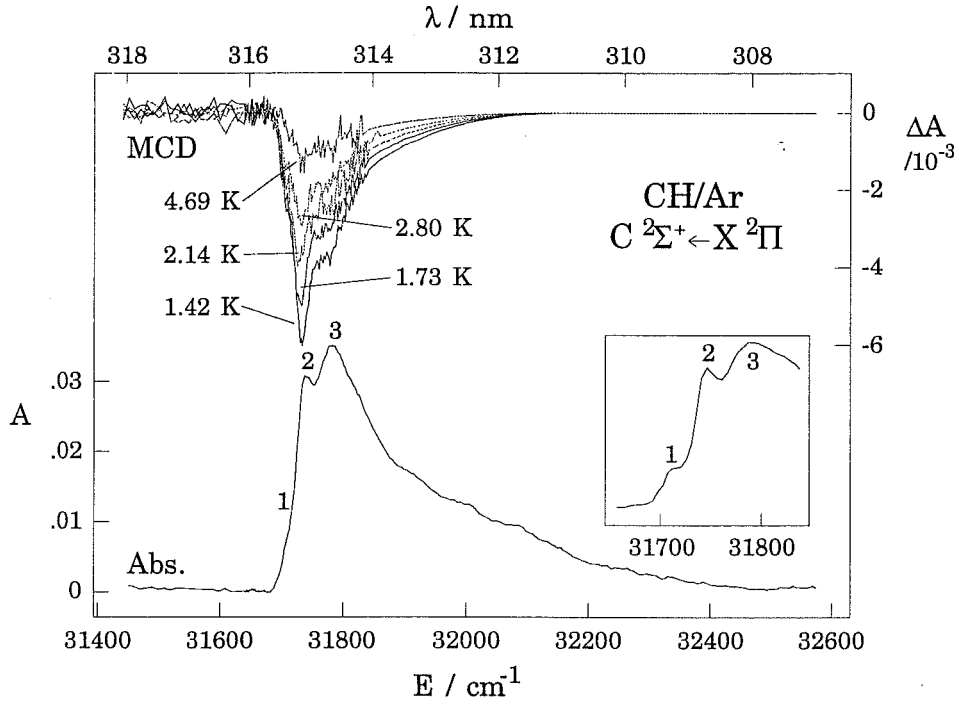

Figure 6.3.11: Top: MCD (ΔA) of the $C\,^2\Sigma^+ \leftarrow X\,^2\Pi$ transition of CH/Ar from 1.42 to 4.69 K (B = 1 T). Bottom: averaged (seven spectra) absorption spectrum ($T \approx 4.68$ K) for the same transition. (Both have been corrected for OH/Ar contamination (Figure 6.3.10).) The inset shows an expanded portion of an absorption spectrum obtained using the He refrigerator ($T \approx 14$ K) that better resolves band 1 (Table 6.3.1). The absorption bands are labelled for cross-referencing with Table 6.3.1.

6.3.4. Moment analysis

In order to quantify the temperature and field dependencies, dimensionless zeroth moment parameters (Section 3.5.1) are defined. The zeroth absorption and MCD moments, $\mathbf{A}_0$ and $\mathbf{M}_0$, are given by eqs (4.3.1) and (4.3.2), respectively.

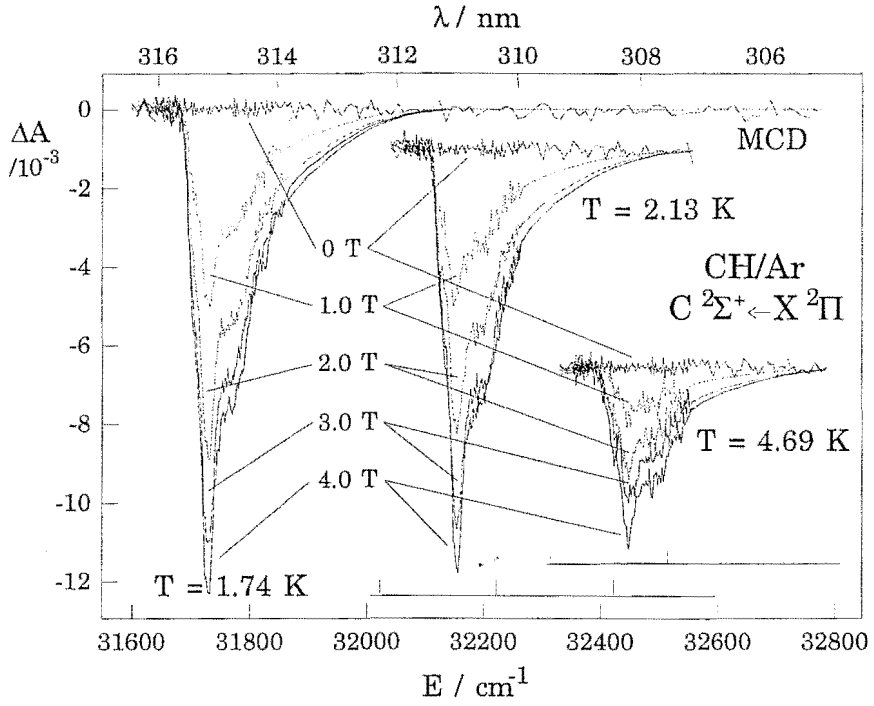

Figure 6.3.12: Magnetic-field dependence, from 0 to 4 T, of the MCD of the $C\,^2\Sigma^+ \leftarrow X\,^2\Pi$ transition of CH/Ar at 1.74, 2.13 and 4.68 K. Data have been corrected for OH/Ar contamination (Figure 6.3.10). (The same ordinate applies for all temperatures.)

The $\mathbf{M}_0/\mathbf{A}_0$ ratios for the CH/Ar temperature-dependence data (B = 1 T) for all three transitions (some spectra for which are illustrated in Figures 6.3.1, 6.3.6 and 6.3.11) are plotted against $1/kT$ in Figure 6.3.13. The saturation behaviour typical of C

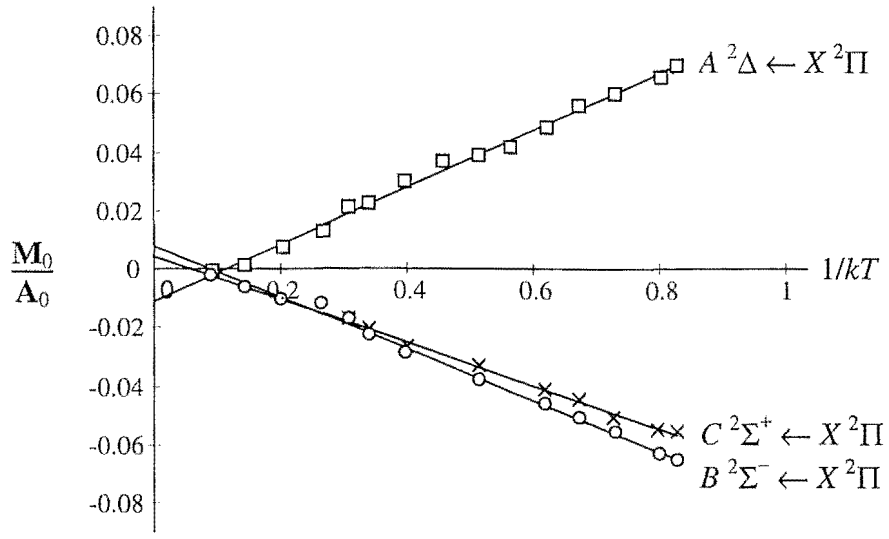

Figure 6.3.13: Temperature-dependence data for the moment ratio $\mathbf{M}_0/\mathbf{A}_0$ as a function of $1/kT$ for CH/Ar $A\,^2\Delta$, $B\,^2\Sigma^-$ and $C\,^2\Sigma^+ \leftarrow X\,^2\Pi$ (B = 1 T).

terms is evident in the field-dependence plots shown in Figures 6.3.14, 6.3.15 and 6.3.16 for the $A\,^2\Delta$, $B\,^2\Sigma^-$ and $C\,^2\Sigma^+ \leftarrow X\,^2\Pi$ systems, respectively, at several temperatures. (It is re-emphasised that the $C\,^2\Sigma^+ \leftarrow X\,^2\Pi$ data are subject to a higher

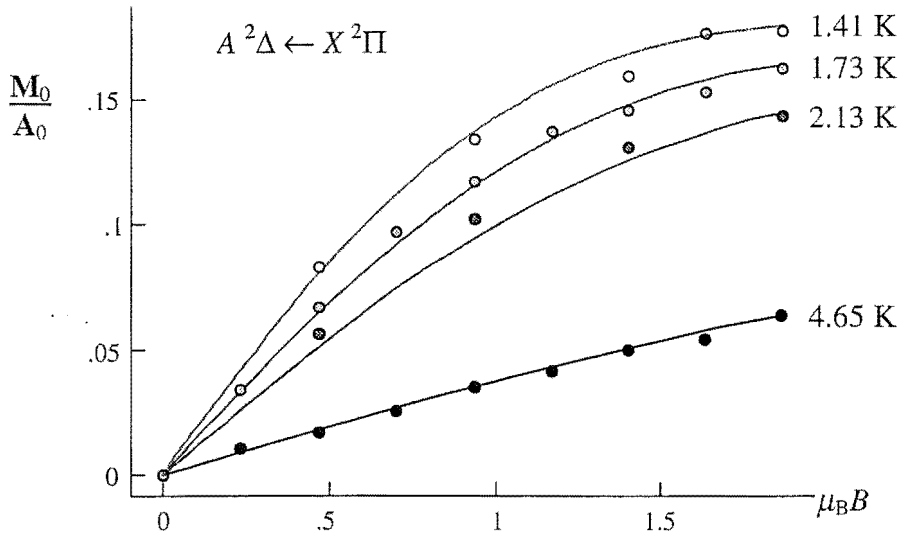

Figure 6.3.14: Field-dependence data for the moment ratio $\mathbf{M}_0/\mathbf{A}_0$ as a function of $\mu_B B$ for CH/Ar $A\,^2\Delta \leftarrow X\,^2\Pi$ at T = 1.41, 1.73, 2.13 and 4.65 K. The curves are best fits to the data of Figures 6.3.2 to 6.3.5 assuming random orientation of CH, and using eqs (6.4.45) and (6.4.58), with ζ_π = 22 cm^{-1} and κ = 0.28 (Section 6.5.1; Table 6.5.1).

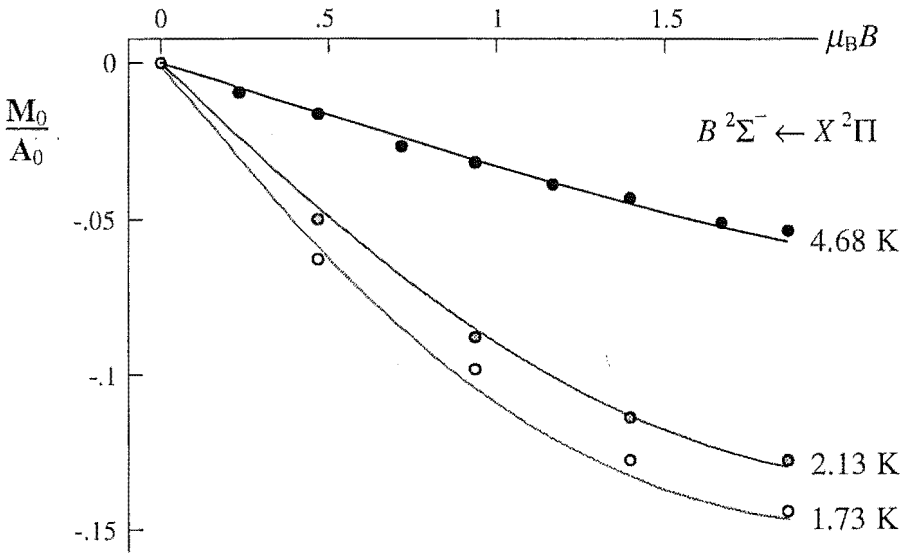

Figure 6.3.15: Field-dependence data for the moment ratio $\mathbf{M}_0/\mathbf{A}_0$ as a function of $\mu_B B$ for CH/Ar $B\,^2\Sigma^- \leftarrow X\,^2\Pi$ at T = 1.73, 2.13 and 4.68 K. The curves are best fits to the data of Figures 6.3.7 to 6.3.9 assuming random orientation of CH, and using eqs (6.4.45) and (6.4.58), with ζ_π = 21 cm^{-1} and κ = 0.24 (Section 6.5.1; Table 6.5.1).

level of uncertainty than the other transitions due to removal of OH/Ar contributions (Section 6.3.3). Nevertheless, Figures 6.3.13 and 6.3.16 suggest that the methodology employed in Section 6.3.3 is reasonable.)

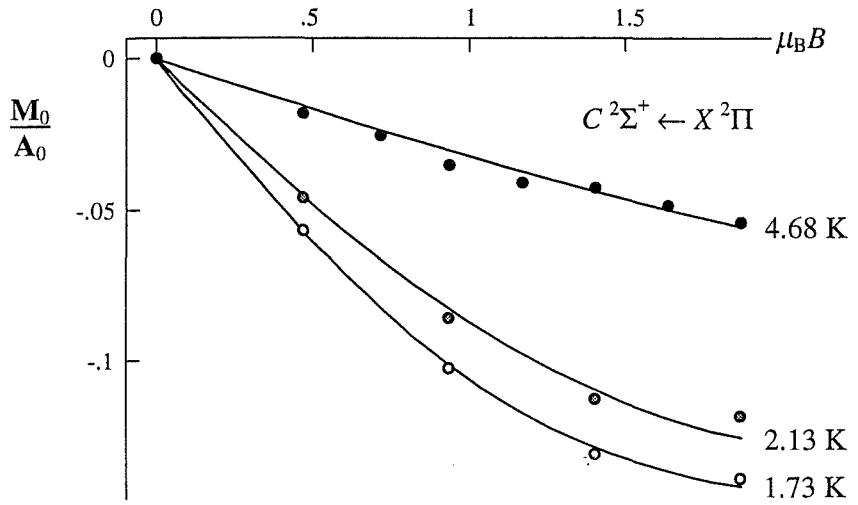

Figure 6.3.16: Field-dependence data for the moment ratio M_0/A_0 as a function of $\mu_B B$ for CH/Ar $C\,^2\Sigma^+ \leftarrow X\,^2\Pi$ at T = 1.73, 2.13 and 4.68 K. The curves are best fits to the data of Figure 6.3.12 assuming random orientation of CH, and using eqs (6.4.45) and (6.4.58), with ζ_π = 21 cm^{-1} and κ = 0.23 (Section 6.5.1; Table 6.5.1).

6.4. Theory

This section describes a SO-CF model developed for CH/Ar. The $X\,^2\Pi$ ground term has a similar treatment to OH/Ar, except that CH/Ar is a regular SO system (it has one rather than three valence π electrons) and has significantly smaller SOC. The reduced SOC requires very careful consideration of the magnitude of the ground-state splitting before a model is proposed and applied to the experimental data. In determining the Zeeman eigenstates within the SO-CF model, it is initially assumed (and later shown to be well founded – Section 6.5) that the Zeeman interactions between the SO-CF levels (Section 6.4.3.1) can be treated by first-order perturbation theory (*i.e.* as B terms).

Three excited terms arising from the first excited configuration (Section 6.4.1) are covered here; the absence of first-order SOC simplifies their treatment. Further, of the $A\,^2\Delta$, $B\,^2\Sigma^-$ and $C\,^2\Sigma^+$ terms, only $A\,^2\Delta$ can undergo CF splitting, which is treated in a manner similar to that for Π states.

In general the treatment of the MCD and absorption follows the methodology used for OH/Ar in Section 4.4.6; *i.e.* it applies to data inside and outside the so-called 'linear-limit',[8] and accounts for orientational averaging. It is expanded, however, by virtue of the possibility of a populated upper SO-CF level in the ground state of CH/Ar. Further, for CH/Ar there are three transitions to be accounted for. Fortunately, due to the principle of spectroscopic stability with respect to choice of the excited-state basis for zeroth and first moments,[8] *C*- and *B*-term contributions to $\mathbf{M}_0$ for each of the three transitions are simply related by a constant factor. *A* terms (Section 6.4.6.3) are considered individually for the transitions, and together with $\mathbf{M}_0$, are used to derive expressions for $\mathbf{M}_1$ inside and outside the linear limit.

6.4.1. Spin-orbit wavefunctions for CH

CH has $\mathbf{C}_{\infty v}$ symmetry, possible basis functions for which are given in Table 4.4.1. The mixing of notations due to Mulliken and Butler is covered in Section 3.2.1.

MOs can be generated for CH, in like manner to NH, but the orbital occupancy is changed since CH has one less valence electron. Figure 6.4.1 shows a schematic MO diagram for CH in which the lowest-energy configuration ($3\sigma^2\ 1\pi^1$) is illustrated. The first excited configuration, $3\sigma^1\ 1\pi^2$, arises from the electronic excitation $1\pi \leftarrow 3\sigma$ shown in the figure.

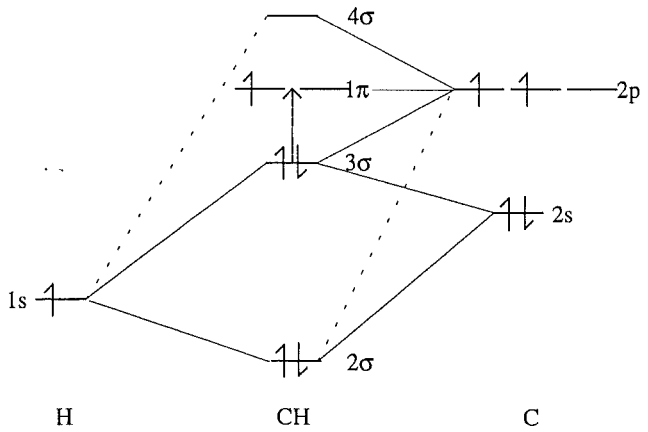

Figure 6.4.1: MO diagram for CH. (The 1σ MO is essentially pure C(1s), and is not shown.) The dashed line shows the lowest-energy electronic excitation, which is investigated in this work.

The ground configuration has only one electron in a partially filled shell (1π), so its orbital irrep (*h*) is Π. The first excited configuration has one σ and two π electrons in partially filled shells, so the orbital irreps are given by $\sigma \otimes \pi \otimes \pi = \Sigma^+ \oplus \Sigma^- \oplus \Delta$

(Section 3.3.1.2(a); Table B.1.2, Appendix B). SL wavefunctions have already been derived for the π^2 ground configuration of NH (Section 5.4.1), and are used after omitting the σ^2 contribution from eq (5.4.6).

The spin irreps (Section 3.3.1.2(b)) are $\frac{1}{2}$ for the ground configuration, and $\frac{1}{2}$ and $\frac{3}{2}$ for the first excited configuration.

Allowed terms are (Section 3.3.1.2(c)) $^2\Pi$ for the ground configuration, and $^4\Sigma^-$, $^2\Delta$, $^2\Sigma^-$ and $^2\Sigma^+$ (in order of ascending energy) for the first excited configuration.

6.4.1.1. SL wavefunctions

SL wavefunctions,[8] $|^{2\Lambda+1}h\ \mathcal{M}\ \theta\rangle$, for the ground configuration are (including the fully occupied 3σ contribution),

$$|^2\Pi\ \pm\tfrac{1}{2}\ +1\rangle = |0^2\ 1^{\pm}\rangle$$

$$|^2\Pi\ \pm\tfrac{1}{2}\ -1\rangle = |0^2\ -1^{\pm}\rangle \qquad (6.4.1)$$

where the notation employed is described in Section 3.3.1.4.

Eq (3.3.6) was used to couple the wavefunctions for the two subconfigurations (σ^1 and π^2) of the first excited configuration. For σ^1, $|\sigma^1\ \Lambda_1\ h_1\ \mathcal{M}_1\ \theta_1\rangle$ were determined by inspection, while for π^2 those of the ground configuration of NH (eq (5.4.6)) were utilised, as noted above. The final SL wavefunctions are,

$$|^4\Sigma^-\ \pm\tfrac{3}{2}\ 0\rangle = |0^{\pm}\ -1^{\pm}\ 1^{\pm}\rangle$$

$$|^4\Sigma^-\ \pm\tfrac{1}{2}\ 0\rangle = \tfrac{1}{\sqrt{3}}\{|0^{\mp}\ -1^{\pm}\ 1^{\pm}\rangle + |0^{\pm}\ -1^{+}\ 1^{-}\rangle + |0^{\pm}\ -1^{-}\ 1^{+}\rangle\}$$

$$|^2\Delta\ \pm\tfrac{1}{2}\ \pm2\rangle = |0^{\pm}\ \pm1^{+}\ \pm1^{-}\rangle$$

$$|^2\Delta\ \mp\tfrac{1}{2}\ \pm2\rangle = |0^{\mp}\ \pm1^{+}\ \pm1^{-}\rangle$$

$$|^2\Sigma^-\ \pm\tfrac{1}{2}\ 0\rangle = \mp\tfrac{1}{\sqrt{6}}\{2|0^{\mp}\ -1^{\pm}\ 1^{\pm}\rangle - |0^{\pm}\ -1^{+}\ 1^{-}\rangle - |0^{\pm}\ -1^{-}\ 1^{+}\rangle\}$$

$$|^2\Sigma^+\ \pm\tfrac{1}{2}\ 0\rangle = \tfrac{1}{\sqrt{2}}\{|0^{\pm}\ -1^{+}\ 1^{-}\rangle - |0^{\pm}\ -1^{-}\ 1^{+}\rangle\} \qquad (6.4.2)$$

6.4.1.2. SO wavefunctions

Section 3.3.1.5 covers the SO coupling (SOC) performed here. Table 6.4.1 gives the spin correlations required to form the symmetry-adapted basis for $\mathbf{SO_3}$ in $\mathbf{C_{\infty v}}$. SO

irreps and partners for terms of the ground and excited configurations are shown in Table 6.4.2, in order of increasing term energy.

Table 6.4.1: Spin correlation from the angular-momentum basis to the $\mathbf{C}_{\infty v}$ basis for $\delta = \frac{1}{2}, \frac{3}{2}$.

$\mathbf{SO}_3 \supset \mathbf{C}_\infty$	$\mathbf{SO}_3 \supset \mathbf{C}_{\infty v} \supset \mathbf{C}_\infty$
$\left\|\frac{1}{2}\ \pm\frac{1}{2}\right\rangle$	$\left\|\frac{1}{2}\ \frac{1}{2}\ \pm\frac{1}{2}\right\rangle$
$\left\|\frac{3}{2}\ \pm\frac{1}{2}\right\rangle$	$\mp\left\|\frac{3}{2}\ \frac{1}{2}\ \pm\frac{1}{2}\right\rangle$
$\left\|\frac{3}{2}\ \pm\frac{3}{2}\right\rangle$	$\left\|\frac{3}{2}\ \frac{3}{2}\ \pm\frac{3}{2}\right\rangle$

Table 6.4.2: SOC irreps and partners resulting from the ground and first-excited configurations of CH.

Term	Orbital irreps	Spin irreps		SOC ($\mathbf{C}_{\infty v} \supset \mathbf{C}_\infty$)		
	$\mathbf{C}_{\infty v}$	$\mathbf{SO}_3$	$\mathbf{C}_{\infty v}$	Irreps	Partners	Level
$X\ ^2\Pi$	1	$\frac{1}{2}$	$\frac{1}{2}$	$\frac{3}{2}$	$\pm\frac{3}{2}$	$^2\Pi_{3/2}$
				$\frac{1}{2}$	$\pm\frac{1}{2}$	$^2\Pi_{1/2}$
$a\ ^4\Sigma^-$	$\tilde{0}$	$\frac{3}{2}$	$\frac{3}{2}$	$\frac{3}{2}$	$\pm\frac{3}{2}$	$^4\Sigma^-_{3/2}$
			$\frac{1}{2}$	$\frac{1}{2}$	$\pm\frac{1}{2}$	$^4\Sigma^-_{1/2}$
$A\ ^2\Delta$	2	$\frac{1}{2}$	$\frac{1}{2}$	$\frac{5}{2}$	$\pm\frac{5}{2}$	$^2\Delta_{5/2}$
				$\frac{3}{2}$	$\pm\frac{3}{2}$	$^2\Delta_{3/2}$
$B\ ^2\Sigma^-$	$\tilde{0}$	$\frac{1}{2}$	$\frac{1}{2}$	$\frac{1}{2}$	$\pm\frac{1}{2}$	$^2\Sigma^-_{1/2}$
$C\ ^2\Sigma^+$	0	$\frac{1}{2}$	$\frac{1}{2}$	$\frac{1}{2}$	$\pm\frac{1}{2}$	$^2\Sigma^+_{1/2}$

SO wavefunctions were derived using eq (3.3.10), and are given in eqs (6.4.3) and (6.4.4) for the ground and first-excited configurations, respectively. The $|^{2\delta+1}h_\Omega\, M_\Omega\rangle$ notation follows the convention described in Section 3.3.1.5, where in $\mathbf{C}_{\infty v}$, $t \equiv \Omega$ and $\tau \equiv M_\Omega$.

$$
\begin{aligned}
|^2\Pi_{3/2}\ \pm\tfrac{3}{2}\rangle &= -|0^2\ \pm 1^\pm\rangle \\
|^2\Pi_{1/2}\ \pm\tfrac{1}{2}\rangle &= \mp|0^2\ \pm 1^\mp\rangle \qquad (6.4.3) \\
|^4\Sigma^-_{3/2}\ \pm\tfrac{3}{2}\rangle &= \pm|0^\pm\ {-1}^\pm\ 1^\pm\rangle \\
|^4\Sigma^-_{1/2}\ \pm\tfrac{1}{2}\rangle &= -\tfrac{1}{\sqrt{3}}\{|0^\mp\ {-1}^\pm\ 1^\pm\rangle + |0^\pm\ {-1}^+\ 1^-\rangle + |0^\pm\ {-1}^-\ 1^+\rangle\} \\
|^2\Delta_{5/2}\ \pm\tfrac{5}{2}\rangle &= |0^\pm\ \pm 1^+\ \pm 1^-\rangle
\end{aligned}
$$

$$|^2\Delta_{3/2}\,\mp\tfrac{3}{2}\rangle = \mp|0^{\mp}\pm1^{+}\pm1^{-}\rangle$$

$$|^2\Sigma^{-}_{1/2}\,\pm\tfrac{1}{2}\rangle = -\tfrac{1}{\sqrt{6}}\{2|0^{\mp}\text{-}1^{\pm}\,1^{\pm}\rangle - |0^{\pm}\text{-}1^{+}\,1^{-}\rangle - |0^{\pm}\text{-}1^{-}\,1^{+}\rangle\}$$

$$|^2\Sigma^{+}_{1/2}\,\pm\tfrac{1}{2}\rangle = -\tfrac{1}{\sqrt{2}}\{|0^{\pm}\text{-}1^{+}\,1^{-}\rangle - |0^{\pm}\text{-}1^{-}\,1^{+}\rangle\} \qquad (6.4.4)$$

Electron-repulsion, SO and CF matrix elements were computed using these wavefunctions.

6.4.2. Matrix elements

6.4.2.1. Electron-repulsion matrix elements

Electron-repulsion matrix elements were evaluated as described in Section 3.3.2.1, and follow the notation given there. The 0 and ±1 partners of the 3σ and 1π orbitals (Figure 6.4.1), respectively, are used as the *a* and *b* labels. (Since the $X\,^2\Pi$ term has only one electron in a partially filled shell, there are no open-shell electron-repulsion matrix elements.)

Three electrons of the first excited configuration occupy partially filled shells, and undergo electron-repulsion interactions. These resultant matrix elements are,

$$\langle^4\Sigma^{-}|\mathcal{H}_{\text{Rep}}|^4\Sigma^{-}\rangle = 2J_{01} - 2K_{01} + J_{1\text{-}1} - K_{1\text{-}1}$$

$$\langle^2\Delta|\mathcal{H}_{\text{Rep}}|^2\Delta\rangle = 2J_{01} - K_{01} + J_{1\text{-}1}$$

$$\langle^2\Sigma^{-}|\mathcal{H}_{\text{Rep}}|^2\Sigma^{-}\rangle = 2J_{01} + K_{01} + J_{1\text{-}1} - K_{1\text{-}1}$$

$$\langle^2\Sigma^{+}|\mathcal{H}_{\text{Rep}}|^2\Sigma^{+}\rangle = 2J_{01} - K_{01} + J_{1\text{-}1} + K_{1\text{-}1} \qquad (6.4.5)$$

Figure 6.4.2 shows the splitting of these terms schematically.

6.4.2.2. Spin-orbit matrix elements

The method used to evaluate SO matrix elements was described in Section 3.3.2.2. As mentioned there, elements involving the raising and lowering operators can be ignored (to first order) in the $\mathbf{C}_{\infty v}$ group.

CH has an orbitally and spin degenerate ground term, resulting in the non-zero diagonal matrix elements,

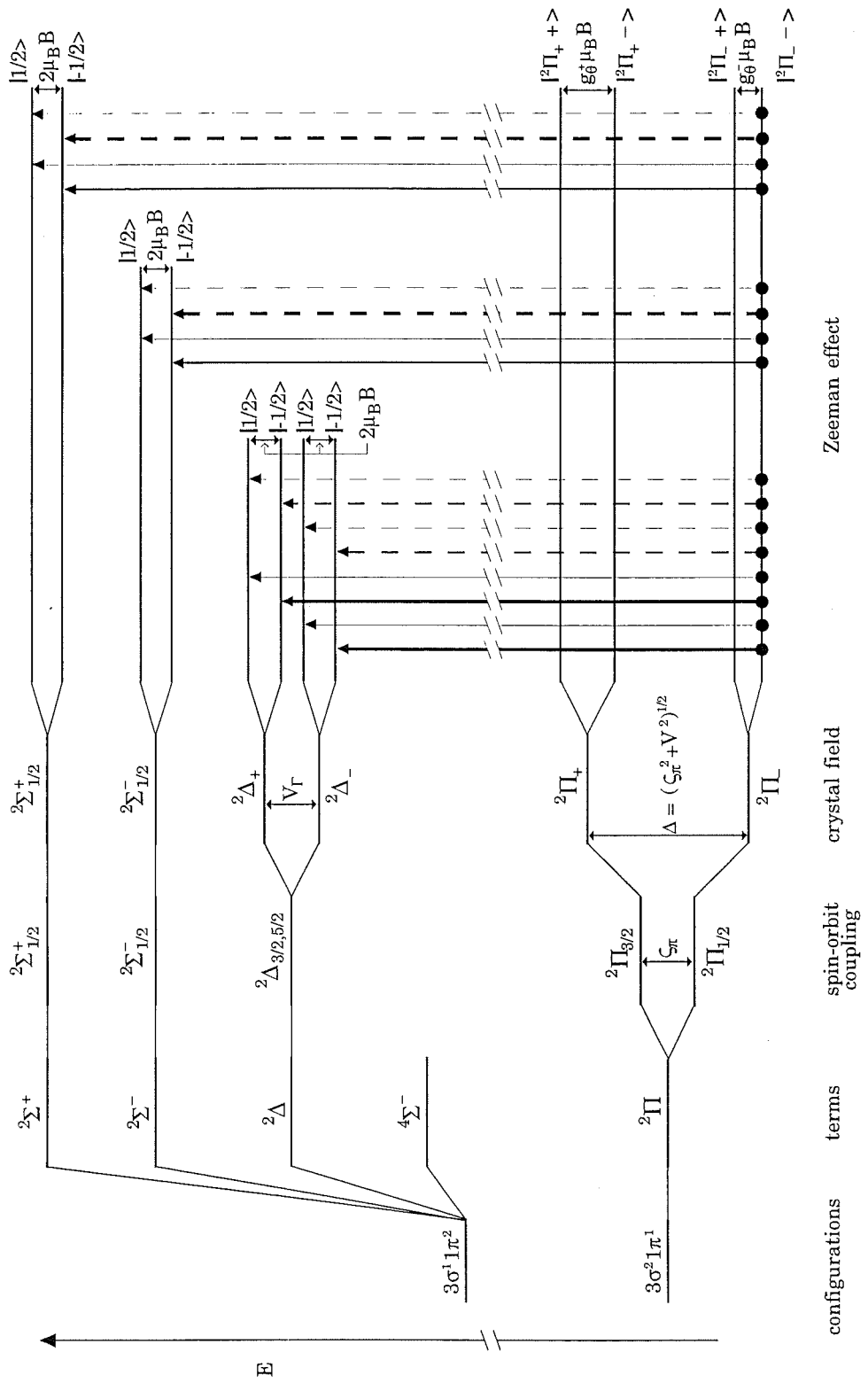

Figure 6.4.2: Energy-level diagram showing the effects of SO, CF and Zeeman interactions on the $X\ ^2\Pi$, $A\ ^2\Delta$, $B\ ^2\Sigma^-$ and $C\ ^2\Sigma^+$ states of CH/Ar. The relative intensities of left- (lcp) and right-circularly polarised (rcp) transitions originating from the $|^2\Pi_-\rangle$ state and terminating in the $A\ ^2\Delta$, $B\ ^2\Sigma^-$ and $C\ ^2\Sigma^+$ manifolds are indicated by the thickness of the lines.

$$\langle {}^2\Pi_{1/2} \pm\tfrac{1}{2}|\mathcal{H}_{SO}|{}^2\Pi_{1/2} \pm\tfrac{1}{2}\rangle = -\tfrac{1}{2}\zeta_\pi$$

$$\langle {}^2\Pi_{3/2} \pm\tfrac{3}{2}|\mathcal{H}_{SO}|{}^2\Pi_{3/2} \pm\tfrac{3}{2}\rangle = \tfrac{1}{2}\zeta_\pi \qquad (6.4.6)$$

where ζ_π is an empirical SO splitting constant for a 1π electron in CH,

$$\zeta_\pi = \pm\langle \pi \pm 1|u_z|\pi \pm 1\rangle \qquad (6.4.7)$$

The energies of the SO levels are therefore,

$$E({}^2\Pi_\Omega) = \zeta_\pi \Lambda (\Omega - \Lambda) \qquad (6.4.8)$$

where Λ and Ω are, respectively, the total orbital angular momentum ($\Lambda = 1$ for a Π term) and SO quantum numbers.

The first excited configuration exhibits no first-order SOC, because it results from coupling between σ^1 and π^2 subconfigurations. The former clearly has no orbital angular momentum, while for the latter the terms are orbitally and/or spin non-degenerate and therefore only undergo higher-order SOC, as was demonstrated for the ground configuration of NH in eq (5.4.12). Non-zero off-diagonal matrix elements occur only between terms with the same value of Ω, and are given in eq (6.4.9). Note that because the energy separations between these terms are large, the SO perturbations are small, and cannot be resolved in this work.

$$\langle {}^2\Sigma^-_{1/2} \pm\tfrac{1}{2}|\mathcal{H}_{SO}|{}^2\Sigma^+_{1/2} \pm\tfrac{1}{2}\rangle = \frac{1}{\sqrt{3}}\zeta_\pi$$

$$\langle {}^2\Sigma^+_{1/2} \pm\tfrac{1}{2}|\mathcal{H}_{SO}|{}^2\Sigma^-_{1/2} \pm\tfrac{1}{2}\rangle = \frac{1}{\sqrt{3}}\zeta_\pi$$

$$\langle {}^4\Sigma^-_{1/2} \pm\tfrac{1}{2}|\mathcal{H}_{SO}|{}^2\Sigma^+_{1/2} \pm\tfrac{1}{2}\rangle = -\frac{2}{\sqrt{3}}\zeta_\pi$$

$$\langle {}^2\Sigma^+_{1/2} \pm\tfrac{1}{2}|\mathcal{H}_{SO}|{}^4\Sigma^-_{1/2} \pm\tfrac{1}{2}\rangle = -\frac{2}{\sqrt{3}}\zeta_\pi \qquad (6.4.9)$$

The SO levels for the $X\,{}^2\Pi$ term are shown in Figure 6.4.2.

6.4.2.3. Crystal-field matrix elements

Evaluation of CF matrix elements was described in Section 3.3.2.3. CH/Ar has a $X\,{}^2\Pi$ ground term, which is the same as OH/Ar (Section 4.4.2.2), and the CF elements are given by eq (4.4.8). (V is defined in exactly the same way as for OH/Ar.) Introduction of the CF is illustrated in Figure 6.4.2.

The $A\,^2\Delta$ term of CH is also susceptible to CF effects, because it is orbitally degenerate. The appropriate CF component must transform as one of the partners of the Γ (or E_4) irrep, since $[\Delta^2] = \Sigma^+ \oplus \Gamma$ (or $[2^2] = 0 \oplus 4$ in Butler notation). These have hexadecapolar symmetry, and due to their high order are probably weak. (This is suggested by the MCD data, since for band 1 (Figure 6.3.1) a moderately sharp A term dominates at warmer temperatures as predicted by the SO treatment of Section 6.4.6.3, not a pseudo-A term or well separated B terms indicated by the Zeeman elements in the SO-CF basis in Section 6.4.4.2. See also Section 6.5.1.) The matrix elements of $\mathcal{H}_{CF}$ are,

$$\langle {}^2\Delta_{5/2}\ \pm\tfrac{5}{2}|\mathcal{H}_{CF}|{}^2\Delta_{3/2}\ \mp\tfrac{3}{2}\rangle = \pm\tfrac{1}{2}V_\Gamma$$

$$\langle {}^2\Delta_{3/2}\ \pm\tfrac{3}{2}|\mathcal{H}_{CF}|{}^2\Delta_{1/2}\ \mp\tfrac{5}{2}\rangle = \mp\tfrac{1}{2}V_\Gamma \qquad (6.4.10)$$

Here $V_\Gamma = \langle 2\|V^4\|2\rangle$ is a one-electron reduced CF matrix element describing the magnitude of the splitting of the $|\Delta\ \pm2\rangle$ orbital components.

6.4.3. SO-CF wavefunctions for CH

The presence of both SO and CF effects causes mixing of the eigenstates of either operator. In this section, SO-CF eigenfunctions for both the $X\,^2\Pi$ and $A\,^2\Delta$ terms are presented.

6.4.3.1. $X\,^2\Pi$ term

SO-CF eigenfunctions and the corresponding eigenvalues for the $X\,^2\Pi$ term were obtained by diagonalisation of the SO-CF hamiltonian matrix (Section 3.3.3), and yield a splitting (Δ) in the $^2\Pi$ manifold of,

$$\Delta = \sqrt{\zeta_\pi^{\,2} + V^2} \qquad (6.4.11)$$

The SO-CF eigenfunctions are then,

$$|{}^2\Pi_-\ \pm\tfrac{1}{2}\rangle = \alpha\,|{}^2\Pi_{1/2}\ \mp\tfrac{1}{2}\rangle \pm \beta\,|{}^2\Pi_{3/2}\ \pm\tfrac{3}{2}\rangle \qquad (6.4.12a)$$

$$|{}^2\Pi_+\ \pm\tfrac{1}{2}\rangle = \mp\beta\,|{}^2\Pi_{1/2}\ \mp\tfrac{1}{2}\rangle + \alpha\,|{}^2\Pi_{3/2}\ \pm\tfrac{3}{2}\rangle \qquad (6.4.12b)$$

where $^2\Pi_-$ and $^2\Pi_+$ respectively designate the lower and upper SO-CF levels, and $\pm\frac{1}{2}$ in the left-hand kets denotes the value of M_S. α and β are mixing coefficients given by eqs

(4.4.11) and (4.4.12), and obey the relations given in eqs (4.4.13) – (4.4.15).

6.4.3.2. A $^2\Delta$ term

The $A\ ^2\Delta$ term has no non-zero first-order SO matrix elements (Section 6.4.2.2), making the derivation of eigenfunctions straightforward. The CF matrix formed according to eq (6.4.10) is diagonalised, yielding,

$$|^2\Delta_- \pm\tfrac{1}{2}\rangle = \tfrac{1}{\sqrt{2}}\{|^2\Delta_{5/2} \pm\tfrac{5}{2}\rangle \mp |^2\Delta_{3/2} \mp\tfrac{3}{2}\rangle\} \qquad (6.4.13a)$$

$$|^2\Delta_+ \pm\tfrac{1}{2}\rangle = \pm\tfrac{1}{\sqrt{2}}\{|^2\Delta_{5/2} \pm\tfrac{5}{2}\rangle \pm |^2\Delta_{3/2} \mp\tfrac{3}{2}\rangle\} \qquad (6.4.13b)$$

6.4.4. Zeeman matrix elements and *g* values

Section 3.3.4 describes the method for evaluation of Zeeman matrix elements and g values.

6.4.4.1. X $^2\Pi$ ground term

The angular momentum matrix elements (assuming $g_e \approx 2$) for the SO-CF states of the $X\ ^2\Pi$ term of CH/Ar are the same as those for $X\ ^2\Pi$ of OH/Ar (Table 4.4.3), although the values of $g_{\parallel}^{\pm}$ differ, as shown in eq (6.4.14).

$$g_{\parallel}^{\pm} \equiv 2\,\langle {}^2\Pi_{\pm} +\tfrac{1}{2}|L_z + 2S_z|{}^2\Pi_{\pm} +\tfrac{1}{2}\rangle = 2(1 \pm \kappa\Lambda) \qquad (6.4.14)$$

$g_{\parallel}^{+}$ and $g_{\parallel}^{-}$ are the g values for the upper and lower SO-CF levels, respectively, when the molecular z axis is aligned parallel to $\boldsymbol{B}$. The $g_{\perp}$ values for the $X\ ^2\Pi$ term are the same as those for OH/Ar in eq (4.4.17).

As in the case of OH/Ar, the g values are not mutually independent: Figure 6.4.3 illustrates their dependencies on κ, where it is noted that the $g_{\parallel}^{+}$ and $g_{\parallel}^{-}$ are inverted with respect to OH/Ar (Figure 4.4.3). Orbital reduction ($\kappa < 1$) yields a non-zero first-order Zeeman splitting for the lower ($^2\Pi_-$) SO-CF level, which is important to the analysis of Section 6.5.

Letting $V \rightarrow 0$, and hence $\kappa \rightarrow 1$, one obtains the Zeeman matrix elements for the SO-only case, where $^2\Pi_- \rightarrow {}^2\Pi_{1/2}$ and $^2\Pi_+ \rightarrow {}^2\Pi_{3/2}$.

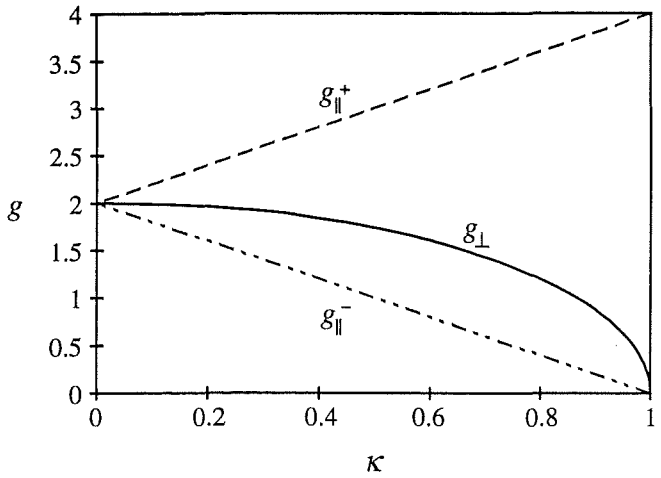

Figure 6.4.3: Dependence of g values for the $X\,^2\Pi$ term of CH/Ar on the orbital reduction factor, κ.

6.4.4.2. A $^2\Delta$ excited term

In the absence of a CF of appropriate symmetry ($V_\Gamma = 0$), the angular momentum matrix elements for $A\,^2\Delta$ of CH are (assuming $g_e \approx 2$),

$$\langle {}^2\Delta_{5/2}\, \pm\tfrac{5}{2} | L_z + 2S_z | {}^2\Delta_{5/2}\, \pm\tfrac{5}{2} \rangle = \pm(\Lambda' + 1)$$

$$\langle {}^2\Delta_{3/2}\, \pm\tfrac{3}{2} | L_z + 2S_z | {}^2\Delta_{3/2}\, \pm\tfrac{3}{2} \rangle = \pm(\Lambda' - 1) \qquad (6.4.15)$$

where Λ' is the orbital angular momentum of the $^2\Delta$ term. After inclusion of the CF ($V_\Gamma \neq 0$) the angular momentum matrices are those given in Table 6.4.3.

Table 6.4.3: Angular momentum matrix elements for the $A\,^2\Delta$ SO-CF states of CH/Ar.

$L_z + 2S_z$	$\lvert {}^2\Delta_-\, -\tfrac{1}{2}\rangle$	$\lvert {}^2\Delta_-\, \tfrac{1}{2}\rangle$	$\lvert {}^2\Delta_+\, -\tfrac{1}{2}\rangle$	$\lvert {}^2\Delta_+\, \tfrac{1}{2}\rangle$
$\langle {}^2\Delta_-\, -\tfrac{1}{2}\rvert$	1	0	Λ'	0
$\langle {}^2\Delta_-\, \tfrac{1}{2}\rvert$	0	-1	0	Λ'
$\langle {}^2\Delta_+\, -\tfrac{1}{2}\rvert$	Λ'	0	1	0
$\langle {}^2\Delta_+\, \tfrac{1}{2}\rvert$	0	Λ'	0	-1

$L_x + 2S_x$	$\lvert {}^2\Delta_-\, -\tfrac{1}{2}\rangle$	$\lvert {}^2\Delta_-\, \tfrac{1}{2}\rangle$	$\lvert {}^2\Delta_+\, -\tfrac{1}{2}\rangle$	$\lvert {}^2\Delta_+\, \tfrac{1}{2}\rangle$
$\langle {}^2\Delta_-\, -\tfrac{1}{2}\rvert$	0	-2	0	0
$\langle {}^2\Delta_-\, \tfrac{1}{2}\rvert$	-2	0	0	0
$\langle {}^2\Delta_+\, -\tfrac{1}{2}\rvert$	0	0	0	-2
$\langle {}^2\Delta_+\, \tfrac{1}{2}\rvert$	0	0	-2	0

6.4.4.3. $B\,^2\Sigma^-$ excited term

In the $B\,^2\Sigma^-$ term, there is no orbital angular momentum and no CF splitting. Hence the Zeeman splitting is approximately isotropic, with $g \approx g_e \approx 2$. The angular momentum matrix elements (Section 3.3.4.1) are,

$$\langle {}^2\Sigma^-_{1/2} \pm\tfrac{1}{2}|L_z + 2S_z|{}^2\Sigma^-_{1/2} \pm\tfrac{1}{2}\rangle = \pm 1 \qquad (6.4.16)$$

6.4.4.4. $C\,^2\Sigma^+$ excited term

Angular momentum matrix elements for the $C\,^2\Sigma^+$ term have a similar form to those of $B\,^2\Sigma^-$ term given in the previous section, since the only angular momentum is due to the spin of a single electron. The elements are,

$$\langle {}^2\Sigma^+_{1/2} \pm\tfrac{1}{2}|L_z + 2S_z|{}^2\Sigma^+_{1/2} \pm\tfrac{1}{2}\rangle = \pm 1 \qquad (6.4.17)$$

6.4.5. Transition-moment matrix elements

Transition moments for $A\,^2\Delta \leftarrow X\,^2\Pi$, $B\,^2\Sigma^- \leftarrow X\,^2\Pi$ and $C\,^2\Sigma^+ \leftarrow X\,^2\Pi$ were evaluated using the method of Section 3.4.2, and the non-zero elements are summarised in Tables 6.4.4, 6.4.5 and 6.4.6, respectively. Initial states are given along the top row and final states down the left hand column. $\mathcal{M}$ is the one-electron reduced transition moment (Section 3.4.2.1) for the orbital excitation $1\pi \leftarrow 3\sigma$,

$$\mathcal{M} = \langle 1\pi \| m^1 \| 3\sigma \rangle \qquad (6.4.18)$$

6.4.6. MCD and absorption

Treatment of CH/Ar generally follows that of OH/Ar (Section 4.4.6), although there are some significant differences. The gas-phase SOC constant of CH $X\,^2\Pi$ is ζ_π = 31.8 cm^{-1},[3] which could be reduced in an Ar matrix due to the external heavy-atom effect.[9,10] It is therefore wise to derive general equations that do not assume the upper SO-CF level ($^2\Pi_+$) in the Ar matrix has a negligible population. The derivation of orientation-dependent wavefunctions for $^2\Pi_-$ and $^2\Pi_+$ initially assumes that the Zeeman interactions between the SO-CF levels are treatable by first-order perturbation theory (*i.e.* as *B* terms). (Without this approximation a 4×4 matrix with 16 non-zero elements must be diagonalised – a problem that is algebraically intractable. In fact, as will be

shown later, the $^2\Pi_+$ level is not significantly populated in these experiments, since the reduction in the SO splitting is more than compensated for by a moderately large CF splitting.)

Table 6.4.4: Transition moments for the $A\ ^2\Delta \leftarrow X\ ^2\Pi_\pm$ SO-CF transitions of CH/Ar.[a]

m^1_{+1}	$\lvert^2\Pi_-\ -\frac{1}{2}\rangle$	$\lvert^2\Pi_-\ \frac{1}{2}\rangle$	$\lvert^2\Pi_+\ -\frac{1}{2}\rangle$	$\lvert^2\Pi_+\ \frac{1}{2}\rangle$
$\langle^2\Delta_-\ -\frac{1}{2}\rvert$	$-\frac{1}{2}\alpha\mathcal{M}$	0	$-\frac{1}{2}\beta\mathcal{M}$	0
$\langle^2\Delta_-\ \frac{1}{2}\rvert$	0	$\frac{1}{2}\beta\mathcal{M}$	0	$\frac{1}{2}\alpha\mathcal{M}$
$\langle^2\Delta_+\ -\frac{1}{2}\rvert$	$-\frac{1}{2}\alpha\mathcal{M}$	0	$-\frac{1}{2}\beta\mathcal{M}$	0
$\langle^2\Delta_+\ \frac{1}{2}\rvert$	0	$\frac{1}{2}\beta\mathcal{M}$	0	$\frac{1}{2}\alpha\mathcal{M}$

m^1_{-1}	$\lvert^2\Pi_-\ -\frac{1}{2}\rangle$	$\lvert^2\Pi_-\ \frac{1}{2}\rangle$	$\lvert^2\Pi_+\ -\frac{1}{2}\rangle$	$\lvert^2\Pi_+\ \frac{1}{2}\rangle$
$\langle^2\Delta_-\ -\frac{1}{2}\rvert$	$-\frac{1}{2}\beta\mathcal{M}$	0	$\frac{1}{2}\alpha\mathcal{M}$	0
$\langle^2\Delta_-\ \frac{1}{2}\rvert$	0	$\frac{1}{2}\alpha\mathcal{M}$	0	$-\frac{1}{2}\beta\mathcal{M}$
$\langle^2\Delta_+\ -\frac{1}{2}\rvert$	$\frac{1}{2}\beta\mathcal{M}$	0	$-\frac{1}{2}\alpha\mathcal{M}$	0
$\langle^2\Delta_+\ \frac{1}{2}\rvert$	0	$-\frac{1}{2}\alpha\mathcal{M}$	0	$\frac{1}{2}\beta\mathcal{M}$

[a] $\mathcal{M}$ is defined in eq (6.4.18).

Table 6.4.5: Transition moments for the $B\ ^2\Sigma^- \leftarrow X\ ^2\Pi_\pm$ SO-CF transitions of CH/Ar.[a]

m^1_{+1}	$\lvert^2\Pi_-\ -\frac{1}{2}\rangle$	$\lvert^2\Pi_-\ \frac{1}{2}\rangle$	$\lvert^2\Pi_+\ -\frac{1}{2}\rangle$	$\lvert^2\Pi_+\ \frac{1}{2}\rangle$
$\langle^2\Sigma^-_{1/2}\ -\frac{1}{2}\rvert$	$\frac{\sqrt{3}}{2}\beta\mathcal{M}$	0	$-\frac{\sqrt{3}}{2}\alpha\mathcal{M}$	0
$\langle^2\Sigma^-_{1/2}\ \frac{1}{2}\rvert$	0	$-\frac{\sqrt{3}}{2}\alpha\mathcal{M}$	0	$\frac{\sqrt{3}}{2}\beta\mathcal{M}$

m^1_{-1}	$\lvert^2\Pi_-\ -\frac{1}{2}\rangle$	$\lvert^2\Pi_-\ \frac{1}{2}\rangle$	$\lvert^2\Pi_+\ -\frac{1}{2}\rangle$	$\lvert^2\Pi_+\ \frac{1}{2}\rangle$
$\langle^2\Sigma^-_{1/2}\ -\frac{1}{2}\rvert$	$\frac{\sqrt{3}}{2}\alpha\mathcal{M}$	0	$\frac{\sqrt{3}}{2}\beta\mathcal{M}$	0
$\langle^2\Sigma^-_{1/2}\ \frac{1}{2}\rvert$	0	$-\frac{\sqrt{3}}{2}\beta\mathcal{M}$	0	$-\frac{\sqrt{3}}{2}\alpha\mathcal{M}$

[a] $\mathcal{M}$ is defined in eq (6.4.18).

Table 6.4.6: Transition moments for the $C\ ^2\Sigma^+ \leftarrow X\ ^2\Pi_\pm$ SO-CF transitions of CH/Ar.[a]

m^1_{+1}	$\lvert^2\Pi_-\ -\frac{1}{2}\rangle$	$\lvert^2\Pi_-\ \frac{1}{2}\rangle$	$\lvert^2\Pi_+\ -\frac{1}{2}\rangle$	$\lvert^2\Pi_+\ \frac{1}{2}\rangle$
$\langle^2\Sigma^+_{1/2}\ -\frac{1}{2}\rvert$	$\frac{1}{2}\beta\mathcal{M}$	0	$-\frac{1}{2}\alpha\mathcal{M}$	0
$\langle^2\Sigma^+_{1/2}\ \frac{1}{2}\rvert$	0	$\frac{1}{2}\alpha\mathcal{M}$	0	$-\frac{1}{2}\beta\mathcal{M}$

m^1_{-1}	$\lvert^2\Pi_-\ -\frac{1}{2}\rangle$	$\lvert^2\Pi_-\ \frac{1}{2}\rangle$	$\lvert^2\Pi_+\ -\frac{1}{2}\rangle$	$\lvert^2\Pi_+\ \frac{1}{2}\rangle$
$\langle^2\Sigma^+_{1/2}\ -\frac{1}{2}\rvert$	$-\frac{1}{2}\alpha\mathcal{M}$	0	$-\frac{1}{2}\beta\mathcal{M}$	0
$\langle^2\Sigma^+_{1/2}\ \frac{1}{2}\rvert$	0	$-\frac{1}{2}\beta\mathcal{M}$	0	$-\frac{1}{2}\alpha\mathcal{M}$

[a] $\mathcal{M}$ is defined in eq (6.4.18).

The CH radicals are initially assumed to be randomly oriented; the averaging procedure of Section 3.4.3.2 is utilised. A significant portion of the CH/Ar data were obtained *outside* the linear limit,[8] so the starting point for the MCD theory is eq (3.4.25), which deals with the most general case in the molecular reference frame.

$\mathbf{M}_0$ comprises contributions from B and C terms, and is treated in two parts. First, C terms are determined explicitly by diagonalisation of the molecular Hamiltonian matrix, including Zeeman elements. Second, in Section 6.4.6.2 first-order perturbation theory is used to deal with the field-induced mixing of states that gives rise to B terms. Finally, in Section 6.4.6.3 $\mathbf{M}_1$ is considered for the case where only the $^2\Pi_-$ level is occupied, and only A terms contribute to $\mathbf{M}_1$. (Considerable complications arise when both levels are populated; Section 3.5.1.2.)

6.4.6.1. Absorption and MCD C terms

In this section, C terms originating from both SO-CF levels of CH/Ar $X\,^2\Pi$ are derived. Expressions are first developed for radicals with their z axes at an angle θ to the field axis Z (Section 3.4.3.2; Figure 3.4.1). Applying eq (3.4.24), the absorption is,

$$\frac{A(E,\theta)}{E} = \frac{1+\cos^2\theta}{4}\gamma c l \sum_{\sigma=\pm}\sum_{\lambda}\sum_{M_S} P_\sigma(M_S)\,(|\langle J\lambda|m_{+1}|^2\Pi_\sigma M_S\rangle|^2 + |\langle J\lambda|m_{-1}|^2\Pi_\sigma M_S\rangle|^2) f_{\lambda,M_S}(E) \qquad (6.4.19)$$

Here $\sigma = \pm$ is a label representing the SO-CF levels of the ground state, and J and λ are the appropriate labels for the excited state. Applying eq (3.4.25) gives the MCD,

$$\frac{\Delta A^1(E,\theta)}{E} = \gamma c l \cos\theta \sum_{\sigma=\pm}\sum_{\lambda}\sum_{M_S} P_\sigma(M_S)\,(|\langle J\lambda|m_{+1}|^2\Pi_\sigma M_S\rangle|^2 - |\langle J\lambda|m_{-1}|^2\Pi_\sigma M_S\rangle|^2) f_{\lambda,M_S}(E) \qquad (6.4.20)$$

The population factors $P_\sigma(M_S)$ in eqs (6.4.19) and (6.4.20) are not easily dealt with, due to their dependence on the relative populations of the $^2\Pi_\sigma$ levels, and $g_\parallel{}^\sigma$ and $g_\perp$ (whose contributions change with θ (eqs (6.4.14) and (4.4.17); Section 3.4.3.2)). Of these factors, the anisotropy of the g values in the $X\,^2\Pi$ term (due to non-zero orbital angular momentum) necessitate the following treatment, since the SO-CF splitting is independent of radical orientation with respect to the laboratory Z axis.

Using the angular momentum matrix elements given in Table 4.4.3, and eq (4.4.22) for transformation to the laboratory reference frame, the non-zero matrix elements of μ_Z within each of the $^2\Pi_\sigma$ levels of the $X\,^2\Pi$ term are,

$$\langle {}^2\Pi_\sigma \pm\tfrac{1}{2}|-\mu_Z B|{}^2\Pi_\sigma \pm\tfrac{1}{2}\rangle = \pm\tfrac{1}{2}\cos\theta\, g_{\|}{}^{\sigma}\mu_B B \tag{6.4.21}$$

$$\langle {}^2\Pi_\sigma \pm\tfrac{1}{2}|-\mu_Z B|{}^2\Pi_\sigma \mp\tfrac{1}{2}\rangle = \mp\tfrac{i}{2}\sin\theta\exp(\pm i\psi)\, g_{\perp}\mu_B B \tag{6.4.22}$$

ψ is the Euler angle defined in Figure 3.4.1. (B terms account for second-order Zeeman interactions *between* SO-CF levels (Section 6.4.6.2).) The Zeeman splitting as a function of θ is obtained by solving a secular equation for the Zeeman interaction that is common to each SO-CF level. The energies are,

$$E_B(\sigma,\pm) = \pm\tfrac{1}{2} g_\theta{}^{\sigma}\mu_B B \tag{6.4.23}$$

Here $E_B(\sigma,\pm)$ gives the energies of the raised and lowered magnetic-field-mixed SO-CF basis functions *within* the $^2\Pi_\sigma$ levels, and $g_\theta{}^{\sigma}$ is,

$$g_\theta{}^{\sigma} = \sqrt{(g_{\|}{}^{\sigma}\cos\theta)^2 + (g_{\perp}\sin\theta)^2} \tag{6.4.24}$$

The eigenfunctions in the Zeeman effect for the $^2\Pi_\sigma$ terms are then,

$$|{}^2\Pi_\sigma \pm\rangle = \pm a_\sigma|{}^2\Pi_\sigma \mp\tfrac{1}{2}\rangle + b_\sigma|{}^2\Pi_\sigma \pm\tfrac{1}{2}\rangle \tag{6.4.25}$$

where the mixing coefficients a_σ and b_σ satisfy,

$$|b_\sigma|^2 = \frac{(g_{\perp}\sin\theta)^2}{2g_\theta{}^{\sigma}(g_\theta{}^{\sigma} - g_{\|}{}^{\sigma}\cos\theta)} \tag{6.4.26}$$

$$|a_\sigma|^2 + |b_\sigma|^2 = 1 \tag{6.4.27}$$

$$|b_\sigma|^2 - |a_\sigma|^2 = \frac{g_{\|}{}^{\sigma}\cos\theta}{g_\theta{}^{\sigma}} \tag{6.4.28}$$

Since the SO-CF splitting is given by Δ (eq (6.4.11)), and using eq (6.4.23), the fractional Boltzmann populations are,

$$P_{-}(\pm) = \frac{1}{Q}\exp\left(\mp\frac{g_\theta{}^{-}\mu_B B}{2kT}\right)\exp(\Delta/2kT) \tag{6.4.29a}$$

$$P_{+}(\pm) = \frac{1}{Q}\exp\left(\mp\frac{g_\theta{}^{+}\mu_B B}{2kT}\right)\exp(-\Delta/2kT) \tag{6.4.29b}$$

where P_- and P_+ are the populations of the $^2\Pi_-$ and $^2\Pi_+$ levels, and the bracketed '+' and '–' indicate the raised and lowered Zeeman states of eq (6.4.23). Q is the partition function,

$$Q = \left[\exp\left(-\frac{g_\theta^- \mu_B B}{2kT}\right) + \exp\left(\frac{g_\theta^- \mu_B B}{2kT}\right)\right]\exp(\Delta/2kT) + \left[\exp\left(-\frac{g_\theta^+ \mu_B B}{2kT}\right) + \exp\left(\frac{g_\theta^+ \mu_B B}{2kT}\right)\right]\exp(-\Delta/2kT)$$

$$= 2\cosh\left(\frac{g_\theta^- \mu_B B}{2kT}\right)\exp(\Delta/2kT) + 2\cosh\left(\frac{g_\theta^+ \mu_B B}{2kT}\right)\exp(-\Delta/2kT) \qquad (6.4.30)$$

Useful relationships for calculation of the MCD are,

$$P_-(-) - P_-(+) = \frac{2}{Q}\sinh\left(\frac{g_\theta^- \mu_B B}{2kT}\right)\exp(\Delta/2kT) \qquad (6.4.31a)$$

$$P_+(-) - P_+(+) = \frac{2}{Q}\sinh\left(\frac{g_\theta^+ \mu_B B}{2kT}\right)\exp(-\Delta/2kT) \qquad (6.4.31b)$$

Eqs (6.4.29) – (6.4.31) demonstrate that calculation of the MCD moments is considerably more complicated than for OH/Ar if both SO-CF levels are occupied. In the case that only $^2\Pi_-$ is populated $P_+(+) = P_+(-) = 0$, and using eq (6.4.30) and replacing $\exp(-\Delta/2kT)$ by 0, eq (6.4.31a) becomes,

$$P_-(-) - P_-(+) = \tanh\left(\frac{g_\theta^- \mu_B B}{2kT}\right) \qquad (6.4.32)$$

Now returning to eqs (6.4.19) and (6.4.20), the absorption and MCD moments (Section 3.5.1.2) are defined as $\mathbf{A}_0^\theta$ and $\mathbf{C}_0^\theta$, respectively (where the latter accounts for only the C-term contribution to $\mathbf{M}_0$). For transitions originating from the Zeeman eigenstates ($\pm$) within each $^2\Pi_\sigma$ level, these moments are given by eqs (6.4.33) and (6.4.34). (The principle of spectroscopic stability[8] has been employed in the choice of excited-state basis functions.) The superscript θ indicates that the moment is specified for a particular orientation of the molecule with respect to the field axis (Z).

$$\mathbf{A}_0^\theta(\sigma,\pm) = \frac{1+\cos^2\theta}{4}\gamma c l \sum_\lambda P_\sigma(\pm)\left(|\langle J\lambda|m_{+1}|^2\Pi_\sigma\pm\rangle|^2 + |\langle J\lambda|m_{-1}|^2\Pi_\sigma\pm\rangle|^2\right) \qquad (6.4.33)$$

$$\mathbf{C}_0^{\theta}(\sigma,\pm) = \gamma c l \cos\theta \sum_{\lambda} P_{\sigma}(\pm) \left(|\langle J\lambda|m_{+1}|^2\Pi_{\sigma}\pm\rangle|^2 - |\langle J\lambda|m_{-1}|^2\Pi_{\sigma}\pm\rangle|^2\right) \qquad (6.4.34)$$

The transition moments from the Zeeman eigenstates of $X\,^2\Pi_\sigma$ to the $A\,^2\Delta$, $B\,^2\Sigma^-$ and $C\,^2\Sigma^+$ manifolds are readily calculated using eq (6.4.25) with Tables 6.4.4, 6.4.5 and 6.4.6, respectively. Using these transition moments with eqs (6.4.33) and (6.4.34), and eqs (4.4.14), (4.4.15) and (6.4.27) – (6.4.31), the absorption and MCD zeroth moments for the three transitions are given by eqs (6.4.35) and (6.4.36); they differ only by constants, $\mathcal{Z}_A$ and $\mathcal{Z}_M$, respectively, which are given in Table 6.4.7.

$$\mathbf{A}_0^{\theta} = \frac{\mathcal{Z}_A \gamma c l (1+\cos^2\theta)\,\mathcal{M}^2}{8} \qquad (6.4.35)$$

$$\mathbf{C}_0^{\theta} = \frac{\mathcal{Z}_M \gamma c l\, \kappa \cos^2\theta\, \mathcal{M}^2}{Q}\left[\frac{g_{\parallel}^-}{g_{\theta}^-}\sinh\left(\frac{g_{\theta}^-\mu_B B}{2kT}\right)\exp(\Delta/2kT) - \frac{g_{\parallel}^+}{g_{\theta}^+}\sinh\left(\frac{g_{\theta}^+\mu_B B}{2kT}\right)\exp(-\Delta/2kT)\right] \qquad (6.4.36)$$

$\mathcal{M}$ was defined in eq (6.4.18).

Table 6.4.7: Coefficients for absorption and MCD moments for the $A\,^2\Delta$, $B\,^2\Sigma^-$ and $C\,^2\Sigma^+ \leftarrow X\,^2\Pi$ transitions of CH/Ar.

Transition	$\mathcal{Z}_A$	$\mathcal{Z}_M$	$\mathcal{Z} = \mathcal{Z}_M / \mathcal{Z}_A$
$A\,^2\Delta \leftarrow X\,^2\Pi$	1	1	1
$B\,^2\Sigma^- \leftarrow X\,^2\Pi$	3/2	-3/2	-1
$C\,^2\Sigma^+ \leftarrow X\,^2\Pi$	1/2	-1/2	-1

Consideration of eq (6.4.36) allows the sign of the zeroth moment of the MCD to be predicted. At low temperatures, the Π_- level is the most populated, so the first term within the square brackets will dominate. The sign of the MCD zeroth moment is then determined by the coefficient $\mathcal{Z}_M$, since all of the other parameters are either squared or intrinsically positive. Hence, the transition $A\,^2\Delta \leftarrow X\,^2\Pi$ should be associated with positive MCD, and the other two transitions with negative MCD, exactly as observed. Furthermore, the fact that C terms arising from the $^2\Pi_-$ level are observed at all temperatures investigated here requires $0 < \kappa < 1$; if $\kappa = 0$, the factor outside the square brackets vanishes, while for $\kappa = 1$, $g_{\parallel}^- = 0$ (eq (6.4.14)). Therefore it

can be concluded that the ground-state orbital angular momentum of CH is partially, but not completely, quenched in an Ar host.

Eqs (6.4.35) and (6.4.36) allow the ratio $\mathbf{C}_0/\mathbf{A}_0$ to be determined for any angle θ. If CH is *Z*-oriented (*i.e.* $\theta = 0$), then

$$\mathbf{C}_0^0/\mathbf{A}_0^0 = \frac{4\mathcal{Z}\kappa}{Q}\left[\sinh\left(\frac{g_\parallel^- \mu_B B}{2kT}\right)\exp(\Delta/2kT) - \sinh\left(\frac{g_\parallel^+ \mu_B B}{2kT}\right)\exp(-\Delta/2kT)\right] \tag{6.4.37}$$

where $\mathcal{Z}$ is the ratio $\mathcal{Z}_M/\mathcal{Z}_A$ (see Table 6.4.7), and hence is unity for $A\,^2\Delta \leftarrow X\,^2\Pi$, and -1 for $B\,^2\Sigma^- \leftarrow X\,^2\Pi$ and $C\,^2\Sigma^+ \leftarrow X\,^2\Pi$.

It is far more likely that the CH molecules are randomly oriented, so $\mathbf{A}_0^\theta$ and $\mathbf{C}_0^\theta$ are averaged over θ (Section 3.4.3.2) to give $\bar{\mathbf{A}}_0$ and $\bar{\mathbf{C}}_0$:

$$\bar{\mathbf{C}}_0/\bar{\mathbf{A}}_0 = 3\mathcal{Z}\kappa\left[\exp(\Delta/2kT)\int_0^1 \frac{1}{Q}\frac{g_\parallel^- \cos^2\theta}{g_\theta^-}\sinh\left(\frac{g_\theta^- \mu_B B}{2kT}\right)d\cos\theta - \exp(-\Delta/2kT)\int_0^1 \frac{1}{Q}\frac{g_\parallel^+ \cos^2\theta}{g_\theta^+}\sinh\left(\frac{g_\theta^+ \mu_B B}{2kT}\right)d\cos\theta\right] \tag{6.4.38}$$

Numerical integration is used to extract various parameters (including κ) from the saturation curves (Figures 6.3.14, 6.3.15 and 6.3.16), as described in Section 6.5.2.

Invoking the linear limit[8] ($\mu_B B << 2kT$; Section 3.4.3), gives $Q \approx 4$ (eq (6.4.30)), and allows the approximation,

$$\sinh\left(\frac{g_\theta^\sigma \mu_B B}{2kT}\right) \approx \frac{g_\theta^\sigma \mu_B B}{2kT} \tag{6.4.39}$$

Defining δ as the fractional population of the $^2\Pi_-$ level, the following are obtained from eq (6.4.29),

$$P_-(-) + P_-(+) = \delta = \tfrac{1}{2}\exp(\Delta/2kT)$$

$$P_+(-) + P_+(+) = 1 - \delta = \tfrac{1}{2}\exp(-\Delta/2kT) \tag{6.4.40}$$

Substitution of eqs (6.4.39) and (6.4.40) with $Q = 4$ into (6.4.37) and (6.4.38), gives the *C*-term contribution to the MCD in the linear limit:

$$\mathbf{C}_0^0/\mathbf{A}_0^0 \approx \frac{2\mathcal{Z}(2\delta - 1 - \kappa)\kappa\mu_B B}{kT} \tag{6.4.41}$$

for the Z-oriented case; and,

$$\bar{\mathbf{C}}_0/\bar{\mathbf{A}}_0 \approx \frac{\mathcal{Z}(2\delta - 1 - \kappa)\kappa\mu_B B}{kT} \tag{6.4.42}$$

for the orientationally averaged case. Note that the $\bar{\mathbf{C}}_0/\bar{\mathbf{A}}_0$ ratio in the linear limit is half that of $\mathbf{C}_0^0/\mathbf{A}_0^0$.

Now the scenario is considered where only the $^2\Pi_-$ level is significantly populated. (Section 6.5.1 shows that this is the case for CH/Ar at $T \lesssim 16$ K.) Using eq (6.4.32), $\mathbf{C}_0^\theta$ of eq (6.4.36) becomes,

$$\mathbf{C}_0^\theta = \frac{\mathcal{Z}_M \gamma c l \kappa g_\parallel^- \cos^2\theta |m|^2}{2g_\theta^-} \tanh\left(\frac{g_\theta^-\mu_B B}{2kT}\right) \tag{6.4.43}$$

Using eqs (6.4.35) and (6.4.43), with $\theta = 0$ the ratio $\mathbf{C}_0/\mathbf{A}_0$ is particularly simple,

$$\mathbf{C}_0^0/\mathbf{A}_0^0 = 2\mathcal{Z}\kappa \tanh\left(\frac{g_\parallel^-\mu_B B}{2kT}\right) \tag{6.4.44}$$

However, as was noted after eq (6.4.37), it is more likely that the CH radicals are randomly oriented in the Ar lattice, and $\mathbf{A}_0$ and $\mathbf{C}_0$ must be orientationally averaged using the procedure described in Section 3.4.3.2. This yields,

$$\bar{\mathbf{C}}_0/\bar{\mathbf{A}}_0 = 3\mathcal{Z}\kappa \int_0^1 \frac{g_\parallel^- \cos^2\theta}{g_\theta^-} \tanh\left(\frac{g_\theta^-\mu_B B}{2kT}\right) d\cos\theta \tag{6.4.45}$$

which, like eq (6.4.38), must be solved numerically.

In the linear limit,[8] one obtains for the Z-oriented case,

$$\mathbf{C}_0^0/\mathbf{A}_0^0 \approx \frac{\mathcal{Z}\kappa g_\parallel^-\mu_B B}{kT} = \frac{2\mathcal{Z}\kappa(1-\kappa)\mu_B B}{kT} \tag{6.4.46}$$

and for the orientationally averaged case,

$$\bar{\mathbf{C}}_0/\bar{\mathbf{A}}_0 \approx \frac{\mathcal{Z}\kappa g_\parallel^-\mu_B B}{2kT} = \frac{\mathcal{Z}\kappa(1-\kappa)\mu_B B}{kT} \tag{6.4.47}$$

Again, $\bar{\mathbf{C}}_0/\bar{\mathbf{A}}_0$ is half $\mathbf{C}_0^0/\mathbf{A}_0^0$. Also, comparing eqs (6.4.45) and (6.4.47), it is clear that $g_\perp$ (through its contribution to g_θ^-; eq (6.4.24)) is only important outside the linear limit.[11]

6.4.6.2. MCD B *terms*

B-term contributions to the MCD[11] are now considered by allowing field-induced mixing of $|^2\Pi_-\rangle$ and $|^2\Pi_+\rangle$. In the first instance, the possibility of the $^2\Pi_+$ level being occupied is considered. Hence, the analysis differs from OH/Ar in that perturbed wavefunctions are computed for *both* $^2\Pi_-$ and $^2\Pi_+$. In doing so it is assumed that the mixing of these levels by the magnetic field is small with respect to the first-order effect, allowing application of perturbation theory.

The Zeeman eigenfunctions $|^2\Pi_\sigma \pm\rangle$ of eq (6.4.25) become,

$$|^2\Pi_\sigma \pm\rangle = |^2\Pi_\sigma \pm\rangle^0 + |^2\Pi_\sigma \pm\rangle' \tag{6.4.48}$$

where the ^{0} and $'$ respectively denote the states in the absence of the perturbation, and the correction for the perturbation. The *B* term arises from the second term, which can be expressed as,[8]

$$|^2\Pi_- \pm\rangle' = -\frac{\mu_B B}{\Delta} \sum_{\nu=\pm} |^2\Pi_+ \nu\rangle^0 \langle ^2\Pi_+ \nu|L_Z + 2S_Z|^2\Pi_- \pm\rangle^0 \tag{6.4.49a}$$

$$|^2\Pi_+ \pm\rangle' = +\frac{\mu_B B}{\Delta} \sum_{\nu=\pm} |^2\Pi_- \nu\rangle^0 \langle ^2\Pi_- \nu|L_Z + 2S_Z|^2\Pi_+ \pm\rangle^0 \tag{6.4.49b}$$

where ν labels the raised and lowered Zeeman eigenfunctions of eq (6.4.25)). Since the Zeeman matrix element is expressed in terms of laboratory-fixed coordinates, eq (6.4.49) must be transformed to the molecular reference frame, in terms of the operators L_z, S_z and L_x, S_x. Following the method of Section 3.4.3.2 the corrections are,

$$|^2\Pi_- \pm\rangle' = -\frac{\mu_B B}{2\Delta}\left[\pm(\cos\theta\, a g_\perp - 2\sin\theta\, b\kappa)|^2\Pi_+ \mp\tfrac{1}{2}\rangle + (\cos\theta\, b g_\perp + 2\sin\theta\, a\kappa)|^2\Pi_+ \pm\tfrac{1}{2}\rangle\right] \tag{6.4.50a}$$

$$|^2\Pi_+ \pm\rangle' = +\frac{\mu_B B}{2\Delta}\left[\pm(\cos\theta\, a g_\perp + 2\sin\theta\, b\kappa)|^2\Pi_- \mp\tfrac{1}{2}\rangle + (\cos\theta\, b g_\perp - 2\sin\theta\, a\kappa)|^2\Pi_- \pm\tfrac{1}{2}\rangle\right] \tag{6.4.50b}$$

Transition moments from these corrected functions are computed in the usual manner (Section 3.4.2), while invoking the principle of spectroscopic stability in the choice of the excited-state basis (Section 6.4.1.2).[8] (Hence for calculation of the moments for $A\,^2\Delta \leftarrow X\,^2\Pi$, the more computation-intensive SO-CF basis for $A\,^2\Delta$ need not be used.) The corrections to the transition moments are combined with the

unperturbed ones, according to eq (4.4.46), to give the total transition moments. In this analysis, $\langle J| = \langle {}^2\Delta_\Omega M_\Omega|$, $\langle {}^2\Sigma^- \pm\tfrac{1}{2}|$ or $\langle {}^2\Sigma^+ \pm\tfrac{1}{2}|$ and $|A\rangle = |{}^2\Pi_\sigma \pm\rangle$.

Evaluation of the $[J|m|A]^2$ (= $2\mathcal{R}_e(\langle J|m_{\pm1}|A\rangle \langle J|m_{\pm1}|A\rangle'^*)$) given in eq (4.4.46) enables calculation of the B-term contribution to the MCD for an orientation θ. These differences have the form, $\cos\theta$ ($[J|m_{+1}|A]^2 - [J|m_{-1}|A]^2$). Summation over all non-zero transitions weighted by their ground-state population factor (eq (6.4.29)), and multiplication by γcl, yields the B-term contribution to the zeroth MCD moment $\mathbf{B}_0^\theta$,

$$\mathbf{B}_0^\theta = -\frac{\mathcal{Z}_M \gamma cl (g_\perp \cos\theta)^2 \mu_B B |\mathcal{M}|^2}{2Q\Delta}\left[\cosh\left(\frac{g_\theta^- \mu_B B}{2kT}\right)\exp(\Delta/2kT) - \cosh\left(\frac{g_\theta^+ \mu_B B}{2kT}\right)\exp(-\Delta/2kT)\right] \qquad (6.4.51)$$

The leading negative sign indicates that the B terms are of *opposite* sign to the C terms. When combined with eq (6.4.35), the results for the Z-oriented ($\theta = 0$) and randomly oriented cases are, respectively,

$$\mathbf{B}_0^0/\mathbf{A}_0^0 = -\frac{2\mathcal{Z} g_\perp^2 \mu_B B}{Q\Delta}\left[\cosh\left(\frac{g_\parallel^- \mu_B B}{2kT}\right)\exp(\Delta/2kT) - \cosh\left(\frac{g_\parallel^+ \mu_B B}{2kT}\right)\exp(-\Delta/2kT)\right] \qquad (6.4.52)$$

$$\bar{\mathbf{B}}_0/\bar{\mathbf{A}}_0 = -\frac{3\mathcal{Z}\mu_B B}{\Delta}\left[\exp(\Delta/2kT)\int_0^1 \frac{1}{Q}(g_\perp \cos\theta)^2 \cosh\left(\frac{g_\theta^- \mu_B B}{2kT}\right) d\cos\theta - \exp(-\Delta/2kT)\int_0^1 \frac{1}{Q}(g_\perp \cos\theta)^2 \cosh\left(\frac{g_\theta^+ \mu_B B}{2kT}\right) d\cos\theta\right] \qquad (6.4.53)$$

In the linear limit, eqs (6.4.39) and (6.4.40) apply, and the following results are obtained for Z-oriented and randomly oriented CH.

$$\mathbf{B}_0^0/\mathbf{A}_0^0 = -\frac{\mathcal{Z}(2\delta - 1) g_\perp^2 \mu_B B}{\Delta} \qquad (6.4.54)$$

$$\bar{\mathbf{B}}_0/\bar{\mathbf{A}}_0 = -\frac{\mathcal{Z}(2\delta - 1) g_\perp^2 \mu_B B}{2\Delta} \qquad (6.4.55)$$

Once again $\bar{\mathbf{B}}_0/\bar{\mathbf{A}}_0$ takes half the value of $\mathbf{B}_0^0/\mathbf{A}_0^0$. These equations also show that when both ${}^2\Pi_-$ and ${}^2\Pi_+$ are occupied (*i.e.* $\delta < 1$), the B-term component of $\mathbf{M}_0$ is reduced in magnitude.

If only the $^2\Pi_-$ level is populated, the above equations simplify dramatically. Using eq (6.4.32), eq (6.4.51) becomes,

$$\mathbf{B}_0^{\theta} = -\frac{\mathcal{Z}_M \gamma c l (g_\perp \cos\theta)^2 \mu_B B |\mathcal{M}|^2}{4\Delta} \qquad (6.4.56)$$

Eq (6.4.56) clearly demonstrates that the *B*-term contribution to $\mathbf{M}_0$ does *not* saturate, but increases linearly with field strength (while $\mu_B B << \Delta$). Likewise, when only $^2\Pi_-$ is occupied, eqs (6.4.52) and (6.4.53) become,

$$\mathbf{B}_0^0/\mathbf{A}_0^0 = -\frac{\mathcal{Z} g_\perp^2 \mu_B B}{\Delta} \qquad (6.4.57)$$

$$\bar{\mathbf{B}}_0/\bar{\mathbf{A}}_0 = -\frac{\mathcal{Z} g_\perp^2 \mu_B B}{2\Delta} \qquad (6.4.58)$$

B-term contributions arising from Zeeman interactions between the terms investigated in this work, or other higher-lying terms, are not considered, because separations are too large to allow significant mixing.

6.4.6.3. MCD A terms and M_1

Contributors to the first MCD moment, $\mathbf{M}_1$, are *A* terms (Section 1.3.2), and *B* and *C* terms displaced from the overall band barycentre, $\bar{E}$ (eq (3.5.13)). $\mathbf{M}_1$, like $\mathbf{M}_0$, is independent of the choice of excited-state basis.[8]

A terms are a temperature-independent consequence of degeneracies in the ground and/or excited states (Section 1.3.2), and their contributions to $\mathbf{M}_1$ are independent of their displacements from $\bar{E}$ (eq (3.5.13)). This section describes the derivation of *A* terms outside the linear limit, before concluding with a presentation of $\mathbf{M}_1$ for the transitions in the case where only the $^2\Pi_-$ level is occupied.

In computing the *A*-term contribution outside the linear limit, the angle-dependent wavefunctions generated for $X\,^2\Pi$ (eq (6.4.25)) are used. These wavefunctions are diagonal in the Zeeman effect within each σ level. (Interactions between levels were accounted for by the *B* terms of the previous section.)

The SO basis is chosen for the $A\,^2\Delta$, $B\,^2\Sigma^-$ and $C\,^2\Sigma^+$ excited terms (eq (6.4.4)). This choice is justified as follows. Firstly, $\mathbf{M}_1$ is insensitive to the choice. Secondly for the case of the $A\,^2\Delta$ term (which is the only excited term that is susceptible to CF splitting) the MCD of band 1 at warmer temperatures (shown in Figure 6.3.1) is

characteristic of a dominant near-pure A-term component rather than a pseudo-A term. It can therefore be concluded that the magnitude of the CF-splitting is negligible in this case (presumably because CFs of Γ symmetry are weak in an Ar matrix). Zeeman matrix elements for these terms are given by eqs (6.4.15), (6.4.16) and (6.4.17), respectively, while the transition moments are described prior to eq (6.4.33). Consideration of the angular dependence of the Zeeman elements and transition moments requires multiplication by a factor of $\cos\theta$ in each case. They are used to compute A terms as follows.

Outside the linear limit the A term is given by,[8]

$$A_1(\sigma) = \sum_{\nu\,\lambda} P_\sigma(\nu)\, A(\lambda\nu) \tag{6.4.59}$$

$A_1(\sigma)$ is the magnitude of the A term arising from transitions originating in the σ level of the ground state; it results from a sum of contributions $A(\lambda\nu)$ from transitions between the individual Zeeman states (designated ν and λ for the ground and excited states, respectively) weighted by the populations of the initial Zeeman state, $P_\sigma(\nu)$ (eq (6.4.29)). $A(\lambda\nu)$ is defined by,

$$\begin{aligned} A(\lambda\nu) = {} & (\langle J\lambda|L_Z + 2S_Z|J\lambda\rangle - \langle {}^2\Pi_\sigma\, \nu|L_Z + 2S_Z|{}^2\Pi_\sigma\, \nu\rangle) \times \\ & (|\langle J\lambda|m_{+1}|{}^2\Pi_\sigma\, \nu\rangle|^2 - |\langle J\lambda|m_{-1}|{}^2\Pi_\sigma\, \nu\rangle|^2) \end{aligned} \tag{6.4.60}$$

Including angle dependence, and denoting the A-term contribution by A_1^θ, yields the following for the three transitions,

$$A_1^\theta({}^2\Delta \leftarrow {}^2\Pi_\sigma) = \tfrac{1}{2}(2-\kappa^2)\mu_B B \cos^2\theta\, |m|^2\, P_\sigma \tag{6.4.61}$$

$$A_1^\theta({}^2\Sigma^- \leftarrow {}^2\Pi_\sigma) = \tfrac{3}{4}\kappa^2\mu_B B \cos^2\theta\, |m|^2\, P_\sigma \tag{6.4.62}$$

$$A_1^\theta({}^2\Sigma^+ \leftarrow {}^2\Pi_\sigma) = \tfrac{1}{4}\kappa^2\mu_B B \cos^2\theta\, |m|^2\, P_\sigma \tag{6.4.63}$$

where

$$P_\sigma = (P_\sigma(+) + P_\sigma(-)) \tag{6.4.64}$$

Apart from the population factors in eqs (6.4.61) to (6.4.63), it is clear that the A terms arising from the two SO-CF levels of the ground state are identical in magnitude and

phase. In addition, each of these expressions is linear in B, so the A-term contribution to the MCD does not saturate with increasing magnetic field.

The role of the orbital reduction factor (κ) in eqs (6.4.61) to (6.4.63) is worthy of special note. After eq (6.4.36) it was noted that κ must be reduced from unity in order to obtain C terms of the sign observed experimentally. In like manner, a reduction of κ can explain the bisignated nature of the MCD for the $A\,^2\Delta \leftarrow X\,^2\Pi$ transition at higher temperatures and stronger fields, and the single-signedness of the other band systems under all conditions investigated in this thesis. In the absence of orbital reduction, the A-term intensities for each transition are in the same ratios as the values of $|\mathcal{J}_M|$ (Table 6.4.7). When $\kappa < 1$, the intensities of the $B\,^2\Sigma^-$ and $C\,^2\Sigma^+$ A terms fall off with κ^2, resulting in rapid intensity loss. Simultaneously, the $A\,^2\Delta$ intensity increases *via* $2 - \kappa^2$ proportionality. Hence when $\kappa < 1$ one might expect to observe an A term for $A\,^2\Delta \leftarrow X\,^2\Pi$, but *not* for the other transitions (see Section 6.5.1).

So far, only the A-term contributions to the first MCD moment have been considered. In order to find the overall first moment, $\mathbf{M}_1^\theta$, the contributions from the $\mathbf{M}_0^\theta(\sigma)$ components are required, where $\mathbf{M}_0^\theta(\sigma) = \mathbf{B}_0^\theta(\sigma) + \mathbf{C}_0^\theta(\sigma)$. $\mathbf{C}_0^\theta(\sigma)$ and $\mathbf{B}_0^\theta(\sigma)$ were calculated in the analysis of the two previous sections, and are given in eqs (6.4.36) and (6.4.51) for the two $^2\Pi_\sigma$ levels. However, in the situation where both SO-CF levels have significant populations, evaluation of $\mathbf{M}_1^\theta$ becomes very difficult because the band barycentre $\bar{E}$ will be temperature dependent (eqs (3.5.3) and (3.5.4)); *i.e.* as T changes the absorption will change. To circumvent this problem, only the case where the $^2\Pi_-$ level is significantly occupied (*i.e.* $P_- = 1$; $P_+ = 0$) is treated here, in which case, $\mathbf{M}_0^\theta$ does *not* contribute to $\mathbf{M}_1^\theta$. (Justification of this assumption follows in Section 6.5.1.) Using eq (3.5.8) with eqs (6.4.61) to (6.4.63) for the $A\,^2\Delta$, $B\,^2\Sigma^-$ and $C\,^2\Sigma^+ \leftarrow X\,^2\Pi$ systems, respectively, the $\mathbf{M}_1^\theta$ are,

$$\mathbf{M}_1^\theta(A\,^2\Delta \leftarrow X\,^2\Pi_-) = \tfrac{1}{2}(2 - \kappa^2)\gamma c l \mu_B B \cos^2\theta\, |\mathcal{M}|^2 \qquad (6.4.65)$$

$$\mathbf{M}_1^\theta(B\,^2\Sigma^- \leftarrow X\,^2\Pi_-) = \tfrac{3}{4}\kappa^2 \mu_B B \cos^2\theta\, |\mathcal{M}|^2 \qquad (6.4.66)$$

$$\mathbf{M}_1^\theta(C\,^2\Sigma^+ \leftarrow X\,^2\Pi_-) = \tfrac{1}{4}\kappa^2 \mu_B B \cos^2\theta\, |\mathcal{M}|^2 \qquad (6.4.67)$$

Eqs (6.4.65) to (6.4.67) with eq (6.4.35) enable the ratio $\mathbf{M}_1/\mathbf{A}_0$ to be evaluated for any orientation, θ. If CH is Z-oriented,

$$\mathbf{M}_1^0/\mathbf{A}_0^0(A\,^2\Delta \leftarrow X\,^2\Pi_-) = 2(2-\kappa^2)\mu_B B \tag{6.4.68}$$

$$\mathbf{M}_1^0/\mathbf{A}_0^0(B\,^2\Sigma^- \leftarrow X\,^2\Pi_-) = 2\kappa^2\mu_B B \tag{6.4.69}$$

$$\mathbf{M}_1^0/\mathbf{A}_0^0(C\,^2\Sigma^+ \leftarrow X\,^2\Pi_-) = 2\kappa^2\mu_B B \tag{6.4.70}$$

Orientational averaging of $\mathbf{M}_1^\theta$ and $\mathbf{A}_0^\theta$ over θ gives,

$$\bar{\mathbf{M}}_1/\bar{\mathbf{A}}_0(A\,^2\Delta \leftarrow X\,^2\Pi_-) = (2-\kappa^2)\mu_B B \tag{6.4.71}$$

$$\bar{\mathbf{M}}_1/\bar{\mathbf{A}}_0(B\,^2\Sigma^- \leftarrow X\,^2\Pi_-) = \kappa^2\mu_B B \tag{6.4.72}$$

$$\bar{\mathbf{M}}_1/\bar{\mathbf{A}}_0(C\,^2\Sigma^+ \leftarrow X\,^2\Pi_-) = \kappa^2\mu_B B \tag{6.4.73}$$

These expressions for Z- and randomly oriented CH/Ar apply both outside and within the linear limit[8] because the assumption that only $^2\Pi_-$ is occupied makes them independent of population factors. Notice that $\bar{\mathbf{M}}_1/\bar{\mathbf{A}}_0$ is half $\mathbf{M}_1^0/\mathbf{A}_0^0$.

6.5. Data analysis and discussion

The experimental data presented in Figures 6.3.1 to 6.3.12 demonstrate temperature and field dependencies indicative of C terms. This section explains the results in terms of the SO-CF model developed in the previous section, and likely sources of observed structure are discussed briefly.

In the only previous work on the MCD of CH/Ar, Rose proposed a model in which total quenching of the orbital angular momentum resulted in near-degenerate Ω = 1/2 and 3/2 SO levels in the $X\,^2\Pi$ ground term.[7] This thesis demonstrates that the splitting of the ground-state term clearly persists in the matrix, and that only the lowest level is occupied at temperatures $\lesssim$16 K.

6.5.1. Consideration of ground-state populations

Assuming, in this section, that CH is randomly oriented in an Ar matrix (*cf.* OH/Ar, Section 4.5.1), the expressions for $\mathbf{C}_0/\mathbf{A}_0$ and $\mathbf{B}_0/\mathbf{A}_0$ given in eqs (6.4.38) and (6.4.53), respectively, have complicated population dependencies. This section shows

that under the conditions of these experiments, only $^2\Pi_-$ is occupied to a measurable extent.

Figures 6.3.14, 6.3.15 and 6.3.16 illustrate the behaviour of $\mathbf{M}_0/\mathbf{A}_0$ as a function of $\mu_B B$ at several temperatures for the $A\,^2\Delta$, $B\,^2\Sigma^-$ and $C\,^2\Sigma^+ \leftarrow X\,^2\Pi$ transitions, respectively. These curves saturate more strongly at lower T, as expected for C terms (eq (6.4.45)), and are observed to tend toward zero as a consequence of the $\sim 1/T$ dependence. At ~16 K, Figure 6.3.13 shows that $\mathbf{M}_0/\mathbf{A}_0 \approx 0$ for all three transitions, indicating the temperature at which the C- and B-term contributions to $\mathbf{M}_0$ (eqs (6.4.45) and (6.4.58)) cancel. At $T > 16$ K the magnetisation curves will be almost linear and have the opposite sign to those illustrated in Figures 6.3.14 to 6.3.16, because at these higher temperatures the MCD will be dominated by B terms (eq (6.4.58)), which do not saturate. Figure 6.3.13 shows the temperature dependence of the $\mathbf{M}_0/\mathbf{A}_0$ data for all three transitions. The slopes of these plots indicate the sign of the pure C-term contributions to the MCD, while the intercepts yield the B-term contributions. Hence the C terms are positive for $A\,^2\Delta \leftarrow X\,^2\Pi$, and negative for $B\,^2\Sigma^-$ and $C\,^2\Sigma^+ \leftarrow X\,^2\Pi$.

Consider the case where a mechanism that quenches the orbital angular momentum ($\kappa = 1$) is absent. One would expect $g_{\parallel}^- = 0$ (eq (6.4.14) and Figure 6.4.3), and C-term contributions to the MCD would arise only from transitions that originate from the upper SO level ($^2\Pi_{3/2}$) of the ground state. Furthermore, since $\delta - 1 \leq 0$, the sign of this MCD would be predicted to be negative for $A\,^2\Delta \leftarrow X\,^2\Pi$, and positive for $B\,^2\Sigma^- \leftarrow X\,^2\Pi$ and $C\,^2\Sigma^+ \leftarrow X\,^2\Pi$ (eqs (6.4.40) to (6.4.42) with Table 6.4.7), exactly the opposite of that observed.

The experimental results can, however, be accounted for by using a SO-CF model (Section 6.4.2.3 *ff.*) that partially quenches the orbital angular momentum ($\kappa < 1$). Figure 6.4.3 shows that this reduction gives a non-zero $g_{\parallel}^-$. It follows, from eqs (6.4.44) to (6.4.47) (with Table 6.4.7), that the C terms can now be associated with transitions originating from the $^2\Pi_-$ level, and that these will be of the *correct* sign (Figures 6.3.13 to 6.3.16). Concomitant with the increase of $g_{\parallel}^-$ is a decrease in the value of $g_{\parallel}^+$ (Figure 6.4.3 and eq (6.4.14)), but $g_{\parallel}^+$ always remains greater than $g_{\parallel}^-$. Hence, if both levels were equally populated, the $^2\Pi_+$ level would always give the stronger C term, and the MCD would still be of the incorrect sign at low temperatures. The experimental observation of single-signed, negative MCD for $B\,^2\Sigma^- \leftarrow X\,^2\Pi$ and $C\,^2\Sigma^+ \leftarrow X\,^2\Pi$

(Figures 6.3.6 to 6.3.12), up to ~16 K for the former, therefore requires that the dominant contribution to the MCD *must* arise from transitions originating from the $^2\Pi_-$ level. This is consistent with the fact that it lies at lower energy and will thus have a greater Boltzmann population. That the MCD of $A\,^2\Delta \leftarrow X\,^2\Pi$ (Figures 6.3.1 to 6.3.5) is predominantly positive is also in agreement with this conclusion. Moreover, the linearity of the fits to the temperature-dependence data (Figure 6.3.13) strongly suggests that the *C*-term contributions to $\mathbf{M}_0/\mathbf{A}_0$ arise *almost exclusively* from the $^2\Pi_-$ level. If the $^2\Pi_+$ level were populated, transitions from it would contribute an oppositely signed *C* term, and since its population increases with temperature, a plot of $\mathbf{M}_0/\mathbf{A}_0$ versus $1/kT$ would deviate from linearity. Contemplation of the effect of the Ar matrix on the embedded radical is entirely consistent with such a conclusion. Ar matrices tend to reduce the SOC coefficient of impurities from the gas-phase value,[9,10] but in spite of this, the ground-state ZFS is actually *increased* by CF effects, according to eq (6.4.11). For temperatures $\lesssim$16 K it is therefore likely that the population of the $^2\Pi_+$ level is negligible. This is assumed in the following analysis.

It now remains to explain the observed dispersion and temperature dependence in the MCD of the lowest-energy band (band 1 of Figure 6.3.1) of the $A\,^2\Delta \leftarrow X\,^2\Pi$ system. The bisignated dispersion at higher temperatures and fields is explicable in terms of a strong *A*-term contribution when κ is small (Section 6.4.4.3, following eq (6.4.64)). Table 6.5.1 of Section 6.5.2 gives $\kappa = 0.26$; using this value with eqs (6.4.61) to (6.4.63) predicts that the *A*-term contribution for $A\,^2\Delta \leftarrow X\,^2\Pi$ is 28 times stronger than those for the other transitions. At temperatures $\gtrsim$7 K, the MCD of this band is predominantly negative, which may seem surprising, since the *C* term is positive. However, the $\mathbf{M}_0/\mathbf{A}_0$ data in Figure 6.3.13 show that the *C*-term intensity is relatively small above 7 K, and the strong *A* term becomes dominant. Positive intensity is depleted by overlap with the negative lobe of a broader positive *A* term centred to the blue (23271 cm^{-1}; Table 6.3.1), while negative intensity is accentuated by the presence of a (temperature-independent) *B*-term contribution. The apparent temperature dependence of the *A* term at warmer temperatures is a consequence of broadening of the band.

6.5.2. Quantification of orbital reduction in $X\,^2\Pi$

The orbital reduction factor, κ, for the $X\,^2\Pi$ term of CH/Ar is extracted from the experimental data by employing a similar procedure to that utilised for OH/Ar (Section 4.5.1), except that the smaller SOC constant of gas-phase CH (relative to OH) precludes assumption of a value for ζ_π in CH/Ar.

On the basis of the argument presented in the preceding section, it was assumed that only the $^2\Pi_-$ level is significantly populated. Expressions for the (zeroth) moment ratios for CH/Ar, assuming initially that they are orientationally disordered, are then given by eqs (6.4.45) and (6.4.58), using the fact that $\mathbf{M}_0 = \mathbf{B}_0 + \mathbf{C}_0$ (Section 6.4.6). The parameter κ was varied for a specific value of ζ_π (using a standard steepest-descent algorithm) to simultaneously fit *all* temperature- and field-dependence data for a particular transition (Figures 6.3.13 – 6.3.16). ζ_π was varied manually and systematically to obtain the lowest sum-of-squared residuals (SSR) in the fitting procedure. (Manual optimisation of ζ_π was required since its very close correlation to κ (eq (4.4.14)) did not permit the two variables to be optimised simultaneously.)

The best fits, illustrated by the curves in Figures 6.3.13 – 6.3.16, provide a credible representation of the experimental temperature-dependence and magnetisation behaviour. In particular, the temperature dependencies of the saturation curves (Figures 6.3.14 – 6.3.16) are accurately reproduced, both in terms of magnitude and the degree of curvature. Table 6.5.1 summarises the final parameters obtained from these fits, and shows the consistent agreement obtained across the three transitions. Combining the results for all three transitions gives a SO parameter of $\zeta_\pi = 21 \pm 1$ cm^{-1} (a reduction of ~11 cm^{-1} from the gas-phase value for CH[3]), and an orbital reduction factor of $\kappa = 0.26 \pm 0.03$.

Table 6.5.1: Parameters for the $A\,^2\Delta$, $B\,^2\Sigma^-$ and $C\,^2\Sigma^+ \leftarrow X\,^2\Pi$ transitions of CH/Ar, assuming random orientation of the CH radical, and that only the $^2\Pi_-$ level is occupied.

Transition	ζ_π / cm^{-1}	κ	V / cm^{-1}	$g_\parallel$	$g_\perp$
$A\,^2\Delta \leftarrow X\,^2\Pi$	22	0.28	77	1.45	1.92
$B\,^2\Sigma^- \leftarrow X\,^2\Pi$	21	0.24	85	1.52	1.94
$C\,^2\Sigma^+ \leftarrow X\,^2\Pi$	21	0.23	89	1.54	1.95
Overall	21 ± 1	0.26 ± 0.03	78 ± 15	1.48 ± 0.07	1.93 ± 0.02

It is noticeable in Table 6.5.1 that there is some degree of variation of κ values obtained for each of the three transitions. This is reflected in the different absolute slopes of the temperature-dependence data in Figure 6.3.13. In the case of the $C\,^2\Sigma^+ \leftarrow X\,^2\Pi$ transition, this is quite understandable, due to the necessity of deconvoluting the CH band system from the stronger band due to OH contamination (Sections 6.2 and 6.3.3). The main reason for the discrepancy between the data for the other two transitions probably lies with uncertainties in determining the absorption baselines at relatively low optical densities.

At this point, it is worth returning to the assumption that the $^2\Pi_+$ level is not significantly populated at the temperatures investigated in this work. With $\zeta_\pi \approx 21$ cm^{-1} and $V \approx 78$ cm^{-1}, eq (6.4.11) gives $\Delta \approx 81$ cm^{-1}. Hence $P_+ \lesssim 10^{-3}$ at $T \lesssim 16$ K, and the assumption is almost certainly justified.

Now the case of preferential orientation of the CH radicals, with their z-axis along the field direction, is considered. Best fits obtained for each band system using ζ_π given in Table 6.5.1, actually yield a SSR ~10% *lower* than that obtained when random orientation is assumed, and decrease the orbital reduction factor to $\kappa = 0.11 \pm 0.02$. At the same time, the CF splitting *increases* to $V = 205 \pm 20$ cm^{-1}. However, it is hard to see that this model is physically realistic for a molecule as small as CH, and the slight gain in the goodness of fit seems insufficient to warrant such a conclusion. Even if the radicals were preferentially oriented, the qualitative aspects of the analysis in this chapter would remain unaltered; the CF-SO model still explains the data, and the population of the upper level is reduced even further.

6.5.3. Structure

In this section, several explanations of the structure in the spectra are considered, keeping in mind that differences between the $A\,^2\Delta$, $B\,^2\Sigma^-$ and $C\,^2\Sigma^+ \leftarrow X\,^2\Pi$ band systems are only explicable in terms of excited-state effects, such as differing rotation selection rules and perturbations resulting from the Ar lattice.

Keyser[5] gives the allowed lines originating from the lowest rotational level of $^2\Pi_{1/2}$ for each band system investigated in this thesis. These transitions are shown in Figure 6.5.1, where Hund's case (b) applies for all terms.[1,3]

Rose[7] assigned fine structure for CH/Ar on the basis of completely quenched orbital angular momentum; *i.e.* that transitions occur from both SO levels of $X\,^2\Pi$. Sections 6.5.1 and 6.5.2 have demonstrated that the orbital angular momentum in the $X\,^2\Pi$ term is *not* completely quenched, and such assignments are therefore erroneous.

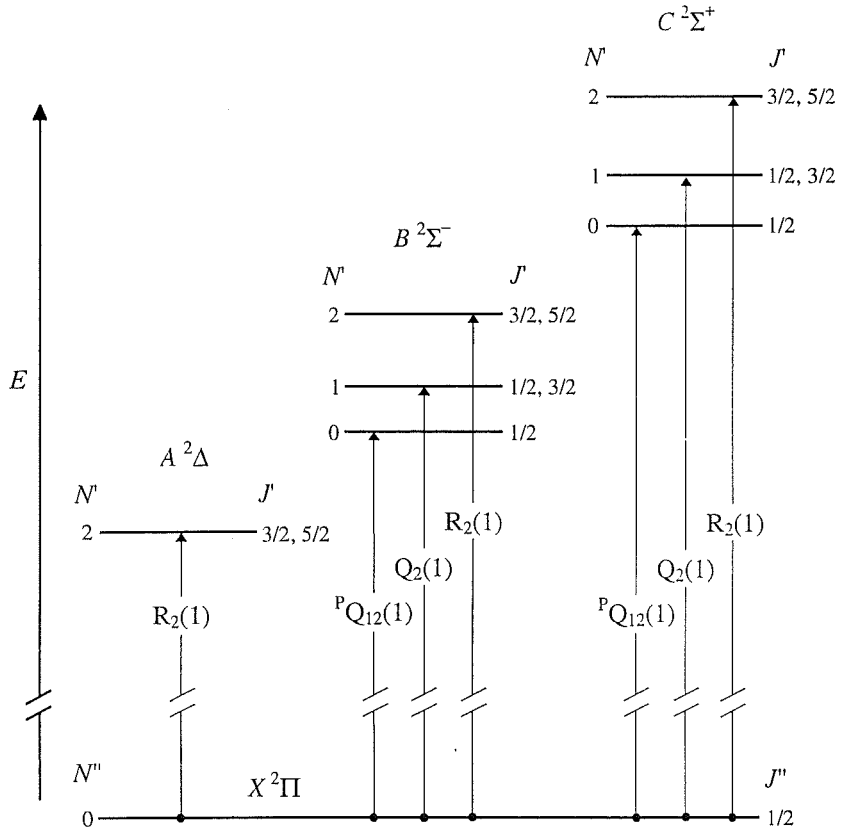

Figure 6.5.1: Energy-level diagram (approximately to scale within the terms) for the allowed lines of $A\,^2\Delta$, $B\,^2\Sigma^-$ and $C\,^2\Sigma^+ \leftarrow X\,^2\Pi$ transitions of CH/Ar that arise from the lowest rotational level of the ground term.[5]

6.5.3.1. $A\,^2\Delta \leftarrow X\,^2\Pi$

There is only one allowed transition for $A\,^2\Delta \leftarrow X\,^2\Pi_{1/2}$ when the lowest rotational level (J = ½) of the initial state is occupied. Hence, as Keyser noted, the structure in this band system can not be due to rotation;[5] nor can it be attributed to hindered rotational (librational) motion. Keyser[5] suggests that the structure may be due to interaction of the CH radical with phonons of the Ar lattice. This could also explain the broad structure to the blue, and bandshapes having a profile similar to that expected for phonon wings.[12] Another possibility is the presence of multiple sites (as observed for OH/Ar; Section 4.5.2.2), or a combination of site and phonon structure. Sites seem

less likely than phonons, because the structure did not change measurably between experiments or with annealing.

6.5.3.2. $B\,^2\Sigma^- \leftarrow X\,^2\Pi$

For the $B\,^2\Sigma^- \leftarrow X\,^2\Pi$ system, the data presented in this thesis allow the author to dispute assignments made by Keyser,[5] in light of a much-improved absorption S/N level (Figure 6.3.6). Bands 2 and 4 of Table 6.3.1 were *not* observed by Keyser, who assigned bands 1 and 3 to $^PQ_{12}(1)$ and $R_2(1)$ (Figure 6.5.1), respectively, since their splitting (76 cm^{-1}) was the same as that of gas phase CH. However, if he had detected band 2, he would have noted that its assignment to $Q_2(1)$ would require an *increase* of ~12 cm^{-1} from the gas-phase $^PQ_{12}(1) - Q_2(1)$ splitting (~25 cm^{-1}).[3] This is physically unreasonable, because a rotational barrier *reduces* the energy of the first rotational level.[13,14] On this basis, and the fact that in this work the $^PQ_{12}(1) - R_2(1)$ splitting is 80 cm^{-1}, structure can not be assigned to free or hindered rotation in the $B\,^2\Sigma^-$ term. (There seems to be no justification for Rose's assignment of a shoulder to $Q_2(1)$, and bands 1 and 2 to $^PQ_{12}(1)$ and $R_2(1)$, respectively, nor of a transition from the lowest rotational level of $X\,^2\Pi$ to the third rotational level of $B\,^2\Sigma^-$.)

Notice that the 37-cm^{-1} splitting between bands 1 and 2 is repeated for bands 3 and 4, and that these pairs show similar relative absorption intensities. It is possible that these indicate the presence of two major sites, with origins corresponding to bands 1 and 3 and lattice-phonon overtones giving bands 2 and 4, respectively. However, this explanation seems rather unlikely, since it hard to reconcile with the MCD, and similar structure would be expected for the other two transitions. An alternative (and probably more likely) explanation, is that there are two local phonons (of ~36 and ~80 cm^{-1}) that account for bands 2 and 3, and which couple to give band 4.

6.5.3.3. $C\,^2\Sigma^+ \leftarrow X\,^2\Pi$

Keyser assigned bands 1, 2 and 3 of the $C\,^2\Sigma^+ \leftarrow X\,^2\Pi$ band system (Figure 6.3.11 and Table 6.3.1) to $^PQ_{12}(1)$, $Q_2(1)$ and $R_2(1)$, respectively (Figure 6.5.1).[5] However, his assignment of band 2 is dubious in that both in his data, and in the data presented here, the $^PQ_{12}(1) - Q_2(1)$ splitting in Ar is *larger* than the gas-phase value of 29 cm^{-1}.[3] A rotational barrier *reduces* the first rotational level's energy with respect to the lowest level.[13,14] Hence the structure is not attributable to rotation or libration, and,

like $A\,^2\Delta$ and $B\,^2\Sigma^- \leftarrow X\,^2\Pi$, site and/or phonon effects in the $C\,^2\Sigma^+$ term are proposed to be responsible.

6.6. Conclusion

MCD and absorption spectra of the $A\,^2\Delta$, $B\,^2\Sigma^-$ and $C\,^2\Sigma^+ \leftarrow X\,^2\Pi$ transitions of CH/Ar demonstrate that the orbital angular momentum of the ground term of CH is partially quenched. A model in which a low-symmetry crystal field reduces the angular momentum accounts for the sign and magnitude of the observed MCD temperature- and magnetic-field dependencies. The model was developed assuming that the ground-state splitting is large enough to allow use of first-order non-degenerate perturbation theory to account for the MCD *B* terms. Moment-analysis data were fitted assuming that the CH radical is randomly oriented and that only the lowest level is significantly populated at $T \leq 16$ K. ζ_π, the empirical SOC coefficient, was found to be 21 ± 1 cm^{-1}, and the orbital reduction factor $\kappa = 0.26 \pm 0.03$, which corresponds to a CF of $V = 78 \pm 15$ cm^{-1}. This gives the SO-CF splitting $\Delta \approx 81$ cm^{-1}, and justifies the assumption that the upper SO-CF level is not significantly populated at 16 K.

Fits to the data assuming preferential orientation with the CH axis aligned along the magnetic-field direction, gave a sum-of-squared residuals ~10% lower than that obtained for randomly oriented radicals. The orbital reduction factor was substantially reduced ($\kappa = 0.11 \pm 0.02$), and the CF splitting increased ($V = 205 \pm 15$ cm^{-1}). However, such preferential orientation does not seem physically likely, and the improved fit is probably fortuitous. In either case, the qualitative aspects of the analysis remain the same.

Qualitative explanations are proffered for some of the structure observed in the spectra. The bisignated MCD of the $A\,^2\Delta \leftarrow X\,^2\Pi$ band system, and single-signed MCD of $B\,^2\Sigma^-$ and $C\,^2\Sigma^+ \leftarrow X\,^2\Pi$, is readily explained by the effects of orbital reduction in the ground state, which substantially enhances the intensity of *A* terms in the former, at the expense of the latter. Other aspects of the observed structure are not attributable to free rotation or libration in the excited states; it is suggested that they may arise from interactions of the CH radical with the Ar lattice, giving rise to different sites and/or (perhaps more likely) coupling with phonon modes.

6.7. References

1. Herzberg, G. *Molecular Spectra and Molecular Structure Volume 1: Spectra of Diatomic Molecules*, 2nd ed.; Krieger: New York, 1950.

2. Huber, K. P.; Herzberg, G. *Molecular Spectra and Molecular Structure, Volume 4: Constants of Diatomic Molecules*; Van Nostrand Reinhold: New York, 1979.

3. Botterud, I.; Loftus, A.; Veseth, L. *Phys. Scr.* **1973**, *8*, 218-224.

4. Robinson, G. W.; McCarty, M. Jr *J. Am. Chem. Soc.* **1960**, *82*, 1859-1864.

5. Keyser, L. F. Ph.D. Dissertation, California Institute of Technology, Pasadena, 1965.

6. Milligan, D. E.; Jacox, M. E. *J. Chem. Phys.* **1967**, *47*, 5146-5156.

7. Rose, J. L. Ph.D. Dissertation, University of Virginia, Charlottesville, 1987.

8. Piepho, S. B.; Schatz, P. N. *Group Theory in Spectroscopy with Applications to Magnetic Circular Dichroism*; Wiley-Interscience: New York, 1983.

9. Samet, C.; Rose, J. L.; Schatz, P. N.; O'Brien, M. C. M. *Chem. Phys. Lett.* **1989**, *159*, 567-572.

10. Lund, P. A.; Smith, D.; Jacobs, S. M.; Schatz, P. N. *J. Phys. Chem.* **1984**, *88*, 31-42.

11. Schatz, P. N.; Mowery, R. L.; Krausz, E. R. *Mol. Phys.* **1978**, *35*, 1537-1557.

12. Rebane, K. K. *Impurity Spectra of Solids*; Plenum Press: New York, 1970.

13. Bondybey, V. E.; Brus, L. E. *J. Chem. Phys.* **1975**, *63*, 794-804.

14. Devonshire, A. F. *Proc. Roy. Soc.* **1936**, *A153*, 601-621.

7. $C_{60}^{\pm}$/Ar

7.1. Introduction

Section 1.1.2 briefly introduced the class of elemental carbon molecules known as the fullerenes. It was noted there the very high symmetry ($\mathbf{I}_h$) and stability of buckminsterfullerene, C_{60}, and its low ionisation potential and high electron affinity. The singly charged ions, which are readily produced electrochemically and in the gas phase, are very interesting in view of their high ground- and excited-state spin and orbital degeneracies (Section 1.3.2). Figure 7.1.1 shows the molecular-orbital (MO) diagram for C_{60}, C_{60}^- and C_{60}^+ assuming $\mathbf{I}_h$ symmetry. The excitations of interest here occur in the near infrared (NIR), and are indicated by arrows on the figure.

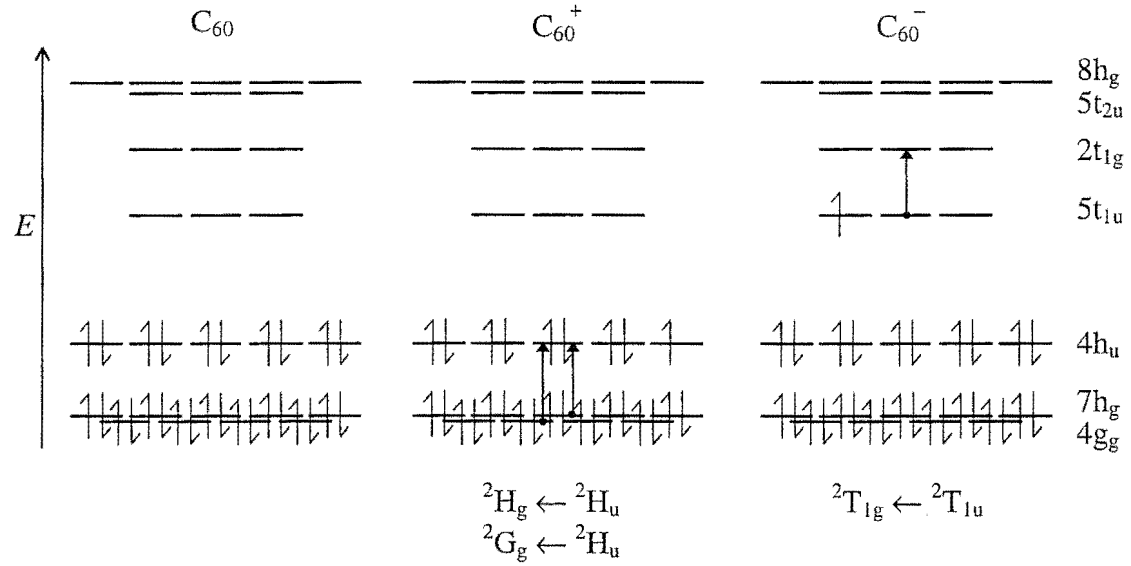

Figure 7.1.1: Partial MO diagram (approximately to scale) for C_{60} and its singly charged ions in $\mathbf{I}_h$ symmetry,[1] showing the transitions considered in this thesis.

Assuming $\mathbf{I}_h$ symmetry, the ground-state terms for C_{60}^+ and C_{60}^- are ^2H_u and $^2T_{1u}$, respectively,[1-4] where the H and T_1 irreps are five- and three-fold degenerate. These high degrees of formal degeneracy have provoked much interest in the literature, and it is now generally accepted that the symmetry of these ions is reduced from $\mathbf{I}_h$ *via* Jahn-Teller (JT) distortions. It is not the purpose of this introduction to provide a thorough review of the experimental and theoretical publications, and only the work of particular relevance to the experimental results of this chapter is presented.

In view of the theoretical predictions (which are performed on isolated molecules; *i.e.*, in the 'gas phase'), and earlier experimental results, the work presented in this thesis aims to provide, *via* the MCD temperature and field dependencies, insight into the nature of the JT distortion of C_{60}^{+} and C_{60}^{-} in an Ar matrix. Using the absorption spectra, a model is proposed for the fine structure in the origin band.

Note that Appendix C gives SO wavefunctions constructed for both ions in $\mathbf{I}_h$ symmetry, and presents the SO, Zeeman and transition-moment matrix elements that were evaluated in that symmetry. Reduction from $\mathbf{I}_h$ symmetry means that those results are not applied here, and they are appended purely for future reference.

7.1.1. C_{60}^{-}

Experimental work

The NIR absorption spectrum of C_{60}^{-} has been investigated at low temperature in organic glasses[5,6] and inert-gas matrices.[7,8] Spectra obtained in both media are better resolved than those observed for solutions at room-temperature.[1,9-11]

In 1991, Kato *et al.*[5] obtained the electronic absorption spectrum of C_{60}^{-} in 2-methyltetrahydrofuran (MTHF), at 77 K, following γ-irradiation of the frozen C_{60} solution, and photobleaching with red light. (γ-irradiation forms a solvent-trapped electron, while photobleaching yields the desired product *via* liberation of the electron, which attaches to C_{60}.) They assigned the band observed at ~9300 cm^{-1} to the origin of the first allowed transition of C_{60}^{-}, $^2T_{1g} \leftarrow {}^2T_{1u}$, and higher-energy bands (~9600 – 14300 cm^{-1}) to vibronic structure. However, only tentative assignments of vibrational structure were made, because correlation with a_g modes of C_{60} was poor, and there was a suspicion (on the basis of a CNDO/S calculation) of the presence of another electronic transition.

C_{60}^{-} was first isolated in an Ar matrix by Gasyna, Andrews, and Schatz in 1992,[7] using the same method as that employed in this thesis (see Section 2.1.2). The NIR electronic absorption spectrum revealed considerable vibronic structure, which they attributed to the a_g and JT-active h_g modes, noting that splittings corresponded satisfactorily with the Raman spectra of a C_{60} thin film.[12] (In unpublished work, Gasyna and Schatz obtained a low-resolution MCD spectrum, which affirms the presence of at least one JT overtone at ~9800 cm^{-1},[13] because of its opposite sign compared with the

origin; see Section 7.3.) Unfortunately, some of the vibronic structure was overlapped by the origin and overtone bands of the lowest-energy electronic transition of C_{60}^{+}/Ar ($\gtrsim$ 10200 cm^{-1}) that was formed simultaneously. In order to identify the contributions due to each ion, CCl_4 was employed as an electron trap to enhance the C_{60}^{+} : C_{60}^{-} ratio. Structure observed in the (0,0) band of C_{60}^{-} was suggested to be due to combined spin-orbit (SO) and JT effects. However, more recently it has been pointed out that the SO coupling (SOC) coefficient in C_{60}^{-} must be small (~0.16 cm^{-1}, or ~1/100 of that for a free carbon atom) because of the large radius of curvature of C_{60};[14,15] hence it is unlikely that Gasyna and Schatz's explanation is correct. An alternative explanation is offered in this thesis.

Fulara, Jakobi and Maier[8] isolated C_{60}^{-} in Ne and Ar matrices in 1993, using a method similar to Gasyna *et al.*,[7] except that Ne- (rather than Ar-) resonance radiation was used as the ionisation source. The Ne matrices exhibit much sharper structure than Ar. Again, C_{60}^{+} ions were produced, but these were isolated in separate experiments (using mass-selection) to give a pure C_{60}^{+} spectrum (see Section 7.1.2). Because they then had a definitive C_{60}^{+}/Ne NIR absorption spectrum, the structure due to C_{60}^{-} in the overlapping spectra could be unambiguously identified. Their vibronic assignments in both Ar and Ne were based on a reduction of symmetry from $\mathbf{I}_h$ to $\mathbf{D}_{5d}$ (Ref. 16; see below) and assume that the electronic transition is $^2E_{1g} \leftarrow {}^2A_{2u}$, with vibrational overtones due only to the totally symmetric a_{1g} mode in $\mathbf{D}_{5d}$ symmetry. Structure in the origin band was suggested to be due to site effects, perhaps because of different distorted geometries being stabilised by the matrix.

In 1995, Kondo *et al.*[6] re-examined the C_{60}^{-} NIR spectra in (polar) MTHF and (non-polar) methylcyclohexane (MCH) solutions at 77 K (using the methodology of Kato *et al.*[5]) to determine solvent effects on the structure of the radical. From their work, and by comparison with the matrix-isolation data,[8] they concluded that the different vibrational structure was a consequence of a reduction from $\mathbf{I}_h$ to $\mathbf{D}_{2h}$ symmetry in MTHF, and to $\mathbf{D}_{5d}$ and/or $\mathbf{D}_{3d}$ in non-polar environments (MCH, Ne and Ar). For the former they assigned two electronic origins, while for the latter they assigned only one (see Section 7.4.1). Recent work with organic glasses at 77 K, and in rare-gas matrices at liquid-He temperatures,[6,8] also suggest that C_{60}^{-} undergoes distortion from $\mathbf{I}_h$ symmetry.

Quantum-mechanical calculations

Quantum-mechanical calculations form a significant portion of the literature on C_{60}^-, but relatively few have sought to compute the favoured structure(s) that results from the JT distortion; these are reviewed below. (Note that the magnitude of the distortion is predicted to be small for C_{60} and its ions because of their relatively large size.[16-18])

Geometry optimisation of C_{60}^- using an unrestricted Hartree-Fock (UHF) semi-empirical calculation (MINDO/3) predicts a reduction of symmetry to $\mathbf{D}_{3d}$ *via* JT distortion.[19] At a higher level of calculation, Koga and Morokuma[16] performed *ab initio* UHF and restricted open-shell Hartree-Fock (ROHF) calculations, finding $\mathbf{D}_{5d}$, $\mathbf{D}_{3d}$ and $\mathbf{D}_{2h}$ structures differing in energy by less than 0.1 kJ mol^{-1}.

Recently, a high-level density-functional calculation by Green *et al.*[3] has correctly predicted the transition energy for the NIR electronic absorption of C_{60}^-, and yielded an electron affinity reasonably close to the experimental value. Moreover, the treatment did not assume $\mathbf{I}_h$ symmetry, but allowed for coupling of JT-active modes (h_g modes in the $^2T_{1u}$ term), and found a $\mathbf{D}_{3d}$ equilibrium geometry, lying 5.0 kJ mol^{-1} below the lowest-energy $\mathbf{I}_h$ geometry.

7.1.2. C_{60}^+

Quantum-mechanical calculations

Assuming $\mathbf{I}_h$ symmetry, the two lowest transitions of C_{60}^+ are $^2H_g \leftarrow {}^2H_u$ and $^2G_g \leftarrow {}^2H_u$, which arise from the excitations shown in Figure 7.1.1. If $\mathbf{I}_h$ symmetry is assumed, theoretical calculations on C_{60}^+ in the $\mathbf{I}_h$ point group (of which there are very few) predict that these transitions lie quite close in energy (Table 7.1.1). The JT theorem requires that $H_{u,g}$ and G_g terms, will be susceptible to distortions along vibrational coordinates of h_g and g_g symmetry.[4,20-23] Bendale, Stanton and Zerner[4] have computationally optimised the C_{60}^+ geometry under distortion from $\mathbf{I}_h$ symmetry. Using the INDO/S semi-empirical quantum-mechanical method they found that the ^2H_u ground-state term of C_{60}^+ can be distorted by JT effects to $\mathbf{D}_{5d}$, $\mathbf{D}_{3d}$ or $\mathbf{D}_{2h}$ symmetry. The $\mathbf{D}_{5d}$ structure is the most stable, being favoured over $\mathbf{D}_{2h}$ and $\mathbf{I}_h$ by 9.2 and 34 kJ mol^{-1}, respectively. The $\mathbf{D}_{3d}$ structure represents a cusp on the potential energy surface, while the fifteen equivalent $\mathbf{D}_{2h}$ structures represent transition states for pseudorotation

between the six equivalent $\mathbf{D}_{5d}$ structures. They calculated an absorption spectrum for the optimised $\mathbf{D}_{5d}$ structure, and found splittings *between* symmetry-lowered components as great as ~3100 cm^{-1}, much larger than the calculated 300-cm^{-1} separation between the $^2H_g \leftarrow {}^2H_u$ and $^2G_g \leftarrow {}^2H_u$ transitions in $\mathbf{I}_h$ symmetry. Further, only one transition from both systems had a non-zero oscillator strength ($^2E_{1g}$ (^2H_g) $\leftarrow {}^2A_{1u}$, at 8630 cm^{-1}).

Table 7.1.1: Computed energies and energy separations for the NIR $^2H_g \leftarrow {}^2H_u$ and $^2G_g \leftarrow {}^2H_u$ transitions of C_{60}^+ assuming $\mathbf{I}_h$ symmetry.

Reference	$E(^2H_g) \leftarrow E(^2H_u)$ / cm^{-1}	$E(^2G_g) \leftarrow E(^2H_u)$ / cm^{-1}	$E(^2G_g) - E(^2H_g)$ / cm^{-1}
1	11900	12400	500
2	8600	8900	300
3	6100	7300	1200
4	9010	9450	440

1. Kato, *et al.*;[5] CNDO/S semi-empirical calculation.
2. Bendale, Stanton and Zerner;[4] INDO/S semi-empirical calculation.
3. Friedman;[24] Huckel-type calculation, including a fairly large Hubbard term.
4. Heath, McGrady and Martin;[1] SCF-Xα-Scattered wave calculation.

Recently Lee *et al.*[25] also predicted a $\mathbf{D}_{5d}$ structure for the ground state of C_{60}^+, using a calculation involving a Su-Schriffer-Heeger model Hamiltonian.

Experimental work

The electronic absorption spectrum of C_{60}^+ in a freon glass at 77 K was obtained by Kato *et al.*[5] in 1991. A small amount of C_{60} was dissolved in a 1:1 $CFCl_3$: CF_2BrCF_2Br mixture, and the frozen solution (77 K) was then subjected to γ-irradiation (forming a solvent-trapped positive hole), before photobleaching with red light yielded C_{60}^+. These workers assigned the band observed at ~10200 cm^{-1} to overlapping origins of the first and second allowed transitions of C_{60}^+; $^2H_g \leftarrow {}^2H_u$ and $^2G_g \leftarrow {}^2H_u$ (Figure 7.1.1). (Vibronic structure in these spectra were not well resolved.) Their assignments were based on peak separations in the C_{60} photoelectron spectrum,[26] and their own calculated absorption spectrum (using the CNDO/S technique; see Table 7.1.1).

Gasyna *et al.*[7] were the first to isolate C_{60}^{+} in an Ar matrix (using the method described in Section 2.1.2); they published the NIR absorption spectrum, including vibronic structure, and MCD of the origin band. Since the vibronic structure of C_{60}^{-}/Ar overlaps C_{60}^{+}/Ar, identification of the C_{60}^{+}/Ar bands was performed using the method noted in Section 7.1.1. These workers concluded that the structure corresponded adequately with that of ($\mathbf{I}_h$) C_{60} in a thin film,[12] but in doing so were able to assign only the lowest-frequency h_g mode. They suggested that structure in the origin band of C_{60}^{+} is the result of combined SO and JT effects, on the basis of the bisignated MCD. However, in light of several theoretical calculations[1,4,5] predicting that the $^2H_g \leftarrow {}^2H_u$ and $^2G_g \leftarrow {}^2H_u$ transitions lie within ~300 – 500 cm^{-1} of each other, and a predicted small SOC coefficient, this seems unlikely.

The definitive NIR to near-UV absorption spectrum of C_{60}^{+}/Ne at 5 K was obtained by Fulara *et al.* by using mass spectrometry to select the C_{60}^{+} ion.[8] This spectrum allowed unambiguous identification of the vibronic structure for the NIR bands of both ions (*cf.* C_{60}^{-} ; Section 7.1.1) in both Ne and Ar, since vibrational energies change little between these media. These workers found that the vibrational structure did *not* correspond to $\mathbf{I}_h$ symmetry, assuming that the C_{60}^{+} mode frequencies do not shift significantly from those of C_{60}. Referencing Bendale *et al.*[4] (see above), the transition was assigned to $^2E_{1g} \leftarrow {}^2A_{1u}$ in $\mathbf{D}_{5d}$ symmetry, and vibrational structure to a_{1g} components arising from symmetry reduction of the h_g modes of $\mathbf{I}_h$. The two peaks observed in the 'origin' band (separated by 67 and 87 cm^{-1} in Ne and Ar, respectively) were tentatively attributed to two electronic transitions, with vibronic progressions built on each.

7.2. Experimental

The apparatus, and experimental procedure, employed for the preparation of $C_{60}^{\pm}$/Ar are described in detail in Section 2.1.2. Samples were prepared in both the He-refrigerator/electromagnet and matrix injection systems (Sections 2.2.1 and 2.2.2, respectively). Matrix preparation using the He refrigerator was found to be far more consistent, and gave higher yields than in the matrix injection system.

The NIR spectra for $C_{60}^{\pm}$/Ar were acquired using MOD4 in the following configuration:

- W lamp (Section 2.3.2.2);
- 590-groove/mm, 1.0-nm-blaze grating (Section 2.3.3.1);
- ~500-μm slits (spectral resolution ~0.8 nm);
- R-316 PMT (Section 2.3.7.1) or BPX-65 photodiode (Section 2.3.7.2).

The S/N level in the MCD is relatively poor due to a relatively low photon flux when using the W lamp, the deterioration of detector response at wavelengths longer than ~1000 nm, and moderately weak MCD.

C_{60}/Ar was prepared in a similar manner to the $C_{60}^{\pm}$/Ar samples (Section 2.1.2), except that the Ar flow was not subjected to a microwave discharge, and the Knudsen-oven temperature was lower (~400 °C). Matrix preparation was undertaken in the He-refrigerator/electromagnet system (Section 2.2.1). The transitions of C_{60}/Ar occur in the visible to near-UV, and their spectra were obtained using MOD4 in an identical configuration to that used for the XH/Ar work (Chapters 4 – 6); *i.e.*,

- Xe-arc lamp (Section 2.3.2.1);
- 1180-groove/mm, 0.3-nm-blaze grating (Section 2.3.3.1);
- 200-μm slits (spectral resolution ~0.16 nm);
- R-376 PMT (Section 2.3.7.1).

7.3. Results

The near-UV absorption spectrum of C_{60}/Ar is presented in Figure 7.3.1, and corresponds well with that of Gasyna *et al.*[27] The inset shows an enlargement of structure assigned to a vibronically allowed $^1T_{2u} \leftarrow {}^1A_{1g}$ transition. Inspection of the data in Figure 7.3.1 made it clearly evident that the structure represents a large number of vibronic (Herzberg-Teller) or false origins in g_g and h_g modes. These assignments are contrary to that of Gasyna *et al.*,[27] but a search of the literature showed that appropriate corrections had already been made by Yabana and Bertsch[28] with the assistance of a cold molecular-beam absorption spectrum obtained by Haufler *et al.*[29] The spectra here are almost identical to those of Ref. 29.

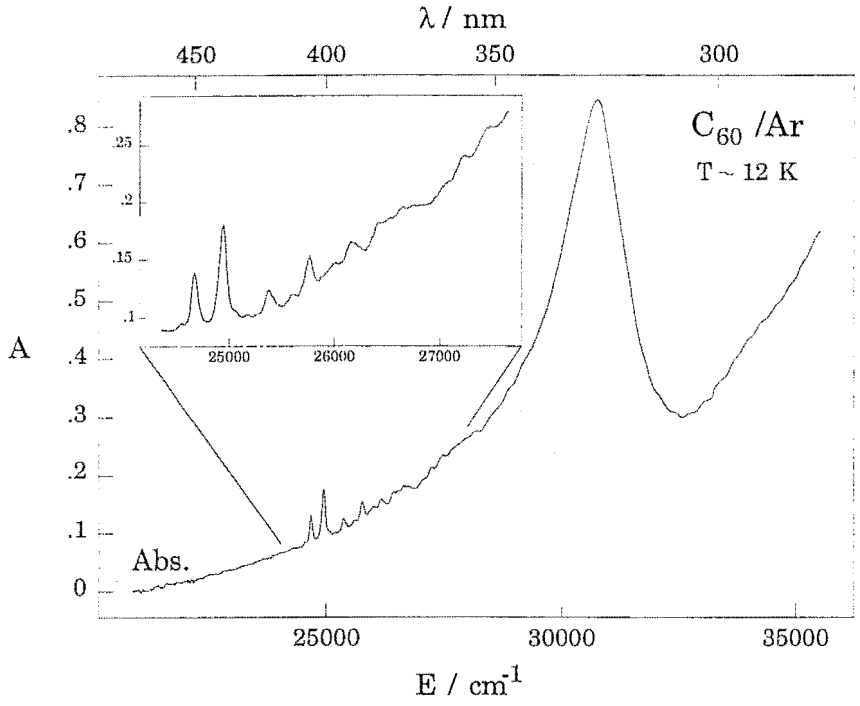

Figure 7.3.1: The near-UV absorption spectrum of C_{60}/Ar at $T \approx 12$ K, obtained using the He-refrigerator/electromagnet system (Section 2.2.1).

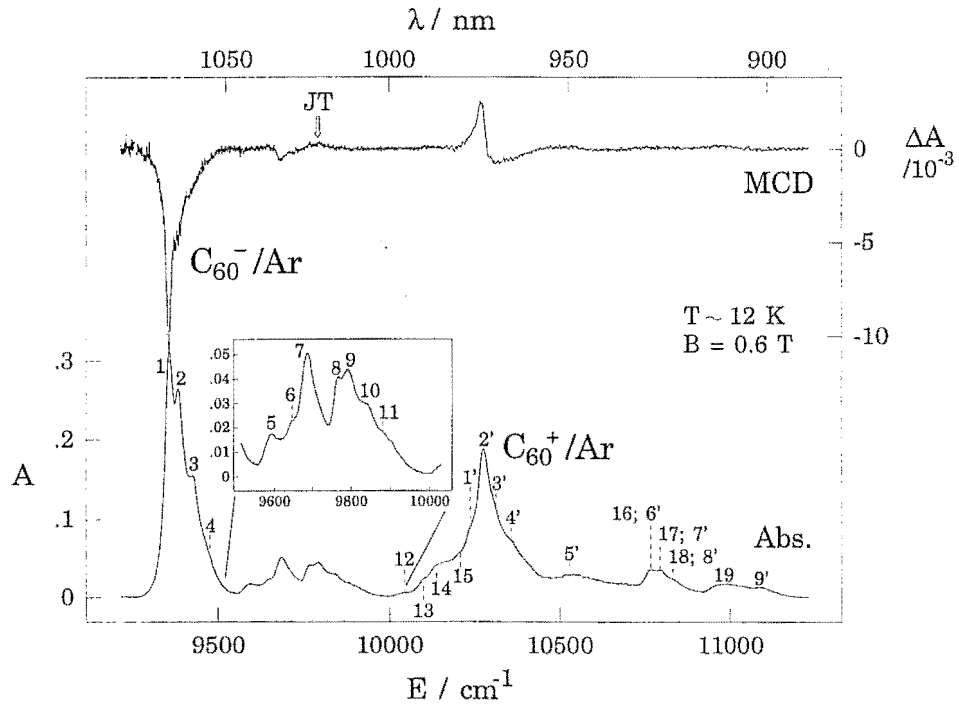

Figure 7.3.2: MCD (ΔA; top) and absorption (A; bottom) for the NIR transitions of $C_{60}^{\pm}$/Ar at $T \approx 12$ K and $B = 0.6$ T obtained using the He-refrigerator/electromagnet system (Section 2.2.1). The inset shows an expanded view of fine structure in the vibronic bands of C_{60}^{-}/Ar. Band numbering is for cross-referencing with Table 7.3.1.

Figure 7.3.2 shows MCD and absorption spectra for C_{60}^{+}/Ar and C_{60}^{-}/Ar obtained using the He-refrigerator/electromagnet system. The vibronic structure observed by Gasyna *et al.*[7] and Fulara *et al.*[8] is reproduced, with the inset showing an expansion of the fine structure in the region of the C_{60}^{-}/Ar vibronic absorption bands. Table 7.3.1 gives the band positions observed in this work; the unprimed numbers refer to bands of C_{60}^{-}/Ar and the primed numbers to C_{60}^{+}/Ar. Bands 4 and 1' in Figure 7.3.2 were not observed by the earlier workers (see below).[7,8] The origin-band MCD of C_{60}^{-}/Ar is single-signed and negative, whilst that of C_{60}^{+}/Ar is bisignated, but asymmetric. The MCD of the vibronic bands aids in their assignment because odd harmonics of JT-active modes are of the opposite sign to the electronic origin. The arrow in Figure 7.3.2 illustrates one such band for C_{60}^{-}/Ar, but the poor MCD S/N precludes identification of others.

Figures 7.3.3 and 7.3.4 illustrate the absorption spectra and temperature dependence of the MCD for the origin-band regions of C_{60}^{-}/Ar and C_{60}^{+}/Ar, respectively. Data in the left-hand panels were obtained using the matrix injection system (B = 4.0 T for C_{60}^{-}/Ar and B = 1.0 T for C_{60}^{+}/Ar), while those in the right-hand panels were obtained using the He-refrigerator/electromagnet system (B = 0.6 T). There is a significant difference in the fine structure obtained using the two apparatuses, with the matrices prepared in the He-refrigerator system showing sharper structure (though not as sharp as that observed by Gasyna *et al.*[7] and Fulara *et al.*[8]). Evidently, the structure is quite sensitive to the deposition conditions; the matrix injection system does not maintain a steady window temperature (~12 – 25 K) due to the tendency of the liquid He flow to surge. On the other hand, the He refrigerator maintains a steady temperature of ~20 K in these experiments. (The temperatures are higher than those employed in the XH/Ar experiments because of the thermal load placed on the window by the Knudsen oven. Gasyna *et al.*[7] and Fulara *et al.*[8] prepared their samples at temperatures of 10 – 12 K.)

Further evidence that the difference in structure arises from the deposition temperature is provided by the absorption spectra presented in Figure 7.3.5. These were obtained using the He-refrigerator/electromagnet system, at temperatures between ~13 and 30 K, *i.e.* as the matrix was successively annealed at higher and higher

Table 7.3.1: Band positions (in cm^{-1}) for structure in the NIR absorption spectra of C_{60}^{-}/Ar and C_{60}^{+}/Ar.[a]

Band number	Gasyna *et al.* [b]	Fulara *et al.* [c]	This work [d]
C_{60}^{-}/Ar			
1	9360	9363	9359
2	9390 (30)		9387 (28)
3	9440 (80)		9426 (67)
4			9476 sh (117)
5		9592 (229)	9595 (236)
6			9644 sh (285)
7	9680 (320)	9678 (315)	9686 (327)
8			9768 (409)
9	9800 (440)	9790 (427)	9792 (433)
10			9842 (483)
11		9895 (532)	9881 sh (522)
12			10033 sh (674)
13			10097 sh (738)
14	10140 (780)	10129 (766)	10139 sh (780)
15			10201 sh (842)
		10661 (1298)	
16 [e]		10770 (1407)	10768 (1409)
17			10795 (1446)
18			10834 sh (1485)
19		10957 (1594)	10984 br (1635)
C_{60}^{+}/Ar			
1'			10237 sh (-37)
2'	10280	10282	10274
3'	10310 (30)		10310 sh (36)
4'	10360 (80)	10355 (73)	10361 (87)
5'	10540 (260)	10526 (244)	10538 br (264)
		10600 (318)	br?
6' [e]		10770 (488)	10768 (494)
7'			10795 (521)
8'			10834 sh (560)
9'		11090 (808)	11090 (816)
		11644 (1362)	
		11882 (1600)	

[a] Band numbering is shown in Figure 7.3.2. Shifts from the lowest-energy origin are given in parentheses.

[b] Ref. 7.

[c] Ref. 8, which unambiguously assigns the transitions of C_{60}^{+}/Ar, *via* mass-selected deposition of C_{60}^{+}.

[d] Uncertainty in band positions ±5 cm^{-1}. sh = shoulder. br = broad.

[e] Both C_{60}^{+}/Ar and C_{60}^{-}/Ar have a band at this wavenumber; Ref. 8. Hence, bands 17 and 18 and 7' and 8' are repeated here for both.

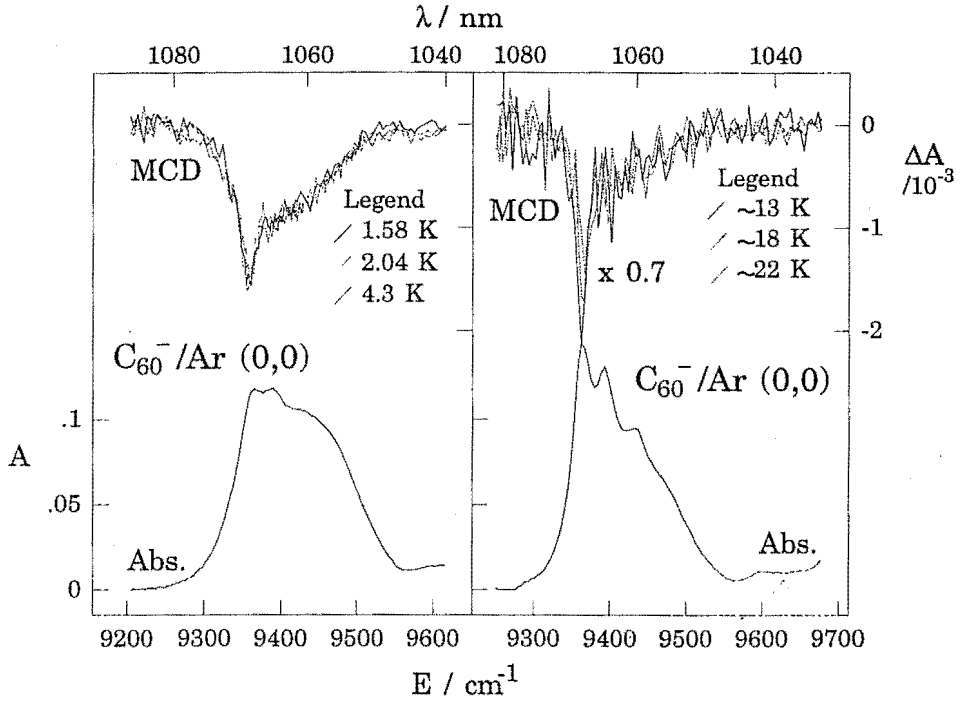

Figure 7.3.3: MCD (ΔA; top) temperature dependence (from 1.58 to ~22 K) and absorption (A; bottom) for the (0,0) band of C_{60}^-/Ar. The left- and right-hand panels respectively illustrate data obtained using the matrix injection (B = 4.0 T) and He-refrigerator/electromagnet (B = 0.6 T) systems. It is proposed that the fine structure variations are due to differing site occupancies.

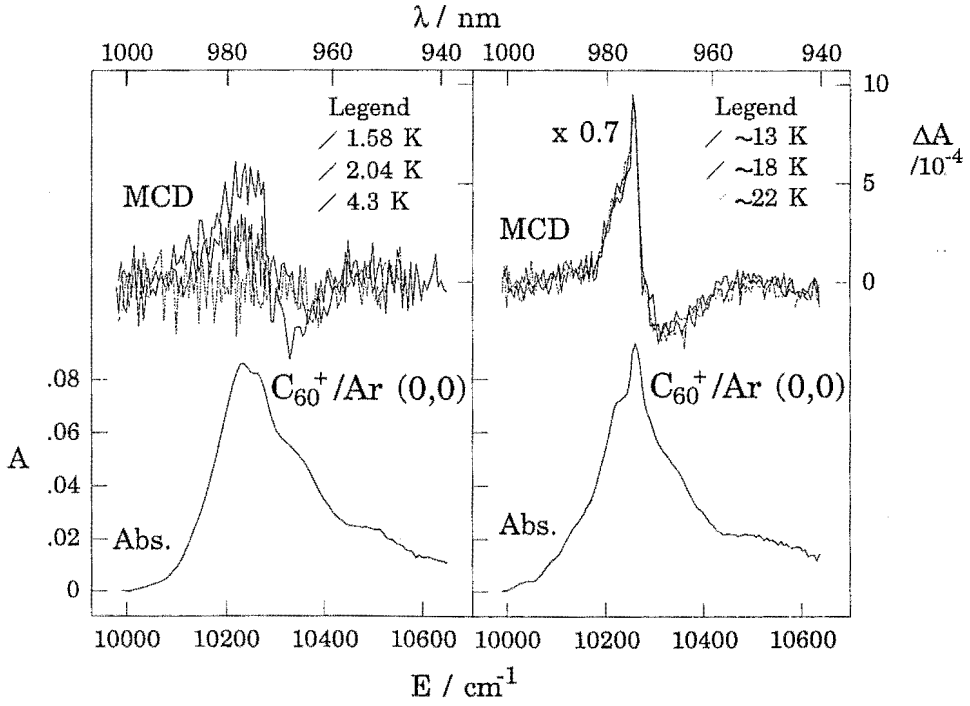

Figure 7.3.4: MCD (ΔA; top) temperature dependence (from 1.58 to ~22 K) and absorption (A; bottom) for the (0,0) band of C_{60}^+/Ar. The left- and right-hand panels respectively illustrate data obtained using the matrix injection (Section 2.2.2) and He-refrigerator/electromagnet (Section 2.2.1) systems. It is proposed that the fine structure variations are due to differing site occupancies.

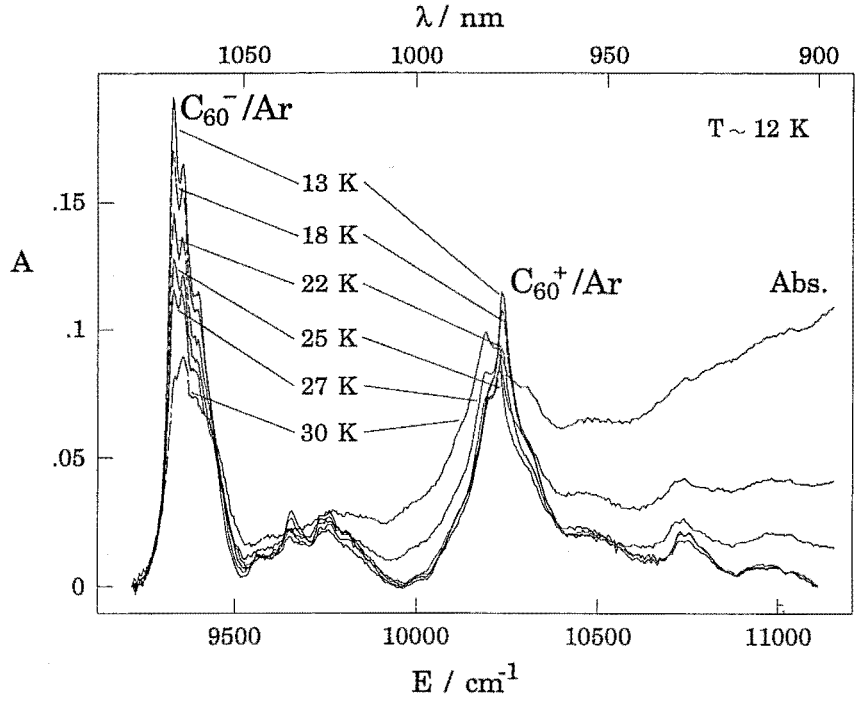

Figure 7.3.5: Absorption spectra for the NIR transitions of $C_{60}^{\pm}/Ar$ over a range of temperatures, demonstrating the effect of anneals on the fine structure observed. Temperatures are approximate, since data were obtained using the He-refrigerator/electromagnet system (Section 2.2.1), which does not permit accurate determination of *T*.

temperatures. The upward-sloping baseline with *E* at higher temperatures is due to degradation of the sample; *i.e.* poorer transmittance. C_{60}^+/Ar and C_{60}^-/Ar annihilate at higher temperatures, as indicated by the loss of overall intensity. More interesting, however, is the fact that both ions show fine-structure variations with increases of temperature, which is retained when the matrix is cooled. Notably, the intensity of the red-most band of C_{60}^-/Ar decreases significantly relative to the two bands at immediately higher energies. In C_{60}^+/Ar the most intense band at ~13 K loses intensity while at the same time the 1' band (~10200 cm^{-1}) gains intensity. The spectra after annealing look very similar to those obtained in the matrix injection experiment. This strongly suggests the appearance of the latter is due to the fluctuations of *T* during deposition, which has the consequence of annealing the matrix as it is formed.

Consideration of the new structure observed in this work, and the changing *relative* intensities with annealing, tend to indicate that the fine structure in the (0,0) bands of both ions is due, at least in part, to different substitutional sites. In particular, the triplet structure in the (0,0) region of C_{60}^-/Ar, ascribed to SO splitting by Gasyna *et*

al.,[7] is almost certainly due to sites. Such an assignment is also more consistent with the expectation of weak SOC in C_{60} systems.[14,15]

Figures 7.3.3 and 7.3.4 show the temperature dependencies of the MCD in the (0,0) regions of C_{60}^{-}/Ar and C_{60}^{+}/Ar, respectively. Moment analysis of the single-signed and negative MCD of C_{60}^{-}/Ar (Section 7.4.1) suggests that the apparent temperature dependence of the data obtained using the He-refrigerator/electromagnet system (right-hand panel) is an artefact due to the poor S/N level. The MCD of C_{60}^{+}/Ar shows a highly unusual *inverse* temperature dependence (*i.e.* its magnitude gets weaker at lower temperatures), but only at the *low* temperatures attained in the matrix injection system.

Figures 7.3.6 and 7.3.7 illustrate the magnetic-field dependencies, at various temperatures, of the MCD of C_{60}^{-}/Ar and C_{60}^{+}/Ar, respectively in the (0,0) regions. The data for C_{60}^{-}/Ar show a *linear* dependence on B within the S/N level. However, for C_{60}^{+}/Ar, the data reveal that at the lower temperatures (1.58 and 2.04 K), increases in field strength serve to *increase* the MCD by a rate that is *greater* than a linear dependence on B, which is again very unusual.

The temperature- and field-dependence data of the (0,0) regions were moment analysed (Section 3.5.1) in order to aid the discussion in the next section. The results of these are presented in the appropriate places, but are really only useful for *qualitative* purposes, because of the relatively poor quality of the MCD data, and the fact that the absorption bands overlap considerably with vibronic structure.

7.4. Discussion

This section seeks to provide a qualitative explanation of the experimental data of Section 7.3.

7.4.1. C_{60}^{-}/Ar

On the basis of the data presented in Figures 7.3.3 and 7.3.6, and with the aid of moment analysis (Section 3.5.1), some qualitative conclusions can be drawn for C_{60}^{-}/Ar. The zeroth MCD moment is used to quantify the temperature and field dependencies of the single-signed MCD of C_{60}^{-}/Ar in the origin region. Figures 7.4.1 and 7.4.2 display the ratios of the zeroth MCD and absorption moments plotted versus $1/kT$ and $\mu_B B$, respectively. ($\mathbf{A}_0$ and $\mathbf{M}_0$ are defined by eqs (4.3.1) and (4.3.2), respectively.)

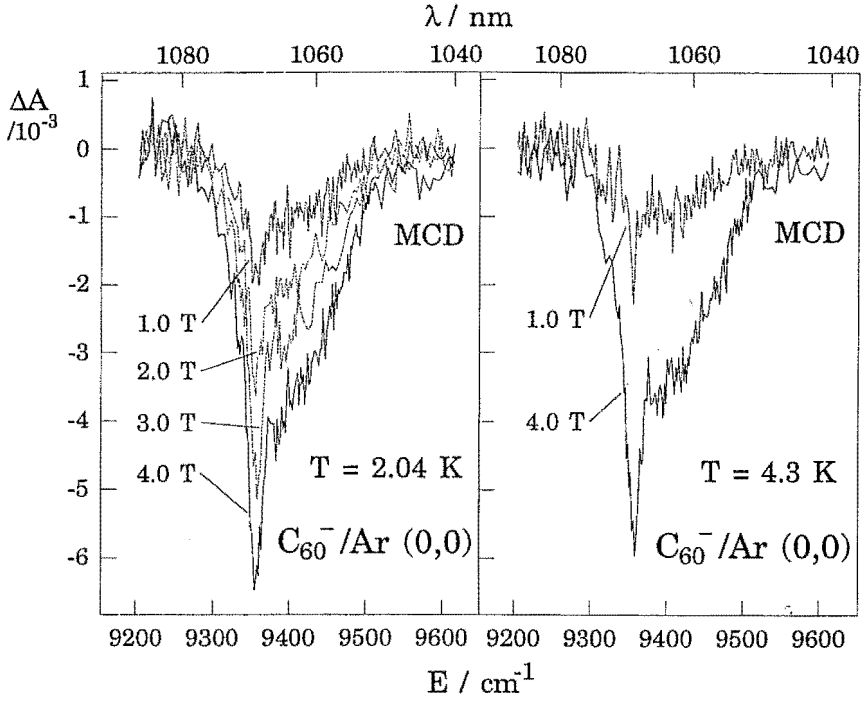

Figure 7.3.6: MCD field dependencies at 2.04 and 4.3 K for the (0,0) band of C_{60}^-/Ar. Data were obtained using the matrix injection system (Section 2.2.2).

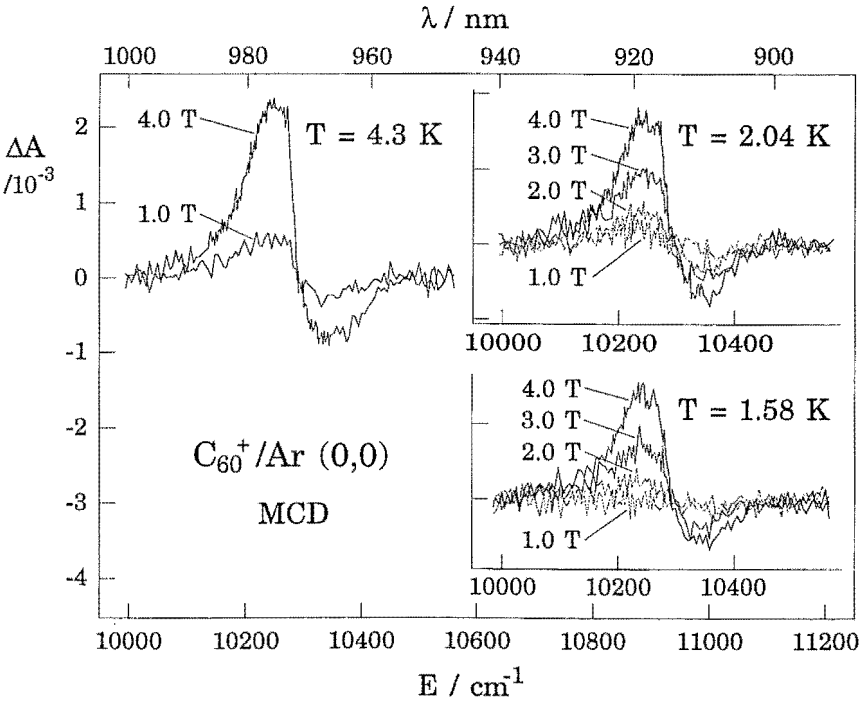

Figure 7.3.7: MCD field dependencies at 1.58, 2.04 and 4.3 K for the (0,0) band of C_{60}^+/Ar. Data were obtained using the matrix injection system (Section 2.2.2).

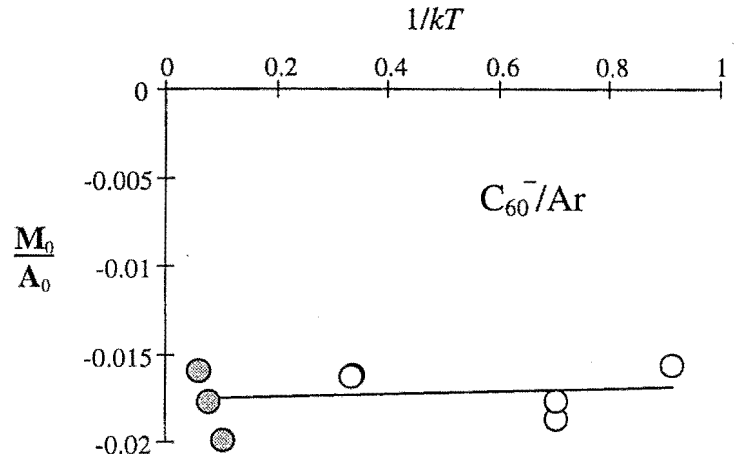

Figure 7.4.1: M_0/A_0 plotted against $1/kT$ for the (0,0) region of C_{60}^-/Ar. The grey and white filled circles represent data obtained using the He-refrigerator and matrix injection systems, respectively. The linear least-squares fit is indicated by the line. The slope ($(8.4 \pm 36) \times 10^{-4}$) is zero within experimental error, indicating an absence of significant temperature dependence.

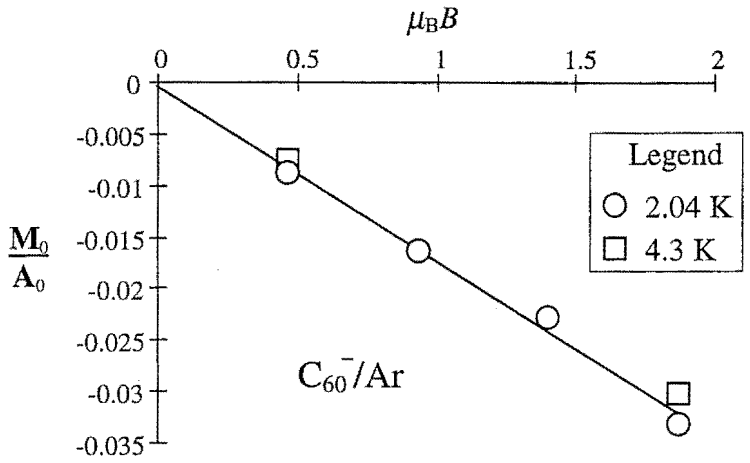

Figure 7.4.2: M_0/A_0 plotted against $\mu_B B$ for the (0,0) region of C_{60}^-/Ar at 2.04 and 4.3 K, for data obtained using the matrix injection system. The linear fit is made to the 2.04-K data.

It can be seen that there is no significant temperature dependence or magnetic saturation of the MCD. These results immediately suggest that *C* terms are very weak or absent, and hence the Zeeman splitting of the ground state is insubstantial. Furthermore, from the single-signed nature of the MCD it can also be concluded that *A*-term contributions are also weak or absent, and hence the MCD must be dominated by *B* terms. In $\mathbf{I}_h$ symmetry, the transition is formally assigned to $^2T_{1g} \leftarrow {}^2T_{1u}$, both the initial and final states for which have three-fold orbital degeneracy. The absence of *A* and *C* terms therefore requires that the orbital angular momenta are either intrinsically weak, or that they are almost totally quenched, presumably by CF and/or vibronic (JT) effects.

Evidence for a significant JT effect can be seen in the vibrational overtones of the C_{60}^-/Ar spectra; in particular, the MCD of band 9 in Figure 7.3.2 is oppositely signed to the origin band, a feature indicative of a JT-active vibration. In $\mathbf{I}_h$ symmetry, T_1 orbital components are susceptible to JT effects due to eight h_g vibrational modes.[30] The observed energy for this excited-state overtone (~430 cm^{-1}; Table 7.3.1) corresponds very well with Raman and inelastic neutron scattering values for the $h_g(7)$ mode of C_{60} (~432 cm^{-1}),[31] which is potentially JT active in both the ground and excited states of C_{60}^-.

Theoretical work by Tosatti, Manini and Gunnarson[14] predicts a significant reduction of the orbital angular momentum of the $^2T_{1u}$ term of C_{60}^-, to give an effective orbital *g* value of 0.43, due to dynamic JT effects. However, this should not be nearly enough to quench the MCD *A* and *C* terms to the degree observed in the current work. On the other hand, EPR studies of C_{60}^- in solution give a ground-state *g* value close to the spin-only value of $g_e \approx 2$,[32,33] indicating essentially complete quenching of the orbital angular momentum. The explication of the earlier EPR and current MCD results almost certainly lies with the notorious susceptibility of dynamic JT effects to stabilisation by crystal fields due to the local environment of a molecule.[34] In the case of dynamic JT effects, the molecule tunnels between equivalent JT-distorted configurations, retaining a time-averaged geometry of the undistorted system. However, at any point in time, the local environment will tend to relax to accommodate the instantaneous geometry of the molecule. If this relaxation occurs on a time scale that is shorter than, or similar to, that of the tunnelling process, it can act to stabilise the current configuration, trapping the molecule in a static JT distortion. This type of effect is sometimes referred to as a crystal-field-stabilised JT (CF-JT) effect, and is well known to cause very substantial (often effectively complete) reductions of orbital angular momenta (the Ham effect).[34] Tosatti *et al.*[14] comment on the possibility of CF-JT effects, and suggest that C_{60}^- may be particularly susceptible to them, on account of the ability of the negative charge to polarise the surroundings. Ar is certainly not immune to polarisation, and it has been seen (*e.g.* in earlier chapters of this thesis) that CF perturbations of the order of 100 cm^{-1} are quite common in Ar matrices. In fact CF-JT effects have been previously observed for (electrically neutral) metallophthalocyanines in Ar matrices,[35-38] and it therefore seems extremely likely that they also occur for other species, including the ions that are of interest in this chapter.

If (as seems almost certain) a static CF-JT effect operates in the ground state of C_{60}^{-}/Ar, then, as noted in Section 7.1.1, $\mathbf{I}_h$ symmetry will not provide a satisfactory description of the structure of the ion. For a h_g JT mode, group theory shows that the possible subgroups of $\mathbf{I}_h$ to be considered[39] are $\mathbf{D}_{5d}$, $\mathbf{D}_{3d}$ and $\mathbf{D}_{2h}$ ($\mathbf{I}_h \supset \mathbf{T}_h \supset \mathbf{D}_{2h}$), for which the reductions of $^2T_{1u}$ and $^2T_{1g}$ are shown in Figure 7.4.3. The ordering of states in Figure 7.4.3 follows that of Lawson *et al.*[40] and Kondo *et al.*[6] for $\mathbf{D}_{5d}$, Green *et al.*[3] and Kondo *et al.*[6] for $\mathbf{D}_{3d}$, and Kondo *et al.*[6] for $\mathbf{D}_{2h}$. Allowed transitions and their polarisations are indicated. (SOC and other effects are ignored.)

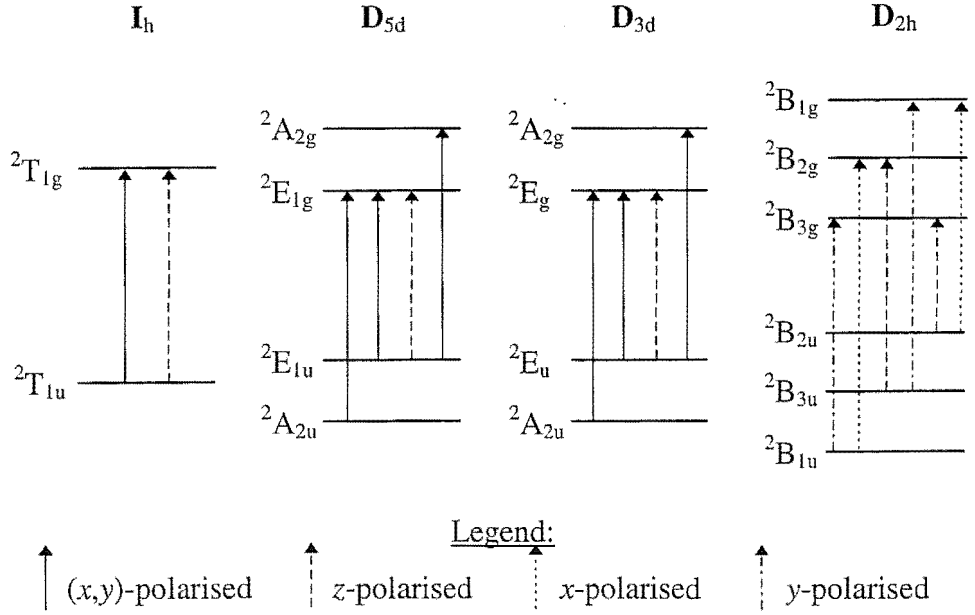

Figure 7.4.3: Symmetry reduction from $\mathbf{I}_h$ of $^2T_{1g} \leftarrow {}^2T_{1u}$ of C_{60}^{-}, showing states and allowed transitions in the $\mathbf{D}_{5d}$, $\mathbf{D}_{3d}$, and $\mathbf{D}_{2h}$ point groups.

$\mathbf{D}_{5d}$ and $\mathbf{D}_{3d}$ exhibit the same type of splitting under symmetry reduction, and can hence be considered together. $^2A_{2u}$ terms are orbitally non-degenerate, and (in the expected absence of significant excited-state SOC) transitions from them will not show MCD temperature dependence. On this basis one might expect that either symmetry may explain the observed spectra. The only allowed transitions terminate in $^2E_{1g}$ ($\mathbf{D}_{5d}$) or ^2E_g ($\mathbf{D}_{3d}$) of the excited-state manifold, and should therefore show *A*-term character unless the excited-state orbital angular momentum is intrinsically small. *B* terms could arise from magnetic-field-induced coupling between the JT-split components of either the ground or excited state. In $\mathbf{D}_{5d}$ and $\mathbf{D}_{3d}$ the *x* and *y* components of the magnetic dipole operator couple $^2A_2$ and $^2E_1$ (or ^2E) terms of the same parity.

The JT theorem states that there will always be a vibration that will lower any electronic degeneracy of a molecule, and this applies equally well to states in $\mathbf{D}_{5d}$ and $\mathbf{D}_{3d}$ symmetry as it does to those in $\mathbf{I}_h$. Thus the $^2E_{(1)}$ levels in Figure 7.4.3 are also susceptible to JT effects, and if CF stabilisation occurs, the appropriate symmetry is D_{2h}. In that case, no orbital degeneracies remain (Figure 7.4.3), but two allowed transitions should occur. This type of model was used by Kondo *et al.*[6] to explain their observation of two bands separated by ~1210 cm^{-1} in work on C_{60}^- in a *polar* organic glass (2-methyltetrahydrofuran) at 77 K. The higher-energy band (10504 cm^{-1}) is not observed in non-polar environments, such as rare-gas matrices, so they suggested that the symmetry reduction was only from $\mathbf{I}_h$ to $\mathbf{D}_{5d}$ or $\mathbf{D}_{3d}$ in these media. It is probably more reasonable to say that further distortions must be small. Note that a reduction to $\mathbf{D}_{2h}$ can not be used to explain the absence of *A*-term-like features, since $\mathbf{M}_1$ is invariant to unitary transformations of the excited-state basis; the loss of pure *A* terms due to CF-JT reduction to $\mathbf{D}_{2h}$ symmetry will be exactly compensated for by *B*-term interactions, which will give rise to a pseudo-*A* term. Thus one is forced to conclude that the excited-state orbital angular momentum must be intrinsically weak.

Assuming effective $\mathbf{D}_{5d}$ or $\mathbf{D}_{3d}$ symmetry, the data presented here suggest that the $^2E_{(1)u}$ terms arising from $^2T_{1u}$ in $\mathbf{I}_h$ symmetry are *not* significantly populated at the temperatures employed ($\lesssim$22 K) in these experiments, since significant changes to the MCD would be expected. A ^2E term has the *potential* to contribute *C* terms to the MCD, and will almost certainly yield *B* terms of different magnitude and/or sign to those of the $^2A_{1g}$ level, and hence the MCD would be temperature dependent. If it is assumed that a population of less than 10% in the $^2E_{(1)u}$ level would have an unobservable effect (within the S/N level) on the MCD, then the CF-JT splitting must be $\gtrsim$37 cm^{-1}.

7.4.2. C_{60}^+/Ar

The bisignated nature of the (0,0) region of C_{60}^+/Ar MCD (Figures 7.3.4 and 7.3.7) means that the use of the first MCD moment is more appropriate than $\mathbf{M}_0$ as a means of quantifying temperature and field dependencies. The results are shown in Figures 7.4.4 and 7.4.5 as the ratios of the first MCD and zeroth absorption moments. ($\mathbf{M}_1$ and $\mathbf{A}_0$ are defined by eqs (5.3.1) and (4.3.1), respectively.) The fitted polynomials qualitatively illustrate the unusual MCD temperature and field dependence of data.

These data do *not* support an $\mathbf{I}_h$ model for C_{60}^{+}/Ar. In that symmetry the ground-state term of C_{60}^{+} is ^2H_g, which has five-fold orbital degeneracy, and should hence show *C*-term temperature (*i.e.*, ~1 / *T* proportionality) and field (*i.e.*, saturation) dependencies. It is very likely that a CF-JT effect operates to lower the symmetry of C_{60}^{+} in the same way as for C_{60}^{-} in Section 7.4.1, which will cause zero-field splittings of both the ground and excited states. Unfortunately, the poor MCD S/N in Figure 7.3.2 precludes identification of any JT-active modes. Hence a more definitive assignment of the vibronic structure than that given by Fulara *et al.*[8] (Section 7.1.2) can not be made from these data.

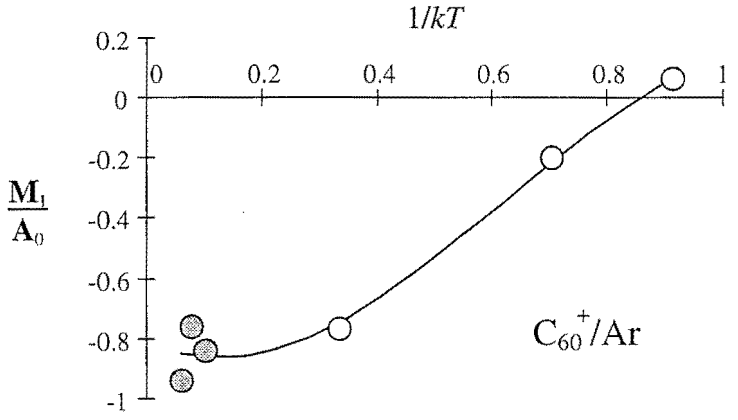

Figure 7.4.4: $\mathbf{M}_1/\mathbf{A}_0$ plotted against $1/kT$ for the (0,0) region of C_{60}^{+}/Ar. The grey- and white-filled circles represent data obtained using the He-refrigerator and matrix injection systems, respectively. The curve is a cubic polynomial fitted to the data to guide the eye.

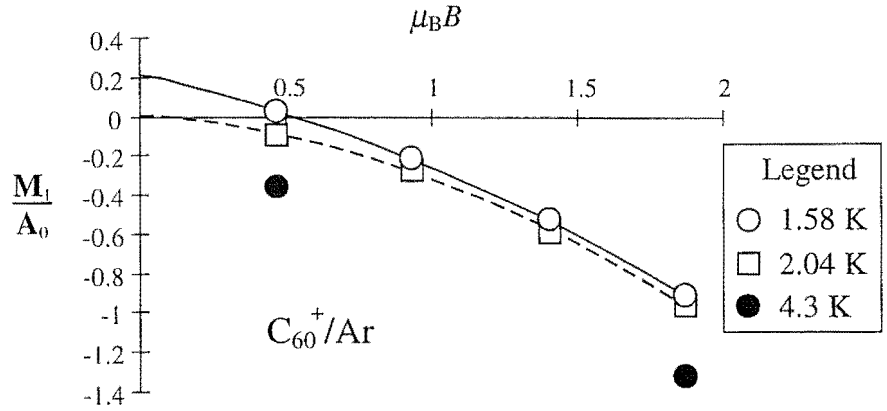

Figure 7.4.5: $\mathbf{M}_0/\mathbf{A}_1$ plotted against $\mu_B B$ for the (0,0) region of C_{60}^{+}/Ar at 1.58, 2.04 and 4.3 K. The full and dashed curves are quadratic polynomials fitted to the 1.58- and 2.04-K data to guide the eye.

The increase in MCD intensity up to ~8 K (Figure 7.4.4), and its temperature independence at the higher temperatures used in the He refrigerator, tend to suggest that there are two close-lying levels arising from the $\mathbf{I}_h$ ground state. The lower one gives very weak (or slightly positive) MCD, while the upper one gives negative MCD. The non-linear increase in the MCD as a function of increasing field strength at the lowest two temperatures could then be due to a Zeeman shift of the upper level. As B is increased, one of the states from this level is shifted to lower energy, raising its occupancy, and hence causing a non-linear increase in the MCD. It is possible that the existence of these levels is a consequence of reduction in symmetry from $\mathbf{I}_h$. Table 7.4.1 gives the correlations from H in the $\mathbf{I}_h$ point group to irreps in possible subgroups. In order for this explanation to be correct, however, the zero-field splittings would have to be ~1/1000 of those calculated by Bendale *et al.*[4] in order to reach near equilibrium populations at ~8 K, where the MCD is approximately linear with field, and becomes almost linear with temperature.

Table 7.4.1: Symmetry reduction of the $\mathbf{I}_h$ irreps H and G.

$\mathbf{I}_h$	$\mathbf{D}_{5d}$	$\mathbf{D}_{3d}$	$\mathbf{D}_{2h}$
H	$A_1 \oplus E_1 \oplus E_2$	$A_1 \oplus E \oplus E$	$A_1 \oplus A_1 \oplus B_1 \oplus B_2 \oplus B_3$
G	$E_1 \oplus E_2$	$A_1 \oplus A_2 \oplus E$	$A_1 \oplus B_1 \oplus B_2 \oplus B_3$

Now the bisignated nature of the (0,0) band MCD is considered. First it is noted that if it corresponds to an A term, it is negative (which is relatively uncommon) and very asymmetric. Gasyna *et al.*[7] proposed that the bisignated MCD was due to combined SO and JT effects in the ^2H_g excited state. However, as was noted in Section 7.1.2, the SO coupling coefficient for C_{60}^+ is likely to be small, and so the SO-JT model is probably incorrect. Theoretical predictions[1,4,5] (Section 7.1.2) suggest that there may in fact be two close-lying electronic origins in the region of the (0,0) band, due to the close proximity of the two lowest-energy excitations ($h_u \leftarrow h_g$ and $h_u \leftarrow g_g$) of Figure 7.7.1. These could explain the observation by Fulara *et al.*[8] of two slightly different vibrational progressions in C_{60}^+/Ne. Close-lying states also give rise to B terms of opposite sign if they interact through magnetic-field effects, which could explain the bisignated MCD. Table 7.4.1 shows the orbital irreps obtained when $\mathbf{I}_h$ symmetry is reduced to $\mathbf{D}_{5d}$, $\mathbf{D}_{3d}$ and $\mathbf{D}_{2h}$ for the ^2H_g and ^2G_g terms of C_{60}^+ considered in this work. In

all three subgroups there is the potential for second-order Zeeman interactions (*e.g.* E_{1g} from ^2H_g with E_{1g} from ^2G_g in $\mathbf{D}_{5d}$) that would produce oppositely signed *B* terms.

7.5. Conclusion

This preliminary work has not provided sufficient information to allow definitive determination of the structures of the ions in Ar matrices. However qualitative analyses of the preliminary absorption and temperature- and field-dependent MCD data for the NIR transitions of C_{60}^-/Ar and C_{60}^+/Ar have enabled several conclusions to be reached.

Structure in the origin bands of both ions can be attributed, at least in part, to the occupation of different sites, because of the variations observed between matrices prepared in the two deposition systems, and the changes that occur as the matrix is annealed. A single JT overtone has been identified from the MCD of the $^2T_{1g} \leftarrow {}^2T_{1u}$ transition (in $\mathbf{I}_h$ symmetry) of C_{60}^-/Ar, but the poor S/N level precludes observation of others for either ion.

Lack of MCD *C* terms and *A* terms for C_{60}^-/Ar is interpreted to indicate (a) that the orbital angular momentum of the ground state is quenched by crystal-field-stabilised Jahn-Teller effects, and (b) that the orbital angular momentum of the excited state is intrinsically weak. A reduction in symmetry to $\mathbf{D}_{5d}$ or $\mathbf{D}_{3d}$ could account for quenching of the ground-state angular momenta. If this is the case, the lack of MCD temperature dependence requires that the splitting of $^2T_{1u}$ must be greater than 35 cm^{-1}, with an orbitally non-degenerate level lying at lower energy.

A MCD magnitude that increases with temperature, and unusual non-linear dependence on magnetic-field strength, were observed for C_{60}^+/Ar at low temperatures. The lack of normal *C*-term field and temperature dependencies suggest that the orbital angular momentum of the ^2H_u ground-state term is either intrinsically weak or strongly quenched. It is suggested that the latter is more likely, with a CF-JT effect giving rise to two close-lying ground-state levels, which reach near equilibrium by ~8 K. The bisignated MCD is possibly due to two nearby excited terms, ^2H_g and ^2G_g in $\mathbf{I}_h$ symmetry, that contribute oppositely signed *B* terms. In $\mathbf{I}_h$ symmetry, there are allowed transitions to both terms, but they will be CF-JT-distorted, and magnetic coupling will occur between the symmetry-reduced levels.

7.6. References

1. Heath, G. A.; McGrady, J. E.; Martin, R. L. *J. Chem. Soc., Chem. Commun.* **1992**, 1272-1274.

2. Negri, F.; Orlandi, F.; Zerbetto, F. *Chem. Phys. Lett.* **1988**, *144*, 31-37.

3. Green, W. H. J.; Gorun, S. M.; Fitzgerald, G.; Fowler, P. W.; Ceulemans, A.; Titeca, B. C. *J. Phys. Chem.* **1996**, *100*, 14892-14898.

4. Bendale, R. D.; Stanton, J. F.; Zerner, M. C. *Chem. Phys. Lett.* **1992**, *194*, 467-471.

5. Kato, T.; Kodama, T.; Shida, T.; Nakagawa, T.; Matsui, T.; Suzuki, S.; Shiromaru, H.; Yamauchi, K.; Achiba, Y. *Chem. Phys. Lett.* **1991**, *180*, 446-450.

6. Kondo, H.; Momose, T.; Shida, T. *Chem. Phys. Lett.* **1995**, *237*, 111-114.

7. Gasyna, Z.; Andrews, L.; Schatz, P. N. *J. Phys. Chem.* **1992**, *96*, 1525-1527.

8. Fulara, J.; Jakobi, M.; Maier, J. P. *Chem. Phys. Lett.* **1993**, *211*, 227-234.

9. Dubois, D.; Kadish, K. M. *J. Am. Chem. Soc.* **1991**, *113*, 4364-4367.

10. Greany, M. A.; Gorun, S. M. *J. Phys. Chem.* **1991**, *95*, 7142-7144.

11. Khaled, M. M.; Carlin, R. T.; Trulove, P. C.; Eaton, G. R.; Eaton, S. S. *J. Am. Chem. Soc.* **1994**, *116*, 3465-3474.

12. Bethune, D. S.; Meijer, G.; Tang, W. C.; Rosen, H. J.; Golden, W. G.; Seki, H.; Brown, C. A.; de Vries, M. S. *Chem. Phys. Lett.* **1991**, *179*, 181-186.

13. Gasyna, Z.; Schatz, P. N. *Private communication* **1992**.

14. Tosatti, E.; Manini, N.; Gunnarsson, O. *Phys. Rev. B* **1996**, *54*, 17184-17190.

15. Adrian, F. J. *Chem. Phys.* **1996**, *211*, 73-80.

16. Koga, N.; Morokuma, K. *Chem. Phys. Lett.* **1992**, *196*, 191-196.

17. Chang, A. H. H.; Ermler, W. C.; Pitzer, R. M. *J. Phys. Chem.* **1991**, *95*, 9288-9291.

18. Negri, F.; Orlandi, G.; Zerbetto, F. *J. Am. Chem. Soc.* **1992**, *114*, 2909-2913.

19. Tanaka, K.; Okada, M.; Okahara, K.; Yamabe, T. *Chem. Phys. Lett.* **1992**, *193*, 101-103.

20. Ceulemans, A.; Fowler, P. W. *J. Chem. Phys.* **1990**, *93*, 1221-1234.

21. Cullerne, J. P.; Angelova, M. N.; O'Brien, M. C. M. *J. Phys.: Condens. Matter* **1995**, *7*, 3247-3269.

22. Cullerne, J. P.; O'Brien, M. C. M. *J. Phys.: Condens. Matter* **1994**, *6*, 9017-9041.

23. Moate, C. P.; O'Brien, M. C. M.; Dunn, J. L.; Bates, C. A.; Liu, Y. M.; Polinger, V. Z. *Phys. Rev. Lett.* **1996**, *77*, 4362-4365.

24. Friedman, B. *Phys. Rev. B* **1993**, *48*, 2743-2747.

25. Lee, K. H.; Lee, H. M.; Chon, H. C.; Park, S. S.; Lee, W. R.; Park, T. Y.; Sun, X. *Bull. Korean Chem. Soc.* **1996**, *17*, 452-457.

26. Lichtenberger, D. L.; Nebesny, K. W.; Ray, C. D.; Huffman, D. R.; Lamb, L. D. *Chem. Phys. Lett.* **1991**, *176*, 203-208.

27. Gasyna, Z.; Schatz, P. N.; Hare, J. P.; Dennis, H. W.; Kroto, H. W.; Taylor, R.; Walton, D. R. M. *Chem. Phys. Lett.* **1991**, *183*, 283.

28. Yabana, K.; Bertsch, G. F. *Chem. Phys. Lett.* **1992**, *197*, 32-37.

29. Haufler, R. E.; Chai, Y.; Chibante, L. P. F.; Fraelich, M. R.; Weisman, R. B.; Curl, R. F.; Smalley, R. E. *J. Chem. Phys.* **1991**, *95*, 2197-2199.

30. Dunn, J. L.; Bates, C. A. *Phys. Rev. B* **1995**, *52*, 5996-6005.

31. Schettino, V.; Salvi, P. R.; Bini, R.; Cardini, G. *J. Chem. Phys.* **1994**, *101*, 1079-11081.

32. Stasko, A.; Brezova, V.; Rapta, P.; Asmus, K.-D.; Guldi, D. M. *Chem. Phys. Lett.* **1996**, *262*, 233-240.

33. Bennati, M.; Grupp, A.; Bauerle, P.; Mehring, M. *Chem. Phys.* **1994**, *185*, 221-227.

34. Englman, R. *The Jahn-Teller Effect in Molecules and Crystals*; Wiley-Interscience: London, 1972.

35. Metcalf, D. H.; VanCott, T. C.; Snyder, S. W.; Schatz, P. N.; Williamson, B. E. *J. Phys. Chem.* **1990**, *94*, 2828-2832.

36. VanCott, T. C.; Koralewski, M.; Metcalf, D. H.; Schatz, P. N.; Williamson, B. E. *J. Phys. Chem.* **1993**, *97*, 7417-7426.

37. VanCott, T. C.; Rose, J. L.; Williamson, B. E.; Boyle, M. E.; Misener, G. C.; Schrimpf, A. E.; Schatz, P. N. *J. Phys. Chem.* **1989**, *93*, 2999-3011.

38. Gasyna, Z.; Metcalf, D. H.; Schatz, P. N.; McConnell, C. L.; Williamson, B. E. *J. Phys. Chem.* **1995**, *99*, 5865-5872.

39. Butler, P. H. *Point Group Symmetry Applications*; Plenum Press: New York, 1981.

40. Lawson, D. R.; Feldheim, D. L.; Foss, C. A.; Dorhout, P. K.; Elliot, C. M.; Martin, C. R.; Parkinson, B. *J. Electrochem. Soc.* **1992**, *139*, L68-L71.

8. FERRICENIUM/AR

8.1. Introduction

8.1.1. Ferrocene – $Fe(cp)_2$

The synthesis of ferrocene in 1951[1,2] was a major factor in the beginnings of organometallic chemistry. Ferrocene has also played an important role in understanding the electronic structure of organometallics. However, a review of these aspects is beyond the scope of this chapter.

Ferrocene has been investigated using MCD by several groups of investigators. It has been studied in organic solution,[3-5] perspex films[5] and inert-gas matrices.[5] The MCD in the blue and near-UV is weak, since it is primarily composed of *B* terms. Ferrocene's radical cation, ferricenium, is a potentially far more interesting species for investigation using MCD, since it has an orbitally degenerate ground state (Section 1.3.2).

8.1.2. Ferricenium – $Fe(cp)_2^+$

Formation of ferricenium in solution is straightforward, since oxidation of ferrocene occurs at -0.400 V versus the Standard Hydrogen Electrode.[6] Furthermore, ferricenium is relatively stable in solution, enabling spectroscopic measurements to be made following bulk electrolysis, without the need for gas-purged or vacuum-tight cells. Such methodology was used by Taylor to generate $Fe(cp)_2^+$ in dichloromethane, using $TBAPF_6$ as the electrolyte.[7] She measured the broad MCD and absorption spectra of the allowed ligand-to-metal charge-transfer (LMCT) transition of ferricenium at room temperature using MOD4. The MCD was moderately strong and positive, in support of the $^2E_{1u} \leftarrow {}^2E_{2g}$ assignment made by Sohn *et al.*[8] for ferricenium in $\mathbf{D}_{5d}$ symmetry. (Prins and Reinders assigned the ground state, using EPR,[9] in agreement with the magnetic-susceptibility data of Hendrickson *et al.*[10])

The low oxidation potential of ferrocene has also been utilised by other workers in the preparation of ferricenium salts. Sohn *et al.*[8] synthesised $[Fe(cp)_2]PF_6$, $[Fe(cp)_2](CCl_3COOH)_3$ and $[Fe(cp)_2]BF_4$, and observed vibrational structure in the $^2E_{1u}$

$\leftarrow {}^2E_{2g}$ transition at 77 K. (The first two compounds were in KBr pellets, while the latter was in aqueous 10-mol L^{-1} LiCl solution.)

The observation of MCD at room temperature by Taylor,[7] and the vibrational structure resolved by Sohn *et al.*,[8] inspired the author to attempt to make $Fe(cp)_2^+$/Ar. If the positive MCD were due to a *C* term, then at low temperatures there should be significant temperature dependence. Additionally, vibrational structure similar to that obtained by Sohn *et al.*[8] could well be obtained because of the low temperature and chemically weak interaction of the Ar solvent. These goals were realised, and this chapter gives a brief account of the first MCD and absorption spectra of $Fe(cp)_2^+$/Ar (with SF_6^- as the counter-ion).

8.2. Experimental

8.2.1. Apparatus for ionisation of volatile compounds for matrix isolation

The apparatus used to prepare $Fe(cp)_2^+$/Ar is shown in Figure 8.2.1. Ferrocene sublimes under vacuum from the cell and is ionised by Ar-resonance radiation produced by the method described in Section 2.1.2. Ejected electrons are subsequently trapped by SF_6 molecules introduced (with or without Ar) into the deposition region through a separate inlet.

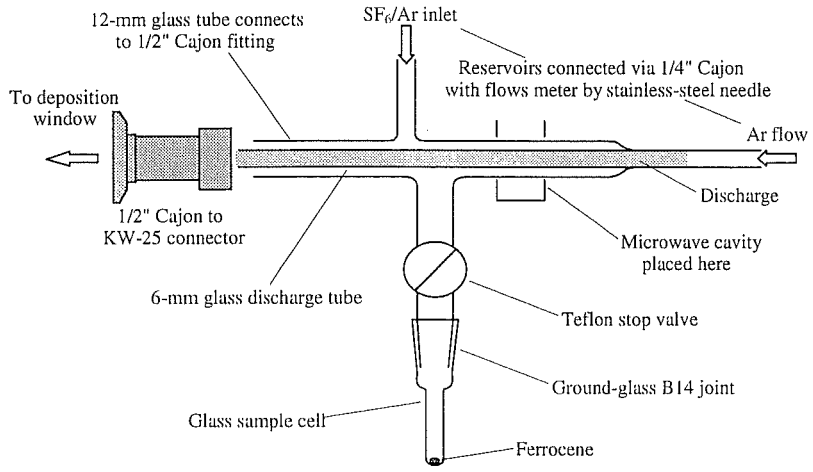

Figure 8.2.1: The glass apparatus designed and successfully employed to prepare $Fe(cp)_2^+$/Ar.

8.2.2. Procedure

Ferrocene (Merck) was placed in the sublimation cell. Since ferrocene sublimes readily under vacuum at room temperature, the cell was pumped down to a moderate vacuum, before the ground-glass stop valve was closed. Matrix preparation was

undertaken as follows, using the He-refrigerator/electromagnet system with MOD4 (Section 2.2.1).

Before starting the discharge, the stop valve was opened so that the resultant sudden rush of ferrocene did not initiate the discharge. The discharge was then started through an ~1 – 2 mmol hr^{-1} flow of Ar, sufficiently well tuned to provide an intense VUV flux at the sample window (Section 2.1.2). Finally, the flow of SF_6 or 1:25 SF_6/Ar (~0.3 – 0.4 or ~1 mmol hr^{-1}, respectively) was initiated, and matrix preparation could occur over a period of ~40 minutes.

It must be emphasised that the methodology described here has not been optimised. However, some useful conclusions can be made. First, it is possible to obtain a small, but spectroscopically useable, yield of $Fe(cp)_2^+$/Ar; second, a high VUV flux is required to make it; and, finally, SF_6 acts as a reasonable electron trap over a range of concentrations. Future work should involve using CCl_4, since it is a more efficient electron scavenger, and could be used in lower concentrations (see Ref. 11) than SF_6. The blue absorption of CCl_4^- does not overlap the $^2E_{1u} \leftarrow {}^2E_{2g}$ transition of ferricenium.

8.3. Results and discussion

8.3.1. Spectral data

Figure 8.3.1 shows the MCD and absorption spectrum of $Fe(cp)_2^+$/Ar obtained using the He-refrigerator/electromagnet system (Section 2.2.1). The temperature was ~14 K, and the magnetic-field strength 0.6 T.

The vibronic structure observed in Figure 8.3.1 is very similar to that obtained for $[Fe(cp)_2^+]PF_6^-$ in KBr pellets at 77 K.[8] Variations are attributable to the differing chemical and physical environments that ferricenium experiences between KBr pellets and Ar matrices. (Note that the optical density is relative low, and there may be baseline artefacts, in the form of broad ripples due to interference fringes of the thin matrix.)

The MCD is single-signed and positive, as observed by Taylor for $Fe(cp)_2^+$ generated electrochemically in dichloromethane.[7] Note, however, that there is one distinct negative-tending dip in the MCD at ~16220 cm^{-1}, which is indicative of a Jahn-Teller (JT) vibration (Section 8.3.3).

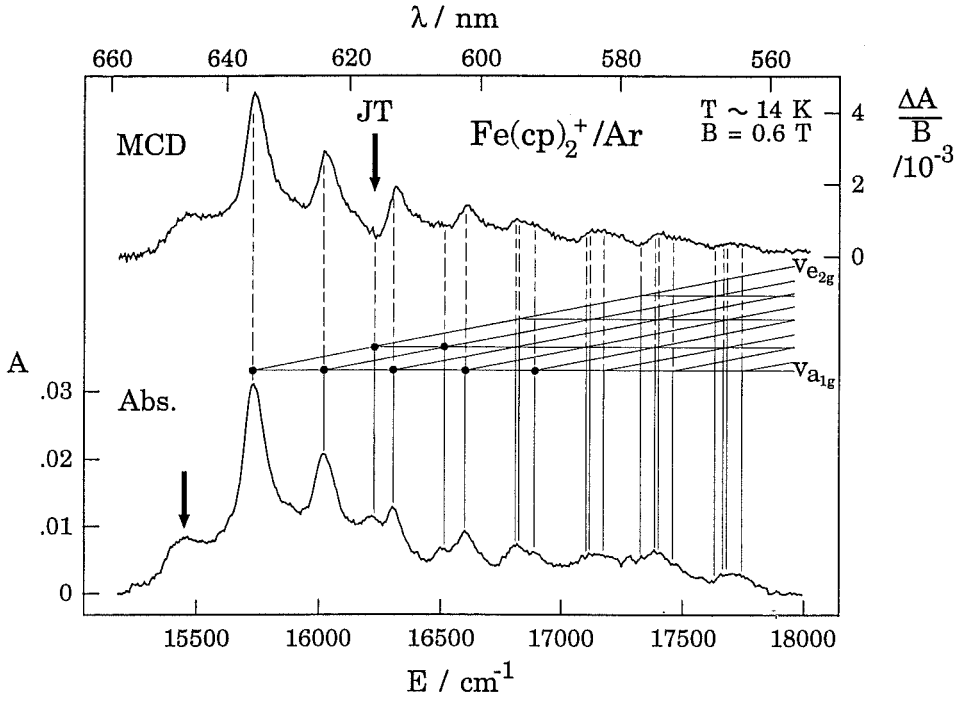

Figure 8.3.1: MCD and absorption spectra for $^2E_{1u} \leftarrow {}^2E_{2g}$ transition of $Fe(cp)_2^+/Ar$ (with SF_6^- as the counter-ion) at $T \approx 14$ K and $B = 0.6$ T. The totally symmetric (a_{1g}) and Jahn-Teller (e_{2g}) vibrational modes (Section 8.3.3) are indicated by the horizontal and sloped lines, respectively. The black dots correspond to bands listed in Table 8.3.2.

8.3.2. The electronic structure of ferricenium

As mentioned in Section 8.1.2, the band system shown in Figure 8.3.1 has been assigned to the $^2E_{1u} \leftarrow {}^2E_{2g}$ LMCT transition. Figure 8.3.2 shows how the transition arises from an excitation between some of the higher-occupied MOs.

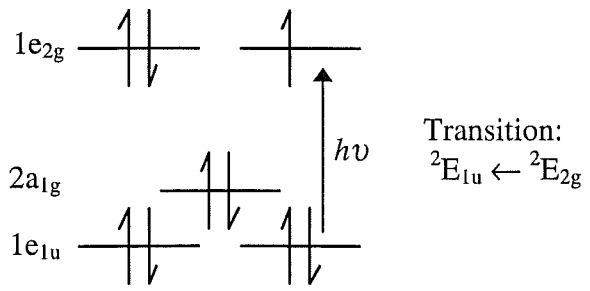

Figure 8.3.2: Partial, schematic MO diagram for $Fe(cp)_2^+$, showing the three highest occupied MOs and the electronic (LMCT) transition that occurs between them and is investigated in this work.

Temperature dependence (between ~14 and 19 K) associated with *C* terms has also been observed, but is not shown here. It provides conclusive evidence of an orbitally degenerate ground state (Section 1.3.2).

8.3.3. Vibrational analysis

First it is noted that at $T < 20$ K, only the lowest vibrational level of the electronic ground state is occupied, so the vibronic structure observed is due to vibrations in only the $^2E_{1u}$ excited state.

8.3.3.1. Progression-building vibrational modes

The only vibrational modes that can appear as Franck-Condon overtones in an electronic transition are those that transform as part of the symmetric squares $[h^2]$ of the orbital irreps of the ground and/or excited states.[12] This always includes the totally symmetric modes (a_{1g} symmetry), which give progressions of bands whose MCD is of the same dispersion and sign as the electronic origin. The other possibilities are JT modes, for which there are two symmetries in the case of a $^2E_{1u} \leftarrow {}^2E_{2g}$ transition in $\mathbf{D}_{5d}$, namely e_{1g} and e_{2g}. Vibrations of the first of these symmetries can be JT active in the ground state, while those of second can be active in the excited state.

As mentioned in Section 8.3.1, JT modes are distinctive in MCD because their odd overtones have signs opposite to that of the electronic origin[13] (giving another example of the utility of MCD). Another occasional feature of progressions in these modes is an uneven energy spacing, due to coupling of two displaced potential-energy surfaces.[13]

8.3.3.2. Assignment of vibrational modes in $Fe(cp)_2^+/Ar$

Previous work on ferricenium salts[8] has shown that there is significant CF splitting (δ') in the $^2E_{1u}$ excited term, evidenced by two (0,0) bands (Table 8.3.1). The same appears to be the case for $Fe(cp)_2^+/Ar$ with the arrow in Figure 8.3.1 indicating the electronic origin due to the lower of the $^2E_{1u}$ levels. Both origins exhibit positive *C* terms in the MCD. Their separation is $\delta' = 285 \pm 10$ cm^{-1}.

Figure 8.3.1 shows the vibrational assignments, which are also presented in Table 8.3.2. (These have only been attempted for overtones built on the more intense, higher-energy origin; bands built on the lower-energy origin are too broad and weak to be easily discerned.) Four members of the most prominent progression are clearly

resolved. They are evenly spaced at ~285 cm^{-1}, and all show positive *C* terms — *i.e.* the same sign as the (0,0) bands. Hence they must represent overtones in a totally symmetric mode, denoted $\nu_{a_{1g}}$ in the following. An overtone in a JT mode (denoted $\nu_{e_{2g}}$ according to the discussion following Table 8.3.2), can be assigned due to the negative tendency of the MCD relative to the rest of the spectrum (Section 8.3.3.1). The wavenumber for the corresponding fundamental is ~480 cm^{-1} (Table 8.3.1). Unfortunately the present data do not afford definitive assignment of higher quanta of this mode. However, a combination band with $\nu_{a_{1g}}$ (also with negative tending MCD) is evident at ~16510 cm^{-1}.

Table 8.3.1: Crystal-field and vibrational parameters for the $^2E_{1u}$ term of ferricenium.

Parameter	$[Fe(cp)_2]PF_6$ *	$[Fe(cp)_2](CCl_3COOH)_3$ *	$Fe(cp)_2^+/Ar$ †
CF splitting, δ'	~ 200 cm^{-1}	140 cm^{-1}	285 ± 10 cm^{-1}
$\nu_{a_{1g}}$	290 – 300 cm^{-1}	300 – 330 cm^{-1}	270 – 300 cm^{-1}
$\nu_{e_{2g}}$	—	—	480 cm^{-1}

* Ref. 8. In a KBr disk at 77 K.

† This work; ± 10 cm^{-1}. Vibrational parameters based on the progression corresponding to the upper CF level.

Table 8.3.2: Vibrational levels and assignments for the upper CF level of the $^2E_{1u}$ term of $Fe(cp)_2^+/Ar$.

E / cm^{-1} *	Assignment
15740	(0,0)
16025	$\nu_{a_{1g}}$
16220	$\nu_{e_{2g}}$
16312	$2\nu_{a_{1g}}$
16510	$\nu_{e_{2g}} + \nu_{a_{1g}}$
16610	$3\nu_{a_{1g}}$
16816	$2\nu_{e_{2g}}$ and $2\nu_{a_{1g}} + \nu_{e_{2g}}$ (?)
16893	$4\nu_{a_{1g}}$

* ± 5 cm^{-1}. The lower CF level has (0,0) at 15466 ± 10 cm^{-1}.

It remains to assign the 480-cm^{-1} JT-active mode. Unfortunately the Raman spectrum of $Fe(cp)_2^+$ (which would show the even-parity modes) does not appear to have been reported. The e_{2g} and e_{1g} modes of ferrocene that lie closest to the wavenumber observed here occur at 600 cm^{-1} (CCC in-plane deformation) and 390 cm^{-1} (ring tilt), respectively.[14,15] Although the energy of the e_{1g} mode is closer to that of the

JT vibration, it is more likely to be the e_{2g} mode that is observed, for the following reasons. The open-shell orbital in the upper state is essentially ligand based, and hence the upper state should show the weak SOC typical of planar π systems.[16] The open-shell orbital in the ground state is predominantly of metal d character, and hence has a relatively large SO splitting (~800 cm^{-1}; Ref. 7). Because SOC tends to quench JT effects,[17] JT activity will be quenched in the $^2E_{2g}$ ground state, but not in the $^2E_{1u}$ excited state, and therefore an e_{2g} mode is expected. The observed frequency does not correspond to those of ferrocene because, (a) vibrational energies will be altered by the ionisation of the molecule; and, (b) the vibration is occurring in an excited state. Hence Raman spectra of $Fe(cp)_2^+$, preferably in the $^2E_{1u}$ excited state, are required to assign the JT mode unambiguously.

8.4. Conclusion

In this chapter, the first MCD and absorption spectra for the $^2E_{1u} \leftarrow {}^2E_{2g}$ LMCT transition of $Fe(cp)_2^+$/Ar have been presented. Both MCD and absorption spectra exhibit vibrational structure. There are two origin bands due to a ~285-cm^{-1} CF splitting of the excited state.[8] Two progression-building vibrational modes have been identified: a totally symmetric mode, $\nu_{a_{1g}}$ (285 ± 15 cm^{-1}), and a Jahn-Teller-active mode, $\nu_{e_{2g}}$ (480 ± 10 cm^{-1}). The JT mode is attributed to an e_{2g} vibration in the excited state, because strong SOC in the ground state will quench its JT susceptibility.

Future work on $Fe(cp)_2^+$/Ar will be carried out by Ms Kirsten Taylor. This will primarily involve improving the experimental method to enhance ion yield, followed by quantification of the MCD temperature dependence using the matrix injection system (Section 2.2.2). Temperature-dependent MCD data should enable extraction of the CF and covalent components of the orbital reduction factor, κ.[7]

Excited-state Raman spectra of ferricenium could enable definitive assignment of the JT-active vibration.

8.5. References

1. Kealy, T. J.; Pauson, P. J. *Nature (London)*, **1951**, *168*, 1039.

2. Miller, S. A.; Tebboth, J. A.; Tremaine, J. F. *J. Chem. Soc.*, **1952**, 632.

3. Nielson, D.; Boone, D.; Eyring, H. *J. Phys. Chem.*, **1972**, *76*, 511.

4. Nielson, D.; Farmer, M.; Eyring, H. *J. Phys. Chem.*, **1976**, *80*, 717.

5. Barton, T. J.; Douglas, I. N.; Grinter, R.; Thomson, A. J. *J. Chem. Soc., Dalton Trans.*, **1972**, 1948.

6. Lide, D. R., Ed. *CRC Handbook of Chemistry and Physics*, 71st ed.; CRC Press: Boca Raton, 1990

7. Taylor, K. C. "*A Theoretical and Experimental Investigation of the Electronic Structure of Ferricenium Using Optical Spectroscopy*", B.Sc.(Hons) Project Report, Department of Chemistry, University of Canterbury, September 1995.

8. Sohn, Y. S.; Henrickson, D. N.; Gray, H. B. *J. Am. Chem. Soc.*, **1970**, *93*, 3603.

9. Prins, R.; Reinders, F. J. *J. Am. Chem. Soc.*, **1969**, *91*, 4929.

10. Henrickson, D. N.; Sohn, Y. S.; Gray, H. B. *Inorg. Chem.*, **1971**, *10*, 1559.

11. Gasyna, Z.; Andrews, L.; Schatz, P. N. *J. Phys. Chem.* **1992**, *96*, 1525-1527.

12. Tsukerblat, B. S. *Group Theory in Chemistry and Spectroscopy*; Academic Press: San Diego, 1994.

13. Samet, C.; Rose, J. L.; Piepho, S. B.; Laurito, J.; Andrews, L.; Schatz, P. N. *J. Am. Chem Soc.* **1994**, *116*, 11109-11119.

14. Fritz, H. P. *Adv. Organometal. Chem.* **1964**, *1*, 239-316.

15. Nakamoto, K. *Infrared and Raman Spectra of Inorganic and Coordination Compounds*, 3rd ed.; Wiley-Interscience: New York, 1978.

16. McClure, D. S. *J. Chem. Phys.* **1952**, *20*, 682-686.

17. Englman, R. *The Jahn-Teller Effect in Molecules and Crystals*; Wiley-Interscience: London, 1972.

9. CONCLUSION

This Ph.D. thesis has described the results of electronic absorption and MCD investigations into a variety of free-radical species matrix-isolated in Ar at cryogenic temperatures.

All spectral data were acquired using a high-resolution simultaneous MCD and absorption spectrometer (MOD4) purpose-built for the project. In terms of the goals set for MOD4, it has performed very well. It has a wider spectral range (UV to NIR), much higher resolution, and better absorption S/N than its predecessor, MOD3; all of these features were necessary for this work. Nevertheless there remain aspects that require further work: (i) stabilisation of the absorption background; (ii) improvement of the MCD S/N level (particular in the NIR); (iii) implementation of Ge photodiode detectors for NIR MCD studies beyond 1100 nm; and, (iv) fixing an electronics 'bug' in the monochromator circuitry, whereby wavelength slews are initiated by electrical noise spikes, due to (for example) switching on other equipment.

The trolley system designed for incorporation of the two matrix-isolation/ cryostat systems in MOD4 has proved very successful, enabling easy interchange of the heavy and unwieldy magnets.

Experimental absorption spectra and MCD temperature and magnetic-field dependencies for OH(D)/Ar, NH(D)/Ar and CH/Ar have been measured and interpreted in terms of a SO-CF model in which orbital angular momentum is partially quenched by CF interactions with neighbouring species in the matrix. The model is consistent with the (physically realistic) expectation of random orientation of the guest species, but does *not* assume the MCD 'linear limit'. Anisotropic g values necessitated the construction of orientation-dependent wavefunctions for the ground state.

The single-signed MCD of the $A\,^2\Sigma^+ \leftarrow X\,^2\Pi$ transition of OH/Ar at ~32150 cm^{-1} shows almost pure C-term character. Only the lowest SO-CF level ($^2\Pi_-$) is occupied at the temperatures investigated (~1.7 – 7 K). The temperature and field dependence of the MCD is due predominantly to C terms, with an additional small B-term contribution arising from a Zeeman interaction between the $^2\Pi_-$ and $^2\Pi_+$ levels. Using $\zeta_\pi = 125 \pm 10$ cm^{-1} (slightly reduced from the gas-phase SO splitting), numerical integration of the experimental $\mathbf{M}_0/\mathbf{A}_0$ data gives a (weighted average) orbital reduction

factor of $\kappa = 0.79 \pm 0.02$, corresponding to a CF of $V = 97 \pm 10$ cm^{-1}. However, structure in the spectra suggests the existence of at least five discrete sites, with orbital reduction factors varying from $\kappa \approx 1$ to 0.5 across the envelope of the transition. This interpretation is also consistent with the similar structure observed in the OD/Ar data.*

MCD temperature and field-dependence data for the $A\,^3\Pi \leftarrow X\,^3\Sigma^-$ band system of NH/Ar has been successfully accounted for in terms of a SO-CF model for $A\,^3\Pi$, and essentially completely quenched ZFS in $X\,^3\Sigma^-$. Numerical integration of the experimental $\mathbf{M}_1/\mathbf{A}_0$ yielded $\zeta_\pi = 33.5 \pm 0.3$ cm^{-1} for the excited term, only a slight reduction from the gas-phase value. Since the first MCD moment is insensitive to CF effects in the excited state, a somewhat tentative CF splitting of $V \approx 75$ cm^{-1} was derived from peak separations. Semiquantitative agreement between the SO-CF theory and experiment was observed in spectral simulations using these values of ζ_π and V. Structure due to librational levels in the excited state, or possibly to coupling with lattice phonons modes, were observed to the blue of the (0,0) SO-CF components. Broadening at warmer temperatures is ascribed to a hot band due to population of a librational level of the $X\,^3\Sigma^-$ term. Finally, a second stable site (~12 cm^{-1} to the red of the main site at 29620 cm^{-1}) accounts for the temperature-independent shoulder observed in these high-resolution spectra.

Fitting of the ND/Ar data in an analogous manner to NH/Ar gave $D \approx 0$ cm^{-1} and $\zeta_\pi = 37.1 \pm 1.0$ cm^{-1}. The latter is ~2.5-cm^{-1} *larger* than the gas-phase value, which was attributed to problems determining the absorption background. Although the spectra of ND/Ar exhibit much broader structure, they behave similarly to those of NH/Ar. Broadening is probably due to compressed rotational levels with respect to NH/Ar and/or different interactions with the Ar host.

CH/Ar has a $X\,^2\Pi$ ground term like OH/Ar, but with significantly smaller SO splitting in the gas phase. Hence a SO-CF model was developed which did *not* assume that only the lower SO-CF level was occupied. However, inclusion of a CF serves to *increase* the splitting from that observed in the gas phase, and at the temperatures used

---

* This work has been published in *The Journal of Physical Chemistry A*, **1997**, *101*, 3119-3124 under the title "Magnetic Circular Dichroism of the Hydroxyl Radical in an Argon Matrix" by Vaughan S. Langford and Bryce E. Williamson.

in this work the population of the upper level is entirely negligible. Temperature and field dependencies of the MCD (the magnitude of which is significantly weaker than OH/Ar) occurs from the $^2\Pi_-$ level occurs because of partial quenching of the orbital angular momentum. Best-fit parameters, obtained by fitting all data for each of the $A\,^2\Delta$, $B\,^2\Sigma^-$ and $C\,^2\Sigma^+ \leftarrow X\,^2\Pi$ transitions, then averaging them, are $\zeta_\pi = 21 \pm 1$ cm^{-1} and $\kappa = 0.26 \pm 0.03$, and consequently $V = 78 \pm 15$ cm^{-1} for randomly oriented CH/Ar. However the possibility of preferentially oriented CH/Ar, with its z axis aligned along the magnetic-field axis, can not be discounted, and fitting gives, for the same ζ_π, $\kappa = 0.11 \pm 0.02$, and hence $V = 205 \pm 15$ cm^{-1}. However, it is considered physically unreasonable for a molecule the size of CH to exhibit such behaviour, and the slightly better fit may be fortuitous. The bisignated MCD of the $A\,^2\Delta \leftarrow X\,^2\Pi$ transition at warmer temperatures and stronger fields, and the single-signed MCD of $B\,^2\Sigma^-$ and $C\,^2\Sigma^+ \leftarrow X\,^2\Pi$ is also explained by orbital reduction. When $\kappa < 1$, the A-term intensity increases for the former, but is reduced for the latter. (The near pure A term suggests that the excited-state CF splitting is very small.) Broadening accounts for temperature dependence in the A-term-dominated MCD of $A\,^2\Delta \leftarrow X\,^2\Pi$ at higher temperatures. Structure in the transitions of CH/Ar has been tentatively assigned to coupling with lattice phonons. Site structure can not be ruled out, although no structural changes were observed between experiments that would support this.

In summary, the SO-CF models developed in this work have been applied successfully to the above monohydrides in Ar matrices. In all cases a significant CF splitting of Π-orbital components has been found. The $X\,^2\Pi$ terms of OH/Ar and CH/Ar indicate a reduction of ~10 cm^{-1} in ζ_π from the gas-phase value. On the other hand, the $A\,^3\Pi$ term of NH/Ar has the same ζ_π value as found in the gas phase. The reason for this difference is not understood, but it is perhaps a consequence of different spin multiplicities of the Π terms. It is concluded that all of these radicals are most likely randomly oriented in Ar matrices.

Future work should include investigating the MCD of CD/Ar, and of the above species in other rare-gas matrices. OH could also be probed in ice, or in MI water clusters, following suitable UV irradiation of the sample to produce the radical. It would also be interesting to apply the theory developed for the first-row monohydrides to the second-row analogues, SiH, PH and SH, which absorb in similar spectral regions.

Preliminary temperature- and magnetic-field dependencies of the NIR MCD of C_{60}^{+}/Ar and C_{60}^{-}/Ar have been presented, but do not allow definitive determination of their structure in Ar matrices. Qualitative analyses of the absorption and temperature- and field-dependent MCD data for C_{60}^{-}/Ar and C_{60}^{+}/Ar have allowed us to attribute structure in the origin bands of both ions, at least in part, to the occupation of different sites.

A JT overtone (h_g symmetry; ~430 cm^{-1}) has been identified from the MCD of the $^2T_{1g} \leftarrow {}^2T_{1u}$ transition (in $\mathbf{I}_h$ symmetry) of C_{60}^{-}/Ar. The absence of MCD *C* terms and *A* terms for C_{60}^{-}/Ar is interpreted to indicate that the orbital angular momentum of the ground state is quenched by crystal-field-stabilised Jahn-Teller (CF-JT) effects, and that the orbital angular momentum of the excited state is intrinsically weak. Symmetry reduction may account for quenching of the ground-state angular momenta.

A MCD magnitude that increases with temperature, and unusual non-linear dependence on magnetic-field strength, were observed for C_{60}^{+}/Ar at low temperatures, and suggest that the orbital angular momentum of the $\mathbf{I}_h$ ^2H_u ground-state term is either intrinsically weak or strongly quenched. The latter is more likely, with a CF-JT mechanism being responsible. The bisignated MCD is possibly due to two transitions to nearby excited terms, ^2H_g and ^2G_g in $\mathbf{I}_h$ symmetry, that contribute oppositely signed *B* terms.

Continuation of the work on $C_{60}^{\pm}$/Ar should seek to obtain absorption and MCD temperature- and field-dependence data over a wider temperature range (~1.4 – 20 K) using the matrix injection system, but with better S/N due to improved NIR detection. Secondly, theory needs to be developed, which would enable unambiguous assignment of the electronic transitions and vibronic structure.

Finally, this thesis has presented the first MCD and absorption spectra of the $^2E_{1u} \leftarrow {}^2E_{2g}$ LMCT transition of ferricenium/Ar (SF_6^- counter-ion). The spectra show well-resolved vibronic structure in agreement with absorption work on crystals at low temperatures. Two progressions are observed because of a CF splitting in the $^2E_{1u}$ excited state. In the stronger, better-resolved progression, the totally symmetric mode has an energy of 285 ± 15 cm^{-1}, while the first harmonic of the Jahn-Teller-active mode lies 480 ± 10 cm^{-1} above the origin. The JT mode is tentatively assigned to an e_{2g} C–C–C deformation mode in the excited state. Future work by Ms Kirsten Taylor will involve acquisition of temperature- and field-dependent MCD data using the matrix

injection system, in order to quantify the orbital reduction of ferricenium/Ar. Excited-state Raman spectra of ferricenium would enable definitive assignment of the JT-active mode.

APPENDICES

Appendix A: Circuit diagrams

A.1. W-lamp power supply (Section 2.3.2.2)

Table A.1.1: Characteristics of the 25-V switch-mode power supply.

Characteristic	Specification
Type	Switch-mode regulated
Voltage	0 to 25 V (knob control)
Current	0 to 10 A (screw potentiometer)
Voltage regulation	0.05%
Current regulation	0.2%

The circuit diagram is shown on the next page.

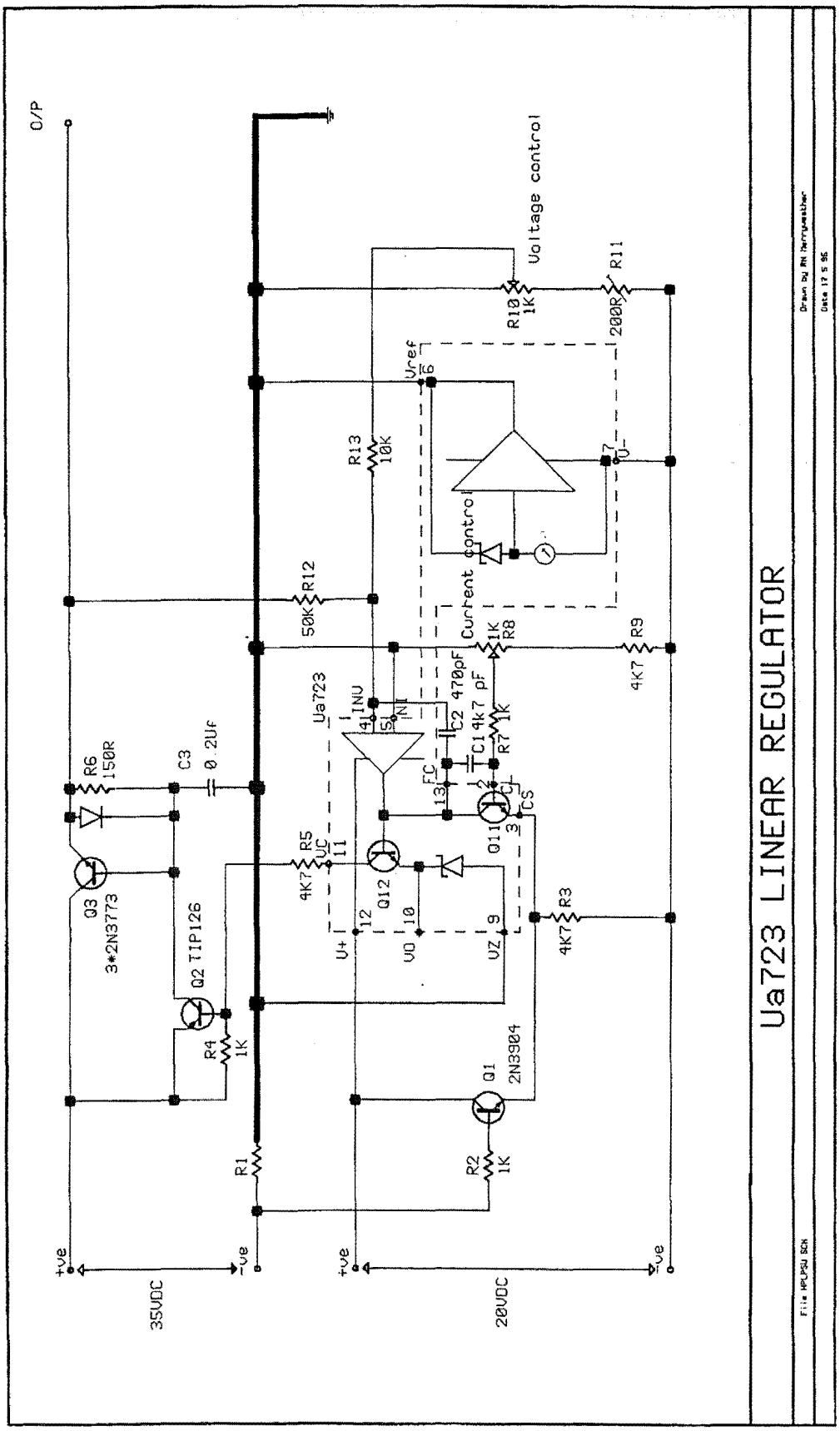

Figure A.1.1: Circuit diagram for W-lamp power supply.

A.2. Monochromator stepper-motor circuitry (Section 2.3.3.2(b))

A.2.1. Driver

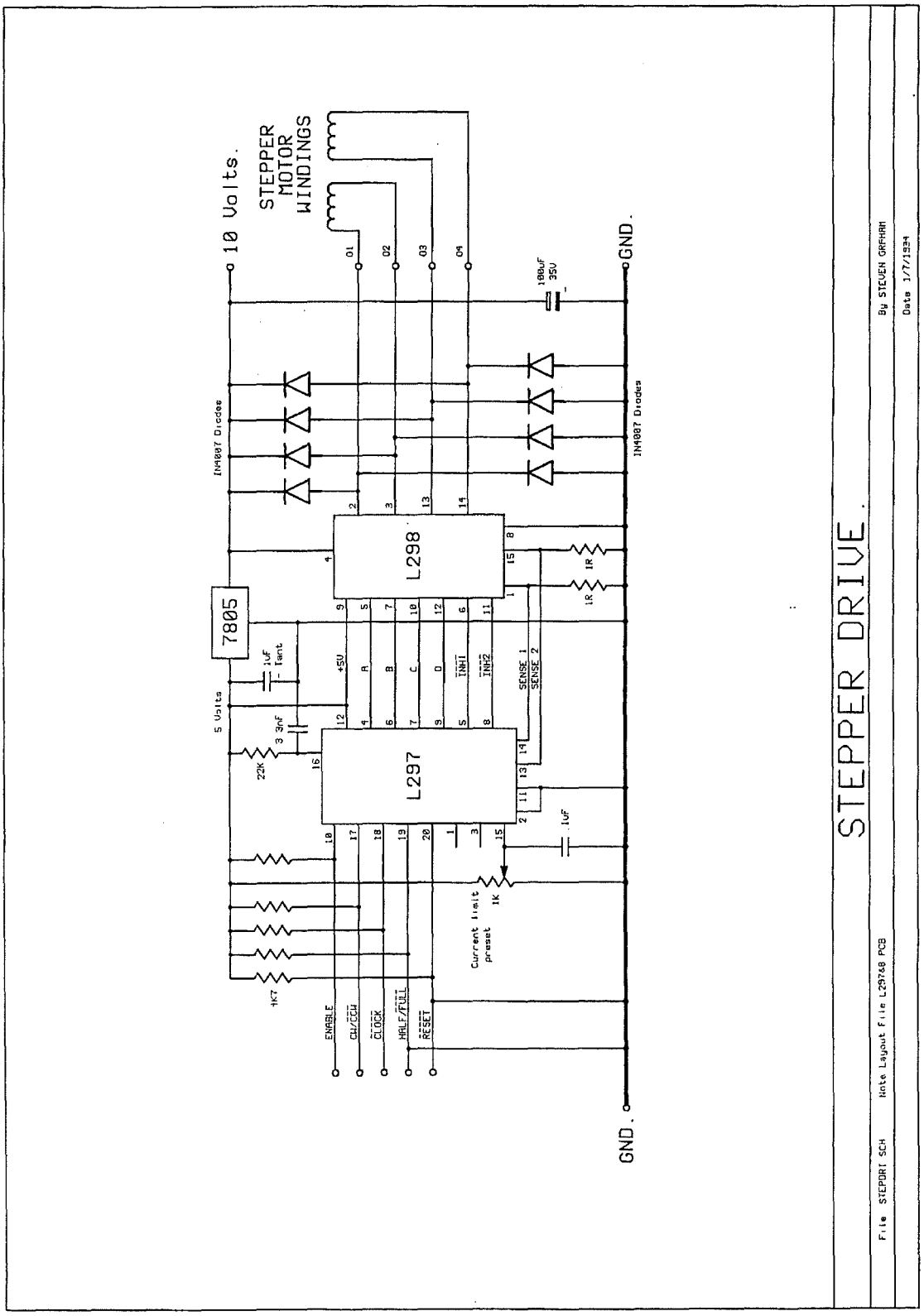

Figure A.2.1: Circuit diagram for monochromator stepper-motor driver.

A.2.2. Controller

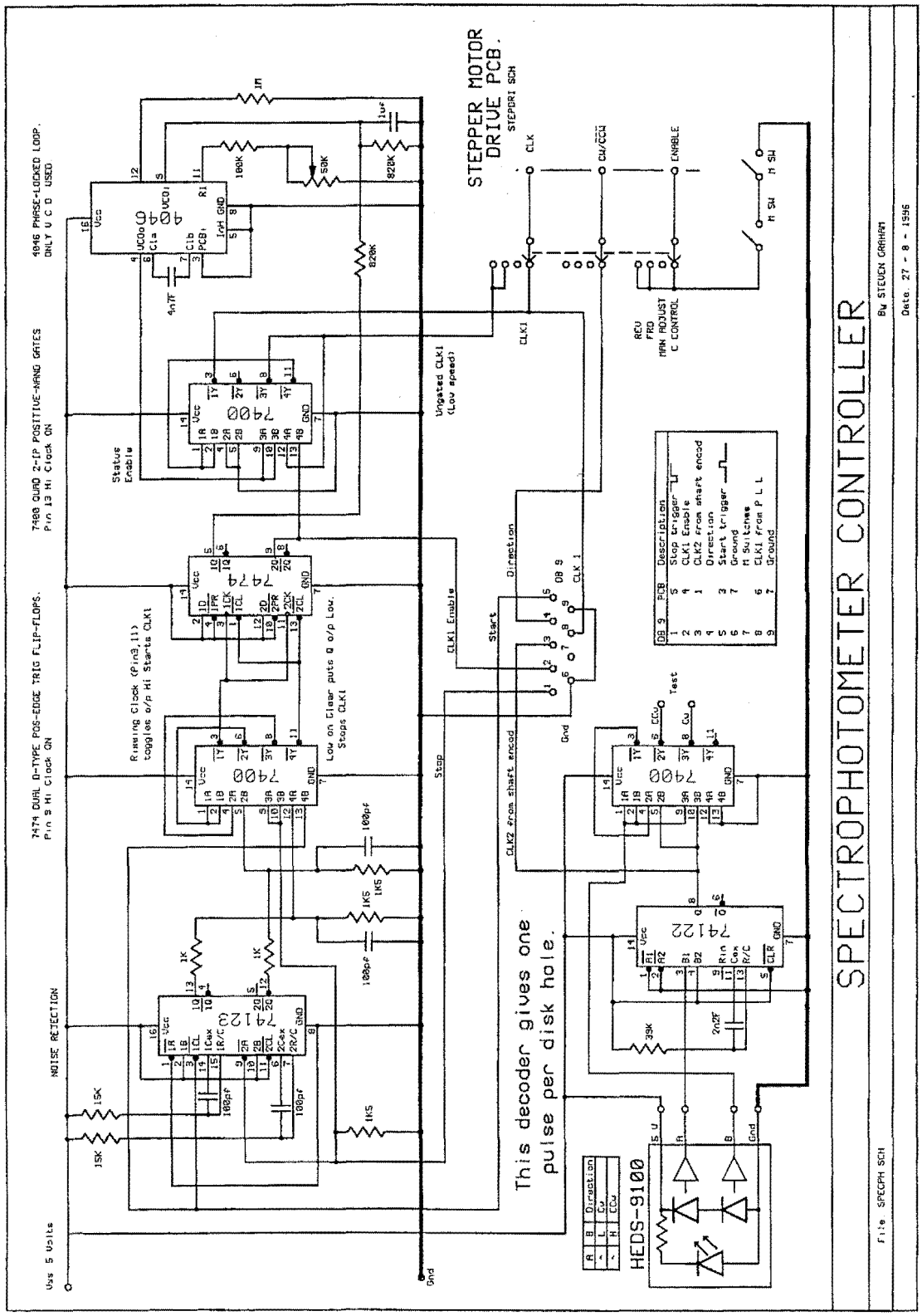

Figure A.2.2: Circuit diagram for monochromator stepper-motor controller.

A.3. HV power supply (Section 2.3.7.1(c))

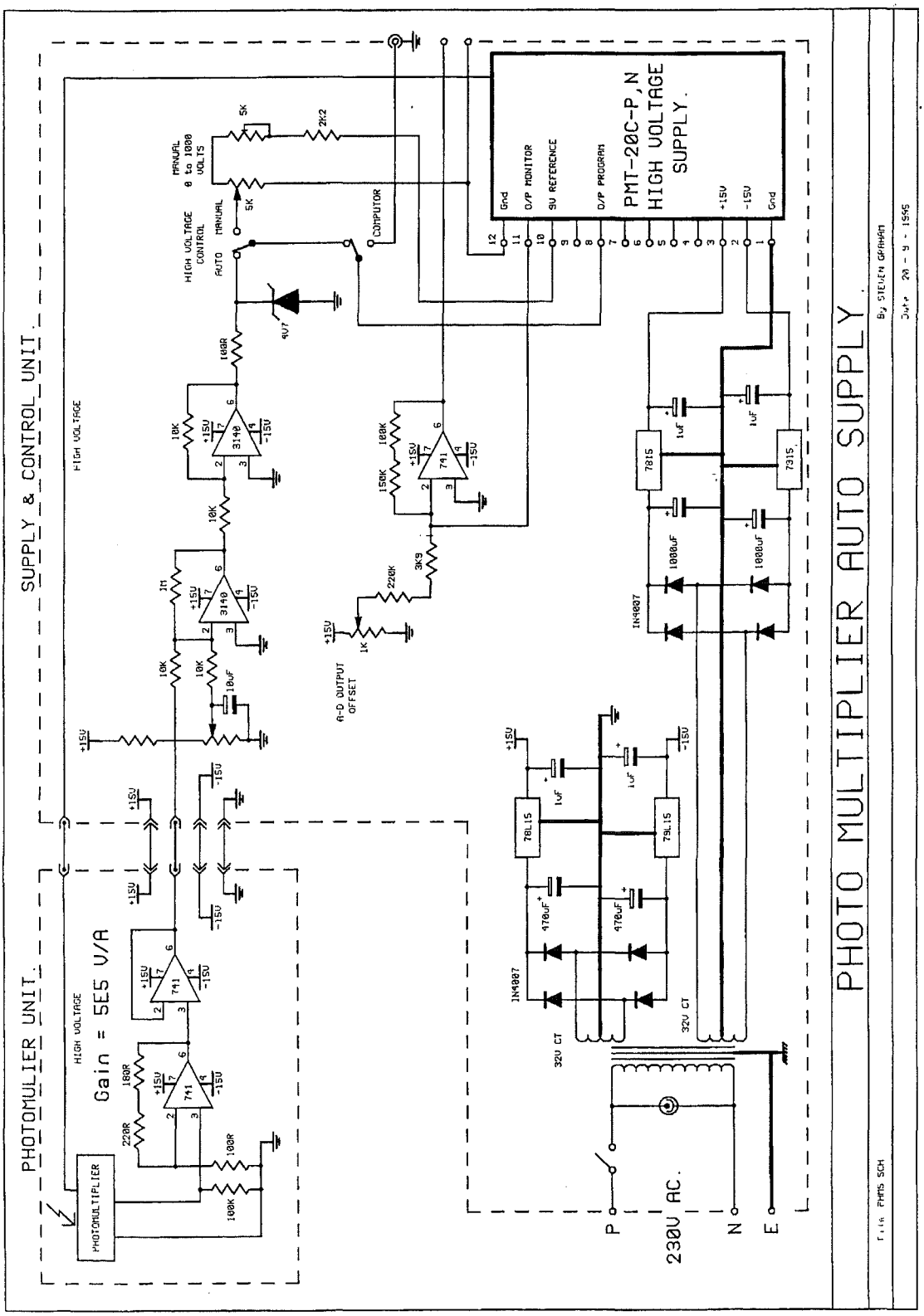

Figure A.3.1: Circuit diagram for photomultiplier high-voltage power supply.

A.4. Programmable amplifier (Section 2.3.9.2(d))

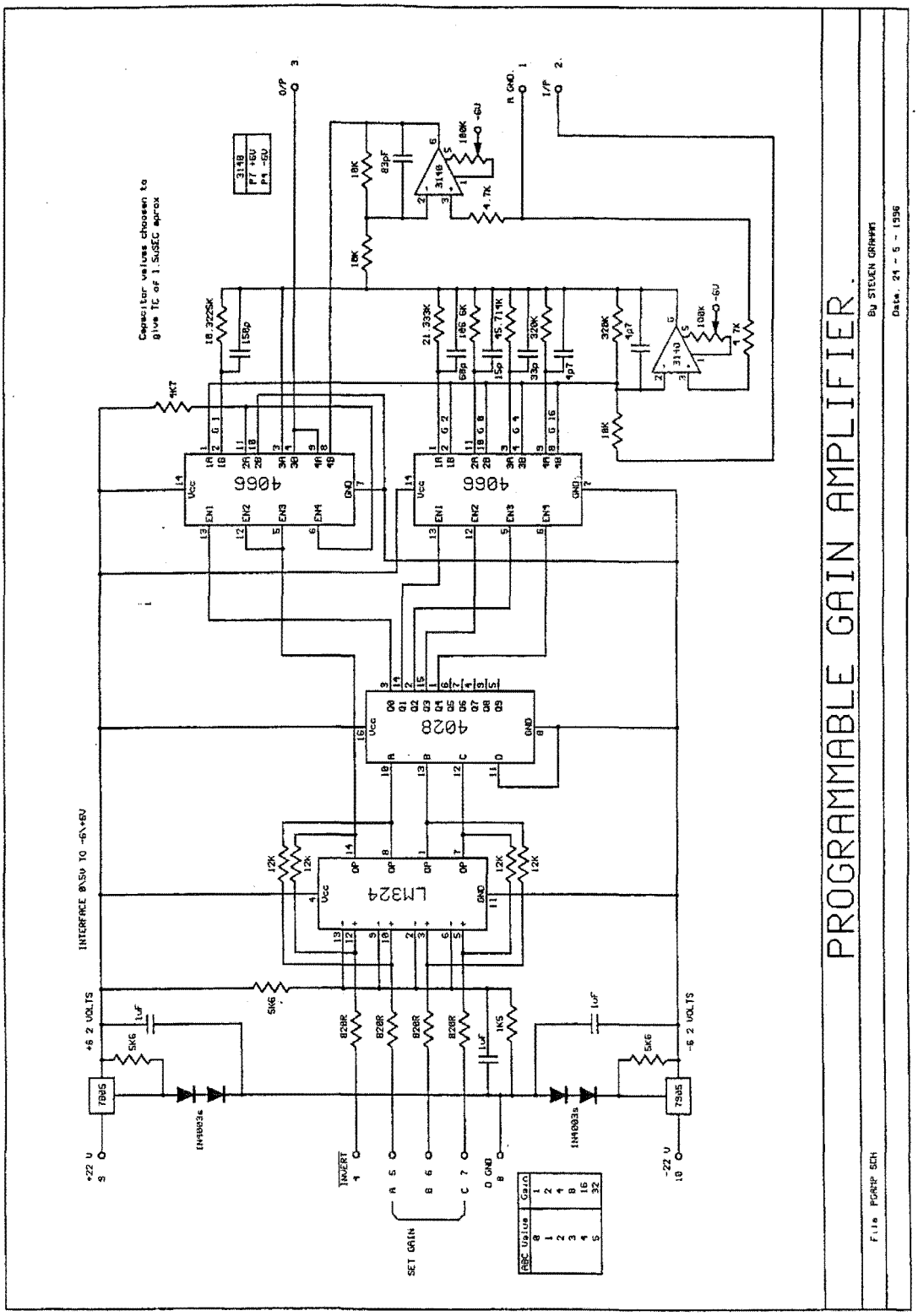

Figure A.4.1: Circuit diagram for progammable amplifier.

Appendix B: Group theory tables

References:

1. Butler, P. H. *Point Group Symmetry Applications*; Plenum Press: New York, 1981.
2. Piepho, S. B.; Schatz, P. N. *Group Theory in Spectroscopy with Applications to Magnetic Circular Dichroism*; Wiley-Interscience: New York, 1983.

B.1. $C_{\infty v}$ point group

2jm for $C_{\infty v}$ in Butler notation

Complex conjugation in $C_{\infty v}$:

$$a^* = a,\ \alpha^* = -\alpha$$

2*jm*s are obtained using the following rules:

$$\begin{pmatrix} \tilde{0} \\ 0 \end{pmatrix} = -1,\ \begin{pmatrix} a \\ \alpha \end{pmatrix} = (-1)^{a-\alpha},\ a \neq \tilde{0}$$

3jm for $C_{\infty v}$ in Butler notation (a partial list)

3*jm* are found using the following rules:

$$\begin{pmatrix} a & b & 0 \\ \alpha & \beta & 0 \end{pmatrix} = \delta_{b,a}\,\delta_{\beta,-\alpha}\,|a|^{-1/2} \begin{pmatrix} a \\ \alpha \end{pmatrix} \qquad \begin{pmatrix} a & a & \tilde{0} \\ a & -a & 0 \end{pmatrix} = \frac{1}{\sqrt{2}};\ \ a, b \neq 0, \tilde{0}$$

$$\begin{pmatrix} a+b & a & b \\ a+b & -a & -b \end{pmatrix} = \frac{1}{\sqrt{2}}(-1)^{2b};\ \ a, b \neq 0, \tilde{0}$$

A partial listing of 3*jm* is given in Table B.1.1.

Table B.1.1: A partial list of $3jm$ for $\mathbf{C}_{\infty v}$.

0	0	0	$3jm$
0	0	0	1

$\tilde{0}$	$\tilde{0}$	0	$3jm$
0	0	0	-1

$\frac{1}{2}$	$\frac{1}{2}$	0	$3jm^{\dagger}$
$\frac{1}{2}$	$-\frac{1}{2}$	0	$\frac{1}{\sqrt{2}}$

$\frac{1}{2}$	$\frac{1}{2}$	$\tilde{0}$	$3jm$
$\frac{1}{2}$	$-\frac{1}{2}$	0	$\frac{1}{\sqrt{2}}$

1	$\frac{1}{2}$	$\frac{1}{2}$	$3jm$
1	$-\frac{1}{2}$	$-\frac{1}{2}$	$-\frac{1}{\sqrt{2}}$
-1	$\frac{1}{2}$	$\frac{1}{2}$	$-\frac{1}{\sqrt{2}}$

1	1	0	$3jm$
1	-1	0	$\frac{1}{\sqrt{2}}$

1	1	$\tilde{0}$	$3jm^{\dagger}$
1	-1	0	$\frac{1}{\sqrt{2}}$

$\frac{3}{2}$	1	$\frac{1}{2}$	$3jm^{\dagger}$
$\frac{3}{2}$	-1	$-\frac{1}{2}$	$-\frac{1}{\sqrt{2}}$
$-\frac{3}{2}$	1	$\frac{1}{2}$	$-\frac{1}{\sqrt{2}}$

$\frac{3}{2}$	$\frac{3}{2}$	0	$3jm^{\dagger}$
$\frac{3}{2}$	$-\frac{3}{2}$	0	$\frac{1}{\sqrt{2}}$

$\frac{3}{2}$	$\frac{3}{2}$	$\tilde{0}$	$3jm$
$\frac{3}{2}$	$-\frac{3}{2}$	0	$\frac{1}{\sqrt{2}}$

2	1	1	$3jm$
2	-1	-1	$\frac{1}{\sqrt{2}}$
-2	1	1	$\frac{1}{\sqrt{2}}$

2	$\frac{3}{2}$	$\frac{1}{2}$	$3jm$
2	$-\frac{3}{2}$	$-\frac{1}{2}$	$-\frac{1}{\sqrt{2}}$
-2	$\frac{3}{2}$	$\frac{1}{2}$	$-\frac{1}{\sqrt{2}}$

2	2	0	$3jm$
2	-2	0	$\frac{1}{\sqrt{2}}$

2	2	$\tilde{0}$	$3jm^{\dagger}$
2	-2	0	$\frac{1}{\sqrt{2}}$

$\frac{5}{2}$	2	$\frac{1}{2}$	$3jm^{\dagger}$
$\frac{5}{2}$	-2	$-\frac{1}{2}$	$-\frac{1}{\sqrt{2}}$
$-\frac{5}{2}$	2	$\frac{1}{2}$	$-\frac{1}{\sqrt{2}}$

3	2	1	$3jm$
3	-2	-1	$\frac{1}{\sqrt{2}}$
-3	2	1	$\frac{1}{\sqrt{2}}$

† $3jm$ changes sign under odd permutation.

Table B.1.2: Direct product table for $\mathbf{C}_{\infty v}$.†

$\mathbf{D}_{\infty}$, $\mathbf{C}_{\infty v}$	0	$\tilde{0}$	a	b
0	0	$\tilde{0}$	a	b
$\tilde{0}$	$\tilde{0}$	0	a	b
a	a	a	$0 \oplus \tilde{0} \oplus (2a)$	$(a+b) \oplus \lvert a-b \rvert$
b	b	b	$(a+b) \oplus \lvert a-b \rvert$	$0 \oplus \tilde{0} \oplus (2b)$

† a and b are numerical irrep labels (*i.e.* Butler notation), while $2a$, $(a+b)$ and $|a-b|$ represent numerical values calculated using these labels.

Table B.1.3: Basis for $\mathbf{D}_{\infty} \supset \mathbf{C}_{\infty}$ defined in terms of the $\mathbf{SO}_3 \supset \mathbf{SO}_2$ basis.[†]

j	$\lvert j\,(\mathbf{SO}_3)\ j_1\,(\mathbf{D}_\infty)\ a_1\,(\mathbf{C}_\infty)\rangle$	$\lvert j\,m\rangle$
0	$\lvert 0\ 0\ 0\rangle$	$\lvert 0\ 0\rangle$
1	$\lvert 1\ \tilde{0}\ 0\rangle$	$\lvert 1\ 0\rangle$
	$\lvert 1\ 1\ -1\rangle$	$\lvert 1\ -1\rangle$
	$\lvert 1\ 1\ 1\rangle$	$\lvert 1\ 1\rangle$
2	$\lvert 2\ 0\ 0\rangle$	$\lvert 2\ 0\rangle$
	$\lvert 2\ 1\ -1\rangle$	$\lvert 2\ -1\rangle$
	$\lvert 2\ 1\ 1\rangle$	$-\lvert 2\ 1\rangle$
	$\lvert 2\ 2\ -2\rangle$	$\lvert 2\ -2\rangle$
	$\lvert 2\ 2\ 2\rangle$	$\lvert 2\ 2\rangle$
⋮	⋮	⋮
$\frac{1}{2}$	$\lvert \frac{1}{2}\ \frac{1}{2}\ -\frac{1}{2}\rangle$	$\lvert \frac{1}{2}\ -\frac{1}{2}\rangle$
	$\lvert \frac{1}{2}\ \frac{1}{2}\ \frac{1}{2}\rangle$	$\lvert \frac{1}{2}\ \frac{1}{2}\rangle$
$\frac{3}{2}$	$\lvert \frac{3}{2}\ \frac{1}{2}\ -\frac{1}{2}\rangle$	$\lvert \frac{3}{2}\ -\frac{1}{2}\rangle$
	$\lvert \frac{3}{2}\ \frac{1}{2}\ \frac{1}{2}\rangle$	$-\lvert \frac{3}{2}\ \frac{1}{2}\rangle$
	$\lvert \frac{3}{2}\ \frac{3}{2}\ -\frac{3}{2}\rangle$	$\lvert \frac{3}{2}\ -\frac{3}{2}\rangle$
	$\lvert \frac{3}{2}\ \frac{3}{2}\ \frac{3}{2}\rangle$	$\lvert \frac{3}{2}\ \frac{3}{2}\rangle$
⋮	⋮	⋮

[†] This table is reproduced from Piepho and Schatz, in which the method for basis generation is described (Appendix F).

B.2. Icosahedral point group (I_h)

Table B.2.1: $2jm$ for the $\mathbf{I_h} \supset \mathbf{D_{5d}} \supset \mathbf{C_{5i}}$ chain in Butler notation.[†]

$\|a\ \alpha\rangle$ (Mulliken notation)	$\|a\ \alpha\rangle$ (Butler notation)	$\begin{pmatrix} a \\ \alpha \end{pmatrix}$	$\|a\ \alpha\rangle^*$ (Butler notation)	$\|a\ \alpha\rangle^*$ (Mulliken notation)
$\|A_1\ 0\rangle$	$\|0\ 0\rangle$	$+1$	$\|0\ 0\rangle$	$\|A_1\ 0\rangle$
$\|E'\ \pm\frac{1}{2}\rangle$	$\|\frac{1}{2}\ \pm\frac{1}{2}\rangle$	±1	$\|\frac{1}{2}\ \mp\frac{1}{2}\rangle$	$\|E'\ \mp\frac{1}{2}\rangle$
$\|T_1\ 0\rangle$	$\|1\ 0\rangle$	-1	$\|1\ 0\rangle$	$\|T_1\ 0\rangle$
$\|T_1\ \pm1\rangle$	$\|1\ \pm1\rangle$	$+1$	$\|1\ \mp1\rangle$	$\|T_1\ \mp1\rangle$
$\|U'\ \pm\frac{1}{2}\rangle$	$\|\frac{3}{2}\ \pm\frac{1}{2}\rangle$	±1	$\|\frac{3}{2}\ \mp\frac{1}{2}\rangle$	$\|U'\ \mp\frac{1}{2}\rangle$
$\|U'\ \pm\frac{3}{2}\rangle$	$\|\frac{3}{2}\ \pm\frac{3}{2}\rangle$	±1	$\|\frac{3}{2}\ \mp\frac{3}{2}\rangle$	$\|U'\ \mp\frac{3}{2}\rangle$
$\|H\ 0\rangle$	$\|2\ 0\rangle$	$+1$	$\|2\ 0\rangle$	$\|H\ 0\rangle$
$\|H\ \pm1\rangle$	$\|2\ \pm1\rangle$	$+1$	$\|2\ \mp1\rangle$	$\|H\ \mp1\rangle$
$\|H\ \pm2\rangle$	$\|2\ \pm2\rangle$	$+1$	$\|2\ \mp2\rangle$	$\|H\ \mp2\rangle$
$\|W'\ \pm\frac{1}{2}\rangle$	$\|\frac{5}{2}\ \pm\frac{1}{2}\rangle$	±1	$\|\frac{5}{2}\ \mp\frac{1}{2}\rangle$	$\|W'\ \mp\frac{1}{2}\rangle$
$\|W'\ \pm\frac{3}{2}\rangle$	$\|\frac{5}{2}\ \pm\frac{3}{2}\rangle$	±1	$\|\frac{5}{2}\ \mp\frac{3}{2}\rangle$	$\|W'\ \mp\frac{3}{2}\rangle$
$\|W'\ \pm\frac{5}{2}\rangle$	$\|\frac{5}{2}\ \pm\frac{5}{2}\rangle$	±1	$\|\frac{5}{2}\ \mp\frac{5}{2}\rangle$	$\|W'\ \mp\frac{5}{2}\rangle$
$\|G\ \pm1\rangle$	$\|3\ \pm1\rangle$	$+1$	$\|3\ \mp1\rangle$	$\|G\ \mp1\rangle$
$\|G\ \pm2\rangle$	$\|3\ \pm2\rangle$	$+1$	$\|3\ \mp2\rangle$	$\|G\ \mp2\rangle$
$\|T_2\ 0\rangle$	$\|\tilde{1}\ 0\rangle$	-1	$\|\tilde{1}\ 0\rangle$	$\|T_2\ 0\rangle$
$\|T_2\ \pm1\rangle$	$\|\tilde{1}\ \pm2\rangle$	$+1$	$\|\tilde{1}\ \mp2\rangle$	$\|T_2\ \mp1\rangle$
$\|E''\ \pm\frac{3}{2}\rangle$	$\|\tilde{\frac{1}{2}}\ \pm\frac{3}{2}\rangle$	±1	$\|\tilde{\frac{1}{2}}\ \mp\frac{3}{2}\rangle$	$\|E''\ \mp\frac{3}{2}\rangle$

[†] Partner labels $\pm\frac{5}{2}$ refer to the $\mathbf{I_h} \supset \mathbf{D_{5d}} \supset \mathbf{C_{5i}}$ chain functions $|\frac{5}{2}\ \pm\frac{5}{2}\ \frac{5}{2}\rangle$.

Table B.2.2: $3jm$ tables for the $\mathbf{I_h} \supset \mathbf{D_{5d}} \supset \mathbf{C_{5i}}$ chain in Butler notation.[‡]

1	$\frac{1}{2}$	$\frac{1}{2}$	$3jm$
0	$\frac{1}{2}$	$-\frac{1}{2}$	$\frac{1}{\sqrt{6}}$
1	$-\frac{1}{2}$	$-\frac{1}{2}$	$\frac{1}{\sqrt{3}}$
−1	$\frac{1}{2}$	$\frac{1}{2}$	$\frac{1}{\sqrt{3}}$

1	1	1	$3jm^{\dagger}$
0	1	−1	$-\frac{1}{\sqrt{6}}$

$\frac{3}{2}$	$\frac{3}{2}$	0	$3jm^{\dagger}$
$\frac{1}{2}$	$-\frac{1}{2}$	0	$\frac{1}{2}$
$\frac{3}{2}$	$-\frac{3}{2}$	0	$\frac{1}{2}$

$\frac{3}{2}$	$\frac{3}{2}$	1	$3jm$
$\frac{1}{2}$	$-\frac{1}{2}$	0	$\frac{1}{\sqrt{60}}$
$\frac{1}{2}$	$\frac{1}{2}$	−1	$-\sqrt{\frac{2}{15}}$
$-\frac{1}{2}$	$-\frac{1}{2}$	1	$-\sqrt{\frac{2}{15}}$
$\frac{1}{2}$	$-\frac{3}{2}$	1	$\frac{1}{\sqrt{10}}$
$-\frac{1}{2}$	$\frac{3}{2}$	−1	$-\frac{1}{\sqrt{10}}$
$\frac{3}{2}$	$-\frac{3}{2}$	0	$\sqrt{\frac{3}{20}}$

2	$\frac{3}{2}$	$\frac{1}{2}$	$3jm$
0	$\frac{1}{2}$	$-\frac{1}{2}$	$\frac{1}{\sqrt{10}}$
0	$-\frac{1}{2}$	$\frac{1}{2}$	$-\frac{1}{\sqrt{10}}$
1	$-\frac{1}{2}$	$-\frac{1}{2}$	$\sqrt{\frac{3}{20}}$
−1	$\frac{1}{2}$	$\frac{1}{2}$	$\sqrt{\frac{3}{20}}$
1	$-\frac{3}{2}$	$\frac{1}{2}$	$-\frac{1}{\sqrt{20}}$
−1	$\frac{3}{2}$	$-\frac{1}{2}$	$\frac{1}{\sqrt{20}}$
2	$-\frac{3}{2}$	$-\frac{1}{2}$	$\frac{1}{\sqrt{5}}$
−2	$\frac{3}{2}$	$\frac{1}{2}$	$\frac{1}{\sqrt{5}}$

1	1	0	$3jm$
0	0	0	$-\frac{1}{\sqrt{3}}$
1	−1	0	$\frac{1}{\sqrt{3}}$

$\frac{3}{2}$	1	$\frac{1}{2}$	$3jm^{\dagger}$
$\frac{1}{2}$	0	$-\frac{1}{2}$	$\frac{1}{\sqrt{6}}$
$-\frac{1}{2}$	0	$\frac{1}{2}$	$\frac{1}{\sqrt{6}}$
$\frac{1}{2}$	−1	$\frac{1}{2}$	$-\frac{1}{\sqrt{12}}$
$-\frac{1}{2}$	1	$-\frac{1}{2}$	$-\frac{1}{\sqrt{12}}$
$\frac{3}{2}$	−1	$-\frac{1}{2}$	$\frac{1}{2}$
$-\frac{3}{2}$	1	$\frac{1}{2}$	$-\frac{1}{2}$

2	1	1	$3jm$
0	0	0	$-\sqrt{\frac{2}{15}}$
0	1	−1	$-\frac{1}{\sqrt{30}}$
1	−1	0	$-\frac{1}{\sqrt{10}}$
−1	1	0	$\frac{1}{\sqrt{10}}$
2	−1	−1	$-\frac{1}{\sqrt{5}}$
−2	1	1	$-\frac{1}{\sqrt{5}}$

2	2	0	$3jm$
0	0	0	$\frac{1}{\sqrt{5}}$
1	−1	0	$\frac{1}{\sqrt{5}}$
2	−2	0	$\frac{1}{\sqrt{5}}$

2	2	1	$3jm^{\dagger}$
0	1	−1	$-\frac{1}{\sqrt{10}}$
0	−1	1	$-\frac{1}{\sqrt{10}}$
1	−1	0	$-\frac{1}{\sqrt{30}}$
1	−2	1	$-\frac{1}{\sqrt{15}}$
−1	2	−1	$-\frac{1}{\sqrt{15}}$
2	−2	0	$-\sqrt{\frac{2}{15}}$

[†] $3jm$ changes sign under odd permutation.

Table continued on next page...

Table B.2.2 (continued)

$\frac{5}{2}$	$\frac{3}{2}$	1	$3jm^{\dagger}$
$\frac{1}{2}$	$-\frac{1}{2}$	0	$-\frac{1}{\sqrt{10}}$
$-\frac{1}{2}$	$\frac{1}{2}$	0	$-\frac{1}{\sqrt{10}}$
$\frac{1}{2}$	$\frac{1}{2}$	−1	$-\frac{1}{\sqrt{20}}$
$-\frac{1}{2}$	$-\frac{1}{2}$	1	$-\frac{1}{\sqrt{20}}$
$\frac{1}{2}$	$-\frac{3}{2}$	1	$-\frac{1}{\sqrt{60}}$
$-\frac{1}{2}$	$\frac{3}{2}$	−1	$\frac{1}{\sqrt{60}}$
$\frac{3}{2}$	$-\frac{1}{2}$	−1	$\frac{1}{\sqrt{10}}$
$-\frac{3}{2}$	$\frac{1}{2}$	1	$-\frac{1}{\sqrt{10}}$
$\frac{3}{2}$	$-\frac{3}{2}$	0	$\frac{1}{\sqrt{15}}$
$-\frac{3}{2}$	$\frac{3}{2}$	0	$\frac{1}{\sqrt{15}}$
$\frac{5}{2}$	$\frac{3}{2}$	1	$\frac{1}{\sqrt{12}}$
$\frac{5}{2}$	$-\frac{3}{2}$	−1	$\frac{i}{\sqrt{12}}$
$-\frac{5}{2}$	$\frac{3}{2}$	1	$\frac{i}{\sqrt{12}}$
$-\frac{5}{2}$	$-\frac{3}{2}$	−1	$\frac{1}{\sqrt{12}}$

$\frac{5}{2}$	2	$\frac{1}{2}$	$3jm^{\dagger}$
$\frac{1}{2}$	0	$-\frac{1}{2}$	$-\frac{1}{\sqrt{10}}$
$-\frac{1}{2}$	0	$\frac{1}{2}$	$\frac{1}{\sqrt{10}}$
$\frac{1}{2}$	−1	$\frac{1}{2}$	$\frac{1}{\sqrt{15}}$
$-\frac{1}{2}$	1	$-\frac{1}{2}$	$\frac{1}{\sqrt{15}}$
$\frac{3}{2}$	−1	$-\frac{1}{2}$	$\sqrt{\frac{2}{15}}$
$-\frac{3}{2}$	1	$\frac{1}{2}$	$-\sqrt{\frac{2}{15}}$
$\frac{3}{2}$	−2	$\frac{1}{2}$	$-\frac{1}{\sqrt{30}}$
$-\frac{3}{2}$	2	$-\frac{1}{2}$	$-\frac{1}{\sqrt{30}}$
$\frac{5}{2}$	2	$\frac{1}{2}$	$\frac{1}{\sqrt{12}}$
$\frac{5}{2}$	−2	$-\frac{1}{2}$	$\frac{i}{\sqrt{12}}$
$-\frac{5}{2}$	2	$\frac{1}{2}$	$\frac{i}{\sqrt{12}}$
$-\frac{5}{2}$	−2	$-\frac{1}{2}$	$\frac{1}{\sqrt{12}}$

$\frac{5}{2}$	$\frac{5}{2}$	0	$3jm^{\dagger}$
$\frac{1}{2}$	$-\frac{1}{2}$	0	$\frac{1}{\sqrt{6}}$
$\frac{3}{2}$	$-\frac{3}{2}$	0	$\frac{1}{\sqrt{6}}$
$\frac{5}{2}$	$-\frac{5}{2}$	0	$\frac{1}{\sqrt{6}}$

3	3	0	$3jm$
1	−1	0	$\frac{1}{2}$
2	−2	0	$\frac{1}{2}$

3	3	1	$3jm^{\dagger}$
1	−1	0	$-\frac{1}{\sqrt{12}}$
1	−2	1	$\frac{1}{\sqrt{6}}$
−1	2	−1	$\frac{1}{\sqrt{6}}$
2	−2	0	$\frac{1}{\sqrt{12}}$

3	2	1	$3jm$
1	0	−1	$\frac{1}{\sqrt{10}}$
−1	0	1	$\frac{1}{\sqrt{10}}$
1	−1	0	$\sqrt{\frac{2}{15}}$
−1	1	0	$-\sqrt{\frac{2}{15}}$
1	−2	1	$\frac{1}{\sqrt{60}}$
−1	2	−1	$\frac{1}{\sqrt{60}}$
2	−1	−1	$-\frac{1}{\sqrt{15}}$
−2	1	1	$-\frac{1}{\sqrt{15}}$
2	−2	0	$-\frac{1}{\sqrt{30}}$
−2	2	0	$\frac{1}{\sqrt{30}}$
2	2	1	$\sqrt{\frac{3}{20}}$
−2	−2	−1	$\sqrt{\frac{3}{20}}$

$i = \sqrt{-1}$.

† $3jm$ changes sign under odd permutation.

‡ Partner labels $\pm\frac{5}{2}$ refer to the $\mathbf{I}_h \supset \mathbf{D}_{5d} \supset \mathbf{C}_{5i}$ chain functions $|\frac{5}{2}\ \pm\frac{5}{2}\ \frac{5}{2}\rangle$.

Table continued on next page...

Table B.2.2 (continued)

3	$\frac{5}{2}$	$\frac{1}{2}$	$3jm$
1	$-\frac{1}{2}$	$-\frac{1}{2}$	$\frac{1}{\sqrt{6}}$
−1	$\frac{1}{2}$	$\frac{1}{2}$	$\frac{1}{\sqrt{6}}$
1	$-\frac{3}{2}$	$\frac{1}{2}$	$\frac{1}{\sqrt{12}}$
−1	$\frac{3}{2}$	$-\frac{1}{2}$	$-\frac{1}{\sqrt{12}}$
2	$-\frac{3}{2}$	$-\frac{1}{2}$	$\frac{1}{\sqrt{12}}$
−2	$\frac{3}{2}$	$\frac{1}{2}$	$\frac{1}{\sqrt{12}}$
2	$\frac{5}{2}$	$\frac{1}{2}$	$-i\sqrt{\frac{3}{40}}+\frac{1}{\sqrt{120}}$
−2	$\frac{5}{2}$	$-\frac{1}{2}$	$\sqrt{\frac{3}{40}}+\frac{i}{\sqrt{120}}$
2	$-\frac{5}{2}$	$\frac{1}{2}$	$-\sqrt{\frac{3}{40}}+\frac{i}{\sqrt{120}}$
−2	$-\frac{5}{2}$	$-\frac{1}{2}$	$i\sqrt{\frac{3}{40}}+\frac{1}{\sqrt{120}}$

$\frac{1}{2}$	3	$\frac{1}{2}$	$3jm^{\dagger}$
$\frac{3}{2}$	−1	$-\frac{1}{2}$	$\frac{1}{2}$
$-\frac{3}{2}$	1	$\frac{1}{2}$	$-\frac{1}{2}$
$\frac{3}{2}$	−2	$\frac{1}{2}$	$\frac{1}{2}$
$-\frac{3}{2}$	2	$-\frac{1}{2}$	$\frac{1}{2}$

$\frac{1}{2}$	$\frac{5}{2}$	1	$3jm^{\dagger}$
$\frac{3}{2}$	$-\frac{1}{2}$	−1	$\frac{1}{\sqrt{6}}$
$-\frac{3}{2}$	$\frac{1}{2}$	1	$-\frac{1}{\sqrt{6}}$
$\frac{3}{2}$	$-\frac{3}{2}$	0	$-\frac{1}{\sqrt{6}}$
$-\frac{3}{2}$	$\frac{3}{2}$	0	$-\frac{1}{\sqrt{6}}$
$\frac{3}{2}$	$\frac{5}{2}$	1	$-i\sqrt{\frac{3}{40}}+\frac{1}{\sqrt{120}}$

$\tilde{1}$	2	1	$3jm$
0	0	0	$-\frac{1}{\sqrt{5}}$
0	1	−1	$\frac{1}{\sqrt{15}}$
0	−1	1	$-\frac{1}{\sqrt{15}}$
2	−1	−1	$-\sqrt{\frac{2}{15}}$
−2	1	1	$-\sqrt{\frac{2}{15}}$
2	−2	0	$-\frac{1}{\sqrt{15}}$
−2	2	0	$\frac{1}{\sqrt{15}}$
2	2	1	$-\sqrt{\frac{2}{15}}$
−2	−2	−1	$-\sqrt{\frac{2}{15}}$

$\tilde{1}$	3	1	$3jm^{\dagger}$
0	1	−1	$-\frac{1}{\sqrt{6}}$
0	−1	1	$\frac{1}{\sqrt{6}}$
2	−1	−1	$-\frac{1}{\sqrt{12}}$
−2	1	1	$-\frac{1}{\sqrt{12}}$
2	−2	0	$-\frac{1}{\sqrt{6}}$
−2	2	0	$\frac{1}{\sqrt{6}}$
2	2	1	$\frac{1}{\sqrt{12}}$
−2	−2	−1	$\frac{1}{\sqrt{12}}$

$\tilde{1}$	$\tilde{1}$	0	$3jm$
0	0	0	$-\frac{1}{\sqrt{3}}$
2	−2	0	$\frac{1}{\sqrt{3}}$

$i=\sqrt{-1}$.

† $3jm$ changes sign under odd permutation.

‡ Partner labels $\pm\frac{5}{2}$ refer to the $\mathbf{I_h} \supset \mathbf{D_{5d}} \supset \mathbf{C_{5i}}$ chain functions $|\frac{5}{2}\ \pm\frac{5}{2}\ \frac{5}{2}\rangle$.

Table continued on next page...

Table B.2.2 (continued)

$3jm$s with repeated representations:

$\frac{5}{2}$	$\frac{5}{2}$	1	$3jm$ $r=0$	$3jm$ $r=1$
$\frac{1}{2}$	$-\frac{1}{2}$	0	$\frac{1}{\sqrt{12}}$	$-\frac{1}{\sqrt{60}}$
$\frac{1}{2}$	$\frac{1}{2}$	-1	0	$\sqrt{\frac{2}{15}}$
$-\frac{1}{2}$	$-\frac{1}{2}$	1	0	$\sqrt{\frac{2}{15}}$
$\frac{1}{2}$	$-\frac{3}{2}$	1	$-\frac{1}{\sqrt{12}}$	$-\frac{1}{\sqrt{60}}$
$-\frac{1}{2}$	$\frac{3}{2}$	-1	$\frac{1}{\sqrt{12}}$	$\frac{1}{\sqrt{60}}$
$\frac{3}{2}$	$-\frac{3}{2}$	0	0	$\frac{1}{\sqrt{15}}$
$\frac{3}{2}$	$\frac{5}{2}$	1	$-\frac{1}{\sqrt{240}}+i\sqrt{\frac{3}{80}}$	$-\frac{i}{\sqrt{48}}-\frac{1}{\sqrt{48}}$
$-\frac{3}{2}$	$\frac{5}{2}$	-1	$-\frac{i}{\sqrt{240}}-\sqrt{\frac{3}{80}}$	$-\frac{i}{\sqrt{48}}+\frac{1}{\sqrt{48}}$
$\frac{3}{2}$	$-\frac{5}{2}$	1	$-\frac{i}{\sqrt{240}}+\sqrt{\frac{3}{80}}$	$-\frac{i}{\sqrt{48}}-\frac{1}{\sqrt{48}}$
$-\frac{3}{2}$	$-\frac{5}{2}$	-1	$-\frac{1}{\sqrt{240}}-i\sqrt{\frac{3}{80}}$	$\frac{i}{\sqrt{48}}-\frac{1}{\sqrt{48}}$
$\frac{5}{2}$	$\frac{5}{2}$	0	$-\frac{2i}{\sqrt{75}}+\frac{\sqrt{3}}{10}$	$-\frac{1}{\sqrt{60}}-\frac{i}{\sqrt{15}}$
$-\frac{5}{2}$	$-\frac{5}{2}$	0	$-\frac{2i}{\sqrt{75}}-\frac{\sqrt{3}}{10}$	$\frac{1}{\sqrt{60}}-\frac{i}{\sqrt{15}}$

$i=\sqrt{-1}$.

† $3jm$ changes sign under odd permutation.

‡ Partner labels $\pm\frac{5}{2}$ refer to the $\mathbf{I_h} \supset \mathbf{D_{5d}} \supset \mathbf{C_{5i}}$ chain functions $|\frac{5}{2}\ \pm\frac{5}{2}\ \frac{5}{2}\rangle$.

Table B.2.3: Direct product table for $\mathbf{I}_h$.

$\otimes$	0	$\frac{1}{2}$	1	$\frac{3}{2}$	2	$\frac{5}{2}$	3	$\tilde{1}$	$\frac{\tilde{1}}{2}$
0	0	$\frac{1}{2}$	1	$\frac{3}{2}$	2	$\frac{5}{2}$	3	$\tilde{1}$	$\frac{\tilde{1}}{2}$
$\frac{1}{2}$	$\frac{1}{2}$	$0 \oplus 1$	$\frac{1}{2} \oplus \frac{3}{2}$	$1 \oplus 2$	$\frac{3}{2} \oplus \frac{5}{2}$	$2 \oplus 3 \oplus \tilde{1}$	$\frac{5}{2} \oplus \frac{\tilde{1}}{2}$	$\frac{5}{2}$	3
1	1	$\frac{1}{2} \oplus \frac{3}{2}$	$0 \oplus 1 \oplus 2$	$\frac{1}{2} \oplus \frac{3}{2} \oplus \frac{5}{2}$	$1 \oplus 2 \oplus 3 \oplus \tilde{1}$	$\frac{3}{2} \oplus \frac{5}{2} \oplus \frac{5}{2} \oplus \frac{\tilde{1}}{2}$	$2 \oplus 3 \oplus \tilde{1}$	$2 \oplus 3$	$\frac{5}{2}$
$\frac{3}{2}$	$\frac{3}{2}$	$1 \oplus 2$	$\frac{1}{2} \oplus \frac{3}{2} \oplus \frac{5}{2}$	$0 \oplus 1 \oplus 2 \oplus 3 \oplus \tilde{1}$	$\frac{1}{2} \oplus \frac{3}{2} \oplus \frac{5}{2} \oplus \frac{5}{2} \oplus \frac{\tilde{1}}{2}$	$1 \oplus 2 \oplus 2 \oplus 3 \oplus 3 \oplus \tilde{1}$	$\frac{3}{2} \oplus \frac{5}{2} \oplus \frac{5}{2}$	$\frac{3}{2} \oplus \frac{5}{2} \oplus \frac{\tilde{1}}{2}$	$2 \oplus \tilde{1}$
2	2	$\frac{3}{2} \oplus \frac{5}{2}$	$1 \oplus 2 \oplus 3 \oplus \tilde{1}$	$\frac{1}{2} \oplus \frac{3}{2} \oplus \frac{5}{2} \oplus \frac{5}{2} \oplus \frac{\tilde{1}}{2}$	$0 \oplus 1 \oplus 2 \oplus 2 \oplus 3 \oplus 3 \oplus \tilde{1}$	$\frac{1}{2} \oplus \frac{3}{2} \oplus \frac{3}{2} \oplus \frac{5}{2} \oplus \frac{5}{2} \oplus \frac{5}{2} \oplus \frac{\tilde{1}}{2}$	$1 \oplus 2 \oplus 2 \oplus 3 \oplus \tilde{1}$	$1 \oplus 2 \oplus 3 \oplus \tilde{1}$	$\frac{3}{2} \oplus \frac{5}{2}$
$\frac{5}{2}$	$\frac{5}{2}$	$2 \oplus 3 \oplus \tilde{1}$	$\frac{3}{2} \oplus \frac{5}{2} \oplus \frac{5}{2} \oplus \frac{\tilde{1}}{2}$	$1 \oplus 2 \oplus 2 \oplus 3 \oplus 3 \oplus \tilde{1}$	$\frac{1}{2} \oplus \frac{3}{2} \oplus \frac{3}{2} \oplus \frac{5}{2} \oplus \frac{5}{2} \oplus \frac{5}{2} \oplus \frac{\tilde{1}}{2}$	$0 \oplus 1 \oplus 1 \oplus 2 \oplus 2 \oplus 2 \oplus 3 \oplus 3 \oplus \tilde{1} \oplus \tilde{1}$	$\frac{1}{2} \oplus \frac{3}{2} \oplus \frac{3}{2} \oplus \frac{5}{2} \oplus \frac{5}{2} \oplus \frac{\tilde{1}}{2}$	$\frac{1}{2} \oplus \frac{3}{2} \oplus \frac{5}{2} \oplus \frac{5}{2}$	$1 \oplus 2 \oplus 3$
3	3	$\frac{5}{2} \oplus \frac{\tilde{1}}{2}$	$2 \oplus 3 \oplus \tilde{1}$	$\frac{3}{2} \oplus \frac{5}{2} \oplus \frac{5}{2}$	$1 \oplus 2 \oplus 2 \oplus 3 \oplus \tilde{1}$	$\frac{1}{2} \oplus \frac{3}{2} \oplus \frac{3}{2} \oplus \frac{5}{2} \oplus \frac{5}{2} \oplus \frac{\tilde{1}}{2}$	$0 \oplus 1 \oplus 2 \oplus 3 \oplus \tilde{1}$	$1 \oplus 2 \oplus 3$	$\frac{1}{2} \oplus \frac{5}{2}$
$\tilde{1}$	$\tilde{1}$	$\frac{5}{2}$	$2 \oplus 3$	$\frac{3}{2} \oplus \frac{5}{2} \oplus \frac{\tilde{1}}{2}$	$1 \oplus 2 \oplus 3 \oplus \tilde{1}$	$\frac{1}{2} \oplus \frac{3}{2} \oplus \frac{5}{2} \oplus \frac{5}{2}$	$1 \oplus 2 \oplus 3$	$0 \oplus 2 \oplus \tilde{1}$	$\frac{3}{2} \oplus \frac{\tilde{1}}{2}$
$\frac{\tilde{1}}{2}$	$\frac{\tilde{1}}{2}$	3	$\frac{5}{2}$	$2 \oplus \tilde{1}$	$\frac{3}{2} \oplus \frac{5}{2}$	$1 \oplus 2 \oplus 3$	$\frac{1}{2} \oplus \frac{5}{2}$	$\frac{3}{2} \oplus \frac{\tilde{1}}{2}$	$0 \oplus \tilde{1}$

Table B.2.4: Correlation table for selected $\mathbf{SO}_3 \supset \mathbf{I} \supset \mathbf{D}_5 \supset \mathbf{C}_5$ partners as $|J\,M\rangle$ partners.

$\mathbf{SO}_3 \supset \mathbf{I} \supset \mathbf{D}_5 \supset \mathbf{C}_5$	$\mathbf{SO}_3 \supset \mathbf{SO}_2$ $(\|J\,M\rangle)$
$\|0\,0\,0\,0\rangle$	$\|0\,0\rangle$
$\|\frac{1}{2}\,\frac{1}{2}\,\frac{1}{2}\,\pm\frac{1}{2}\rangle$	$\|\frac{1}{2}\,\pm\frac{1}{2}\rangle$
$\|1\,1\,\tilde{0}\,0\rangle$	$\|1\,0\rangle$
$\|1\,1\,1\,\pm1\rangle$	$-\|1\,\pm1\rangle$
$\|2\,2\,0\,0\rangle$	$-\|2\,0\rangle$
$\|2\,2\,1\,\pm1\rangle$	$\mp\|2\,\pm1\rangle$
$\|2\,2\,2\,\pm2\rangle$	$-\|2\,\pm2\rangle$
$\|3\,3\,1\,\pm1\rangle$	$\|3\,\pm1\rangle$
$\|3\,3\,2\,\pm2\rangle$	$\mp\sqrt{\frac{2}{5}}\|3\,\pm2\rangle + \sqrt{\frac{3}{5}}\|3\,\mp3\rangle$
$\|3\,\tilde{1}\,\tilde{0}\,0\rangle$	$-\|3\,0\rangle$
$\|3\,\tilde{1}\,2\,\pm2\rangle$	$\mp\sqrt{\frac{3}{5}}\|3\,\pm2\rangle - \sqrt{\frac{2}{5}}\|3\,\mp3\rangle$
$\|\frac{7}{2}\,\frac{\tilde{1}}{2}\,\frac{3}{2}\,\pm\frac{3}{2}\rangle$	$-\sqrt{\frac{7}{10}}\|\frac{7}{2}\,\pm\frac{3}{2}\rangle \pm \sqrt{\frac{3}{10}}\|\frac{7}{2}\,\mp\frac{7}{2}\rangle$

Appendix C: SO theory for C_{60}^+ and C_{60}^- in I_h symmetry

C.1. Introduction

This appendix presents spin-orbit (SO) wavefunctions and SO, Zeeman and transition-moment matrix elements for the three lowest-lying terms of C_{60}^+ and C_{60}^- (Chapter 7) assuming icosahedral ($\mathbf{I_h}$) symmetry. The Jahn-Teller (JT) effect acts to distort the structure of these ions away from the $\mathbf{I_h}$ symmetry of C_{60} (Section 1.1.2), because JT-active vibrational modes act to lower the high degree of orbital degeneracy present in the ions (Section 7.1).

C.1.1. Notation

The mixing of the natural (or Butler)[1] and Mulliken[2] notations employed in this appendix was described in Section 3.2.1. Irrep labels for $\mathbf{I_h}$ are given in Table C.1.1.

Table C.1.1: Butler and Mulliken notation for $\mathbf{I_h}$, with branching for the $\mathbf{I_h} \supset \mathbf{D_{5d}} \supset \mathbf{C_{5i}}$ chain given in the former notation.

$\mathbf{I_h}$ irreps		$\mathbf{D_{5d}}$ irreps	$\mathbf{C_{5i}}$ irreps
Butler	Mulliken		
0	A_1	0	0
$\frac{1}{2}$	E'	$\frac{1}{2}$	$\pm\frac{1}{2}$
1	T_1	0, 1	0, ±1
$\frac{3}{2}$	U'	$\frac{1}{2}, \frac{3}{2}$	$\pm\frac{1}{2}, \pm\frac{3}{2}$
2	H (or V)	0, 1, 2	0, ±1, ±2
$\frac{5}{2}$	W'	$\frac{1}{2}, \frac{3}{2}, \pm\frac{5}{2}$	$\pm\frac{1}{2}, \pm\frac{3}{2}, \frac{5}{2}$ [a]
3	G (or U)	1, 2	±1, ±2
$\tilde{1}$	T_2	$\tilde{0}$, 2	0, ±2
$\frac{\tilde{1}}{2}$	E"	$\frac{3}{2}$	$\pm\frac{3}{2}$

[a] Since the irrep $\frac{5}{2}$ of $\mathbf{I_h}$ is non-degenerate in $\mathbf{C_{5i}}$ (it is a repeated representation), the partners are generally designated according to the $+\frac{5}{2}$ and $-\frac{5}{2}$ of $\mathbf{D_{5d}}$, although this is not strictly correct.

According to standard convention, lower case Mulliken notation is used for orbital designations. The '*g*' or '*u*' subscripts represent the even and odd parity, respectively, of orbitals and states in a centrosymmetric point group.

Determinantal wavefunctions and SL wavefunctions use the notation described in Section 3.3.1.4, while that used for SO wavefunctions differs slightly from that covered in Section 3.3.1.5.

C.1.2. The MOs of C_{60} and its singly charged ions

The electronic configurations treated in this appendix are only given in terms of the few highest occupied MOs, that is those involved in the transitions dealt with here. They have been derived from the results of an *ab initio* calculation,[3] and are used to determine occupancies and hence wavefunctions (Section 3.3.1.1). The orbitals about the HOMO-LUMO gap are illustrated in Figure 7.1.1, with occupancies corresponding to C_{60}, C_{60}^{+} and C_{60}^{-}.

C.2. C_{60}^{+}

C.2.1. Construction of SO wavefunctions for C_{60}^{+}

Figure 7.1.1 shows that the transitions of C_{60}^{+} considered in this thesis are from the fully occupied $4g_g$ and $7h_g$ orbitals lying just below the HOMO ($4h_u$), to the hole left in the HOMO as a consequence of ionisation. The ground, first-excited and second-excited configurations are hence [... $(4g_g)^8$ $(4h_g)^{10}$ $(7h_u)^9$], [... $(4g_g)^8$ $(4h_g)^9$ $(7h_u)^{10}$] and [... $(4g_g)^7$ $(4h_g)^{10}$ $(7h_u)^{10}$], respectively. All of these have only one open subconfiguration, which is treated by the hole-particle formalism — Section 3.3.1.4. No orbital or spin coupling is required since each state arises from a single hole; the terms are hence ^2H_u, ^2H_g and ^2G_g in order of the configurations above (*i.e.* in increasing energy).

(a) SL wavefunctions

Ground- and excited-term SL wavefunctions (Section 3.3.1.4) were formed by inspection. They are,

$$|^2H_{u,g}\ \pm\tfrac{1}{2}\ 2\rangle = |\text{-}2_{u,g}^{\ \pm}\text{-}1_{u,g}^{\ 2}\ 0_{u,g}^{\ 2}\ 1_{u,g}^{\ 2}\ 2_{u,g}^{\ 2}\rangle$$

$$|^2H_{u,g}\ \pm\tfrac{1}{2}\ 1\rangle = |\text{-}2_{u,g}^{\ 2}\text{-}1_{u,g}^{\ \pm}\ 0_{u,g}^{\ 2}\ 1_{u,g}^{\ 2}\ 2_{u,g}^{\ 2}\rangle$$

$$|^2H_{u,g}\ \pm\tfrac{1}{2}\ 0\rangle = |\text{-}2_{u,g}^{\ 2}\text{-}1_{u,g}^{\ 2}\ 0_{u,g}^{\ \pm}\ 1_{u,g}^{\ 2}\ 2_{u,g}^{\ 2}\rangle$$

$$|^2H_{u,g}\ \pm\tfrac{1}{2}\ \text{-}1\rangle = |\text{-}2_{u,g}^{\ 2}\text{-}1_{u,g}^{\ 2}\ 0_{u,g}^{\ 2}\ 1_{u,g}^{\ \pm}\ 2_{u,g}^{\ 2}\rangle$$

$$|^2H_{u,g}\,\pm\tfrac{1}{2}\,\text{-}2\rangle = |\text{-}2_{u,g}^{\,2}\,\text{-}1_{u,g}^{\,2}\,0_{u,g}^{\,2}\,1_{u,g}^{\,2}\,2_{u,g}^{\,\pm}\rangle \qquad \text{(C.2.1)}$$

for the ground (odd parity) and first-excited (even parity) terms, while for the second excited term they are,

$$|^2G_g\,\pm\tfrac{1}{2}\,2\rangle = |\text{-}2_g^{\,\pm}\,\text{-}1_g^{\,2}\,1_g^{\,2}\,2_g^{\,2}\rangle$$

$$|^2G_g\,\pm\tfrac{1}{2}\,1\rangle = |\text{-}2_g^{\,2}\,\text{-}1_g^{\,\pm}\,1_g^{\,2}\,2_g^{\,2}\rangle$$

$$|^2G_g\,\pm\tfrac{1}{2}\,\text{-}1\rangle = |\text{-}2_g^{\,2}\,\text{-}1_g^{\,2}\,1_g^{\,\pm}\,2_g^{\,2}\rangle$$

$$|^2G_g\,\pm\tfrac{1}{2}\,\text{-}2\rangle = |\text{-}2_g^{\,2}\,\text{-}1_g^{\,2}\,\text{-}1_g^{\,2}\,2_g^{\,\pm}\rangle \qquad \text{(C.2.2)}$$

(b) SO wavefunctions

SO coupling is undertaken following the methodology of Section 3.3.1.5, and the resulting levels are shown in Table C.2.1. Note that the ^2H_u and ^2H_g terms are treated equivalently and are summarised on the same row.

Table C.2.1: SOC in C_{60}^{+}.

Term	Orbital irreps	Spin irreps		SOC [a]	
	$\mathbf{I_h}$	$\mathbf{SO_3}$	$\mathbf{I_h}$	Irreps	Levels
$^2H_{u,g}$	$2_{u,g}$	$\frac{1}{2}$	$\frac{1}{2}$	$\frac{5}{2}$ $\frac{3}{2}$	$^2H_{u,g}\,\frac{5}{2}$ $^2H_{u,g}\,\frac{3}{2}$
^2G_g	3_g	$\frac{1}{2}$	$\frac{1}{2}$	$\frac{5}{2}$ $\frac{\bar{1}}{2}$	$^2G_g\,\frac{5}{2}$ $^2G_g\,\frac{\bar{1}}{2}$

[a] The direct-product table for $\mathbf{I_h}$ is given in Table B.2.3 of Appendix B, while the SO partners can be found in Table C.1.1.

The SO wavefunctions for each level were derived using eq (3.3.10), and are given in eq (C.2.3) for the ground and first-excited configurations ('*u*' and '*g*' parity, respectively), and eq (C.2.4) for the second excited configuration. The required 2*jm* and 3*jm* are given in Tables B.2.1 and B.2.2, respectively, of Appendix B. Notation is slightly different to that used elsewhere in this work for SO wavefunctions (Section 3.3.1.5). An intermediate label, *t*', corresponding to the representatives in $\mathbf{D_{5d}}$, is included to remove the ambiguity (of the repeated representation) of the $\frac{5}{2}$ representative in the chain. (See the footnote to Table C.2.1.) The SO wavefunctions are denoted

$|^{2S+1}h_{g,u}\, t\, t'\, \tau\rangle$, where all parameters except t' have been defined previously (see particularly Section 3.3.1.5). $i = \sqrt{-1}$.

$$|^2H_{u,g}\,\tfrac{5}{2}\,\tfrac{5}{2}\,\tfrac{5}{2}\rangle = -\tfrac{1}{\sqrt{2}}\{|\text{-}2_{u,g}{}^2\,\text{-}1_{u,g}{}^2\,0_{u,g}{}^2\,1_{u,g}{}^2\,2_{u,g}{}^-\rangle - i|\text{-}2_{u,g}{}^+\,\text{-}1_{u,g}{}^2\,0_{u,g}{}^2\,1_{u,g}{}^2\,2_{u,g}{}^2\rangle\}$$

$$|^2H_{u,g}\,\tfrac{5}{2}\,\bar{\tfrac{5}{2}}\,\tfrac{5}{2}\rangle = \tfrac{1}{\sqrt{2}}\{|\text{-}2_{u,g}{}^+\,\text{-}1_{u,g}{}^2\,0_{u,g}{}^2\,1_{u,g}{}^2\,2_{u,g}{}^2\rangle - i|\text{-}2_{u,g}{}^2\,\text{-}1_{u,g}{}^2\,0_{u,g}{}^2\,1_{u,g}{}^2\,2_{u,g}{}^-\rangle\}$$

$$|^2H_{u,g}\,\tfrac{5}{2}\,\tfrac{3}{2}\,\tfrac{3}{2}\rangle = \tfrac{1}{\sqrt{5}}\{2\,|\text{-}2_{u,g}{}^2\,\text{-}1_{u,g}{}^+\,0_{u,g}{}^2\,1_{u,g}{}^2\,2_{u,g}{}^2\rangle + |\text{-}2_{u,g}{}^-\,\text{-}1_{u,g}{}^2\,0_{u,g}{}^2\,1_{u,g}{}^2\,2_{u,g}{}^2\rangle\}$$

$$|^2H_{u,g}\,\tfrac{5}{2}\,\tfrac{3}{2}\,\bar{\tfrac{3}{2}}\rangle = \tfrac{1}{\sqrt{5}}\{2\,|\text{-}2_{u,g}{}^2\,\text{-}1_{u,g}{}^2\,0_{u,g}{}^2\,1_{u,g}{}^-\,2_{u,g}{}^2\rangle - |\,2_{u,g}{}^2\,\text{-}1_{u,g}{}^2\,0_{u,g}{}^2\,1_{u,g}{}^2\,2_{u,g}{}^+\rangle\}$$

$$|^2H_{u}\,\tfrac{5}{2}\,\tfrac{1}{2}\,\tfrac{1}{2}\rangle = -\tfrac{1}{\sqrt{5}}\{\sqrt{3}\,|\text{-}2_{u,g}{}^2\,\text{-}1_{u,g}{}^2\,0_{u,g}{}^+\,1_{u,g}{}^2\,2_{u,g}{}^2\rangle + \sqrt{2}\,|\text{-}2_{u,g}{}^2\,\text{-}1_{u,g}{}^-\,0_{u,g}{}^2\,1_{u,g}{}^2\,2_{u,g}{}^2\rangle\}$$

$$|^2H_{u,g}\,\tfrac{5}{2}\,\tfrac{1}{2}\,\bar{\tfrac{1}{2}}\rangle = -\tfrac{1}{\sqrt{5}}\{\sqrt{3}\,|\text{-}2_{u,g}{}^2\,\text{-}1_{u,g}{}^2\,0_{u,g}{}^-\,1_{u,g}{}^2\,2_{u,g}{}^2\rangle - \sqrt{2}\,|\text{-}2_{u,g}{}^2\,\text{-}1_{u,g}{}^2\,0_{u,g}{}^2\,1_{u,g}{}^+\,2_{u,g}{}^2\rangle\}$$

$$|^2H_{u,g}\,\tfrac{3}{2}\,\tfrac{3}{2}\,\tfrac{3}{2}\rangle = \tfrac{1}{\sqrt{5}}\{2\,|\text{-}2_{u,g}{}^-\,\text{-}1_{u,g}{}^2\,0_{u,g}{}^2\,1_{u,g}{}^2\,2_{u,g}{}^2\rangle - |\text{-}2_{u,g}{}^2\,\text{-}1_{u,g}{}^+\,0_{u,g}{}^2\,1_{u,g}{}^2\,2_{u,g}{}^2\rangle\}$$

$$|^2H_{u,g}\,\tfrac{3}{2}\,\tfrac{3}{2}\,\bar{\tfrac{3}{2}}\rangle = -\tfrac{1}{\sqrt{5}}\{2\,|\text{-}2_{u,g}{}^2\,\text{-}1_{u,g}{}^2\,0_{u,g}{}^2\,1_{u,g}{}^2\,2_{u,g}{}^+\rangle + |\text{-}2_{u,g}{}^2\,\text{-}1_{u,g}{}^2\,0_{u,g}{}^2\,1_{u,g}{}^-\,2_{u,g}{}^2\rangle\}$$

$$|^2H_{u,g}\,\tfrac{3}{2}\,\tfrac{1}{2}\,\tfrac{1}{2}\rangle = \tfrac{1}{\sqrt{5}}\{\sqrt{3}\,|\text{-}2_{u,g}{}^2\,\text{-}1_{u,g}{}^-\,0_{u,g}{}^2\,1_{u,g}{}^2\,2_{u,g}{}^2\rangle - \sqrt{2}\,|\text{-}2_{u,g}{}^2\,\text{-}1_{u,g}{}^2\,0_{u,g}{}^+\,1_{u,g}{}^2\,2_{u,g}{}^2\rangle\}$$

$$|^2H_{u,g}\,\tfrac{3}{2}\,\tfrac{1}{2}\,\bar{\tfrac{1}{2}}\rangle = -\tfrac{1}{\sqrt{5}}\{\sqrt{3}\,|\text{-}2_{u,g}{}^2\,\text{-}1_{u,g}{}^2\,0_{u,g}{}^2\,1_{u,g}{}^+\,2_{u,g}{}^2\rangle + \sqrt{2}\,|\text{-}2_{u,g}{}^2\,\text{-}1_{u,g}{}^2\,0_{u,g}{}^-\,1_{u,g}{}^2\,2_{u,g}{}^2\rangle\}$$

(C.2.3)

$$|^2G_{g}\,\tfrac{5}{2}\,\tfrac{5}{2}\,\tfrac{5}{2}\rangle = -\tfrac{1}{\sqrt{20}}\{(3+i)\,|\text{-}2_{g}{}^+\,\text{-}1_{g}{}^2\,1_{g}{}^2\,2_{g}{}^2\rangle - (1-3i)\,|\text{-}2_{g}{}^2\,\text{-}1_{g}{}^2\,1_{g}{}^2\,2_{g}{}^-\rangle\}$$

$$|^2G_{g}\,\tfrac{5}{2}\,\bar{\tfrac{5}{2}}\,\tfrac{5}{2}\rangle = -\tfrac{1}{\sqrt{20}}\{(1+3i)\,|\text{-}2_{g}{}^+\,\text{-}1_{g}{}^2\,1_{g}{}^2\,2_{g}{}^2\rangle + (3-i)\,|\text{-}2_{g}{}^2\,\text{-}1_{g}{}^2\,1_{g}{}^2\,2_{g}{}^-\rangle\}$$

$$|^2G_{g}\,\tfrac{5}{2}\,\tfrac{3}{2}\,\tfrac{3}{2}\rangle = \tfrac{1}{\sqrt{2}}\{|\text{-}2_{g}{}^2\,\text{-}1_{g}{}^+\,1_{g}{}^2\,2_{g}{}^2\rangle + |\text{-}2_{g}{}^-\,\text{-}1_{g}{}^2\,1_{g}{}^2\,2_{g}{}^2\rangle\}$$

$$|^2G_{g}\,\tfrac{5}{2}\,\tfrac{3}{2}\,\bar{\tfrac{3}{2}}\rangle = \tfrac{1}{\sqrt{2}}\{|\text{-}2_{g}{}^2\,\text{-}1_{g}{}^2\,1_{g}{}^-\,2_{g}{}^2\rangle - |\text{-}2_{g}{}^2\,\text{-}1_{g}{}^2\,1_{g}{}^2\,2_{g}{}^+\rangle\}$$

$$|^2G_g\,\tfrac{5}{2}\,\tfrac{1}{2}\,\tfrac{1}{2}\rangle = |\text{-}2_g^{\,2}\,\text{-}1_g^{\,-}\,1_g^{\,2}\,2_g^{\,2}\rangle$$

$$|^2G_g\,\tfrac{5}{2}\,\tfrac{1}{2}\,\bar{\tfrac{1}{2}}\rangle = -|\text{-}2_g^{\,2}\,\text{-}1_g^{\,2}\,1_g^{\,+}\,2_g^{\,2}\rangle$$

$$|^2G_g\,\tfrac{1}{2}\,\tfrac{3}{2}\,\tfrac{3}{2}\rangle = \tfrac{1}{\sqrt{2}}\{|\text{-}2_g^{\,2}\,\text{-}1_g^{\,+}\,1_g^{\,2}\,2_g^{\,2}\rangle - |\text{-}2_g^{\,-}\,\text{-}1_g^{\,2}\,1_g^{\,2}\,2_g^{\,2}\rangle\}$$

$$|^2G_g\,\tfrac{1}{2}\,\tfrac{3}{2}\,\bar{\tfrac{3}{2}}\rangle = \tfrac{1}{\sqrt{2}}\{|\text{-}2_g^{\,2}\,\text{-}1_g^{\,2}\,1_g^{\,-}\,2_g^{\,2}\rangle + |\text{-}2_g^{\,2}\,\text{-}1_g^{\,2}\,1_g^{\,2}\,2_g^{\,+}\rangle\}$$

(C.2.4)

C.2.2. Spin-orbit matrix elements

C_{60}^{+} is an inverted SO system. The SO matrix elements were evaluated as described in Section 3.3.2.2. Unlike linear molecules (such as XH, with $\mathbf{C}_{\infty v}$ symmetry) elements involving the raising and lowering operators must be evaluated in $\mathbf{I}_h$.

The angular momentum operators, $j^{\pm}$ and j_z, act on the $|j\,m\rangle$ of the $\mathbf{SO}_3 \supset \mathbf{SO}_2$ basis. Hence the $\mathbf{SO}_3 \supset \mathbf{I}_h \supset \mathbf{D}_{5d} \supset \mathbf{C}_{5i}$ chain must be correlated to the $\mathbf{SO}_3 \supset \mathbf{SO}_2$ chain, allowing evaluation of $\boldsymbol{s} \bullet \boldsymbol{u}$ (eq (3.3.18)). Table B.2.4 of Appendix B gives the correlations required for the wavefunctions treated here. Erroneous SO matrix elements are obtained if this procedure is neglected.

Applying the correlation involves substituting the $\mathbf{SO}_3 \supset \mathbf{SO}_2$ equivalent of the $\mathbf{I}_h \supset \mathbf{D}_{5d} \supset \mathbf{C}_{5i}$ chain for the orbitals, followed by evaluation the matrix elements that the Wigner-Eckart theorem (Section 3.2.4) has shown are non-zero. Computational effort required for evaluation of these elements is also reduced by virtue of the Wigner-Eckart theorem relating all to a single reduced SO matrix element.

For the ground configuration, the SO matrix elements are,

$$\langle {}^2H_u\,\tfrac{5}{2}\,t\,\tau|\mathcal{H}_{SO}|{}^2H_u\,\tfrac{5}{2}\,t\,\tau\rangle = -\zeta$$

$$\langle {}^2H_u\,\tfrac{3}{2}\,t'\,\tau'|\mathcal{H}_{SO}|{}^2H_u\,\tfrac{3}{2}\,t'\,\tau'\rangle = \tfrac{3}{2}\zeta \qquad \text{(C.2.5)}$$

where the t,τ and t',τ' correspond to all possible chains resulting from the irreps $\frac{5}{2}$ and $\frac{3}{2}$, respectively, in $\mathbf{I}_h$. ζ is the empirical SOC coefficient for the ground term of C_{60}^{+}, and is defined by the equation,

$$\zeta = \hbar^2\langle\xi\rangle \qquad \text{(C.2.6)}$$

with $\langle\xi\rangle$ the expectation value of the SOC coefficient.

The levels of the first excited configuration have the matrix elements,

$$\langle {}^2H_{g\,\frac{5}{2}}\ t\ \tau|\mathcal{H}_{SO}|{}^2H_{g\,\frac{5}{2}}\ t\ \tau\rangle = -\zeta'$$

$$\langle {}^2H_{g\,\frac{3}{2}}\ t'\ \tau'|\mathcal{H}_{SO}|{}^2H_{g\,\frac{3}{2}}\ t'\ \tau'\rangle = \tfrac{3}{2}\zeta' \qquad \text{(C.2.7)}$$

where ζ' is the empirical SOC coefficient for the first-excited configuration of C_{60}^{+}, and is defined analogously to ζ in eq (C.2.6).

SO matrix elements in the second excited configuration are given by eq (C.2.8), with ζ'' defined similarly to ζ and ζ' above.

$$\langle {}^2G_{g\,\frac{5}{2}}\ t\ \tau|\mathcal{H}_{SO}|{}^2G_{g\,\frac{5}{2}}\ t\ \tau\rangle = -\tfrac{1}{2}\zeta''$$

$$\langle {}^2G_{g\,\frac{1}{2}}\ t'\ \tau'|\mathcal{H}_{SO}|{}^2G_{g\,\frac{1}{2}}\ t'\ \tau'\rangle = \tfrac{3}{2}\zeta'' \qquad \text{(C.2.8)}$$

C.2.3. Zeeman matrix elements in the SO states

The longitudinal Zeeman energy, E_{Zeeman}, corresponding to the Zeeman operator, $\mathcal{H}_B$, is given by eq (3.3.28). The SO basis is *not* diagonal in Zeeman operator.

Non-zero diagonal Zeeman matrix elements in the ${}^2H_u$ and ${}^2H_g$ terms are, in units of $\hbar$ and assuming $g_e \approx 2$,

$$\langle {}^2H_{u,g\,\frac{5}{2}\,\frac{3}{2}\,\pm\frac{3}{2}}|L_z + 2S_z|{}^2H_{u,g\,\frac{5}{2}\,\frac{3}{2}\,\pm\frac{3}{2}}\rangle = \pm\tfrac{9}{5}$$

$$\langle {}^2H_{u,g\,\frac{5}{2}\,\frac{1}{2}\,\pm\frac{1}{2}}|L_z + 2S_z|{}^2H_{u,g\,\frac{5}{2}\,\frac{1}{2}\,\pm\frac{1}{2}}\rangle = \pm\tfrac{3}{5}$$

$$\langle {}^2H_{u,g\,\frac{3}{2}\,\frac{3}{2}\,\pm\frac{3}{2}}|L_z + 2S_z|{}^2H_{u,g\,\frac{3}{2}\,\frac{3}{2}\,\pm\frac{3}{2}}\rangle = \pm\tfrac{6}{5}$$

$$\langle {}^2H_{u,g\,\frac{3}{2}\,\frac{1}{2}\,\pm\frac{1}{2}}|L_z + 2S_z|{}^2H_{u,g\,\frac{3}{2}\,\frac{1}{2}\,\pm\frac{1}{2}}\rangle = \pm\tfrac{2}{5} \qquad \text{(C.2.9)}$$

while the off-diagonal matrix elements are,

$$\langle {}^2H_{u,g\,\frac{5}{2}\,\pm\frac{5}{2}\,\frac{5}{2}}|L_z + 2S_z|{}^2H_{u,g\,\frac{5}{2}\,\mp\frac{5}{2}\,\frac{5}{2}}\rangle = \mp 3i\mu_B B$$

$$\langle {}^2H_{u,g\,\frac{5}{2}\,\frac{3}{2}\,\pm\frac{3}{2}}|L_z + 2S_z|{}^2H_{u,g\,\frac{3}{2}\,\frac{3}{2}\,\pm\frac{3}{2}}\rangle = \mp\tfrac{2}{5}\mu_B B$$

$$\langle {}^2H_{u,g\,\frac{3}{2}\,\frac{3}{2}\,\pm\frac{3}{2}}|L_z + 2S_z|{}^2H_{u,g\,\frac{5}{2}\,\frac{3}{2}\,\pm\frac{3}{2}}\rangle = \mp\tfrac{2}{5}\mu_B B$$

$$\langle {}^2H_{u,g\,\frac{5}{2}\,\frac{1}{2}\,\pm\frac{1}{2}}|L_z + 2S_z|{}^2H_{u,g\,\frac{3}{2}\,\frac{1}{2}\,\pm\frac{1}{2}}\rangle = \pm\tfrac{\sqrt{6}}{5}\mu_B B$$

$$\langle {}^2\mathrm{H}_{u,g}\,\tfrac{3}{2}\,\tfrac{1}{2}\,\pm\tfrac{1}{2}|L_z + 2S_z|{}^2\mathrm{H}_{u,g}\,\tfrac{5}{2}\,\tfrac{1}{2}\,\pm\tfrac{1}{2}\rangle = \pm\frac{\sqrt{6}}{5}\mu_B B \qquad \text{(C.2.10)}$$

Of these matrix elements, the first corresponds to the Zeeman splitting of the $|{}^2H_{u,g}\,\frac{5}{2}\,\pm\frac{5}{2}\,\frac{5}{2}\rangle$ states by $6\mu_B B$ if they were diagonal in the Zeeman operator.

For the ${}^2G_g$ states of the second-excited configuration, there are no non-zero diagonal Zeeman matrix elements. However, there are non-zero off-diagonal elements,

$$\langle {}^2\mathrm{G}_g\,\tfrac{5}{2}\,\tfrac{3}{2}\,\pm\tfrac{3}{2}|L_z + 2S_z|{}^2\mathrm{G}_g\,\tfrac{1}{2}\,\tfrac{3}{2}\,\pm\tfrac{3}{2}\rangle = \pm 2$$

$$\langle {}^2\mathrm{G}_g\,\tfrac{1}{2}\,\tfrac{3}{2}\,\pm\tfrac{3}{2}|L_z + 2S_z|{}^2\mathrm{G}_g\,\tfrac{5}{2}\,\tfrac{3}{2}\,\pm\tfrac{3}{2}\rangle = \pm 2 \qquad \text{(C.2.11)}$$

which will lower degeneracy.

C.2.4. Transition-moment matrix elements for the ${}^2H_g$, ${}^2G_g \leftarrow {}^2H_u$ transitions of C_{60}^+

Transition-moment matrix elements were evaluated using the method described in Section 3.4.2. They conform to the convention described therein, and not the one used in Ref. 2.

In $\mathbf{I}_h$ the electric dipole moment operator, $\boldsymbol{m}$, transforms as t_{1u} ($\equiv 1^-$ in Butler's notation, with the parity denoted by the superscript '–', not to be confused with spin orbitals). Allowed transitions occur when the direct product of the orbital irreps contains t_{1u} (Section 3.4.1). Using Table B.2.3 of Appendix B, both $h_u \leftarrow h_g$ and $h_u \leftarrow g_g$ are allowed, since,

$$h_u \otimes h_g = a_{1u} \oplus t_{1u} \oplus t_{2u} \oplus 2h_u \oplus 2g_u$$

$$h_u \otimes g_g = t_{1u} \oplus t_{2u} \oplus 2h_u \oplus g_u \qquad \text{(C.2.12)}$$

Hence ${}^2H_g \leftarrow {}^2H_u$ and ${}^2G_g \leftarrow {}^2H_u$ are allowed.

The Wigner-Eckart theorem is used to relate the transition moments for each component of the orbital transition to a single one-electron reduced transition moment $\mathcal{M}$ (Section 3.4.2.1). In isotropic point groups, such as $\mathbf{I}_h$, the total intensity, which is proportional to $|\mathcal{M}|^2$, is shared equally between z-polarised, lcp and rcp transitions (after a summation is made over the individual polarisations). (This provides a useful check of the reduced transition moments computed for orbital (Section 3.4.2.1) and state (Section 3.4.2.2) transitions.) The sum over all three polarisations gives the total

intensity $|m|^2$ in the absence of spin. Since the terms are spin-doublets, the total intensity is $2|m|^2$.

Introduction of spin means that SOC must be treated, increasing the number of transitions, but sharing the intensity between them. Transitions between each level τ must be considered individually, but all can be presented in terms of m using the Wigner-Eckart theorem following simplification to the one-electron transition moment (Section 3.4.2.2).

Transition moments for the $^2H_g \leftarrow {}^2H_u$ and $^2G_g \leftarrow {}^2H_u$ transitions of C_{60}^+ are given in Tables C.2.2 and C.2.3. Notes on the presentation of the matrix elements are given below each table.

C.3. C_{60}^-

C.3.1. Construction of SO wavefunctions for C_{60}^-

In its ground state, the C_{60}^- ion has the same filled orbital configuration as C_{60}, but with an electron in what was the LUMO of C_{60}, $5t_{1u}$ (Figure 7.1.1).

(a) SL wavefunctions

All of the orbital configurations treated in this work have only one electron in a partially filled shell, so the resulting SL wavefunctions are generated by inspection. Note that the second excited configuration is ignored, because transitions from the ground configuration are Laporte forbidden.

The ground and first-excited configurations of C_{60}^- are $[C_{60}](5t_{1u})^1$ and $[C_{60}](5t_{1u})^0(2t_{1g})^1$ (where $[C_{60}]$ represents the ground-state C_{60} configuration), giving rise to $^2T_{1u}$ and $^2T_{1g}$ terms, and SL wavefunctions,

$$|^2T_{1u,g}\ \pm\tfrac{1}{2}\ 1\rangle = |1_{u,g}^{\pm}\rangle$$

$$|^2T_{1u,g}\ \pm\tfrac{1}{2}\ 0\rangle = |0_{u,g}^{\pm}\rangle$$

$$|^2T_{1u,g}\ \pm\tfrac{1}{2}\ -1\rangle = |-1_{u,g}^{\pm}\rangle \qquad \text{(C.3.1)}$$

The third excited configuration (corresponding to an allowed transition from the $^2T_{1u}$ ground term; Section C.3.4) is $[C_{60}](5t_{1u})^0(2t_{1g})^0(5t_{2u})^0(8h_g)^1$ — a ^2H_g term — giving,

Table C.2.2: Transition moments for the $^2H_g \leftarrow {}^2H_u$ transition of $\mathbf{I_h}$ C_{60}^+.

m^1	$\|^2H_u\ \frac{5}{2}\ \bar{\frac{5}{2}}\ \frac{5}{2}\rangle$	$\|^2H_u\ \frac{5}{2}\ \frac{3}{2}\ \bar{\frac{3}{2}}\rangle$	$\|^2H_u\ \frac{5}{2}\ \frac{1}{2}\ \bar{\frac{1}{2}}\rangle$	$\|^2H_u\ \frac{5}{2}\ \frac{1}{2}\ \frac{1}{2}\rangle$	$\|^2H_u\ \frac{5}{2}\ \frac{3}{2}\ \frac{3}{2}\rangle$	$\|^2H_u\ \frac{5}{2}\ \frac{5}{2}\ \frac{5}{2}\rangle$
$\langle^2H_g\ \frac{5}{2}\ \bar{\frac{5}{2}}\ \frac{5}{2}\|$	0	$-\sqrt{20}i$			$-\sqrt{20}$	$-10i$
$\langle^2H_g\ \frac{5}{2}\ \frac{3}{2}\ \bar{\frac{3}{2}}\|$	$-\sqrt{20}i$	6	8			$-\sqrt{20}$
$\langle^2H_g\ \frac{5}{2}\ \frac{1}{2}\ \bar{\frac{1}{2}}\|$		-8	2	$\sqrt{72}$		
$\langle^2H_g\ \frac{5}{2}\ \frac{1}{2}\ \frac{1}{2}\|$			$-\sqrt{72}$	-2	-8	
$\langle^2H_g\ \frac{5}{2}\ \frac{3}{2}\ \frac{3}{2}\|$	$\sqrt{20}$			8	-6	$\sqrt{20}i$
$\langle^2H_g\ \frac{5}{2}\ \frac{5}{2}\ \frac{5}{2}\|$	$10i$	$\sqrt{20}$			$\sqrt{20}i$	0
$\langle^2H_g\ \frac{3}{2}\ \frac{3}{2}\ \bar{\frac{3}{2}}\|$	$\sqrt{5}i$	2	1			$\sqrt{5}$
$\langle^2H_g\ \frac{3}{2}\ \frac{1}{2}\ \bar{\frac{1}{2}}\|$		$-\sqrt{6}$	$-\sqrt{6}$	$-\sqrt{3}$		
$\langle^2H_g\ \frac{3}{2}\ \frac{1}{2}\ \frac{1}{2}\|$			$\sqrt{3}$	$\sqrt{6}$	$-\sqrt{6}$	
$\langle^2H_g\ \frac{3}{2}\ \frac{3}{2}\ \frac{3}{2}\|$	$-\sqrt{5}$			1	-2	$-\sqrt{5}i$

m^1	$\|^2H_u\ \frac{3}{2}\ \frac{3}{2}\ \bar{\frac{3}{2}}\rangle$	$\|^2H_u\ \frac{3}{2}\ \frac{1}{2}\ \bar{\frac{1}{2}}\rangle$	$\|^2H_u\ \frac{3}{2}\ \frac{1}{2}\ \frac{1}{2}\rangle$	$\|^2H_u\ \frac{3}{2}\ \frac{3}{2}\ \frac{3}{2}\rangle$
$\langle^2H_g\ \frac{5}{2}\ \bar{\frac{5}{2}}\ \frac{5}{2}\|$	$\sqrt{5}i$			$\sqrt{5}$
$\langle^2H_g\ \frac{5}{2}\ \frac{3}{2}\ \bar{\frac{3}{2}}\|$	2	$\sqrt{6}$		
$\langle^2H_g\ \frac{5}{2}\ \frac{1}{2}\ \bar{\frac{1}{2}}\|$	-1	$-\sqrt{6}$	$-\sqrt{3}$	
$\langle^2H_g\ \frac{5}{2}\ \frac{1}{2}\ \frac{1}{2}\|$		$\sqrt{3}$	$\sqrt{6}$	-1
$\langle^2H_g\ \frac{5}{2}\ \frac{3}{2}\ \frac{3}{2}\|$			$\sqrt{6}$	-2
$\langle^2H_g\ \frac{5}{2}\ \frac{5}{2}\ \frac{5}{2}\|$	$-\sqrt{5}$			$-\sqrt{5}i$
$\langle^2H_g\ \frac{3}{2}\ \frac{3}{2}\ \bar{\frac{3}{2}}\|$	9	$-\sqrt{54}$		
$\langle^2H_g\ \frac{3}{2}\ \frac{1}{2}\ \bar{\frac{1}{2}}\|$	$\sqrt{54}$	3	$-\sqrt{72}$	
$\langle^2H_g\ \frac{3}{2}\ \frac{1}{2}\ \frac{1}{2}\|$		$\sqrt{72}$	-3	$\sqrt{54}$
$\langle^2H_g\ \frac{3}{2}\ \frac{3}{2}\ \frac{3}{2}\|$			$-\sqrt{54}$	-9

Notes:

1. The initial states (^2H_u term) are shown along the top row of the table (designated by their spin orbit irrep and partner), and the final states (^2H_g term) down the left hand column.

2. All matrix elements are in terms of $\mathcal{M}_h / \sqrt{750}$, where

$$\mathcal{M}_h = \langle h_u \| m^1 \| h_g \rangle,$$

the one-electron reduced matrix element for the transition, $4h_u \leftarrow 7h_g$.

3. Transition polarisation is shown by the shading:

$m_0 = z$ polarised
m_{-1} = right circularly polarised
m_{+1} = left circularly polarised

Table C.2.3: Transition moments for the $^2G_g \leftarrow {}^2H_u$ transition of I_h C_{60}^+.

m^1	$\|^2H_u\ \frac{5}{2}\ \bar{\frac{5}{2}}\ \frac{5}{2}\rangle$	$\|^2H_u\ \frac{5}{2}\ \frac{3}{2}\ \bar{\frac{3}{2}}\rangle$	$\|^2H_u\ \frac{5}{2}\ \frac{1}{2}\ \bar{\frac{1}{2}}\rangle$	$\|^2H_u\ \frac{5}{2}\ \frac{1}{2}\ \frac{1}{2}\rangle$	$\|^2H_u\ \frac{5}{2}\ \frac{3}{2}\ \frac{3}{2}\rangle$	$\|^2H_u\ \frac{5}{2}\ \frac{5}{2}\ \frac{5}{2}\rangle$
$\langle^2G_g\ \frac{5}{2}\ \bar{\frac{5}{2}}\ \frac{5}{2}\|$	0	$\sqrt{5}(-3+i)/2$			$\sqrt{5}(1+3i)/2$	$3+i$
$\langle^2G_g\ \frac{5}{2}\ \frac{3}{2}\ \bar{\frac{3}{2}}\|$	$\sqrt{5}(3+i)/2$	-3	1			$\sqrt{5}(1+3i)/2$
$\langle^2G_g\ \frac{5}{2}\ \frac{1}{2}\ \bar{\frac{1}{2}}\|$		-1	4	$-\sqrt{18}$		
$\langle^2G_g\ \frac{5}{2}\ \frac{1}{2}\ \frac{1}{2}\|$			$\sqrt{18}$	-4	-1	
$\langle^2G_g\ \frac{5}{2}\ \frac{3}{2}\ \frac{3}{2}\|$	$\sqrt{5}(-1+3i)/2$			1	3	$\sqrt{5}(3-i)/2$
$\langle^2G_g\ \frac{5}{2}\ \frac{5}{2}\ \frac{5}{2}\|$	$3-i$	$\sqrt{5}(-1+3i)/2$			$\sqrt{5}(-3-i)/2$	0
$\langle^2G_g\ \frac{1}{2}\ \frac{3}{2}\ \bar{\frac{3}{2}}\|$	$\sqrt{5}(-3+i)/2$	-5	5			$\sqrt{5}(1-3i)/2$
$\langle^2G_g\ \frac{1}{2}\ \frac{3}{2}\ \frac{3}{2}\|$	$\sqrt{5}(-1-3i)/2$			5	5	$\sqrt{5}(-3-i)/2$

m^1	$\|^2H_u\ \frac{3}{2}\ \frac{3}{2}\ \bar{\frac{3}{2}}\rangle$	$\|^2H_u\ \frac{3}{2}\ \frac{1}{2}\ \bar{\frac{1}{2}}\rangle$	$\|^2H_u\ \frac{3}{2}\ \frac{1}{2}\ \frac{1}{2}\rangle$	$\|^2H_u\ \frac{3}{2}\ \frac{3}{2}\ \frac{3}{2}\rangle$
$\langle^2G_g\ \frac{5}{2}\ \bar{\frac{5}{2}}\ \frac{5}{2}\|$	$\sqrt{20}i$			$\sqrt{20}$
$\langle^2G_g\ \frac{5}{2}\ \frac{3}{2}\ \bar{\frac{3}{2}}\|$	4	$\sqrt{24}$		
$\langle^2G_g\ \frac{5}{2}\ \frac{1}{2}\ \bar{\frac{1}{2}}\|$	-2	$-\sqrt{24}$	$-\sqrt{12}$	
$\langle^2G_g\ \frac{5}{2}\ \frac{1}{2}\ \frac{1}{2}\|$		$\sqrt{12}$	$\sqrt{24}$	-2
$\langle^2G_g\ \frac{5}{2}\ \frac{3}{2}\ \frac{3}{2}\|$			$\sqrt{24}$	-4
$\langle^2G_g\ \frac{5}{2}\ \frac{5}{2}\ \frac{5}{2}\|$	$-\sqrt{20}$			$-\sqrt{20}i$
$\langle^2G_g\ \frac{1}{2}\ \frac{3}{2}\ \bar{\frac{3}{2}}\|$				
$\langle^2G_g\ \frac{1}{2}\ \frac{3}{2}\ \frac{3}{2}\|$				

Notes:

1. The initial states (^2H_u term) are shown along the top row of the table (designated by their spin orbit irrep and partner), and the final states (^2G_g term) down the left hand column.
2. All matrix elements are in terms of $\mathcal{M}_g / \sqrt{300}$, where

   $$\mathcal{M}_g = \langle h_u \| m^1 \| g_g \rangle,$$

   the one-electron reduced matrix element for the transition, $7h_u \leftarrow 4g_g$.
3. Transition polarisation is indicated by the shading:

   $m_0 = z$ polarised
   m_{-1} = right circularly polarised
   m_{+1} = left circularly polarised

$$|^2H_g \pm\tfrac{1}{2}\ 2\rangle = |2_g^{\pm}\rangle$$

$$|^2H_g \pm\tfrac{1}{2}\ 1\rangle = |1_g^{\pm}\rangle$$

$$|^2H_g \pm\tfrac{1}{2}\ 0\rangle = |0_g^{\pm}\rangle$$

$$|^2H_g \pm\tfrac{1}{2}\ -1\rangle = |-1_g^{\pm}\rangle$$

$$|^2H_g \pm\tfrac{1}{2}\ -2\rangle = |-2_g^{\pm}\rangle \qquad \text{(C.3.2)}$$

(b) SO wavefunctions

SO wavefunctions for C_{60}^- were formed by applying the method of Section 3.3.1.5. The SO levels are shown in Table C.3.1, where, since the $^2T_{1u}$ and $^2T_{1g}$ terms have equivalent treatments, they are summarised on the same row.

Table C.3.1: SOC in C_{60}^-.

Term	Orbital irreps	Spin irreps		SOC [a]	
	$\mathbf{I}_h$	$\mathbf{SO}_3$	$\mathbf{I}_h$	Irreps	Levels
$^2T_{1u,g}$	$1_{u,g}$	$\frac{1}{2}$	$\frac{1}{2}$	$\frac{3}{2}$ $\frac{1}{2}$	$^2T_{1u,g}\ \frac{3}{2}$ $^2T_{1u,g}\ \frac{1}{2}$
^2H_g	2_g	$\frac{1}{2}$	$\frac{1}{2}$	$\frac{5}{2}$ $\frac{3}{2}$	$^2H_g\ \frac{5}{2}$ $^2H_g\ \frac{3}{2}$

[a] The direct-product table for $\mathbf{I}_h$ is given in Table B.2.3 of Appendix B, while the SO partners can be found in Table C.1.1.

The SO wavefunctions for each level were derived using eq (3.3.10), and are given in eq (C.3.3) for the ground and first-excited configurations, and (C.3.4) for the third excited configuration. Further details are given in Section C.2.2, where the notation is also described.

$$|^2T_{1u,g}\ \tfrac{3}{2}\ \tfrac{3}{2}\ \pm\tfrac{3}{2}\rangle = |\pm 1_{u,g}^{\pm}\rangle$$

$$|^2T_{1u,g}\ \tfrac{3}{2}\ \tfrac{1}{2}\ \pm\tfrac{1}{2}\rangle = \mp\frac{1}{\sqrt{3}}\left\{\sqrt{2}\,|0_{u,g}^{\pm}\rangle - |\pm 1_{u,g}^{\mp}\rangle\right\}$$

$$|^2T_{1u,g}\ \tfrac{1}{2}\ \tfrac{1}{2}\ \pm\tfrac{1}{2}\rangle = \pm\frac{1}{\sqrt{3}}\left\{|0_{u,g}^{\pm}\rangle + \sqrt{2}\,|\pm 1_{u,g}^{\mp}\rangle\right\} \qquad \text{(C.3.3)}$$

$$|^2H_g\ \tfrac{5}{2}\ \pm\tfrac{5}{2}\ \tfrac{5}{2}\rangle = \mp\frac{1}{\sqrt{2}}\left\{|\mp 2_g^{\mp}\rangle - i\,|\pm 2_g^{\pm}\rangle\right\}$$

$$|^2H_g\,\tfrac{5}{2}\,\tfrac{3}{2}\,\pm\tfrac{3}{2}\rangle = \frac{1}{\sqrt{5}}\{\,2\,|\pm1_g^{\pm}\rangle \pm |\pm2_g^{\mp}\rangle\}$$

$$|^2H_g\,\tfrac{5}{2}\,\tfrac{1}{2}\,\pm\tfrac{1}{2}\rangle = -\frac{1}{\sqrt{5}}\{\sqrt{3}\,|0_g^{\pm}\rangle \pm \sqrt{2}\,|\pm1_g^{\mp}\rangle\}$$

$$|^2H_g\,\tfrac{3}{2}\,\tfrac{3}{2}\,\pm\tfrac{3}{2}\rangle = \pm\frac{1}{\sqrt{5}}\{2\,|\pm2_g^{\mp}\rangle \mp |\pm1_g^{\pm}\rangle\}$$

$$|^2H_g\,\tfrac{3}{2}\,\tfrac{1}{2}\,\pm\tfrac{1}{2}\rangle = \pm\frac{1}{\sqrt{5}}\{\sqrt{3}\,|\pm1_g^{\mp}\rangle \mp \sqrt{2}\,|0_g^{\pm}\rangle\} \qquad \text{(C.3.4)}$$

C.3.2. SO matrix elements

C_{60}^- is a regular SO system. Its SO matrix elements were evaluated as described in Section 3.3.2.2. It is again emphasised that elements involving the raising and lowering operators must be evaluated (Section C.2.2).

For the ground configuration, the SO matrix elements are,

$$\langle^2T_{1u}\,\tfrac{1}{2}\;t'\;\tau'|\mathcal{H}_{SO}|^2T_{1u}\,\tfrac{1}{2}\;t'\;\tau'\rangle = -\zeta$$

$$\langle^2T_{1u}\,\tfrac{3}{2}\;t\;\tau|\mathcal{H}_{SO}|^2T_{1u}\,\tfrac{3}{2}\;t\;\tau\rangle = \tfrac{1}{2}\zeta \qquad \text{(C.3.5)}$$

where the t,τ and t',τ' correspond to all possible chains resulting from the irreps $\frac{3}{2}$ and $\frac{1}{2}$ respectively, in $\mathbf{I}_h$. ζ is the empirical SOC coefficient for the ground configuration of C_{60}^-, which is defined by the equation,

$$\zeta = \hbar^2\langle\xi\rangle \qquad \text{(C.3.6)}$$

$\langle\xi\rangle$ is the expectation value of the SOC coefficient.

The levels of the first-excited configuration have the matrix elements,

$$\langle^2T_{1g}\,\tfrac{1}{2}\;t\;\tau|\mathcal{H}_{SO}|^2T_{1g}\,\tfrac{1}{2}\;t\;\tau\rangle = -\zeta'$$

$$\langle^2T_{1g}\,\tfrac{3}{2}\;t'\;\tau'|\mathcal{H}_{SO}|^2T_{1g}\,\tfrac{3}{2}\;t'\;\tau'\rangle = \tfrac{1}{2}\zeta' \qquad \text{(C.3.7)}$$

where ζ' is the empirical SOC coefficient for the first-excited configuration of C_{60}^-, and is defined analogously to ζ in eq (C.3.6).

SO matrix elements in the third-excited configuration are given in eq (C.3.8), with ζ'' defined similarly to the ζ and ζ'.

$$\langle^2H_u\,\tfrac{3}{2}\;t'\;\tau'|\mathcal{H}_{SO}|^2H_u\,\tfrac{3}{2}\;t'\;\tau'\rangle = -\tfrac{3}{2}\zeta''$$

$$\langle {}^2H_u \tfrac{5}{2}\, t\, \tau | \mathcal{H}_{SO} | {}^2H_u \tfrac{5}{2}\, t\, \tau \rangle = \zeta'' \qquad \text{(C.3.8)}$$

C.3.3. Zeeman matrix elements in the SO states

The longitudinal Zeeman energy, E_{Zeeman}, corresponding to the Zeeman operator, $\mathcal{H}_B$, is given by eq (3.3.28).

The diagonal elements for the states of the ground and first excited term ($^2T_1$ with odd and even parity, respectively), are (assuming $g_e \approx 2$), in units of $\hbar$,

$$\langle {}^2T_{1u,g}\, \tfrac{3}{2}\, \tfrac{3}{2}\, \pm\tfrac{3}{2} | L_z + 2S_z | {}^2T_{1u,g}\, \tfrac{3}{2}\, \tfrac{3}{2}\, \pm\tfrac{3}{2} \rangle = \pm 2$$

$$\langle {}^2T_{1u,g}\, \tfrac{3}{2}\, \tfrac{1}{2}\, \pm\tfrac{1}{2} | L_z + 2S_z | {}^2T_{1u,g}\, \tfrac{3}{2}\, \tfrac{1}{2}\, \pm\tfrac{1}{2} \rangle = \pm\tfrac{2}{3}$$

$$\langle {}^2T_{1u,g}\, \tfrac{1}{2}\, \tfrac{1}{2}\, \pm\tfrac{1}{2} | L_z + 2S_z | {}^2T_{1u,g}\, \tfrac{1}{2}\, \tfrac{1}{2}\, \pm\tfrac{1}{2} \rangle = \pm\tfrac{1}{3} \qquad \text{(C.3.9)}$$

while the off-diagonal matrix elements are,

$$\langle {}^2T_{1u,g}\, \tfrac{3}{2}\, \tfrac{1}{2}\, \pm\tfrac{1}{2} | L_z + 2S_z | {}^2T_{1u,g}\, \tfrac{1}{2}\, \tfrac{1}{2}\, \pm\tfrac{1}{2} \rangle = \mp\tfrac{\sqrt{2}}{3}$$

$$\langle {}^2T_{1u,g}\, \tfrac{1}{2}\, \tfrac{1}{2}\, \pm\tfrac{1}{2} | L_z + 2S_z | {}^2T_{1u,g}\, \tfrac{3}{2}\, \tfrac{1}{2}\, \pm\tfrac{1}{2} \rangle = \mp\tfrac{\sqrt{2}}{3} \qquad \text{(C.3.10)}$$

Non-zero diagonal Zeeman matrix elements in the states of the third excited term are the same as those of the first excited term of C_{60}^+ (eqs (C.2.9) and (C.2.10)).

C.3.4. Transition-moment matrix elements for the $^2T_{1g}$, $^2H_g \leftarrow {}^2T_{1u}$ transitions of C_{60}^-

As noted in Section C.2.4, the electric dipole moment operator $\boldsymbol{m}$ transforms as t_{1u} in $\mathbf{I}_h$ ($\equiv 1^-$ in Butler's notation[1]). Allowed transitions (Section 3.4.1) require that the direct product of the orbital irreps contain t_1 ($\equiv 1$). From the direct product table (Table B.2.3 of Appendix B) the following results are obtained for excitations to the two excited configurations:

$$t_{1u} \otimes t_{1g} = a_{1u} \oplus t_{1u} \oplus h_u$$

$$t_{1u} \otimes h_g = t_{1u} \oplus t_{2u} \oplus h_u \oplus g_u \qquad \text{(C.3.11)}$$

Transitions to each of the excited $^2T_{1g}$ and ^2H_g terms are allowed, for which transition moment matrix elements are given in Tables C.3.2. and C.3.3, respectively.

Table C.3.2: Transition moments for the $^2T_{1g} \leftarrow {}^2T_{1u}$ transition of $\mathbf{I_h}$ C_{60}^-.

m^1	$\|^2T_{1u}\ \frac{1}{2}\ \bar{\frac{1}{2}}\rangle$	$\|^2T_{1u}\ \frac{1}{2}\ \frac{1}{2}\rangle$	$\|^2T_{1u}\ \frac{3}{2}\ \bar{\frac{3}{2}}\rangle$	$\|^2T_{1u}\ \frac{3}{2}\ \bar{\frac{1}{2}}\rangle$	$\|^2T_{1u}\ \frac{3}{2}\ \frac{1}{2}\rangle$	$\|^2T_{1u}\ \frac{3}{2}\ \frac{3}{2}\rangle$
$\langle^2T_{1g}\ \frac{1}{2}\ \bar{\frac{1}{2}}\|$	2	$\sqrt{8}$	$-\sqrt{3}$	$\sqrt{2}$	-1	
$\langle^2T_{1g}\ \frac{1}{2}\ \frac{1}{2}\|$	$-\sqrt{8}$	-2		1	$-\sqrt{2}$	$-\sqrt{3}$
$\langle^2T_{1g}\ \frac{3}{2}\ \bar{\frac{3}{2}}\|$	$\sqrt{3}$		3	$-\sqrt{6}$		
$\langle^2T_{1g}\ \frac{3}{2}\ \bar{\frac{1}{2}}\|$	$\sqrt{2}$	-1	$\sqrt{6}$	1	$-\sqrt{8}$	
$\langle^2T_{1g}\ \frac{3}{2}\ \frac{1}{2}\|$	1	$-\sqrt{2}$		$\sqrt{8}$	-1	$\sqrt{6}$
$\langle^2T_{1g}\ \frac{3}{2}\ \frac{3}{2}\|$		$\sqrt{3}$			$-\sqrt{6}$	-3

Notes:

1. The initial states ($^2T_{1u}$ term) are shown along the top row of the table (designated by their spin orbit irrep and partner), and the final states ($^2T_{1g}$ term) down the left hand column.

2. All matrix elements are in terms of $\mathcal{M}_t / \sqrt{54}$, where

   $$\mathcal{M}_t = \langle t_{1g} \| m^1 \| t_{1u} \rangle,$$

   the one-electron reduced matrix element for the transition, $2t_{1g} \leftarrow 5t_{1u}$.

3. Transition polarisation is shown by the shading:

   $m_0 = z$ polarised
   m_{-1} = right circularly polarised
   m_{+1} = left circularly polarised

Table C.3.3: Transition moments for the $^2H_g \leftarrow {}^2T_{1u}$ transition of I_h C_{60}^-.

m^1	$\|^2T_{1u}\ \frac{1}{2}\ \frac{1}{2}\ \bar{\frac{1}{2}}\rangle$	$\|^2T_{1u}\ \frac{1}{2}\ \frac{1}{2}\ \frac{1}{2}\rangle$	$\|^2T_{1u}\ \frac{3}{2}\ \frac{3}{2}\ \bar{\frac{3}{2}}\rangle$	$\|^2T_{1u}\ \frac{3}{2}\ \frac{1}{2}\ \bar{\frac{1}{2}}\rangle$	$\|^2T_{1u}\ \frac{3}{2}\ \frac{1}{2}\ \frac{1}{2}\rangle$	$\|^2T_{1u}\ \frac{3}{2}\ \frac{3}{2}\ \frac{3}{2}\rangle$
$\langle^2H_g\ \frac{3}{2}\ \frac{3}{2}\ \bar{\frac{3}{2}}\|$	$-\sqrt{75}$		3	$-\sqrt{6}$		
$\langle^2H_g\ \frac{3}{2}\ \frac{1}{2}\ \bar{\frac{1}{2}}\|$	$-\sqrt{50}$	5	$\sqrt{6}$	1	$-\sqrt{8}$	
$\langle^2H_g\ \frac{3}{2}\ \frac{1}{2}\ \frac{1}{2}\|$	-5	$\sqrt{50}$		$\sqrt{8}$	-1	$\sqrt{6}$
$\langle^2H_g\ \frac{3}{2}\ \frac{3}{2}\ \frac{3}{2}\|$		$-\sqrt{75}$			$-\sqrt{6}$	-3
$\langle^2H_g\ \frac{5}{2}\ \bar{\frac{5}{2}}\ \frac{5}{2}\|$			$-\sqrt{45}i$			$-\sqrt{45}$
$\langle^2H_g\ \frac{5}{2}\ \bar{\frac{3}{2}}\ \frac{3}{2}\|$			-6	$-\sqrt{54}$		
$\langle^2H_g\ \frac{5}{2}\ \frac{1}{2}\ \bar{\frac{1}{2}}\|$			3	$\sqrt{54}$	$\sqrt{27}$	
$\langle^2H_g\ \frac{5}{2}\ \frac{1}{2}\ \frac{1}{2}\|$				$-\sqrt{27}$	$-\sqrt{54}$	3
$\langle^2H_g\ \frac{5}{2}\ \frac{3}{2}\ \frac{3}{2}\|$					$-\sqrt{54}$	6
$\langle^2H_g\ \frac{5}{2}\ \frac{5}{2}\ \frac{5}{2}\|$			$\sqrt{45}$			$\sqrt{45}i$

Notes:

1. The initial states ($^2T_{1u}$ term) are shown along the top row of the table (designated by their spin orbit irrep and partner), and the final states (^2H_g term) down the left hand column.

2. All matrix elements are in terms of $\mathcal{M}_h / \sqrt{450}$, where

$$\mathcal{M}_h = \langle h_g \| m^1 \| t_{1u} \rangle,$$

the one-electron reduced matrix element for the transition, $8h_g \leftarrow 5t_{1u}$.

3. Transition polarisation is indicated by the shading:

$m_0 = z$ polarised
m_{-1} = right circularly polarised
m_{+1} = left circularly polarised

C.4. References

1. Butler, P. H. *Point Group Symmetry Applications*; Plenum Press: New York, 1981.

2. Piepho, S. B.; Schatz, P. N. *Group Theory in Spectroscopy with Applications to Magnetic Circular Dichroism*; Wiley-Interscience: New York, 1983.

3. Heath, G. A.; McGrady, J. E.; Martin, R. L. *J. Chem. Soc., Chem. Commun.* **1992**, 1272-1274.